SEISMIC BEHAVIOUR OF SMA-REINFORCED SLENDER CONCRETE SHEAR WALLS

Mena Morcos

A Thesis Submitted to
The Faculty of Graduate Studies

In Partial Fulfillment of the Requirements
For the Degree of

Master of Applied Science

Graduate Program in
Civil Engineering

York University
Toronto, Ontario

April 2021

ABSTRACT

Superelastic Shape Memory Alloys (SE-SMA) have provided a viable novel alternative to conventional steel reinforcement for the construction of earthquake-resilient structures. The capacity of SE-SMA to recover from high strains upon unloading provides the mechanism required to develop self-centering smart structures. Shear walls are routinely used seismic force resisting systems in concrete construction, which makes them qualified candidates for the application of SE-SMA longitudinal reinforcement. The integration of SE-SMA into a hybrid-reinforced flexural system is expected to rectify inelastic lateral displacements and economize the cost of post-disaster repair. A large-scale slender superelastic Nitinol-reinforced concrete shear wall was tested numerically and experimentally, along with a control specimen, under quasi-static load reversals to assess seismic performance. The results of the SE-SMA wall demonstrated efficient dissipation of seismic energy to achieve high drift recovery and easily repairable damage, suggesting a low probability of demolition and substantial savings over the lifetime of the structure.

Dedicated to the memory

of my brother

Peter Morcos

ACKNOWLEDGEMENTS

I would like to express sincere gratitude and appreciation to my supervisor Professor Dan Palermo for his enduring mentorship, guidance, and patience throughout the journey of this research. Without his support and ambition this opportunity would not have been possible. His humble but strong leadership provided the freedom to explore and grow towards my professional interests. Professor Palermo is a wealth of wisdom and knowledge and an encouraging example to be all that you can be.

I also extend appreciation to Dr. Stavroula Pantazopoulou for fostering a greater interest and knowledge in earthquake engineering and her coaching in academia. Much gratitude to Dr. Medhat Shehata for his continual academic and professional guidance from undergrad, in the industry, and through to graduate school. Likewise, many thanks to Mr. John Cseff for guiding me through the start of my career in structural engineering and for imparting insightful knowledge through our conversations about approaching design challenges.

The gracious support and understanding expressed by the Department of Civil Engineering, through a difficult personal loss at the start of the program, is deeply appreciated and valued towards the achievement of this milestone.

Many thanks for the help of the technical staff of the Structures High Bay Lab: Melessa Salem, Riad Rajab, and Kunjan Rupakheti. Thanks also to Adam McLean for his help in the machine shop. The construction of the shear walls and assembly of the test setup would not have been accomplished without the many days, long nights – and very early mornings pouring concrete – spent in the lab with the help of Adrien Sparling, Michael Armando Soto Rojas, Roberto Salazar, and many other lab friends.

I am grateful for the generous donations of construction materials from Mansteel Limited, CRH – Dufferin Concrete, Burnco Mfg. Inc., and Sika Canada.

Most importantly, to my selfless and loving parents Montasser and Ragaa Morcos, I can never repay you for all you do for me, including your encouragements, support, and sacrifices which allowed me to pursue and fulfill my academic ambitions. I hope to make you proud always. The support of family is not complete without my siblings John and Mary. Thank you for believing in me and for always being there.

Last, but not least, I would like to express my warmest appreciation to my dearest friend Christina Sagos, as well as to my friends Eric Sousa, Bakir Fayad, Michael Araujo, Vinh Dinh, and Kenneth Ekka for being there for me throughout the highs and lows of this journey.

Nevertheless, many thanks to everyone who has been there for me in any way throughout this invaluable experience.

TABLE OF CONTENTS

LIST OF FIGURES

LIST OF TABLES

NOTATION

A_s	Austenite material phase transformation start temperature
A_f	Austenite material phase transformation finish temperature
f'_c	Compressive strength of concrete cylinder at 28 days
M_s	Martensite material phase transformation start temperature
M_f	Martensite material phase transformation finish temperature
T	Temperature
V	Base shear
V_y	Base shear at yield
Δ	Lateral translation
δ	Displacement
δ_o	Initial displacement
δ_y	Yield displacement
δ_u	Ultimate displacement
ε	Strain
ε_y	Strain at yield
θ	Rotation
θ_{max}	Maximum rotation
σ	Stress
σ^{As}	Austenite material phase transformation start stress
σ^{Af}	Austenite material phase transformation finish stress
σ^{Ms}	Martensite material phase transformation start stress
σ^{Mf}	Martensite material phase transformation finish stress
Ø	Diameter

CHAPTER 1

Introduction

1.1 Background

The demand for sustainable, earthquake-resilient structures in the 21st century is more than ever, pushing the limits of the seismic design of reinforced concrete structures, and facilitating a need for the introduction of novel smart materials for structural applications. Starting in the 1950's, advances in the design of reinforced concrete structures for sufficient seismic resistance has in large been limited to the use of conventional materials such as Portland cement concrete and black carbon steel reinforcement for construction of rigid frame structures. The general availability and economy of these conventional materials, compounded by the lack of adequate analytical tools (Paulay, 1975), influenced a limited understanding of the seismic behaviour of structures, compelling the use of rudimentary static loading and behaviour assumptions for structural design (Fintel, 1991).

In common practice, it is presumed that a structure designed in accordance with the local building code will achieve adequate seismic performance. Earthquake loads are historically accounted for as simple lateral loads countered by a proportional lateral strength and stiffness, known as force-based design (Mitchell et al., 2010). However, observation of actual structural performance, under the governing design assumptions of the relevant time, prompts periodic updates to the building codes to refine design methodology. As experience with the seismic behaviour of structures since the 1950's has demonstrated, moment-resisting frame construction is not the most economical, and the brittle response of shear walls is a misconception (Fintel, 1991). Traditional ductile reinforced concrete structures, built to code, sustain permanent deformations while dissipating seismic energy, suffering extensive and costly damages. More so, traditional means of seismic design do not consider the non-structural components associated with the construction and commissioning of a structure for its intended purpose, which accounts for approximately 80 percent of the overall cost, and become the costliest loses (Fintel, 1991). While there are economic benefits in tending towards the minimum accepted tolerances of the building code, non-technical decision-makers expect an overall greater level of certainty when it comes to the seismic performance of a structure.

Through the last quarter of the 20th century, seismic design has evolved towards performance-based design. Seismic events through the 1970's burdened the Federal Emergency Management Agency (FEMA) with significant post-disaster aid and repair costs, prompting the pursuit of a new approach to designing earthquake-resilient structures to repress future insurance claims. Performance-based design is the means by which the seismic behaviour of a

structure is determined prior to final design and construction to achieve a quantified limit on structural and non-structural losses (Priestley, 2000). The demands of building developers, owners, insurers, and relevant stakeholders are categorized into four performance objectives: Operational, Immediate Occupancy, Life Safety, and Collapse Prevention (Yazgan, 2010). Each performance level is defined by a drift threshold, a lateral displacement ratio relative to the height of the structure, prognosticating a degree of structural damage from an earthquake. The residual drift retained by the structure inevitably determines its performance against serviceability limits and the feasibility of repair.

The iterative process of performance-based design starts with a defined objective – a target displacement (Elnashai and Pinho, 1998) – followed by revisions of preliminary design, and assessment of seismic performance prior to construction. The structural performance objective gives reference to the acceptance criteria. From this initiative, non-linear finite element analysis (NLFEA) software was developed in the 1990's to enable the numerical simulation and study of seismic performance by observation of progressive strength and stiffness degradation, known as a pushover analysis. The total lateral displacement (δ_u) experienced at the top of the structure is representative of the intensity of the design seismic event. When plotted against base shear (V), a pushover curve is developed showing the elastic (δ_o to δ_y) and inelastic (δ_y to δ_u) capacities of the structure, which is indicative of the degree of damage experienced proportional to increasing seismic intensity. The overall objective is to have a structural system which adheres to the standards of the building code while significantly increasing the certainty of seismic resilience. Excessively superseding the minimum requirements of the building code, implies using more materials for larger structural sections to remain within the elastic range (δ_y, V_y), which is correlative to higher construction costs. This also adversely attracts greater seismic loading due to the increased weight and stiffness of the structure. The pushover curve is illustrated in Figure 1.1.

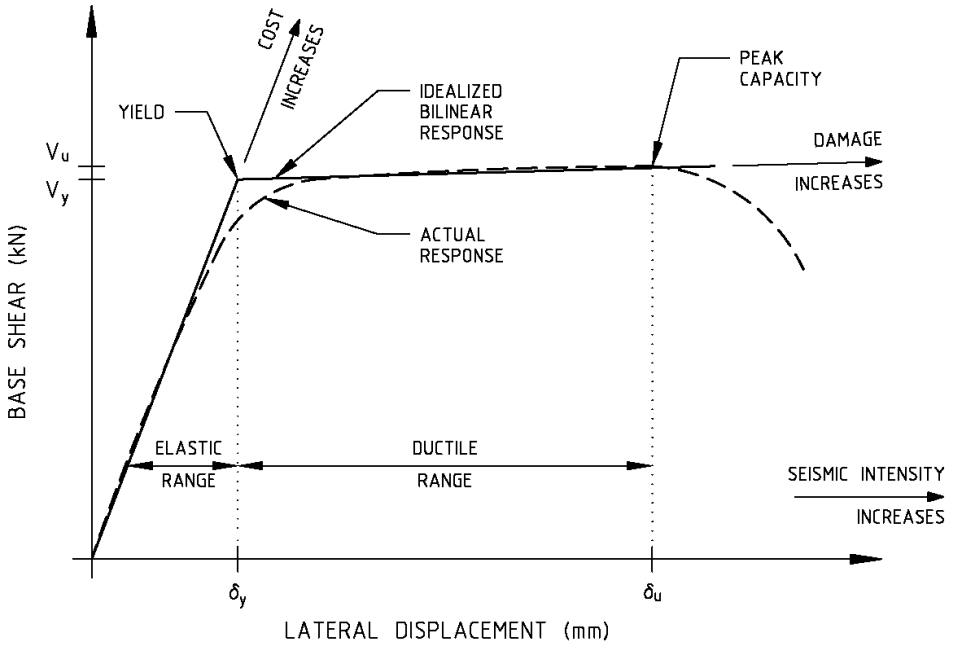

Figure 1.1. Pushover analysis curve.

Reinforced concrete shear walls are a commonly used lateral force resisting system for structures around the world due to their efficient resistance to seismic loading and relatively lower cost (Fintel, 1991). Shear walls function by resisting loading that is applied along the plane formed by the height and length, effectively behaving as a diaphragm. The diaphragm characteristic enables resistance to inter-story shear, structural torsion, and helps transfer gravity loads to the foundation. The utility of shear walls separates them into two distinct categories: slender and squat. Slender walls have a height-to-length aspect ratio equal to or greater than two. Slender shear walls are primarily utilized as in-plane lateral force resisting systems in mid to high-rise structures, such as commercial buildings, where the connected reinforced concrete, or structural steel, frame supports most of the gravity loads. Slender shear walls typically have a flexural behaviour, likened to a vertical cantilever beam. This type of wall can be found along the perimeter or forming hollow center cores, which are utilized as elevator shafts or stairwells, surrounded by an unobstructed open space, such as for office buildings. Squat walls have an aspect ratio of less than two and commonly found in low to mid-ride buildings. Squat shear walls can have a compounded purpose as loadbearing in addition to providing in-plane lateral force resistance, failing due to excessive shear. The shear walls can be found along the perimeter or distributed internally, also serving as space dividers as found in residential structures. Both types of shear walls are favoured in seismic applications because of their high structural utility and easy, fast, and inexpensive construction, for a lightweight structure. The structural use of shear walls is illustrated in Figure 1.2, and the force distribution is presented in Figure 1.3.

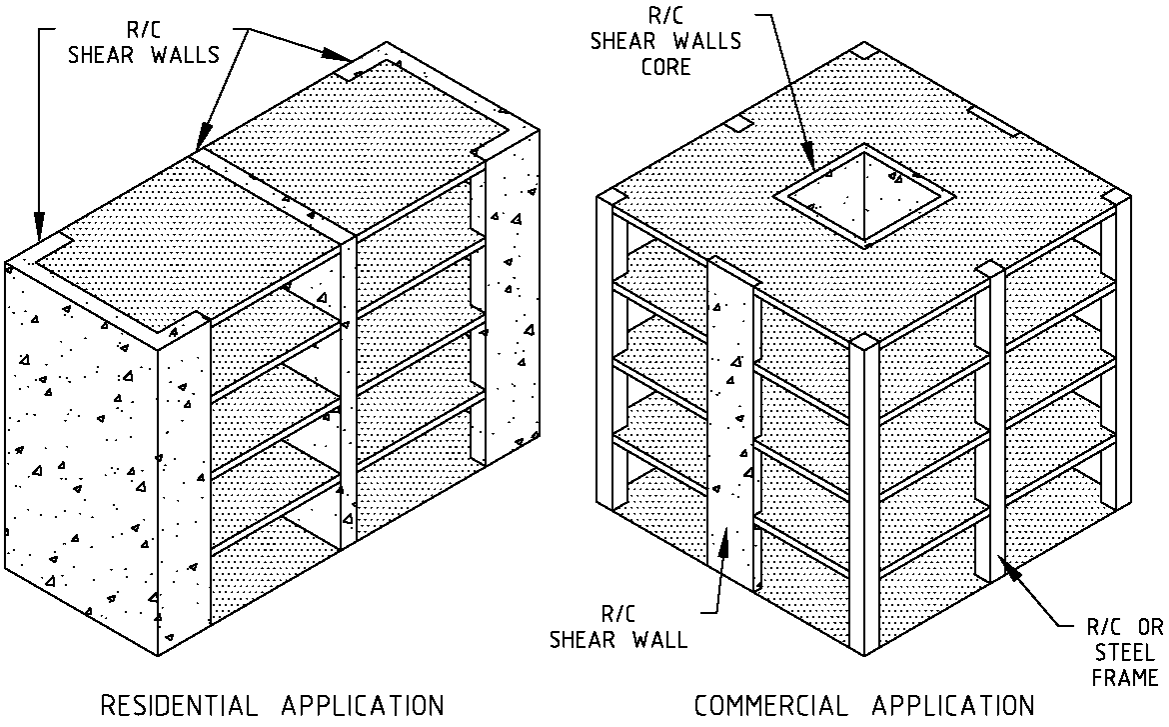

Figure 1.2. Structural applications of shear walls.

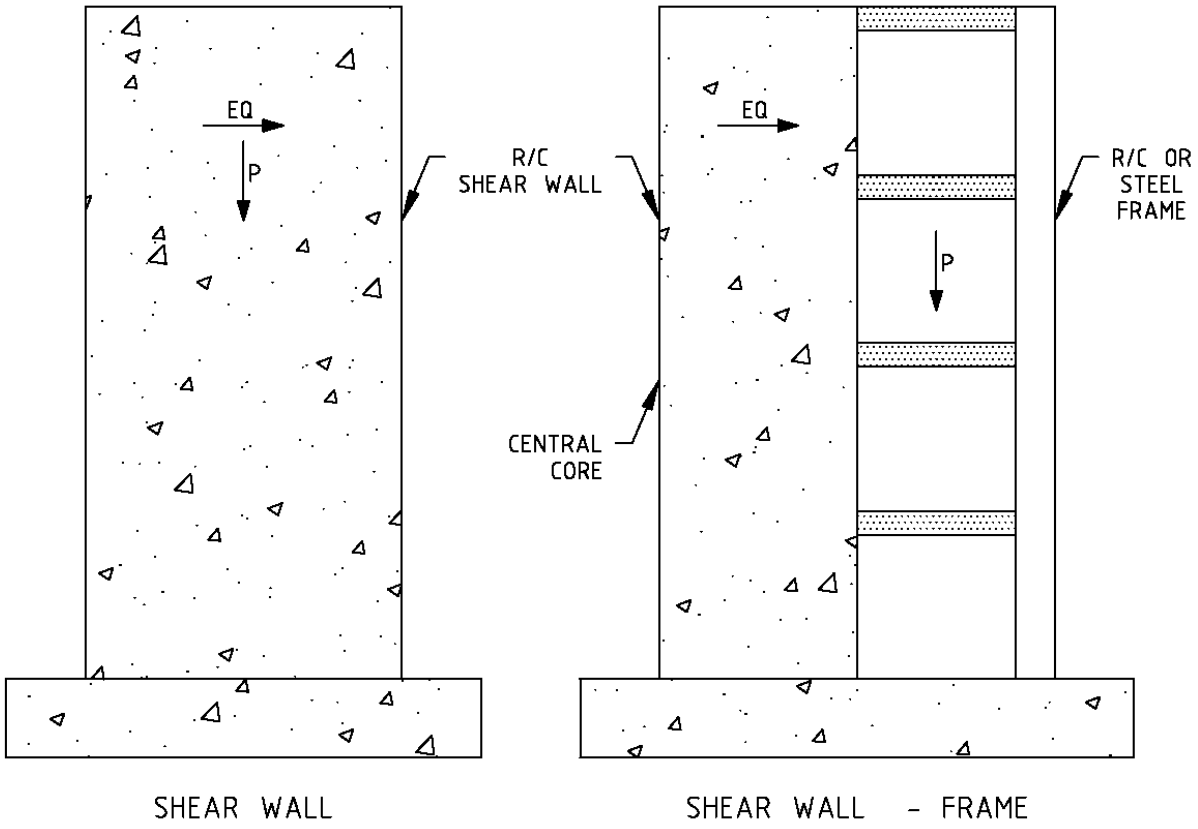

Figure 1.3. Load distribution for shear wall structural systems.

Shear walls, as a primary structural system for tall buildings, have an inherent resilience to earthquakes. A survey of the aftermath of earthquakes around the world, starting in 1960, points to structures integrating shear walls having suffered significantly less damage than structures with ductile moment-resisting frames, taking into consideration that early construction of shear walls did not include specific detailing for ductility (Fintel, 1991). Flexural ductility is the desired seismic response for shear walls, as is a common attribute of tall cantilever walls with a slender aspect ratio. The arrangement of longitudinal reinforcement across the boundaries and the web of a shear wall should be as such that the flexural strength does not exceed the corresponding shear strength for the design moment capacity of the structure. A shear wall with adequate detailing of reinforcement for flexure and shear will exhibit a drift (δ) at the free end achieved by maximum rotation (θ_{max}) from flexure, and minimum lateral translation due to shear (Δ), as illustrated in Figure 1.4. Ductile flexure curvature is maximized when vertical reinforcement is concentrated towards the boundaries, while web reinforcement also contributes (Paulay, 1975). However, shear strength significantly drops, below flexural strength, as diagonal shear cracks develop from the load reversal cycles experienced during an earthquake. Transverse reinforcement (stirrups), work with longitudinal reinforcement, to provide the shear strength required to sustain a predominant flexural behaviour. Adequately detailing a shear wall for ductility prevents collapse in severe earthquakes, and mitigates non-structural damages at moderate intensities (Paulay, 1975).

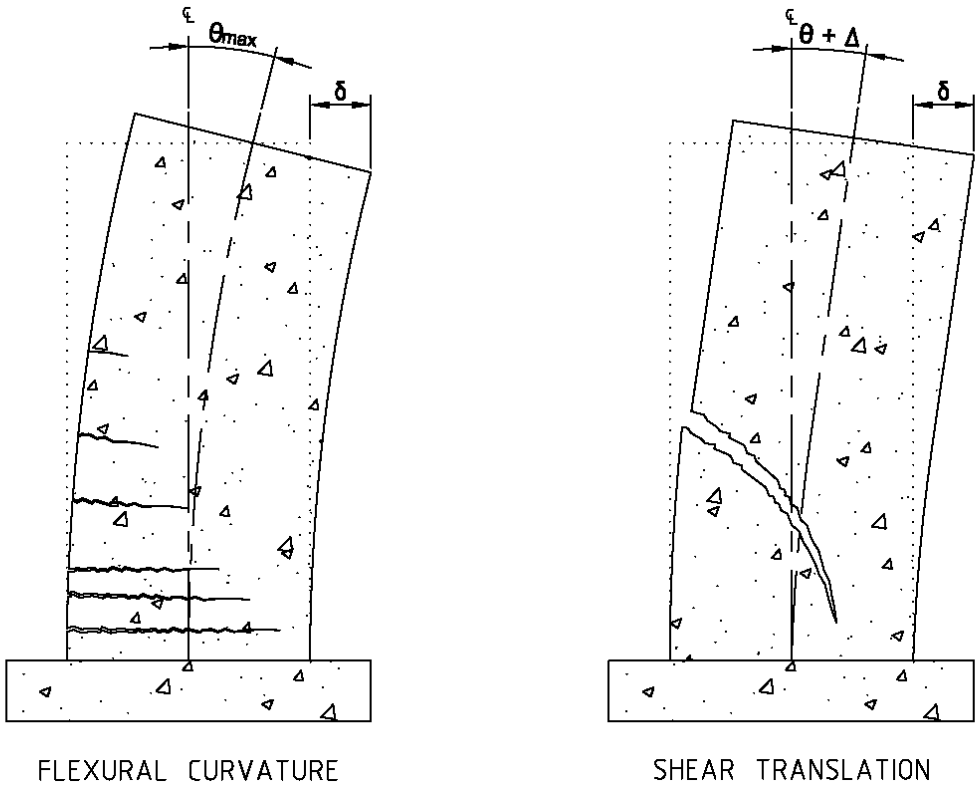

Figure 1.4. Flexural curvature and shear translation.

The use of conventional black carbon steel for reinforcement presents a predicament in the feasibility of repair due to the degree of damage sustained by a structure in direct relation to yielding and rupture. The plastic hinge zone, above the foundation, of a slender shear wall is where most of the damage occurs. At the boundaries on each end of the shear wall, the cracked concrete has negligible contribution in the dissipation of seismic energy, so the vertical steel reinforcement becomes the primary dampening mechanism against the loads induced by oscillating seismic excursions (Paulay, 1980). Under post-yield tension, the steel reinforcement experiences increasing inelastic strain leading to reduced cross sections and plastic elongation. Upon load reversal, now under compression, the steel reinforcement is subject to the Bauschinger effect, having a reduced resistance contribution in the compression zone and is more susceptible to buckling. Buckling is achieved consequentially to a series of cycle-induced elongations which have a ratcheting effect on the structure. The ratcheting effect widens the predominant crack, usually at the base of the shear wall, elevating the entire structure, and reducing the concrete contact area within the compression zone. Under the combined weight of the structure and the lateral loading of an earthquake, the elongated longitudinal reinforcement in the boundaries of the wall buckle when compressed. Increasing seismic intensity inevitably causes the reinforcement in the boundaries to rupture causing severe and sudden strength degradation. More so, the reduction of flexural strength reduces the capacity of the shear-resistance mechanism promoting the propagation of wide cracks

with minimal recovery (Paulay, 1980). The accumulation of damage leads to undesirable repair costs among other economic losses (Ramirez and Miranda, 2012).

Shape memory alloys (SMA) is a contemporary state-of-the-art technology available as an alternative reinforcement for the development of sustainable reinforced concrete smart structures capable of adapting to contemporary demands. Since the 1950's the Canadian approach to seismic design has changed drastically. The force-based methodology does not correlate accurately with damage in comparison to a performance-based approach (Cordone et al., 2010). A performance-based design technique builds upon displacement (Priestly, 1993). To address the incompatibilities between design philosophy and material limitations, and to facilitate balance between functionality and economy, years of research and development have investigated various mechanisms to absorb and divert seismic energy applied to a structure (Ozbulut et al., 2011). Among the researched technologies are varieties of the novel SMA smart materials, which facilitate a viable and sustainable alternative to conventional steel reinforcement. Furthermore, the medical, aerospace, robotics, automotive, consumer electronics, and many other technology industries, such as NASA, have demonstrated and advanced the use of SMA, allowing it to become more affordable and feasible to be explored as a new construction material. Unlike conventional steel, SMA has exhibited characteristics of a much greater capability to significantly recover from large deformations, and reduced corrosion. The mechanical advantage of strain recovery inherit in SMA implies a greater control over damage and the post-disaster state of a structure, by design. As such, this presents an opportunity to, efficiently and economically, realize the structural performance objectives of non-technical stakeholders. In conjunction with the principles of earthquake engineering, the use of SMA as an alternative reinforcement material enables the realization of smart structures.

1.2 Shape Memory Alloys

The onset of discovering shape memory alloys started with the discovery of the irreversible martensite material phase in steel, during the 1890's by Adolf Martens (Lagoudas, 2008). The first SMA was later discovered in 1932 by Arne Ölander, a Swedish physicist, as a gold-cadmium alloy (AuCd) (Mohd Jani et al., 2013). By 1938, copper-based alloys with zinc (CuZn), and tin (CuSn), were introduced for the same purpose by Greninger and Mooradian (Kheirikhah et al., 2011). The thermoplastic behaviour of steel was not understood until 1949, until the reversible thermoelastic martensite phenomenon was discovered through more elaborate studies of copper-based alloys and compared to carbon steel (Kurdyumov and Khandros, 1949). The discovery of the reversible thermoelastic martensite material phase stimulated a greater interest in discovering a larger variety of thermoelastic alloys, however, these materials remained without application for a while (Lagoudas, 2008). In 1963, the "titanium-nickel system" was introduced for the first time after observations of "highly interesting and dynamic property changes" at near room temperature (Buehler et al., 1963). Buehler demonstrated the reversible thermoelastic martensite transformation with a thin wire of a 0.02inch (0.508mm) diameter, composed of 55.4% nickel, retaining a coiled shape at room temperature, and straightening out "in less than one second" only once submersed in hot water (Buehler et al., 1963). By 1971, the nickel-titanium (NiTi) alloy was popularized by the Naval Ordinance Laboratory (NOL) in the USA,

referred to as NiTiNOL (Huang et al., 2010). The Nitinol SMA is composed of approximately 56% nickel and 44% titanium (Abdulridha et al., 2013). Approximately 30 SMAs have been identified up to this point (Janke et al., 2005). Relevant SMAs are categorized into iron-based (Fe-) and copper-based (Cu-) groups, however the most preferable for structural applications is Nitinol (Alam et al., 2007).

Shape memory alloys have two predominant material phases: Martensite and Austenite. These material phases refer to the body-centered cubic crystal structure of the alloy. Shifting between the two distinct material phases, SMAs can exhibit a shape memory effect (SME) and a superelastic effect (SE). The crystal structure of SMAs is illustrated in Figure 1.5.

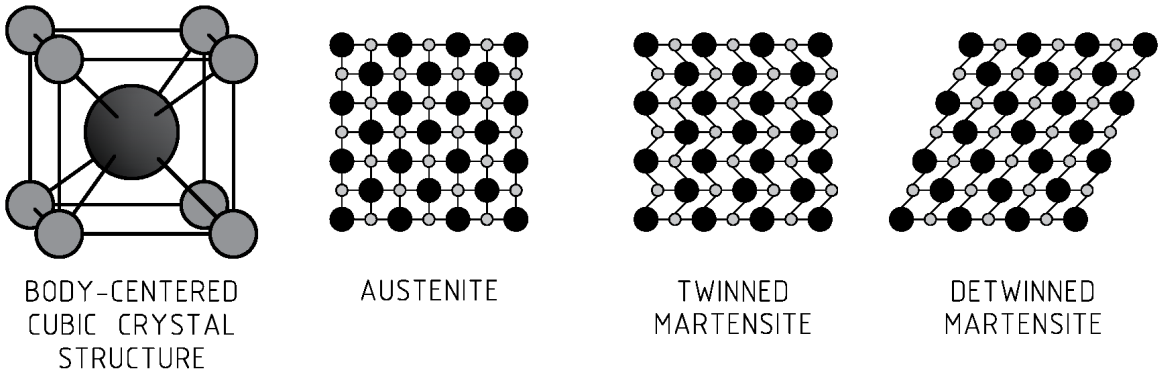

Figure 1.5. Crystal structure and material phase configurations of shape memory alloys.

The shape memory effect is achieved through the martensite crystal structure, which is present in two states: twinned and detwinned. A SMA specimen exhibiting the SME characteristic will start in the twinned martensite crystal configuration and can be deformed with mechanical or thermal stress (σ). Deformation of the specimen shifts the crystal structure towards the detwinned martensite configuration, where the deformity is retained upon unloading. The stress-strain curve for SME-SMA looks similar to the behaviour of steel, shown in Figure 1.6a. The SME-SMA specimen recovers its initial shape with the application of heat. Heat induces a shift in the crystal structure towards the austenite crystal configuration, which continues to shift to the twinned martensite configuration upon cooling, and there by achieving the initial shape. This relationship between the twinned martensite phase and the detwinned martensite phase is a combination of physical deformation followed by heating, then cooling (Ozbulut et al., 2011). Notably, the thermal cycle for the martensite material phase has been observed to also work in a cycle going from high temperatures to lower temperatures (Buehler et al., 1963). The behaviour and crystal phase transformation of SME-SMA is illustrated in Figure 1.6b.

The superelastic effect is achieved when the SMA specimen is in the austenite crystal configuration. The SMA specimen transforms into the detwinned martensite phase through mechanical straining (ε). The superelastic phenomenon is attributed to near complete recovery when axial strain is applied to an SE-SMA specimen below a strain limit of 6-8%, (Ozbulut et al., 2011). The SE-SMA specimen ruptures at approximately 12% axial strain. The

superelastic behaviour is presented in Figure 1.7a. To achieve superelasticity, heat treatment of the SMA is performed outside of the ambient temperature range for the intended use of the specimen in order to maintain a stable austenite phase. For structural applications, the functional ambient temperature range, is estimated between -20°C and 60°C (Janke et al., 2005). As such, SMA intended for structural applications is conditioned for austenite stability at a temperature below -20°C, as shown in Figure 1.7b. The SE-SMA used in this research is Nitinol. Nitinol is preferred for structural applications for its high strain recovery, high fatigue resistance, and high corrosion (Abdulridha and Palermo, 2017).

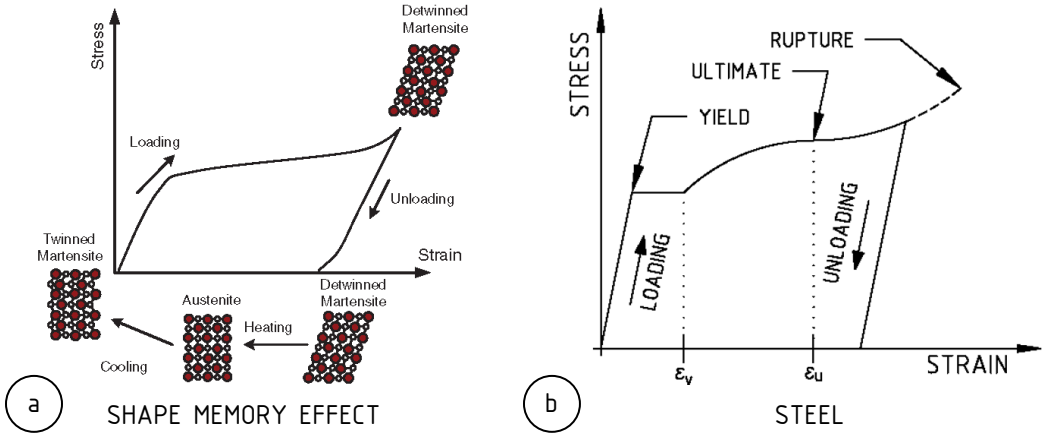

Figure 1.6. Material stress-strain curvatures for: (a) shape memory effect in shape memory alloys (Ozbulut et al., 2011); (b) carbon steel.

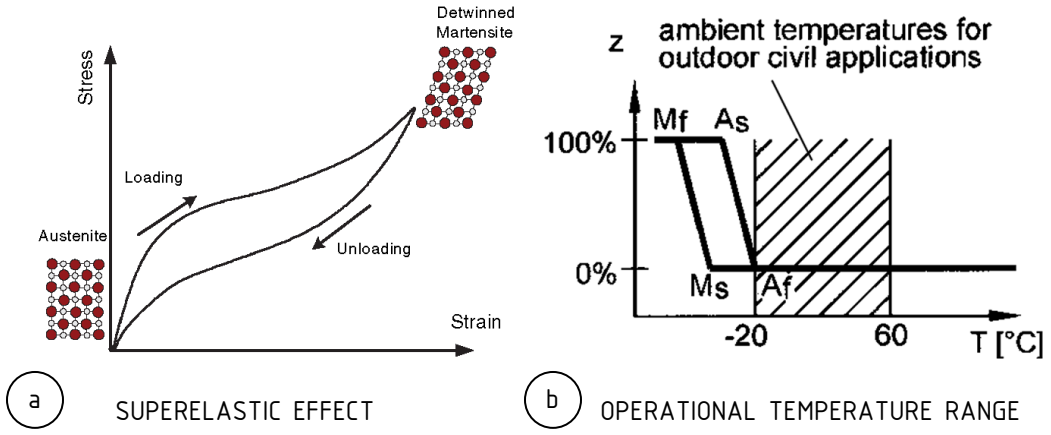

Figure 1.7. Superelastic shape memory alloys: (a) phase transformation cycle (Ozbulut et al., 2011); (b) functional temperature range (Janke et al., 2005).

1.3 Theory

Seismic design has traditionally utilized the principle of ductility to increase the seismic resiliency of structures, however, this consumes more materials and increases cost. The balance between cost and design demands places a limit on the post-disaster integrity and serviceability of a structure. A reinforced concrete structure absorbs and dissipates seismic energy through the formation of plastic hinges, consequential to the yielding of conventional steel reinforcement. Plastic hinges are commonly found at critical locations throughout moment-resisting systems, such as at the interface of beam-to-columns joints, and the base of shear walls and bridge piers. A residual drift or deflection at the free-end, or a rotation at the fixed-end, of an unloaded structure or structural element is indicative of permanent damage, which is a source of hazard to occupants and accumulates to high financial losses. The post-yield capacity of steel limits salvaging due to increasing permanent damages. The damage is commonly a collection of dispersed wide cracks due to the steel-concrete bond, yielded or ruptured steel reinforcement, and crushing of concrete. Researchers have predominantly investigated copper (Cu-) and iron (Fe-) based alloys, as well as the nickel-titanium (NiTi) alloy, which are all common commercially available smart materials, to substitute conventional steel reinforcement (Huang et al., 2010). Nitinol (NiTi) presents the most adaptable, sustainable, and economic solution utilizing SMA to resolve the engineering problems arising from damages sustained by reinforced concrete structures during an earthquake.

The governing theory for this research proposes that superelastic Nitinol SMA can be used, in the form of smooth round bars, as an alternative reinforcement, within the plastic hinge region of a reinforced concrete slender shear wall, to achieve self-centering and minimize damage. The Nitinol reinforcement is mechanically coupled to conventional steel reinforcement outside of the plastic hinge region for anchorage. Bond slip between the smooth bar surface and concrete will transfer the majority of flexure-induced tensile strain to the Nitinol, thereby limiting concrete cracking. The use of superelastic Nitinol complements the philosophy of performance-based design by providing a mechanism with which displacement and residual drifts can be controlled and minimized. The theory is illustrated in Figure 1.8.

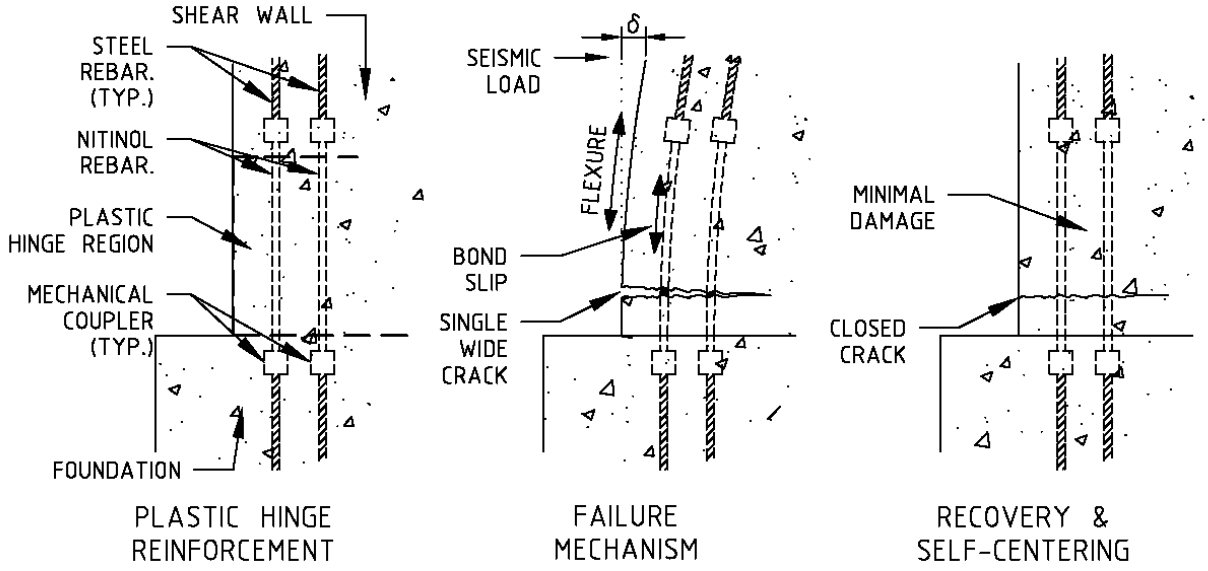

Figure 1.8. Function of Nitinol reinforcement in a slender concrete shear wall.

1.4 Research Objectives

The central objective of this research is to utilize the high-strain recoverability of superelastic Nitinol SMA, as an alternative longitudinal reinforcement in the boundaries of the plastic hinge region, to achieve a self-centering slender reinforced concrete shear wall structure. The intended outcome of the study is to assess the seismic behaviour of the hybrid Nitinol-reinforced shear wall to promote the use of smart materials for new construction of sustainable smart structures with reduced post-disaster repair costs and preserve serviceability. To achieve this objective, two large-scale reinforced concrete slender shear walls are constructed: a Nitinol SMA-reinforced shear wall, and a control conventionally reinforced shear wall. Each wall is tested in-plane through a quasi-static reverse cyclic loading protocol to simulate an earthquake.

Secondary objectives of the study are to:

- Contribute to a limited dataset and knowledgebase on the use of superelastic Nitinol reinforcement in slender reinforced concrete shear walls;
- Investigate the effect of removing starter bars;
- Utilize a less invasive mechanical reinforcement coupler.

1.5 Research Novelty

Nitinol is used to develop self-centering and economically repairable structures. However, no methodological seismic loading standard exists to govern the reverse cyclic laboratory testing of reinforced concrete specimens. Past studies recommend that Nitinol be coupled with non-invasive devices positioned outside of the plastic hinge region, and that shear starter bars at the base tend to shift damage, expected to occur at the base, to above the starter bars. The novelty of the research is in the investigation of a Nitinol-reinforced slender concrete shear wall tested to a synthesized loading protocol, while using non-invasive coupling outside of the plastic hinge region, and the elimination of shear starter bars. Furthermore, the slender SMA wall tested in this study contributes to the very limited experimental data available on SMA-hybrid shear walls, yet slender shear walls are routinely used as the main seismic-force resisting system in concrete construction. In addition, the test data from this study will be critical to continued development of SMA constitutive models, and procedures to accurately model SMA-reinforced concrete structures.

1.6 Report Layout

The contents of this thesis are organized into a series of seven chapters. Chapter 1 is an introduction to the research, detailing the fundamental background concepts motivating the study of the behaviour of shape memory alloy-reinforced shear walls in context of seismic-resilience. The chapter addresses the evolution and requirements of the seismic design philosophy, the discovery and material characteristics of shape memory alloys, and the background

theory governing the study. Chapter 2 includes an extensive and critical review of literature pertinent to reinforced concrete structures utilizing superelastic shape memory alloys as alternative reinforcement. The specific focus is on the study of slender shear walls. An auxiliary review of comparable structures, and relevant experimental studies is also provided. Chapter 3 addresses the proceedings of the experimental program to produce and investigate two slender reinforced concrete shear wall specimens. The material properties, construction process, instrumentation, test setup, and testing procedure are discussed in detail. Chapter 4 focuses on a predictive finite element analysis of both shear wall specimens using an array of material constitutive models in program VecTor2, a non-linear finite element analysis (NFLEA) software developed at the University of Toronto. The results of the experimental study are presented in Chapter 5. This chapter contains the responses, failure mechanisms, and behavioural observations for each wall. Chapter 6 is a discussion of the experimental results and findings. An interpretation and analysis of the results is followed by a comparison of the seismic performance of both walls. Finally, Chapter 7 is a cumulation of conclusions and recommendations, and addresses future works. All auxiliary information is provided in a series of appendices at the end of the thesis.

CHAPTER 2

Literature Review

2.1 Introduction

This chapter presents a comprehensive literature review of publications related to reinforced concrete shear walls and the integration of shape memory alloys (SMA) for structural applications, in the context of performance based seismic design. The literature indicates a limited availability of research conducted on the application of the Nitinol Shape Memory Alloy (SMA) as a novel reinforcement alternative for reinforced concrete (RC) construction. Traditional RC construction utilizes deformed steel bars to resolve the low tensile strength and ductility of concrete. Reinforced concrete shear walls commonly suffer costly damages and retain permanent lateral deformations from a seismic event in direct relation to the strain capacities of conventional construction materials. Shape memory alloys, a smart material, present a solution attuned to the control and recovery of lateral displacement.

2.2 Shear Walls

The behaviour of slender reinforced concrete shears walls under seismic loading has been the research focus of many as an efficient lateral force resisting system. The components of a shear wall and how they respond under loading have been long examined to identify opportunities to improve design parameters and to economize construction.

An experimental study by Oesterle et al. (1976) identified design features limiting the inelastic seismic performance of conventional reinforced concrete shear walls, designed to the 1971 ACI Building Code without seismic detailing, when subjected to lateral load reversal. The experiment considered the shape of the shear wall cross-section, the amounts of longitudinal and transverse reinforcements, boundary element confinement, concrete strength, and applied axial load. The results indicated that appropriate detailing of the flexural reinforcement in the boundaries significantly improved the inelastic performance of the shear wall. Confining reinforcement is required in the boundaries to prevent buckling of the longitudinal bars. However, high concentrations of longitudinal reinforcement in the boundaries produced high compressive strains on the concrete. The loss of compression concrete further impeded the inelastic response of the wall. More so, the study highlighted the importance of mitigating out-of-plane

displacement of the compression boundary to maintain the lateral strength of the wall while axial loading is applied. Transverse shear reinforcement was applied to satisfy the minimum code requirements.

An experimental study was devised by Corley, Fiorato, and Oesterle (1981) to determine the factors influencing the strength and deformation capacities of isolated walls. The study found that the section shape of a reinforced concrete shear wall has a significant influence on its strength and deformation capacities. A set of common shear wall cross-sections is presented in Figure 2.1. Given the design concrete strength, the arrangements of reinforcements across the footprint of the cross-section influences the moment-to-shear ratio and the axial compressive strength of the concrete wall. The arrangements of the reinforcements are a result of balancing between the physical restrictions of the cross-section, on variables like size and quantity, and achieving the desired performance from the wall. The arrangement of longitudinal reinforcement defines the flexural capacity of the wall, and by definition sets the maximum shear capacity. A balance is required between having a uniform distribution of longitudinal reinforcement over the cross-section and placing concentrations in the end boundary elements. Walls with concentrations of longitudinal reinforcement in boundary element, and have a relatively thin web, are more likely to attract large shear forces and suffer web crushing. In contrast, a uniform distribution of the longitudinal reinforcement is correlated to reducing the rotational capacity of the wall. However, boundary elements are favoured for increasing resistance to sliding, and sustaining the integrity of the shear and axial load capacities of the wall once the web becomes damaged. Boundary elements would be especially helpful in walls with a flexural response, where load reversal beyond the yield point had a reductive influence on the strength and deformation capacities of the wall. Squat walls were not impacted by this degradation but are rather defined by the limitations of web crushing. As such, the study determined that load history is among the significant factors influencing the strength and deformation capacities of existing structures.

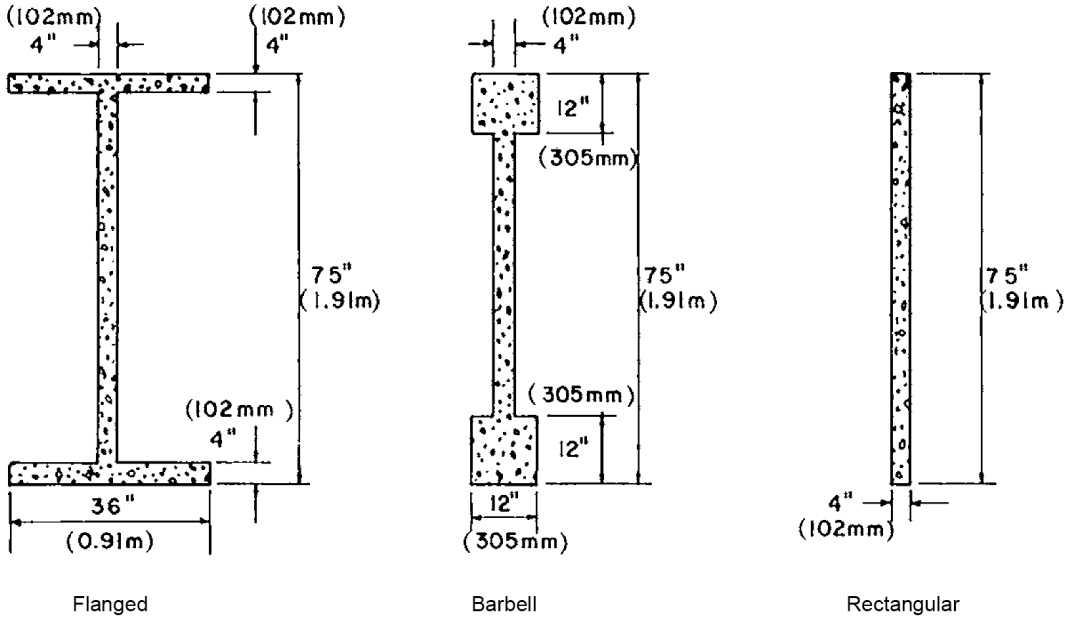

Figure 2.1. Shapes of shear wall cross-sections (Corley, Fiorato, and Oesterle, 1981).

Sittipunt and Wood (1995) elaborated on the shear failure of concrete walls during earthquakes in relation to the configuration of web reinforcement. The numerical study investigated a variety of distributions of longitudinal reinforcement across the web and assessed the impact of the configurations on the cyclic response of the walls. The objective was to address lateral strength and stiffness degradation as a result of web crushing under cyclic loading. The study found that introducing diagonal reinforcement across the web, within the plastic hinge region, minimized shear distortion. The results also indicted that that the diagonal reinforcement improved energy dissipation and diminished the probability of shear failure.

Further reverse cyclic experimental testing was conducted on slender reinforced concrete shear walls by Pilakoutas and Elnashai (1995). The study found that excessive application of shear reinforcement beyond the minimum requirement had insignificant contribution to improving the hysteretic performance of slender shear walls.

2.3 Shape Memory Alloys

Shape memory alloys (SMA) have provided an array of solutions for many growing industries, including the medical, automotive, mechanical, and aerospace fields. Products that utilize shape memory alloys typically require high force application, large strains within a small temperature range, and overall versatility and ease of use. These commercial products commonly employ the benefits of free recovery to regain a distinct shape through the application of heat, or superelastic recovery which is mechanized by the storage of potential energy retained from recoverable strains (Darjan and Dolinsek, 2007). There are approximately 30 types of shape memory alloys available (Debbarma and Saha, 2012) as thin films, wires, and bars. These SMA materials are trainable for sensing and actuation at the molecular level (Huang, et al., 2010). Commonly, they can be trained and actuated by mechanically or by using heat. Some other variants of the material are manipulated by using light/laser, or a magnetic field.

2.3.1 Material Behaviour

Shape memory alloys are composed of at least two elements and interchange between two material phases within an operational temperature range. The concentrations of the elemental constituents determine how the alloy responds to thermal stimulus to shift between material phases (Lagoudas, 2008). At low temperatures, SMA's are in the martensite phase. At high temperatures, the crystal structure of the alloys transforms to the austenite configuration. The transformation between the material phases and crystal structures is generally induced by thermal or mechanical loading, or a combination of both.

The martensite phase has two variants of the monoclinic crystal structure: twinned and detwinned. At a fixed temperature (T), an SMA in the twinned configuration can be transformed to the detwinned configuration by mechanically stressing (σ) the material. The reorientation of the crystals is retained, and so is the deformed shape (ε) of the materials, upon removal of the applied load. This phenomenon is referred to as the shape memory effect (SME).

When detwinned martensite is heated (T), the crystal structure transforms towards the austenite configuration. The austenite material phase is present in a single cubic crystal orientation. When mechanical stress (σ) is applied to austenitic SMA, the crystal structure shifts towards detwinned martensite. Once the stress is removed, the crystal orientation of the SMA material reverts to the austenite phase to recovers its original shape (ε). This phenomenon is called superelasticity or the pseudoelastic effect.

The fundamental relationship between the shape memory effect and the superelasticity of SMA is found in the reversible shear lattice distortion of the crystal structure of the material (Lagoudas, 2008). When martensitic SMA is heated it shifts to the austenite phase in a process called reverse transformation. When the same material is cooled, it shifts back to twinned martensite in a process referred to as forward transformation.

The thermal and mechanical phase transformation relationship of SMA is summarized in Figure 2.2.

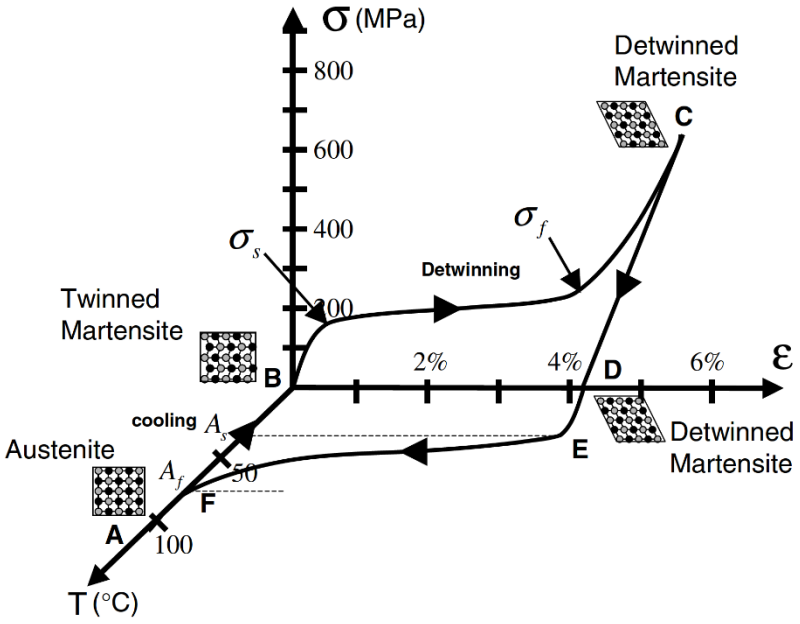

Figure 2.2. Thermal-mechanical phase transformation relationship of shape memory alloys (Lagoudas, 2008).

2.3.1.1 Shape Memory Effect

The shape memory effect (SME) is attained from a SMA material starting in the twinned martensite phase. The deformed shape is retained once the mechanical stress is unloaded, given that the thermal conditions remain below the start transformation temperature for the austenite material phase (A_s) (Lagoudas, 2008). A shape memory alloy material possessing the SME property is trained into the twinned martensite phase first by heating into complete austenite transformation, then cooling to an operational temperature below the start transformation temperature for the martensite material phase (M_s) (Lagoudas, 2008).

The shape memory effect is further broken down into a one-way effect and a two-way effect. The one-way shape memory effect describes a condition where the SMA material retains its distorted form, but remembers its original shape upon heating, and continues to maintain the original shape once cooled down. One-way shape memory is the commonly attributed feature to SMA materials. The two-way shape memory effect is when the SMA material is trained through a sequence of cyclic thermomechanical repetitions to remember two deformed shapes. The two shapes become interchangeably achievable through heating and cooling (Alaneme and Okotete, 2016). However, the two-way shape memory effect is an indicator of degradation in the SMA material. The permanent shape retained by the SMA is a result of irreversible dislocation of the crystal structure from thermal cycling (Van Humbeeck, 1991). The degradation of the hot and cold shapes converges towards a stabilized strain variation.

The thermomechanical behaviour of the shape memory effect, for stress induced transformation, was studies and presented in mathematics expressions by Tanaka, Kobayashi, and Sato (1986) for constitutive modeling.

2.3.1.2 Superelasticity

Superelasticity, or the pseudoelastic effect, is a stress induced behaviour dependant on the austenite material parent phase. The superelastic property is commonly employed at a constant nominal operation temperature beyond the finish transformation temperature for austenite (A_f). A superelastic SMA material remains elastic until phase transformation is initiated when the applied stress equals the detwinned martensite start transformation stress (σ^{Ms}). Throughout the martensite phase transformation, the SMA material exhibits a yielding stress-strain (σ-ε) relationship, followed by some strain hardening towards the martensite finish transformation stress (σ^{Mf}). The martensitic SMA material heron retains an elastic behaviour with an increase in applied stress, similar to the austenitic elastic response. Upon unloading, the SMA material recovers from elongation strain along a path determined by martensitic elasticity until the residual stress reduces to the austenite start transformation stress (σ^{As}), at which large strain recovery is triggered over the course of the reverted phase transformation. Beyond the austenite finish transformation stress (σ^{Af}), the stress-strain relationship of the SMA material decays according to austenitic elasticity as unloading continues (Lagoudas, 2008). The stress-strain cycle of superelastic SMA is seen in Figure 2.3.

Further studies on the cyclic behaviour of superelastic SMA has highlighted the benefits of self-centering, and the inherent flaws of cumulative plastic offset in strain recovery and a diminishing hysteresis. Sets of superelastic SMA 25.4mm diameter bars and 1.8mm diameter wires were tested experimentally for their cyclic properties by DesRoches, McCormick, and Delemont (2004), considering the influences of cross-section, loading history and load rate. The study strongly suggested that superelastic SMA bars had highly similar results to those of SMA wire, contrary to the previously limited knowledge on the cyclic behaviour of SMA bars and the studies in the early 1990's which stipulated the inability of SMA bars to achieve superelasticity. The result showed that the cross-section of the material has no baring on the degree of strain recovery. Residual strain and the hysteretic response were correlated to the loading history. Residual strain in both the bars and wires increased with each consecutive cycle by up to about 520% from 2% strain to 6% strain. The rate of increase in residual strain was observed to diminish and approach stability with additional cycles at 6% strain. The intervals of strain targets and the repetition of cycles influenced the rate of

degradation of the loading and unloading plateau stresses. The loading plateau stress of the SMA wire degraded by up to about one-third the initial value over the course of subsequent strain cycles. In contrast, the degradation of the loading plateau stress in the bar was up to approximately 8.5%, however the initial value was about 30% lower than the that of the SMA wire. The unloading plateau stress of the wire was insignificant, relative to a 3% diminution for the SMA bar. The lower initial value of the loading plateau stress for the SMA bar resulted in an increasingly diminishing hysteretic pattern which is expressive of a lower energy dissipation capacity than found with wires. Furthermore, strain rate was found to have a negligible impact on the self-centering capacity of the SMA specimens.

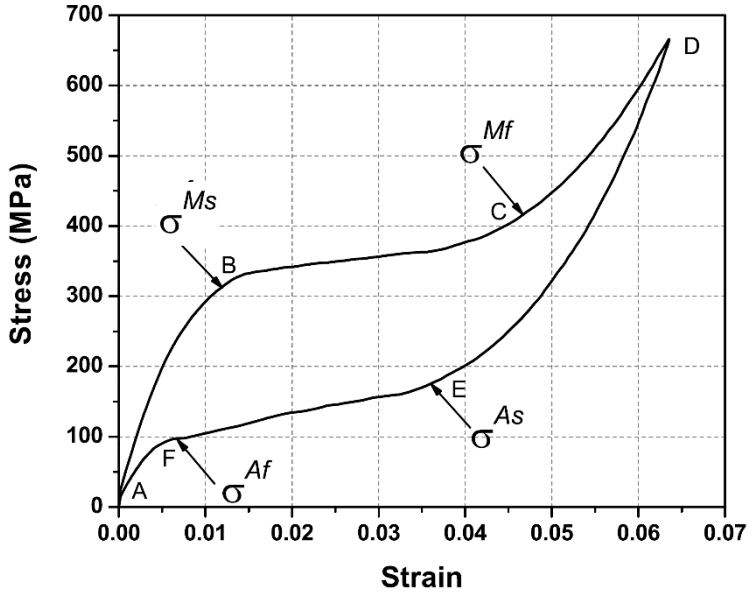

Figure 2.3. Stress-strain cycle of a superelastic SMA material (Lagoudas, 2008).

Piedboeuf, Gauvin, and Thomas (1998) investigated the damping behaviour of shape memory alloys in relation to the effects of strain amplitude and frequency and temperature under dynamic loading conditions to develop a numerical model to predict energy dissipation and a loss factor. The loss factor is defined by a numerical relationship between the maximum potential energy and the dissipated energy for a non-linear viscoelastic material. Superelastic SMA 100μm wire was used for the experimental investigation. To stabilize the superelasticity of the wires, all specimens were conditioned prior to testing by undergoing a set of 100 cycles to 4.5% strain at 5Hz. The specimens were then tested under tensile cyclic loading following a sinusoidal strain function. The strain amplitudes were 2%, 3%, and 4%. The strain frequencies included 0.01Hz, 0.1Hz, 1Hz, 5Hz, and 10Hz. The temperature settings were 25°C and 35°C. The combination of parameters resulted in testing of 120 specimens. The results showed a direct correlation between an increase in the maximum strain energy and increasing the strain amplitude, which also increased the capacity for energy dissipation. Changes in frequency presented a sequence of changes in the hysteresis. A tenfold increase from the lowest frequency to 0.1Hz caused the loading plateau stress to increase and the unloading

plateau stress to decrease, overall increasing the dissipated energy by approximately 15%. The dissipated energy appears to diminish at higher frequencies. A subsequent tenfold increase in the frequency to 1Hz caused the loading plateau stress to continue increasing, however the unloading plateau remains at approximately the same stress but is significantly shortened. At a higher frequency of 10Hz, the loading plateau appears to stagnate, and the unloading plateau stress significantly increases, overall leading to the lowest level of dissipated energy. The variation in levels of energy dissipation with frequency are dependant on the strain amplitude, becoming more definitive as strain amplitude increases. An increase in temperature was found to have a linear relationship with uniformly increasing the hysteresis upwards. However, the increased ambient temperature had no impact on the level of energy dissipation but did lower the energy loss factor. More details pertinent to the loss factor can be found in the journal paper. The results are cumulated into a Fourier three harmonic sine series model for modeling the dynamic behaviour of superelastic SMA.

Superelastic SMA is prone to fracturing due to fatigue under cyclic loading which raises question about its stability and lifetime reliability. Van Humbeeck (1991) highlights that over a large number of loading cycles, defects accumulate in the crystal structure of the SMA material throughout loading, which adversely hinders the stress-induced martensitic transformation, leading to sequences of internal microcracks, which when connected result in fracturing. Superelastic alloys with a fine material grain were found to be more resistant to fatigue, when compared to alloys with a coarse grain.

2.3.2 Types of Shape Memory Alloys

Many types of shape memory alloys have been discovered and synthesized from various metals. The most prominent shape memory alloy is Nitinol (NiTi), produced from nickel and titanium. Other popular shape memory alloys are copper-based (Cu-) and iron-based (Fe-), among many other lesser-known alloys.

2.3.2.1 Nitinol

The shape memory effect was first discovered in the Nitinol (NiTi) alloy in 1962 (Tanaka, Kobayashi, and Sato, 1986). The phenomenon was described as an "*... unusual behavior... limited to NiTi alloys* [with near equal composition]. *... having a nickel content of approximately 55 percent by weight.*" (Cross, Kariotis, and Stimler, 1969). In 1969, a founding investigation by Cross, Kariotis, and Stimler at the Goodyear Aerospace Corporation was release on the characterized properties of Nitinol for the National Aeronautics and Space Administration (NASA). Three fundamental nickel-rich (Ni), nominal 55% weight content, compositions of Nitinol were used under three different martensite training temperatures to produce rod, wire, and foil specimens. The nickel content varied between 52% to 56% by weight for the set of Nitinol compositions used in this study and classified as suitable for shape recovery. The Nitinol provided by the Naval Ordinance Laboratory contained 6.5% cobalt (Co) by weight substitution for nickel, enabling a significantly lower transformation temperature at about -196°C, which allows for controlled production of

superelastic Nitinol that is suitable for applications in harsh ambient sub-zero environments. This Nitinol was identified as 'Type A'. Two other compositions were provided by an alternative source. The second Nitinol composition, designated as 'Type B', had a fixed weight content of 55% nickel and 7% carbon (C) with titanium (Ti) making up the balance. The third composition, identified as 'Type C', was proportioned by weight at 54.6% nickel, 6% carbon, and 0.6% sulfur (S). The reasoning for the additional compositions was not provided.

Three types of specimens were produced from each of the Nitinol compositions. Nitinol rods were produced in diameter sizes of 7.62mm from Type A, 5.08mm from Type B, and 15.875mm from Type C. Wires in diameter sizes of 2.54mm, 0.508mm, 0.381mm, and 0.254mm were drawn at about -23°C for Nitinol Type A through a temperature-controlled procedure. Wires of the same diameter sizes were cold drawn from rods for Nitinol of Type B and Type C, at temperatures below the martensite start transformation temperatures (M_s). Nitinol foils were produced for all three compositions in thicknessed of 0.1524mm (foil 1) and 0.0762mm (foil 2). For Nitinol Type A, rod and wire specimens had a martensite start transformation temperature of -51°C, -62°C for the thicker foil, and -65°C for the thinner foil. For Nitinol Type B, rod and wire specimens had a temperature of 18°C, 24.4°C for foil 1, and 24°C for foil 2. For Nitinol Type C, all specimens had a martensite start transformation temperature of 40.6°C. The variations in the start temperatures are related to material processing requirements, necessitated by the objectives of the study, and constituted the versatility of Nitinol applications. The production details and annealing methods for each of the specimens are discussed more elaborately by the authors in the report.

Contrary to earlier findings suggesting limited use of Nitinol with caution, the results of this study validated new application opportunities for space exploration and established fundamental design specifications for a multitude of industries. The experiment looked for consistency in the stress-strain behaviour of Nitinol throughout cooling and heating and to substantiate the expectations for tensile performance. Strain recovery, structural properties, and physical properties were among the defined characteristics. Temperature is a key influencing factor in how the Nitinol specimens behaved across all three compositions. When heated, the 0.2% offset yield stress of Nitinol increased across the phase transformations and seemed to reverse when cooled. Heating Nitinol above the martensite start transformation temperature produced a significant increase in the elastic modulus, estimated in the range of fourfold. The greater stiffness is observable starting at the austenite start transformation temperature and increases towards stability at the maximum allowable temperature for stress-induced martensite transformation (M_d). Cooling the Nitinol has a reverse effect on the elastic modulus. Collectively, the specimens were recorded to achieve complete strain recovery from a maximum range of 6% to 8% strain. Beyond 8% strain, deformation recovery was recorded at upward of 90%. The wire specimens were able to demonstrate approximately 690MPa tensile recovery stress along the unloading plateau from a maximum strain of 8%. The overarching conclusion from the study was that appropriately processed Nitinol can reliably and consistently maintain a desired mechanical performance regardless of composition and product size. Electrical resistance versus temperature profiles were determined to be a viable tool for monitoring transformation temperatures during processing and thereby enable greater control over the variables influencing the recovery behaviour in the final product. Recovery performance is dependant on processing history.

Industrial favour of Nitinol is due to its highest mechanical and material performance among shape memory alloys. Nitinol gained popularity due to its demand in the medical industry because of its good biocompatibility

(Huang, et al., 2010). The preferred SMA for structural seismic design is the NiTi alloy (Abdulridha et al., 2013). The corrosion-resistant Nitinol is preferred for its hysteric dampening and self-centering abilities when used for structural applications. Industry demand for Nitinol, for its superior quality, has generated competitive pricing. In a two-part investigation Tyber et al. (2007) and McCormick et al. (2007) studied Nitinol extensively for application in structural engineer. Tyber et al. (2007) addressed the material properties of Nitinol from the perspectives of material scientists and structural engineers with respect to the challenges hindering the adoption of the material for design and construction. The fundamental knowledge of Nitinol is a product of experimentation using research grade materials carefully processed through very high heat treatment to address the transformation temperatures, and many do not report on the mechanical performance. For practical applications, heat treatment techniques are a common challenge for anyone using Nitinol. Tyber et al. (2007) explains that the industrial processes used are typically either traditional to adhere to founding methods or become trade secrets based on undisclosed developments. In both cases, manufacturers generally employ whichever means they find best for producing a Nitinol product with the transformation temperatures specified by the customer. Nitinol wires, tubes, and strips are commonly tested specimens for material characterization, thermo-mechanical properties, and formation of constitutive models. The expensive method of cold drawing impeded mechanical testing on bars of a larger diameters, such as suitable for structural applications. The compatibilities and performance differences between cold drawn and hot-rolled products are not well understood. The available knowledge when employed in engineering design is an idealized approximation of the mechanical behaviour of Nitinol.

The two-part experiment used superelastic Nitinol composed of 55.95% nickel by weight for hot-rolled bar specimens of 12.7mm, 19.1mm, and 31.8mm diameter sizes. Specific details of the processing and heat treatment are presented by Tyber et al. (2007). The bar specimen diameters are the equivalent of #4, # 6, and close to #10 (32.3mm diameter) from the imperial reinforcing bar sizes; respectively No. 13, No. 19, and No. 32 in metric. The specimens closely resemble 10M (11.3mm diameter), 20M (19.5mm diameter), and 30M (29.9mm diameter) reinforcing bars from the Canadian sizes.

Tyber et al. (2007) reported new fundamental findings for the material characterization of large diameter Nitinol bars with respect to the mechanical processing and heat treatment of the material. Repetitive mechanical processing of hot-rolled bars slightly reduced the material grain size for increased strength and resilience to plastic dislocation of the Nitinol crystals. However, minimal grain size difference was observed in comparison to cold drawn bars. Another finding was regarding the aging of Nitinol and its usefulness to engineers. The phase transformations to austenite and martensite are ideal when the Nitinol alloy is perfectly equiatomic. However, commercial Nitinol is most commonly available in nickel-rich compositions which disrupt the complete phase transformations as commonly understood to occur. Contrary to this disruption, the study found that appropriate aging of nickel-rich Nitinol stabilized the crystal structure of the material to make it more adaptable for shape memory or superelastic engineering applications. Overall, the characteristic similarities make using hot-rolled bars feasible, mitigating the need for the more expensive cold drawn product.

McCormick et al. (2007) reported on the mechanical behaviour of large diameter Nitinol bars, using coupons and full-scale samples, under cyclic loading and earthquake loading. The coupons were extracted from each bar size to a

length of 63.5mm and 1mm thickness. The coupons were taken from two locations along the diameter of each bar to allow for further investigation of the findings presented by Tyber et al. (2007). The first coupon was taken from the center of the bar, and the other was taken from towards the edge. The full-scale specimens were tapered to avoid stress concentrations at the grips. The 12.7mm, 19.1mm, and 31.8mm were tapered to 6.35mm, 12.7mm, and 25.4mm, respectively. The tapered diameters are representative of #2 (No. 6), #4 (No. 13), and #8 (No. 25) bars. To Canadian standards, the 6.35mm bar is similar to smooth bars sometimes used for stirrups or welded mesh reinforcement, the 12.7mm bar is closest to a 10M bar, and the 25.4mm bar is closest to a 25M bar (25.2mm diameter). Cyclic loading consisted of 20 cycles to 6% strain to observe the degradation of properties. Earthquake loading was simulated by tension-only cycling to a sequential buildup of strain increments to 6% strain to contrast behavioural changes induced by nonuniform loading. The results found that repetitive cycling gradually reduced the loading plateau stress by approximately 38% independent of bar size. This degradation was linked more so to artifacts deposited during processing, referred to as precipitates, than to grain size. The coupons were sparsely useful in connecting material characteristics to the results of cyclic loading of full-scale bars, due to the heterogeneous matrix of Nitinol found across the diameter of the bars, which was restricted by the narrow section of the coupons. However, strain recovery and viscous damping improved as bar size decreased. Earthquake loading and cyclic loading did not produce any significant differences in the mechanical behaviour of the Nitinol bars. Overall, the mechanical testing of the Nitinol bars corroborated the usefulness of large diameter bars for structural applications as determined from the material characterization study.

2.3.2.2 Alternative Shape Memory Alloys

The most common alternatives to Nitinol are copper-based and iron-based shape memory alloys. Copper (Cu)-based SMA's offer the benefit of low cost due to material and ease of processing (Huang, et al., 2010). Copper-based alloys are an intermediate option between superior NiTi-based alloys and place above iron-based alloys due to greater shape memory and superelastic performance (Sutou, et al., 2004). Iron (Fe)-based SMA's are the least expensive and most suitable for infrequent actuation, however, are also the weakest alternative (Huang, et al., 2010).

The copper-aluminum (CuAl) alloy is the fundamental constituent of commercial copper-based SMA alternatives. Dasgupta (2014) elaborates on the state-of-the-art of Cu-based alloys to address their applicability, challenges, and future potential. Copper-based SMA's include two other base alloys with zinc (Zn-) and tin (Sn-). However, all three base alloys present challenges with cold working and thermal stability among other mechanical shortcomings, as binary amalgams. Other elements are added to the base alloys to produce compositions with improved properties. Experimenting on ternary and quaternary alloys with various element concentrations has achieved isolated improvements in mechanical and thermal properties. The copper-aluminum-nickel (CuAlNi) alloy and copper-zinc-aluminum (CuZnAl) alloys have been the focus of many research efforts given their wholistic responses to the shape memory effect, superelasticity, and include the temperature memory effect. The commercial availability of products from these alloys is impeded by poor mechanical performance including brittleness, low strength, degradation of recovery capacity, and limited operation at temperatures beyond 150°C. Recorded results have attributed the product

flaws to the nature of the material properties of copper-based SMA's, such as the coarse grain sizes of the material microstructure and high sensitivity to common contaminants like oxygen and carbon. For this reason, copper-based alloys tend to remain quite expensive to manufacture and mostly utilized in more advanced applications. Dasgupta (2014) projects that, with continued research and development, future syntheses of copper-based alloys will find applications in structural engineering among other technology industries. The envisioned applications include self-repairing structures, and sensory networks to locate defects and provide data to monitor performance history.

Sutou et al. (2004) reported some improved performance with ductile copper-aluminum-manganese-based (CuAlMn-) alloys for shape memory and superelasticity. The study was driven by the endeavour to enhance the strain capacity of these alloys to beyond their 2% limit. A relationship was established between the diameter of the alloy grain relative to the diameter of the round wire or bar and the degree of superelasticity. As the diametric ratio increased, so did the superelastic capacity. The study pursued precise addition of various constituents to the base alloy in combination with thermomechanical treatment to alter the grain size of the microstructure as a solution. Superelasticity with near complete recovery was achieved from 7% strain for a diametric ratio of 4.54, setting the most compatible performance to Nitinol. The high superelasticity was demonstrated with a wire made of an alloy containing 0.5% Cobalt. The CuAlMn-based alloys in the commercial market are recommended for medical application and other industries producing electronics and micromechanical devices.

In a review of iron-based shape memory alloys, by Cladera et al. (2014) for civil engineering applications, iron-manganese-silicon-based (FeMnSi-) alloys were identified to have suitable commercial potential among the known compositions. Two groups of iron-based SMA's were identified. The first group of alloys contained combinations exhibiting similar martensitic transformation as found in Nitinol. Among this group, the iron-nickel-cobalt-aluminum-tantalum-boron (FeNiCoAlTaB) alloy was presented in 2010 for its superelastic recovery from over 13% strain at room temperature and having a tensile strain of 1200MPa. Similarly, the iron-manganese-aluminum-nickel (FeMnAlNi) alloy was able to recover from over 5% strain at room temperature and had a rupture strain of about 8%. The applicability of both alloys as a construction material is hindered by the high cost associated with special production requirements, signaling the need for further development. The second group contains alloys capable of the shape memory effect, including FeMnSi-based alloys. The alloys in this group are attributed with low cost and ease of use. Further development among this group has identified compositions capable of generating high recovery stresses within a relatively lower temperature range of 130°C to 500°C. The iron-based alloys in development are projected to serve the purpose of prestressing tendons for structural repair or reinforcement in new construction, while remaining inexpensive and recyclable due to the iron-base of the material. The alloys are also expected to have a higher elastic stiffness, in contrast to Nitinol, and good corrosion resistance.

Czaderski et al. (2014) elaborate on the use of iron-based SMA's as a construction material in the form of near surface-mounted reinforcing strips as an alternative to fiber-reinforced polymer strips. The study used a novel iron-manganese-silicon-chromium-nickel-vanadium, carbon (FeMnSiCrNiV,C) alloy produce the reinforcement strips. The iron alloy strips would eliminate the need for mechanical prestressing, instead depending on thermal initiation of the shape memory effect, which would be triggered by resistive heating from an electric current.

2.4 Structural Applications of Shape Memory Alloys

The application of shape memory alloys across many industries, including civil engineering, is fueled by the intent to attain control of passive and active smart actuation and sensory behaviour (Song, Ma, and Li, 2006). Civil engineering applications benefits from the reversibility of SMA phase transformations for strain recovery, energy dissipation, and damping. The phase transformation path between austenite and martensite, for superelasticity, improves the hysteretic response of structures towards self-centering. The martensitic transformation sequence, for shape memory, promotes adaptation and self-healing against damages in construction materials. A large focus within research efforts has been put on controlling structural behaviour against earthquakes (Menna, Auricchio, and Asprone, 2015). Superelastic SMA's are favoured for enabling a structure with the smart feature of self-centering. A structure utilizing superelastic SMA also benefits from the ability to control service load deformation, retard load transmission for large displacements, and displacement control under extreme loading. As such, SMA's are used in a variety of ways for reinforced concrete structures and steel structures, as well as for the development of evolved construction materials.

2.4.1 Reinforced Concrete Structures

Among the SMA's commercially available, Nitinol is most favoured for reinforced concrete structural applications to address the growing demands for challenging, adaptable, economic, and sustainable structures (Janke, et al., 2005). Most applications have been related to controlling the response of concrete structures to the impact of seismic events. Some initiatives have focused on vibration control, pre/post-stressing, and re-centering of new structures, repaired structures, and retrofitting projects. These structural applications have increased the demand for the manufacture of larger diameter Nitinol bars in contrast to the commonly available wire sizes frequently used in other industries. As a construction material, Nitinol has superior mechanical properties among the known alternative SMA's including high corrosion resistance and high fatigue resistance, making it suitable for scenarios of cyclic loading.

Canadian and American researchers have implemented Nitinol SMA as a reinforcement alternative in structural elements such as shear walls, beams, and columns for resilience against seismic loading (Palermo, Youssef, and Alam, 2013). The experimental studies for new construction have idealized the placement of superelastic Nitinol in the plastic hinge region and coupling it to conventional deformed steel reinforcing bars for anchorage beyond the limits of where a concentrated network of damage is expected to occur. This reinforcement configuration results in an economic hybrid Nitinol-steel reinforced system. A common finding in the test results of the hybrid systems was a prevalence of self-centering over the conventional steel-reinforced counterparts. More so, the damages to the Nitinol -reinforced concrete structures appeared to be more contained. Chang and Araki (2016) explain that, aside from the damaged concrete, the lateral energy delivered to the structure is partially absorbed by the superelastic Nitinol and is dissipated through the rectification of the laterally deformed structure, increasing the feasibility of its repair.

2.4.1.1 Shear Walls

In a first of its kind experimental study, Abdulridha and Palermo (2017) investigated the seismic performance of a slender hybrid Nitinol-steel reinforced concrete shear wall. The study compared the reverse cyclic lateral loading response of the Nitinol-reinforced concrete shear wall against that of a conventional control specimen to evaluate the efficacy of integrating superelastic Nitinol reinforcement for seismic resilience. A typical shear wall specimen had a cross-section measuring 1000mm long by 150mm thick. The height of the shear wall was 2200mm. The wall sat on top of a 500mm thick foundation block and at the top had a cap beam with a cross section of 400mm by 400mm. Superelastic Nitinol 0.5inch (12.7mm) diameter round smooth bars were used to replace the 10M (11.3mm diameter) deformed steel bars in the boundaries of the plastic hinge region. The 1200mm long Nitinol bars were spliced to 15M (16mm diameter) deformed steel bars at 950mm above the top of the foundation to position the mechanical connection outside of the plastic hinge region, which was numerically estimated to a height of 760m from the base. The remaining length of the Nitinol bars was embedded and spliced at 250mm within the foundation block. The stock barrel screw lock coupler that was used to splice the Nitinol had an insufficient grip and required heavy modification. The quantity of screw locks was doubled, and the coupler was welded to the deformed steel reinforcement to allow the Nitinol to be inserted to the total length of the coupler to be gripped by both sets of screw locks at each end. This configuration later proved detrimental to the post-testing integrity of the Nitinol reinforcement as a bar was found fractured at the coupler. The longitudinal reinforcement bars in the boundary elements were restrained against buckling using 10M steel ties along the height of the wall. Both walls had identical shear reinforcement details and shear starter bars extending 300mm into the web of the wall from the base. Typical reinforcement details are shown in Figure 2.4a. Both walls were tested under a lateral loading protocol derived from the ATC-24 standard. No axial load was applied to idealize the conditions for investigation of residual displacements. The shear walls specimens were anchored to the laboratory floor and a lateral displacement was applied through the centre of the cap beam using a hydraulic actuator. The test setup was later modified to include a brace along the length of the cap beam to maintain an in-plane displacement trajectory, which became an evident necessity at 36mm displacement (1.5% drift) of the conventional wall.

The test results indicated good structural compatibility in the Nitinol-reinforced wall and improved seismic performance. The control specimen had an average yield at 9.4mm displacement (0.39% drift) under a load of 116kN. The Nitinol-reinforced wall had an average yield at 26.4mm displacement (1.1% drift) under a load of 112kN. Yielding at about three timed the displacement of the control specimen, the Nitinol-reinforced wall appeared to have 35% the stiffness of its counterpart at about a 3% lower load. The steel-reinforced wall reached an average peak strength of 156kN at 76mm displacement (3.2% drift). The Nitinol-reinforced wall had an average peak strength of 133kN at 72mm displacement (3% drift). The hysteretic responses reflected similar peak strengths at about the same drift level, however, the Nitinol-reinforced wall had about 15% less strength and a reduced ductility. Abdulridha and Palermo (2017) explained that Nitinol-reinforced flexural elements typically experience greater yield displacement due to the lower elastic modulus of Nitinol. Subsequently, greater flexural strain demand is transferred to the stiffer longitudinal steel reinforcing bars in the web of the slender shear wall. These factors manifested in the rupturing of the principal web reinforcement and the abrupt rupturing of the Nitinol bar in the boundary of the Nitinol-reinforced wall. As such,

it is recommended that comparing drift capacities overall is a more adequate means of examining the response of flexural Nitinol-reinforced shear walls. The wide hysteresis of the steel-reinforced wall indicated greater energy dissipation in comparison to the pinched hysteresis of the Nitinol-reinforced wall, however, self-centering was more evident in the later. At the end of testing, The Nitinol-reinforced wall was able to achieve 92% recovery from lateral displacement compared to 31% by the steel-reinforced wall. The high lateral recovery capacity of the Nitinol-reinforced wall also rectified rotation and shear strain in addition to closing cracks by an average of 88% as compared to 24% in the conventional wall. Overall, the damage sustained by the Nitinol-reinforced wall was significantly less and more readily repairable at the completion of testing. The crack pattern at 3% drift (72mm displacement) is shown in Figure 2.4b for the steel-reinforced wall and in Figure 2.4c for the Nitinol-reinforced wall.

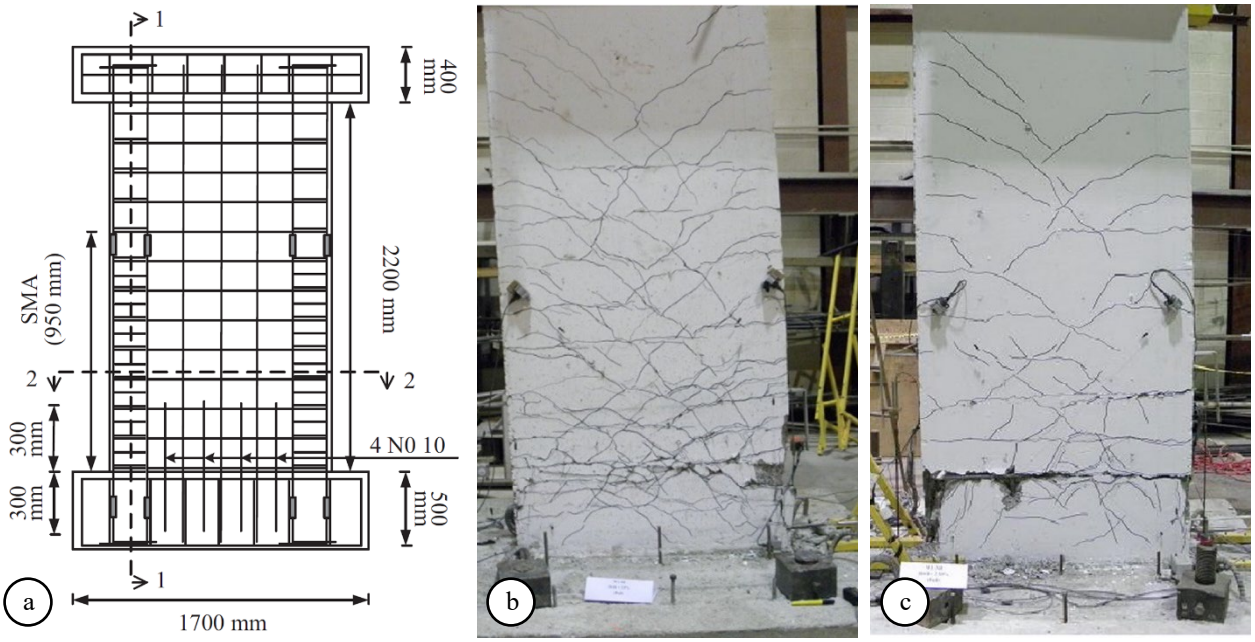

Figure 2.4. Slender shear walls: (a) reinforcement details; and damage patterns at 3% drift for (b) steel-reinforced wall; and (c) Nitinol-reinforced wall (Abdulridha and Palermo, 2017).

The study by Abdulridha and Palermo (2017) included a 2-dimentional numerical simulation of the shear walls using nonlinear finite element analysis (NLFEA) software VecTor2. The walls were modelled using a planar element mesh of multiple regions with assigned material properties. The behaviours and characteristics of concrete and steel were governed by material constitutive models. In a similar fashion, Abdulridha and Palermo (2017) developed a constitutive model to closely represent the true hysteretic response of superelastic Nitinol, including improved features for the gradual increase in residual plastic strain when unloaded and degradation of the lower stress plateau. The newly developed Nitinol constitutive model led to accurate prediction of the hysteretic response and failure mode of the experimental specimen.

Wang and Zhu (2018) conducted a numerical study on similar rectangular section large-scale four-story slender Nitinol-reinforced concrete shear walls. The walls had an aspect ratio of 3 with a height of 3660mm and a length of 12200mm. The walls had a thickness of 102mm with equal story heights at 915mm. Eight longitudinal Nitinol bars were embedded and spliced to deformed steel bars within each of the boundary regions and equally divided over two reinforcement curtains. Steel jackets were placed around the end boundaries to protect the wall from spalling and toe crushing throughout the load reversal cycles. More details on the reasoning for the length of the Nitinol bars and detailing of the boundaries within the plastic hinge region are available in the paper by Wang and Zhu (2018). The walls were benchmarked under reverse cyclic loading, using software OpenSees, prior to a comprehensive parametric study considering the variability of some design parameters. The investigation considered the effects of the axial compressive load ratio, length of end boundaries, and reduced lower plateau stress. The results showed near complete lateral displacement recovery for up to the peak 2.5% drift. At 2.5% drift, the highest axial strain in the Nitinol bars was approximately 3.3%, leaving a wide margin for ductility and self-centering, relative to the nominal 6% axial strain recoverability limit for Nitinol. Increasing the length of the end boundaries, by up to half the length of the wall at 610mm, increased the drift recovery and resulted in minor damage not requiring repair, contrary to the expectation of rocking and a large gap at the base of the wall. In contrast, the wall models with the initial end boundary length of 172mm, also had high lateral drift recovery, however required repair to the web of the wall. Overall, the results suggest that applying traditional design parameters of reinforced concrete walls to Nitinol-reinforced walls may not be the most efficient way of harnessing the seismic resiliency of a self-centering structure.

A numerical study including rectangular section walls and coupled walls was completed by Ghassemieh, et al. (2012) using program ABAQUS for dynamic loading. The rectangular section walls had an aspect ratio of 3 at a height of 15000mm and a length of 5000mm. The walls were 300mm thick. The coupled walls had similar dimensions, except the length of each wall was 3000mm. The coupling beams were 2400mm long with a cross-section that is 600mm deep by 300mm wide. Both walls represented five story structures with equal interstory heights of 3000mm. To investigate the elimination of residual drift in buildings, the study opted to replace all longitudinal conventional reinforcing bars throughout the total height of the shear walls with Nitinol. The principal reinforcement in the coupling beams of the coupled walls were also replaced with Nitinol. Different diameters and spacings were considered for the Nitinol bars to address the required reinforcement percentages in contrast to using conventional deformed steel. Based on preceding findings, a simplified material constitutive model was programed for the SMA material, assuming no cyclic strength degradation and no residual strain upon unloading. The bond relationship between the SMA reinforcing bars and concrete was not explicitly stipulated by the authors. Thus, it is assumed that the full replacement with Nitinol bars implies only a material change but maintains the same bond conditions as for deformed steel bars. The time history simulations used ground motion records from two seismic events. The results for both types of wall showed significant recovery capacity over their conventional counterparts. The regular shear wall had 60% and 75% reduction of residual displacements for the two earthquakes. The residual displacements of the coupled wall were reduced by about 83%. Maximum displacements were also reduced by about 46% for the coupled wall, but no significant change was recorded for the regular shear wall. Based on the presented results, the walls were remodeled to include different

ratios of steel and Nitinol, which shoed further improvement in the dynamic response of the walls. It was concluded that the improvement was dependant on the percentage of Nitinol reinforcement.

2.4.1.2 Beams

In a report to the Nevada Department of Transportation, Ayoub, Saiidi, and Itani (2003) detailed an exploratory experimental study on Nitinol SMA-reinforced concrete beams and cubes. The objective was to use superelastic Nitinol to observe its performance in confining concrete, reducing unloaded crack widths, and minimize plastic deformations resulting from cyclic loading. At the time of the study no research had been done on confining concrete with Nitinol, and little research was available on the use of superelastic Nitinol reinforcement in concrete structures. Eight concrete beam specimens were all built the same with a reduced mid-section to allow for external coupling of the reusable Nitinol bars. Each beam was 1525mm long (60inch). The mid-section of the beam measured 152mm deep by 127mm wide (6inch by 5inch) over a length of 711mm. The reduced depth of the mid-section allowed for placement of the Nitinol tension reinforcement at variable depths from the extreme compression fiber. The ends of the beam had a cross-section measuring 305mm deep by 127mm wide (12inch by 5inch). A variety of combinations of steel and Nitinol bars were arranged over the eight beams using 9.525mm diameter and 12.7mm diameter superelastic Nitinol bars of 127mm lengths. The 9.525mm bar was reduced at mid-length to a diameter of 6.35mm, and the 12.7mm bar was reduced to a diameter of 9.525mm. The Nitinol bars were integrated into the beams using threaded mechanical couplers. The ends of the beams were over-reinforced for strength. The beams were tested under cyclic loading at increasing increments of half the yield load, under a consistent loading rate. Eleven 152mm (6inch) concrete cubes were made to investigate confinement as well as reduced crack widths and overall damage. Two orthogonal holes were left through the centre of cube to fit the two diameter sizes of Nitinol bars. The Nitinol bars had threaded anchorage and bore against 4inch thick steel plates at each end to produce confinement. The cubes were tested under uniaxial monotonic and cyclic loading until a significant drop in bearing strength was detected. The test results from the beams showed great ability to control deformation when using superelastic Nitinol reinforcement (Saiidi, et al., 2007). Nitinol-reinforced beams had compatible ductility to the steel-reinforced beams, but with approximately 60% lower stiffness. Plastic deflection was reduced by up to 75% in the Nitinol-reinforced beams. The average residual displacement for a Nitinol-reinforced beams was less than one-fifth of that in the control specimens, which retained approximately 4.25 times greater strain. The test results from the cubes indicated a need for continued research and refinement of experimental approaches to investigate the confinement of concrete with Nitinol. The peak bearing strength of Nitinol-confined cubes was approximately 73% of the capacity of the steel-confined counterparts. The lower modulus of elasticity of Nitinol allowed early crushing of concrete at lower loads. Overall, the described method of confining concrete with Nitinol rods did not produce any improvement in deformation recovery. Hybrid Nitinol-steel reinforced concrete systems were deemed most effective and efficient for deformation recovery.

Abdulridha, et al. (2013) expanded on the investigation of SMA-reinforced concrete beams, using a hybrid reinforced system with embedded superelastic Nitinol reinforcing bars. Seven simply supported flexure-controlled beams were designs using deformed steel and Nitinol bars. The beams were 2800mm long, with a supported clear

span of 2400mm. the cross-section was 125mm wide and 250mm deep. The 600mm long Nitinol reinforcing bars were spliced by threaded couplers to conventional deformed steel bars at mid-span. Each Nitinol bar was machined over 300mm centred at mid-length to reduce the diameter from 12.7mm to 9.5mm for controlled failure away from the coupled ends. More so, the couplers were positioned outside of the anticipated flexural plastic hinge region to maintain the integrity of the splice. The beams intended for monotonic and cyclic loading had the Nitinol bars positioned as tension retracement only. Three other beams intended for reverse cyclic loading had the Nitinol bars positioned in a symmetrical manner for both tension and compression reinforcement, as seen in Figure 2.5. Experimental testing followed two main loading protocols. Monotonic loading was applied in increments of 5kN until failure. Cyclic and reverse cyclic testing followed the displacement-controlled protocol of the ATC-24 standard. The Nitinol reinforcement significantly improved the performance of the flexural beams in contrast to the conventional specimens. The Nitinol-reinforced beams exhibited similar ductility but a higher peak load capacity than steel-reinforced beams. Under cyclic loading, the Nitinol-reinforced beams dissipated a similar amount of energy as the steel-reinforced beams. The energy dissipation of the Nitinol-reinforced beams under reverse cyclic loading was approximately 54% of the conventional beams, however, lower residual deflection and smaller crack widths were directly observed. The Nitinol-reinforced beams had displacement recoveries mostly above 80%, whereas the steel-reinforced beams had average recoveries of approximately 26% under cyclic loading and 17% under reverse cyclic loading. Crack widths were able to recover by upward of 80% for the Nitinol-reinforced beams but remained well below 50% for the conventional beams. Overall, the large Nitinol reinforcing bars demonstrated consistent and reliable behaviour in agreement with the results produced from other experiments with smaller specimens.

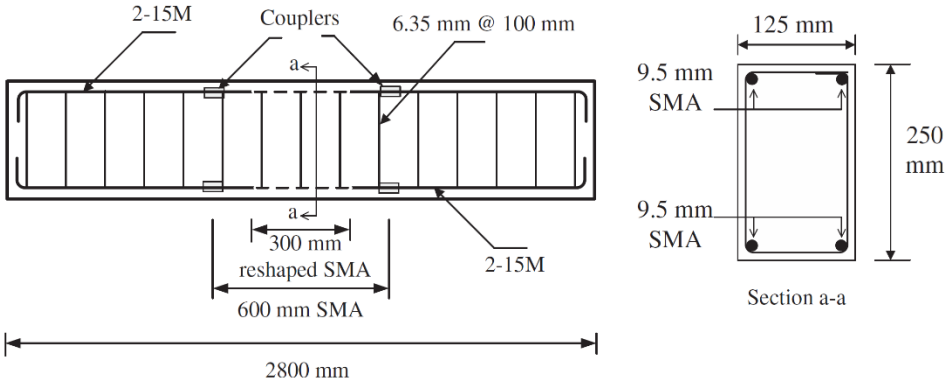

Figure 2.5. Detailing of Nitinol-reinforced concrete beam (Abdulridha, et al., 2013).

Alternatively, Deng, Li, and Sun (2006) investigated concrete beams reinforced with embedded shape memory Nitinol wires. A total of 25 beam specimens were made using cross-sections of 50mm by 50mm or 40mm by 40mm, all at 465mm lengths. Most beams were reinforced with three or four 2.5mm diameter Nitinol wires. Only one beam was reinforced with two 3.5mm diameter wires. All Nitinol wires were pre-strained at room temperature to 8%, except

for one beam with wires strained to 6%, and embedded as tension reinforcement. The bond relationship with concrete and end constraints for the Nitinol wire reinforcements were not specified. The Nitinol wire reinforcements in all beams were actuated by raising the temperature of the material with an electric current. As the heated Nitinol recovered its original length, it induced an eccentric compressive force causing deflection at the midspan of the beams, which was recorded. The results highlighted correlations for recovery energy, pre-strain, and size of reinforcement. The most effective method of activation was through gradual increase of electric current. However, the thermoelectric energy dissipated to actuate the shape memory Nitinol was independent of the procedure for the applied actuation method. Greater pre-strain was directly correlated with greater flexural deflection. Finally, it was identified that smaller diameter Nitinol wires had better actuation performance than an arrangement of larger wires of equal total cross-sectional area. As the findings seemingly direct attention to towards the bond condition between Nitinol and concrete, the practicality of the presented work is suggested for further research.

A similar experimental initiative was undertaken by Rojob and El-Hacha (2018) using shape memory iron-based SMA reinforcing bars in reinforced concrete beams. The beam specimens 2000mm long, with a clear span of 1800mm. the cross section was 305mm deep by 150mm wide. The beams were design as under-reinforced elements for ductile flexural failure. The 14.3mm diameter iron-SMA bars were produced as 1000mm long elements without a surface finish. Each beam was cast with a centerline groove along the tension fiber for near surface mounting of the iron-SMA bar. The anchored bars were then heated to initialize the shape memory effect to produce a prestressing force before being bonded in place with a cement-based grout. The iron-SMA reinforced beams were tested under 650 freeze-thaw cycles, through -34°C to +34°C, while supporting a load equal to 50% of the ultimate capacity of a control un-strengthened specimen. The sustained load was approximately equivalent to the service load expected to be carried by the beam. Another set of beams was produced but tested at room temperature for benchmarking. The strengthened beams exposed to the freeze-thaw cycles performed much better than their unstrengthen counterparts, but with minor strength variation from their replicated specimens tested at room temperature. The freeze-thaw cycles had deteriorated the cement-based grout to leave the iron-SMA bar exposed and unbonded, however, higher corrosion resistance was observed when compared to the corrosion accumulated by the internal deformed steel reinforcement. The strengthened beams exposed to extreme environmental conditions were able to demonstrate a satisfactory performance concluding with ductile failure as ideally expected from reinforced concrete beams. The near surface application is recommended for strengthening and rehabilitation projects. However, improvement of the surface finish is recommended to improve the bond to the existing surrounding material.

2.4.1.3 Columns

Nakashoji (2014) conducted a study on superelastic Nitinol-reinforced columns to improve the seismic behaviour of bridge piers. Two concept specimens and one control specimen were constructed at 30% scale. The specimens were designed to be tested as single column bridge piers. Each column had a 457mm (18inch) square cross-section and a height of 1575mm (62inch). The height of the columns was determined from the shortest pier of a reference bridge, as it is expected to have the greatest shear demand. A total of 16 longitudinal reinforcing bars were placed in a circular

arrangement and confined by spiraling transverse reinforcement. The 12.7mm diameter superelastic Nitinol bars were placed at the base of the column within the plastic hinge region and spliced to the deformed steel bars using mechanical couplers for headed bars. The Nitinol bars were embedded at two different projections within the columns to evaluate the impact of length on performance. In the first column, the Nitinol bars projected by 457mm (18inch), and by 343mm (13.5inch) in the second column. The Nitinol bars in both columns were embedded into the foundations by approximately 51mm (2inch). The coupled ends were presumably placed outside of the plastic hinge region, as later indicated from backtracked calculations of the lengths of the plastic hinge for each column. Both columns reinforced with Nitinol bars in the plastic hinge region were cast to full height using an engineered cementitious composite mix (ECC) in place of conventional normal concrete. The control specimen was reinforced with conventional deformed steel and completely cast with normal concrete. The loading point was integrated into the top of each column through a uniform cross-section. The foundation blocks were designed as rigid elements to anchor the column specimens against the applied lateral loads during testing. The detailing of a typical column specimen is presented in Figure 2.6.

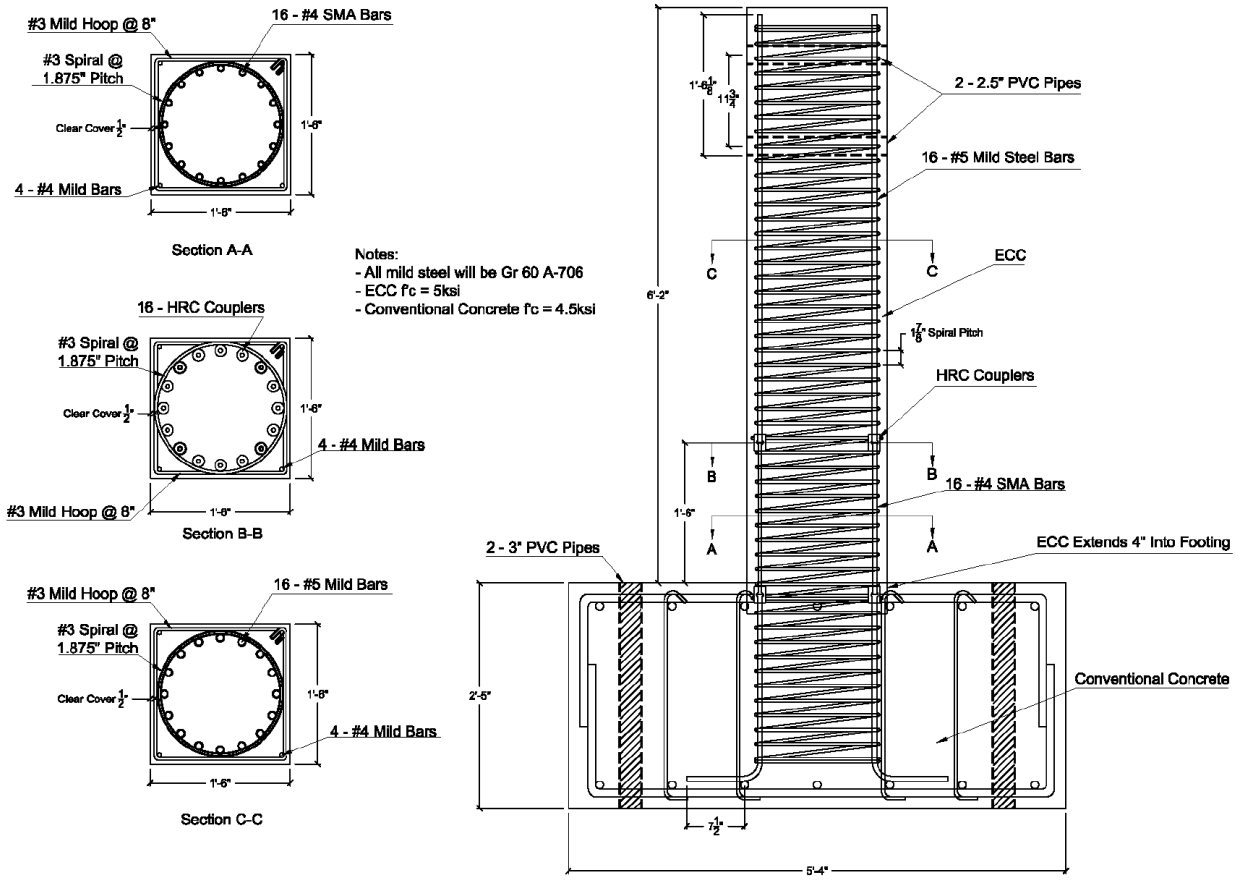

Figure 2.6. Reinforcement detailing of a 30% scale Nitinol-reinforced bridge pier column specimen (adapted from Nakashoji, 2014).

The columns were tested under lateral reverse cyclic loading with a scaled axial load of 663kN to simulate the tributary weight of the superstructure from the reference bridge. The custom cyclic loading protocol followed a pattern of two cycles at each drift level as summarized in Table 2.1. Lateral displacements were applied at a rate of 25.4mm/min (1inch/min) for drift levels below 3%. For 3% drift and higher, lateral displacements were applied at a rate of 127mm/min (5inch/min). A hydraulic actuator was used to impose drift in the positive and negative directions before unloading to complete the cycle. The experimental setup is presented in Figure 2.7.

Table 2.1. Custom reverse cyclic loading protocol (adapted from Nakashoji, 2014)

Drift (%)	0.25	0.5	1.0	2.0	3.0	4.0	5.0	6.0	8.0	10.0	12.0
Displacement (inch)	0.155	0.31	0.62	1.24	1.86	2.48	3.1	3.72	4.96	6.2	7.44
Displacement (mm)	3.9	7.9	15.7	31.5	47.2	63.0	78.7	94.5	126.0	157.5	189.0

Figure 2.7. Typical experimental test setup for reverse cyclic loading of bridge pier columns (Nakashoji, 2014).

For numerical analysis and parametric study using program OpenSees, four Nitinol bar specimens were sampled for tensile testing. Two bars were 457mm long and the other two were 343mm long to match the bars used in the column specimens. One bar of each length was used for standard testing according to ASTM F2516. The other two

bars were tested following a cyclic tensile loading profile of two cycles at each strain target, which started with quarter intervals of 1% strain, followed by two cycles at each increment increasing by 1% up to 8% strain. Each Nitinol coupon was coupled to #5 (15.9mm diameter) deformed steel bars at each end to replicate the in-situ loading conditions of the Nitinol reinforcement, and to provide an improved grip over the smooth surface of the Nitinol bars. The bars tested according to ASTM F2516 ruptured at approximately 7% strain. Both coupons experienced a facture occurring at the base of the transition to one of the headed ends. The other two bars tested through cyclic loading completed strain cycles to 6% before failing. The longer bar ruptured in a similar manner to the others at the transition to one of the headed ends, and the shorter bar ruptured along its length. It was speculated that the heat applied during the forging process of the headed ends may have locally altered the properties of the Nitinol bars leading to fracturing at the base of the transition to the rest of the bar. The results of the numerical analysis and parametric study are discussed in detail in the thesis publication by Nakashoji (2014). The tested properties of the Nitinol coupons are summarized in Table 2.2.

Table 2.2. Performance points for wall SWN (adapted from Nakashoji, 2014)

Parameter	**Expected**	**Average Measured**	
		18inch Bars	**13.5inch Bars**
Austenite modulus, k_1	5500 ksi (37900MPa)	4450 ksi (30682 MPa)	4880 ksi (33646 MPa)
Post yield stiffness, k_2	250 ksi (1725 MPa)	260 ksi (1793 MPa)	265 ksi (1827 MPa)
Austenite yield strength, f_y	55 ksi (380 MPa)	51 ksi (352 MPa)	57 ksi (393 MPa)
Lower plateau stress factor, β	0.65	0.41	0.35
Secondary post-yield stiffness ratio, α	0.3	0.38	0.3
Ultimate Strain, ε_u	10%	6.50%	6%

The experimental testing of the columns ended at different drift levels in relation to the fracturing of the longitudinal reinforcement and significant drop in lateral load capacity. The column with the 457mm long Nitinol bars concluded testing at the end of one cycle to 12% drift. At the conclusion of 11% drift, two Nitinol bars had ruptured, followed by four more bars rupturing through the negative excursion to 12% drift. The column with the 343mm long Nitinol bars completed one cycle of 8% drift before concluded testing at the end of 10% drift. The first rupture of a Nitinol bar occurred during the first negative excursion to 6% drift, however, the column maintained more than 85% of its load capacity. Four additional bars ruptured throughout the 8% drift cycle. An additional six Nitinol bars fractured throughout the 10% drift cycle. The control column concluded testing at the end of one cycle of 8% drift. The first rupture of a longitudinal bar occurred during the second negative excursion to 6% drift. The longitudinal bars

continued to rupture throughout the 8% drift cycle. The results reflected the favourable performances of the Nitinol-reinforced columns. The column with the long Nitinol bars had an approximately 83% greater drift capacity, and the column with the short Nitinol bars had approximately 33% greater capacity, over the conventional reinforced concrete column. When benchmarked at 3% drift, the Nitinol-reinforced columns had recovered by approximately 95% compared to approximately 50% for the control column. The residual drift of the column with the long bars was approximately 0.17%, and 0.15% for the column with the short bars, in comparison to approximately 1.5% for the control column. The self-centering capacity of the columns was not hindered by the shortened length of the superelastic Nitinol bars. The ECC supplemented the performance by limiting the damage to a singular major crack at the base of the columns and some minor spalling. In the control column, damage included major spalling, crushing of the concrete through to the core, and buckling of the longitudinal reinforcement. When the concrete was removed for further inspection of the tested columns, it was observed that the Nitinol bars had ruptured along their length or at the transition to one of the headed ends. Nonetheless, the rupturing of the Nitinol bars had occurred at such a severe drift level that it is suspected to have little to no bearing on the performance of the Nitinol-reinforced columns. Tazarv and Saiidi (2017) elaborate on improving the performance of the column by confining the plastic hinge with FRP.

Billah and Alam (2012) conducted a similar analytical investigation on hybrid Nitinol-reinforced columns, where deformed steel longitudinal reinforcement was completely replaced with combinations of Nitinol, fiber reinforced polymer (FRP) bars, and stainless steel. Deformed steel bars were used only for transverse reinforcement. The objective of the study was to assess corrosion-resistant and damage reducing reinforcement combinations. Three longitudinal reinforcement combinations were considered. Combination A used Nitinol bars in the plastic hinge, coupled to stainless steel bars. Combination B used Nitinol bars in the plastic hinge, coupled to FRP bars. Combination C used stainless steel bars in the plastic hinge, coupled to FRP bars. The Nitinol bar had a 20.6mm diameter, the #6 FRP bar had a 19.1mm diameter, and the 20M stainless steel bar had a 19.5mm diameter. For control, a column with continuous stainless steel longitudinal reinforcement was considered. It is presumed from the available figures that the stainless steel bars are deformed, the FRP bars are glass fiber and sand coated with epoxy, and the Nitinol bars are smooth. These surface conditions presented compatibility challenges for mechanical coupling. Combinations of modified screw-lock couplers and epoxy were tested against slip to determine the best coupling arrangement for each combination of longitudinal bars. The columns had a 450mm square cross-section and a total height of 3200mm. The plastic hinge was estimated to a height of 468mm, which was intersected by the couplers for each of the eight longitudinal bars in each column. Normal concrete was used for all columns. Specific details of the constitutive material models and model parameters used for analysis in program SeismoStruct are discussed more elaborately by Billah and Alam (2012). The columns resembled ground level interior columns of a six-story building in Vancouver, Canada. A constant axial load of 400kN was applied to simulate the tributary gravity load supported by the column. The column models were subjected to a quasistatic monotonic loading and a dynamic time history analysis. The pushover analysis was used to characterize the initial stiffness, yield displacement, peak shear capacity and onset of concrete crushing of the columns. The columns were then subjected to 20 different ground motion records ranging in magnitude from 6.5 to 6.9. The dynamic analysis was used to determine the demand capacities for base shear, energy dissipation, and residual displacement for each column. The columns integrating Nitinol typically had a base shear

capacity to demand ratio slightly below 2, whereas the columns with stainless steel bars through the plastic hinge had ratios slightly above 2. The stainless steel control column had the greatest ductility, which was approximately 50% greater than the column with the stainless steel and FRP combination, 80% greater than the Nitinol and stainless steel combination, and 200% greater than the Nitinol and FRP combination. Of the three reinforcement combinations, the column with stainless steel and FRP had the highest energy dissipation. However, the predominant advantage was found in columns integrating Nitinol reinforcement in the plastic hinge, which had reduced residual displacement by up to 87% and were more likely to remain serviceable after an earthquake. The column reinforced with the Nitinol and FRP combination was the most preferred system for seismic resilience and low maintenance cost.

An experimental study relevant to columns by Shin and Andrawes (2010) explored the use of the nickel-titanium-niobium (NiTiNb) ternary alloy, a nickel-titanium SMA variant, for spiralled confinement of concrete. The test specimens were sets of 152mm diameter cylinders, 305mm tall, cast using normal concrete. Cylinders confined with NiTiNb spirals, cylinders additionally confined with glass fiber reinforced polymer (GFRP) wrap, and cylinders confined with GFRP wrap only were to be tested under uniaxial compression against unconfined control cylinders. The spiral was made of 2mm diameter wire. The GFRP wrap had a thickness of 0.11mm. The spiral was pitched at 13mm for cylinders confined by the SMA wire only. Two other sets were produced for cylinders additionally confined by GFRP wrap. The first set of cylinders was wrapped with two layers of GFRP and confined with the SMA wire at a pitch of 25mm. The second set of cylinders was wrapped with four layers of GFRP and confined with the SMA wire at a pitch of 13mm. Four other sets of GFRP confined cylinders were produced with of 2, 4, 8, and 10 layers. The NiTiNb alloy was first pre-strained to 6% before being applied to the concrete cylinders. The shape memory effect of the NiTiNb alloy was then triggered by evenly heating the spiral in an oven to 160°C to produce a confining pressure through the recovery stress of the alloy. The cylinders confined by the NiTiNb spiral increased in compressive strength by approximately 21% and had an ultimate strain that was approximately 24 times greater relative to unconfined concrete cylinders. The combination of the SMA spiral with GFRP wrap delayed rupturing of the GFRP wrap which allowed the concrete cylinder to withhold its peak strength to failure by up to 60%. The ultimate strain of the hybrid confined cylinders increased by approximately 30 times for two layers of GFRP, and by approximately 25 times for four layers of GFRP wrap. The application of shape memory NiTiNb spirals to confine concrete presents a feasible rehabilitative means of confining concrete to improve ductility.

2.4.1.4 Beam-Column Joints

Youssef, Alam, and Nehdi (2008) integrated superelastic Nitinol reinforcing bars into beam-column joints to improve their seismic behaviour at the plastic hinge. Two 75% scale experimental beam-column joint specimens were constructed. The Nitinol-reinforced specimen had four 20.6mm diameter smooth Nitinol bars spliced to 20M (19.5mm diameter) deformed steel longitudinal reinforcement at the end of the beam interfacing the column. The 450mm long Nitinol bars were coupled using conventional barrel couplers with screw lock bolts. The Nitinol bars projected 360mm into the end of the beam where the couplers were intersected by the end of the estimated length of the plastic hinge. The remaining 90mm of the Nitinol bars were embedded into the column and coupled to hooked deformed steel bars.

An identical beam-column joint specimen was constructed using conventional materials for control. The beam-column joint was derived from an eight-story reinforced concrete reference building situated in western Canada. The specimen is constructed to resemble an exterior configuration centered along the sixth floor. The beam and column were scaled to a depth of 400mm and a width of 250mm. The beam had a length of 1830mm from the centerline of the column and was aligned at mid-height. The column had a total height of 3000mm. The reinforcement detailing typical beam-column joint specimen is presented in Figure 2.8.

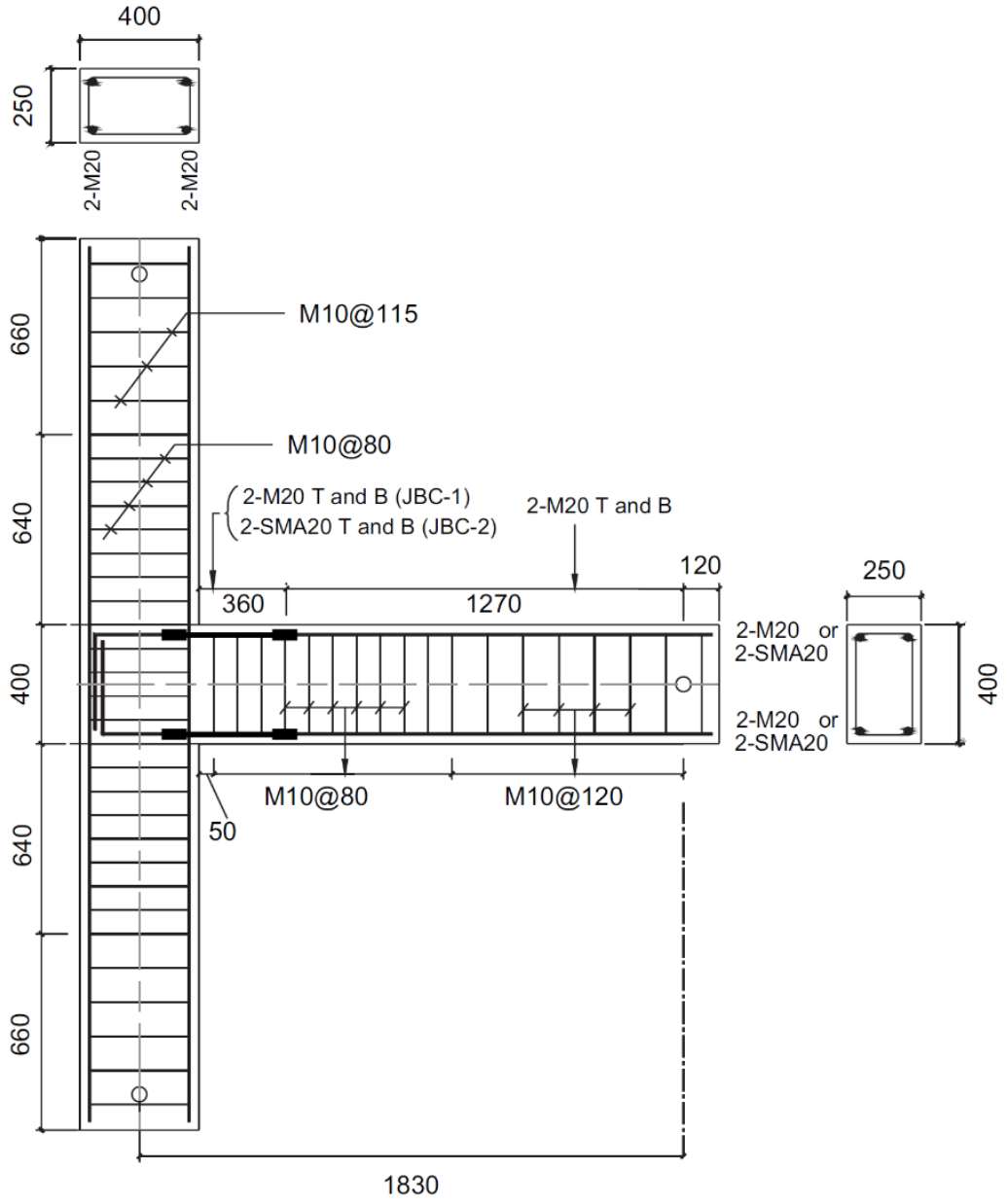

Figure 2.8. Typical beam-column joint specimen (adapted from Youssef, Alam, and Nehdi, 2008).

The test setup was arranged so that the column was pinned at the top and bottom, coinciding with the points of contraflexure, and the free end of the beam was supported by the hydraulic actuator which would impose the reverse cyclic loading sequence. A secondary hydraulic actuator maintained a scaled constant axial load of 350kN to the column to account for the tributary gravity load supported by it. Loading at the end of the beam was applied in two stages. The first stage was load-controlled. The sequence started with two cycles at 10% of the estimated yield capacity of the beam. The following two cycles were imposed to observe flexural cracking. Another two cycles were subsequently applied to yield the longitudinal reinforcement. Determining the yield load and displacement marked the end of the first stage. The second loading stage was displacement-controlled. The displacement amplitude was increased by an increment of the yield displacement for each consecutive set of two cycles. The displacement sequence concluded in correlation to a minimum story drift level of 7.9%, to exceed the collapse limit of the structure. The results support the future use of Nitinol to construct moment resisting frame structures with higher resilience to seismic events. At the conclusion of testing, the Nitinol-reinforced beam-column joint specimen had approximately 60% lower residual story drift than the control specimen, equating to an approximate recovery of 75%. Although the Nitinol-reinforced beam-column joint specimen dissipated less energy, the self-centering mechanism was evident. The use of superelastic Nitinol in the beam-column joint promoted ease of repair and maintained the integrity of the column by relocating to the onset of the plastic hinge away from the face of the column by an approximate distance equal to half the depth of the beam.

A similar experiment was later completed by Nehdi, Alam, and Youssef (2010) to include FRP bars in conjunction with the aforementioned Nitinol bars for application to structures constructed in corrosive environments. The Nitinol-FRP hybrid beam-column joint specimen suffered from slippage of the FRP bars from the couplers, however, the collected data still expressed negligible residual strain in the Nitinol bars. Regardless of the slippage of the FRP bars, the specimen was still able to support approximately 89% of its load capacity beyond collapse.

Suhail, et al. (2015) investigated an alternative approach to reinforcing beam-column joints externally using SMA and steel brackets. The study looked to resolve the challenges in externally confining concrete columns including non-circular sections by utilizing the shape memory effect of SMA materials. Different schematics are proposed by Suhail, et al. (2015) for retrofitting of the beam-column joints in seismically deficient reinforced concrete structures.

2.4.1.5 Prestressing Tendons

Nitinol has also been used for structural application as prestressing tendons for reinforced concrete structures. In one instance, a study by Shahin, Meckl, and Jones (1997) investigated the reduction of vibrations in a building by applying external Nitinol tendons. The analytical study compared the results of passive superelastic tendons and active shape memory tendons in minimizing the displacement difference between the base and the floor mass of a single story structure when exposed to a sinusoidal ground motion. In two geometrically similar simulation models, two tendons were applied in an opposing diagonal formation between the top and bottom of two flexible walls supporting the floor mass. The passive tendons were used to reduce vibration by increasing structural stiffness, thus the diameter of the tendons became the controlling variable. The active tendons functioned to reduce vibration by means of

contraction to produce opposing forces induced by the austenitic transformation from heating. The passive and active tendons were able to reduce the difference in displacement between the base and the floor mass by factors of 12 and 19, respectively. The shape memory tendons were approximately 60% more effective at controlling vibration of the structure.

Maji and Negret (1998) looked at utilizing shape memory Nitinol wires to apply additional restressing to concrete structures. The experimental study used 0.64mm diameter Nitinol wires to prestress two types of concrete mortar beams. Each beam measured 305mm long with a cross-section of 25mm wide and 13mm deep. The first beam was reinforced with a single prestressed four-wire strand, and the second type of beam was reinforced with two strands of the same. The reinforcement was centered at 1.9mm from the bottom of each beam. The beams were placed in a pure flexure loading assembly with a displacement gauge to measure deflection at the center of the beam upon activation of the shape memory effect of the Nitinol strands. The twisted wire strands were able to effectively provide sufficient mechanical bond to the mortar to transfer the prestressing stresses to the beam. These results facilitate a means to rectify prestressing losses in conventional steel tendons over time. More so, the capacity of reinforced concrete beam can be increased to meet future demands using the same prestressing technique.

Further experimental investigation on the use of Nitinol, and a variant of it, for prestressing tendons in concrete mortar beams was conducted by El-Tawil and Ortega-Rosales (2004). The objective of the research was to demonstrate a means of post-tensioning without the use of jacking equipment and to rectify short-term and long-term prestressing losses. Nitinol was used as 2.5mm diameter wires. Alternatively, the nickel-titanium-niobium (NiTiNb) ternary alloy was used in the form of 6.3mm diameter wires. Preliminary investigation resulted in the Nitinol wires posing challenges in maintaining the recovery stress at room temperature, prompting use of the proprietary NiTiNb alloy for beam reinforcement. Five beams were constructed at a length of 380mm with a cross-section measuring 25mm wide and 38mm deep. Prior to application, the ternary alloy reinforcement wires were prestressed to 15% strain. In two beams the ternary alloy reinforcement was embedded along the centerline of the beam, in the other two beams the wire reinforcement was embedded eccentrically. Post-tensioning was induced by heating the pre-strained tendons with an electric current. One additional beam reinforced in a similar manner to the first set was constructed, with the exception that the tendon was not pre-strained, to be used as a control specimen. All five beams were tested in a pure flexure test setup. The results highlighted the challenges in using shape memory Nitinol tendons as a permanent prestressing solution since precise temperature conditions are required to sustain the recovery stress, which made the application impractical in this study. The NiTiNb alloy presented a viable option, however, the recovery stress was approximately 45% lower when produced from a pre-strain of 15%. The performance of the NiTiNb alloy suggests that it is a more suitable candidate for commercial prestressing applications.

2.4.2 Structural Steel Connections

Steel structures have utilized shape memory alloys, including Nitinol, for fasteners and restrainers to improve the performance of end connections and achieve greater versatility of function under various loading conditions. Nitinol tendons and bars have been implemented in different forms to control the response of moment connections with partial

fixity. Ocel et al. (2004) used martensitic Nitinol bars to restrain the flanges of a beam to its supporting element, with the intention of recovering the functionality of the deformed connection with the application of heat. The experiment was successfully repeatable after recovering the initial shape of the tendons. Speicher, DesRoches, and Leon (2010) experimented with the same concept but using superelastic Nitinol tendons to harvest the benefit of self-centering. Further numerical and practical studies have been conducted on the design of beam-to-column connections using Nitinol by Yam et al. (2015).

2.4.3 Other Structural Applications

Nitinol has been further utilized in both its superelastic and shape memory phases to produce innovative products for structural applications. Research and development in earthquake engineering accelerated the implementation of Nitinol based technology to produce auxiliary structural elements such as bracing members, dampers and isolators, and bridge deck restrainers.

2.4.3.1 Bracing Members

Bracing members are common efficient structural elements used to stiffen structures against swap. In the context of seismic design, Effendy, et al. (2006) used SMA bars [assumed to be Nitinol based on the provided material properties] as external brace members to enhance the seismic performance of reinforced concrete squat walls. The objective of the study was to increase the ductility and energy dissipation capacity of shear walls in low-rise structures. Two types of SMA bracing bars were compared under reverse cyclic loading. The barbell type squat shear wall test specimens were fitted on both sides with a set of diagonal bracing members. One shear wall specimen had superelastic SMA braces and the other specimen had shape memory SMA braces. A displacement-controlled lateral load reversal sequence was applied to each wall until failure. A typical braced squat wall specimen tested to 1% drift is presented in Figure 2.9. The SMA bracing members improved the performance of the squat shear walls, however, with variable trade-offs. The wall with the superelastic braces had approximately 12% greater ductility and the highest strength at approximately 28% greater than the control specimen. The wall with the shape memory braces had the greatest ductility at approximately 29% greater and a strength improvement of approximately 17% over the control wall. However, the wall with the shape memory braces retained the greatest residual displacement, and the wall with the superelastic SMA bars was challenged with buckling of the bracing elements at the ultimate displacement of 2% drift. The hysteretic responses show that the wall with the shape memory braces dissipated more energy than the superelastic braced specimen. Overall, the SMA braces achieved the common benefit of diverting damage away from the end boundaries of the wall in comparison to the conventional control wall.

Auricchio, Fugazza, and DesRoches (2006) completed a similar numerical study using large diameter superelastic Nitinol bars to brace low-rise to mid-rise structural steel buildings. A dynamic analysis comparison of the superelastic Nitinol bracing members was made against buckling-restrained steel braces for control. The Nitinol bracing members

were significantly favoured for their ability to self-center the structures and minimize residual interstory displacements. However, some concern was raised regarding the high forces developed during the martensitic transformation and the rigidity of the connections to the structure which way inadvertently cause damage to the primary beams and columns. As such, further research is recommended to refine the design parameters for superelastic Nitinol bracing elements.

Scaled model shake table experimental tests conducted by Lafortune, et al. (2007) elaborated on the use of Nitinol bracing members to further assess their benefits. In this study shape memory pre-strained Nitinol and superelastic Nitinol were compared against conventional steel. The results indicated that the best seismic performance was obtained from shape memory Nitinol braces that were pre-strained between approximately 1% to 1.5%, after which the benefits diminished. The pre-strained Nitinol braces were successfully able to reduce the maximum displacement of a structure by dissipating a significantly larger amount of energy throughout the drift. The experimental results were later verified numerically and were found consistent.

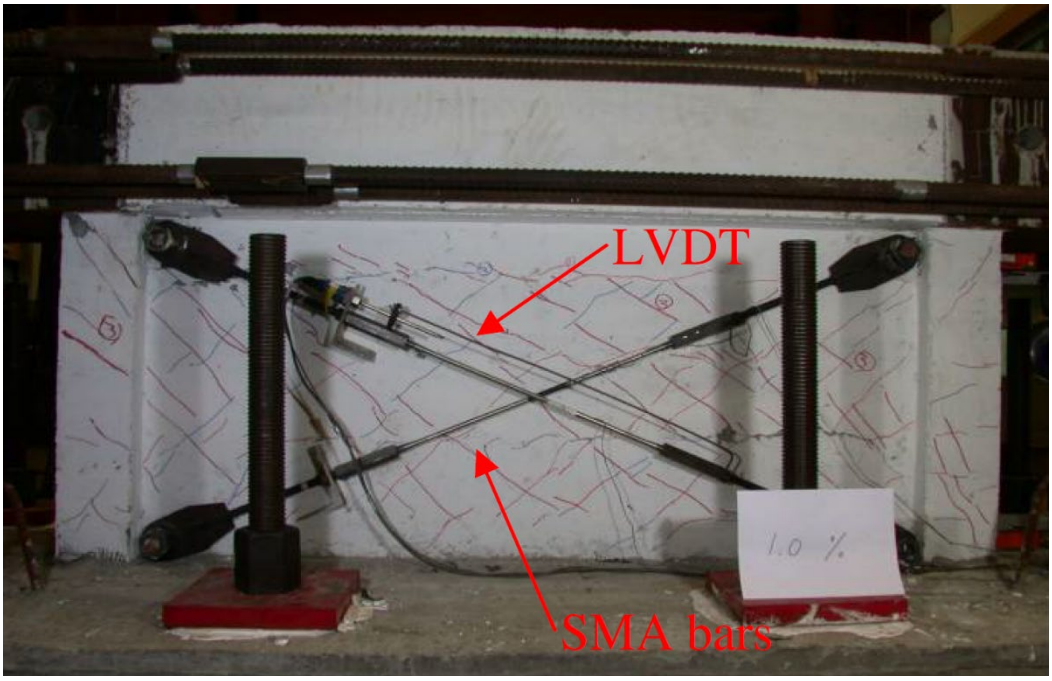

Figure 2.9. Squat shear wall specimen externally braced with Nitinol bars (Effendy, et al., 2006).

2.4.3.2 Dampers and Isolators

Dampers and isolators are evolving protective technologies used to control the response of structures to seismic excitation. Dampers help by absorbing some of the seismic energy, whereas isolators interrupt the transmission of that energy from the ground and into the structure. Experimental and analytical research initiatives have integrated Nitinol to advance the development of seismic dampers and isolators.

A barrel-shaped piston-type damping device was developed by Zuo, et al. (2006) using superelastic Nitinol 1mm diameter wires within a self-contained system. Inside the damper, a sequence of Nitinol wires produced a restrictive force against the sleeve of opposing pistons to generate the damping effect from the induced friction. The Nitinol wire dissipated energy by maintaining a frictional resistance for small displacements and supplemented the damping response by straining under larger displacements. The damping device was experimentally tested under dynamic loading in an environment with a 25°C ambient temperature. The damper was evaluated based on its response to the influence of loading frequency and displacement amplitude. The loading frequency was found to have negligible impact. The displacement amplitude correlated with the strain level and phase transformation of the superelastic Nitinol. Within the austenite elastic range, the damper showed little change in stiffness and the dissipated energy related linearly with the applied displacement. When the displacement amplitude became large enough to produce sufficient strain in the Nitinol for martensitic transformation, the secant stiffness of the damper decreased, however, the dissipated energy increased. At this stage, the damping effect became a product of the frictional resistance, between the pistons and the sleeve, which is generated by the recovery force in the superelastic Nitinol wires. The design schematic of the piston-style damper is presented in Figure 2.10.

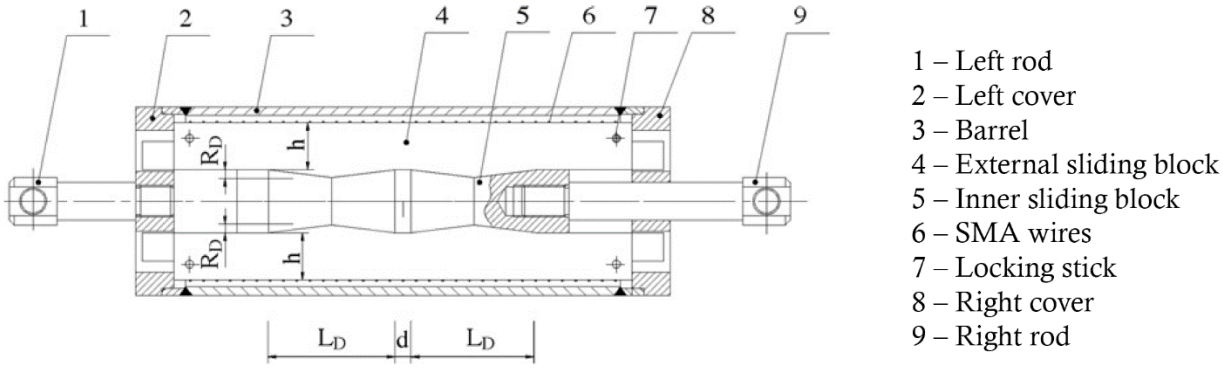

Figure 2.10. Piston-style damper with Nitinol wire (adapted from Zuo, et al., 2006).

The damping device created by Clark, et al. (1995) was constructed using fine 0.447mm diameter superelastic Nitinol wires configured in layered loops anchored by steel connections at each end. The damping device, which is suited for low to mid-rise buildings, was configured as an individual unit or a paired set. Prior to testing, the damper devices were pre-strained to 6% to condition the wires to a uniform state. Each device was then tested in-plane under a sinusoidal dynamic loading protocol. The dynamic testing considered the variability of load frequency, strain amplitude, and ambient temperature to characterize the failure mechanism and the ultimate capacity for each device. A nonlinear finite element analytical study was performed to verify the results using a six-story building model. The results were generally consistent and predictable but sensitive to differences in strain rate and loading history. Overall, the paired damper had the best performance, whereas the single damper presented variable responses, requiring further investigation. A quantified control of the wire strain conditioning is speculated to mitigate performance variations.

Dolce, Cardone, and Ponzo (2006) discuss the design of a similar device using a fine-tuned set of superelastic Nitinol wires to produce a seismic base isolator. The base isolation systems using Nitinol presented the benefit of self-centering, but had the disadvantage of transmitting high frequency vibrations, and inducing high interstory accelerations.

2.4.3.3 Bridge Deck Restrainers

Superelastic Nitinol has been used to develop a variety of bridge deck restrainers to control the displacement and unseating of the superstructure during seismic events. The restraining devices can be applied in new construction, or for repair and retrofitting. The restrainer design investigated by DesRoches and Delemont (2002) was tested at full-scale using superelastic Nitinol bars. The tension-only design proposed that the travelling end of the bar would be mounted to the underside of the girder and the opposite end would be fixed to the pier or abutment. A three-span bridge with simply supported girders was used as the reference structure for the design of the restrainer. The end spans measure 12.2m and the middle span measured 24.4m. The dimensions of the bar were suited to the details of the bridge with a tolerance to temperature-induced changes in the Nitinol. Each restrainer bar had a total length of 280mm at a diameter of 38.1mm, which was tapered down to an effective length of 152.4mm at a diameter of 25.4mm. The ends of each bar were threaded for mounting including a gap for thermal tolerance. The bars were assessed experimentally and by nonlinear analysis through a cyclic loading sequence to 8% strain. The results presented a superior performance in comparison to a steel cable restrainer used for control. The Nitinol restrainer behaved much more effectively at reducing displacements at the abutments and over the piers, by an approximate range of 42% to 63%, due to the increased stiffness from strain hardening of the Nitinol. The Nitinol was able to dissipate an overall comparable amount of energy by remaining elastic throughout multiple cycles of large displacements. The Nitinol restrainer maintained minimal residual deformations unlike the continuous plastic deformation of the steel cable restrainer. The Nitinol bar restrainer concept is presented in Figure 2.11.

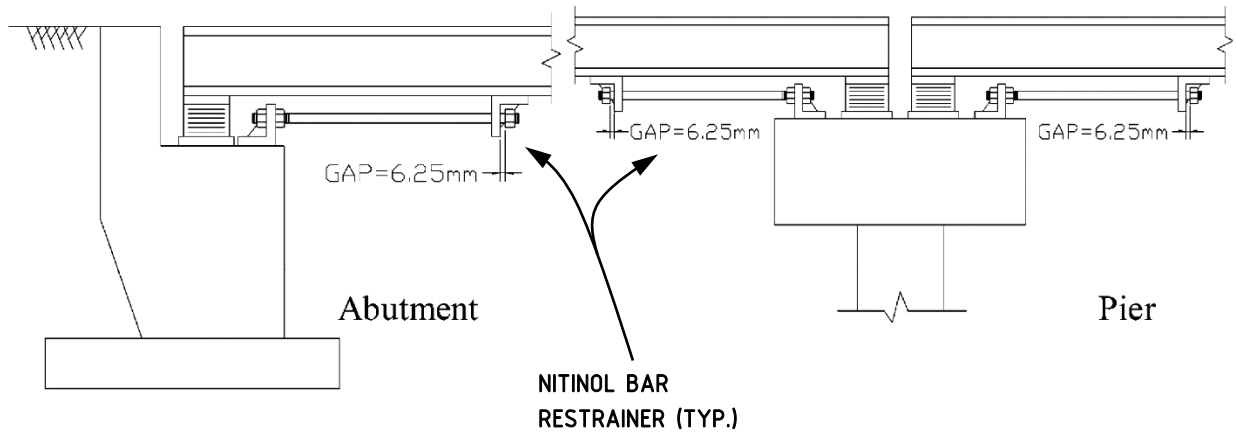

Figure 2.11. Nitinol bar bridge deck restrainer (adapted from DesRoches and Delemont, 2002).

Choi, Lee, and Choei (2009), elaborated on the bar restrainer design by seeking to improve its utility throughout both the tension and compression branches of the loading cycle. Axial compression of Nitinol bars risks the potential of buckling and designing to prevent it adds material and complexity which increases the cost of the restrainer device. Bending the Nitinol bar is a more efficient and practical method of resisting lateral load reversals. The study repeated a similar experiment using an identical superelastic Nitinol bar specimen as described by DesRoches and Delemont (2002). Instead of controlling displacement through axial tension loading, Choi, Lee, and Choei (2009) altered the end conditions of the bar to take advantage of strain recovery from single and double bending. For single bending, the bar was fixed on one end and allowed to translate and rotate on the opposite end using a ball joint. For double bending, the bar was only allowed to translate on the opposite end. The bar was tested under variable loading speed and displacement amplitudes. The results of the new bending bar design showed significant performance improvement. The double bend increased the stiffness of the bar by about five times over a single bend. Similarly, damping increased by approximately 67% as compared to when the bar is under tension. The benefit of strain hardening to control large displacements was the same under bending as observed under tension. Overall, the bending bar restrainer is speculated to significantly reduce damages caused by large displacements at the end of the girders such as collision of concrete elements, and destruction of bearings and expansion joints. The Nitinol bending bar restrainer concept is presented in Figure 2.12.

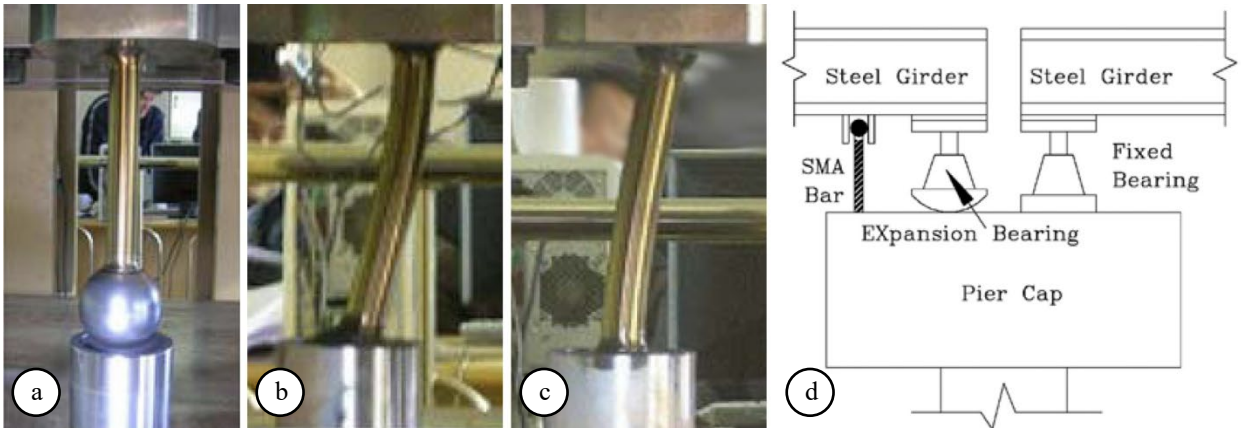

Figure 2.12. Nitinol bending bar restrainer: (a) assembly; (b) single bending, (c) double bending; and (d) application to a bridge deck (adapted from Choi, Lee, and Choei, 2009).

Johnson, et al. (2008) used superelastic Nitinol wires for an alternative bridge deck restrainer which would be used to connect the ends of box girders together against large displacements. The 1160mm long restrainer was made using a bundle of 84 wires and a bundle of 130 wires to be compared to a steel control specimen. The Nitinol wire had a diameter of 0.584 mm. A restrainer was mounted on each side to link two concrete box girders throughout shake table testing using ground motion records. The Nitinol had compatible strength to the steel retraining, however, was

more durable at maintaining strength and stiffness throughout several loading cycles. The Nitinol restrainer dampened the acceleration of the girders and reduced the maximum in-span displacement between by approximately 50%, in addition to achieving near complete displacement recovery to prevent unseating from the bearings. The concept of the Nitinol wire restrainer and its application are presented in Figure 2.13.

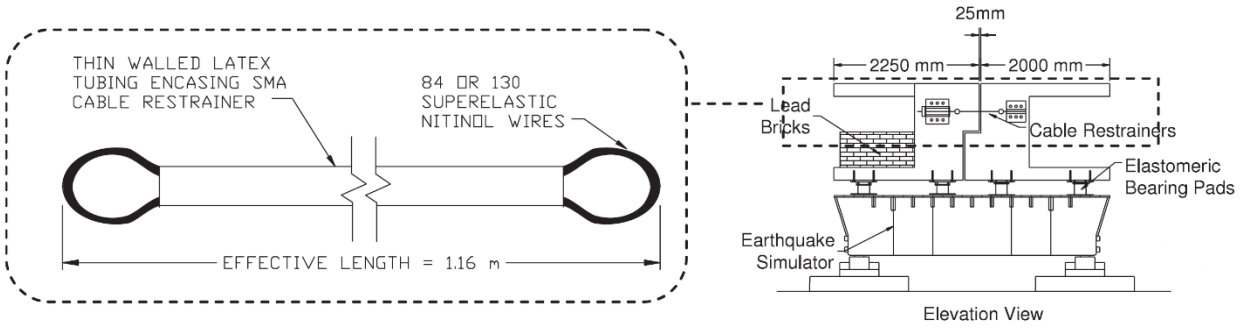

Figure 2.13. Nitinol wire restrainer (on left) applied to concrete box girders (on right) (adapted from Johnson, et al., 2008).

2.4.4 Hybrid Composites

The superelastic and shape memory properties of Nitinol contribute substantial mechanical possibilities never before possible with such high versatility in conventional construction materials. Among the smart materials employed in construction, Nitinol has the most diverse characteristics including high ductility, corrosion resistance, deformation recovery, damping capacity, and durability. When Nitinol is combined with other smart materials, smart composites are developed to provide economically feasible custom solutions to complex structural challenges. A popular research topic is the integration of Nitinol and glass fiber reinforced polymer (GFRP) for reinforcing bars. The intended product is an economic high strength, ductile, and corrosion-free reinforcement alternative. Another topic of interest is the embedment of Nitinol in engineered cementitious composite (ECC) to achieve more durable plastic hinges in reinforced concrete structures.

2.4.4.1 Fiber Reinforced Polymers Hybrid

The connection between Nitinol and glass fiber reinforced polymers (GFRP) has raised interest and challenges, drawing responses on both the macro and micro level. The smooth yet hard surface of round Nitinol bars is sensitive to pressure concentrations, and the epoxy sand coating or deformed epoxy jacket on GFRP bars is susceptible to stripping. A variety of efforts are explored to successfully achieve a Nitinol-GFRP hybrid.

Alam, Youssef, and Nehdi, (2010) addressed an economic and effective means to couple Nitinol and GFRP bars. The objective of their study was to utilize the high strength of GFRP while allowing Nitinol to achieve its superelastic

strain capacity under cyclic loading. The tested product was a modified barrel-type coupler with additional rows of screws, which is expected to sufficiently produce the full capacity of both Nitinol and GFRP. The results established some coupling parameters and limitations. To couple the Nitinol without damaging it, the screws had to have flattened tips, to a diameter of 7mm, for sufficient grip and to achieve full strain capacity. However, the modified screw lock coupler modification did not work for the GFRP bars. The suggested solution was to weld a steel tube, at a length of at least 18 times the diameter of the GFRP bar, to the modified screw lock coupler. The GFRP bar would then be anchored into the welded steel tube using an epoxy adhesive. Iterative experimental testing verified the efficacy of this Nitinol-GFRP hybrid reinforcement coupler configuration.

Micro level solutions have been explored to produce Nitinol-GFRP composite reinforcing bars. A round reinforcing bar design was explored by Wierschem and Andrawes (2010), as seen in Figure 2.14, which proposed replacing 25% of the volume of glass fiber with 0.5mm diameter Nitinol wire. The Nitinol-GFRP composite specimen was gauged against a conventional GFRP control coupon. The addition of Nitinol fibers increased the ductility of GFRP by approximately 64%. The Nitinol-GFRP hybrid was able to maintain approximately 28% of its strength at 3.8% strain, whereas the GFRP specimen ruptured at 57% lower strain. The energy dissipation of the Nitinol-GFRP hybrid was estimated at 2.6 times greater than for conventional GFRP.

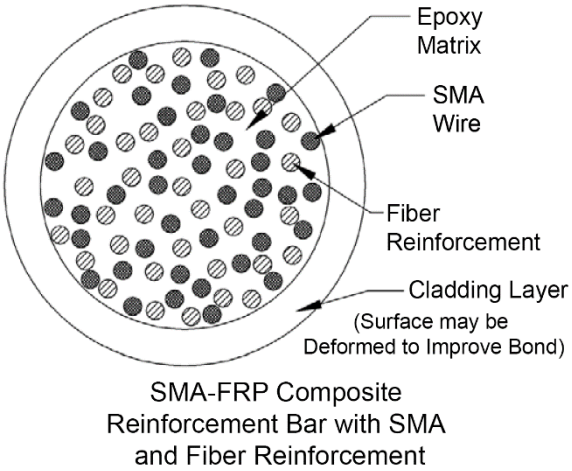

Figure 2.14. Cross-section of round superelastic Nitinol-GFRP hybrid bar concept (adapted from Wierschem and Andrawes, 2010).

A more elaborate experimental study of a square reinforcing bar concept was explored by Zafar and Andrawes (2013). The square Nitinol-GFRP hybrid bars were produced using similar 0.5mm diameter superelastic Nitinol wires embedded in an epoxy matrix with glass fibers. The study included formulation of a custom high elongation resin that would be durable under tensile cyclic loading. The matrix of the Nitinol-GFRP hybrid was inspected and verified for bond, air voids, and damages on a microscopic level, as seen in Figure 2.15a. The fiber content of the Nitinol-GFRP

specimen contained approximately 47% Nitinol by volume. One Nitinol-GFRP reinforcing bar included 22 Nitinol wires. The experimental testing included cyclic axial tension, and for the first time, axial compression, especially for a Nitinol-GFRP hybrid specimen. To include axial compression in the loading cycles, a Nitinol-FRP specimen was produced using 13 wires. The cyclic stress-strain response of the Nitinol-FRP coupon is presented in Figure 12.15b. The reasoning and outcome from this test are discussed in more detail by Zafar and Andrawes (2013). Testing also included flexural loading of a reinforced concrete T-beam. The T-beam specimen was 250mm long, coinciding with the available length of the Nitinol-GFRP reinforcing bars. The depth of the beam was 51mm, with the flange width of 64mm, and a web width of 25mm. The embedded Nitinol-GFRP reinforcing bars were left unfinished with a smooth surface as manufactured. The T-beam was tested under a total of four quasistatic cycles to a sequence of target displacements. The results showed that the combination of Nitinol and GFRP together produced a reinforcing bar with increased stiffness and strength, when compared to the properties of superelastic Nitinol. However, the Nitinol-GFRP reinforcing bars had the advantage of increase ductility and energy dissipation. Buckling of the Nitinol-FRP coupon during cyclic loading limited the ductility of the specimen to 3.9. The sequence of failure under compression started with debonding of the Nitinol wire from the resin at 6% strain, followed by crushing of the resin at 7% strain. At the conclusion of testing the T-beam, crack widths were observed to recover by approximately 96% correlating with near complete deflection recovery.

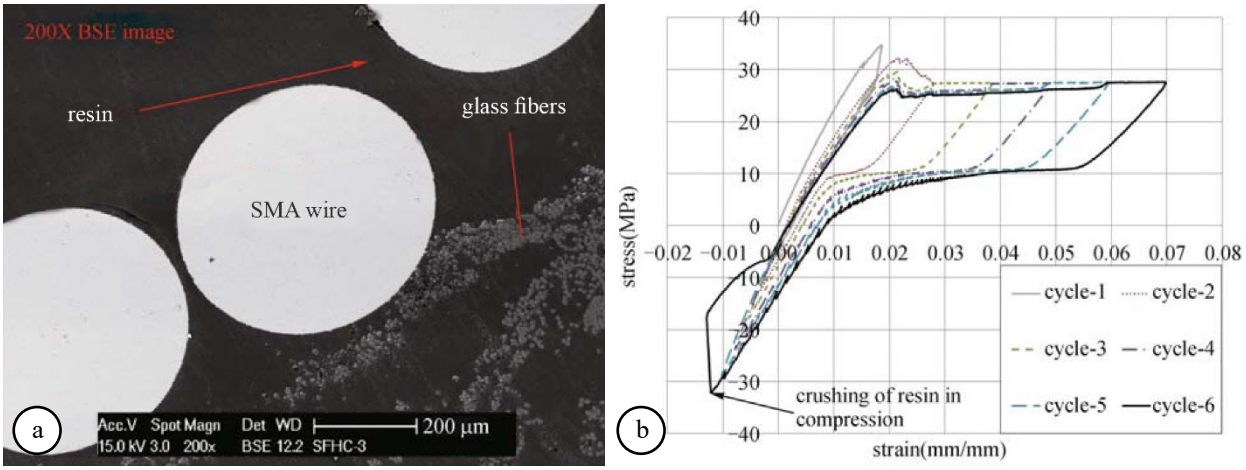

Figure 2.15. Superelastic Nitinol-GFRP hybrid: (a) 200x magnification of back-scatter electron image of fibers in resin; and (b) reverse cyclic stress-strain response of a Nitinol-FRP coupon (adapted from Zafar and Andrawes, 2013).

The results and concepts presented for a Nitinol-GFRP reinforcing bar suggest the possibility of three advantages relevant to the construction of reinforced concrete structures with seismic resilience. The advantages are:

1- The combination of Nitinol and GFRP provides a means of producing reinforcing bars with fine-tuned stiffness, strength, and ductility.

2- Nitinol wire is more readily available commercially due to high demand from other industries, which makes it cheaper than Nitinol bars (Wierschem and Andrawes, 2010). The substitution of a portion of the Nitinol with GFRP further economizes the production of reinforcing bars made of smart materials.
3- The encasement of Nitinol-FRP or Nitinol-GFRP in resin presents a medium which can be easily modified to economically produce improved bond with concrete (Wierschem and Andrawes, 2010) by applying a roughened surface such as sand coating with epoxy or a deformed polymer sheathing.

2.4.4.2 Engineered Cementitious Composites

Li, Li, and Song (2015) investigated the application of superelastic Nitinol wires embedded in engineered cementitious composite (ECC) to produce a novel composite material, in contrast to the reinforcement of ECC with Nitinol bars, such as found in the works of Saiidi and Wang (2006), and Saiidi, et al. (2015). The experimental study is motivated by the tensile strain compatibility and high deformation recovery of superelastic Nitinol and ECC. The details of the specimens and experimental testing program are discussed elaborately by Li, Li, and Song (2015). The conclusions of the study are drawn from the cyclic loading of flexural specimens made with the Nitinol-ECC composite material. The common advantages of Nitinol and ECC, minute residual deformation and high strain recovery, were obvious observations. The Nitinol-ECC material was able to limit the widths of open cracks to below 0.04mm consistently across an array of microcracks. The cracks were observed to completely, even when induced by large displacements. A closer investigation of the tested flexural specimens revealed that the Nitinol-ECC material did not show signs of debonding, deep crack propagation, or spalling. The experiment was successfully able to produce a ‘self-repairing’ flexural specimen.

2.5 Constitutive Modelling of Shape Memory Alloys

The introduction of the novel Nitinol material into the design and construction industry has raised interest in harnessing its benefits by predicting its behaviour through mathematical expressions. Since superelastic Nitinol is the more prevalent choice for structural applications, it will be the main focus for the topic of constitutive modeling.

Profiling the function of Nitinol has posed some challenges due to its variable thermomechanical responses, its physical properties, and integration compatibility. Nitinol remains temperature sensitive regardless of superelastic or shape memory training, which has implications on the proportions of energy dissipation and strain recovery. The austenite to martensite material phase transformation is exothermic, and the reverse is endothermic (Piedboeuf, Gauvin, and Thomas, 1998). At low loading frequencies of 0.01Hz and lower, the temperature of superelastic Nitinol will rise above its ambient environment, causing an increase in the upper plateau stress. Throughout the unloading branch, the temperature of the Nitinol will drop below the ambient environment, which is correlated with a degradation of the lower plateau stress. The widened hysteretic loop indicates greater energy dissipation, however, the reduction

of the lower plateau recovery stress results in increasing retention of residual displacement, and thereby a reduced self-centering capacity. The temperature gradient which develops across the diameter of Nitinol bars, as compared to wires, and the rate at which the thermal gradient equalizes, is also an influencing factor in the thermomechanical response of Nitinol. More so, extensive studies since the 1970's have identified a consistent observation of asymmetric stress-strain responses for superelastic Nitinol under axial tension and compression (Tyber, et al., 2007). Idealization of the tension and compression responses, by symmetrizing a singular numerical expression, has been cause for concern by researchers, especially when the numerical model is intended for implementation in high risk applications. The constitutive modeling of Nitinol is a complex challenge due to the variety of variables influencing the intricate stress-strain-temperature relationships of the material (Piedboeuf, Gauvin, and Thomas, 1998). As a result, an evolving series of material constitutive models have endeavoured to achieve true representation of the actual behaviour of superelastic Nitinol.

An early example of a material constitutive model for superelastic Nitinol is found in the work of Auricchio and Sacco (1997). The stress-strain behaviour is expressed according to the classical Euler-Bernoulli beam theory, using data from experimental studies on superelastic Nitinol orthodontic and commercial straight wires. Using agreeable experimental results and analytical estimation, the model is made to differentiate between the tensile and compressive behaviours of superelastic Nitinol, and account for the difference in austenitic and martensitic material stiffnesses. The product is a simple linear model, presented in Figure 2.16, intended for analysis of one-dimensional elements.

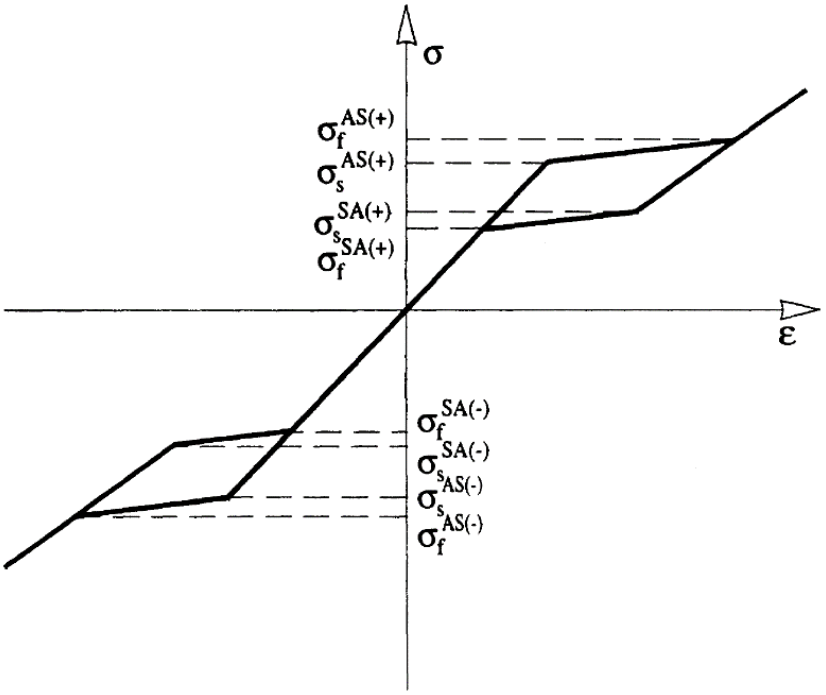

Figure 2.16. Early constitutive material model of superelastic Nitinol for 1D finite element analysis (Auricchio and Sacco, 1997).

Other developments of material constitutive models relevant to superelastic Nitinol are discussed elaborately by De la Flor, Urbina, and Ferrando (2006) and Paiva and Savi (2006). The superelastic Nitinol constitutive model contemporary to this study is the material model developed by Abdulridha and Palermo (Abdulridha, et al., 2013). The model is intended for nonlinear finite element analysis of reinforced concrete structural elements. The model contributes multiple improvements including differentiating between the loading branch and the unloading branch, differentiating between austenite and martensite elasticities, capturing residual strain offset, and implementing the degradation of the lower plateau stress over the course of cyclic loading. However, the model assumes identical material behaviour under both tension and compression. It is presumed that the condition of embedment in concrete and restraint against buckling is the reasoning behind the symmetry of axial responses in the model. The model is presented in Figure 2.17.

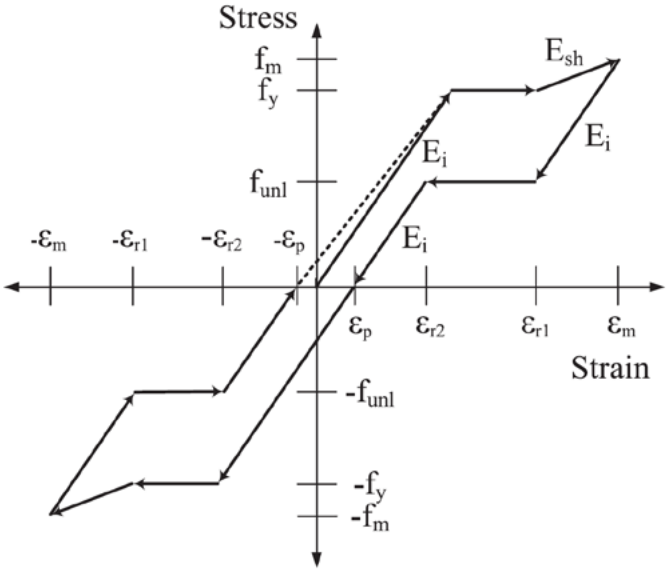

Figure 2.17. Abdulridha and Palermo superelastic Nitinol material constitutive model (Abdulridha et al., 2013).

The available constitutive models for superelastic Nitinol present viable options for analytical simulations. A common observation is the shared characteristic of a thermostable material hysteretic response. While it is true that the Nitinol will remain superelastic beyond the austenite finish transformation temperature for a given operational range, the hysteretic response will change throughout the range, which may be a point for further investigation.

2.5.1 Bond Behaviour in Concrete

The implementation of superelastic Nitinol in reinforced concrete analytical models is typically accompanied by an assumption of no bond to concrete, based on experimental observations, due to the unfinished smooth surface of

bars and straight wires. The difficulty and cost in manufacturing and machining Nitinol has made it impractical to implement surface deformations on bars, and other solutions are not always directly obvious or need special modifications. Kuang and Ou (2008) infused an ECC mix with brittle adhesive-filled fibers to create a Nitinol-reinforced self-repairing beam. The idea was for the adhesive released from the brittle fibers to seal and strengthen cracks in the beam once it has recovered under the strain recovery stress of the Nitinol wire. It was found that the adhesive released throughout the microcracks was able to resist opening under consecutive load cycles, but the adhesion was not effective at improving the bond between the Nitinol wire and concrete in the self-repaired beam. The study by Choi, et al. (2014) found that increasing the confining pressure on cold-drawn Nitinol produced the most effective bond to concrete. The additional normal confining pressure was produced by using pre-strained Nitinol fibers, which were then heated to enlarge their diameter. The study concluded that using dog-bone-shaped fibers, which had a similar bond strength to the heated fibers, is a more applicable practical solution. On a large scale, the suggested bog-bone fibers solution is synonymous with anchoring a smooth Nitinol bar at each end by means of headed ends or coupling to deformed steel reinforcement, in which case bond to concrete is still not achieved. An experimental study using twisted strands of Nitinol wire was able to report good bond to concrete due to mechanical interlocking (Maji and Negret, 1998).

Given the indicated need for mechanical interlock at the surface, Billah and Alam (2016) investigated the bond behaviour of sand-coated superelastic Nitinol reinforcing bars embedded in concrete cylinders. The experiment used 450mm long Nitinol bars with diameters of 20mm and 32mm. The bars were separated into sets identified by bar diameter, sand grain size, and embedment length. The sand grain sizes used were 0.3mm and 0.6mm. The epoxy sand coating increased the diameter of each bar by approximately 3mm to 4mm. A general observation was that cylinders embedded with sand-coated Nitinol had a splitting failure, whereas smooth Nitinol bars simply slipped under load. Testing showed that epoxy sand-coating effectively provided a surface interlocking mechanism to improve the bond between Nitinol bars and concrete. The 20mm diameter Nitinol bars coated with 0.6mm sand grains were able to achieve an average maximum bond strength 45% greater than the smooth control bars and maintained a 29% greater average residual bond strength. When 0.3mm sand-coating was applied, the Nitinol bars had an average maximum bond strength of 12% greater than the smooth control bars, however, the average residual bond strength reduced by 6%. The factors considered towards the performance and strength of the bond were concrete strength, bar diameter, concrete cover, embedment length, and surface condition of the bar. The results indicated that for both smooth and sand-coated bars, the influence of concrete cover was negligible, but coarser sand grains provided better interlock which increased bond strength. Billah and Alam (2016) concluded with the development of an expression to estimating bond strength for sand-coated Nitinol bars. The estimates were almost identical to the experimental results. More so, the developed expression was found to be closely compatible with the bond strength expression for sand-coated FRP bars in the Canadian Highway Bridge Design Code CSA S6.

2.6 Seismic Design

The seismic resilience afforded to structures by means of reinforced concrete shear walls (Paulay, 1975) encourages the adaptation of displacement-based seismic design, where a structure can be designed to remain inherently operational post-disaster (Priestley, 2000). The experimental work of Thomsen IV and Wallace (2004) exemplifies how slender walls can be detailed for displacement control. An emphasis is made on the importance of considering the cross-section of the wall and detailing of the boundaries. The introduction of superelastic Nitinol as an alternative reinforcement, compliments both the principles of displacement-controlled seismic design and the flexural behaviour of slender shear walls, by facilitating a mechanism for strain recovery. The application of superelastic Nitinol longitudinal reinforcement, in the boundaries of a slender shear wall, is expected to rectify inter-story drifts and reduce overall residual displacement of the structure. However, the implementation of embedding longitudinal Nitinol reinforcement in concrete would be partial to new construction.

2.6.1 Retrofitting and Repair

Where an existing conventional concrete shear wall may be feasible to repair post disaster (Vecchio, et al., 2002), it is possible to also retrofit it with superelastic Nitinol to meet the standards of performance-based seismic design. Cortés-Puentes (2017) used external superelastic Nitinol braces to rectify a drifted squat shear wall and control its lateral displacement in future seismic events. Zaidi, Palermo, and Dragomirescu (2017) discuss the repair of a damaged slender shear wall reinforced with superelastic Nitinol. In comparison to a similar wall constructed with conventional materials, the Nitinol reinforcement embedded in the boundaries did not require replacement or repair. The repaired Nitinol-reinforced wall continued to self-center from up to 2% drift.

2.7 Summary

In this chapter a comprehensive literature review was completed to address the underlaying fundamental concepts leading up to the experimental investigation of slender Nitinol-reinforced concrete shear walls, and to highlight their importance and relevance among the completed works pertinent to it. The failure mechanism of conventional slender reinforced concrete shear walls was reviews to identify the relationships between reinforcement distribution and performance. The fundamental behaviours of shape memory alloys and the available variety was surveyed in relation to reinforced concrete construction. Superelastic Nitinol was identified as the most favourable shape memory alloy for structural applications due to its superior mechanical and physical properties. The use of Nitinol for structural steel construction, retrofitting products, and protective seismic devices was also explored. The versatile use of Nitinol was also examined as a component in hybrid composites such as fiber reinforced polymers (FRP) and engineered cementitious composites (ECC). Given the novelty of Nitinol in the design and construction industry and its unique behaviours, a review of material constitutive models was completed to understand the benefits and limitations of

numerical models current to the study. Finally, given the implied application of superelastic Nitinol in new construction of reinforced concrete structures, a brief review was completed on the use of superelastic Nitinol for repair and retrofitting, which revealed its efficacy in continuing to control the displacement of rehabilitated structures.

CHAPTER 3

Experimental Program

3.1 Introduction

An experimental program was designed to study the behaviour of two large-scale reinforced concrete shear walls. The study is a comparative effort to gain a better understanding of the behaviour of Nitinol shape memory alloy (SMA) reinforced concrete against conventionally reinforced concrete under seismic loading. This chapter discusses the design, material properties, and construction process of both shear walls, followed by the test setup, and testing program used for experimental evaluation. The utilization of Nitinol SMA reinforcement is demonstrated in conjunction with conventional steel, through a non-invasive coupling device, for a hybrid reinforcement system. The Nitinol SMA is positioned within the plastic hinge region where the greatest damage is expected to surface. Both walls were positioned and tested in an identical manner using relevant quasi-static reverse cyclic loading standards. Data was collected through a comprehensive set of instruments.

3.2 Shear Wall Specimens

For this study two ductile slender reinforced concrete wall specimens were adopted from the study previously conducted by Abdulridha (2013). Some dimensions were slightly modified to accommodate anchorage points and instrumentation constraints; however, each wall is geometrically identical. The walls measure 2200mm in height and 1000mm in length, yielding a slenderness ratio of 2.2. Each wall is 150mm thick. The rectangular cross-section contains boundary elements at each end of the web with a 150mm by 150mm footprint. Each wall sits on top of a thick foundation block measuring 500mm in depth, 1600mm in length, and 1000mm in width for a stiff base. The length of the foundation block was adapted for a total of six anchorage points through the depth and into the strong floor of the Structures Laboratory (Lab). The anchorage points are positioned three on each side of the wall, spaced evenly along the length at 600mm center-to-center. Finally, each wall is topped off with a stiff cap beam with a cross-section of 400mm in depth by 400mm in width, and 1600mm length. The length of the cap beam was adapted for mounting a hydraulic actuator between the wall and the strong wall in the Structures Laboratory. The typical geometry of a wall is illustrated in Figure 3.1.

The walls were named ‘SWS-R’ and ‘SWN’. Specimen SWS-R is the steel-reinforced wall, and the name denotes Shear Wall Steel-reinforced – Repair. This wall is conventionally reinforced with steel to serve as a control. While casting the wall, some poor consolidation of concrete occurred along the base and required repair. The repair was performed using premixed self-consolidating concrete, and as such the ‘-R’ became a significant denotation. The name SWN refers to Shear Wall Nitinol-reinforced.

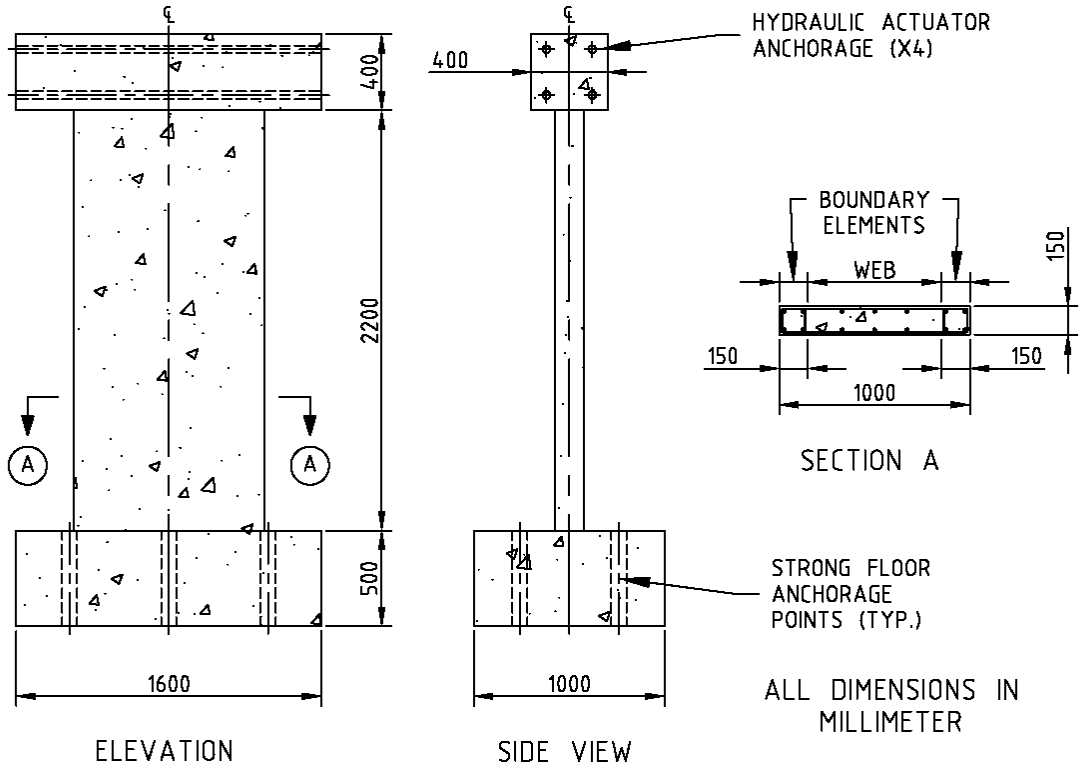

Figure 3.1. Dimensions of the walls.

3.3 Design of Shear Walls

The adopted shear walls were designed according to the seismic provisions of CSA A23.3-04, Section 21. The specimens were designed as ductile slender walls. The longitudinal reinforcement is arranged across the web and the two boundary elements to attain a predominant flexural behaviour. The transverse reinforcement is expected to provide sufficient strength against any major shear cracking. In the test condition, the walls are intended to behave as single degree-of-freedom cantilever systems, mimicking the response of perimeter walls found in mid-to-high rise structures. The design calculations are available in Appendix A of the thesis by Abdulridha (2013).

3.3.1 Reinforcement Details

Wall SWS-R was reinforced entirely using conventional deformed steel. The detailing of the reinforcement accounts for a 20mm concrete cover on all sides of the wall. In the longitudinal direction, the reinforcement was divided into three distinct sections, the web and two boundary elements on either end. Two curtains of 10M bars (11.3mm diameter) were used to distribute the longitudinal reinforcement, with each bar hooked at both ends. The longitudinal reinforcement in the web were arranged in two rows of three, spaced at 150mm apart. The reinforcement arrangement in the boundaries are identical, using a total of four bars over two rows, spaced at 120mm apart. The spacing between the closest reinforcement bars of the web and boundaries is 190mm. All the longitudinal reinforcement bars extend to the bottom of the reinforcement cage of the foundation block, and through to the top of the cage in the cap beam. The transverse reinforcement was made of 10M closed stirrups, encompassing the two rows of seven longitudinal bars, spaced at 150mm along the height of the wall. A total of 15 stirrups were used. The four longitudinal bars in each boundary were restrained in the transverse direction using 10M closed buckling prevention ties. The ties were spaced at 75mm over a height of 1100mm from the base of the wall to exceed the height of the plastic hinge region. Beyond this point, the buckling prevention ties were spaced 150mm to the top of the wall. The detailing of Wall SWS-R is illustrated in Figure 3.2. The plastic hinge was estimated to have a minimum height of 720mm from the base, according to Equation 3.1 from Clause 21.5.2.1.2, where l_w is the length of the wall, and h_w is the height of the wall.

$$(0.5 \cdot l_w) + (0.1 \cdot h_w) \qquad \text{[Eq. 3.1]}$$

The reinforcement details of Wall SWN are similar to Wall SWS-R. The difference is in the reinforcement details of the boundary elements where Nitinol SMA reinforcing bars were used within the plastic hinge zone. In each boundary, the four deformed steel bars were replaced with four, smooth Nitinol round bars (12.7mm diameter). Each Nitinol bar measures 1200mm in length, where 900mm is utilized within the height of the plastic hinge region, and 300mm is embedded into the foundation block. Each Nitinol bar was coupled at each end to deformed steel reinforcement. The deformed steel reinforcement in the boundaries, above the plastic hinge region, are #13 bars (12.7mm diameter), which extend to the top and anchored into the cap beam. Likewise, #13 bars were coupled to the opposite end of the Nitinol bars embedded in the foundation block for anchorage. The #13 bars were used as the nearest size to 10M bars due to lack of availability to the coupling manufacturer. The reinforcement arrangement of Wall SWN is presented in Figure 3.3.

The detailing of the cap beam and foundation block are identical for both walls, using a 50mm cover. The cap beam is reinforced in the longitudinal direction using a total of ten, 10M bars over the cross section. The bars were arranged in a row of four bars along the top and bottom with a spacing of 90mm, and a middle row of two bars. All longitudinal bars were hooked at both ends and spliced to the opposite bar. The transverse reinforcement was formed using eight sets of 10M u-shaped bars spliced together to create stirrups, spaced at 215mm. The foundation block is similarly reinforced in the longitudinal direction with 15M bars (16mm diameter), with a single row of eight bars at the top and bottom of the cross-section. A set of eight stirrups were formed similarly using 15M bars.

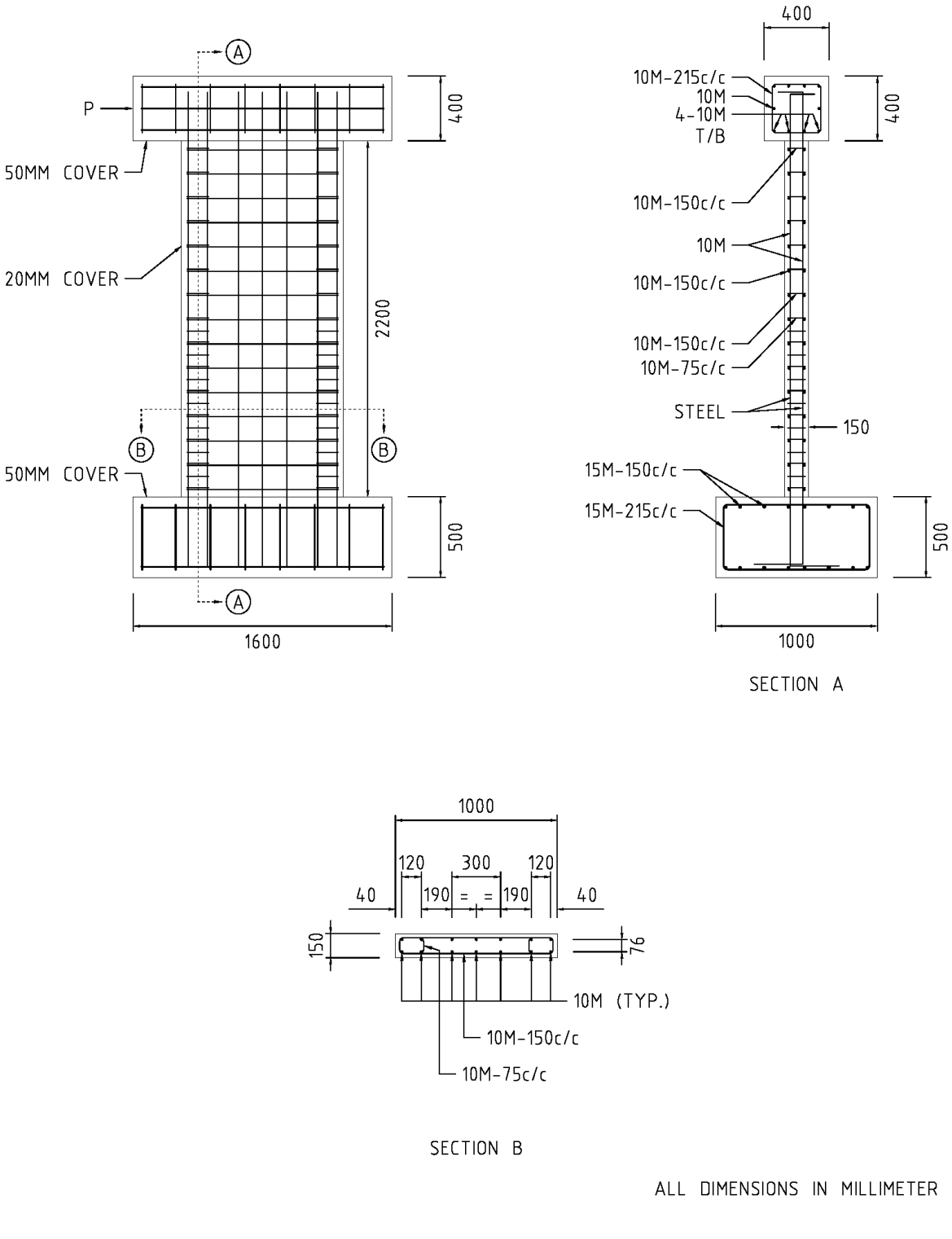

Figure 3.2. Reinforcement details for steel-reinforced Wall SWS-R.

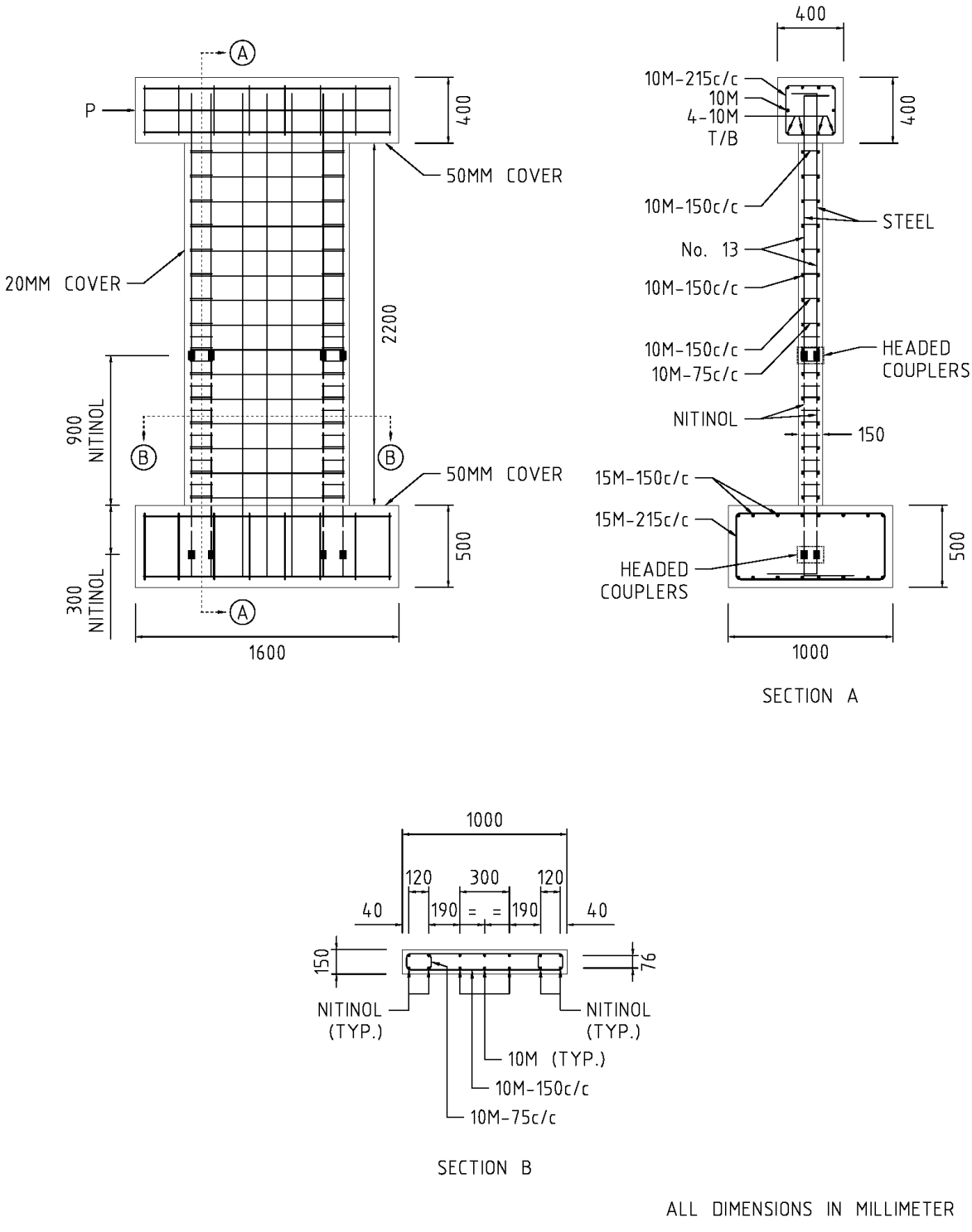

Figure 3.3. Reinforcement details for Nitinol SMA-reinforced Wall SWN.

3.3.2 Reinforcement Coupling System

The reinforcement coupler used is a non-invasive mechanical cylindrical device which draws together the ends of two headed reinforcement bars passing through the coupler. This coupler was selected to avoid notching in the stress-sensitive material of the Nitinol SMA bars. In comparison, the common means of coupling steel reinforcement with screw-lock couplers has proven detrimental to a previous study as it led to local stress concentrations resulting in fracturing of an SMA bar (Abdulridha, 2013). The coupler used is a threaded, two-part set of male and female components which come together to adjoin the reinforcement bars, as shown in Figure 3.4a. Each component of the coupler has an annulus cross-section, sized to splice #13 (metric) (Ø12.7mm) size Nitinol and steel bars. The couplers were pre-applied by the manufacturer to the ends of the reinforcement bars prior to forging the conical heads on the reinforcement as required. The male and female components have inner conical seats which force the opposing conical ends of the reinforcement bars together to form a confined continuous bearing connection. The coupler was assembled by torqueing together each component to a minimum of 100 lbs-ft (136Nm) to form a short smooth cylinder measuring 51mm in length and 35mm diameter. The couplers were utilized to splice the Nitinol-steel reinforcement above the plastic hinge region in the boundary elements of the wall (Figure 3.4b), and within the foundation block (Figure 3.4c).

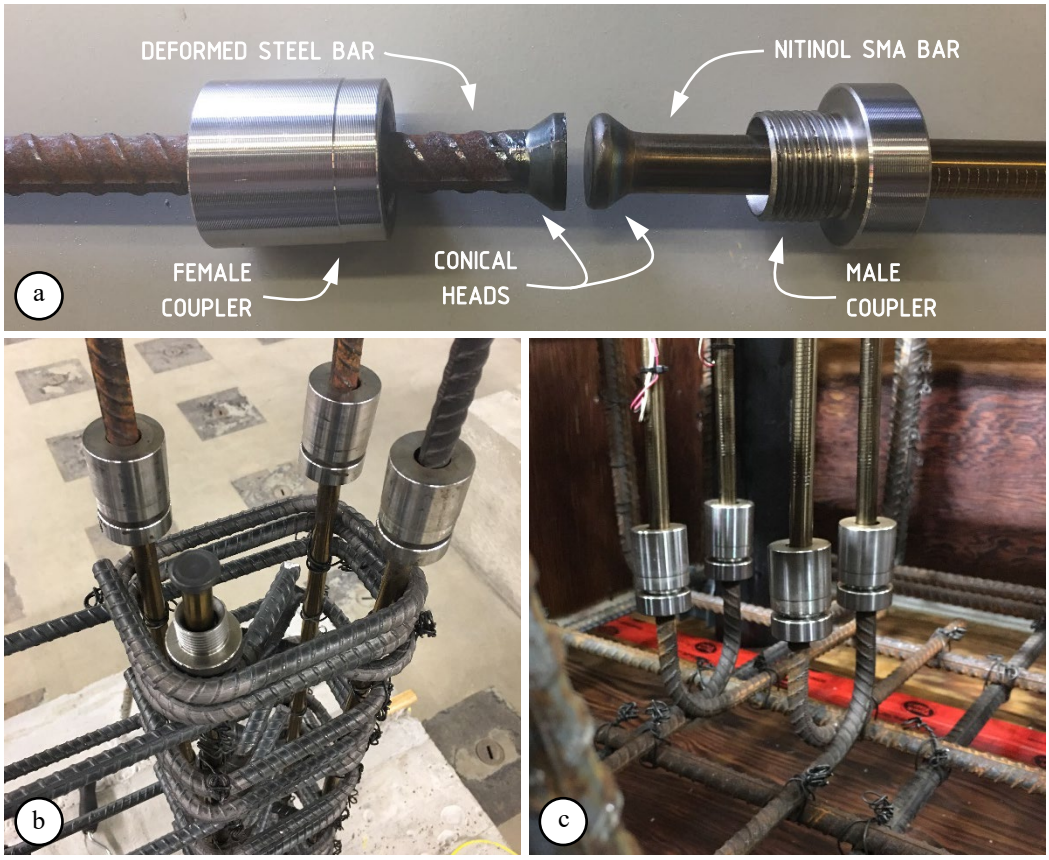

Figure 3.4. Coupling of reinforcement: (a) headed bars; (b) in boundary element; and (c) within foundation block.

The production material of the coupling device is to the discretion of the manufacturer to use either AISI Grade 1144 or Grade 1141 steel. The couplers used in this project are assumed to be made of Grade 1141 steel to conservatively assume the lower bound material capacity of the product. AISI Grade 1141 steel is rated to have a yield strength of 360MPa, a tensile strength of 675MPa, an elastic modulus of approximately 200GPa, and an elongation of 22% at rupture. Adequate material testing of the coupling device is beyond the scope of this research. Further technical information on the HRC 500/510 XTENDER Mechanical Coupler product is available through the manufacturer and supplier Headed Reinforcement Corporation.

3.4 Material Properties

This section discuses the properties of the materials used in the construction of the steel-reinforced and Nitinol-reinforced walls. A total of four types of materials were used. The reinforcement materials are steel, and the Nitinol (NiTi) shape memory alloy (SMA). The concrete that was used is normal concrete, and self-consolidating concrete (SCC) which was applied for a local repair.

3.4.1 Reinforcement

The material properties of all reinforcement bars were determined using available ASTM standards, and engineering judgement where specific guidelines were not available. Steel reinforcement coupons were prepared and subject to monotonic tensile testing according to ASTM A370. The Nitinol SMA reinforcement coupons were prepared and tested in tension according to ASTM F2516. The ASTM A1034 standard served as the best available guide for testing coupled reinforcement, as well as for forming a tensile cyclic loading protocol. All reinforcement coupon sets were tested in a displacement-controlled device (Universal Testing Machine) under monotonic and cyclic loading to establish a stress-strain curve. Steel coupons were additionally tested through a single 6% strain loading cycle for comparison to Nitinol.

The cyclic tensile loading protocol is determined using best judgement for number of strain cycles and according to the guidelines of ASTM A1034, while satisfying the requirements of ASTM A370 and F2516. The division of cycles was determined by harmonizing a set of targets to capture cyclic responses at key points of relevance. Of interest were capturing multiple cycles within the yielding range of SMA up to and including 2% strain, then moving on to capture cycles up to and including 6% strain at the onset of mechanically induced strain hardening in superelastic Nitinol SMA. Considering the potential for rupture of the SMA, cycles were applied to include the response at 12% strain and 16% strain prior to rupture. As a result, the tensile cyclic loading protocol followed a series of single cycles at increments of 0.5% for strain from 0% to 2%, 1% increments to 6%, 2% increments to 12%, 4% increments to 20%, and finally to rupture.

3.4.1.1 Steel

The walls were predominantly reinforced with deformed steel bars. The reinforcement was sourced from multiple suppliers and production batches, as available to the project, and as such were identified for differentiation of material properties for similar type bars. Reinforcement of designations 10M (from both suppliers A and B) and 15M are to Canadian specifications CAN/CSA-G30.18 Grade 400W (ASTM A615 Grade 60 equivalent). Steel reinforcement designated #13 is to American standards, ASTM A706 Grade 60, as available to and supplied by the coupling manufacturer. Deformed bars of designation 10M(a) were used to assemble the longitudinal and transverse reinforcements of Wall SWS-R, as well as for its cap beam. The longitudinal reinforcement in the web of Wall SWN used 10M(b) bars, as well as for all the transverse reinforcement across the length of the wall, and the buckling prevention ties throughout each boundary. The reinforcement cage of the cap beam was assembled also using 10M(b) bars. The longitudinal reinforcements in the boundaries of Wall SWN are of designation #13, coupled to Nitinol reinforcement above and below the plastic hinge region. The foundation blocks of both walls were assembled from 15M bars in the longitudinal and transverse directions.

The steel coupons produced from the steel stockpiles measured a length of 700mm each, accounting for a grip length of 100mm on each end, for a clear length of 500mm. Each coupon was loaded at a rate of 3.5mm/min (range of 3.125 to 31.25mm/min) throughout yielding and until the onset of strain hardening. Thereafter, a loading rate of 30mm/min (range of 25 to 250mm/min) was used until rupture. Slow loading rates were used to complement the effects of quasi-static loading. The cross-section of each coupon was reduced over the gauge length of 50mm to achieve controlled collection of data, including rupture, by an extensometer. The mechanical values obtained are an average of testing a minimum of three bars for each of the rebar stockpiles. The average results of the tension tests are summarized in Table 3.1. The stress-strain response for a sample 10M(a) coupon is presented in Figure 3.5. The stress-strain responses for all other deformed steel reinforcement bars are available in Appendix A.

Table 3.1. Steel reinforcement mechanical properties

Rebar		Diameter (mm)	Yield		Modulus of Elasticity (GPa)	Strain Hardening (%)	Tensile		Rupture (%)
			Strength (MPa)	Strain (%)			Strength (MPa)	Strain (%)	
10M	a	11.3	488	0.3	163	2.7	608	15.4	26.7
	b	11.3	530	0.3	162	2.3	698	14.8	27.1
15M		16	480	0.3	170	3.1	581	14.1	26.3
#13		12.7	482	0.3	161	2.1	645	14.8	27.5

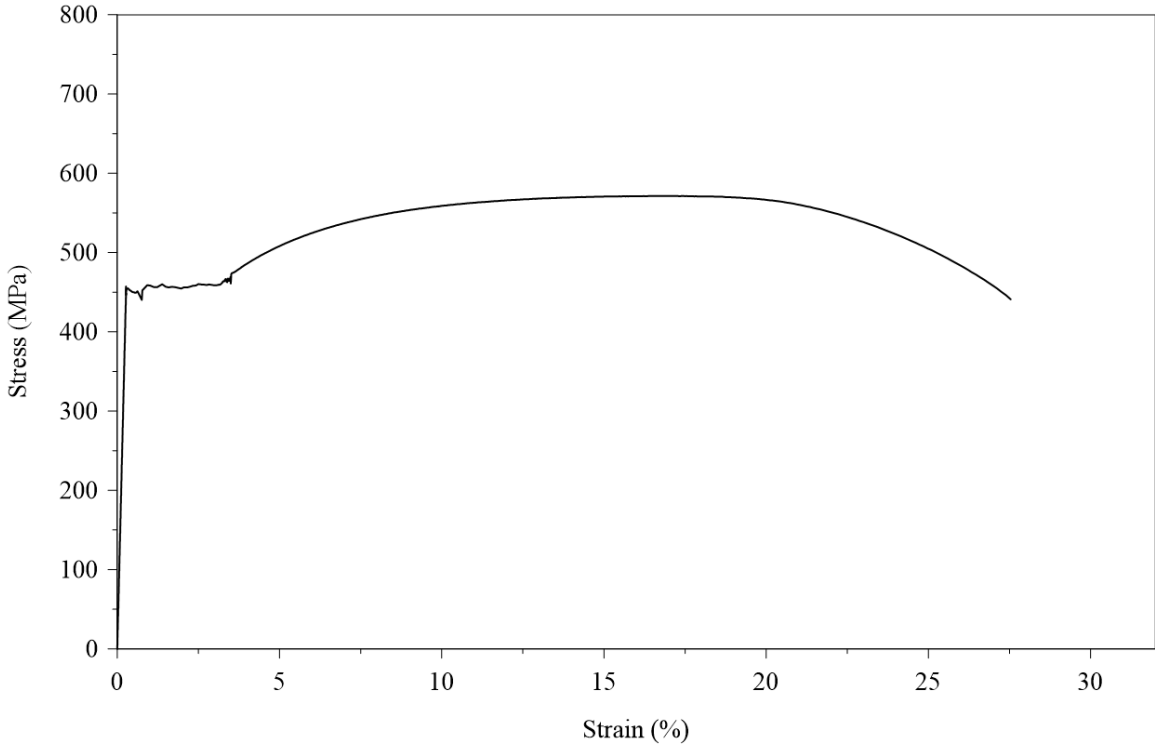

Figure 3.5. Sample stress-strain response of a 10M reinforcing bar.

3.4.1.2 Nitinol

Superelastic Nitinol SMA was used as the longitudinal reinforcement within the boundary elements of the Nitinol-reinforced shear wall (SWN). The Nitinol bars were annealed to maintain the austenite material phase, at a starting temperature (A_s) of -30°C, for superelastic behaviour in operational ambient temperatures above the finishing temperature of -10°C (A_f). The general physical, mechanical, and chemical properties of the Nitinol alloy were provided by the manufacturer and are presented in Table 3.2. Further technical information is available through the manufacturer and supplier SAES Smart Materials.

The mechanical properties of the Nitinol reinforcement were determined according to the ASTM F2516 standard at room temperature of 22°C ±2°C. Standard testing followed a sequence of loading to 6% strain, unloading, then reloading again until the tensile strength was achieved. For a clear length of 300mm, each coupon was loaded at a constant rate of 2.0mm/min, remaining below the maximum allowable rate of 3mm/min throughout completion of the 6% strain cycle and also remaining below the 30mm/min allowable loading rate for loading to failure.

Each Nitinol coupon was coupled to #13 deformed steel bars, using the non-invasive mechanical couplers, to simulate the actual loading mechanism as used in the construction of the Nitinol reinforced wall. The coupled steel bars on each end of a Nitinol coupon were used for gripping the coupon assembly within the tensile testing equipment. The cross-section of each Nitinol coupon was uniformly reduced at mid-length over a gauge length of 50mm to achieve controlled complete data collection by the extensometer. A total of three coupons were tested. The first two coupons

were tested, and averaged, to determine standard material properties, and the last coupon was used for cyclic testing. The average mechanical properties of the monotonically tested Nitinol coupons are presented in Table 3.3. A typical Nitinol coupon test setup is presented in Figure 3.6. The stress-strain response of Nitinol is presented in Figure 3.7.

Table 3.2. Manufacturer provided Nitinol reinforcement properties

Physical Properties	**Density**	6500		kg/m^3
	Modulus of Elasticity (thermomechanical)	75 40	(Austenite) (Martensite)	GPa
	Modulus of Elasticity (mechanical)	38	(Austenite)	GPa
Mechanical Properties	**Yield Strength**	345		MPa
	Ultimate Tensile Strength	965 – 1500		MPa
	Total Elongation Capacity	10 – 15		%
	Permanent Set (after 6% strain)	0.1 – 0.2		%
	Austenite Start Temperature (A_s)	-30		°C
	Austenite Finish Temperature (A_f)	-10		°C
Chemical Properties	**Nickel**	55.95		%
	Titanium	43.99		%
	Elemental Balance	0.06		%

Table 3.3. Nitinol reinforcement properties

Upper Plateau (at 3% strain during initial loading)	435	MPa
Lower Plateau (at 2.5% strain during unloading)	195	MPa
Residual Elongation (difference at 7.0MPa stress, after 6% strain)	0.25	%
Yield Strength	338	MPa
Modulus of Elasticity (mechanical)	42	GPa
Tensile Strength	1034	MPa
Uniform Elongation	16	%

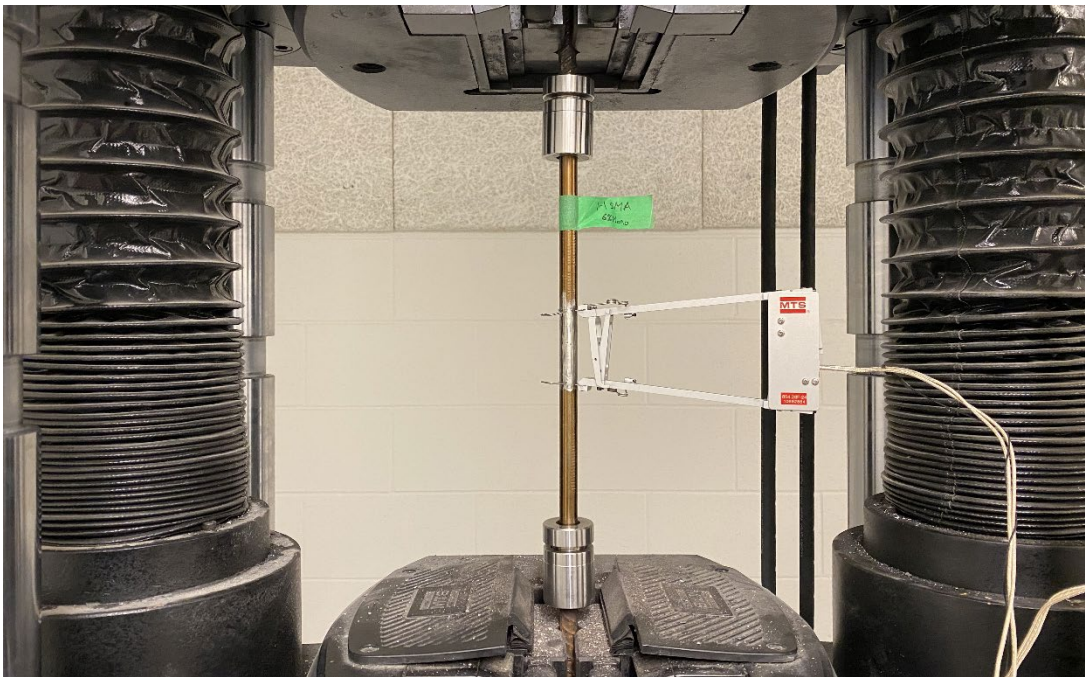

Figure 3.6. Tensile test setup of coupled Nitinol coupon assembly.

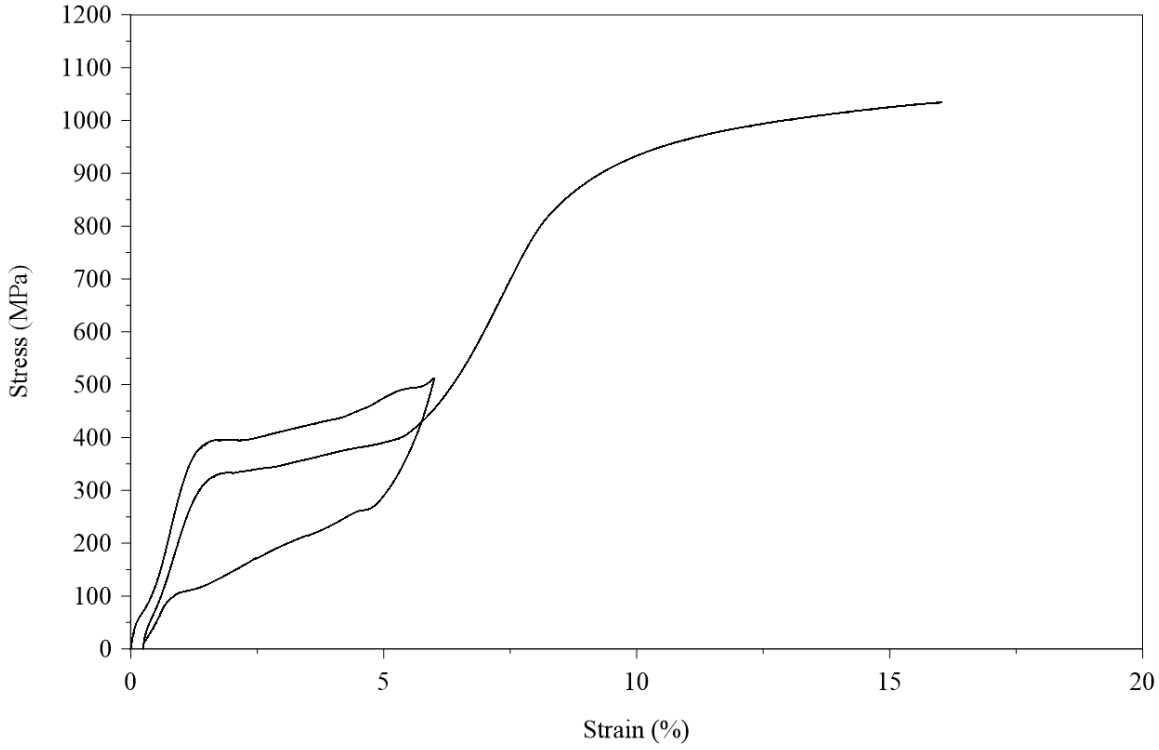

Figure 3.7. Sample stress-strain response of a 12.7mm diameter Nitinol SMA reinforcing bar.

The first coupon was mounted to the prescribed assembly as presented in Figure 3.6. However, the test setup was later modified for the second Nitinol test coupon and changed again for the third coupon. The second Nitinol coupon was gripped by the couplers in place of the deformed steel. The idea to grip the coupon from the couplers was adopted from the anchorage the couplers provide due to their larger diameter and bearing against the concrete beyond the plastic hinge region. The test setup was finally modified, and maintained as the most reliable approach, to grip the Nitinol from each end. The details of the outcomes in each coupon test are discussed in further details in Chapter 5 – Experimental Results. Photos of the modified test setups, and the monotonic and cyclic stress-strain responses from the Nitinol reinforcement tension specimens are included in Appendix A.

3.4.2 Concrete

The material properties of concrete were determined for each batch according to ASTM standards. The laboratory set the field conditions for the construction site of the walls. Two types of concrete were used for construction. Truck-mixed normal concrete was predominantly used to cast both walls. Truck-mixed fresh concrete was delivered to the laboratory from a local batch plant. Upon delivery, the concrete was first sampled (ASTM C172) and tested to pass parameters for slump (ASTM C143), air content (ASTM C231), and temperature (ASTM C1064) to determine suitability for casting into the formwork. Packaged dry blended material for self-consolidating concrete (SCC) was prepared (ASTM C387) and used as a repair material for Wall SWS-R to remedy a localized region of poor consolidation. The pre-blended SCC product was mixed with potable water and tested for slump (ASTM C1611) prior to application. All casting was completed within one hour from the time of batching (ASTM C94), with exception of the product specification for SCC.

Moulded cylinders of fresh concrete (ASTM C31) and fresh SCC (ASTM C1758) were prepared for each batch of concrete to be used to determine compressive strength. A total of 20 to 30 moulded cylinders were made for each batch. All cylinders were demoulded after 28 – 36 hours and stored next to their respective wall in the laboratory to cure under the same conditions at room temperature (CSA A23.2, Section 9). The concrete cylinders were tested in a load-controlled hydraulic device at a stress rate complying with 0.25 ± 0.05MPa/s (ASTM C39). Compressive strength measurements were collected and averaged from a minimum of three cylinders at the ages of 3 days, 7 days, 14 days, 21 days, and at 28 days. At the time of testing the respective wall, the age of the concrete cylinders was noted, and compressive strength was averaged from six cylinders. Determining the post-peak properties of concrete is outside of the scope of this study due to equipment limitations. The restrictions include a limited load capacity and inadequate means of collecting synchronized stress and strain readings from a displacement-controlled device.

3.4.2.1 Normal Concrete

Three batches of truck-mixed fresh concrete were used for construction. The first batch was to cast the foundation block of Wall SWS-R. The second batch was used to cast Wall SWS-R and the foundation for Wall SWN. The third

batch was to cast Wall SWN. The properties of the concrete mix design are tabulated in Table 3.4. The compression specimens were made using 150mm by 300mm cylindrical moulds (ASTM C31). The average compressive strength for Wall SWS-R at 28 days was 47.2MPa. At the time of testing, the concrete was 500 days old and had an average compressive strength of 50.8MPa. The average compressive strength for Wall SWN at 28 days was 36.4MPa. At the time of testing, the concrete was 410 days old and had an average compressive strength of 39.3MPa. Maturity curves and additional details are available in Appendix A.

Table 3.4. Mix design properties of normal concrete

Design Strength	30	MPa
Aggregate Size	14	mm
Slump	100	mm
Entrained Air Content	6	%
Acceptable Temperature Range (CSA A23.1 Table 14)	10 – 30	°C

3.4.2.2 Self-Consolidating Concrete

One batch of machine-mixed self-consolidating concrete was prepared at room temperature in the laboratory. The pre-blended packaged SCC product used was Sika Sikacrete-08 SCC. The batch volume was sufficient for both casting and preparation of moulded cylinders. The SCC product had a maximum aggregate size of 8mm and a design strength of 55MPa. The slump measured an average of 660mm, satisfying the product prescribed range of 600 to 700mm. The compression specimens were made using 100mm by 200mm cylindrical moulds (ASTM C31). The average compressive strength at 28 days was 57.3MPa. At the time of testing, the concrete was 405 days old and had an average compressive strength of 73.4MPa. The maturity curve for SCC and additional details are available in Appendix A.

3.5 Construction of Shear Walls

The construction of each wall occurred in five phases. The first phase was the production of formwork. The second phase was the assembly of the reinforcement cages. The third phase was applying internal instrumentation. The fourth phase was the production of the specimens. The fifth phase was surface preparation for the application of external instrumentation and visual inspection for post-casting damage.

Phase one of the construction occurred in two stages. In the first stage, the design of reusable formwork was executed. A 3D model was designed and virtually assembled to determine functionality, dimensions, compile quantities, and a cost estimate. The formwork was designed to be readily available and easily assembled to produced

geometrically identical walls. In the second stage the modular reusable formwork was custom fabricated and produced using plywood sheets and lumber as customary for concrete construction. In total the formwork is compiled of 15 modules: five panels for the foundation block, six panels for the wall, and four modules for the cap beam. The 3D design model of the modular reusable formwork is presented in Figure 3.8.

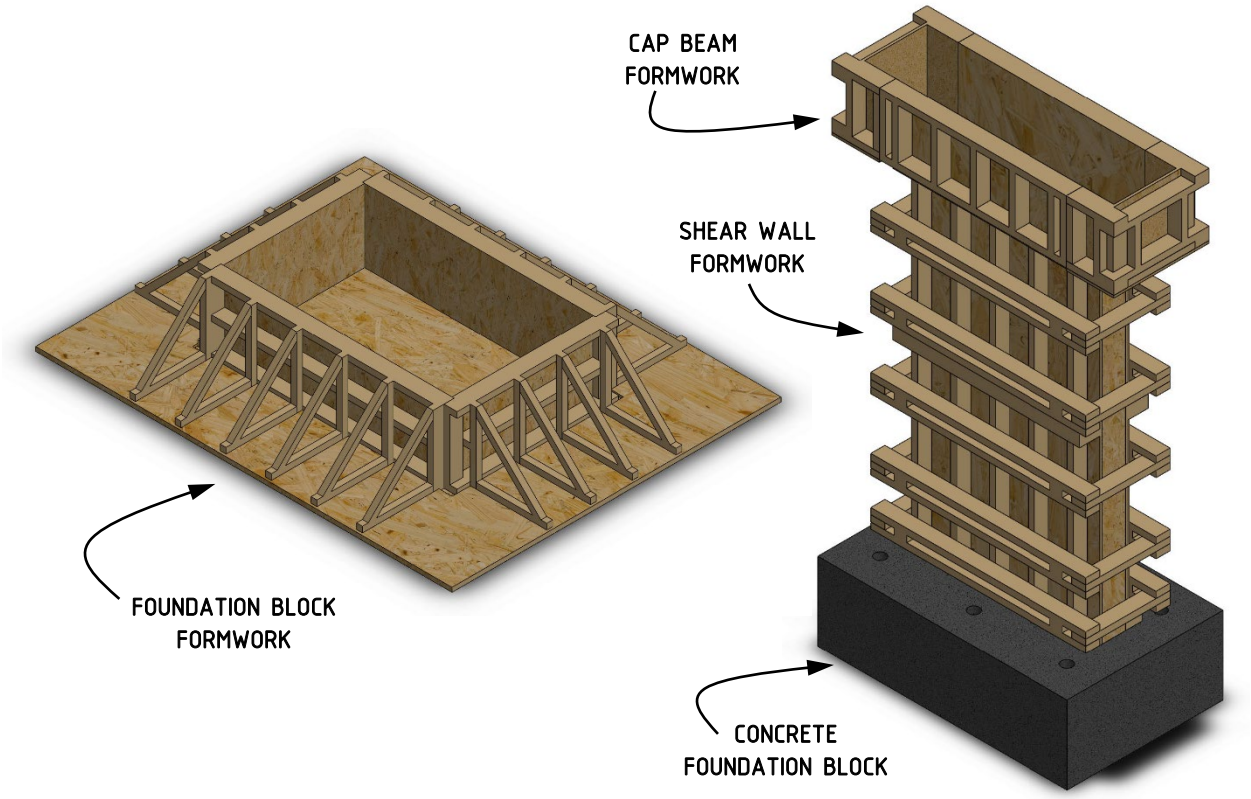

Figure 3.8. Assembled 3D model of reusable modular formwork: foundation block (left); shear wall and cap beam (right).

Phase two of construction occurred in three stages. The first stage was the assembly of the foundation block reinforcement cage. The longitudinal reinforcement was assembled first by splicing the hooked ends to form rectangular loops. Then, the transverse reinforcement was assembled in the same manner before being fitted around the longitudinal reinforcement to form the cage. The spacing of the longitudinal reinforcement was slightly modified to accommodate six symmetrically placed 2.5in. diameter PVC conduits, spaced at 600mm center-to-center, over the footprint of the foundation block. The PVC conduits were used to allow for anchorage of the wall to the strong floor of the laboratory. The spacing of the longitudinal reinforcement around the centerline of the cage was maintained to adequately accommodate the embedment of the longitudinal reinforcement of the wall cage. Hooked U-shaped lifting lugs were lastly fitted to the reinforcement cage of the foundation block. The assembled reinforcement cage and the

configured components of the foundation block are presented in Figure 3.9. In stage two the reinforcement cage of the wall was assembled. Each hooked longitudinal reinforcing bar in the first curtain was spliced at both ends to the bar adjacent to it in the second curtain. The adjoined longitudinal reinforcement was then fitted into the reinforcement cage of the foundation block and fixed in place at the required dimensions across the length of the wall. The procedure for assembling the wall reinforcement cage for Wall SWN was similar to of Wall SWS-R, except for the application of the couplers to the four Nitinol bars in each boundary. The smooth Nitinol SMA reinforcement were coupled to hooked deformed steel reinforcement within the foundation block and beyond the height of the plastic hinge region spanning the height of the wall and embedded within the cap beam. At this point, the assembly of reinforcement cages was interrupted for the casting of the concrete foundation block. The transverse reinforcement for each wall was fabricated as singular hoops for shear and buckling prevention ties. The shear reinforcement and buckling prevention ties were sequentially assembled around the longitudinal reinforcement as required. The assembled wall reinforcement cages are presented in Figure 3.10. In the third stage the reinforcement cage of the cap beam was assembled in a similar manner to the previous cages, however, this cage was not directly mounted and set aside for ease of construction, to be connected once the formwork was in place. The cap beam reinforcement cage is shown in Figure 3.11.

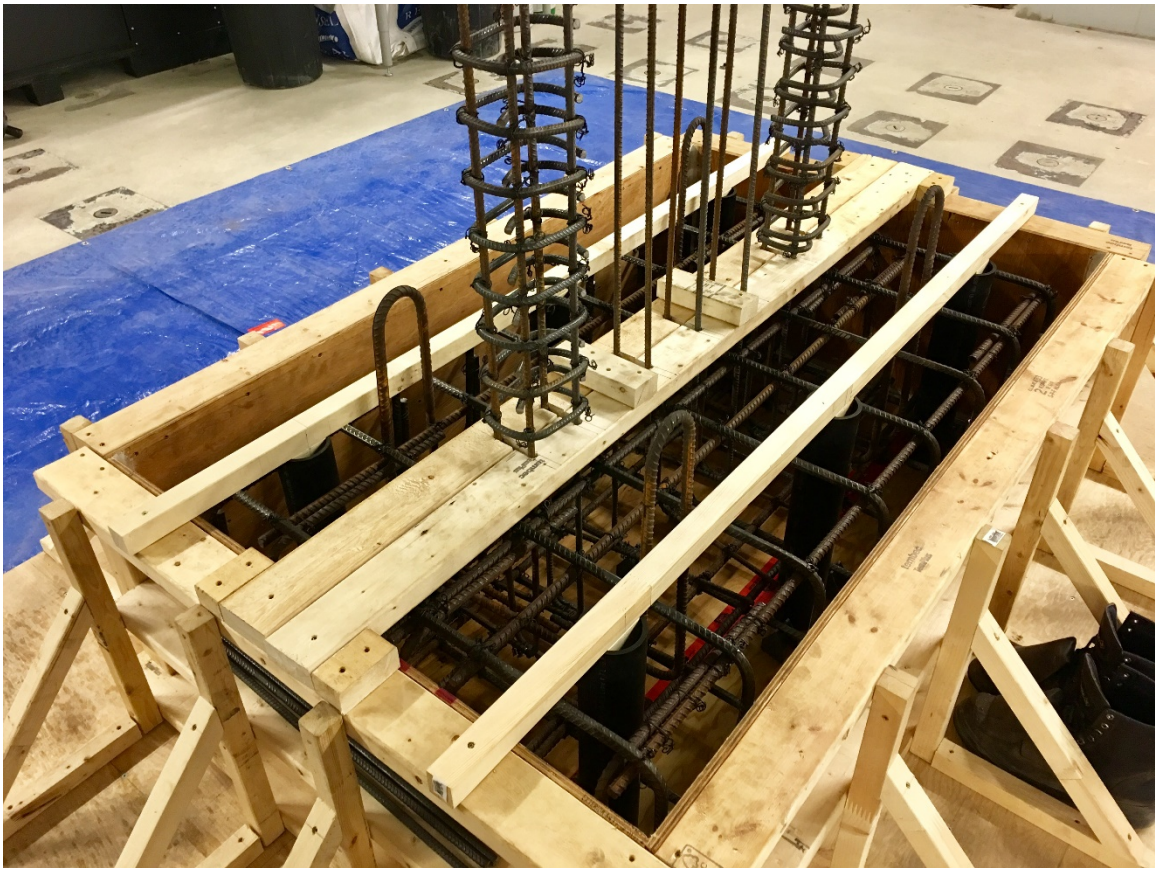

Figure 3.9. Assembled reinforcement cage of foundation block including anchorage conduits and lifting lugs.

Figure 3.10. Assembled wall reinforcement cages for: Wall SWS-R (left); Wall SWN with couplers (right).

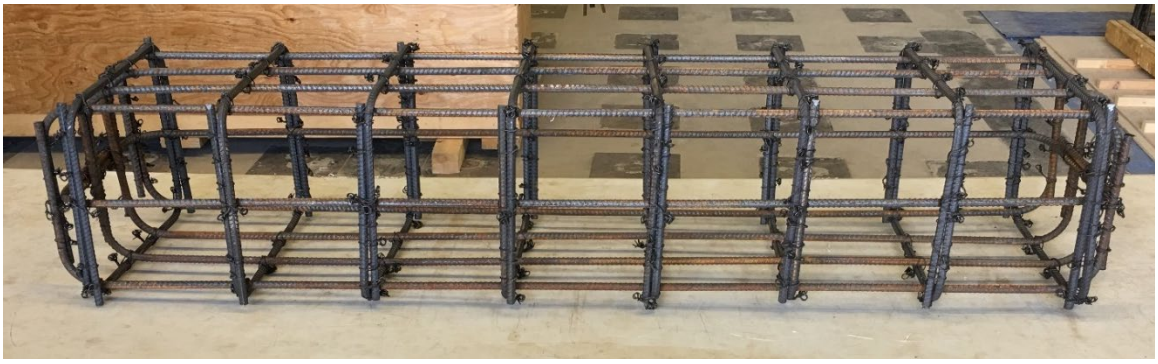

Figure 3.11. Assembled cap beam reinforcement cage.

Phase three of construction included the application of strain gauges. Strain gauges were predominantly applied to the longitudinal reinforcement and select shear reinforcement within the plastic hinge zone. The designated locations for applying the strain gauges on the assembled cage were filed down to a smooth surface measuring approximately 1in (25 mm) in length as required to adhere the sensor. The strain gauges were then applied with a series of adhesive and protective layers of super glue, Kapton tape, nitrile rubber, Teflon tape, and a hardening epoxy to protect the sensor from the placement of concrete. The signal wires attached to the strain gauges were routed along the wall reinforcement cage and clustered at four locations in a manner as to not influence the onset of damage during experimental testing at the protruding wire clusters. The strain gauges applied to Wall SWS-R were 10mm long standard strain gauges with an elongation limit of up to 2%. The same standard strain gauges were applied to the majority of Wall SWN, apart from the post-yield strain gauges which were applied to the Nitinol bars on the anterior side of the wall. The post-yield strain gauges were 10mm in length and have a strain capacity of up to 15%. The strain gauges were generally applied in the same locations and in the same wall reinforcement cages, presented in Figure 3.12. Wall SWN had an additional four standard strain gauges applied to the outer most Nitinol bars in each boundary to allow for monitoring of strain penetration into the foundation block.

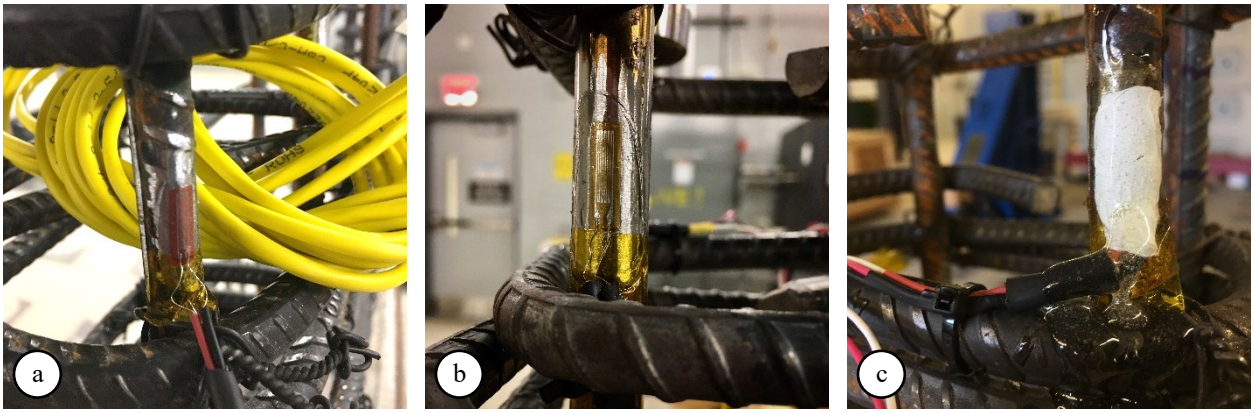

Figure 3.12. Strain gauges applied to reinforcement: (a) standard; (b) post yield; and (c) epoxy coated strain gauge.

Phase four occurred in two stages and was repeated twice to first construct the foundation block, and then the wall and cap beam. In the first stage the modular formwork was prepared with a coating of nonstaining form-release oil (CSA A23.1, Section 6), then assembled and sealed with silicon caulking to close any minor gaps between the panels. In the second stage, truck-mixed concrete was cast using a concrete bucket. When the foundation block was cast, the cold joint at the surface was intentionally left rough over the footprint of the wall to promote adherence between the hardened concrete and the fresh concrete of the wall. The cold joint was additionally mechanically roughened to eliminate any smooth surfaces, as shown in Figure 3.13. The formwork panels for the shear wall were assembled around the reinforcement cage, resting at the surface of the foundation block, with a snap-tie system to maintain the thickness of the wall over its height against the hydraulic pressure of the fresh concrete. The snap-ties

were locked in place external to the formwork using steel wedges bearing against the walers. The snap-ties were applied in rows colinear with the walers, concentrated at the bottom over the surface of the foundation, and then spaced out evenly over the remaining height of the wall. The assembly of the shear wall formwork is exhibited in Figure 3.14. The formwork for the cap beam was then assembled atop the wall formwork and the reinforcement cage for the cap beam was positioned. Four, 1in-diameter PVC conduits were then routed along the length of the cap beam, spaced symmetrically at 184mm center-to-center over the cross-section of the beam to allow for attachment to the hydraulic actuator with threaded rods. Finally, the wall and cap beam were cast monolithically as shown in Figure 3.15.

Figure 3.13. Mechanically roughened cold joint over footprint of wall.

Figure 3.14. Assembly of wall formwork panels around the reinforcement cage using the snap-tie system.

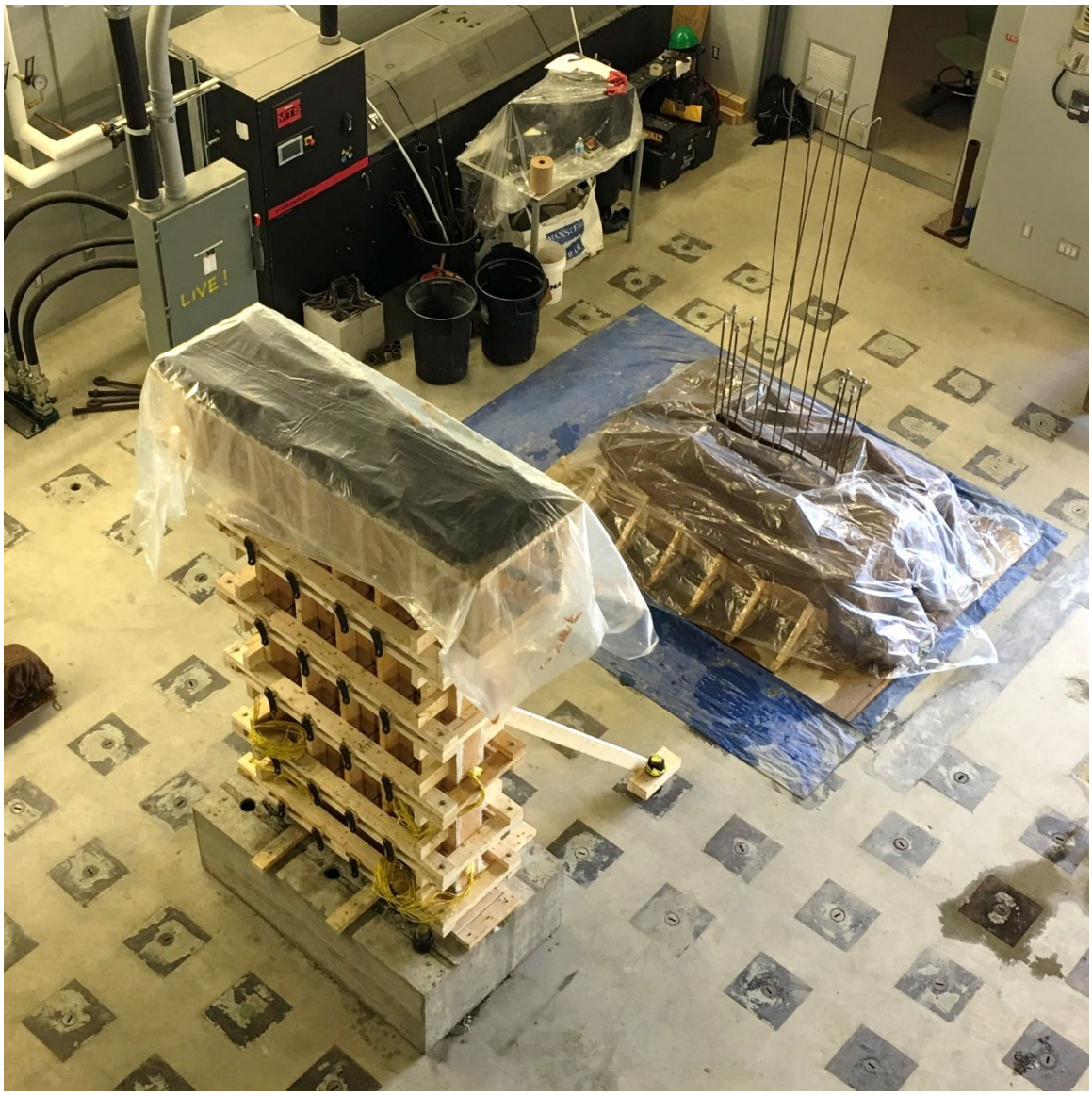

Figure 3.15. Casting and curing of walls: Wall SWS-R (left); and the foundation block of Wall SWN (right).

Phase five included demoulding the specimens and applying a white coating. Formwork was stripped from the concrete walls after a minimum of 24 hours (CSA A23.1, Section 6). The entire surface of each wall, including the cap beam and the top surface of the foundation block, were then coloured white. A water-based staining and non-sealing surface primer was used to prepare the surface to allow for tracing and measuring of cracks during experimental testing. Latex paint and similar elastic surface preparation products were avoided to prevent the covering of microcracks. The anterior face of each wall was later prepared with a 50mm by 50mm grid to reference the location of cracks and aid in the position of external instruments. The demoulded and prepared walls are presented in Figure 3.16.

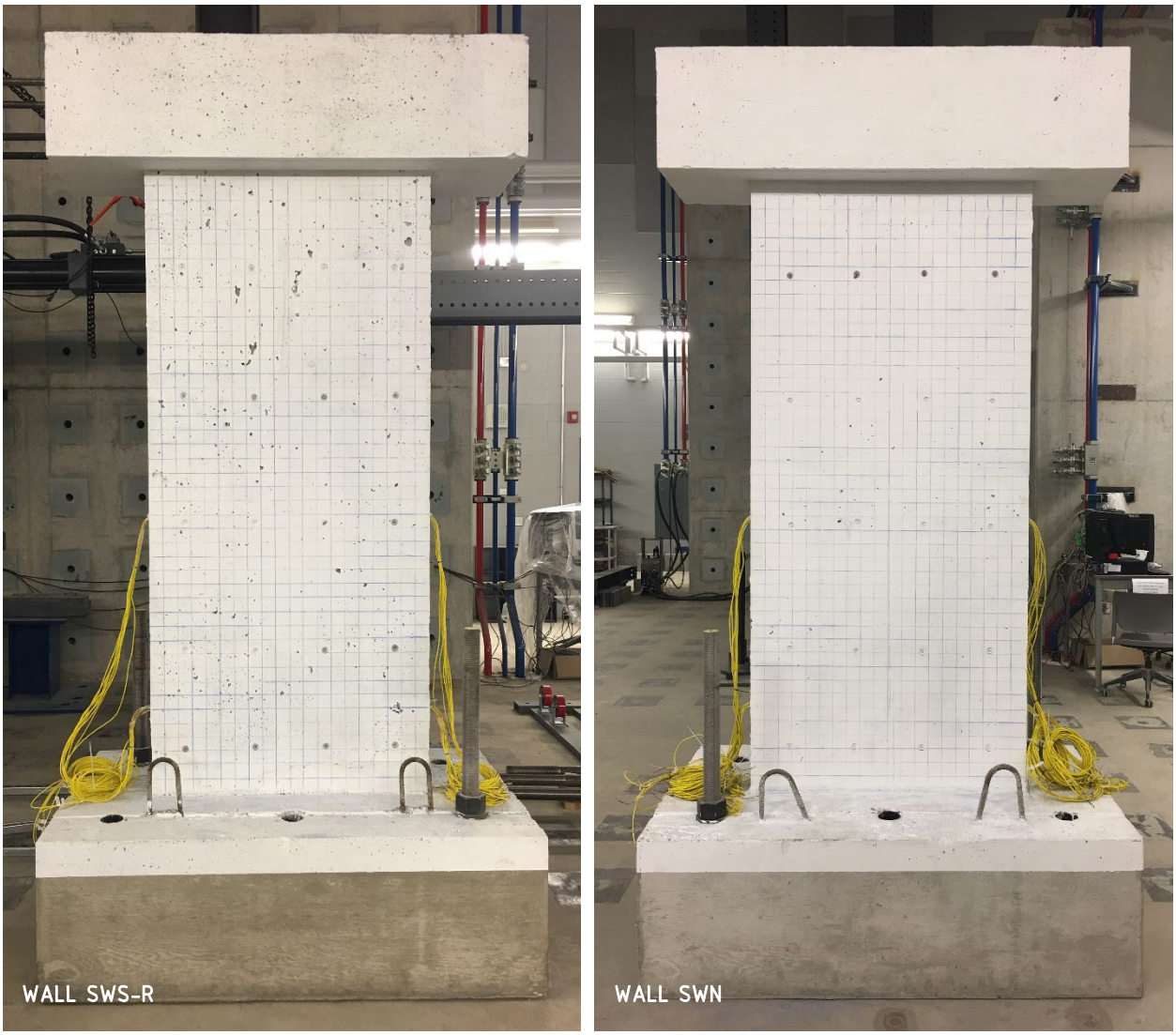

Figure 3.16. Walls prepared for experimental testing: Wall SWS-R (left); and Wall SWN (right).

Further details and photos of the construction process of the walls are available in Appendix B.

3.5.1 Repair

While casting Wall SWS-R (formerly named SWS) an unanticipated equipment difficulty was encountered while attempting to consolidate the concrete in the formwork. While the equipment issue was later resolved towards pouring the upper half of the wall, consolidating the base of the wall became obstructed with fresh concrete and became challenging to achieve without promoting over-consolidation or introducing unintentional air voids. Attempts were made external to the formwork to promote consolidation but had minimal impact without causing significant damage.

The extent of poor consolidation was realized once wall SWS was demoulded. The depth of honeycombing ranged in severity. The extent of honeycombing at the base of the left boundary measured 200mm across the length of the wall, 150mm from the top of the foundation, and penetrated through the thickness of the wall. The defect at the base of the right boundary was similar to the left. Poor consolidation was less severe over the web, measuring about 400mm across from the right boundary, 100mm in height, and did not extend beyond the 20mm cover. The honeycombing pattern over the web from the right boundary was similar on both sides of the wall. The regions of poor consolidation are presented in Figure 3.17.

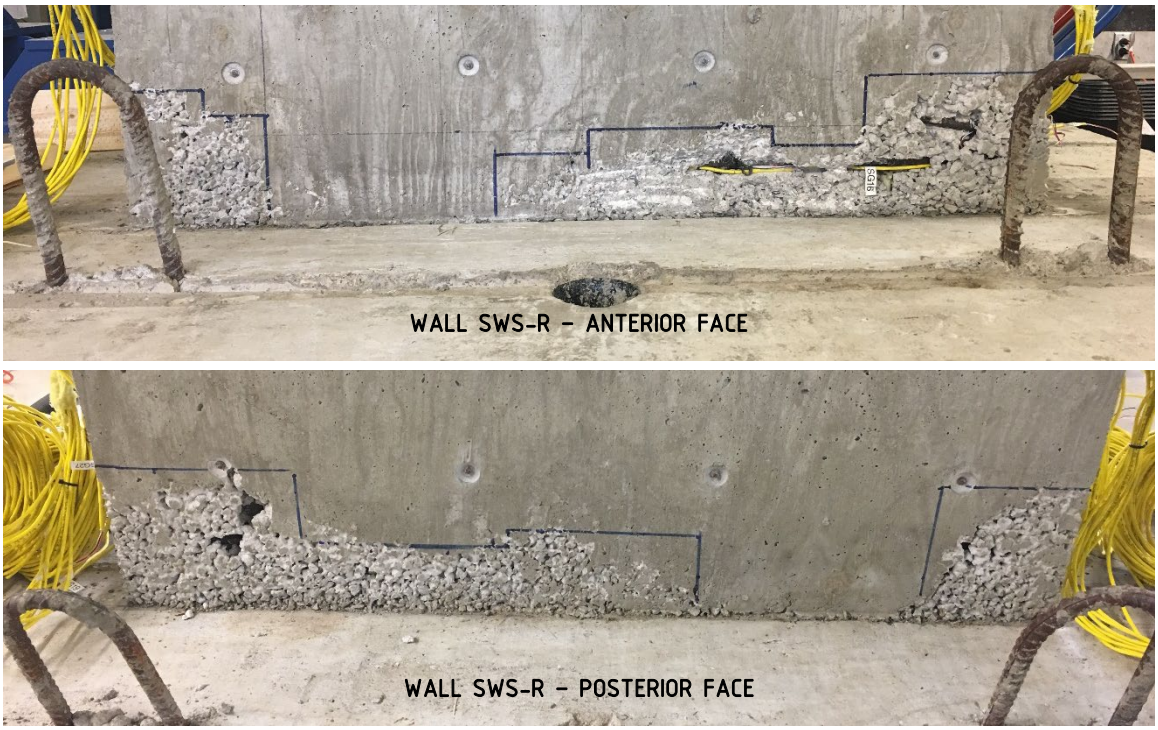

Figure 3.17. Regions of poor consolidation in Wall SWS-R.

The regions of poor consolidation were chipped away by applying several passes with a bushing tool to avoid imposing unintentional weakening of the boundaries at the base. The prepared regions are shown in Figure 3.18. Formwork was constructed and applied all around the base of Wall SWS-R to cast the repair material. The strength of the concrete, aggregate size for the shallowest depth of the removed honeycombing, cohesiveness of the material, and ease of application were determining factors in deciding to use self-consolidating concrete (SCC) as the repair material. The packaged Sika Sikacrete-08 SCC product was used. The repaired regions in Wall SWS-R are presented in Figure 3.19. Further information and photos regarding the repair are included in Appendix B.

Figure 3.18. Prepared repair regions on posterior side of Wall SWS-R: right boundary (left), and left boundary (right).

Figure 3.19. Repaired regions in Wall SWS-R.

3.6 Test Setup

The experimental testing of the walls required the completion of three major tasks. The first task was the complete instrumentation of each wall to characterize the structural response to quasi-static displacement cycles. The second task was the assembly of an adequate test frame to facilitate in-plane testing of the walls. The final task was to set up a data acquisition system to collect and output synchronized instrumentation readings.

3.6.1 Instrumentation

The instrumentation of each wall is composed of a set of external and internal sensors. The external sensors were a set of cable and linear potentiometers and a hydraulic actuator, positioned as shown in Figure 3.20, to collect displacements and force data. A total of 14 cable potentiometers were used: four of CP-300 units, five of CP-600 units, and five of CP-1250 units. A total of two linear potentiometers were used from the LP-100 set. The value following the 'CP-'or 'LP-' notation indicated the total stroke value of the sensor in millimeters. A stiff instrumentation frame was mounted to each end of the foundation block to support instruments CP-E-1250 and CP-C-600 on the right, and CP-B-600 on the left, to collect lateral displacement readings along the height of the wall relative to the base. Instruments CP-A-600 and CP-B-300 were mounted to the test frame to gauge the total actuator displacement and sliding of the wall relative to the laboratory floor, respectively. The majority of the remaining potentiometers were fixed to the wall. The cluster of CP-(A to D)-1250 instruments were mounted within an 800mm by 800mm square, at 100mm from the base of the wall, over the plastic hinge region to collectively measure and determine shear strain, according to the method by Massone and Wallace (2004). Instruments CP-D-600 and CP-E-600 were used to measure vertical displacement between the underside of the cap beam and the top of the foundation. Instruments CP-C-300 and CP-D-300 were used to measure the slip and elongation of reinforcement at the base of the wall just above the foundation. Potentiometer CP-A-300 was used to measure slip of the wall at the interface with the foundation. Lastly, instruments LP-A-100 and LP-B-100 were used to measure the uplift of the wall relative to the laboratory strong floor. For Wall SWN, instruments CP-(A to D)-1250 were positioned on the posterior face of the plastic hinge to avoid accidental contact with the extended cables while tracing cracks. The hydraulic actuator had a total stroke capacity of 500mm and force capacity of 250kN in tension or compression. The hydraulic actuator was anchored on the far end to the strong wall of the laboratory. The piston end of the actuator was bearing against a 10mm thick, 300mm by 300 steel plate used to distribute the pushing force on the left end of the cap beam. Four threaded rods were routed through the cap beam to attach the wall to the actuator. On the right end of the cap beam, the threaded rods distributed the pulling force over the cross-section of the cap beam using a similar 10mm thick steel plate. The external instruments were supplemented by a set of cameras to capture high resolution video and photos. The internal instruments were an array of strain gauges applied to the reinforcement within the plastic hinge region. A total of 33 strain gauges were applied to the Wall SWS-R, and 37 strain gauges to Wall SWN. Each wall had 21 strain gauges applied on the anterior reinforcement curtain, and 12 strain gauges on the posterior curtain. Wall SWN had an additional four strain gauges applied to the outer most Nitinol bars of each boundary, below the surface of the

foundation to measure yield penetration. Wall SWS-R used standard 10mm long unidirectional strain gauges, as presented in Figure 3.21. Wall SWN used a combination of unidirectional standard and post-yield strain gauges, each 10mm in length. The post-yield strain gauges were applied to the Nitinol bars of the anterior curtain only, within the plastic hinge region. The layout of strain gauges for Wall SWN is presented in Figure 3.22. The positioning of the instruments was adopted from the test setup prepared for the experimental testing conducted by Abdulridha (2013) and modified as required for this study. Raw data is available in Appendix C. Auxiliary details for the instrumentation frame are in Appendix D.

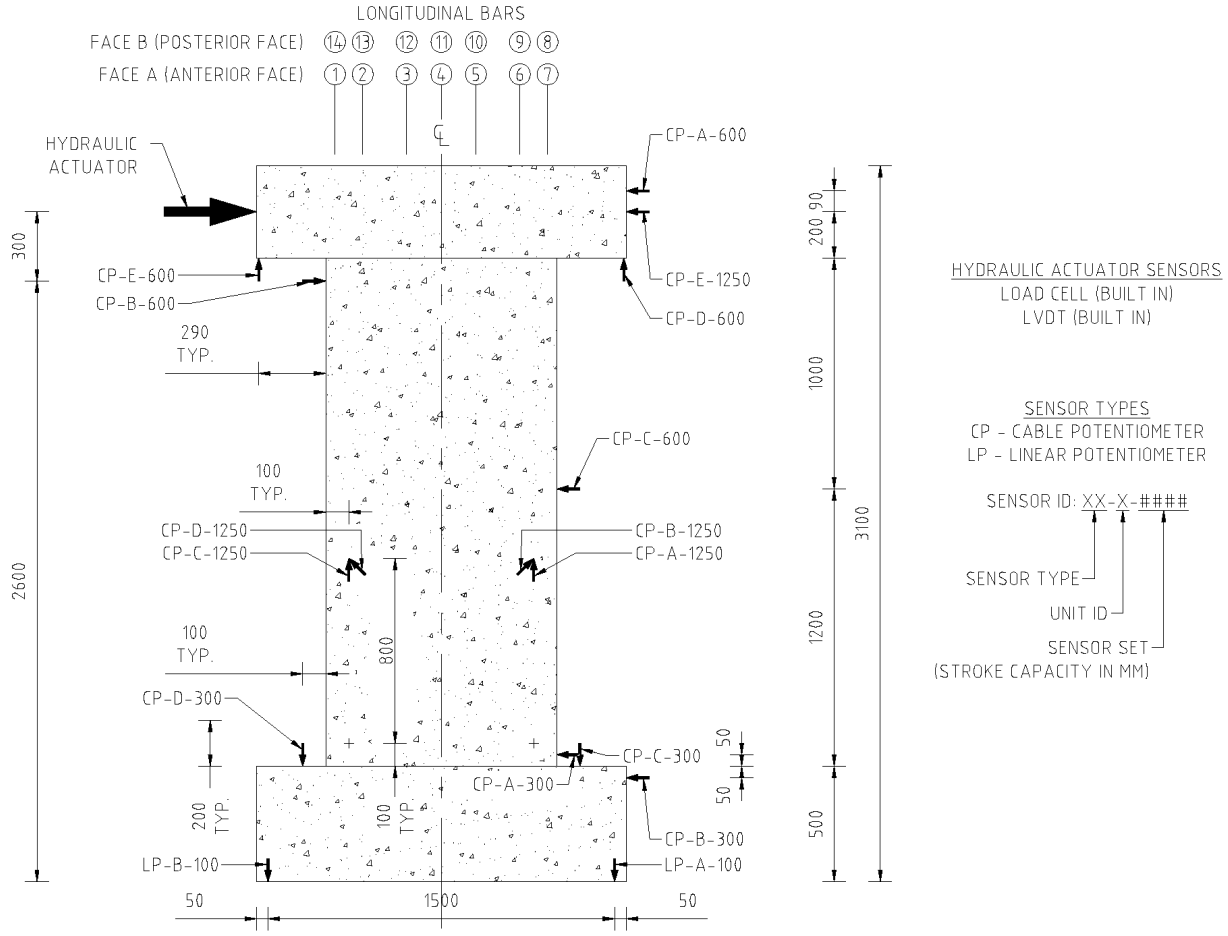

Figure 3.20. General instrumentation map.

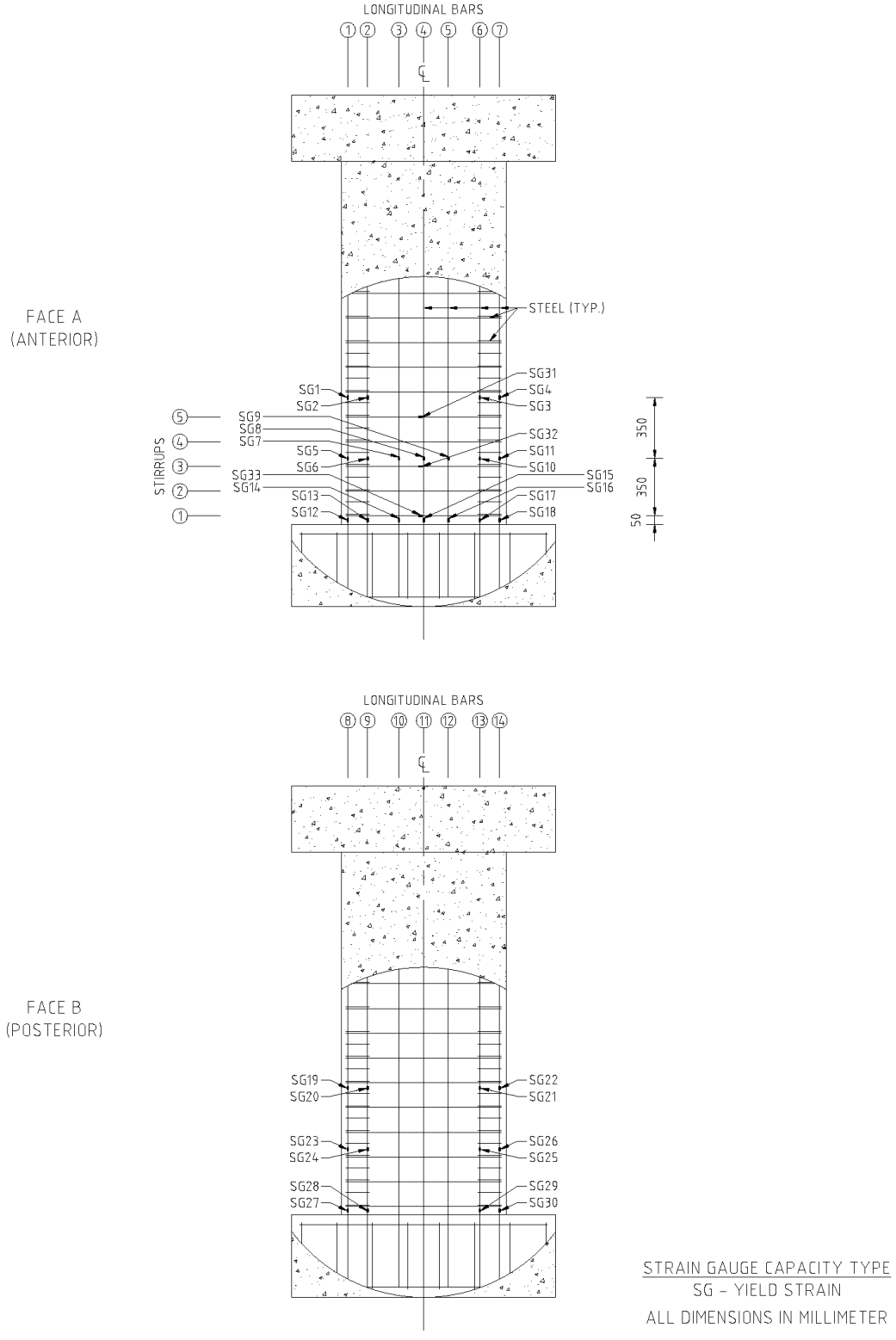

Figure 3.21. Strain gauge map for Wall SWS-R.

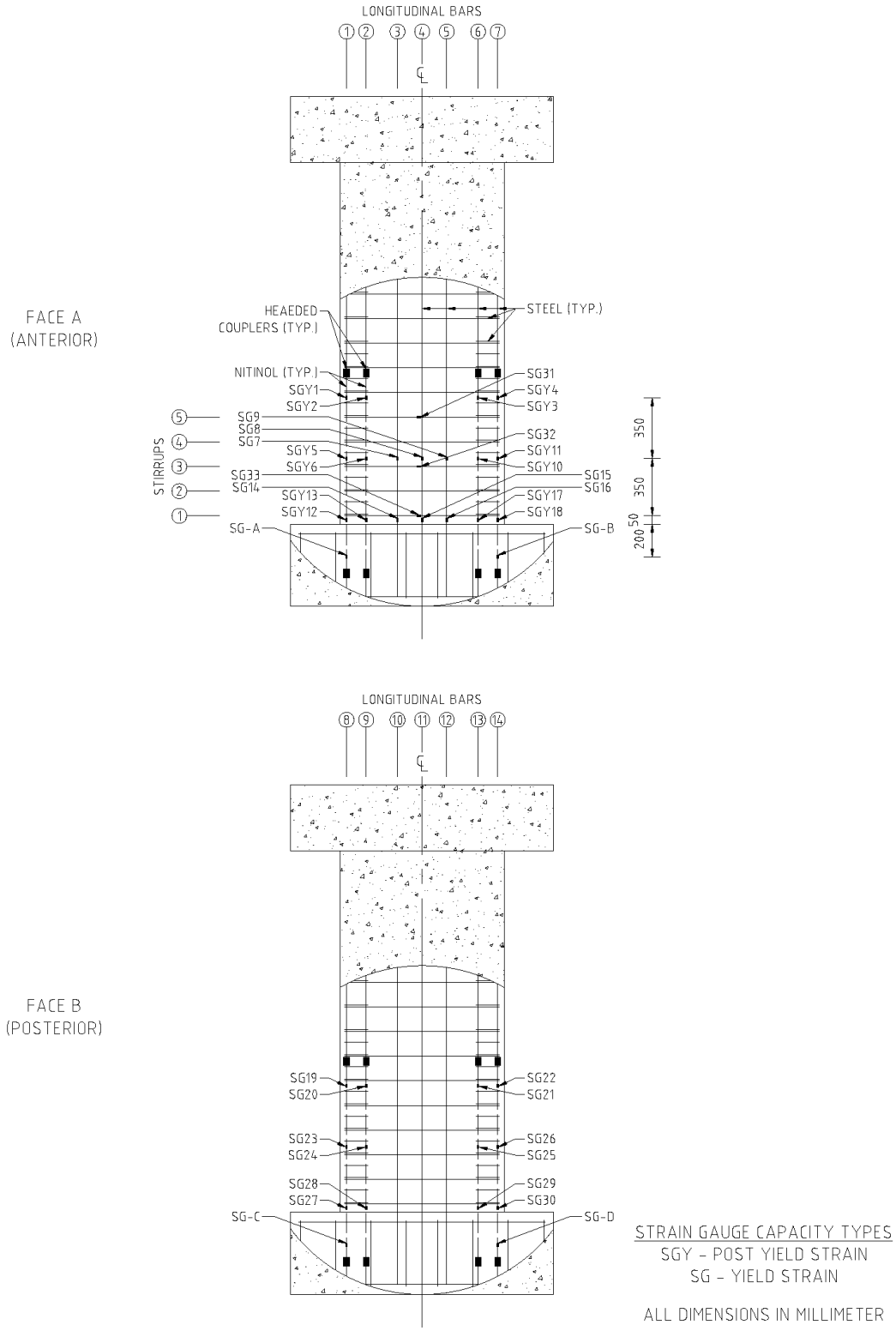

Figure 3.22. Strain gauge map for Wall SWN.

3.6.2 Test Frame

The test frame was assembled to provide a stiff structure that restrains displacement to within a single plane. The test frame was assembled using a set of W200x52 structural steel sections including four columns and four beams. Each column was anchored to the strong floor of the laboratory with four anchor rods. The columns were positioned along the length of the shear wall in two rows spaced at 600mm on each side form the centerline. In each row the columns were spaced at 3000mm apart. The two rows of columns were connected using semi-fixed bolted connections with two crossbeams of the same structural section to adjoin adjacent columns. The flexural capacity of the columns was expected to provide the majority of lateral resistance to out-of-plane displacements. The crossbeams were connected at a height of 1700mm from the ground to provide a sufficient clearance above the actuator. The columns in each row were then connected to each other with a steel beam of the same structural section, supporting the lateral bracing system. The test frame and lateral bracing system were virtually assembled in a scaled 3D model to assist with efficient assembly by first assessing the positioning of equipment and to determine any physical constrains. The assembled test frame 3D model is presented in Figure 3.23. The hydraulic actuator was mounted to the strong wall using a loading beam, a component of the laboratory loading system. The lateral bracing system was designed to withstand lateral loading due to accidental torsion inherent in the structure, determined according to the seismic provisions of CSA A23.3 for concrete structures. The lateral bracing system was designed according to CSA S16-14, and assembled using a modified C150x19 structural steel channel, with industrial grade unidirectional 6in. casters. The lateral bracing system is displayed in Figure 3.24. Further details on the lateral bracing system are available in Appendix E. More information on the design and development of the loading system is available in Appendix F.

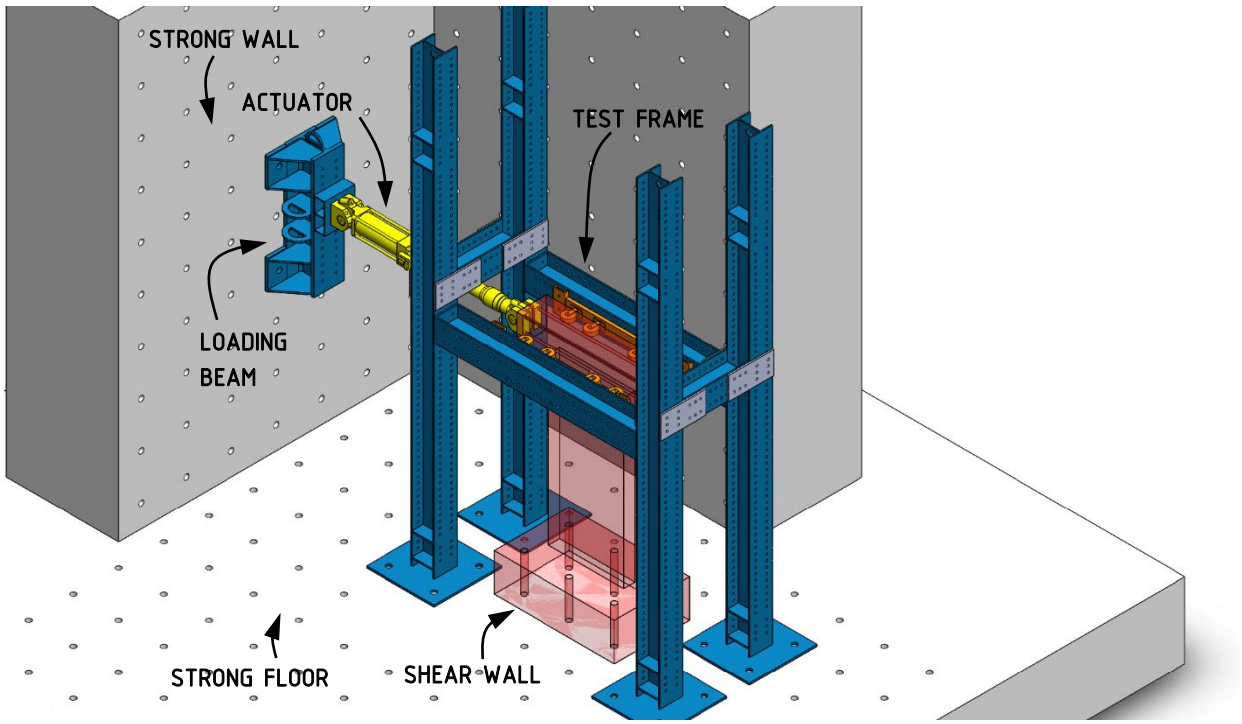

Figure 3.23. A 3D model of the assembled test frame.

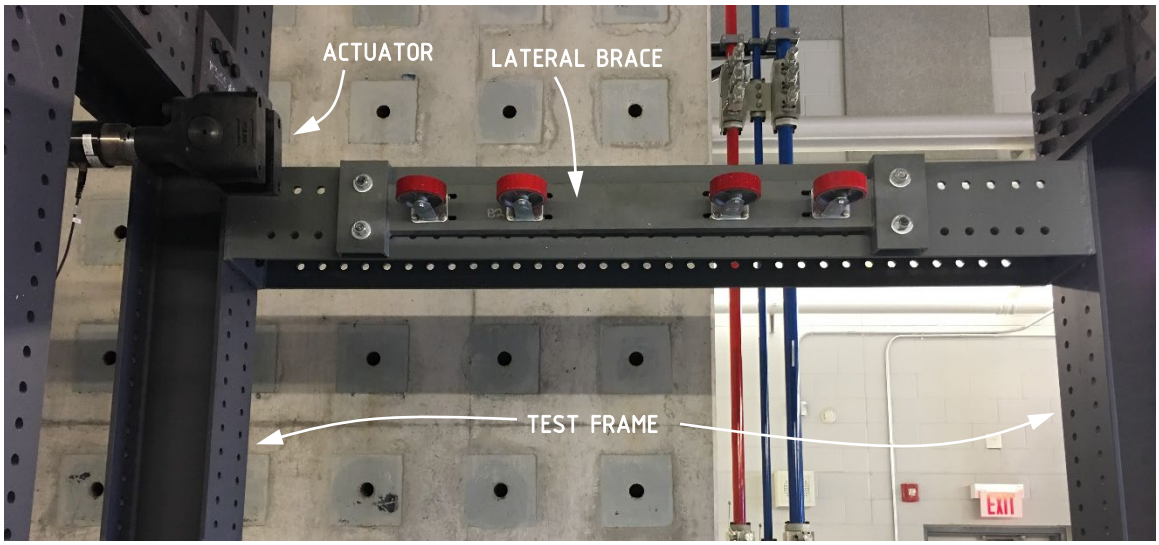

Figure 3.24. Lateral brace member mounted on the test frame.

3.6.3 Data Acquisition

Data acquisition was setup using a network of software suites and a combination of hardware. At the center of the setup was the laboratory computer which was used to control incoming and outgoing signals throughout the operation. The computer hosted two data collection applications: HBM Catman and MTS MultiPurpose Elite. The MultiPurpose Elite software was used solely to control the operation of the hydraulic actuator and to collect data from its load cell and LVDT devices. This software communicated with a signal controller unit which was connected to a hydraulic distribution manifold and a hydraulic power unit to drive the actuator displacements. Data was collected at a frequency of 10Hz, which provided an almost instantaneous refresh rate of live readings, to enable timely control of the actuator against the potential of haphazard communication lag between electronic devices. The HBM Catman software was used to log raw experimental data for all instruments, including synchronized signals from the actuator load cell and LVDT, at a frequency of 1Hz. The signal from the primary lateral displacement gauge (CP-E-1250) at the center of the cap beam was cloned to an additional port and read at a frequency of 50Hz to provide redundancy of live readings independent of the software used to control the actuator. Data from the clone signal was logged for lag calibration, if required. Signals from the instruments were collected using HBM data logging hardware (DAQ). A total of four DAQ units were used. The instrumentation for each wall occupied a total of 50 ports on the DAQ units. The laboratory computer and the data logging hardware were supported by a backup battery power supply, as a customary safety requirement in standards for experimental testing, to allow for sufficient time to save data and safely shut down the equipment in case of loss of power or an emergency. The hydraulic power unit was supplied by a dedicated power source and was set to a fail-safe mode which instantly relieves hydraulic pressure from the actuator. A flowchart of the data acquisition setup is presented in Figure 3.25.

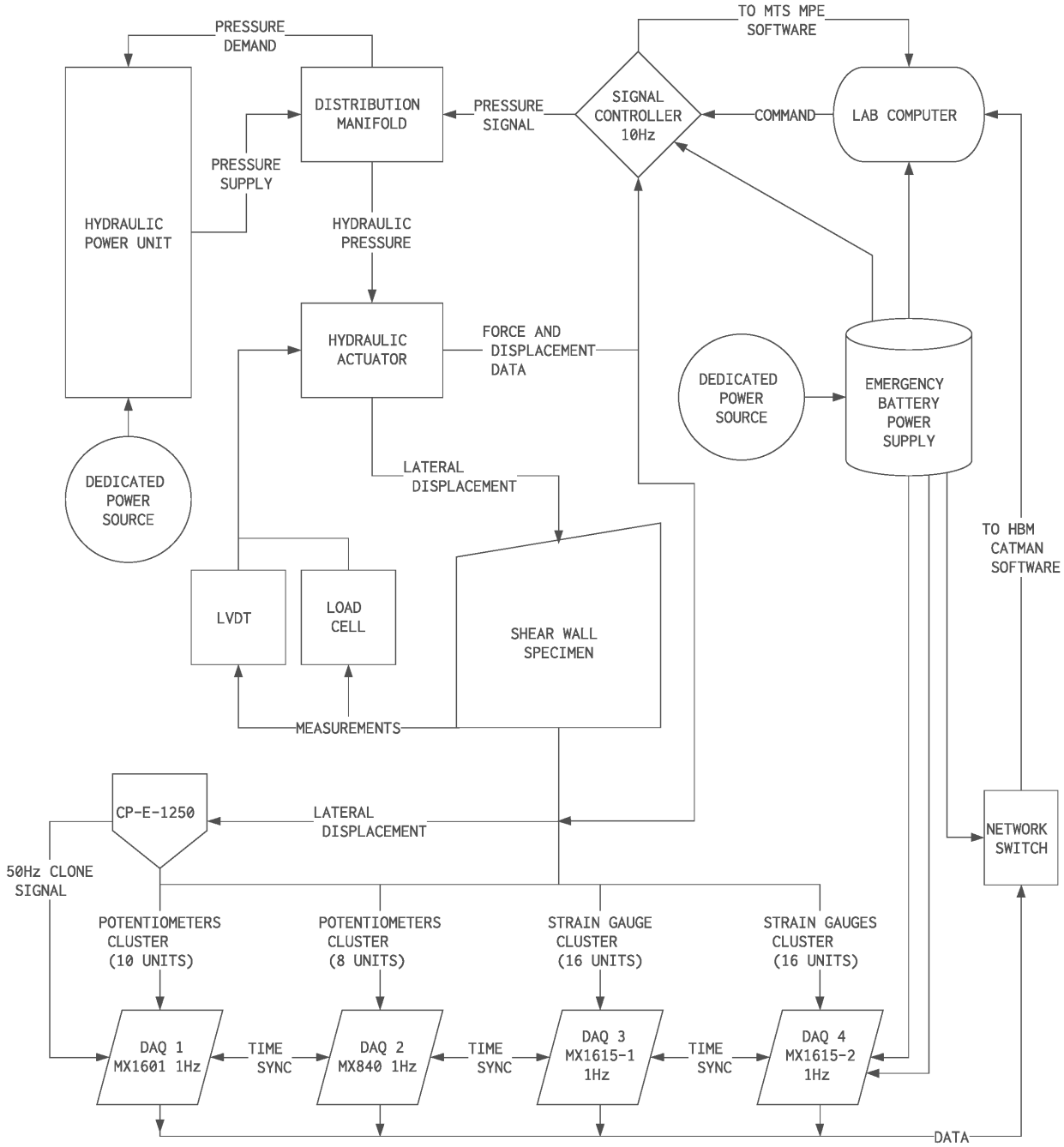

Figure 3.25. Data acquisition flowchart.

3.7 Test Program

The focus of the experimental test program is to study the structural performance of slender concrete shear walls in severe earthquakes. As such, a series of reverse cyclic quasi-static displacements are used to simulate seismic loading in which deterioration and safety govern considerations of failure.

3.7.1 Loading Protocol

The loading protocol for the experimental program was determined as a result of a comprehensive review of available literature on reverse cyclic loading, and by engineering judgement. A review of available loading protocols indicated that no standard is directly available for the pseudo-static seismic loading of reinforced concrete structures. Most of the available loading protocols pertain to steel and wood structures, and one protocol for masonry. A list and comparison of the available cyclic loading protocols is summarized by Krawinkler (2009).

For testing reinforced concrete structures, it was deemed most relevant to evaluate the use of the ATC-24 (1992) protocol and the FEMA 461 (2007) protocol as a more recent standard for reverse cyclic loading of structural components. The ATC-24 (1992) loading protocol, which pertains to steel structures, was predominantly used as it was largely referred to by the FEMA 261 (2007) protocol, however with some minor differences. Building upon the ATC-24 (1992) method, a displacement-controlled loading protocol was extrapolated around the yield point of each wall for the elastic and plastic ranges. The yield displacement of each wall was estimated by numerical analysis models to be approximately 10mm for Wall SWS-R, and approximately 23mm for Wall SWN. The series of displacements was unified, and the cycle counts for each wall were adjusted accordingly. ATC-24 (1992) suggested that force-controlled cycles be implemented up to 75% of the elastic range of the structure for more accurate control against high initial stiffness, however, this was omitted in favour of a consistent displacement-controlled protocol following FEMA 461 (2007). The cycle count at each displacement level was maintained according to the pattern prescribed by ATC-24 (1992), however, for displacements below yield, the cycle count was reduced by half to three. Unloading at each stage was force and time controlled to preserve any residual plastic deformations and to maintain similarity to the loading rate. A summary of the displacements sequence is presented in Table 3.5.

The gradual displacement increases over a low cycle count, as shown in Figure 3.26, is desirable for experimental testing as it intermittently limits the extent of damage, in brittle reinforced concrete structures, and allows for observation of extenuating damage at higher displacements. The ultimate lateral displacement of 120mm (5% drift), however unlikely in a seismic event, was used as a termination point ensuring severe strength and stiffness deterioration of the walls. This value was determined with consideration to the displacement capacities of the actuator and the attached instruments, as well as the physical limitations of the test setup.

Within the MultiPurpose Elite software, the loading protocol was programmed as a sequence of logical steps, each step containing the algorithm for a set of loading cycles within a specific displacement range. To account for rigid body movement during testing, the actuator was limited by a displacement range instead of a specific

displacement. The displacement ranges varied by judgement of amplitude and translation limits. The programming logic of the loading protocol is available in Appendix G.

Table 3.5. Displacements sequence

No.	Drift (%)	Displacement (mm)	Cycles		Loading Rate (mm/min)	Unloading Duration (min)
			Wall SWS-R	Wall SWN		
1	0.05	1.2	3	3	3	0.4
2	0.10	2.4	3	3	3	0.8
3	0.20	4.8	3	3	3	1.6
4	0.30	7.2	3	3	3	2.4
5	0.40	9.6	3 (yield)	3	3	3.2
6	0.50	12	3	3	3	4
7	1.00	24	3	3 (yield)	6	4
8	1.50	36	2	3	6	6
9	2.00	48	2	3	6	8
10	2.50	60	2	2	15	4
11	3.00	72	2	2	15	4.8
12	3.50	84	2	2	15	5.6
13	4.00	96	2	2	15	6.4
14	4.50	108	2	2	15	7.2
15	5.00	120	2	2	15	8

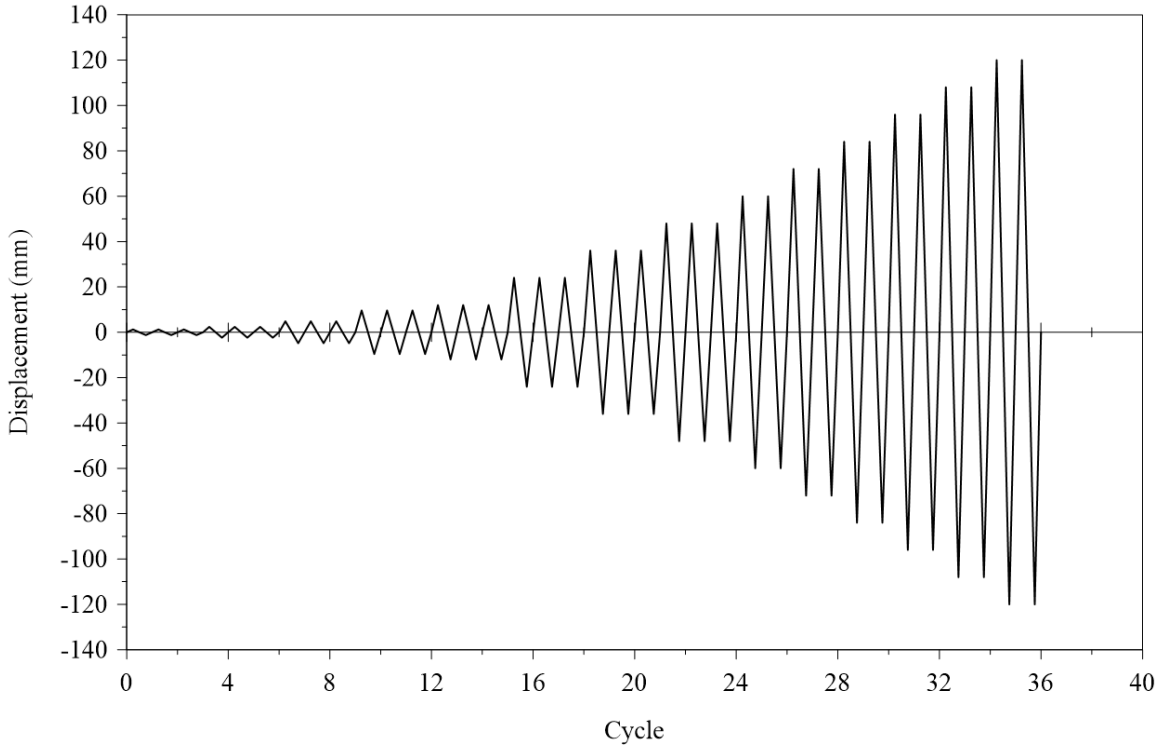

Figure 3.26. Reverse cyclic displacement protocol based on ATC-24 (1992).

CHAPTER 4

Preliminary Numerical Modelling

4.1 Introduction

A preliminary numerical investigation was conducted to predict the seismic performance of the superelastic Nitinol shape memory alloy (SE-SMA) reinforced slender concrete shear wall against the steel-reinforced control wall, using non-linear finite element analysis (NFLEA). The study is to investigates the variations in damage and the ability to recover from imposed lateral displacements. In this chapter, the development of the finite element models and the results of the numerical assessment are presented.

4.2 Development of Shear Wall Models

Two simulation models of ductile shear walls were developed for nonlinear finite element analyses (NLFEA) to investigate the seismic performance of self-centering structures when reinforced with the superelastic Nitinol shape memory alloy (SE-SMA). The models were assembled in FormWorks version 3.8. The dimensions were adopted from the shear wall specimens studied by Abdulridha (2013). A typical wall model had an aspect ratio of 2.2, having a length of 1000mm and height of 2200mm. The wall maintained a 150mm thick rectangular cross-section, rationed with 200mm long end boundaries. The wall specimen rested on a foundation block measuring 1600mm in length, 1000mm in width, and 500mm deep. The foundation block was sized to accommodate six anchor points divided over two rows along the length of the wall. The anchors were positioned at 600mm center-to-center, offset by 200mm from the ends of the pedestal. A cap beam was placed at the top of the wall and was used to transmit the cyclic lateral displacements. The beam had a cross-section of 400mm by 400mm and was 1600mm long.

The structural details of the walls were based on the seismic provisions of CSA A23.3. Identical deformed steel reinforcement details were used for the longitudinal reinforcement in the boundaries and the web, and the transverse shear reinforcement and buckling-prevention ties for both walls. The boundaries contained four, 10M (11.3mm diameter) bars and the web had six bars spaced evenly about the center of the wall. The longitudinal bars were placed in two curtains. All transverse reinforcement were made from 10M bars. In the Nitinol-reinforced wall, the longitudinal steel reinforcement in the boundaries were replaced within the estimated 1000mm height of the plastic

hinge region with smooth Nitinol SE-SMA bars (12.7mm diameter). The Nitinol bars were coupled to conventional steel bars for anchorage beyond the plastic hinge region of the wall and within the foundation block. The Nitinol bars extended 900mm into the boundaries and 300mm into the foundation block. The reinforcement details are further discussed in Section 3.3.1 of Chapter 3 (Experimental Program). The control wall was named SWS to denote 'Shear Wall – Steel-reinforced'. The Nitinol-reinforced wall was named SWN to denote 'Shear Wall – Nitinol-reinforced'.

4.2.1 Finite Element Modelling

Modelling the shear walls required some preplanning to overcome new geometric limitations and improve the availability of post-processing metrics for an accurate numerical prediction. In the study by Abdulridha (2013), the model mesh consisted of 100mm by 100mm rectangular elements. The large size of the rectangular elements imposed some geometric restrictions against investigating damage in the concrete cover at the ends of the wall, precise monitoring of crack locations and propagation, examining localized stresses and bond conditions in the longitudinal reinforcement, and integrating the new coupler system of this present study. The 20mm concrete cover over the end boundaries required discretization to allow for isolated detection of damage (cracks, spalling, or crushing). In the previous study (Abdulridha, 2013), the walls had shear starter bars projecting 300mm from the foundation into the web section of the wall, which shifted the critical damage away from the base. The removal of the shear starter bars in this study was speculated to increase damage along the base of the wall within a 300mm high region. It was anticipated that a finer mesh would present a diversified array of localized stresses and isolate singular cracks for a more realistic depiction of the damage. A mesh of higher element resolution would also improve investigation of yield penetration and the bond-slip relationship of the smooth Nitinol bars with the concrete. The couplers used to splice the Nitinol bars have a significantly wider diameter which was suspected to provide additional bearing anchorage at the ends. However, the 50mm length of the couplers would not align well with a larger rectangular element to give an identifiable localized response. To resolve the geometric and investigative limitations in the model, the mesh was discretized using 50mm by 50mm elements. The smaller element size provided a resolution four times greater than in the previous study.

Modelling the walls was completed in three stages. The first stage was defining the materials for rectangular elements and truss elements. The rectangular element materials contained the properties of concrete and smeared reinforcement. The properties of any reinforcements that were consistent over a region were unified into the rectangular element material in place of a composite system. Six rectangular element material types were prepared. Material types for the web, boundary region within the plastic hinge, and boundary region above the plastic hinge had smeared in-plane and out-of-plane transverse reinforcement properties. The out-of-plane reinforcement was based on the out-of-plane legs of the ties in the boundary regions. The cover was represented by a non-reinforced element material type. The cap beam and foundation block were represented by separate materials, each hosting the respective smeared properties for longitudinal and transverse reinforcements. The truss elements held properties for a singular material and were utilized to model the longitudinal reinforcing bars in the boundaries and web sections of the walls. The deformed steel truss elements were assumed to be perfectly bonded to the concrete and anchored with hooked

ends. The set of truss elements was expanded to model the smooth Nitinol bars, the couplers (35mm diameter), and the alternative American deformed No. 13 steel bars (12.7mm diameter) provided by the coupling manufacturer. A bond-slip property was defined for use with the smooth Nitinol bars, in conjunction with the pre-set condition for hooked ends to engage the anchorage and splicing provided by the couplers. The bond-slip behaviour was captured with link elements, which are placed between the concrete and truss bar elements. All other truss elements in the expanded set were assumed to have the same bond relationship as the deformed steel element.

The second stage was to create the finite element mesh. The mesh consisted of rectangular element regions and localized truss element reinforcements. A total of nine rectangular element regions were defined to form a basic wall model as presented in Figure 4.1. Each region was associated with the material type that contained the appropriate smeared transverse reinforcement ratio(s). The web region was modelled first to define the core aspect ratio of the rectangular elements at 1:1. The mesh of the boundary regions was predominantly populated with elements at the 1:1 ratio and was completed with elements at a 5:3 ratio adjacent to the ends of the wall. The end cover was modelled as an individual region to distinguish cover damage from other damage accumulating in neighbouring elements. The mesh of the concrete cover was limited to elements at a 5:2 ratio. The material types for the regions of the cap beam and foundation block both included smeared longitudinal reinforcement. The regions of the cap beam and foundation block were intentionally modelled with high reinforcement ratios for high stiffness to ensure complete transmission of the displacements into the wall. The aspect ratio of the elements in the mesh of the cap beam and foundation block conformed variably to the mesh pattern of the wall. The region types with their dimensions and reinforcement ratios are listed in Table 4.1. The longitudinal reinforcement was modelled using truss elements. A total of seven trusses were discretized. Each truss represented two bars to account for the two curtains of longitudinal reinforcement. Each truss bar was embedded into the cap beam at 100mm below the top, and into the foundation block at 100mm above the bottom. In Wall SWS, all seven trusses across the boundaries and the web were appropriated with conventional Canadian 10M deformed steel properties. In Wall SWN, the truss bars in the boundaries were replaced with Nitinol SE-SMA truss bars within the plastic hinge and linked to coupler truss bars at each end positioned at 900mm above the base of the wall and 300mm into the foundation. The coupler truss bars were spliced to conventional American No. 13 truss bars extending through the wall into the cap beam and within the foundation block. The truss bars in the web remained the same as in Wall SWS. A complete wall model contained 1580 rectangular elements and 406 truss bar elements.

In the third stage, the support conditions and load were defined. The wall was anchored using three sets of anchor rod supports spaced at 600mm about the centerline of the wall. In the model, each set contained three pin supports spaced at 50mm apart to simulate the actual distributed restraint of each anchor rod to be used for experimental testing. Loading was applied to the wall by imposing a lateral displacement at a node along the center of the cap beam. Loading was applied in displacement increments until the target was achieved or failure occurred. The self-weight of the wall was excluded on the premiss that it was a negligible gravity load and would have negligible influence on the performance of the wall under quasi-static lateral loading.

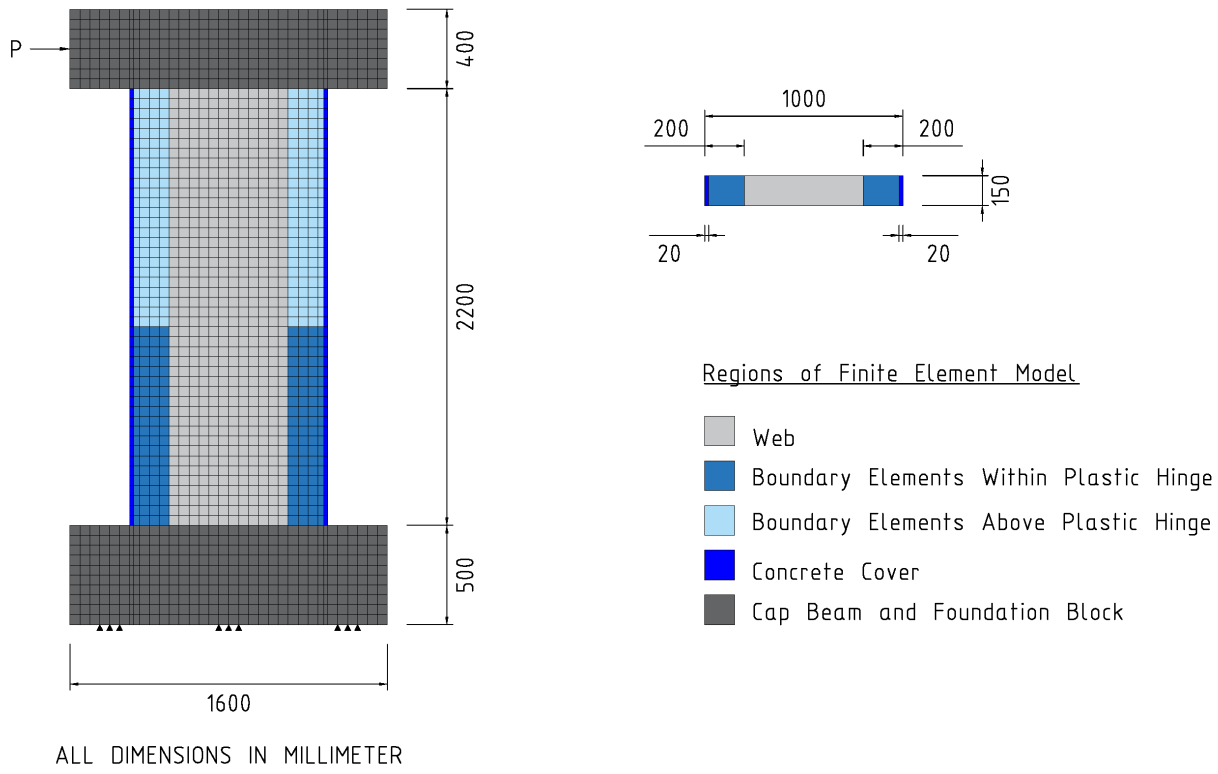

Figure 4.1. Regions of a typical finite element wall model.

Table 4.1. Region types and properties

Region Type	**Dimensions**		**Reinforcement Ratio**
Web	H: 2200mm	W: 600mm	In-plane: 0.889%
Boundary – Within Plastic Hinge	H: 1000mm	W: 180mm	In-Plane: 2.667%; Out-of-plane: 1.852%
Boundary – Above Plastic Hinge	H: 1200mm	W: 180mm	In-Plane: 1.778%; Out-of-plane: 1.111%
Concrete Cover	H: 2200mm	W: 20mm	Not Applicable
Cap Beam	H: 400mm	W: 1600mm	Longitudinal: 20%; Transverse: 20%
Foundation Block	H: 500mm	W: 1600mm	Longitudinal: 20%; Transverse: 20%

Two finite element models were developed for this study: Wall SWS and Wall SWN. Wall SWN was reinforced with the Nitinol SE-SMA bars in both boundaries and served the focus of this research. Wall SWS was used for control as a conventional reinforced concrete wall. The finite element models are presented in Figure 4.2.

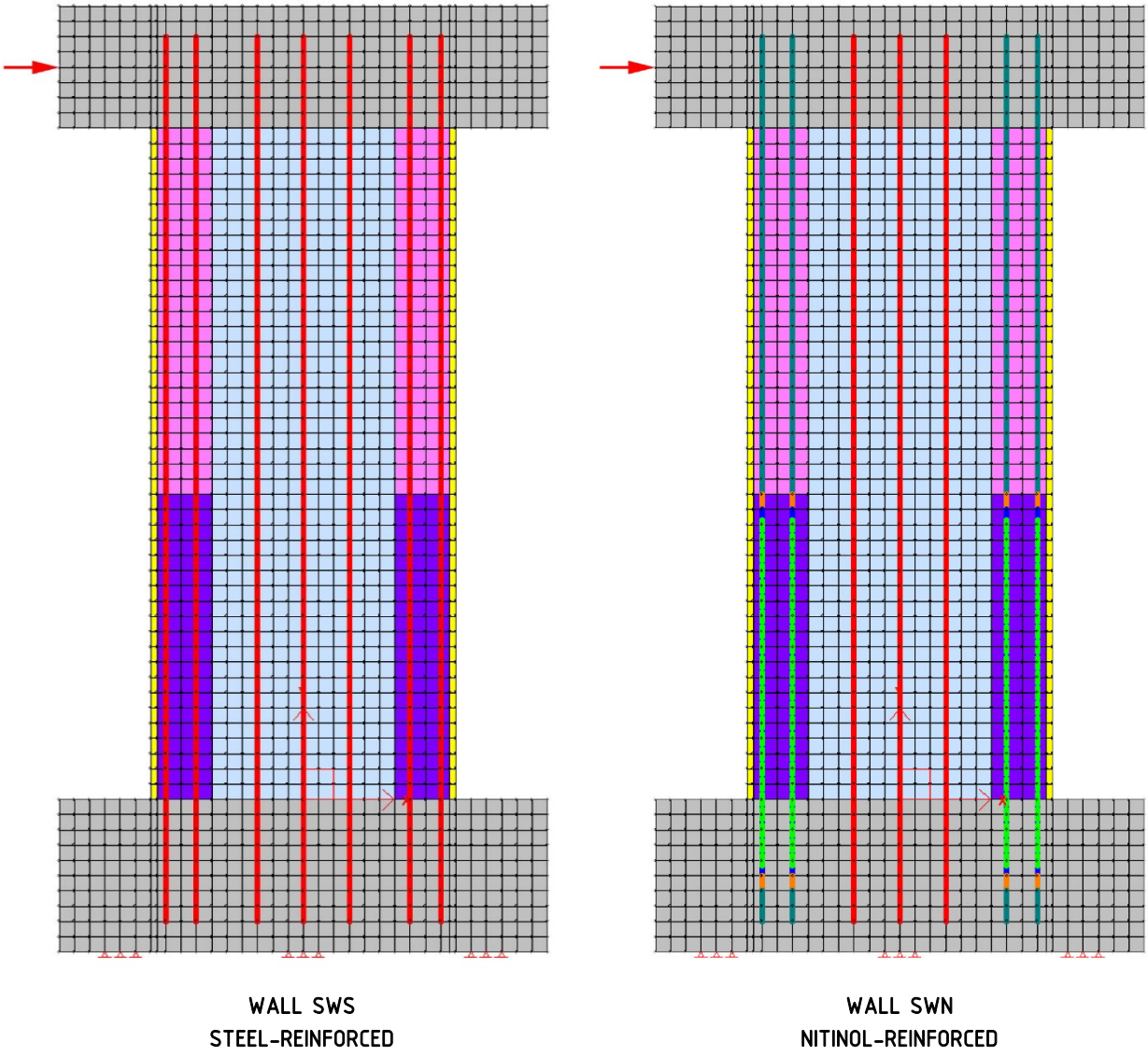

Figure 4.2. Finite element models of Walls SWS (left) and SWN (right).

4.2.1.1 Material Properties

Material properties were determined from concrete cylinders and steel reinforcement coupons for each wall. The Sika Sikacrete-08 self-consolidating concrete (SCC) product was available as a repair material. The properties of concrete are available in Table 4.2. Only steel reinforcement coupons were tested towards numerical modelling. Manufacturer provided details were used for the Nitinol and the couplers. Nitinol coupons were reserved for the experimental study. The reinforcement properties for Wall SWS are in Table 4.3, and in Table 4.4 for Wall SWN.

Table 4.2. Concrete mechanical properties for walls

Wall	**Type**	f'_c **(MPa)**	**Aggregate Size (mm)**
SWS	30MPa Normal Concrete	47.2	14
SWN	30MPa Normal Concrete	36.9	14
Repair Material	Sika Sikacrete-08 SCC	57.3	8

Table 4.3. Reinforcement mechanical properties for steel-reinforced Wall SWS

Rebar	**Diameter (mm)**	**Yield Strength (MPa)**	**Modulus of Elasticity (GPa)**	**Strain Hardening (%)**	**Tensile Strength (MPa)**	**Rupture (%)**
10M	11.3	454.4	159.5	3.5	570	29.4
15M	16	472.5	178.1	3.0	578	26.7

Table 4.4. Reinforcement mechanical properties for Nitinol-reinforced Wall SWN

Rebar	**Diameter (mm)**	**Yield Strength (MPa)**	**Modulus of Elasticity (GPa)**	**Strain Hardening (%)**	**Tensile Strength (MPa)**	**Rupture (%)**
10M	11.3	529.4	185.2	2.2	686.5	27.5
15M	16	472.5	178.1	3	578	26.7
#13	12.7	474.5	180.7	2.1	639.5	27.9
Nitinol	12.7	380	41	6	900	12
Coupler	35	690	200	4	795	35

4.2.1.2 Repair of Steel-Reinforced Wall SWS

The steel-reinforced wall revealed some areas of poor consolidation along the base after casting and removing of the formwork. The base of the right boundary had a defective region measuring about 200mm wide by 150mm high and penetrated about 35mm into the anterior and posterior faces and through the end cover. The honeycombing spread inwards from the right boundary by about 400mm across the web over a height of about 100mm. The region was similar on both faces of the wall with a penetration depth of about 20mm. Less severe honeycombing surrounded the base of the left boundary. The defect was isolated to a similar region for the right boundary at a depth of about 20mm on all sides. The wall was locally repaired and renamed 'SWS-R' to reflect the modification and used as the new control model. The model of Wall SWS was used for reference. The modified wall model with the discretized repaired regions is displayed in Figure 4.3.

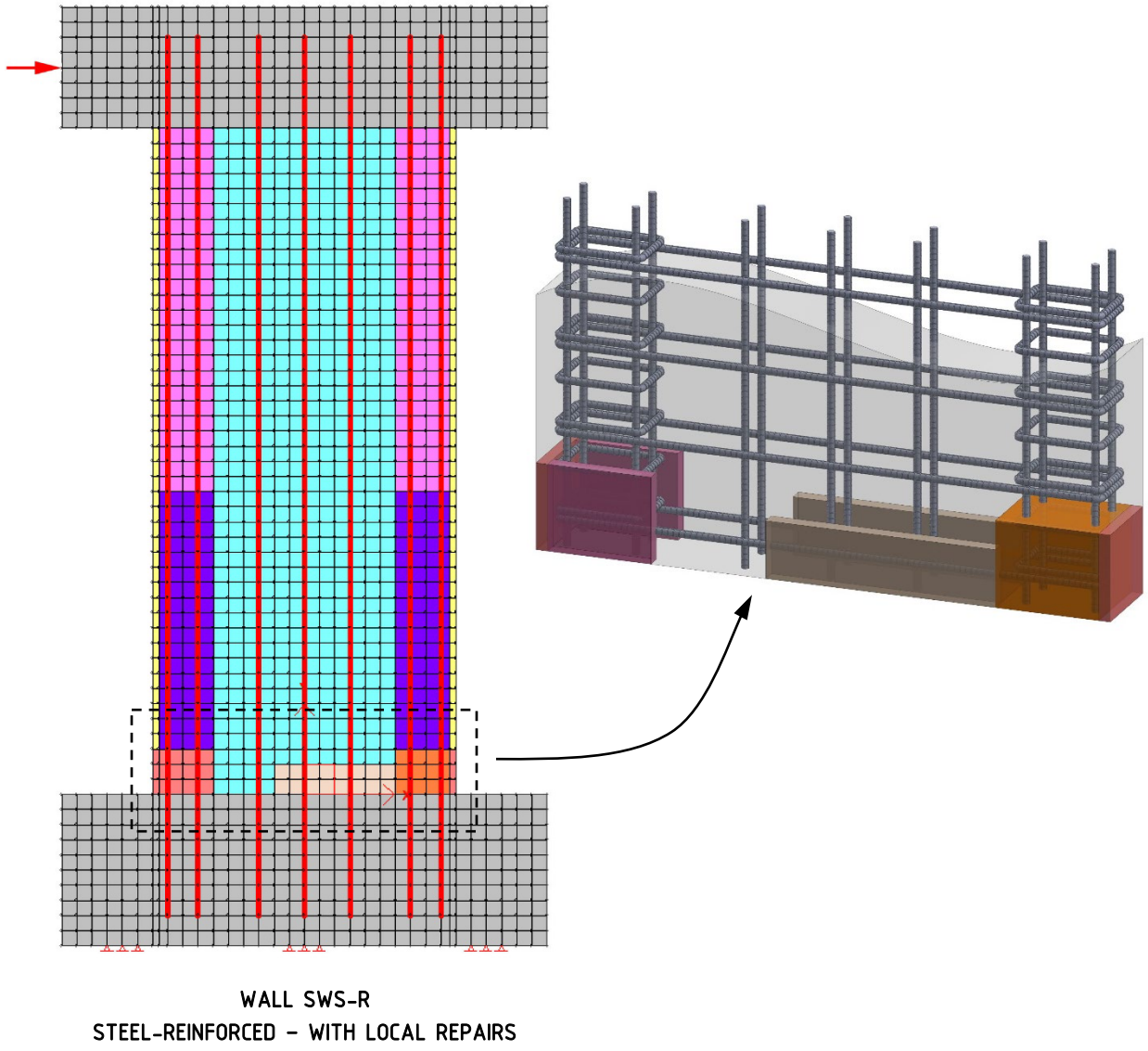

Figure 4.3. Arrangement of finite element repair layers for Wall SWS-R.

All defective regions were repaired with the Sika Sikacrete-08 SCC product. The defective region at the base of the right boundary was completely removed and filled with the SCC repair material. All other defective regions were repaired to a depth of 25mm. The repaired regions were discretized in layers of concrete elements with proportioned smeared reinforcement ratios as applicable. The layer of SCC through the base of the right boundary was smeared with 100% of the relevant transverse reinforcement. The 25mm thick repair layers over the web and the base of the left boundary were smeared with 25% of the respective reinforcement ratios for the regions. The remaining 100mm thick layer of original normal concrete retained 50% of the reinforcement ratio per region. The end cover layers were not reinforced. Negligible difference was found between the performance of the repaired steel-reinforced wall model and the original control wall model.

4.3 Non-Linear Finite Element Analysis

The VecTor2 analysis software was used for non-linear finite element analysis. The numerical methodology is built on the philosophies of the Modified Compression Field Theory (Vecchio et al., 1986) and the Disturbed Stress Field Model (Vecchio, 2000). The software includes a library of additional constitutive models for the realistic simulation of construction materials. Program VecTor2 uses stiffness matrices to analyze models assembled with low-powered, planar-stress elements and truss-bar elements. A planar-stress element is defined by four nodes and a truss-bar element is defined by two nodes. The properties attributed to each element are used in the analysis to capture the second-order effects of compression softening, tension stiffening, and tension softening, to name a few. A finite element model is loaded incrementally towards a target value of force or displacement. The performance of the structure is defined by an iterative algorithm using the secant stiffness. The cumulative results of the analyses are presented in the orthotropic stress elements as a sequence of crack widths and orientations. The results are visualized in the post-processing software Augustus (Wang and Vecchio, 2002).

4.3.1 Loading Protocol

The walls were simulated in-plane under monotonic loading and reverse cyclic loading. The wall models were loaded at the center of the cap beam at a height of 2400mm from the base.

Modelling was initialized with a pushover analysis of the walls. Each wall was displaced by trial of approximated values based on previous studies to achieve failure. The results of monotonic loading were used to estimate the yield displacement of each wall, according to the method by Park (1989), to extrapolate the loading protocol for reverse cyclic loading. The approximated yield of Wall SWS-R was 12mm at 130kN and 32mm at 140kN for Wall SWN.

Quasi-static load reversals were applied to each wall model to simulate a seismic event. The loading protocol was developed based on the guidelines of the ATC-24 (1992) standard. To apply an identical loading sequence to both models, the displacement intervals were defined as multiples of the yield displacement of Wall SWS-R. The loading

sequence is presented in Table 4.5. To allow for future repair of the walls, loading was terminated at 3.5% drift (84mm displacement). The displacement cycles are presented in Figure 4.4.

Table 4.5. Displacements sequence

No.	**Drift (%)**	**Displacement (mm)**	**Cycles**
1	0.08	2	3
2	0.17	4	3
3	0.25	6	3
4	0.50	12	3 (yield)
5	0.75	18	3
6	1.00	24	3
7	1.25	30	3
8	1.50	36	3
9	1.75	42	3
10	2.00	48	3
11	2.25	54	3
12	2.50	60	2
13	3.00	72	2
14	3.50	84	2

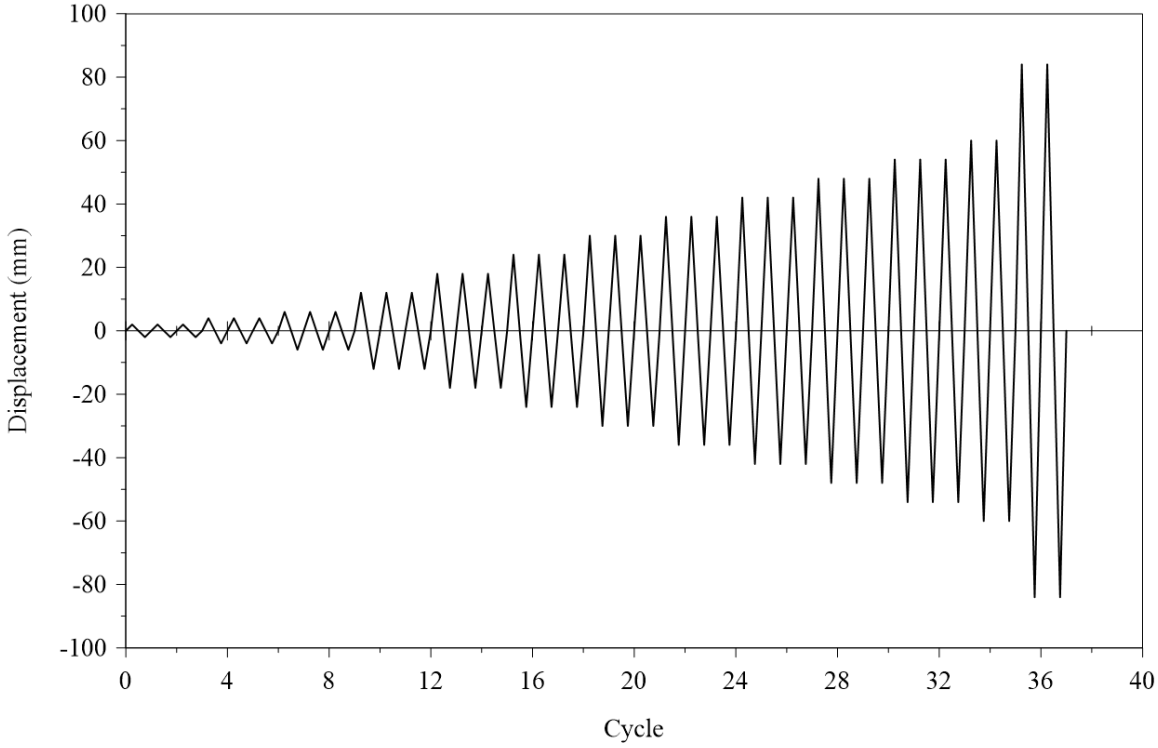

Figure 4.4. Displacement reversal cycles.

4.3.2 Constitutive Models

The VecTor2 default 'Basic' set of constitutive models were used for analysis. The constitutive models for concrete are listed in Table 4.6. The constitutive models for reinforcement and bond are listed in Table 4.7. The basic analysis settings are listed in Table 4.8. Additional details on the default constitutive models and analysis settings can be found in the VecTor2 & FormWorks User's Manual – Second Edition (Wong, Vecchio, and Trommels, 2013).

Table 4.6. Concrete constitutive models

Parameter	**Model**
Compression Pre-Peak	Hognestad (Parabola)
Compression Post-Peak	Modified Park-Kent
Compression Softening	Vecchio 1992-A (e1/e2-Form)
Tension Stiffening	Modified Bentz 2003
Tension Softening	Bilinear
FRC Tension	Not Considered
Confined Strength	Kupfer / Richart
Dilation	Variable – Orthotropic
Cracking Criterion	Mohr-Coulomb (Stress)
Crack Stress	Basic (DSFM/MCFT)
Crack Width Check	Aggregate/2.5 Max Crack Width
Crack Slip	Walraven
Creep and Relaxation	Not Considered
Hysteretic Response	Nonlinear with Plastic Offsets

Table 4.7. Reinforcement and bond constitutive models

Parameter	**Model**
Hysteretic Response	Bauschinger Effect (Seckin)
Dowel Action	Tassios (Crack Slip)
Buckling	Akkaya 2012 (Modified Dhakal-Maekawa)
Concrete Bond	Eligehausen

Table 4.8. Analysis settings

Parameter	**Settings**
Strain History	Previous Loading Considered
Strain Rate Effects	Concrete: Not Considered Steel Reinforcement: Not Considered
Structural Damping	Not Considered
Geometric Nonlinearity	Considered
Crack Spacing	CEB-FIP 1978-Deformed Bars

4.3.2.1 Superelastic Nitinol Shape Memory Alloy Model

The constitutive model for the superelastic Nitinol shape memory alloy used in this assessment was developed by Abdulridha et al. (2013). The model has two trilinear envelopes representing the loading and unloading responses of the SMA material. The loading branch defines the stress-strain path for the elastic response, yielding (mechanically induced detwinned martensite transformation), and strain hardening. The unloading branch defines the strain recovery phase and captures the plastic offset. The residual plastic deformations are formed when the martensitic Nitinol begins to strain harden beyond 6 to 8% strain. A representation of the superelastic Nitinol SMA numerical model is presented in Figure 4.5.

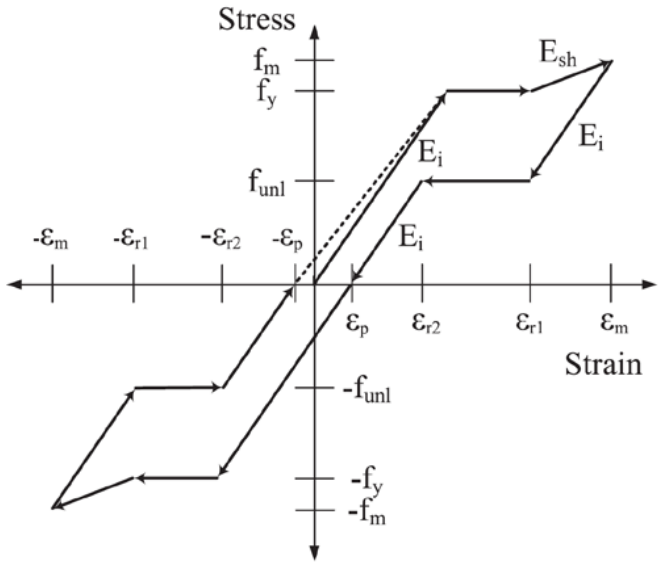

Figure 4.5. Superelastic Nitinol shape memory alloy constitutive model (Abdulridha et al., 2013).

4.4 Results

The results of the numerical analyses are presented in this section. The performance of each wall is averaged from the responses of positive and negative directions loading.

4.4.1 Load-Displacement

Quasi-static load reversal was used to predict the seismic performance from the wall models. Wall SWS-R presented wide hysteretic loops. Yielding of the longitudinal steel bars in the boundaries and the web led to early achievement of the peak load. Negligible difference was found in the hysteretic responses of Wall SWS-R and Wall SWS in relation to the repair. The self-centering capacity of Wall SWN was immediately evident from a pinching trend in the hysteretic response around the origin. The stiffer steel bars in the web yielded prior to yielding of the Nitinol bars, which remained within the strain recovery limit of 6%. The smaller modulus of elasticity of the Nitinol bars led to a large global yield displacement of the wall. The envelopes of the pushover analyses highlight the strength losses resulting from reverse cyclic loading. Wall SWS-R maintained a 14% reduction in strength in the positive direction before stiffening towards 3% drift (72mm displacement). The strength stagnated at about 16% below the monotonic loading envelope in the negative direction. Wall SWN had an average cyclic strength drop of less than 5%. The hysteretic response of Wall SWS-R is presented in Figure 4.6, and in Figure 4.7 for Wall SWN. The hysteretic performances of the walls are summarized in Table 4.9.

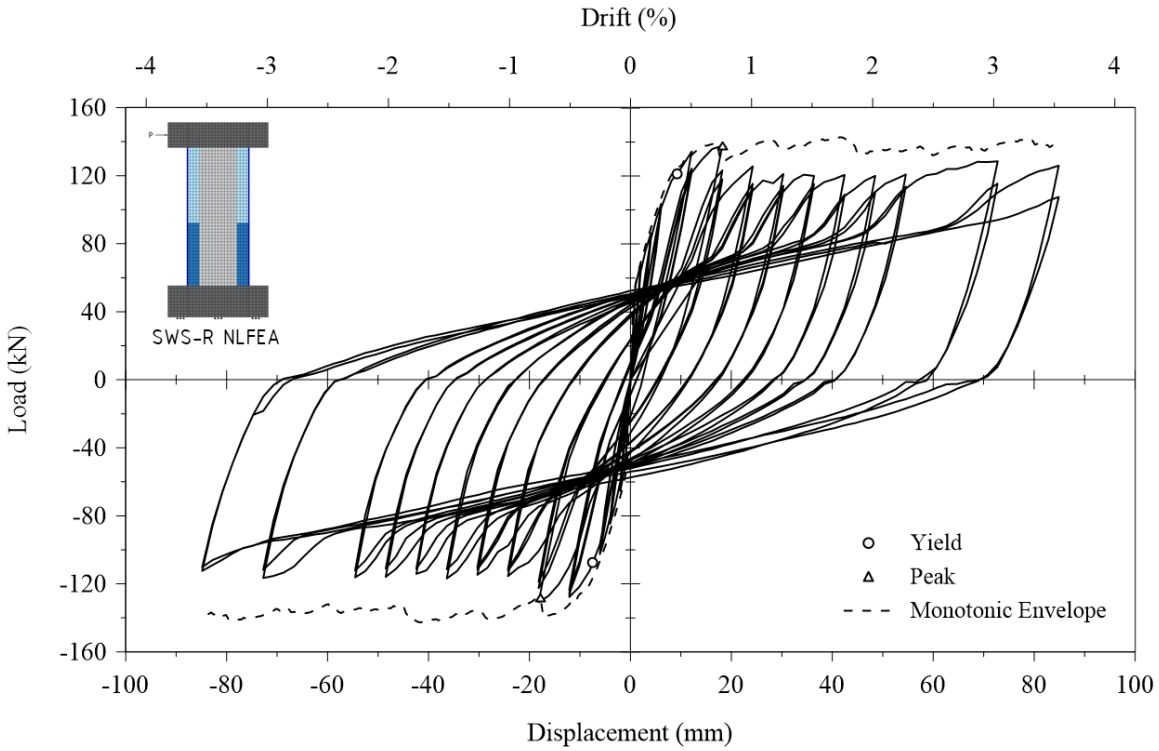

Figure 4.6. Load-displacement response of Wall SWS-R with monotonic loading envelope.

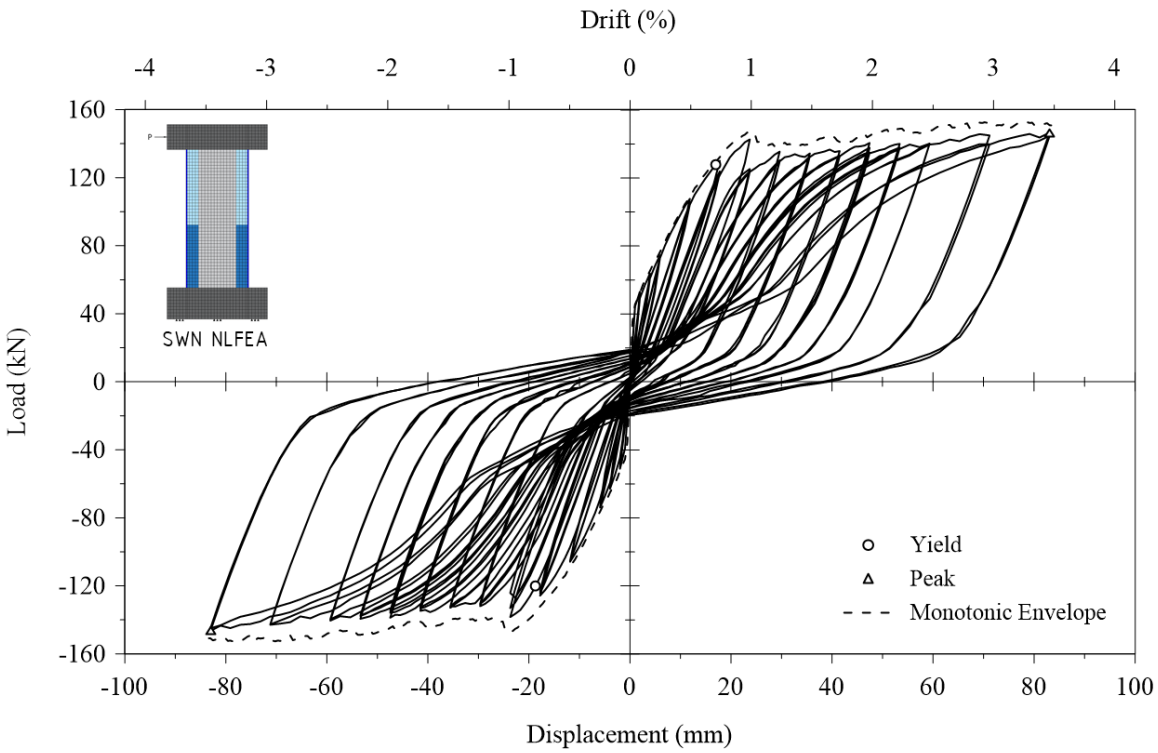

Figure 4.7. Load-displacement response of Wall SWN with monotonic loading envelope.

Table 4.9. Yield and peak displacements

Response	Wall SWS-R				Wall SWN			
	Yield		Peak		Yield		Peak	
	+	–	+	–	+	–	+	–
Displacement (mm)	9.2	7.4	18	18	17	19	83	83
Drift (%)	0.38	0.31	0.76	0.74	0.71	0.78	3.5	3.5
Load (kN)	121	108	138	128	128	120	147	147

4.4.2 Strength and Stiffness

Both walls maintained compatible high strength retention, with a minimum of 92%, based on a comparison of the second loading repetition to the first loading repetition Wall SWS-R presented a maximum difference of 7% less retention at the terminal drift of 3.5% (84mm displacement), as shown in Figure 4.8. The initial stiffness of Wall SWN was approximately 20% less than that of Wall SWS-R, in correlation to the lower stiffness of the Nitinol bars in the boundaries. The walls had identical stiffness at 0.75% drift (18mm displacement.). Thereafter, Wall SWN maintained a greater stiffness by up to 31%. The stiffness degradation of both walls is presented in Figure 4.9.

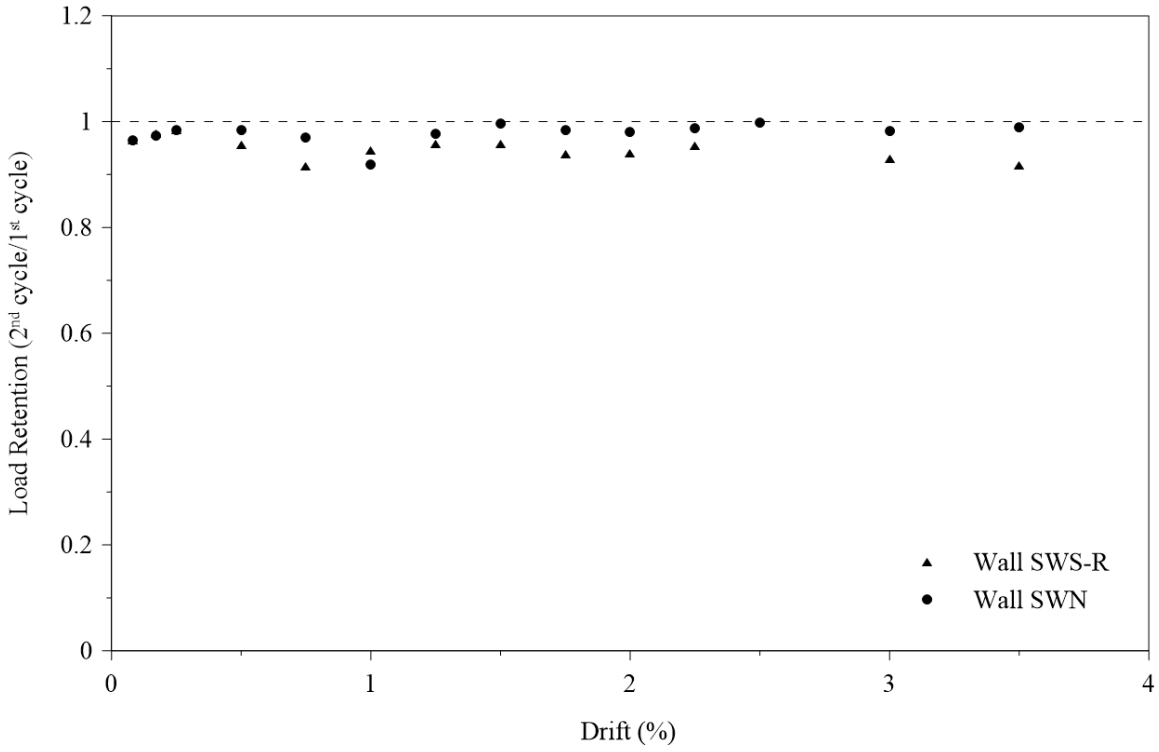

Figure 4.8. Strength retention.

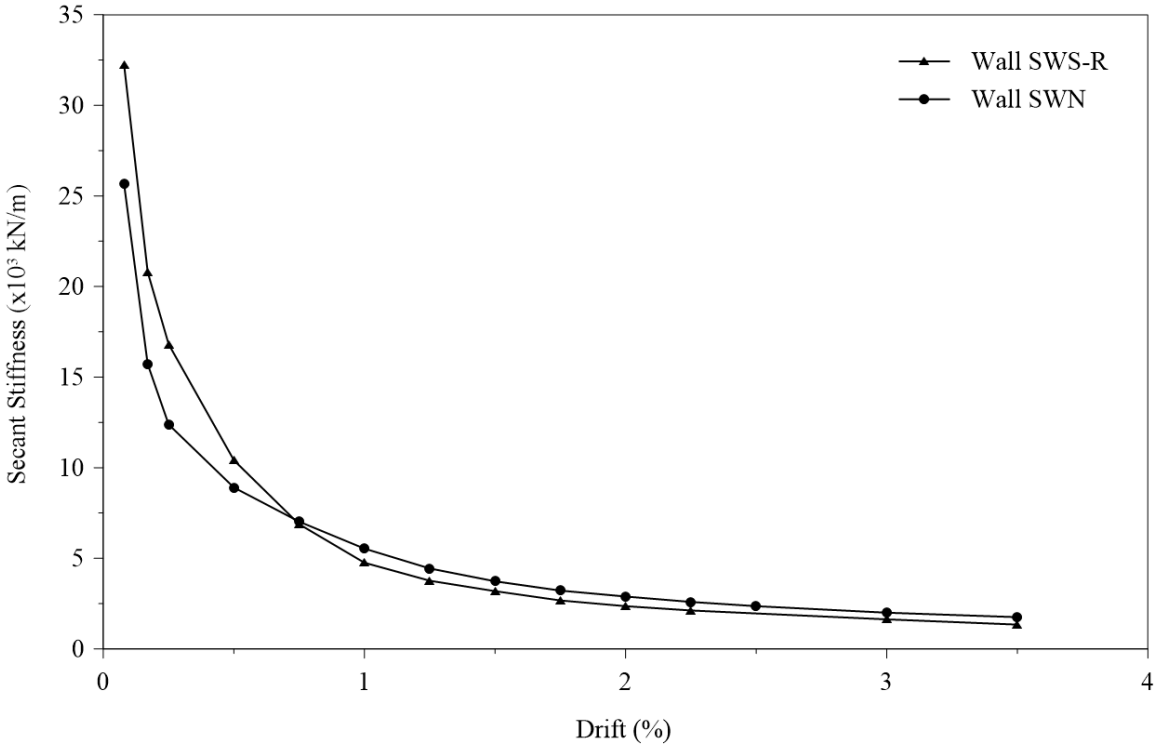

Figure 4.9. Stiffness degradation.

4.4.3 Ductility and Recovery

Wall SWS-R had a ductility of 10.2 and Wall SWN had a ductility of 4.7. The earlier onset of yielding of the steel reinforcement in the boundaries contributed to a lower yield displacement of Wall SWS-R. The lower stiffness of the Nitinol bars led to a softened hysteretic response of Wall SWN and a delayed yielding of the structure. Wall SWN is expected achieve higher drift recovery at displacements prior to the global yield displacement.

Recovery (*%*), was determined by Equation 4.1. The difference between the target displacement (Δ_{max}) and the residual displacement ($\Delta_{residual}$) of the first cycle when unloaded, is weighed against the target displacement.

$$Recovery\ \% = \frac{\Delta_{max} - \Delta_{residual}}{\Delta_{max}} \cdot 100\% \qquad \text{[Eq. 4.1]}$$

Both walls presented high drift recovery for up to 0.25% drift (6mm displacement). Wall SWN retained high drift recovery up to 0.75% drift (18mm displacement). As plastic deformations accumulated, Wall SWN maintained a higher level of drift recovery at an average of about 2.3 times greater than Wall SWS-R, indicating a high tendency towards self-centering, due to the superelasticity of the Nitinol bars. At 2.5% drift (60mm displacement), Wall SWN recovered approximately 61%, whereas Wall SWS-R recovered approximately 24%. Based on the study by Ramirez

and Miranda (2012), Wall SWN has less than 10% chance of being demolished, whereas Wall SWS-R has approximately an 80% chance. The recovery responses for Wall SWS-R and SWN are presented in Figure 4.10.

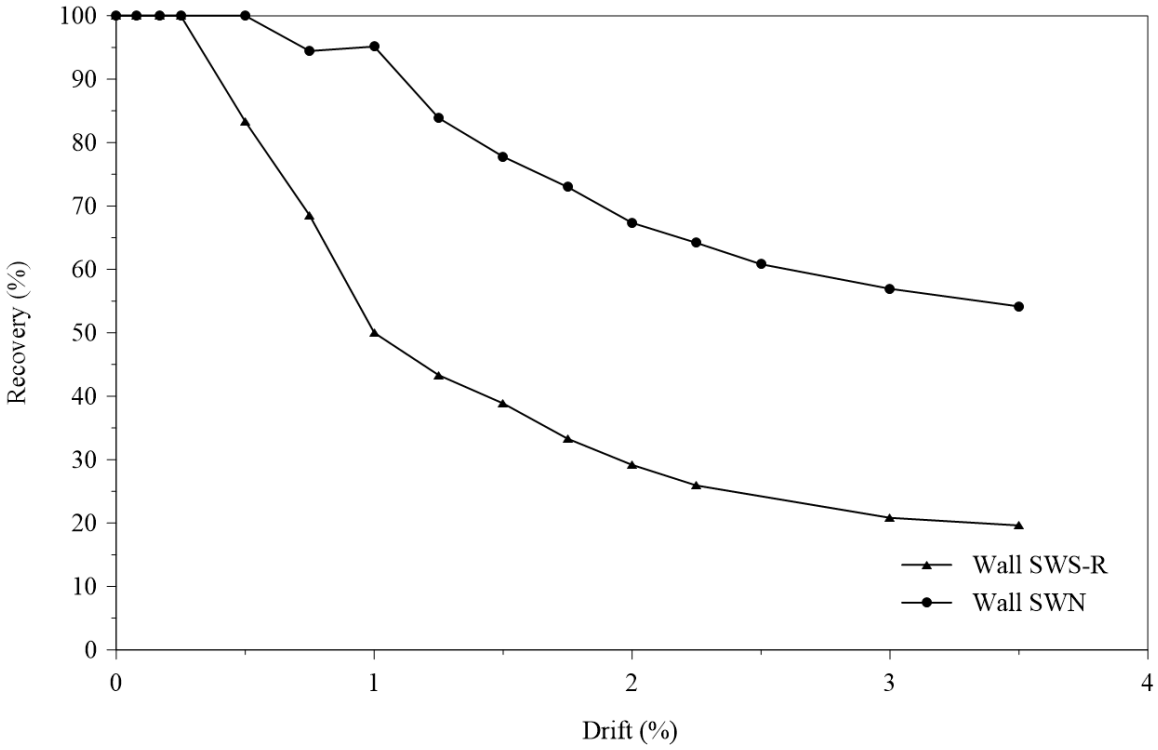

Figure 4.10. Drift recovery capacity.

4.4.4 Energy Dissipation

Wall SWS-R had wide hysteretic loops indicating greater energy dissipation than anticipated from the narrower pinched loops of Wall SWN. The first cyclic repetition at the ultimate drift to 3.5% (84mm displacement) are provided in Figure 4.11, while the energy dissipation trends for both walls are presented in Figure 4.12. The walls had compatible energy dissipation up to 0.5% drift (12mm displacement), varying by about 20%. Wall SWS-R had a peak dissipation difference of 177% over Wall SWN at 1% drift (24mm displacement). Thereafter, Wall SWS-R continued to maintain greater energy dissipation, however with a diminishing difference. At 2.5% drift (60mm displacement) Wall SWS-R dissipated about 57% more energy than Wall SWN. At the ultimate displacement level, the difference in energy dissipation of Wall SWS-R was reduced to about 41% greater than Wall SWN.

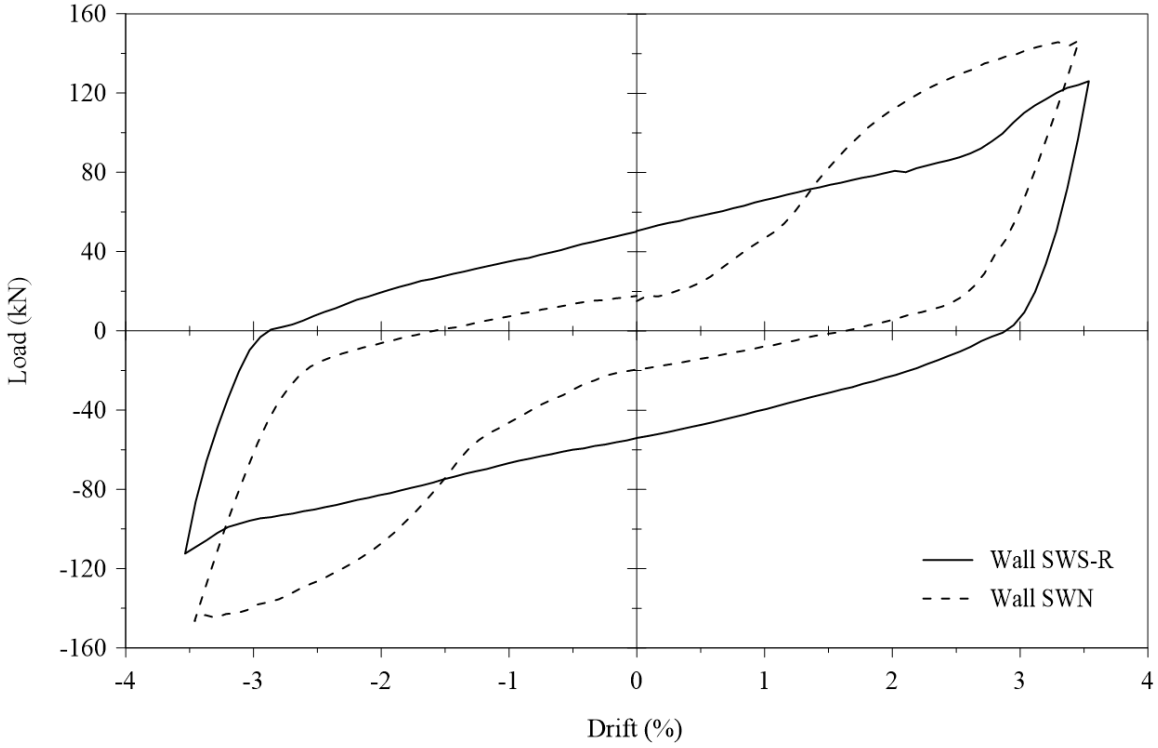

Figure 4.11. First cyclic repetition at 3.5% drift.

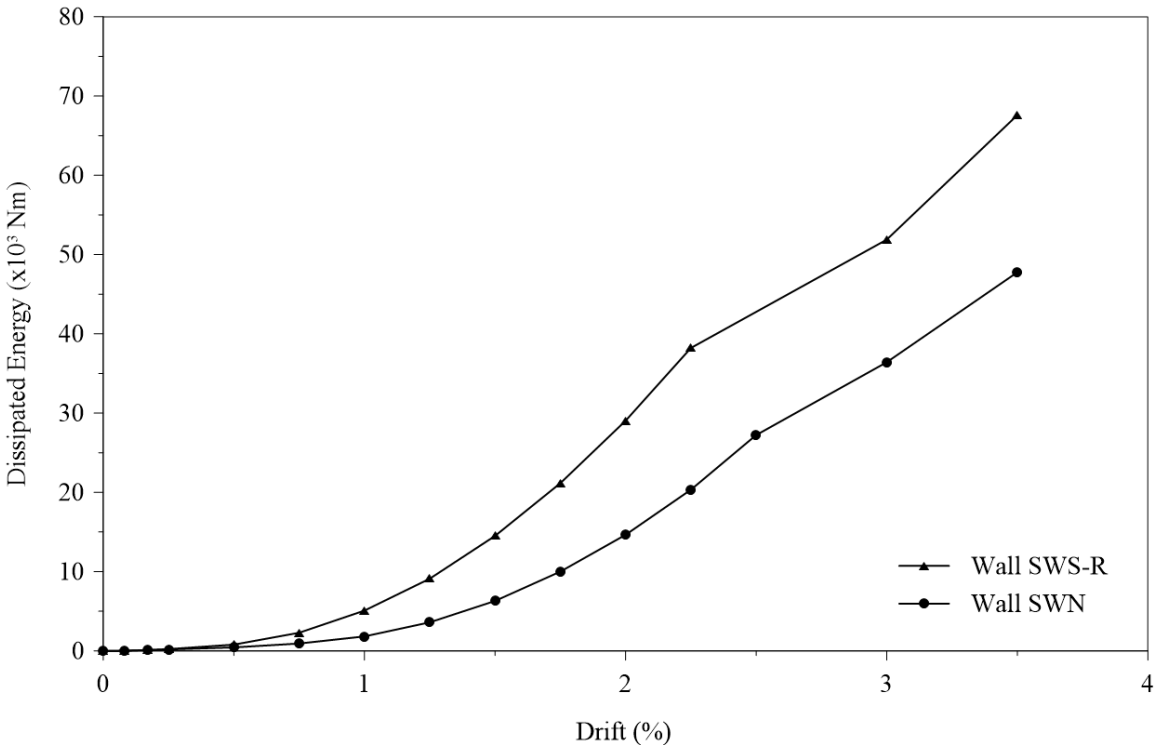

Figure 4.12. Dissipated energy.

4.4.5 Failure Mechanism

The predicted damage mechanisms are summarized in Table 4.10. No rupturing of the reinforcement was captured.

Table 4.10. Predicted damage mechanisms

Order of Failure	Wall SWS-R		Wall SWN	
	Displacement (mm)	Failure Type	Displacement (mm)	Failure Type
1	1	First Flexure Crack	1	First Flexure Crack
2	2	Cover Loss	6	First Shear Crack
3	3	First Shear Crack	12	Longitudinal Steel Yield, Web
4	8	Global Yield Displacement	17	Cover Loss
5	24	Longitudinal Steel Yield	18	Global Yield Displacement
6	54	Toe Crushing	18	Nitinol Yield, Boundaries

4.4.5.1 Cracking Characteristics

The damage in each wall initiated with an array of flexural cracks and some shear cracking across the web. Common to both walls was a predicted concentration of damage extending approximately 300mm up from the base of the walls.

Wall SWS-R developed a concentration of cracks towards the bottom of the plastic hinge, accompanied by a widening flexural crack running along the base. The model exhibited loss of the concrete cover at the ends of the wall at 0.08% drift (2mm displacement). The SCC repair material was predicted to have crushed at 2.25% drift (54mm displacement). At 2.5% drift (60mm displacement), Wall SWS-R had an elaborate network of shear and flexural cracks within the plastic hinge region. The crack pattern over the height of the wall was mostly populated by shear cracks fanning across the boundaries and the web from both ends. The predicted crack pattern at 2.5% drift for Wall SWS-R is presented in Figure 4.13.

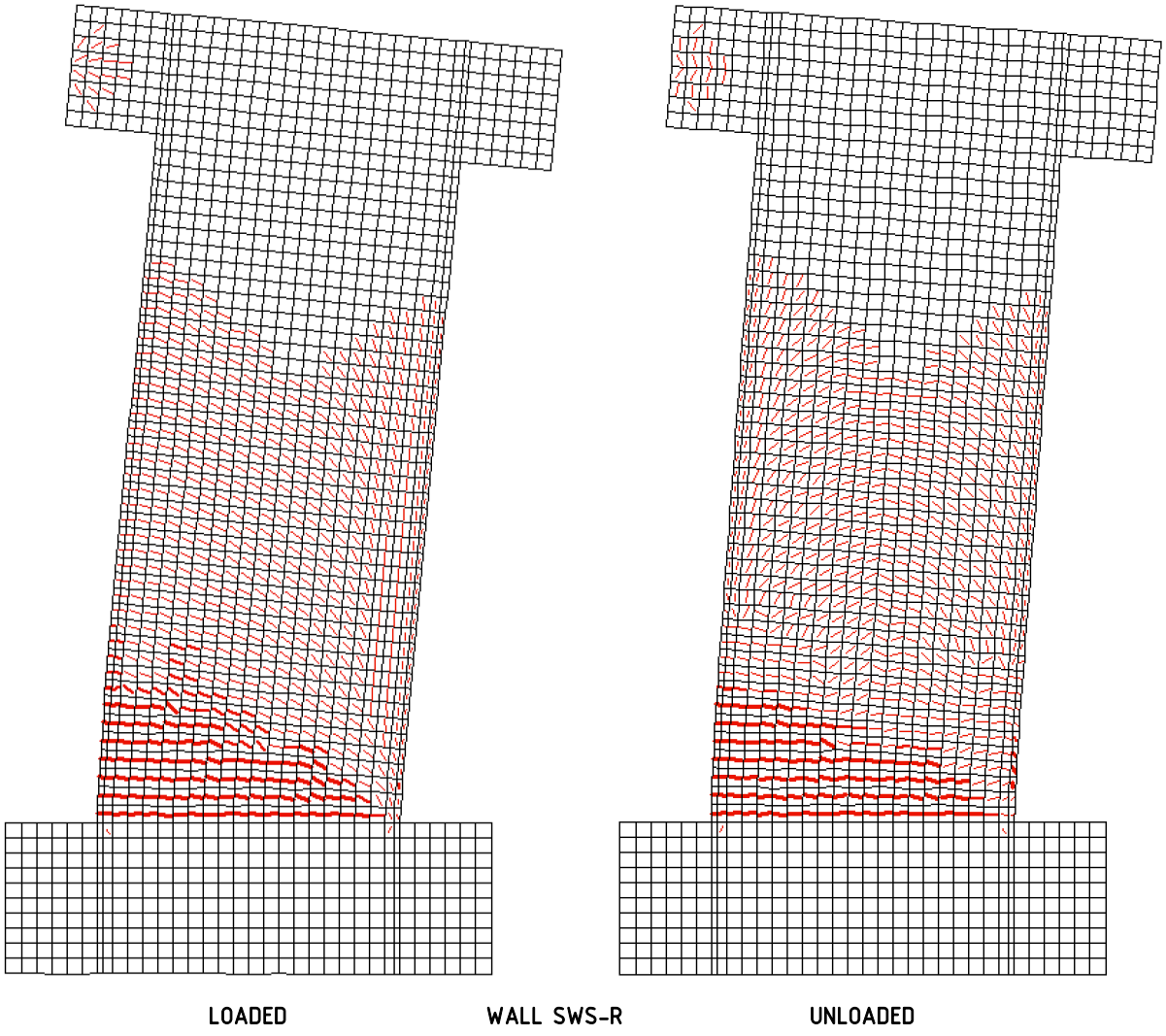

Figure 4.13. Crack pattern of Wall SWS-R at 2.5% drift: loaded (right); and unloaded (left).

Wall SWN developed a dominant flexural crack along the base as a result of the poor bond between the smooth Nitinol bars and the concrete. The model predicted that the concrete end cover would be lost at the boundary under compression as the wall reached the global yield displacement at approximately 0.75% drift (18mm displacement). Concrete crushing was not observed up to 3.5% drift. At 2.5% drift (60mm displacement), Wall SWN presented cracks appearing to initiate over the web and diminish towards the boundaries. The concrete regions of the boundaries reinforced with superelastic Nitinol experienced minimal cracking. The predicted crack pattern at 2.5% drift for Wall SWN is presented in Figure 4.14.

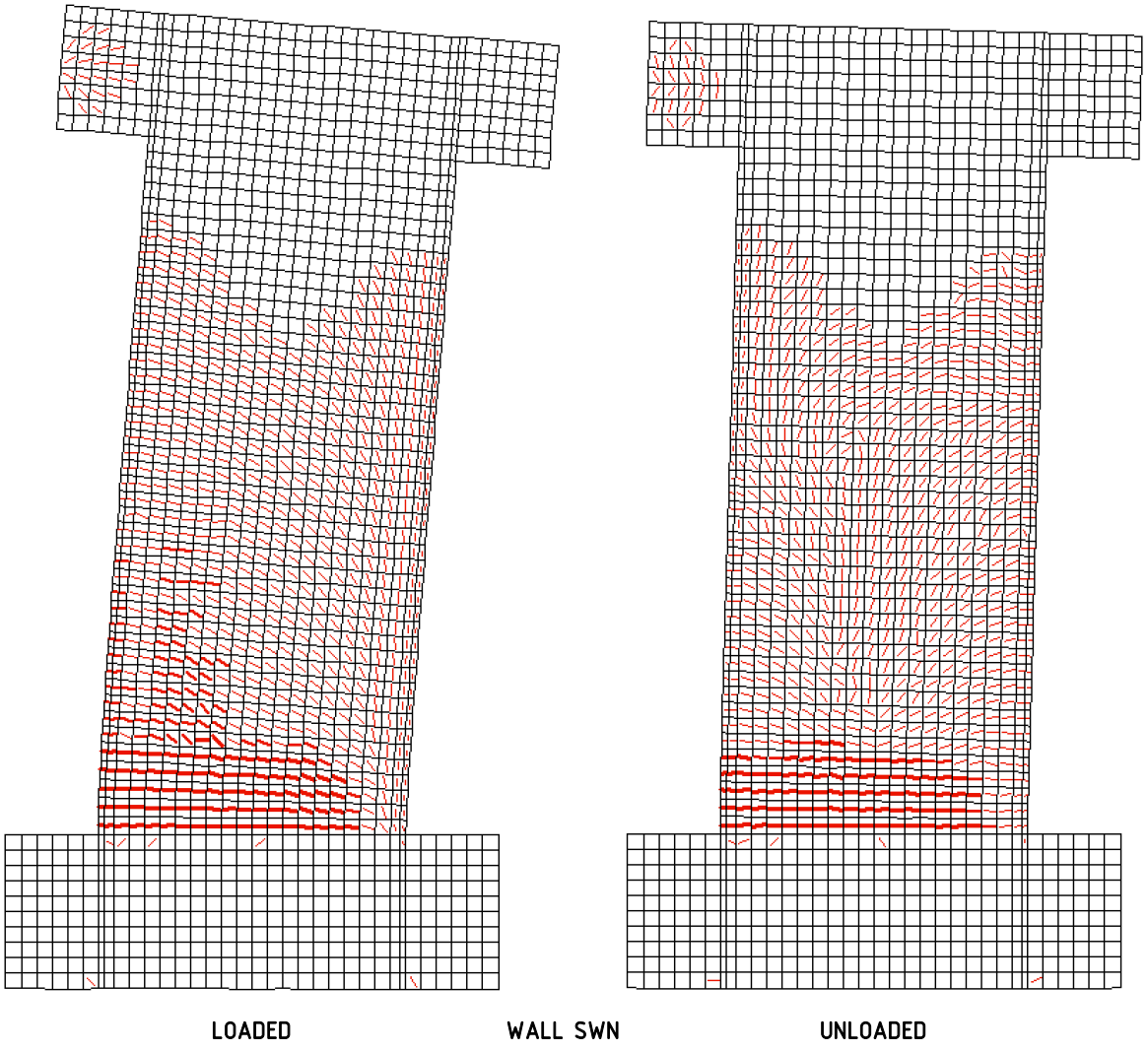

Figure 4.14. Crack pattern of Wall SWN at 2.5% drift: loaded (right); and unloaded (left).

CHAPTER 5

Experimental Results

5.1 Introduction

This chapter presents the results of the experimental testing of two walls: the steel-reinforced Wall SWS-R, and the hybrid steel and superelastic Nitinol-reinforced Wall SWN. Both walls were subjected to a sequence of quasi-static load reversals at the same drift levels to study the seismic response of each wall. To develop an understanding of the mechanical properties of the novel Nitinol reinforcement, tension tests were conducted on both deformed steel coupons and smooth superelastic Nitinol coupons for comparison. Both materials were used as longitudinal reinforcement within the boundaries of each respective wall and were therefore expected to significantly influence the behaviour of the slender walls. The load-displacement response for each wall was collected through a set of instruments and presented herein as raw data. Furthermore, the anterior face of each wall was photographed to study the development of cracking patterns over the course of displacements. As each wall was subjected to reverse cyclic loading, strain measurements were recorded from the reinforcement at various locations throughout the plastic hinge region on both faces of each wall. The collected data and observations are used to characterize the seismic response of the walls.

5.2 Reinforcements Tension Testing

Tension tests were performed to study the mechanical differences between conventional deformed steel and superelastic Nitinol. A set of tension tests were performed using 10M (Ø 11.3mm) steel bars, from the batch used for the reinforcement of Wall SWS-R, and smooth superelastic Nitinol (Ø 12.7mm) bars, from the batch used to construct Wall SWN.

Three coupons of the Nitinol material were tested against deformed steel counterparts. The initial coupon configuration for the Nitinol bars intended for tensile loading to be transmitted through the mechanical couplers via the spliced deformed steel where the grips were attached. The concept was that gripping the coupled steel for the tension tests would simulate the same anchorage condition in the constructed wall.

The first coupon was mounted, for monotonic testing, to the prescribed assembly as presented in Figure 5.1(a). Data was collected using an extensometer at a reduced cross-section, measuring approximately Ø12.0mm over a length of 60mm, at mid-length of the Nitinol bar. The tension specimen was monotonically loaded to 6% strain, unloaded, then reloaded towards achieving tensile strength. In this configuration, when the Nitinol bar reached 7% strain, the deformed steel bar coupled at the top end ruptured. The data collected by the extensometer over the reduced cross-section was used to compile the results of the monotonic test of this specimen, however, there was a lack of values for uniform elongation and tensile strength. An inspection of the couplers showed that they remained tightly connected throughout testing, maintaining bearing of the coupled steel to the Nitinol bar. No observable deformations or damage were sustained by the couplers.

The failure of the first coupon prompted the modification of the second coupon assembly so that the gripping of the Nitinol specimen should be from the couplers, as shown in Figure 5.1(b). The idea to grip the Nitinol coupon from the couplers is adopted from the anchorage the couplers provide due to their larger diameter and bearing against the concrete beyond the plastic hinge region. This specimen was monotonically loaded and failed at approximately 7% strain. It was observed that the coupon was susceptible to rupturing at the location of the transition from the diameter of the smooth bar to the conical head at either end, which occurred at the top end at approximately 8.5% strain across the reduced cross-section. The coupon was further modified to remove the remining conical head. The superelasticity and low residual elongation of Nitinol facilitated the reloading of the modified coupon to complete the reloading branch to a controlled rupture within the reduced cross-section.

The third Nitinol coupon was modified to remove the conical heads and the diameter of the cross-section was further reduced to approximately Ø10mm using gradual transitions over a length of 90mm. This tension coupon was successfully tested by gripping the Nitinol bar for direct application of tension, as seen in Figure 5.1(c). The coupon endured eight out of the intended thirteen axial strain cycles, discussed in Section 3.4.1 of Chapter 3. Failure was observed just below the top length of the gradual transition to the reduced cross-section. Given the location of the rupture, it is suspected that the failure occurred due to localized stress concentration promoted by inadequate machining of the transition to the reduced cross-section, and less due to strength degradation.

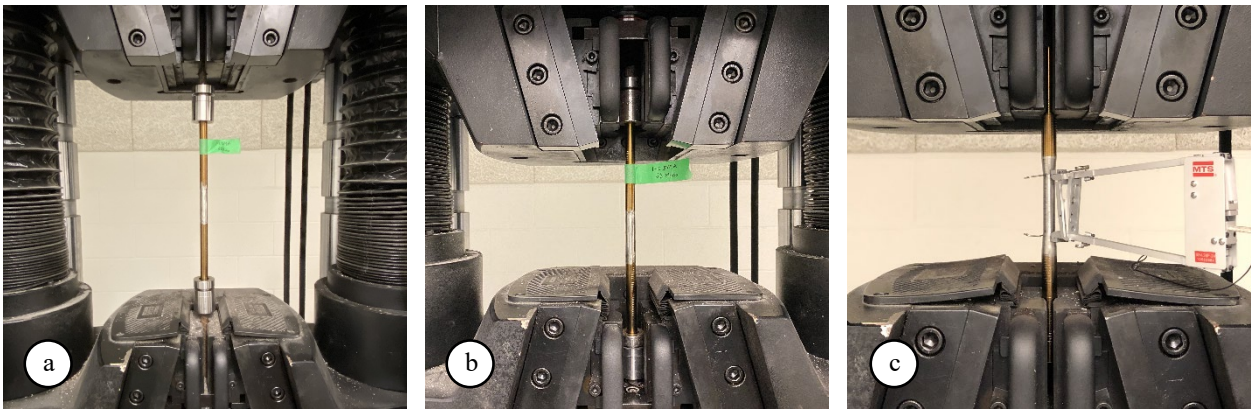

Figure 5.1. Nitinol tension coupons: (a) steel grip; (b) coupler grip; and (c) bar grip.

A comparative set of 10M deformed steel bars were tested in the same manner as the Nitinol coupons under monotonic loading with a 6% strain cycle, and cyclic loading subject to the same set of axial strain targets. All the steel bars were previously prepared with a reduced cross-section at mid-length to capture a controlled rupture within the span of the extensometer. Each steel coupon was directly loaded from either end.

Comparative monotonic tensile testing of the second Nitinol coupon and a 10M deformed steel bar was conducted to study the variation in responses. The stress-strain curve of the sampled superelastic Nitinol coupon presented a flag-shaped response. Upon initial loading, the Nitinol bar had a stiffness of approximately 38GPa and yielded at approximately 333MPa. The upper plateau strength measured 412MPa at 3% strain (ASTM F2516), while the lower plateau strength of the unloading branch measured 172MPa at 2.5% strain (ASTM F2516). The residual elongation, upon unloading from 6% strain, was gauged at a stress level of 7MPa to retain a 0.24% strain offset. On the reloading branch, the Nitinol bar achieved a tensile strength of 1034MPa at a uniform elongation of 16%. In comparison, the sampled 10M steel coupon exhibited a much larger elastic modulus of 189GPa. The steel bar yielded at 510MPa. The upper plateau strength of the steel bar corresponds with the onset of strain hardening which measured 582MPa at 3% strain. The unloading branch from 6% strain for the steel bar appeared to have a more linear response without presenting a lower plateau strength. At 7MPA a residual elongation of 5.6% strain was retained. The steel bar achieved a tensile load of 663MPa and ruptured at 22.4% uniform elongation. The stress-strain curves for both coupons are presented in Figure 5.2.

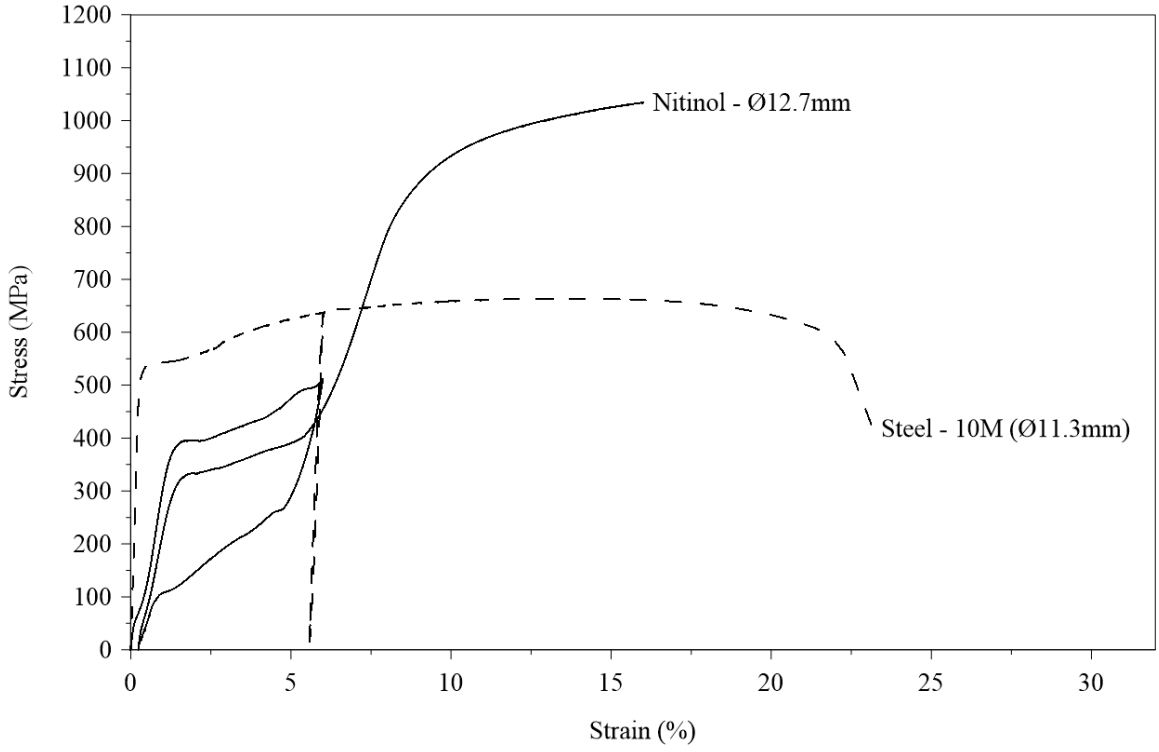

Figure 5.2. Monotonic tension test result for a Nitinol coupon and 10M deformed steel coupon.

Another comparative test was conducted on a second set of Nitinol and 10M steel reinforcement coupons to study the response of the materials under cyclic loading. The Nitinol coupon endured eight progressive strain cycles before rupturing at approximately 7.2% strain, while loading towards the 8% strain cycle. The hysteretic response of the Nitinol coupon had a progressive strength decay in both the upper plateau and the lower plateau. The first measurable upper and lower plateau strengths are from the 3% strain cycle (ASTM F2516). The upper plateau strength for the 3% strain cycle measured 406MPa. The upper plateau strength of the 6% strain cycle dropped by approximately 6.6% to 379MPa. The 3% strain cycle had a lower plateau strength of 309MPa, which dropped by approximately 60.2% to 123MPa in the 6% strain cycle. The hysteretic response of the Nitinol indicated no effect on residual elongation, which was approximately 0.19% from the 6% strain cycle. The Nitinol coupon ruptured at 7.1% uniform elongation at a tensile strength of 633MPa. The hysteresis of the 10M steel bar matched very closely to the envelope of the monotonic response. The only observable difference is a reduction in the uniform elongation capacity which dropped by approximately 20% to 19% strain. In each cycle, for both the Nitinol and steel, the stiffness of the materials appears to be sustained through loading and unloading. The cyclic stress-strain curves for both the 10M and Nitinol coupons are presented in Figure 5.3.

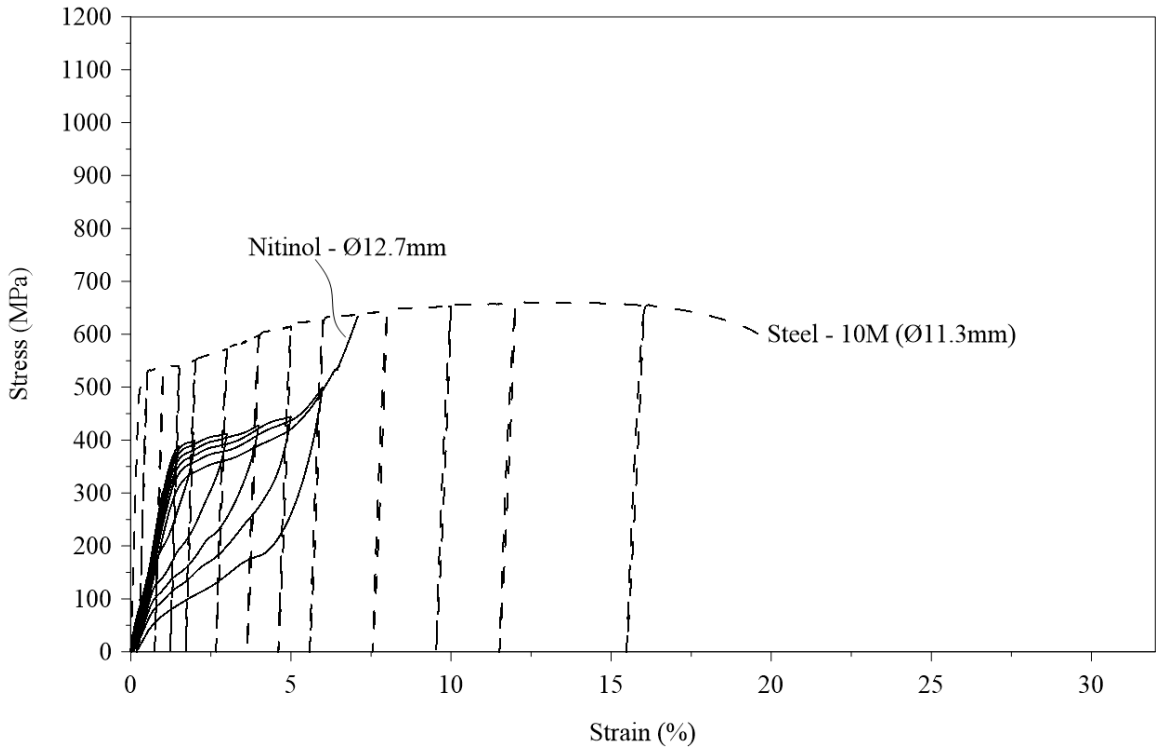

Figure 5.3. Cyclic tension test result for a Nitinol coupon and 10M deformed steel coupon.

The design values for the mechanical properties of the 10M steel bar and other deformed steel reinforcements, as well as the superelastic Nitinol reinforcement, are available in Section 3.4.1 in Chapter 3 (Experimental Program). Further information is available on the results of the reinforcement tension testing in Appendix A.

5.3 Load-Displacement Response

The primary load-displacement response measurement for each wall was based on a cable potentiometer (CP-E-1250) which was mounted to the instrumentation frame on the right end of the wall and connected colinearly with the center of the cap beam at an elevation of 2400mm from the top of the foundation block.

Experimental testing started with Wall SWS-R. The initial displacement to 1.2mm (0.05% drift) produced hairline flexural cracking along the base from positive loading, and at approximately 150mm above the base from negative loading. Each crack measured approximately 150mm in length. Lateral displacement to 2.4mm (0.1% drift) produced a new flexural crack which spanned the length of the wall at approximately 350mm above the base. At a displacement of 4.8mm (0.2% drift), shear cracking formed from the left and right sides of the wall at approximately 950mm from the base. New flexural cracks formed in addition to the flexural cracks which had formed with previous displacements and had now propagated across the length of the wall, spaced apart by approximately 150mm over the 1000mm height of the plastic hinge region. The accumulated damaged at this stage within the plastic hinge was augmented throughout displacement cycles to 7.2mm (0.3% drift) and to 9.6mm (0.4% drift). A single flexural crack had also developed at a height of approximately 1250mm from the base. The displacement cycles to 12mm (0.5% drift) widened the flexural crack at the base to become a major crack. New shear cracks developed from both ends of the wall at approximately 1400mm from the base. Displacement to 24mm (1.0% drift) caused the expansion of shear cracks and the development of new cracks. One major shear crack was evident across the plastic hinge, sloping from the top left. A fanned cracking pattern also became apparent from the left side on the upper half of the wall. At this state of testing, intensifying damage was observed at the base of the wall, specifically in the repaired regions. Vertical cracking separating the concrete end cover began to develop at the base of each boundary from displacement cycles to 36mm (1.5% drift). The damage sustained by the wall continued to intensify through the displacement cycles to 48mm (2.0% drift). The toe at the base of each boundary became significantly cracked and spalling became visible. By the end of the displacement cycles to 60mm (2.5% drift), the right toe was completely crushed. The concrete cover of the left toe became completely separated in addition to spalling of large fragments. In the first positive load excursion to 72mm displacement (3.0% drift), the two outermost reinforcing bars of the left boundary ruptured at approximately 40mm to 50mm above the foundation, and the reinforcing bars in the right boundary began to buckle. In the subsequent negative loading, the stiffness of the wall was significantly lower than exhibited at the previous displacement level. At the peak of the negative loading branch, the two outermost reinforcing bars of the right boundary ruptured at approximately 50mm above the base, and the reinforcing bars in the left boundary buckled. In the second positive loading branch, the remaining two reinforcing bars in the left boundary ruptured and the two remaining reinforcing bars in the right boundary were severely buckled. Wall SWS-R completed the second negative excursion to conclude

testing. When the damaged concrete was chipped away for inspection after testing, it was revealed that longitudinal reinforcement bars in the web section had also sustained some buckling. The hysteretic response of Wall SWS-R is presented in Figure 5.4.

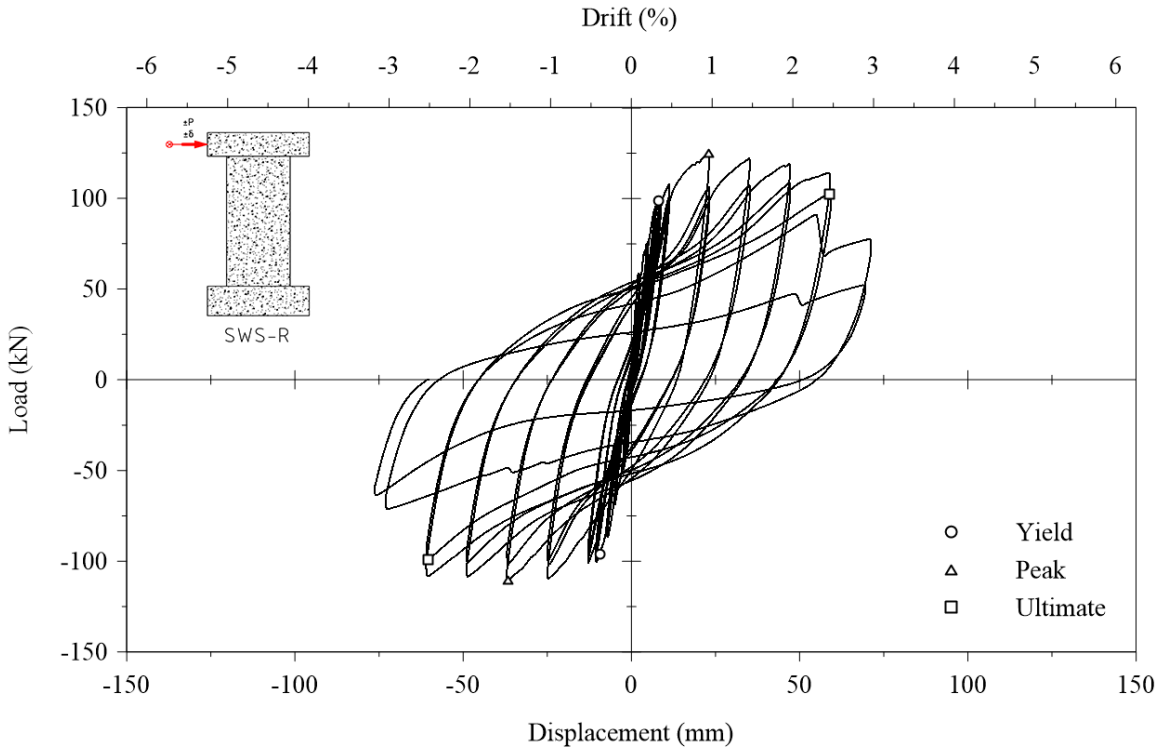

Figure 5.4. Load-displacement response of Wall SWS-R.

The testing of Wall SWN followed the same displacement sequence as Wall SWS-R. The initial loading branch to 1.2mm displacement produced a 400mm long crack across the base of the wall from the left end. The same crack propagated across the length of the wall with displacements to 2.4mm. No other cracks were evident. The displacement cycles to 4.8mm presented a 900mm long flexural crack at approximately 300mm and a flexural-shear crack at approximately 150mm above the base. The displacement cycles to 7.2mm formed one major flexural crack spanning the length of the wall at approximately 300mm from the base and another flexure crack spanned the length of the wall at approximately 1100mm above the foundation. Three vertical cracks also developed symmetrically, spaced at 150mm, over the longitudinal reinforcement of the web. The vertical cracks surface at approximately 350mm above the base, and each measured approximately 150mm in length. At the top of the vertical cracks, a horizontal crack had also formed across the web and terminated at 200mm from each end of the wall. The displacement cycles to 9.6mm unevenly propagated the vertical cracks to approximately 150mm above the base of the wall and to approximately 600mm. A second horizontal crack also formed across the web at approximately 650mm from the base. The major crack at approximately 300mm from the base that had previously formed became significantly wider. The second

flexural crack at 1100mm above the base extended across the length of the wall. The displacement cycles to 12mm lengthened the cracks which previously developed across the web to almost reach across the wall. The vertical cracks extended by an average of 50mm to measure between 250mm to 300mm in length. Additional flexural cracks formed with displacement cycles to 24mm, the highest being at 1550mm above the foundation. Fanned flexural-shear cracks formed in the upper half of the wall with displacement cycles to 36mm. The flexural cracks across the wall at the base and 300mm above the base were approximately 3mm wide. All other cracks had significantly less wide.

At this stage in testing, an intermission in the loading sequence led to an inadvertent calibration error which caused displacements to be skewed toward the negative direction. As a result, three additional cycles were imposed at the 1.5% drift level (36mm displacement) in the positive direction, and for the negative cycles the wall was loaded to the 2.5% drift level (60mm displacement). The 2% drift level (48mm displacement) was missed in the negative direction as a result. The 2% drift level (48mm displacement) in the positive direction was completed with the 3% drift (72mm displacement) in the negative direction. The displacement cycles to 48mm initiated new flexural-shear cracks in the upper half of the wall and extended existing cracks. The highest flexural-shear crack was at 1900mm from the base. The major flexural cracks near the bottom of the wall reached widths of 6mm and 14mm at the base. When unloaded, the crack widths measured 0.5mm and 9mm at the base. Spalling occurred on the right side of the wall along the major flexural crack adjacent the foundation through the 60mm displacement (2.5% drift) cycles in the positive direction. The 1.0% drift skew in the negative direction carried over to 3% drift (72mm displacement) in the positive direction. At 72mm displacement, the wall began to rock about the two major flexural cracks at the base and crushing initiated at the toe of the right boundary. The skew was subsequently corrected by shifting the drift offset in the positive direction. As a result of the correction the 3.5% drift level (84mm displacement) in the positive direction was missed, and an additional two cycles were imposed at 4% drift (96mm displacement) in the negative direction. The displacement skew provided a brief opportunity to observe the impact of asymmetric loading cycles, which is a closer representation of in-situ seismic loading. Thereafter, the displacement cycles maintained symmetrical drift levels. The wall appeared to have maintained a plateaued response from 2.5% drift through 4% drift under negative loading.

The displacement to 96mm (4% drift) widened the crack at the base to approximately 38mm. The second major flexural crack measured 5mm in width. New flexural-shear cracks formed in the top half of the wall and the toe of each boundary continued to crush. The set of longitudinal bars at the right end of the web ruptured at the peak of the first negative loading excursion to 108mm displacement (4.5% drift). Subsequently, the center set of longitudinal bars in the web ruptured during the first negative loading branch to 120mm displacement (5% drift). Some observation of buckling was made of the left end longitudinal reinforcement in the web. During the second positive loading excursion to 120mm displacement, the last set of longitudinal reinforcement in the web ruptured. The test was terminated upon unloading. The wall maintained a plateaued response from 4% drift to 5% drift under positive loading. The damaged concrete of Wall SWN was then removed along the base for closer inspection of the longitudinal reinforcement. The web reinforcing bars appeared to have mostly ruptured at just above the surface of the foundation block and showed severe buckling. In contrast, the superelastic Nitinol reinforcing bars in the boundaries did not show any visible signs

of damage. As concrete was removed around the couplers above the plastic hinge, it became evident they were in excellent condition. The hysteretic response of Wall SWN is presented in Figure 5.5.

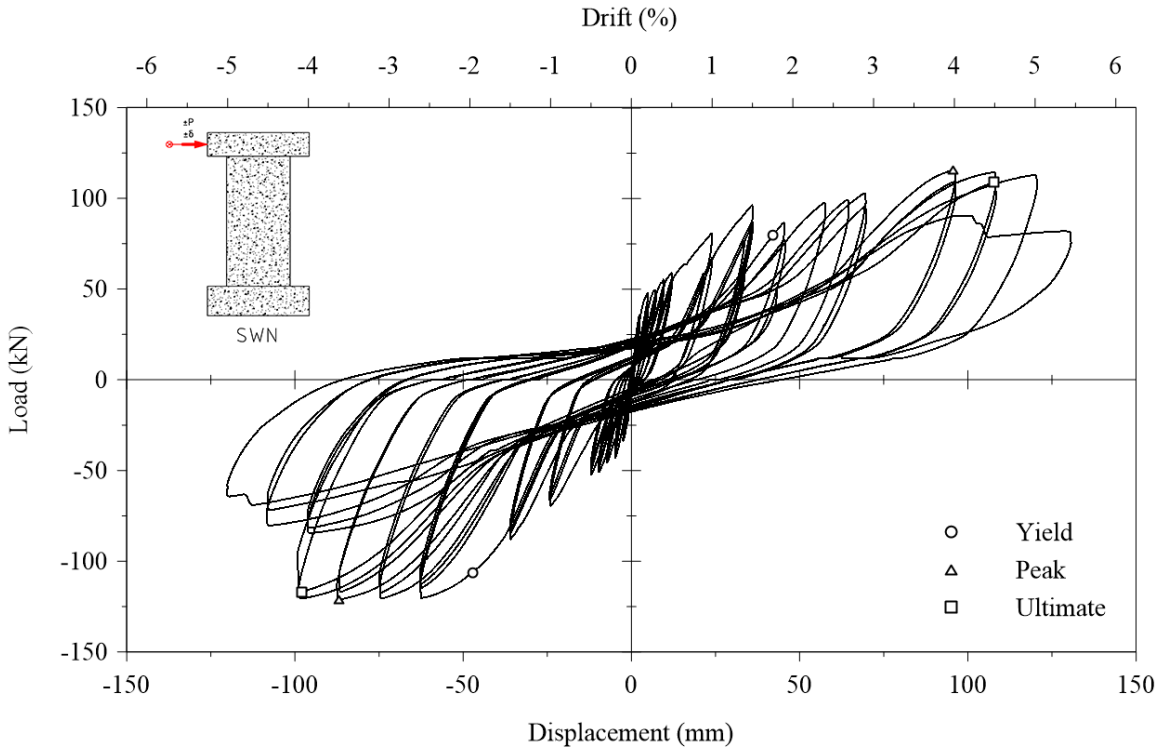

Figure 5.5. Load-displacement response of Wall SWN.

The yield displacement, peak load, and ultimate displacement performance points were determined from the hysteresis response of each wall using the method by Park (1989). The performance points of each wall were assessed for both the positive and negative directions of loading, and then averaged for an overall result. The performance points for Wall SWS-R are summarized in Table 5.1, and in Table 5.2 for Wall SWN. Supplementary performance points gauging the yield secant stiffness and ductility values for both walls were derived from the response of each wall. Wall SWS-R had a higher yield secant stiffness in the positive direction of 12.22 x10^3 kN/m, compared to 10.32 x10^3 kN/m in the negative direction. In the positive direction, the wall sustained a ductility of 7.3, and in the negative direction it experienced a ductility of 6.5. In contrast, Wall SWN had significantly lower yield secant stiffnesses measuring 1.90 x10^3 kN/m in the positive direction, and 2.25 x10^3 kN/m in the negative direction. The reduction in yield stiffness in the positive direction is a result of the additional load cycles sustained at 1.5% drift, below the yield displacement threshold. The wall had a ductility of 2.6 in the positive direction, and a ductility of 2.1 in the negative direction. The greater ductility value in the positive direction is a result of the displacement jump from 3% drift to 4% drift which interrupted the gradual degradation pattern, and thus extended the ultimate displacement of the wall. The

jump from 1.5% drift to 2.5% drift in the negative direction appears to have had minimal impact on the performance of the wall. The average supplementary performance points are presented in Table 5.3.

Table 5.1. Performance points for Wall SWS-R

Response	Yield			Peak			Ultimate		
	Disp. (mm)	Drift (%)	Load (kN)	Disp. (mm)	Drift (%)	Load (kN)	Disp. (mm)	Drift (%)	Load (kN)
+	8.1	0.34	99	23	0.96	125	59	2.45	102
–	9.3	0.39	96	37	1.53	111	61	2.52	99
Avg.	8.7	0.36	98	30	1.24	118	60	2.49	101

Table 5.2. Performance points for Wall SWN

Response	Yield			Peak			Ultimate		
	Disp. (mm)	Drift (%)	Load (kN)	Disp. (mm)	Drift (%)	Load (kN)	Disp. (mm)	Drift (%)	Load (kN)
+	42	1.75	80	96	3.99	116	108	4.49	109
–	47	1.97	106	87	3.62	121	98	4.09	117
Avg.	45	1.88	93	91	3.80	118	103	4.29	113

Table 5.3. Supplementary performance points

Performance Point	Shear Walls		
	SWS-R	SWN	
Yield Secant Stiffness	11.26	2.07	$x10^3$ kN/m
Ductility	6.9	2.3	

5.3.1 Lateral Displacements

Lateral displacements were recorded at three additional locations along the height of each wall. Instrument CP-B-600 measured lateral displacements from the left just below the cap beam (elevation 2100mm). Instrument CP-C-600 measured lateral displacements from the right at mid-height (elevation 1200mm). Instrument CP-C-300 was mounted on the right end of the wall to monitor sliding at 50mm above of the foundation block. The lateral displacements along the height of Wall SWS-R are presented in Figure 5.6, and in Figure 5.7 for Wall SWN.

The general shape of the lateral displacement hystereses along the height of each wall appeared similar to the primary load-displacement response from the center of the cap beam. Significant hysteretic shape variations were only visible in the sliding displacements measured at the base of each wall.

At the 2.5% drift threshold (60mm target displacement), Wall SWS-R drifted to approximately 95% (56mm) of the target displacement at just under the cap beam, 52% (31mm) at mid-height, and slid by 20% (12mm). In the negative direction, at just under the cap beam the wall drifted to approximately 83% (51mm), and to 53% (33mm) at mid-height. The wall slid towards the negative direction by approximately 10.6mm when loaded, but the base remained in a position to the right of the centerline by 2% (1mm) of the target displacement. At the base of Wall SWS-R, sliding was generally limited to a range of -4mm to 4mm up to the end of the first cycle at 2% drift (48mm displacement). The range of sliding then began to widen and skew towards the positive direction. The range of sliding shifted to -2mm to 8mm with the completion of the second cycle to 2% drift. It was observed that there was significant cracking around the toes of the wall. At 2.5% drift, sliding continued to skew to a range of 1mm to 12mm with the first cycle, then shifted to 8mm to 19mm with the second cycle, as the right toe was completely crushed. In the first cycle to 3% drift, sliding reached 28mm in the positive direction. At this point, the displacement sensor (CP-A-300) was removed to prevent damage to the instrument.

The positive and negative displacement profiles for Wall SWN, at the 2.5% drift threshold, appeared more symmetrical. In the positive direction, at just under the cap beam, the wall drifted by approximately 92% (55mm) of the target displacement, 51% (30mm) at mid-height, and slid by 5% (3mm) at the base. In the negative direction, displacement just under the cap beam reached approximately 82% (49mm), 48% (29mm) at mid-height, and slid by 7% (4mm). Wall SWN had a wide sliding range of -14mm to 9mm covering all the displacement cycles up to and including 5% drift (120mm). The increase in magnitude of sliding appears proportional and consistent with the primary load-displacement response of the wall, for the most part. A singular jump is observed between the final positive displacement cycle at 3% drift to the first displacement cycle at 4% drift, which shifts from approximately 4mm to approximately 6mm, respectively. The right toe had suffered some crushing throughout the cycles to 3% drift. The subsequent crushing of the toe on each end of the wall influenced the wide range of sliding.

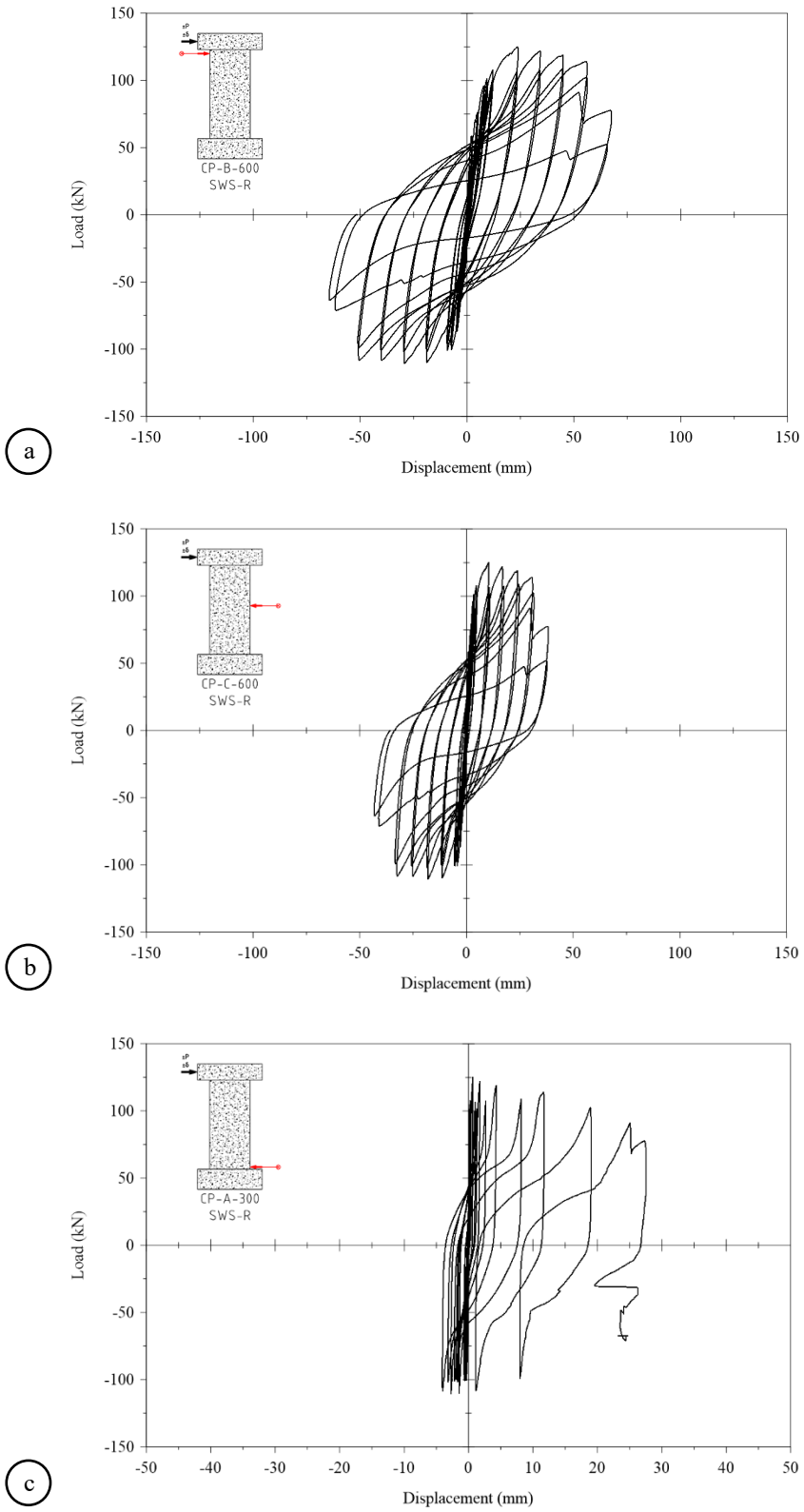

Figure 5.6. Lateral displacements over the height of Wall SWS-R at: (a) under cap beam; (b) mid-height; and (c) base.

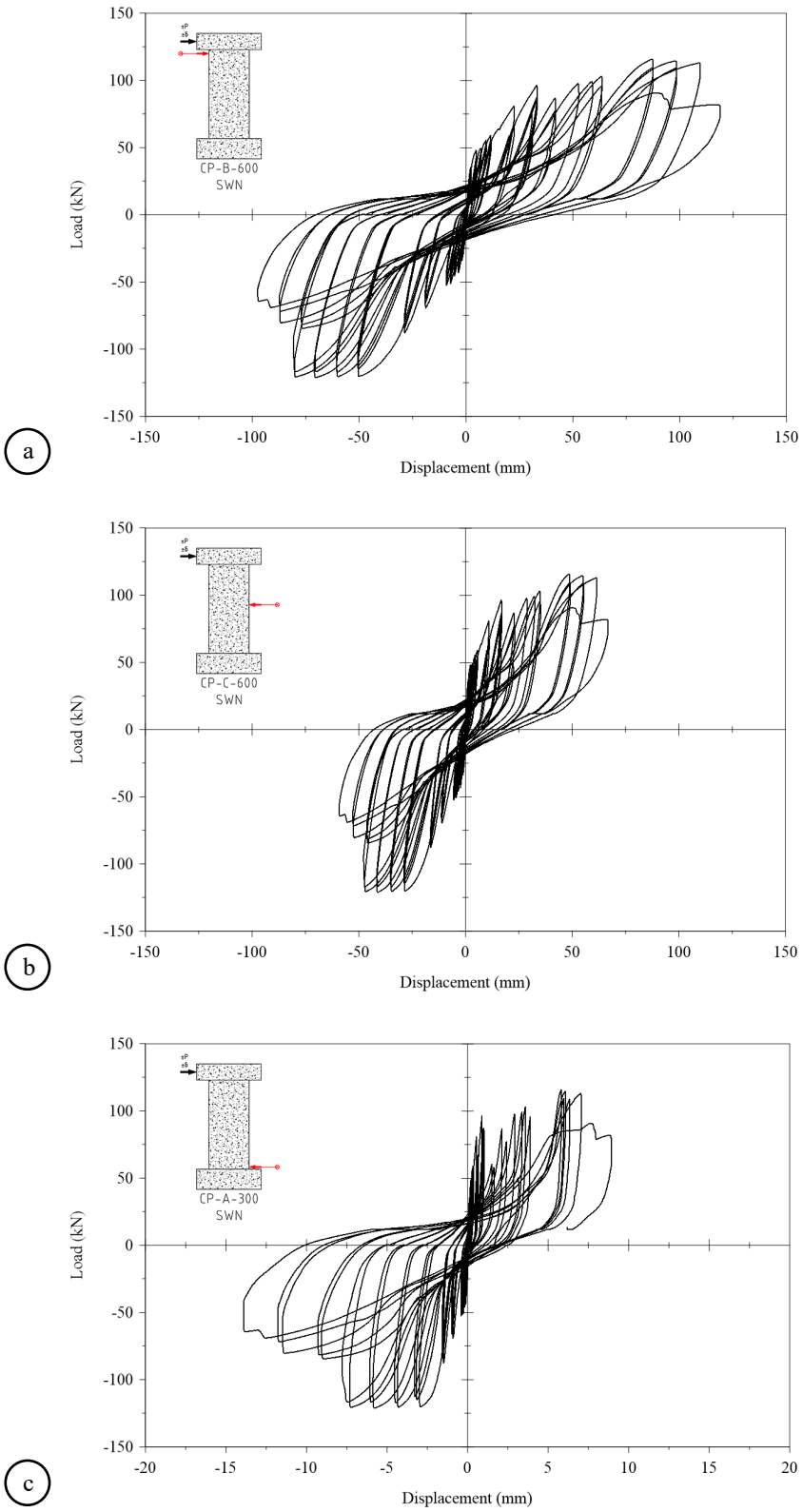

Figure 5.7. Lateral displacements over the height of Wall SWN at: (a) under cap beam; (b) mid-height; and (c) base.

5.3.2 Vertical Displacements

Vertical displacements were recorded using pairs of instruments at three locations on each wall. Instruments CP-E-600 and CP-D-600 were connected on the left and right, respectively, between the top of the foundation block and the underside of the cap beam to gauge the vertical displacements at the top level. The instruments monitored vertical displacements at a 300mm offset from each end of the wall. Instruments CP-C-1250 and CP-A-1250 were connected on the left and right, respectively, over an 800mm by 800mm footprint concentric to the plastic hinge region to record the vertical displacements associated with plastic hinge deformation. Instruments CP-D-300 and CP-C-300 were connected to the wall on the left and right, respectively, at 200mm from the top of the foundation block to monitor vertical displacements along the base of the wall due anchorage slip. The instruments at the base had an approximate distance of 1100mm between them.

The positive vertical displacements, at all three locations in both walls, were obvious. The measurements recorded by instruments on the left side of the walls had hysteretic patterns similar to that of the primary lateral load-displacement under positive loading. Instruments on the right end of the walls had cyclic responses similar to that of the primary response under negative loading. The responses of Wall SWS-R presented wide cycles, while the cycles of Wall SWN were pinching towards the origin upon unloading. Negative vertical displacements were also presented but were most distinct in the measurements at the cap beams, and at the base of Wall SWN. It was observed that the negative readings at the cap beam of Wall SWN were approximately double that of Wall SWS-R. At the base of Wall SWN, the negative vertical displacements were significantly noticeable at every target displacement. The measurements over the plastic hinge regions, and at the base of Wall SWS-R, had sub-millimeter readings. The vertical displacement values at 2.5% drift and at the limits of positive and negative loading are summarized in Table 5.4 for both walls SWS-R and SWN. The vertical displacements at all three locations in Wall SWS-R produced wide cyclic responses. The vertical displacement at the cap beam is the overall resultant for the wall. The vertical displacement hysteretic responses from Wall SWS-R are presented in Figure 5.8 for the left end, and Figure 5.9 for the right end. The vertical displacement results for Wall SWN are presented in a similar fashion with the instruments on the left end presented in Figure 5.10, and the instruments on the right end presented in Figure 5.11.

Table 5.4. Vertical displacements

Instrument	SWS-R Vertical Displacements				SWN Vertical Displacements			
	Positive Loading		Negative Loading		Positive Loading		Negative Loading	
	2.5% Drift (mm)	Limit (mm)	2.5% Drift (mm)	Limit (mm)	2.5% Drift (mm)	Limit (mm)	2.5% Drift (mm)	Limit (mm)
Cap Beam								
CP-D-600 [R]	-7.5	-8.3	29.1	35.2	-7.9	-21.0	29.7	59.5
CP-E-600 [L]	30.9	36.7	-5.3	-5.3	32.3	64.1	-7.8	-13.8
Plastic Hinge								
CP-A-1250 [R]	0.2	-0.3	7.2	7.2	0.03	-0.3	6.1	9.6
CP-C-1250 [L]	7.4	7.4	0.6	-0.2	5.8	8.1	0.2	-0.2
Base								
CP-C-300 [R]	-0.9	-0.9	20.1	29.6	-1.7	-7.9	16.0	42.8
CP-D-300 [L]	18.1	28.1	0.6	-0.4	17.7	45.3	-2.2	-4.3

[R] denotes instrument mounted on right end of the wall

[L] denotes instrument mounted on left end of the wall

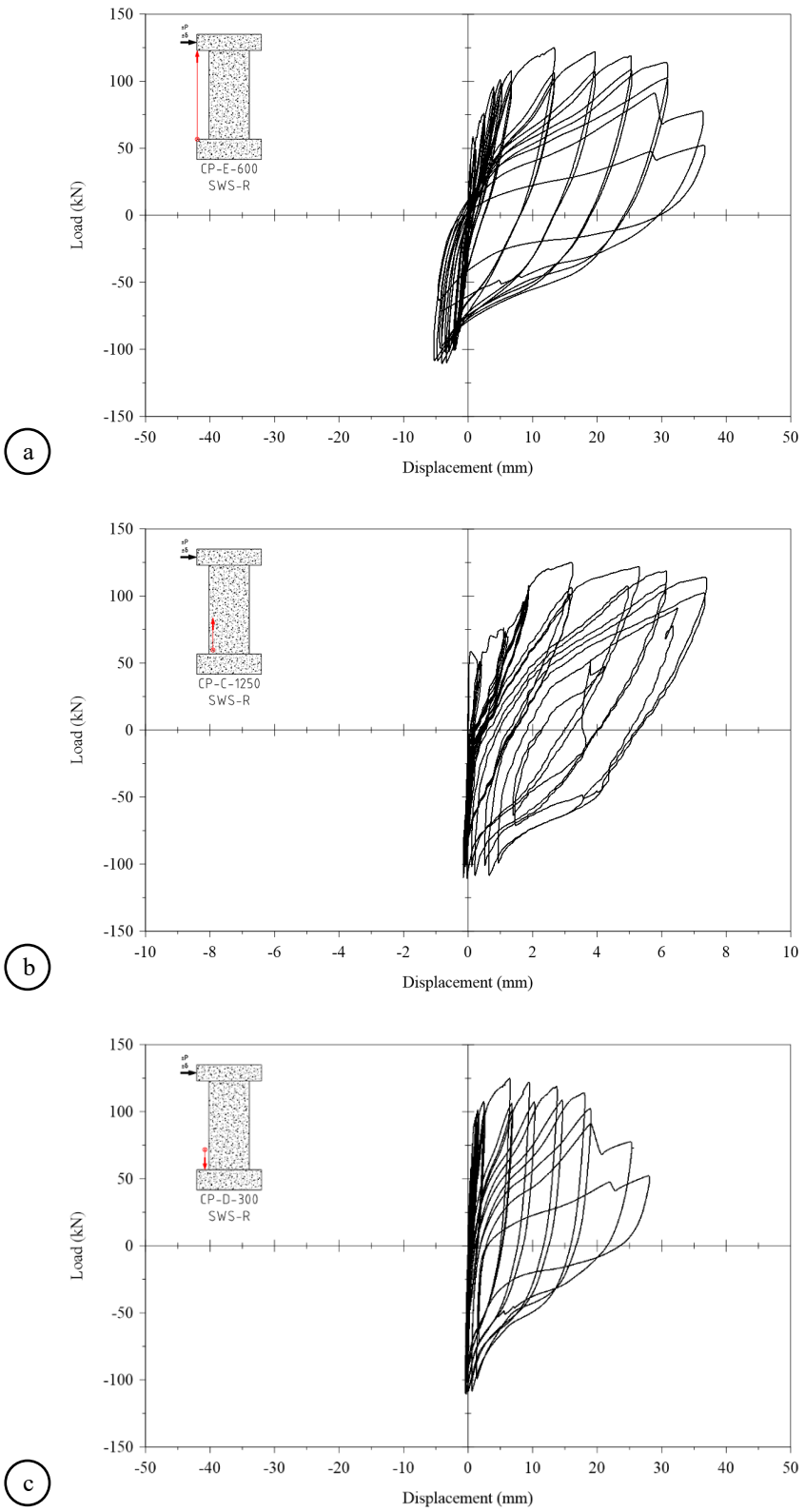

Figure 5.8. Vertical displacements on the left end of Wall SWS-R at: (a) under cap beam; (b) plastic hinge; and (c) base.

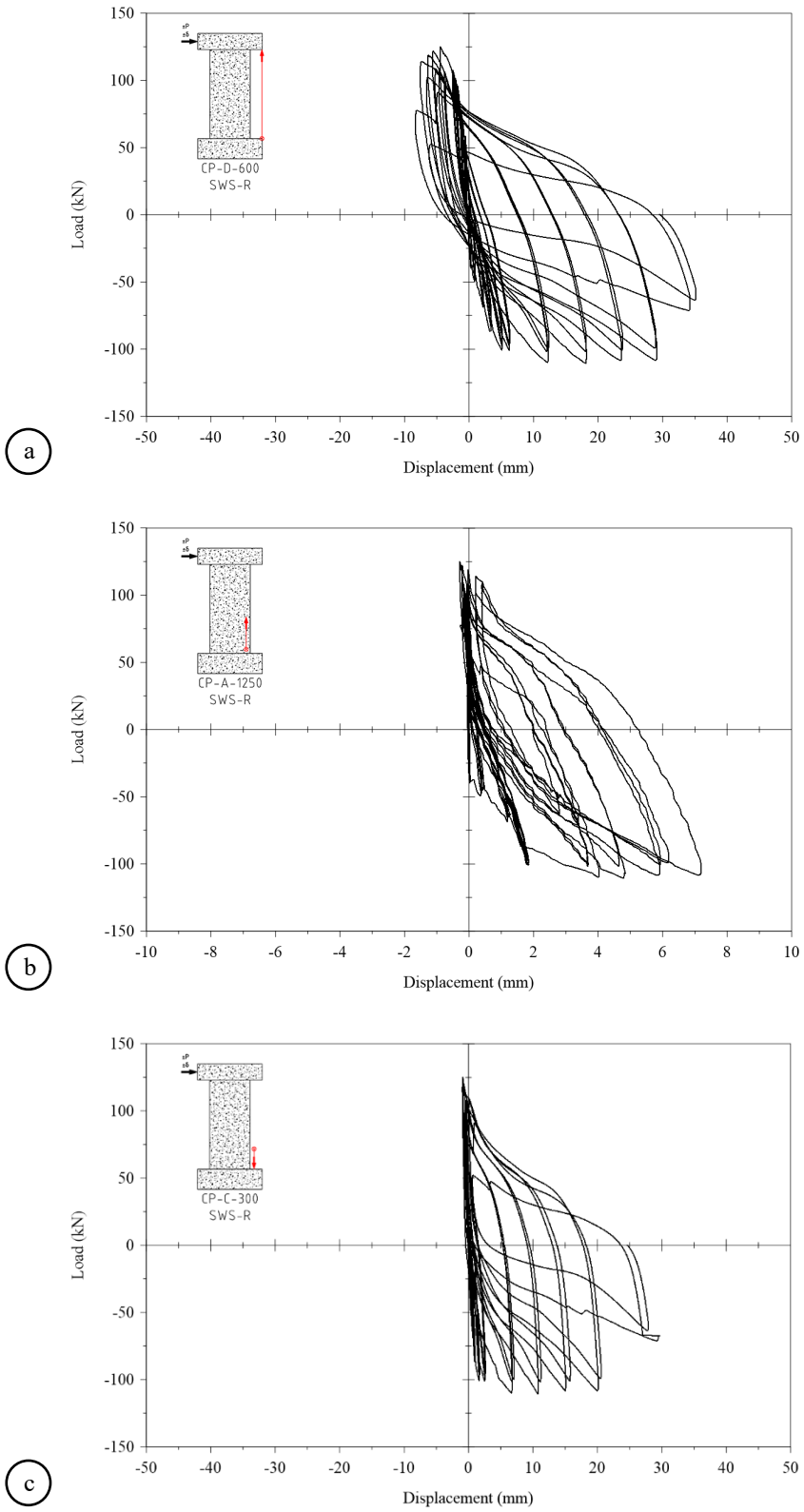

Figure 5.9. Vertical displacements on the right end of Wall SWS-R at: (a) under cap beam; (b) plastic hinge; and (c) base.

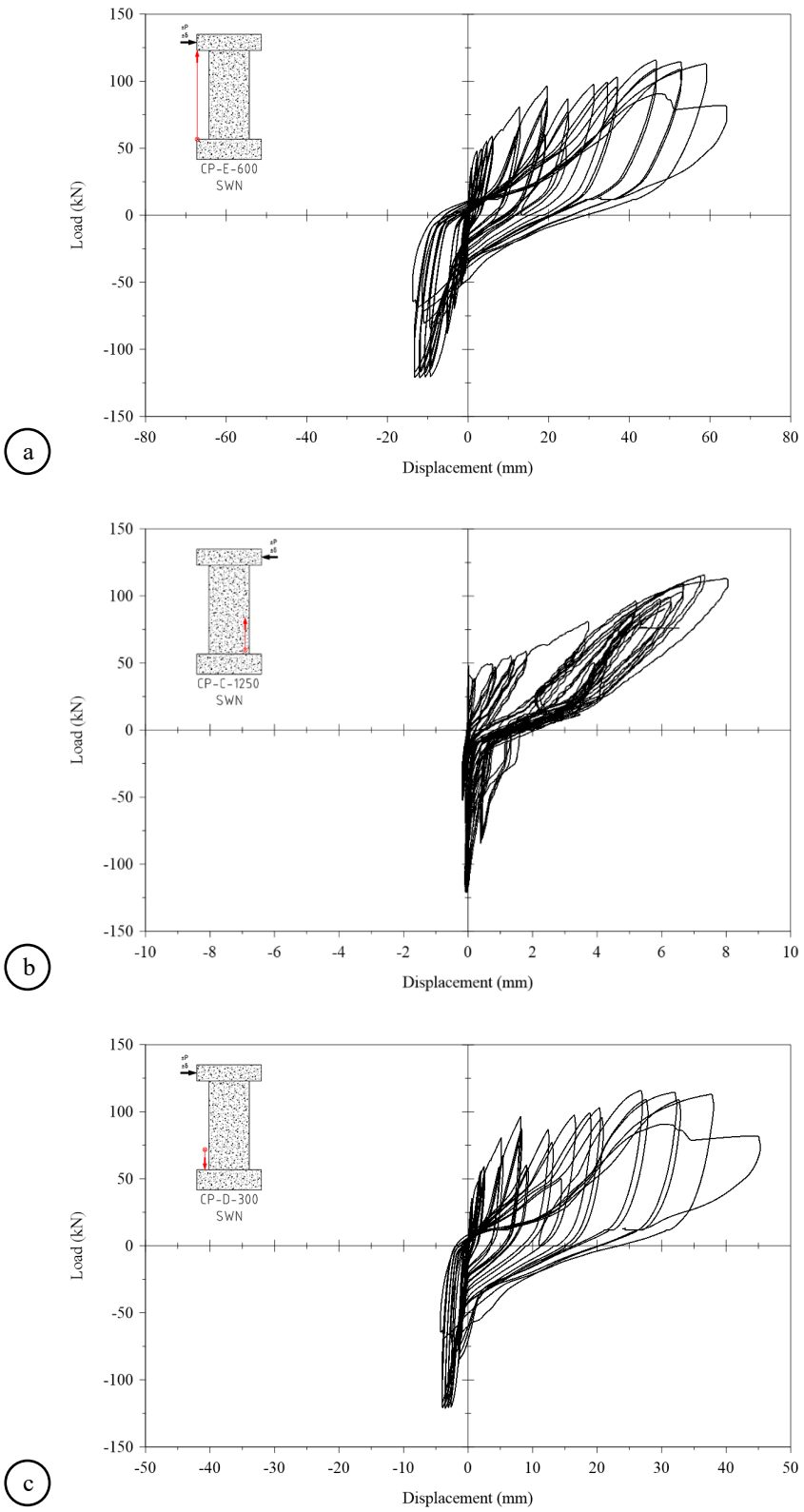

Figure 5.10. Vertical displacements on the left end of Wall SWN at: (a) under cap beam; (b) plastic hinge; and (c) base.

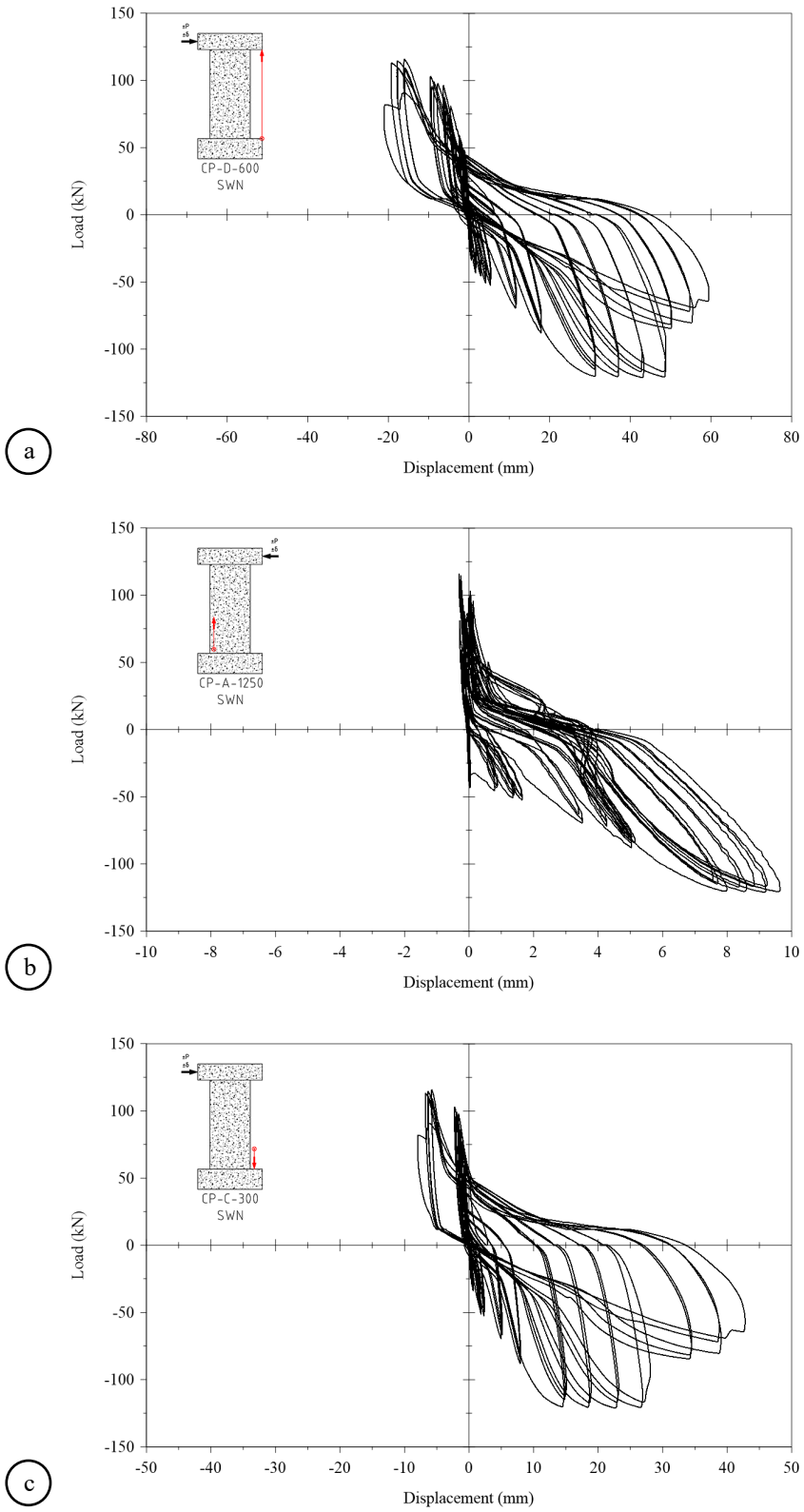

Figure 5.11. Vertical displacements on the right end of Wall SWN at: (a) under cap beam; (b) plastic hinge; and (c) base.

5.3.3 Rigid Body Displacements

Rigid body displacements were monitored for each of the anchored wall specimens. Instrument CP-C-300 was mounted to the test frame and connected to the right end of the foundation block to record sliding of the entire structure. Uplift of each wall was monitored by instruments LP-A-100 and LP-B-100, which were mounted to the right and left ends of the foundation block, respectively. Rigid body sliding and uplift values at 2.5% drift and at the limits of positive and negative loading are summarized in Table 5.5 for both walls SWS-R and SWN. A common observation of both walls during testing was that each foundation block had developed a hairline fracture at approximately half-length. The fractures were determined to be a result of irregular surface flatness of the laboratory strong floor at the test site. An inspection of the sliding and uplift values for both walls indicated that a possible slight concavity over the surface of the laboratory floor influenced the degree of rigid body displacements, against the applied anchorage. The suspected concavity would have reduced the uniformity of contact over the footprint of the foundation block, which would limit frictional resistance leading to sliding, and allowing rocking about a high point.

Table 5.5. Rigid body displacements

Movement	SWS-R Rigid Body Displacements				SWN Rigid Body Displacements			
	Positive Loading		Negative Loading		Positive Loading		Negative Loading	
	2.5% Drift (mm)	Limit (mm)	2.5% Drift (mm)	Limit (mm)	2.5% Drift (mm)	Limit (mm)	2.5% Drift (mm)	Limit (mm)
Sliding	2.87	2.87	-0.29	-0.29	0.44	0.52	-0.054	-0.21
Uplift (right)	-4.92	-4.92	0.71	0.72	-0.67	-0.91	0.82	1.25
Uplift (left)	3.44	3.46	-0.74	-0.75	0.21	0.34	-0.27	-0.31

The rigid movements of Wall SWS-R appear to have been influenced by a high point located closer to the left end. The reduced contact area over the right half of the foundation block promoted a gradual skew in sliding towards the direction of positive displacement. Under negative loading, sliding was limited to below -0.5mm. Uplift on the left end was most salient under positive loading. Instrument LP-A-100 on the right end progressively compressed to almost -5mm, while instrument LP-B-100 on the left end progressively expanded up to approximately 3.5mm. With negative loading, uplift of the structure was contained to below ±1mm on both ends. The rigid body displacement responses for Wall SWS-R are presented in Figure 5.12.

The anchorage of Wall SWN was modified by applying additional mechanically assisted torque to the anchor rods, which reduced the degrees of sliding and uplift. However, the results depicted similar trends to those of the steel-reinforced control specimen. Sliding maintained a positive skew at 2.5 times the magnitude of the negative direction. The most substantial uplift occurred on the right end under negative loading, elevating by approximately 1.25mm. The rigid body displacement responses for Wall SWN are presented in Figure 5.13.

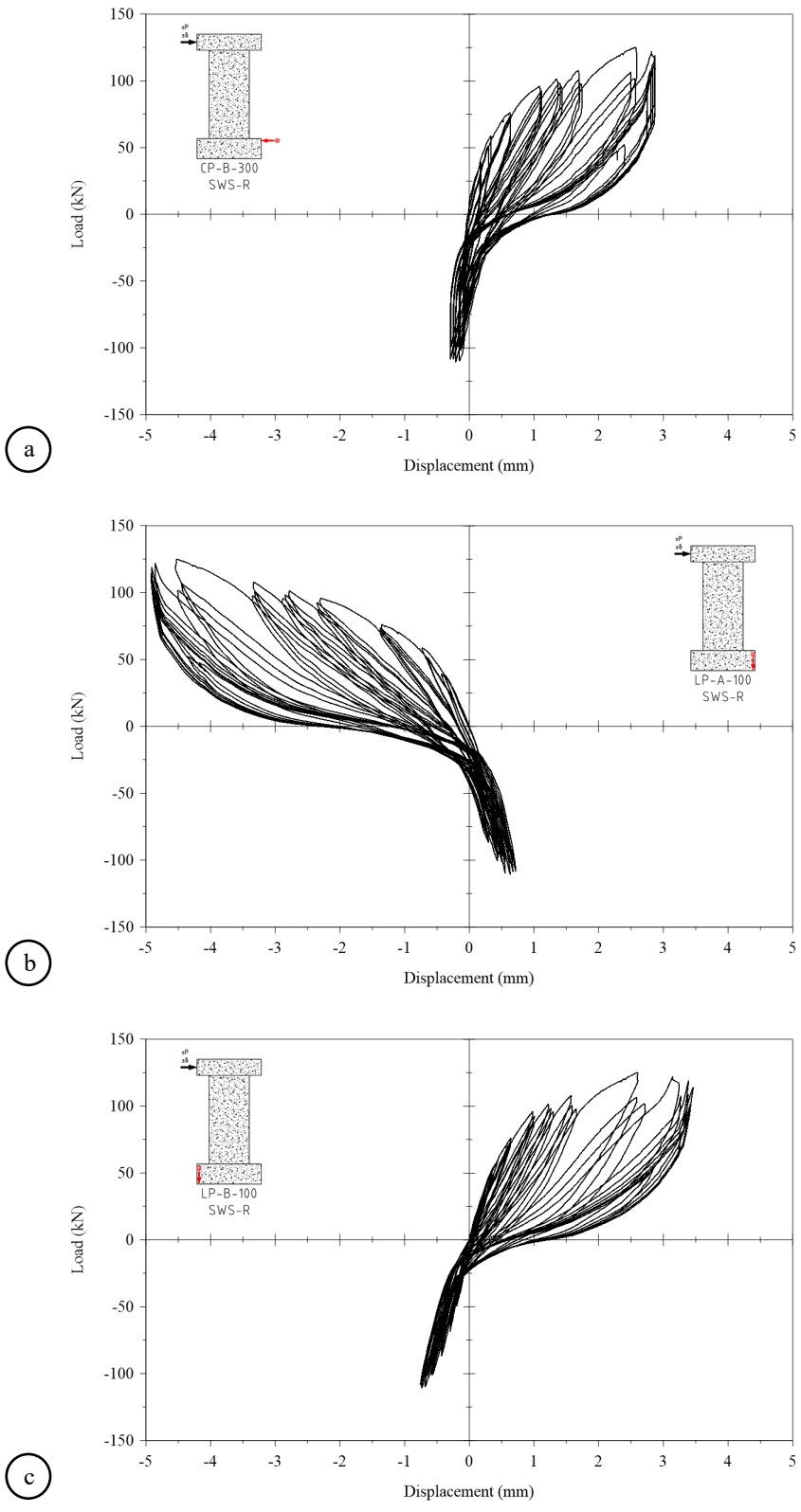

Figure 5.12. Rigid body displacements of Wall SWS-R: (a) sliding; (b) uplift on right end; and (c) uplift on left end.

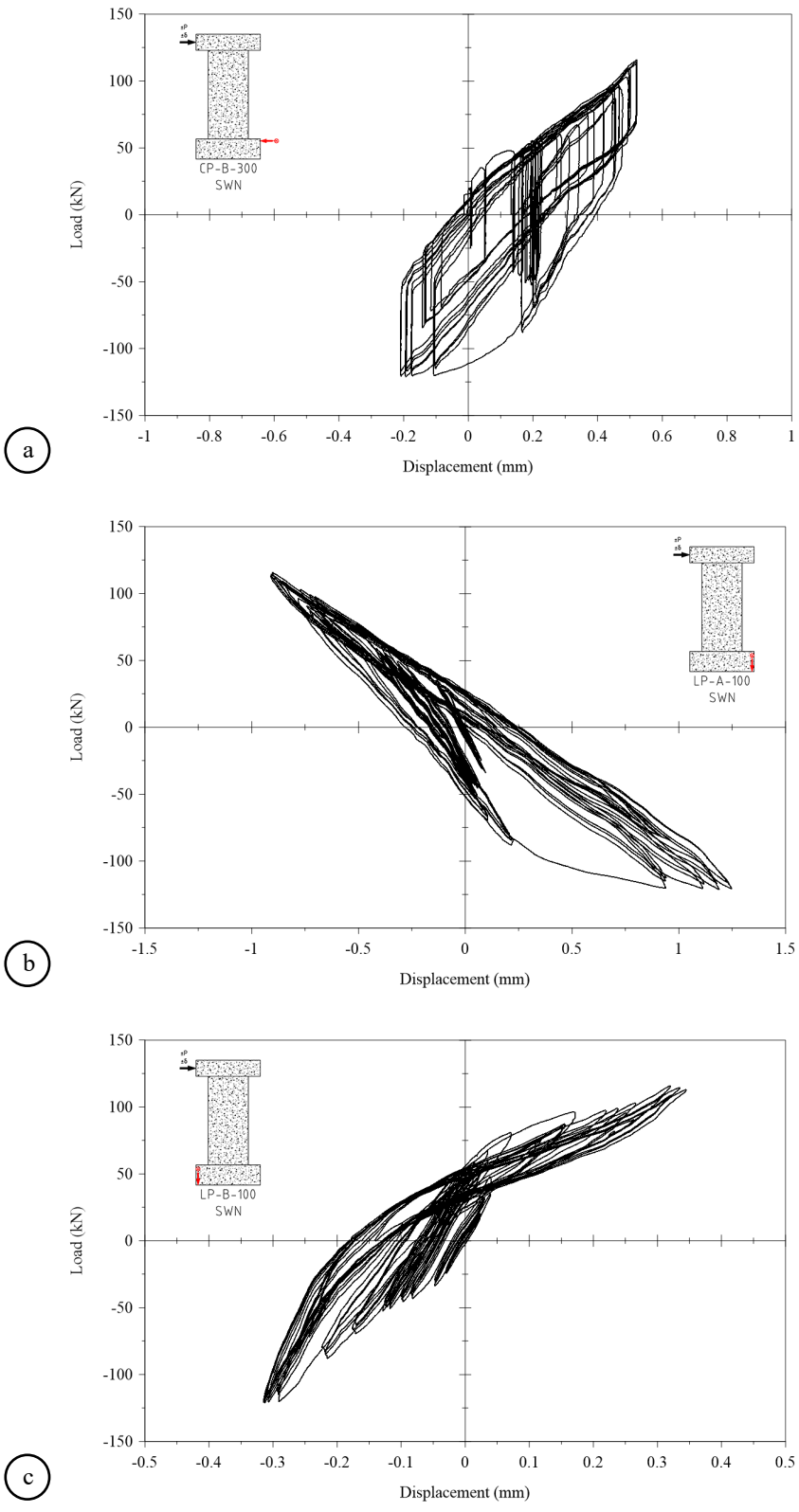

Figure 5.13. Rigid body displacements of Wall SWN: (a) sliding; (b) uplift on right end; and (c) uplift on left end.

5.4 Cracking Characteristics

The development of cracks was monitored, on the anterior face of each shear wall, to characterize their types, widths, locations, and lengths in correlation to the lateral displacements. Of interest are the crack patterns which are expressive of the failure mechanism for each wall. As such, the crack patterns formed relative to the yield displacement, peak load, and ultimate displacement performance points were inspected. The formation of the first flexural crack and the first shear crack were also investigated as initial damages, in contrast to the crack patterns at the 2.5% drift threshold, which is representative of near collapsed structures with severe damage (Yazgan, 2010). Toe crushing at each end of the shear walls was also observed as a notable failure type. The progressive development of crack patterns at each stage of the failure mechanism for each wall presented variations in crack locations and widths. Only the cracks with the highest influence on the failure mechanism are discussed in detail in this section. Further details on crack widths and locations are available in the tables of Appendix H. The damage mechanisms for Wall SWS-R and SWN are presented chronologically by displacement in Table 5.6. The crack patterns are presented in parallel for both walls in the unloaded state to the order of the damage mechanism of Wall SWS-R. The crack patterns and damages formed in each wall was traced throughout the final cycle of each relevant displacement. The crack patterns at each target displacement are presented in the unloaded state of the final cycle in Appendix I for both walls.

Table 5.6. Damage mechanisms

Order of Damage	Wall SWS-R		Wall SWN	
	Displacement (mm)	**Damage Type**	**Displacement (mm)**	**Damage Type**
1	1.2	First Flexure Crack	1.2	First Flexure Crack
2	7.2	First Shear Crack	2.4	First Shear Crack
3	9.6	Yield Displacement	48	Yield Displacement
4	36	Peak Load	60	2.5% Drift
5	36	Toe Crushing	96	Peak Load
6	60	2.5% Drift	108	Toe Crushing
7	72	Ultimate Displacement	120	Ultimate Displacement

The first flexural crack in Wall SWS-R occurred under positive loading through the last cycle to 1.2mm displacement (0.05% drift). The hairline crack developed along the base to a length of approximately 160mm. Negative loading is suspected to have produced the first flexural crack at the right end, from the same final cycle to 1.2mm displacement, at a height of 150mm, just above the repair region in the right boundary, which extended by approximately 140mm. The crack appeared to be a hairline separation between the SCC repair material and the cast-in-place concrete of the wall. The posterior face of the wall did not show indication of a related crack, yielding the

penetration depth of the flexure crack through the thickness of the wall as inconclusive. The base of the wall on the right end did not show any visible indication of flexural cracking under negative loading. The first flexural crack in Wall SWN surfaced along the base under positive loading with the final cycle to 1.2mm displacement and propagated by 390mm. The first flexural crack under negative loading also occurred along the base through the final cycle to 1.2mm displacement and reached approximately 500mm in length. Both cracks had hairline widths when open under load. The first flexural cracks in both walls are presented in Figure 5.14.

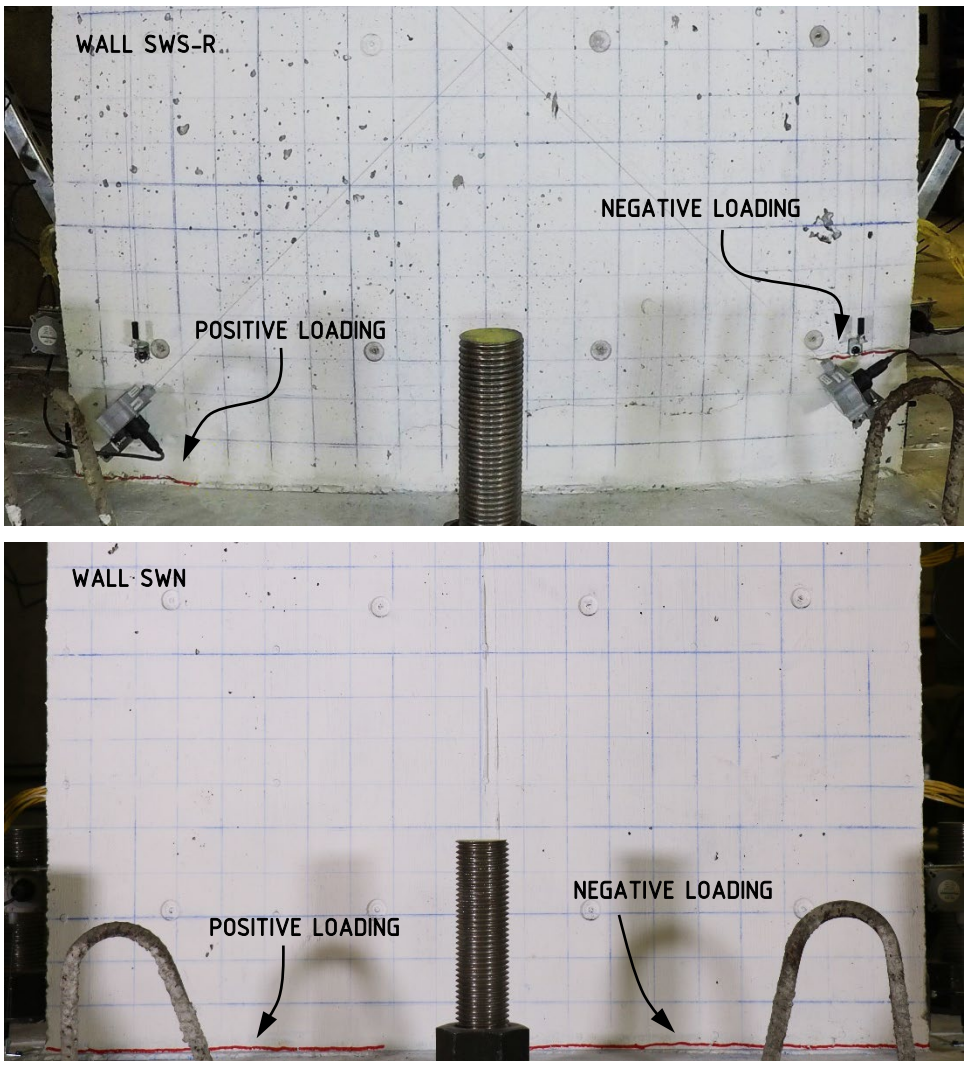

Figure 5.14. First flexural cracks on walls SWS-R (top) and SWN (bottom).

The first shear crack to occur in Wall SWS-R formed under positive loading in the final cycle to 7.2mm displacement (0.3% drift). The crack propagated across the web, continuing from the end of a flexural crack that had previously formed at a height of approximately 1390mm from the base. The diagonal crack started forming at

approximately 350mm from the left and continued inward by 200mm. The crack had an open width of 0.004mm. Before this shear crack formed, what appears to be a shear crack had formed earlier under negative loading in the final cycle to 2.4mm displacement (0.1% drift). The suspected shear crack started to form from the end of a flexure crack coinciding at the top of the repair region at 150mm from the base. The shear crack started at approximately 140mm in from the right end of the wall and spread across by approximately 70mm. This shear crack is only found over the repair material and for this reason, is suspected to be a surface fracture only. The first shear crack in Wall SWN was observed earlier under positive loading during the final cycle to 2.4mm displacement. The crack formed from the right end of a previous flexural crack present cross the web. The shear crack started at approximately 650mm from the left end of the wall and at 160mm from the base. The crack extended towards the right by approximately 125mm and terminated at 50mm above the base. The crack width measured 0.1mm under load, and closed to a hairline width upon unloading. The first shear cracks in both walls are presented in Figure 5.15.

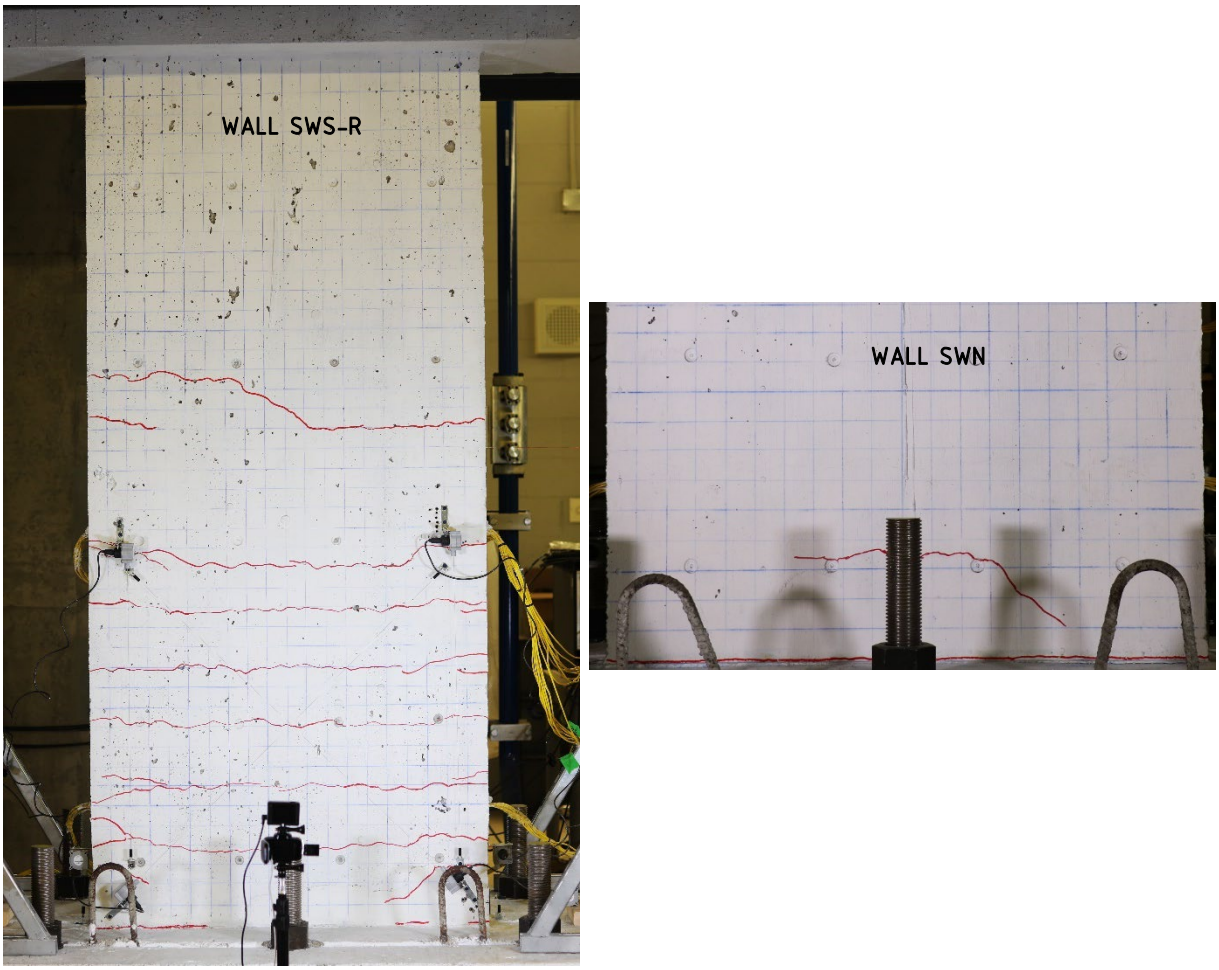

Figure 5.15. First shear cracks on walls SWS-R (left) and SWN (right).

The crack patterns coinciding with the yield displacement of each wall presented distinct characteristics and differences. Wall SWS-R yielded in the positive and negative directions while loading to the 9.6mm target displacement (0.4% drift). The crack pattern for Wall SWS-R, shown in Figure 5.16, exhibited a predominance of flexural cracks up to a height of approximately 1400mm. Ten flexural cracks were spaced over the height of the wall by an average of 150mm. It was observed that for six of the flexural cracks, which had developed over the plastic hinge region, they had developed on adjacent elevations and propagated to meet. The flexure crack along the base had the most significant open width at 1mm upon loading in both the positive and negative directions. The crack closed to a hairline width upon unloading. Additionally, two more shear cracks had developed above the plastic hinge region under negative loading. One shear crack formed directly from the right end of the wall at a height of approximately 1410mm from the base and extended approximately 260mm across the wall. The second shear crack propagated across the web from the end of a pre-existing flexure crack starting from the right end at a height of 1100mm from the base. The shear crack started at 350mm inward from the right end of the wall and extended across the web by approximately 230mm. The first shear crack to form on the wall, as previously described, was now intercepted, and terminated by a flexural crack extending from the right end of the wall at an elevation of approximately 1250mm from the base. Cracks on the left end of the wall had a maximum width of 0.1mm. Crack widths on the right end of the wall ranged from hairline thickness to 0.3mm wide.

Wall SWN reached a positive and negative yielding displacement while loading to the 48mm target displacement (2% drift). The yield crack pattern for Wall SWN, shown in Figure 5.16, presented a mix of flexural cracks, shear cracks, and vertical cracks. The flexural cracks amounted to ten fractures spaced 150mm over the height of the wall up to approximately 1400mm from the base. The flexure crack along the base was accompanied by a second prominent flexure crack at an elevation of approximately 300mm. The crack along the base had an open width of 9mm under positive loading and closed to 6mm. Under negative loading, the crack opened to 14mm, and closed to 9mm. The flexure crack at 300mm elevation opened to 5mm under positive loading and closed to 1.5mm. Under negative loading it opened to 6mm and closed to 0.5mm. Most flexural cracks had extended to merge at the same elevation, while some flexural cracks within the plastic hinge region appeared to only develop outwards from the centre of the wall over the web. Most of the flexure cracks which had developed over the web appeared to progress into shear cracks on each end towards the boundaries, while some were extended by meeting widening flexure cracks through the end boundaries at the same elevation. The shear cracks above the plastic hinge region had a fanning formation from the right end and left end of the wall. Positive loading produced two shear cracks across the left boundary and partially over the web at elevations of 1700mm and 1550mm from the base. Negative loading produced three shear cracks fanning from the right end at approximate elevations of 1880mm, 1710mm, and 1570mm from the base, all reaching across the wall by an average of 450mm. At an elevation of approximately 1250mm from the base, two shear cracks had developed over the web from the ends of positive and negative loading flexure cracks. The crack propagation from the left had initiated at approximately 300mm inward from the left and extended to approximately 670mm across the wall. The crack propagating from the right started at approximately 400mm inward from the right and crossed the web by approximately 350mm to intercept a flexure crack. Vertical cracks were observed over the plastic hinge region only and were all colinear with the longitudinal reinforcement in the web. The vertical crack on the left of the centerline of

the wall, by 150mm, was intercepted by flexure cracks, and intermittently connected over a length of approximately 700mm, starting at 150mm from the base. The vertical crack colinear with the centerline also started at 150mm above the base and reached a length of approximately 280mm. The vertical crack to the right of the centerline, by 150mm, discontinuously covered a length of approximately 650mm, and was intercepted by flexural cracks. The vertical crack started at the base of the wall and extended by approximately 90mm, then followed by two consecutive disjointed crack lengths of 150mm each from an elevation of 350mm over the base. The vertical cracks all maintained hairline widths when loaded.

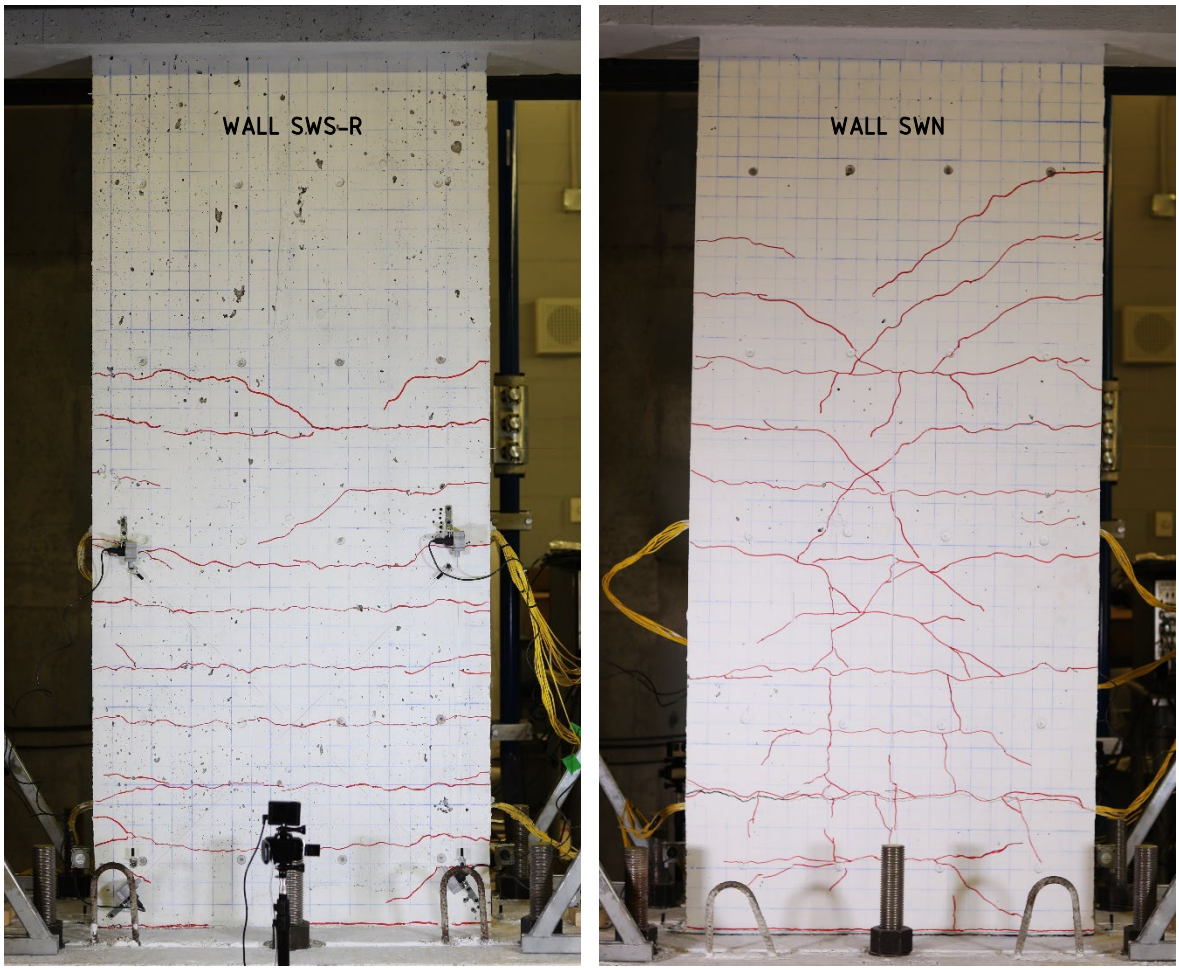

Figure 5.16. Crack patterns at yielding of walls SWS-R (left) and SWN (right).

The existing crack patterns of each wall were augmented at the peak load. Both walls experienced some form of localized damage in addition to sprawled cracks.

Wall SWS-R reached the peak load at 23mm displacement in the positive direction, and at 37mm displacement in the negative direction. The crack pattern presented in Figure 5.17 for Wall SWS-R was traced throughout the final cycle of the 36mm target displacement. Positive loading produced two new shear cracks. The highest shear crack was at an elevation of 1650mm from the base and extended by approximately 230mm from the left. The crack had a hairline width when open. The second shear crack was at approximately 100mm below it and propagated inward from the left by 350mm to intercept an existing shear crack present from yielding of the wall. The crack had an open width of 0.2mm and closed to a hairline width. A major disjointed shear crack had also formed across the wall, starting from the end of a pre-existing short flexure crack at an elevation of 1150mm from the base. The major shear crack extended by 650mm across the length of the wall and terminated at the intersection with a flexure crack at 200mm from the right end of the wall and 150mm above the base. At the initiation point of the major shear crack, it had an open width of 0.15mm, and at the end it had an open width of 0.4mm. The crack closed at the initiation point to a hairline width, and slightly closed to 0.3mm at the end. The separation crack at the base of the wall had an open width of approximately 8mm and closed to approximately 3mm. The flexure crack running across the length of the wall at approximately 200mm from the base, had an open width of approximately 1mm, and closed to a hairline at the left end, but maintained approximately a 1mm width over the web. A cluster of cracking formed around the right toe, over a region measuring 150mm by 150mm. The right toe also showed some indication of the SCC repair material separating from the wall. Negative loading presented two new shear cracks from the right end, and some concentration of cracking near the left toe. The top shear crack was at an elevation of 1500mm from the base, and the other new shear crack was running across the web near the base of the wall. The shear crack at the top spread by 200mm inward from the right and connected to a previous shear crack below it. The shear crack near the base appears to have branched out from the widening flexure crack at 200mm up form the base. The shear crack started at approximately 600mm inward from the right end and stretched by 150mm across the web before terminating at 50mm above the base. The left toe showed some wide cracking accompanied by some loose debris within a region measuring 50mm by 50mm. The crack along the base reached an open width of approximately 5mm on the right end and closed to a width of approximately 1mm. The flexure crack at 200mm above the base had an open width of 0.5mm which closed to 0.25mm. The same crack was approximately 2mm wide over the web and closed to approximately 1mm.

Wall SWN reached the peak load at 96mm displacement in the positive direction, and at 87mm displacement in the negative direction. The crack pattern presented in Figure 5.17 for Wall SWN was traced throughout the final cycle of the 96mm target displacement. Both positive loading and negative loading showed little variation to most of the pre-existing crack pattern, with exception of the addition of a shear crack, some spalling, and some cracking around the toes. Most of the cracks experienced minor widening of the existing cracks with most of the damage becoming concentrated at the base separation crack and a secondary major flexural crack at approximately 350mm above the base. Positive loading presented a new shear crack from the left end at an elevation of 1850mm. The shear crack extended approximately 210mm across the wall. The pre-existing shear crack below it extended by approximately 200mm to intercept a shear crack from the right end, following the fanning pattern. The crack along the base had an

open width of approximately 35mm, which closed to approximately 12mm. The secondary major flexure crack had an open width of 8mm and closed to 1.25mm. No explicitly new cracks were presented with the completion of negative loading. The only distinct damage was a spalled region near the right end of the wall along the elevation of the secondary major flexural crack. The spall was offset by 40mm from the right end and measured approximately 15mm wide, 170mm long, and 10mm deep. The crack along the base had an open width of 38mm and closed to 12mm. The secondary major flexure crack had an open width of 5mm and closed to 2mm. Both toes showed a crack contained within a region measuring 50mm by 50mm.

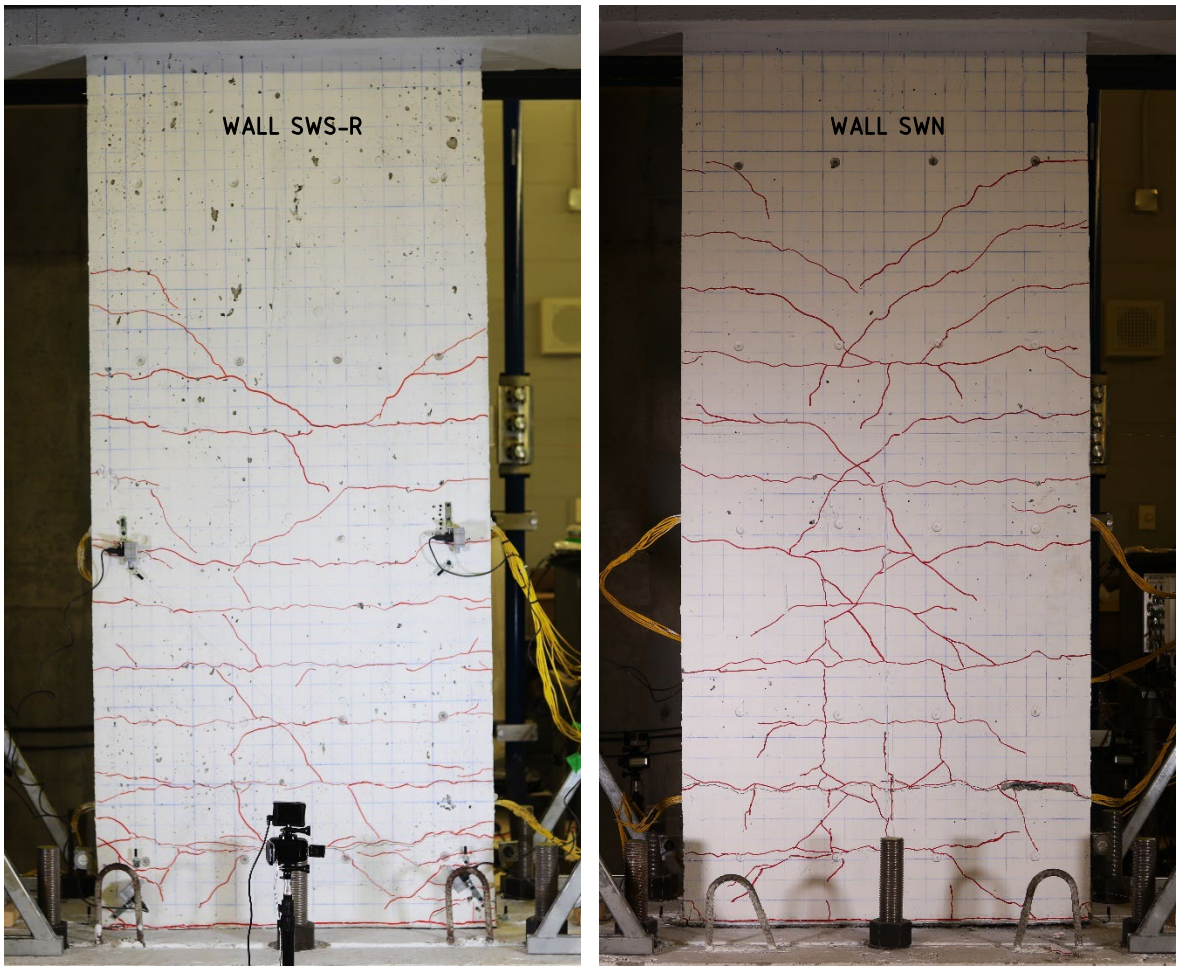

Figure 5.17. Crack patterns at peak load of walls SWS-R (left) and SWN (right).

Both walls experienced toe crushing as part of the failure mechanism. Wall SWS-R exhibited the onset of toe crushing first on the left end through the negative loading branch of the second cycle to 36mm displacement (1.5% drift.). The onset of crushing of the right toe followed through the positive loading branch of the final cycle to 36mm displacement. The onset of damage to the toes at 36mm displacement are shown in Figure 5.18a. The damaged toes

progressively deteriorated as the wall reached failure at 72mm displacement (3% drift). Deterioration of the left toe on the posterior face expanded to include spalling of the end cover along with a region measuring 50mm across and 150mm high. The right toe experienced spalling of the end cover along with a region measuring 200mm wide by 150mm high. Both crushed toes were surrounded by neighbouring regions on both faces of the wall showing signs of partially detached spalls and crushed concrete. Figure 5.18b shows the extend of damage to the toes on the posterior face of the wall. The toes of Wall SWN began to show damage at 108mm displacement (4.5% drift), as evident on the posterior face of the wall, shown in Figure 5.19. The left toe crushed during negative loading of the first cycle, and the right toe crushed with positive loading of the second cycle. Both toes maintained their level of damage through the final displacement cycles to 120mm displacement (5% drift). The damaged region of the left toe was maintained to approximately 25mm wide by 110mm high, with some surface spalling to a depth of approximately 10mm at the base. The crushed region on the right toe measured approximately 70mm wide by 60mm high, with spalling of small fragments. The damage of both toes was relatively similar on both faces of the wall.

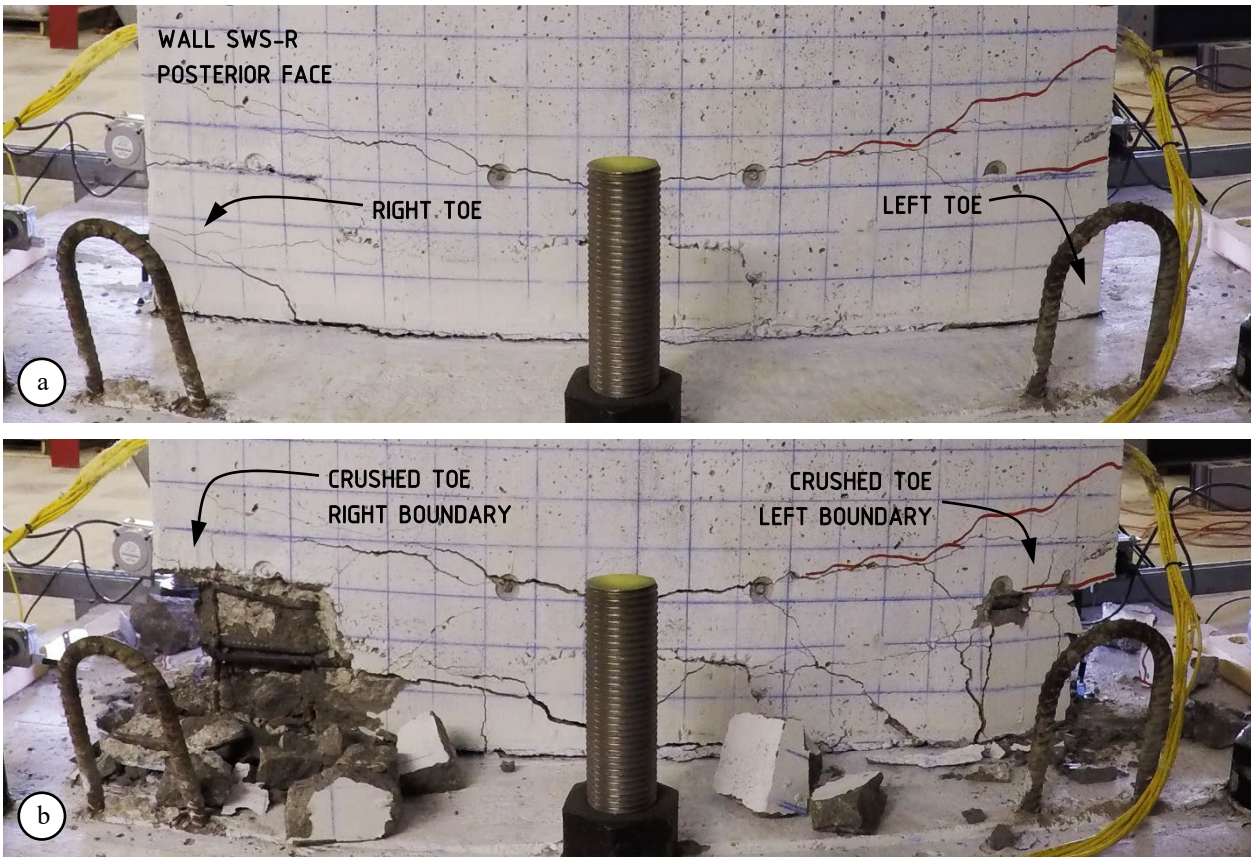

Figure 5.18.Crushed toes of Wall SWS-R: (a) onset at 36mm displacement; and (b) at 72mm displacement.

Figure 5.19. Crushed toes of walls SWN at 108mm displacement.

At the 2.5% drift threshold (60mm displacement) Wall SWS-R had more damage along the base, than Wall SWN. Wall SWS-R presented significant damage over the length of the wall along the base within 200mm. The cracks were mostly clustered towards the boundaries. With positive loading, the crack along the base of the wall had an approximate open width of 10mm, measured at approximately 100mm inward from the left end due to the obstruction by spalling concrete from the left toe. The crack closed to approximately 3mm. The secondary major crack near the base appeared to have a diminishing width due to the deteriorated concrete surrounding it which had a series of other widening cracks. The secondary major crack had an open width of 1.25mm and closed to 0.8mm. Neighbouring cracks had open widths ranging from 1.25mm to 8mm and closed widths between 0.9mm to 5mm. With negative loading, the crack along the base opened to approximately 7mm, inward by 200mm from the right end, and closed to approximately 1mm. The secondary major crack was surrounded by various cracks and partially sustained a width of approximately 2mm. Under positive loading, the base crack in Wall SWN had an open width of 12mm and closed to 9mm. The secondary major flexure crack had an open width of 5mm which closed to 1.25mm. With negative loading, the base crack opened to 19mm and closed to 13mm. The secondary flexure crack opened to 7mm and closed to 2mm. Some spalling occurred along this crack near the right end of the wall. The crack patterns at 2.5% drift for both walls are presented in Figure 5.20.

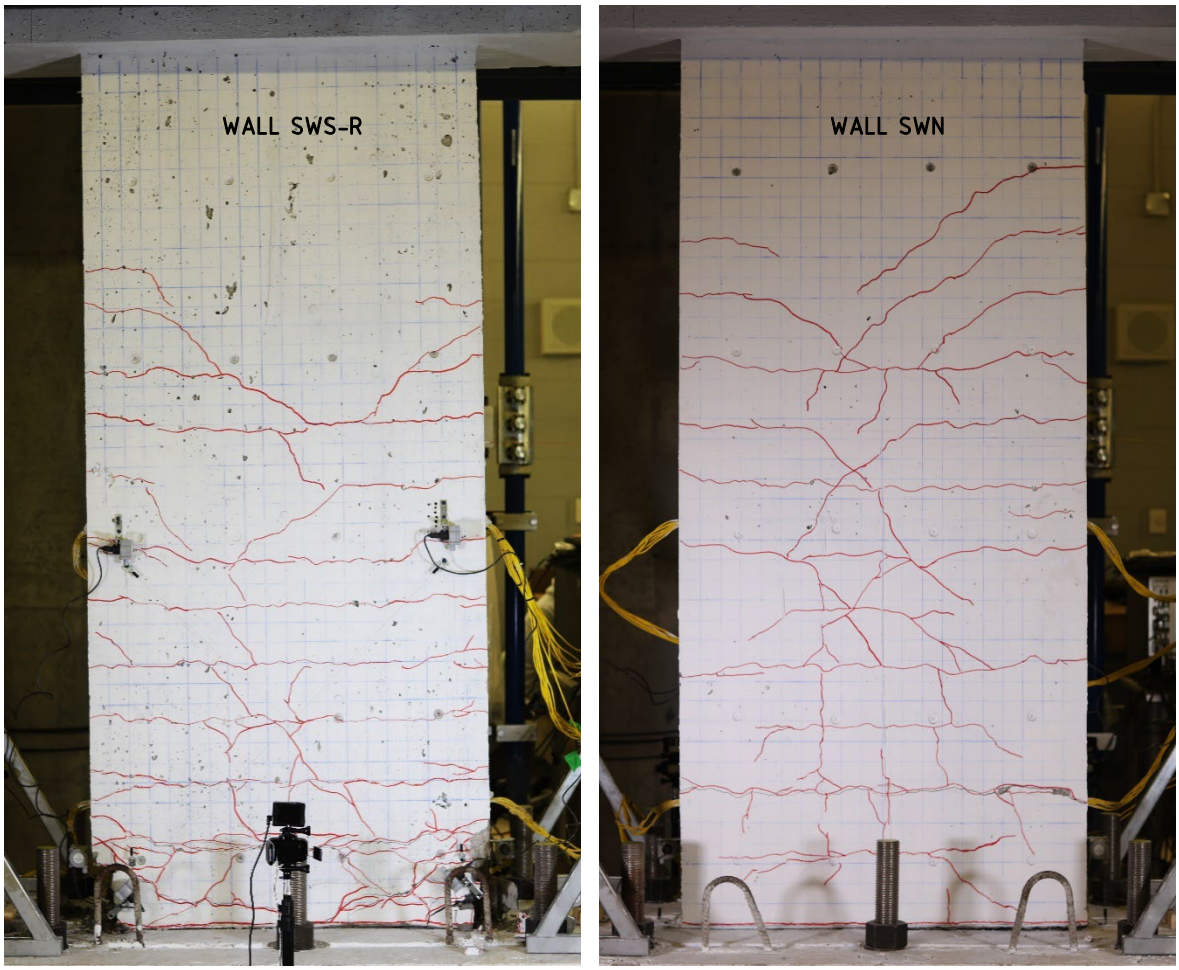

Figure 5.20. Crack patterns at 2.5% drift of walls SWS-R (left) and SWN (right).

Wall SWS-R reached an average ultimate displacement of 60mm under positive and negative loading and was followed by a final subsequent displacement to 72mm, at which the base was completely deteriorated. The toes were surrounded with spalled concrete and debris, the largest fragment measured approximately 50mm by 50mm. The bulk of the SCC repair material at the base of the right boundary had spalled. The crack along the base was obstructed by some of the loose debris. Under load, it had an open width of approximately 8mm to 10mm, measured at 250mm inwards from both ends. The crack closed to approximately 3mm at the left end and closed to approximately 5mm on the right end. The secondary major flexural crack maintained 2mm at its widest point for part of its length near the right end of the wall. The remainder of the cracks across the wall did not show any expansion. Wall SWN reached an average ultimate displacement of 103mm under positive and negative loading and was pushed to a final subsequent displacement of 120mm. The crack pattern remained largely unchanged. The crack along the base had an open width of 37mm under positive loading and closed to 30mm. The secondary major flexure crack had an open width of 7mm and closed to 1.25mm. Under negative loading, the base crack opened to 38mm and closed to 18mm. The secondary

major crack opened to 4mm and closed to 1.25mm. All other cracks had a maximum open width of 0.2mm on both the left and right ends. All cracks closed to a hairline width. The crack patterns of both walls at their final displacement are displayed in Figure 5.21.

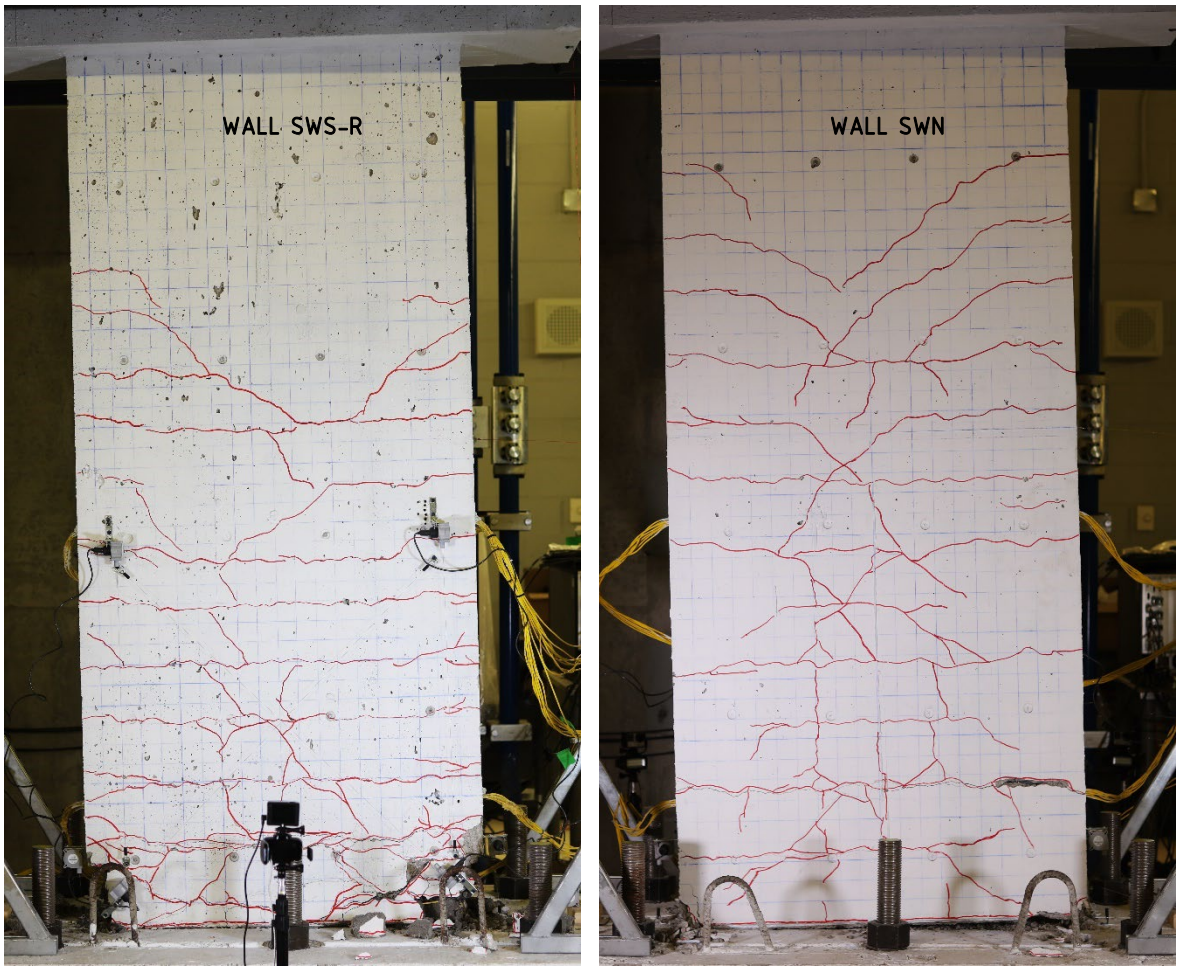

Figure 5.21. Crack patterns at the final displacements of walls SWS-R (left) and SWN (right).

5.5 Reinforcement Strains

Strain gauges were used to monitor the axial strain of three distinct reinforcements: the longitudinal bars in the boundaries, longitudinal bars in the web, and transverse bars. Strain gauges were dispersed over the anterior face (Side A) of each wall and limited to the boundaries on the posterior face (Side B), to collect strain data from within the plastic hinge region, as discussed in Section 3.6.1 of Chapter 3. The strain gauges used on both walls had a nominal strain limit of 2%. Other strain gauges used had the prefix 'SGY', which were exclusive to Wall SWN and had a nominal strain limit of 15%. Results were collected for all active strain gauges, however, not all units remained functional for the full duration of the test. Strain gauges SG30, SG14, and SG31 were sampled for representative hysteretic responses from the same locations on each wall for parallel results. Strain gauge SG30 was mounted on the outmost bar of the right boundary at an elevation of approximately 30mm from the base. Strain gauge SG14 was mounted to the leftmost longitudinal bar, at 150mm from the centerline, of the web at an elevation of approximately 30mm from the base. Strain gauge SG31 was mounted to the transverse bar located closer to the top of the plastic hinge region at an elevation of approximately 650mm from the base. The results from each of the three explicit reinforcements are presented for each wall. The hysteretic response of each strain gauge was terminated at a point determined by the onset of excessive obstruction of readings due to signal noise or indication of physical damage. Appendix C contains the complete sets of strain gauge hysteretic responses for Wall SWS-R and Wall SWN.

Strain gauge SG30 of Wall SWS-R exhibited wide hysteretic loops, as observed in Figure 5.22a. The response indicted yielding of the longitudinal bar at the base while loading to the first cycle of 12mm displacement (0.5% drift). The yield plateau concluded at 1.49% strain, under approximately 104kN of force. Under negative loading, plastic deformation of the bar was emphasized through a positive shift in the value of compressive strain to 0.120%, under a load of approximately -99kN. The remaining cycles were mostly confined to within the envelope of the first cycle. Strain readings were terminated during positive loading in the first cycle of 24mm displacement (1% drift). Strain gauge SG14 captured a predominantly elastic response up to the completion of the first cycle to 9.6mm displacement (0.4% drift), as presented in Figure 5.22b. The bar yielded during positive loading of the second cycle to form a plateau up to 0.649% strain, under a force of approximately 95kN. Readings were terminated after unloading. Strain gauge SG31 remained mostly under tension throughout the duration of testing, as illustrated in Figure 5.22c. The response appears to have developed a progressive positive skew upon positive loading of the last cycle to 12mm displacement. Shear cracks across the plastic hinge region were visible hereafter. Axial strains for the three sample strain gauges, measured at the performance points of Wall SWS-R, are available in Table 5.7.

Strain gauge SG30 of Wall SWN presented slender hysteretic loops from the superelastic Nitinol longitudinal bar, as displayed in Figure 5.23a. The maximum residual strain was approximately 0.009% from a maximum strain of 0.219%, under approximately 58kN, during in the first cycle to 12mm displacement. The response was terminated along the positive loading branch of the first cycle to 24mm displacement. Strain gauge SG14, presented in Figure 5.23b, expressed a yielding plateau at the onset of positive loading to 12mm displacement, which reached 0.785% strain under approximately 57kN of force. Strain gauge SG31 maintained a tensile response throughout the duration of testing, as evident in Figure 5.23c. Two minor plateaus formed in both the positive and negative loading branches of the first cycles to 7.2mm displacement (0.3% drift) and 9.6mm displacement. At 7.2mm displacement no visible

cracks were present at the transverse bar or in its vicinity. At 9.6mm displacement, a flexural crack developed across the web of the wall colinear with the shear reinforcement bar. A major plateau formed upon positive loading in the first cycle to 24mm displacement. Shear cracks were observed, near the top of the plastic hinge region, propagating over the web towards the transverse bar. Axial strains for the three sample strain gauges, measured at the performance points of Wall SWN, are available in Table 5.8.

Table 5.7. Axial strain samples from Wall SWS-R

Wall Performance Points	**Axial Strain**					
	Positive Loading (%)			**Negative Loading (%)**		
	SG30	**SG14**	**SG31**	**SG30**	**SG14**	**SG31**
Yield	0.286	0.257	0.00264	-0.0998	0.0363	-0.000643
Peak	-	-	0.00541	-	-	0.0186
Ultimate	-	-	0.0431	-	-	0.0345
2.5% Drift	-	-	0.0431	-	-	0.0344
Strain Limit	1.80	0.649	0.0533	-0.144	-0.0197	-0.00241

- denotes unavailable strain gauge reading

Table 5.8. Axial strain samples from Wall SWN

Wall Performance Points	**Axial Strain**					
	Positive Loading (%)			**Negative Loading (%)**		
	SG30	**SG14**	**SG31**	**SG30**	**SG14**	**SG31**
Yield	-	-	0.0711	-	-	0.0568
Peak	-	-	0.0992	-	-	0.0654
Ultimate	-	-	0.0978	-	-	0.0669
2.5% Drift	-	-	0.0832	-	-	0.0495
Strain Limit	0.287	0.785	0.101	-0.194	-0.129	-0.00124

- denotes unavailable strain gauge reading

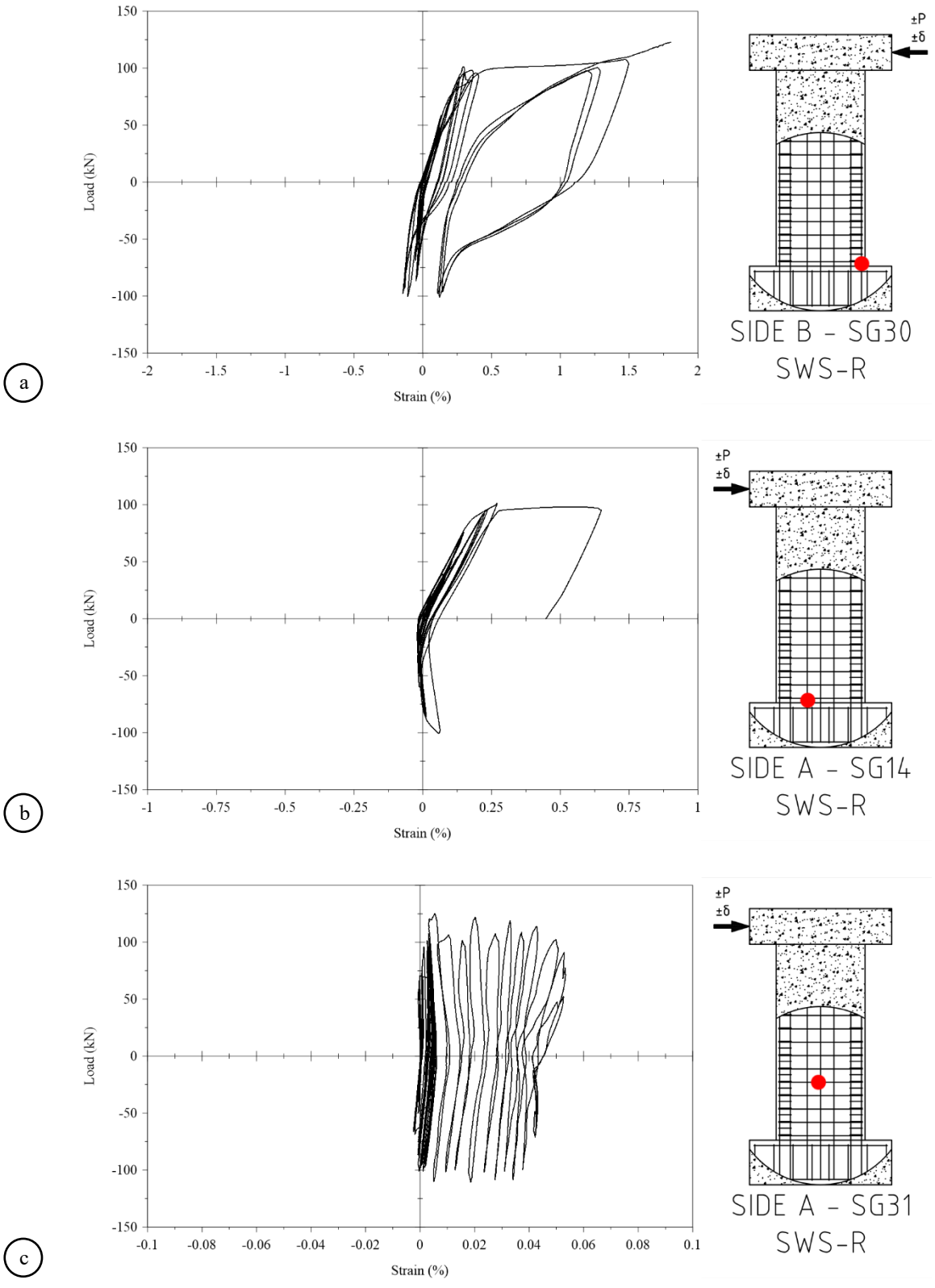

Figure 5.22. Samples of strain gauge responses from Wall SWS-R: (a) longitudinal reinforcement in left boundary; (b) longitudinal reinforcement in web; and (c) transverse reinforcement.

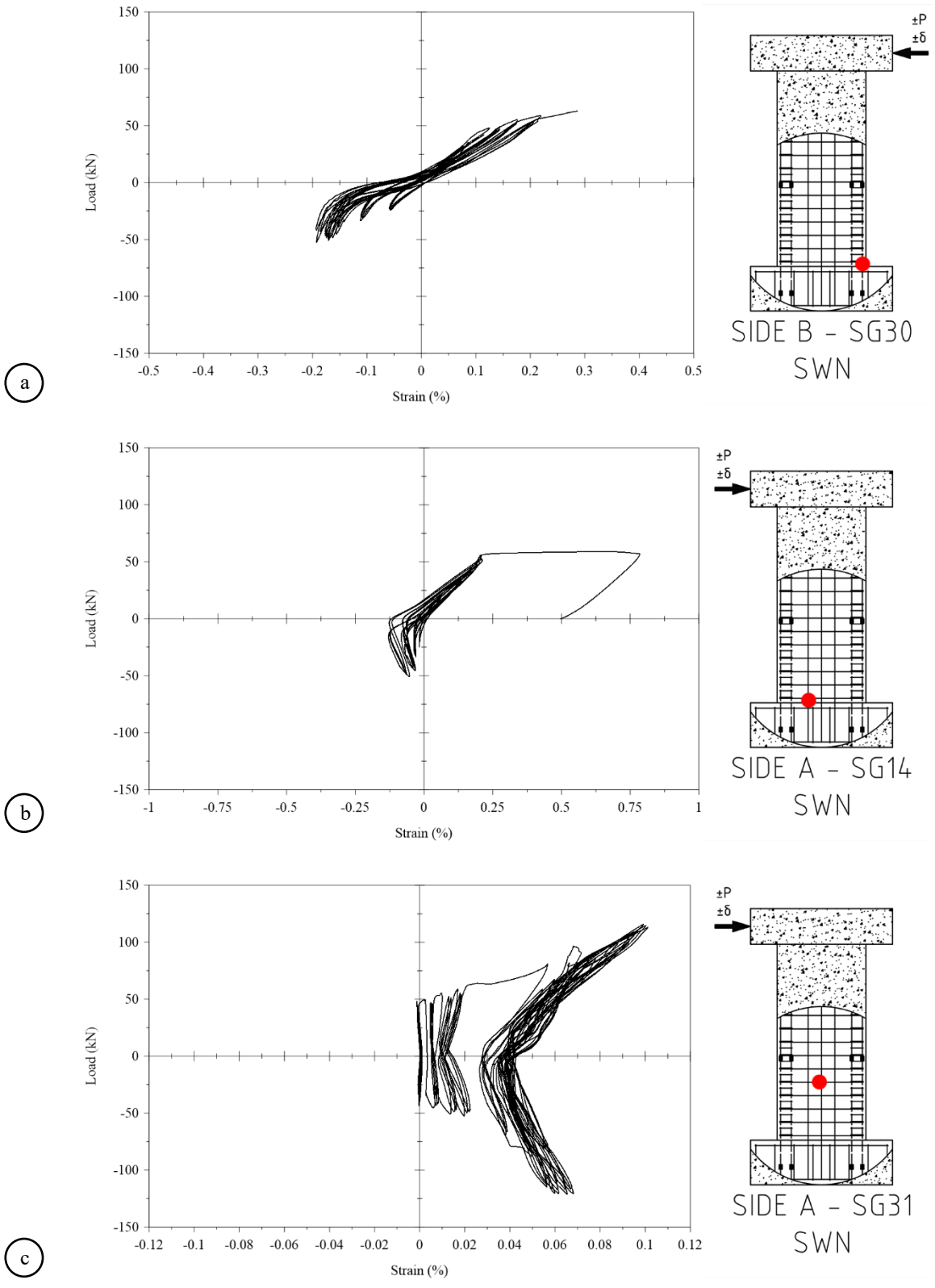

Figure 5.23. Samples of strain gauge responses from Wall SWN: (a) longitudinal reinforcement in left boundary; (b) longitudinal reinforcement in web; and (c) transverse reinforcement.

CHAPTER 6

Discussion of Experimental Results

6.1 Introduction

This chapter provides a discussion of the experimental results of a hybrid steel and superelastic Nitinol-reinforced concrete shear wall (SWN) in comparison to a conventional steel-reinforced counterpart (SWS-R). The raw data sets from experimental testing were used to express the seismic performance of each structure to examine the benefits of integrating superelastic Nitinol shape memory alloy (SMA) reinforcing bars in slender concrete walls. The anticipated outcome was a self-centering structure with minimal damage.

6.2 Behaviour of Shear Walls

The seismic behaviour of the slender walls was benchmarked at each of the target drift levels. Each wall was assessed in both the positive and negative displacement directions. Results were primarily collected from the peak of the first cycle at each target displacement. The additional cycles at each target displacement provided secondary data expressive of performance degradation. Throughout the performance metrics, a particular emphasis is placed on the 2.5% transient drift (60mm displacement) marker as a reference for severe damage and to examine the response of each structure at the threshold of collapse (Yazgan, 2010). The performance assessment includes a review of the lateral displacement profiles, strength and stiffness, ductility and recovery, energy dissipation, rotation, and shear distortion. The comparative assessment also reviews the distribution of elemental failure (flexure, shear, and sliding) and the failure mechanism of each wall. The overall performance of each wall is a product of the average performance from the positive and negative displacements. However, isolated results from each loading direction were used for some performance assessment where it was necessary to convey a distinct outcome. Isolated performance results for positive and negative loading of each wall are available in Appendix J.

Notably, the performance assessments of the Nitinol-reinforced wall (SWN) exclude two drift targets. A displacement calibration error resulted in missing the 3.5% drift target in the positive direction, and the 2% drift target in the negative direction. More details are available on this in Section 5.3 of Chapter 5. The steel-reinforced control shear wall (SWS-R) covered all drift targets in both loading directions.

6.2.1 Lateral Displacement Profiles

The lateral displacement of each wall was profiled along the height for both the positive and negative displacement directions at 2.5% drift (60mm displacement). Lateral displacements were recorded at four elevations: just above the base, mid-height, top of the wall, and center of the cap beam, as described in Section 5.3.1 of Chapter 5. The profiles of each wall were visually assessed for an indication of the overall structural response. Each profile expressed a geometric combination of four distinct responses: flexure, shear, rocking, and sliding, as the reference diagrams show in Figure 6.1.

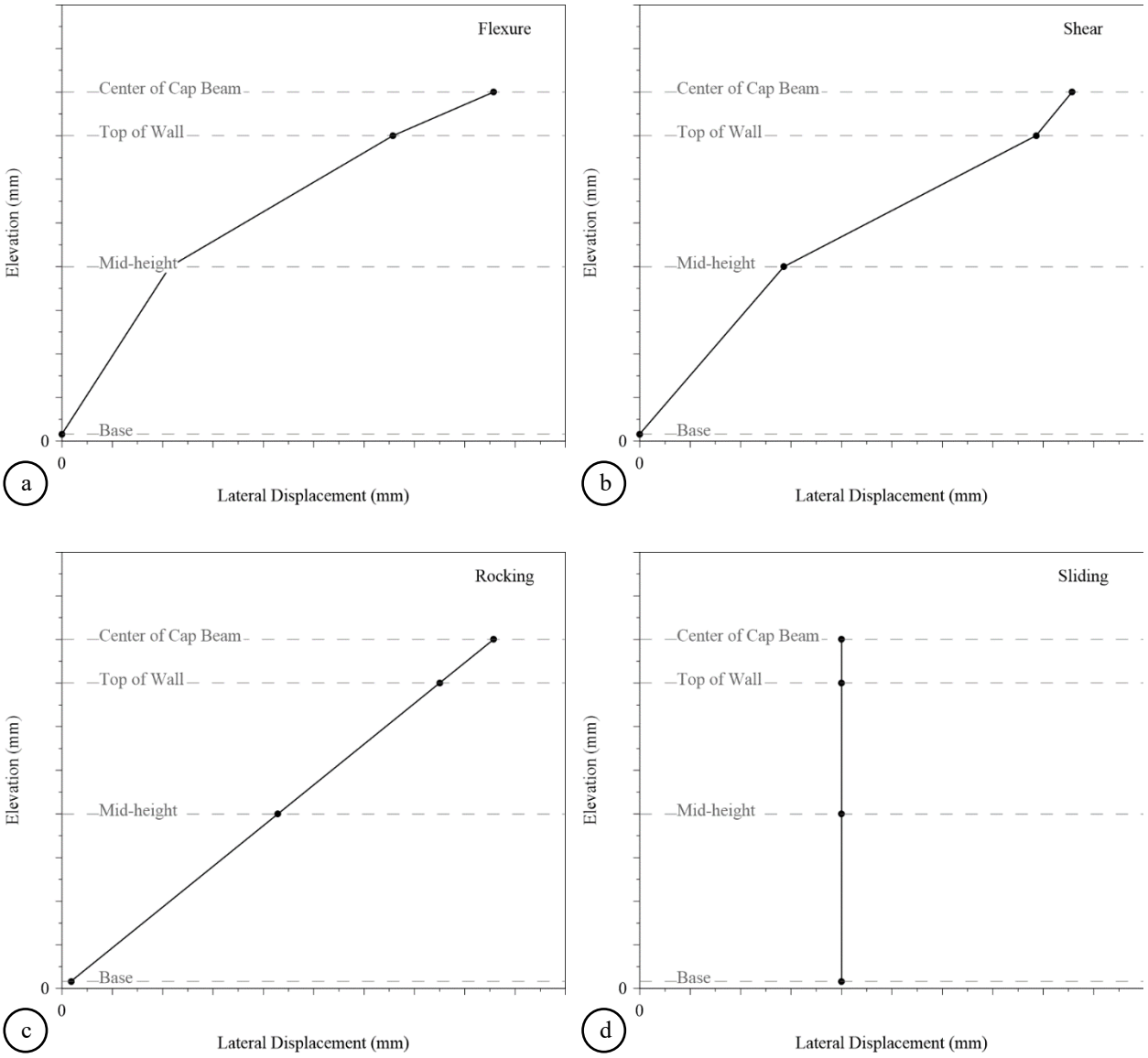

Figure 6.1. Reference displacement profiles: (a) flexure; (b) shear; (c) rocking; and (d) sliding.

A flexural response has a bowed profile with the base at near zero displacement and the shallowest slope at the top end. A shear profile has a steep slope at the top end indicating displacement induced by lateral translation. Rocking maintains a uniform slope along the entire profile. Sliding is profiled by translation at the base.

Wall SWS-R presented asymmetrical profiles, relative to Wall SWN. The positive profile of Wall SWS-R presented a distinct tri-linear response influenced by sliding and shear. The base of the wall slid to approximately 20% of the target displacement. At mid-height, the profile was displaced by 52% of the target and pivoted forward, then maintained a more vertical relation between the displacement at the top of the wall and the centre of the cap beam. The top of the wall displaced by 95% relative to the target displacement at the cap beam. The positive profile of Wall SWN maintained a more linear response between the base and the top of the wall, with some minor sliding at the base. The wall slid by 5% and displaced at mid-height by 50% of the target displacement. The overall linearity of the profile expressed the rocking which predominantly occurred at the base due to the development of a widening major crack. The slight bow forward from mid-height is a result of additional minor rocking which occurred at a secondary major flexural crack across the plastic hinge. The top end of the profile exhibited a slight increase in slope indicating some shear distortion. However, the top of the wall displaced by 92% of the target, having a shallower slope than Wall SWS-R, due to the increased rotation from secondary rocking.

Without the significant sliding displacement experienced by Wall SWS-R in the positive direction, both walls would have had similar positive profiles expressing an influence from rocking and shear distortion. The cracking characteristics of both walls at 2.5% drift showed patterns of shear cracks over the plastic hinge region. On both walls the major crack along the base was observed to retain an opening at the left end of the wall when unloaded, while resting on the right toe, being the pivoting point for rocking. The secondary pivoting point above the base on Wall SWN exhibited similar attributes at rest. Figure 6.2 presents the locations of the pivot points and outlines the path along the traced intermittent shear cracks for each wall.

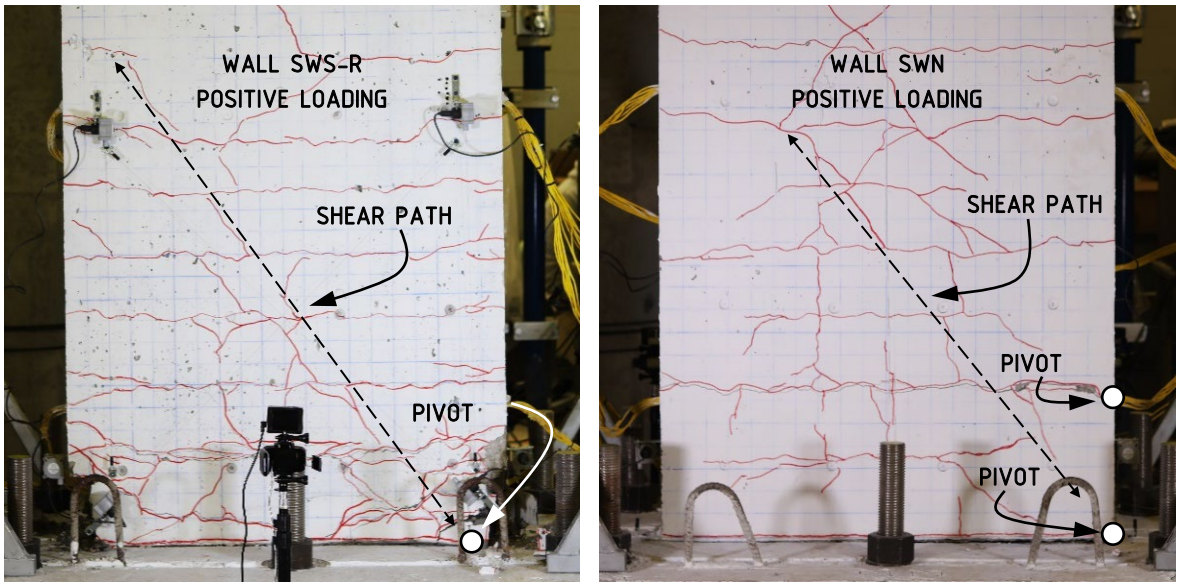

Figure 6.2. Shear paths and rocking pivot points developed under positive loading at 2.5% drift, unloaded.

The negative profile of Wall SWS-R showed an unusual convexity in the profile about the mid-height, followed by a shallow slope. Under negative loading, Wall SWS-R slid towards the negative direction but lagged behind the centerline by 2% of the target displacement. In contrast, base sliding of Wall SWN was proportional with positive loading at 5% of the target drift. At this point in testing the toe of the left boundary of Wall SWS-R was significantly crushed, thus shifting the extreme compression fiber, and the pivoting point of rocking, inward. The combination of a rightward offset to the centerline at the base and rocking about a shifted pivot resulted in the forward appearance of the displacement at mid-height, giving the overall impression of a convex profile. At mid-height, the wall had displaced by 53% of the target, while Wall SWN had displaced by 45%. The displacements at the top of the wall and at the center of the cap beam relatively coincided for both walls at 83% for Wall SWS-R, and 80% for Wall SWN, relative to the transient 2.5% drift target.

Both walls shared similar general trends throughout their negative loading profiles, indicating overall similar responses. Both walls had a relatively linear negative profile between the base and the top of the wall, followed by a shallower slope relating the top of the wall to the center of the cap beam. The overall response of both walls was governed by flexure and rocking. Figure 6.3 presents the locations of the pivot points for each wall.

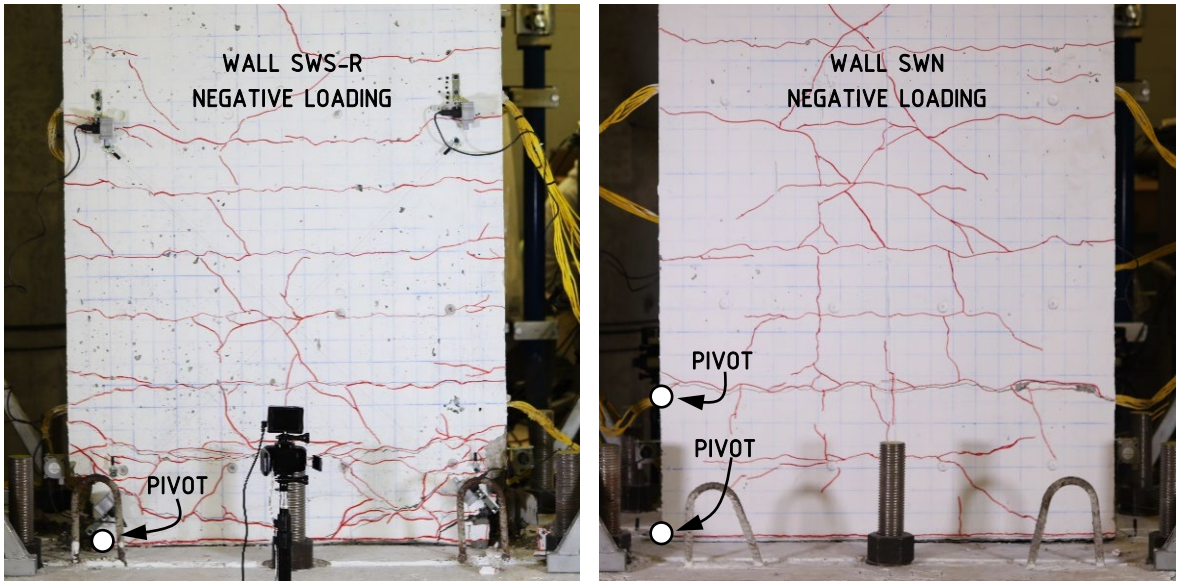

Figure 6.3. Rocking pivot points developed under negative loading at 2.5% drift, unloaded.

The profiles of Wall SWS-R presented unique responses. The positive loading profile is influenced by base sliding and shear distortion. The negative loading profile is the product of flexure and rocking with the influence of a base sliding offset. Wall SWN presented mostly mirrored profiles. The positive loading profile was influenced by rocking and shear distortion, whereas the negative loading profile was a result of rocking and flexure. The positive and negative profiles of walls SWS-R and SWN are presented in Figure 6.4.

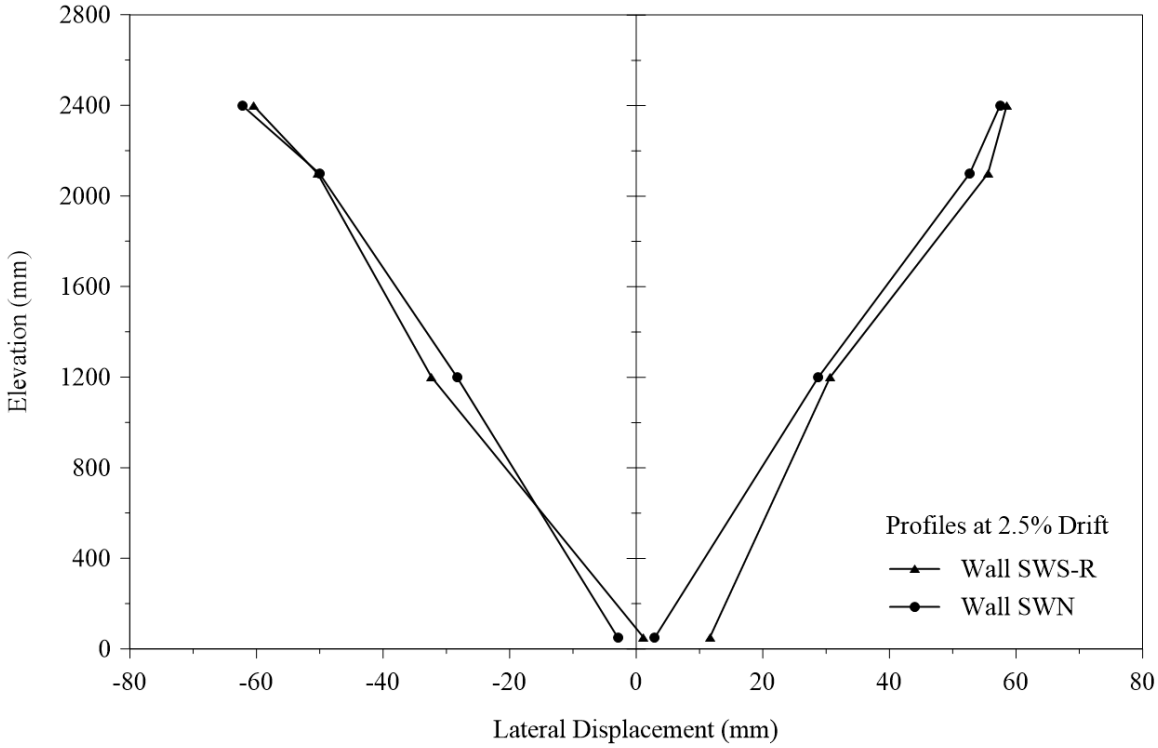

Figure 6.4. Lateral displacement profiles.

6.2.2 Strength and Stiffness

The impact of sequential reverse cyclic loading on strength retention was assessed by proportioning the peak load of the second displacement cycle against the peak load of the first displacement cycle at each drift target. The strength of Wall SWS-R deteriorated by up to 3% before yielding near 0.4% drift (9.6mm displacement). At 0.5% drift (12mm displacement), the strength dropped by 5% as the flexural crack along the base widened, influencing the response of the wall towards rocking. Wall SWN presented up to 10% in strength loss to 0.5% drift, with progressive development of some flexural cracks. At 1% drift (24mm displacement), Wall SWS-R developed a major flexural shear crack across the plastic hinge region which led to an 8% drop in strength. In contrast, the strength of Wall SWN dropped by 16% at the same drift level as the number of flexural cracks increasing by 80%. Wall SWS-R accumulated damage resulting in a strength loss of 10% as it reached its peak load at approximately 1.5% drift (36mm displacement). The flexural depth of the wall became shortened by the partially crushed toes at each end. As Wall SWN yielded at 2% drift (48mm displacement), the strength dropped by 11% due to significant widening across the entire lengths of the major flexural cracks at the base and across the plastic hinge, defining the two pivoting points for rocking at each end. At 2.5% drift (60mm displacement), Wall SWN had almost complete strength retention, whereas Wall SWS-R weakened by 9%. The terminal drift to 3% (72mm displacement) presented the greatest strength loss for Wall SWS-R at 22%, corresponding to the consecutive rupturing of the longitudinal reinforcement in the boundaries. Reaching peak load at 4% drift (96mm displacement), Wall SWN deteriorated by 50% less than Wall SWS-R did at its capacity. Overall,

walls SWS-R and SWN achieved strength compatibility with average peak strengths of 118kN. The final cycle set at 5% drift (120mm displacement) resulted in the largest strength loss for Wall SWN at 28%. The superelasticity of the Nitinol reinforcing bars in the boundaries shifted some of the concentration of flexural strain in the cracked section to the stiffer steel longitudinal reinforcing bars in the web. As a result, the steel bars progressively ruptured or severely buckled in pairs throughout each cycle. The superelastic Nitinol bars remained undamaged. Figure 6.5 presents the average strength retention at each drift target for Wall SWS-R and Wall SWN. Table 6.1 summarizes the sequence of average strength degradation over the salient damage indicators for each wall.

The secant stiffness references the damaged state of the structure against its initial condition. The lower elastic modulus of the longitudinal Nitinol reinforcing bars, placed in the boundaries of Wall SWN, resulted in an average initial secant stiffness at 57% of the stiffness of the steel-reinforced control wall. Wall SWS-R maintained a diminishing stiffness gap to Wall SWN beyond 0.4% drift. Benchmarked at 2.5% drift, the walls presented compatible stiffness, differing by approximately 3%. Both walls achieved compatible stiffness through different types of damages with varying severity. The crushed toes of the boundary presented the most severe and dominating damage of Wall SWS-R. The softening at each end was augmented by a widening flexural crack and a dense network of cracks across the length of the wall, all contained within 200mm above the foundation. In comparison, Wall SWN featured two wide flexural cracks extending the length of the wall along the base and at 300mm. Wall SWN maintained a 49% greater secant stiffness over Wall SWS-R at its final drift of 3%. The stiffness degradation of both walls is presented in Figure 6.6.

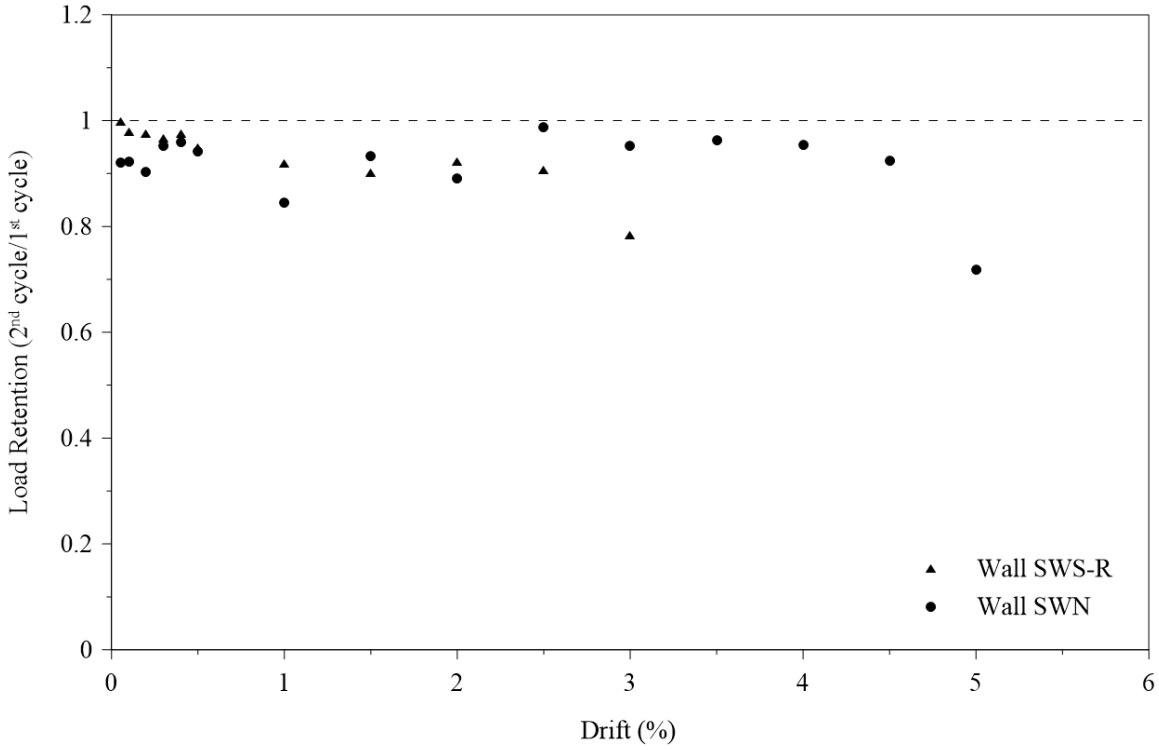

Figure 6.5. Strength retention.

Table 6.1. Damage mechanism strength losses

Order of Damage	Wall SWS-R			Wall SWN		
	Drift (%)	Damage Type	Strength Loss (%)	Drift (%)	Damage Type	Strength Loss (%)
1	0.05	First Flexure Crack	0	0.05	First Flexure Crack	8
2	0.3	First Shear Crack	3	0.1	First Shear Crack	8
3	0.4	Yield Displacement	2	2	Yield Displacement	11
4	1.5	Peak Load	10	2.5	2.5% Drift	1
5	1.5	Toe Crushing	10	4	Peak Load	5
6	2.5	2.5% Drift	9	4.5	Toe Crushing	8
7	3	Ultimate Displacement	22	5	Ultimate Displacement	28

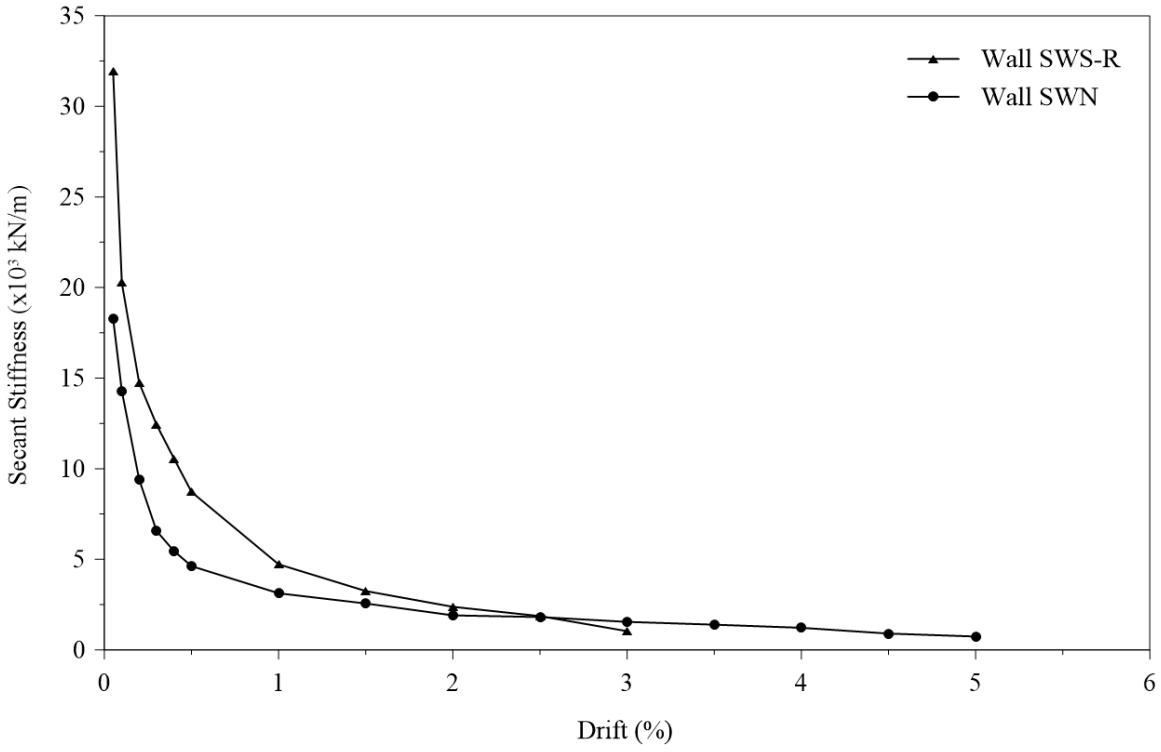

Figure 6.6. Stiffness degradation.

6.2.3 Ductility and Recovery

The Nitinol-reinforced Wall SWN had a delayed yield response (Park, 1989), correlating the ductility of the wall to one third the ductility of Wall SWS-R. The delay is attributed to the overall lower stiffness of Wall SWN, as influenced by the superelastic Nitinol longitudinal reinforcement in the boundary elements.

Recovery (%), was determined by Equation 6.1. The difference between the target displacement (Δ_{max}) and the residual displacement ($\Delta_{residual}$) of the first cycle when unloaded, is weighed against the target displacement.

$$Recovery\ \% = \frac{\Delta_{max} - \Delta_{residual}}{\Delta_{max}} \cdot 100\% \qquad \text{[Eq. 6.1]}$$

Wall SWS-R presented almost identical recovery trends for positive and negative loading. The recovery behaviour of Wall SWS-R, under positive and negative loading, deviated beyond 0.1% drift from a generally declining trend, increasing in recovery and peaking at 0.3% drift, before continuing to decay. At 0.1% drift, the control wall recovered by an average of 77%. At 0.3% drift, the wall had an average recovery of approximately 85%. It was observed that there was no new formation of flexure cracks beyond this drift level. The distribution of tensile strain over a larger number of cracks helped alleviate the otherwise higher strain concentrations, which previously caused localized elongations in the longitudinal reinforcement. For this reason, the conventionally reinforced wall experienced a brief improvement in drift recovery. Thereafter, the average recovery of Wall SWS-R continued to decay.

Wall SWN presented two distinct recovery responses due to the occurrence of a sequence of anomalies in the loading protocol, as discussed in Section 5.3 of Chapter 5. The recovery trends of Wall SWN maintained similar decay paths up to 1%, then increased slightly at 1.5%. In contrast to the steel-reinforced specimen, Wall SWN had an average recovery of approximately 79% at 0.1% drift and an average of 70% at 0.3% drift. The slight increase in recovery at 1.5% drift is due to a sudden dispersion of flexure and shear cracks over the height of the wall. The distribution of damage helped reduce further plastic deformation from forming over the plastic hinge region as a result of tensile strain concentrations in the longitudinal reinforcement at the two major flexural cracks, specifically for the stiffer deformed steel bars in the web. Hereafter, the positive recovery branch fluctuated between approximately 60% to 80% recovery, and the negative recovery branch continued to decay gradually. At 2% drift, the positive recovery branch spiked to 75%. Prior excessive cycling at 1.5% drift had softened the concrete structure allowing it to displace further under a lower load demand and without a significant increase in plastic damage. The positive recovery branch continued to decline towards 3% drift after which the anomalies in the loading protocol were rectified. At 4% drift, positive recovery spiked to approximately 69% as a spalled portion along the secondary major crack was dislodged resulting in a fine closed crack width. Positive recovery reduced to approximately 63% at 5% drift. The negative recovery branch maintained a reductive trend beyond 1.5% drift.

If comparing the recovery at 2.5% drift, Wall SWN has a recovery of approximately 66% from the positive loading branch and approximately 50% from the negative loading branch, as compared to an average recovery of approximately 25% by Wall SWS-R from both loading branches. The positive and negative recovery branches for Wall SWS-R are displayed in Figure 6.7, and in Figure 6.8 for Wall SWN.

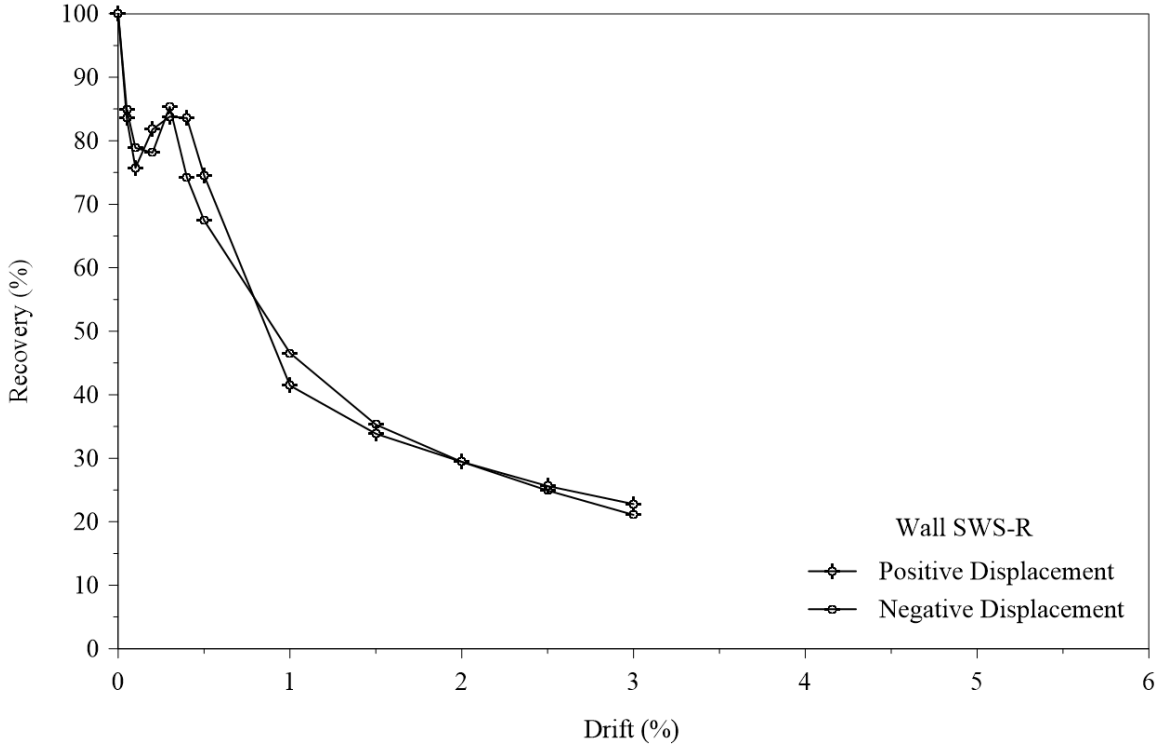

Figure 6.7. Drift recovery of Wall SWS-R.

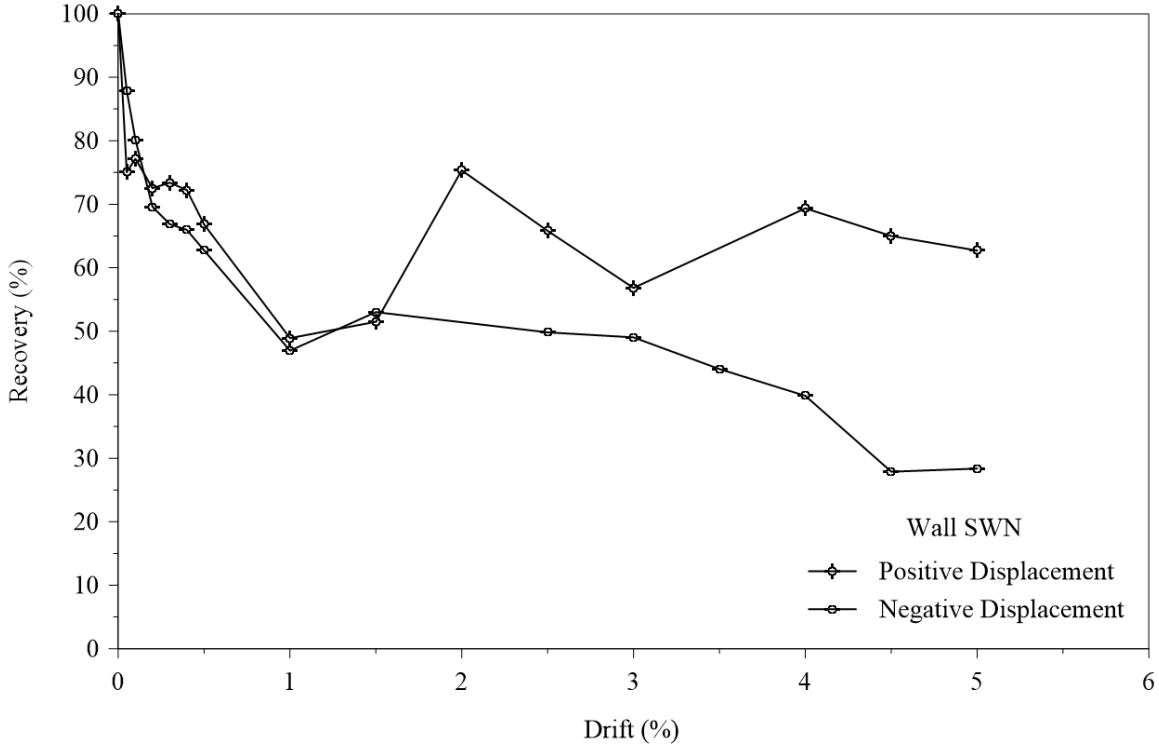

Figure 6.8. Drift recovery of Wall SWN.

Residual drift was assessed at 2.5% drift in relation to the probability of demotion as prescribed by Ramirez and Miranda (2012). The results of the positive recovery branch for Wall SWN indicate that in the event of asymmetrical seismic loading, the probability of demolition may increase. The softening of the structure as observed in the results due to excessive cycling at +1.5% drift supports this hypothesis. The probability curves are presented in Figure 6.9. The probability values for each wall are proportional approximations from the intersection of the residual drift with the probability curve. A summary of the probabilities of demolition is presented in Table 6.2.

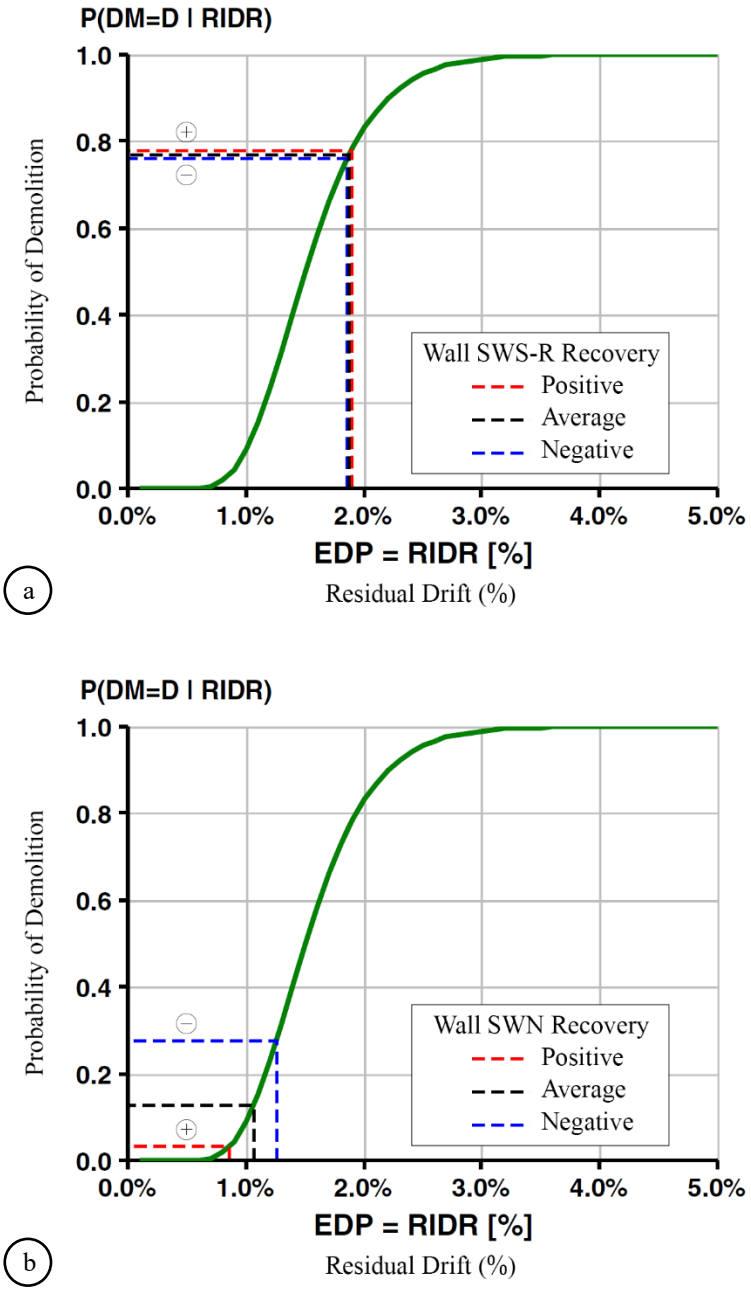

Figure 6.9. Probability of demolition: (a) Wall SWS-R; and (b) Wall SWN (adapted from Ramirez and Miranda, 2012).

Table 6.2. Probability of demolition at 2.5% drift

Recovery Branch	Wall SWS-R			Wall SWN		
	Recovery (%)	Residual (%)	Probability	Recovery (%)	Residual (%)	Probability
Positive	25.64	1.86	0.78	65.82	0.85	0.03
Negative	24.93	1.88	0.76	49.81	1.25	0.27
Average	25.28	1.87	0.77	57.81	1.05	0.15

6.2.4 Energy Dissipation

The complete response of the first cycle at each target displacement was used to establish the energy dissipation. The wide displacement loops of Wall SWS-R were characterized with steep unloading branches. Wall SWN maintained more slender loops tending towards pinching at the origin. The consistency of symmetrical drift in Wall SWN was interrupted by a second iteration of redundant skewed cycling at 1.5% drift followed by asymmetrical loading at 2%, 2.5%, and 3% drift. Wall SWN is assessed at the +2.5% drift range as it bears the impact of asymmetric and excessive loading. The first cycle loops at +2.5% drift for walls SWS-R and SWN are presented in Figure 6.10.

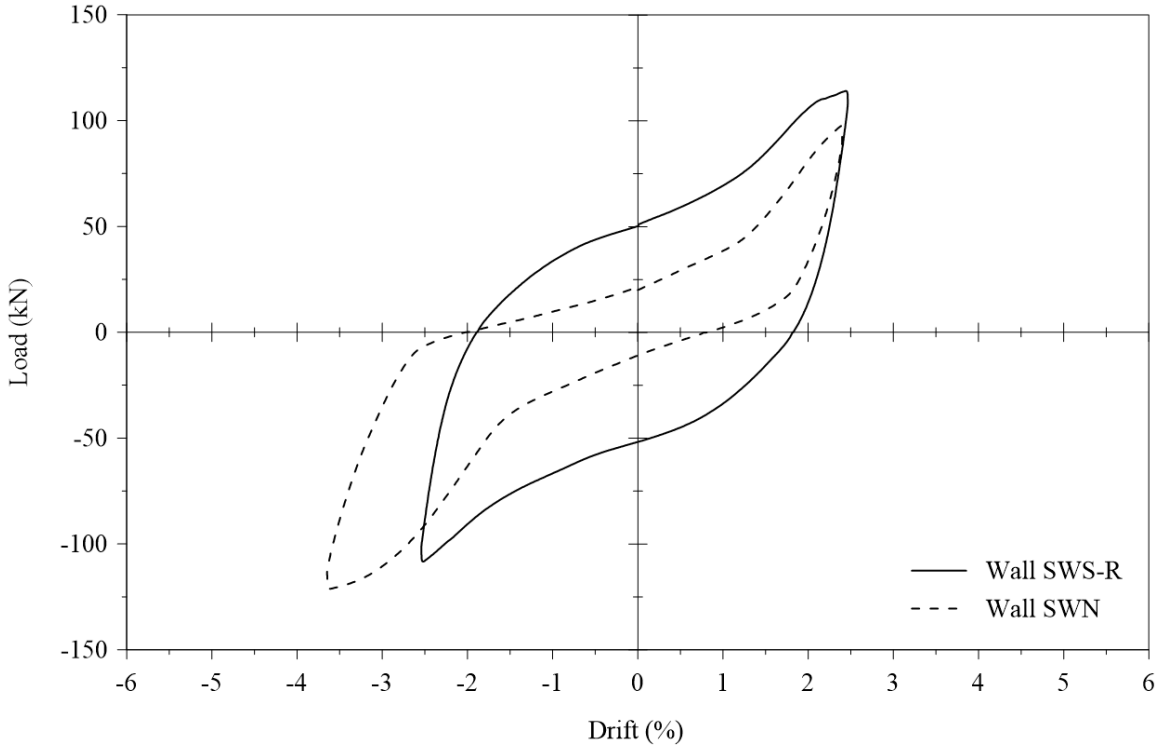

Figure 6.10. First cycle at +2.5% drift.

The unloading branches in the positive displacement quadrant, emphasize the self-centering mechanism inherent in Wall SWN due to its capacity to store more elastic potential energy than its conventional counterpart, Wall SWS-R, as illustrated in Figure 6.11. The overall difference in loop width can be attributed to the lower energy required to displace the less stiff Wall SWN, and its ability to store a portion of the applied displacement energy towards recovery.

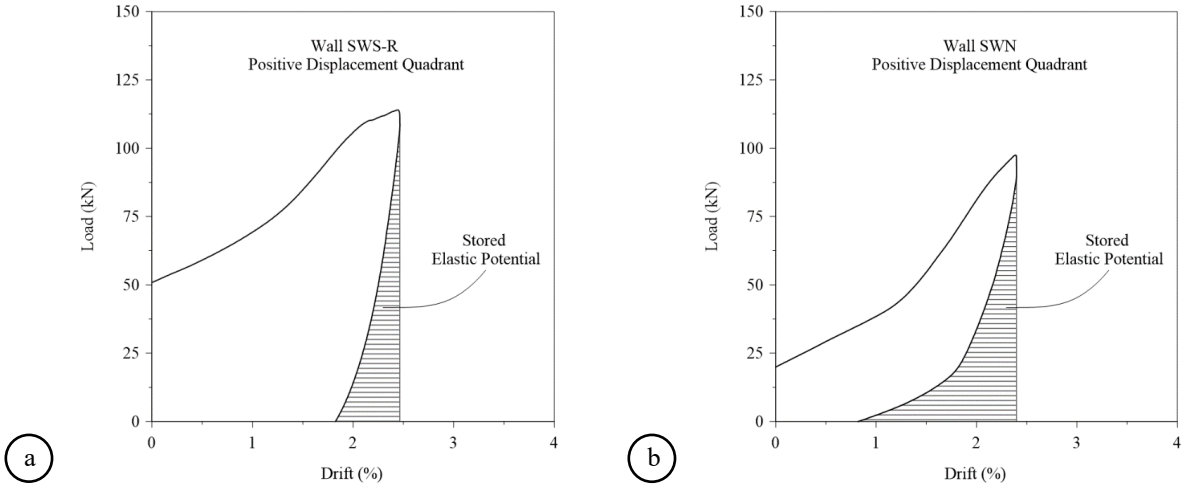

Figure 6.11. Stored Elastic potential energy: (a) Wall SWS-R; and (b) Wall SWN.

The energy dissipation for Wall SWN at 2.5% drift was calculated at two separate drift cycles for the positive and negative responses due to the anomalies in the loading protocol for this wall. The negative response was produced first during the +1.5% to -2.5% drift range. Concurrently, in the positive loading direction, three additional cycles of +1.5% drift were applied. The positive response was produced in the second drift succession, following the repetition at 1.5% drift, during the +2.5% to -3.5% drift range. Under positive loading, Wall SWN dissipated approximately 30% less energy than under negative loading as a direct result of the additional energy dissipated at +1.5% drift. Wall SWS-R was assessed from a single cycle at ±2.5% drift. Under negative displacement, Wall SWS-R dissipated 2% less energy and retained 5% larger elasticity than when displaced in the positive direction. The energy dissipation values at 2.5% drift are summarized in Table 6.3. Figure 6.12 shows the total dissipated energy through the first cycle at each drift level for both walls.

Table 6.3. Energy dissipation at 2.5% drift

Wall	Positive Displacement		Negative Displacement	
	Dissipated Energy ($x10^3$ Nm)	**Stored Elastic Potential ($x10^3$ Nm)**	**Dissipated Energy ($x10^3$ Nm)**	**Stored Elastic Potential ($x10^3$ Nm)**
SWS-R	5.55	0.54	5.43	0.56
SWN	2.17	0.82	3.05	1.14

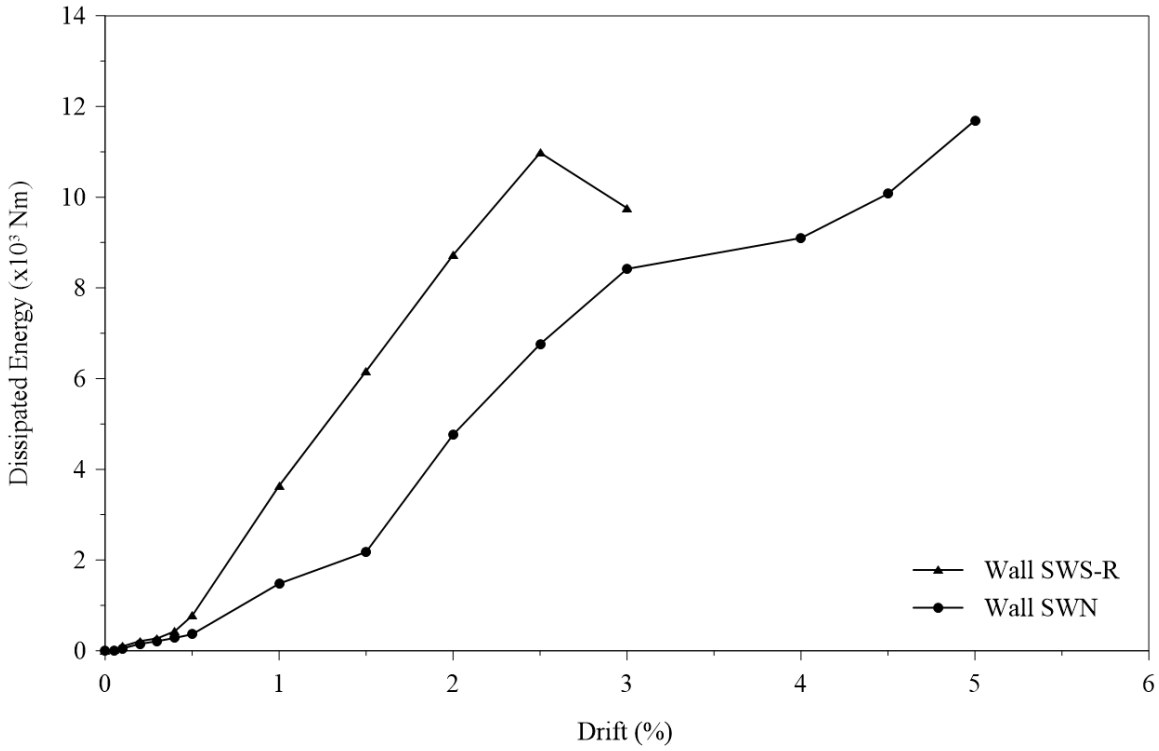

Figure 6.12. Dissipated energy.

6.2.5 Rotation

Rotation was monitored at three locations on each wall. Rotation (θ) was determined using the left (V_1) and right (V_2) vertical displacement values, set apart at a specified distance (l), as expressed by Equation 6.2 (Massone and Wallace, 2004). The overall rotation of the walls was monitored at the cap beam. Intermediate rotations were monitored at the plastic hinge region and at the base.

$$\theta = \frac{V_1 - V_2}{l} \qquad \text{[Eq. 6.2]}$$

The overall average rotation of Wall SWN was approximately 30% greater than Wall SWS-R at 2.5% drift. The difference is attributed to the lower stiffness of the Nitinol-reinforced walls and the development of two dominant flexural cracks. Rocking at the base had a major contribution towards the total rotation of each wall. The wider major flexural crack on Wall SWN caused the wall to rotate at the base by an average of 16% more than Wall SWS-R. The second major flexural crack contributed to an average of 12% more rotation over the plastic hinge. The self-centering capacity of Wall SWN is evident in the slender cycles of the hysteretic responses. The rotation hystereses for Wall SWS-R are presented in Figure 6.13, and in Figure 6.14 for Wall SWN. Further information is available in Appendix J.

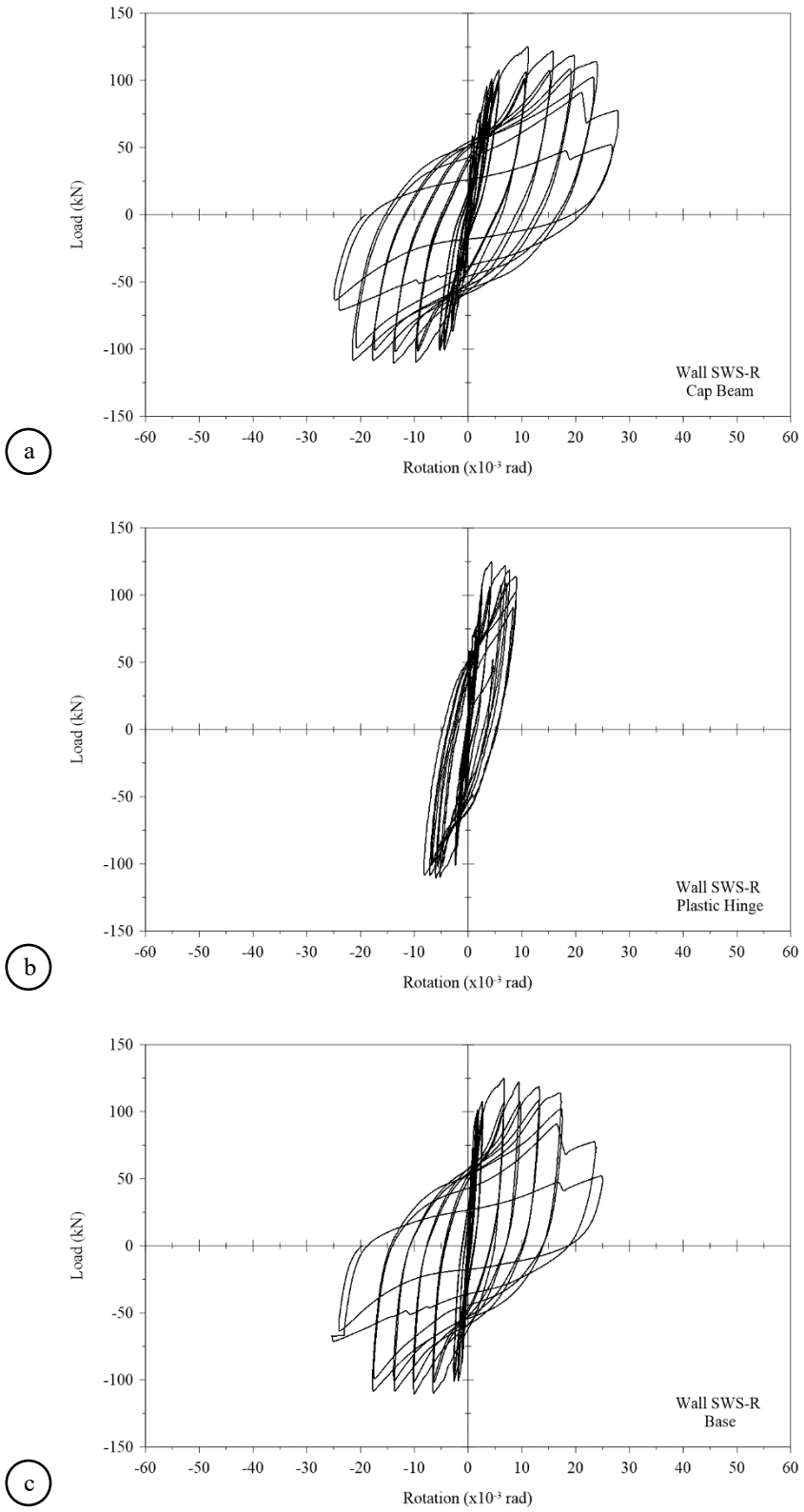

Figure 6.13. Rotation hystereses of Wall SWS-R at: (a) cap beam; (b) plastic hinge; and (c) base.

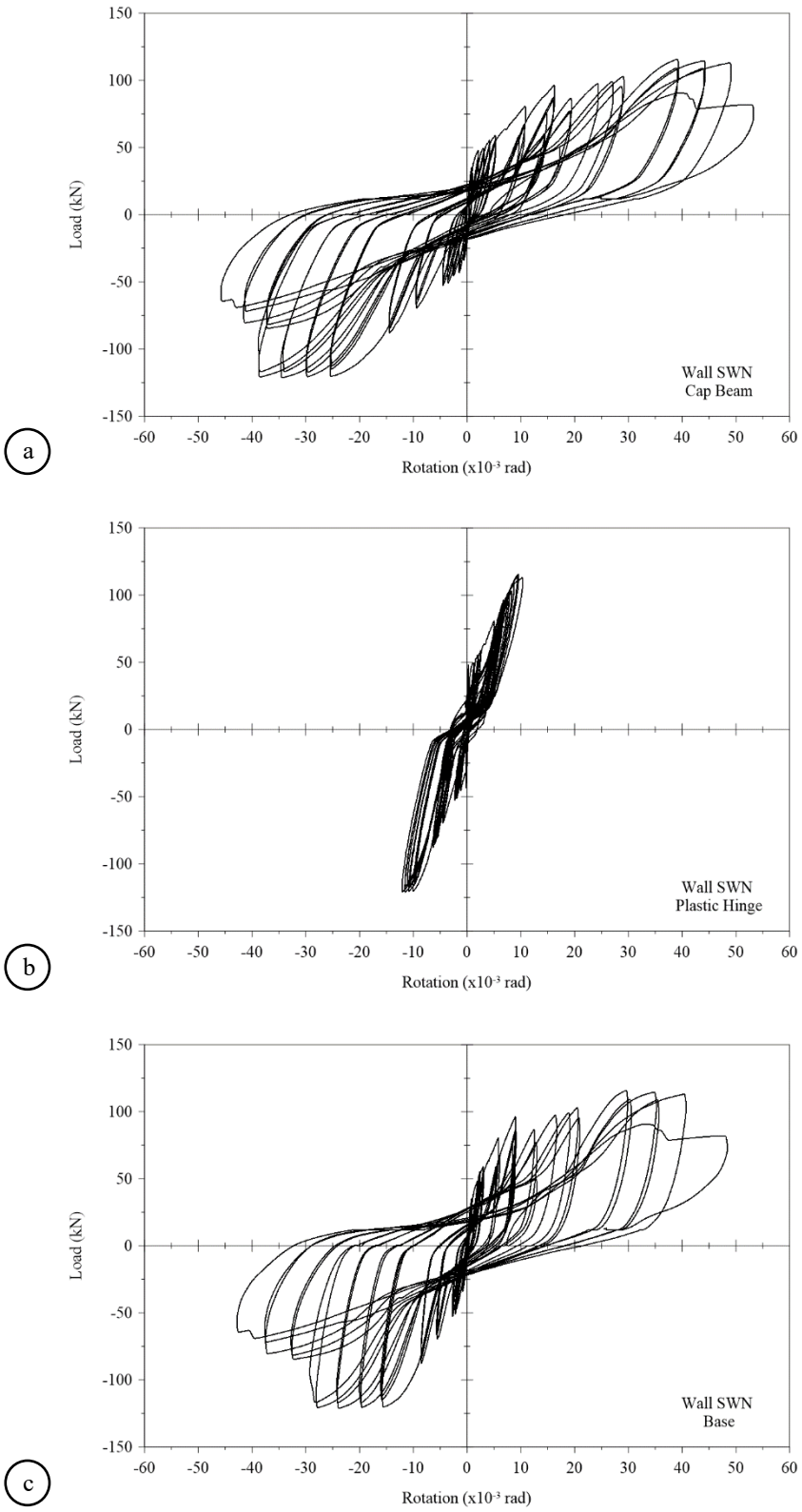

Figure 6.14. Rotation hystereses of Wall SWN at: (a) cap beam; (b) plastic hinge; and (c) base.

6.2.6 Shear Distortion

Shear distortion was monitored over the plastic hinge of each wall. Diagonal expansion and retraction measurements were recorded by instruments CP-B-1250 on the right end and CP-D-1250 on the left end, which were mounted diagonally across an 800mm by 800mm reference plane concentric to the plastic hinge region. The average shear distortions (γ_{avg}) were determined using Equation 6.3 (Oesterle et al., 1976). The equation approximates shear distortions for reinforced concrete structures by averaging angular changes to the reference plane on the left and right ends, measured in radians. The variables d_1 and d_2 represent the undistorted diagonal lengths across the reference plane for the instrument on the right and on the left, respectively. The variables δ_1 and δ_2 represent the changes in diagonal lengths of d_1 and d_2, respectively. The undistorted dimensions of the reference frame are represented by the variables h for height and l for length.

$$\gamma_{avg} = \frac{(\delta_1 \cdot d_1) - (\delta_2 \cdot d_2)}{2 \cdot h \cdot l} \quad \text{[Eq. 6.3]}$$

Wall SWS-R maintained narrow shear distortion loops up to 0.5% drift, followed by significantly widening loops thereafter. Wall SWN maintained narrow loops with pinching around the origin upon unloading throughout testing. The use of superelastic Nitinol longitudinal reinforcement in the boundaries reduced the extent of shear failure and promoted recovery. At the conclusion of testing at 3% drift, Wall SWS-R had approximately 30% greater shear distortion under positive loading, and approximately 20% greater distortion under negative loading, than Wall SWN achieved at 5% drift. The shear distortion values at each of the structural performance points of each wall, as well as at the 2.5% drift threshold and at the limits of positive and negative loading, are provided in Table 6.4. The shear distortion hystereses of walls SWS-R and SWN are presented in Figure 6.15 and Figure 6.16, respectively.

Table 6.4. Shear distortions

Performance Point	**Shear Distortion**			
	Wall SWS-R		**Wall SWN**	
	Positive Loading ($x10^{-3}$ rad)	**Negative Loading ($x10^{-3}$ rad)**	**Positive Loading ($x10^{-3}$ rad)**	**Negative Loading ($x10^{-3}$ rad)**
Yield	0.499	-0.573	2.49	-2.29
Peak	2.01	-3.82	4.62	-4.37
Ultimate	7.48	-6.15	4.64	-4.51
2.5% Drift	7.48	-6.16	3.14	-3.07
Limit	7.74	-6.16	5.41	-4.69

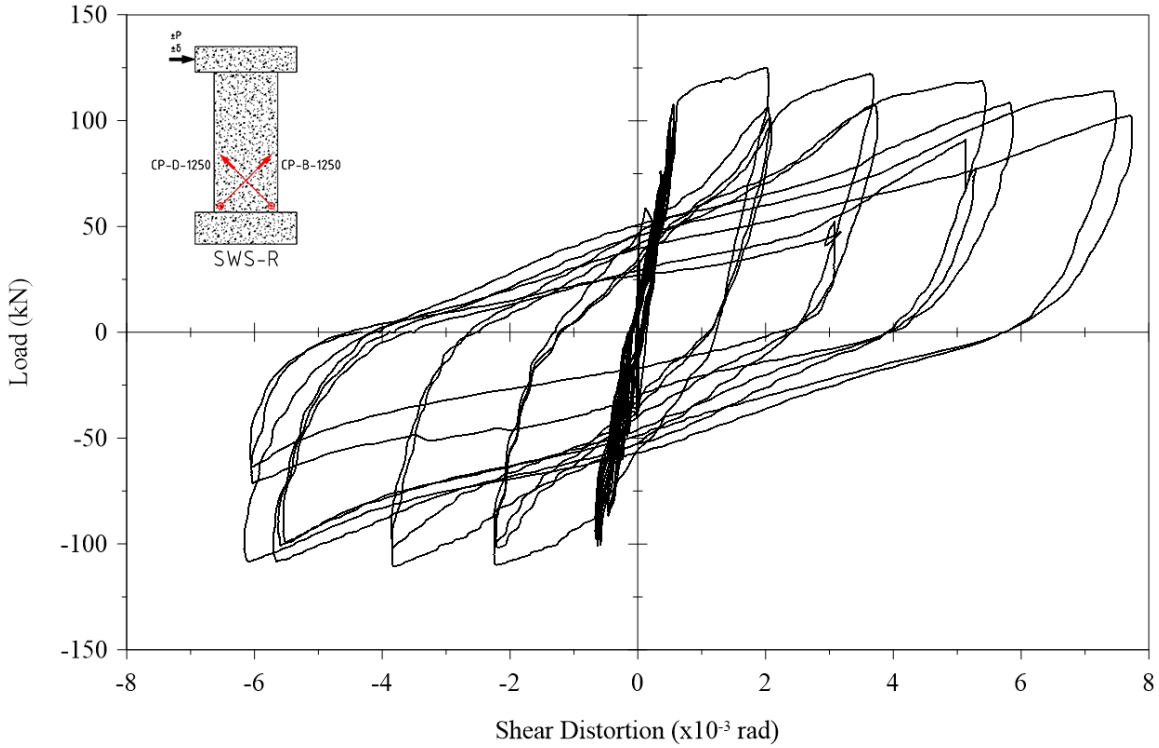

Figure 6.15. Shear distortion of Wall SWS-R.

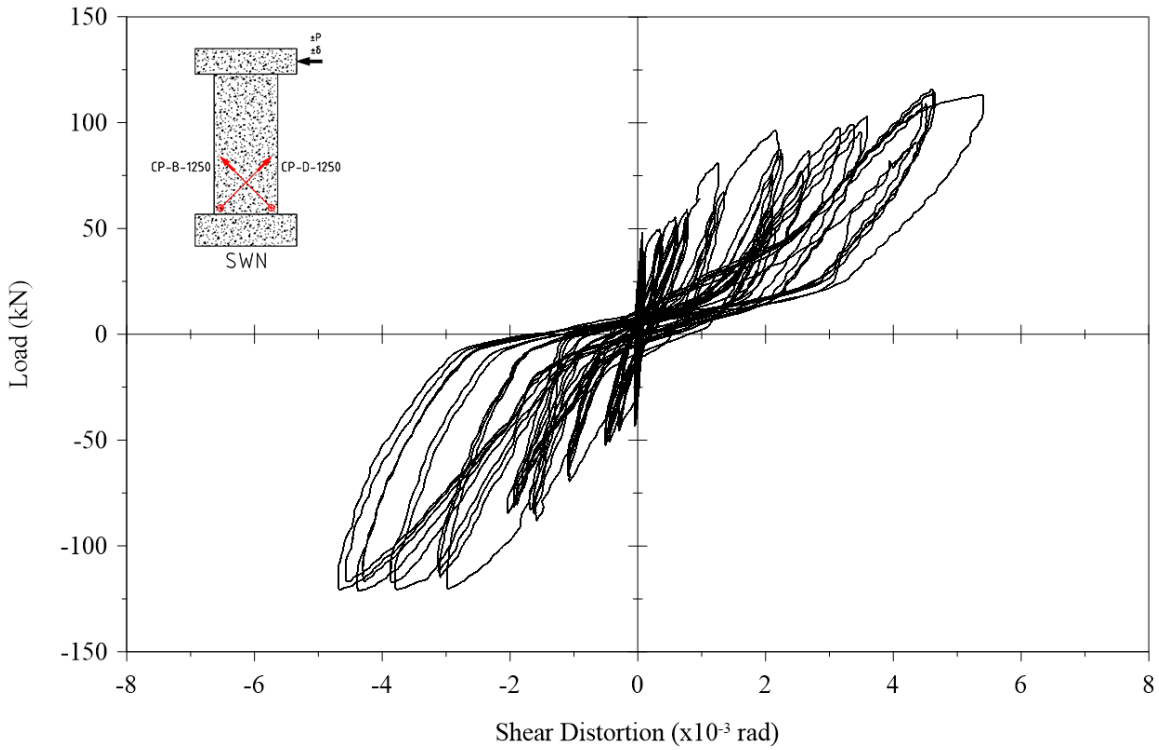

Figure 6.16. Shear distortion of Wall SWN.

6.2.7 Distribution of Flexure, Shear, and Sliding

The deformation response of each wall was evaluated by scaling the distribution of flexure, shear, and sliding. The methodology for determining the distribution of deformation was adopted from the procedure outlined by Massone and Wallace (2004). The geometric relations for curvature and skew were defined by mathematical expressions to produce the lateral displacement values for flexure and shear, respectively, at the top of the first story. A story is defined as the rectangular region over which the instrumentation is positioned in pairs for shear (CP-B-1250 and CP-D-1250) and flexure (CP-A-1250 and CP-C-1250). For this study, the plastic hinge region served as the location of the first story. The instrumentation was configured as described in Section 3.6.1 of Chapter 3.

Displacement due to flexure is expected to account for approximately 70% of the total displacement at the top of the first story in slender walls, and account for a much higher contribution at the top (Massone and Wallace, 2004). However, the variation in distribution of deformation is relative to the slenderness of the wall. Given a fixed length and variable height, the slenderness of the aspect ratio directly influences the flexural stiffness of the wall beyond the plastic hinge, which dictates the curvature in the upper portion of the wall. The most severe damage in both walls was embodied within the plastic hinge region, which was approximately equal to half of the height of the walls. Beyond the plastic hinge region, the upper halves of the walls remained mostly linear with damage limited to fewer cracks with mostly hairline widths. Considering the limited damage and linearity in the upper halves of the walls, it was accepted that the total lateral displacement of the wall, as measured by instrument CP-E-1250 at the center of the cap beam, would be closely proportional to the lateral displacement at the top of the first story. As such the proportions of lateral displacement at the top of the first story were used to ration the distribution of the total lateral displacement at the top of the wall.

Total lateral displacement (U_{total}) at the top of the first story is expressed in Equation 6.4a by Massone and Wallace (2004) as the summation of displacements due to shear ($\overline{U}_s$) and flexure (U_f). The expression was modified for this study to express the total lateral displacement at the top of the wall by including the contribution from sliding (U_{sl}), as shown in Equation 6.4b.

$$U_{total} = \overline{U}_s + U_f \qquad \text{[Eq. 6.4a]}$$

$$U_{total} = \overline{U}_s + U_f + U_{sl} \qquad \text{[Eq. 6.4b]}$$

The simplified expression in Equation 6.5 combines the instrumentation measurements for shear and flexure to determine the total lateral displacement at the top of the first story. The instruments were separated by a length (l) and height (h) of 800mm over the plastic hinge. The variables D_1^{meas} and D_2^{meas} denote the measurements of diagonal lengths across the plastic hinge when the wall is loaded. The changes in lengths measured by the diagonal instruments were added to the diagonal constant to calculate the values of the diagonal length variables. The variables V_1 and V_2 denote the changes in height over the plastic hinge on the left and right, respectively.

$$U_{total} = \frac{\sqrt{D_1^{meas2} - (h + V_2)^2} - \sqrt{D_2^{meas2} - (h + V_1)^2}}{2} \quad \text{[Eq. 6.5]}$$

The flexure displacement was calculated using Equation 6.6. The variable θ denotes rotation and was determined using Equation 6.2. The variable h_1 denotes the height of the first story and is therefore equal to the constant h at 800mm. The variable α is a factor expressing the fraction from the top of the first story to the centroid of curvature. The value of factor α is 0.67, as recommended and applied by Massone and Wallace (2004) and other researchers for slender shear walls with rectangular cross-sections. More information on the relevance of the value of the factor α is available elsewhere (Ali 1990).

$$U_f = \alpha \cdot \theta \cdot h_1 \quad \text{[Eq. 6.6]}$$

The outputs of the total displacement expression (Equation 6.5) and flexural displacement expression (Equation 6.6) were used in a rearranged form of Equation 6.4a to calculate shear displacement. The results of shear displacement and flexure displacement were then weighed against the calculated total displacement to determine the distribution of deformation at the first story. The total lateral displacement of Wall SWS-R at the top of the first story was accounted for by an average of approximately 74% flexure and 26% shear for all drift targets. Wall SWN had an average distribution of approximately 73% flexure and 27% shear.

Equation 6.4b was rearranged to subtract displacement due to sliding from the overall lateral displacement at the top of the wall. The remainder was rationed given the distribution at the top of the first story to output the displacement values at the top of the wall for shear and flexure deformations. The breakdown of lateral displacements was then weighed against the total lateral displacement at the top of the wall to determine the distribution of flexure, shear, and sliding at each drift target.

When considering sliding, the distribution slightly changed, however, flexure remained the dominant source of deformation. At 2.5% drift, Wall SWS-R had averaged contributions of 59% from flexure, 21% from shear, and 20% from sliding. The distributions under positive loading and negative loading for Wall SWS-R are presented in Figure 6.17. In contrast, Wall SWN had averaged contributions of 67% from flexure, 25% from shear, and 8% from sliding. The distributions under both loading direction of Wall SWN are presented in Figure 6.18. Further details on the distributions of flexure, shear, and sliding deformations are individualized for each target displacement, under positive and negative loading, for each wall in Appendix K. Note that the effect of base rocking was not considered and could be included as a component in Equation 6.4b.

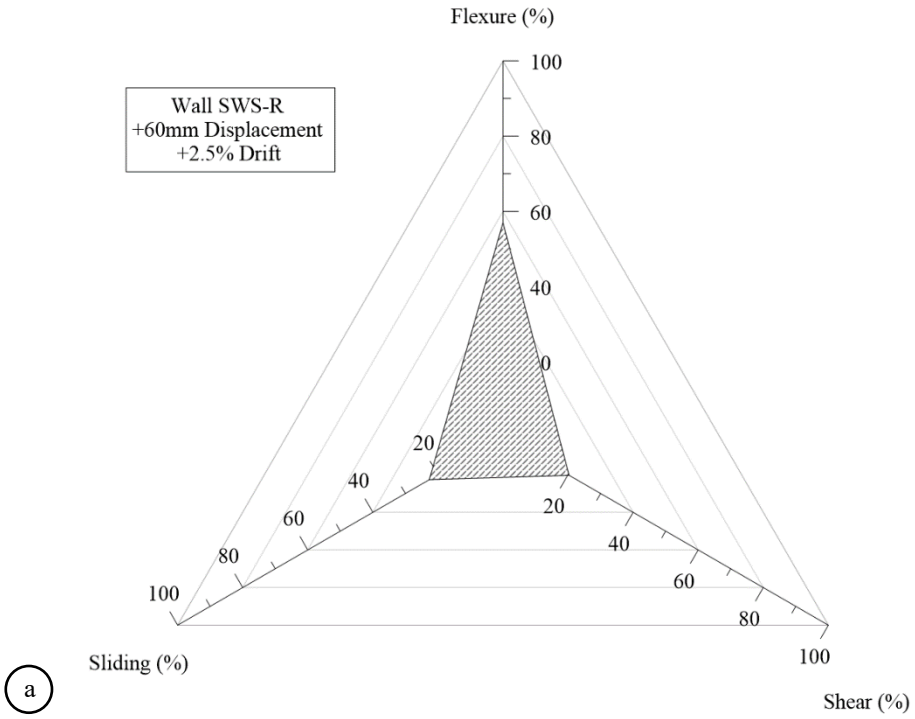

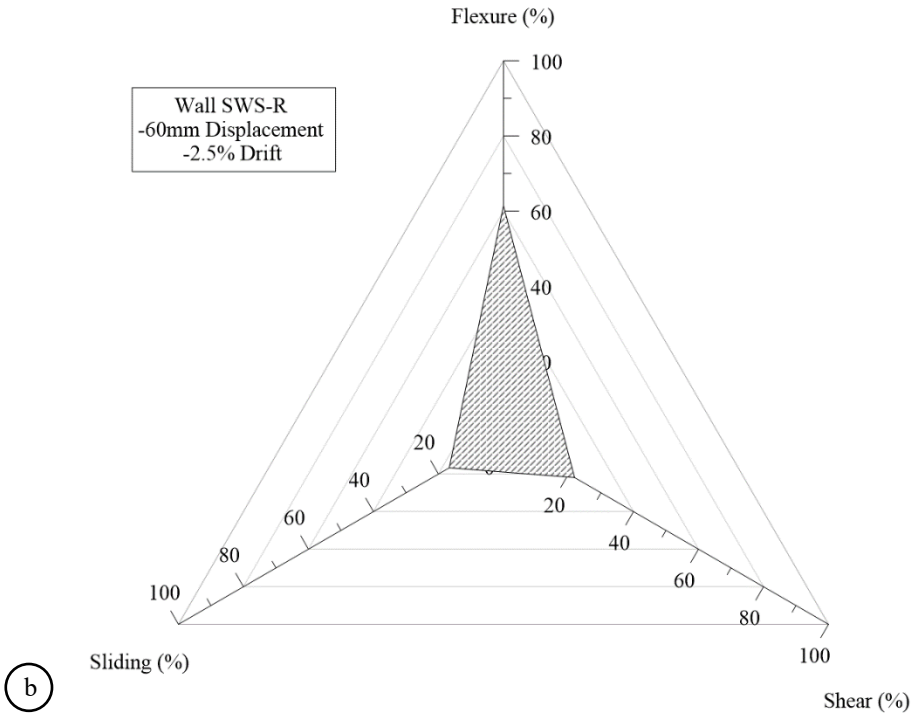

Figure 6.17. Distribution of flexure, shear, and sliding deformation in Wall SWS-R under: (a) positive loading; and (b) negative loading.

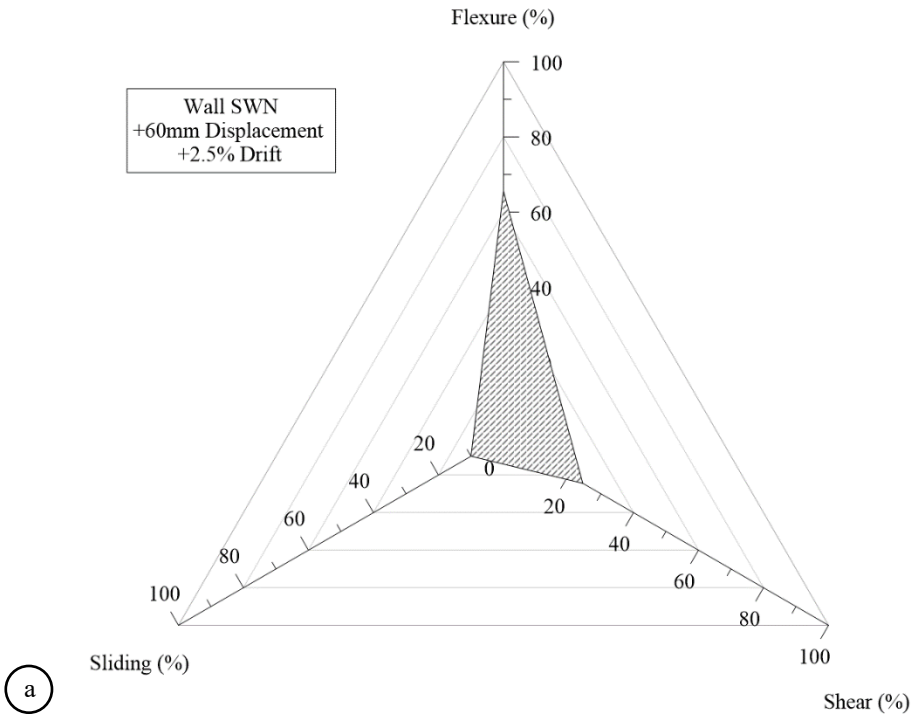

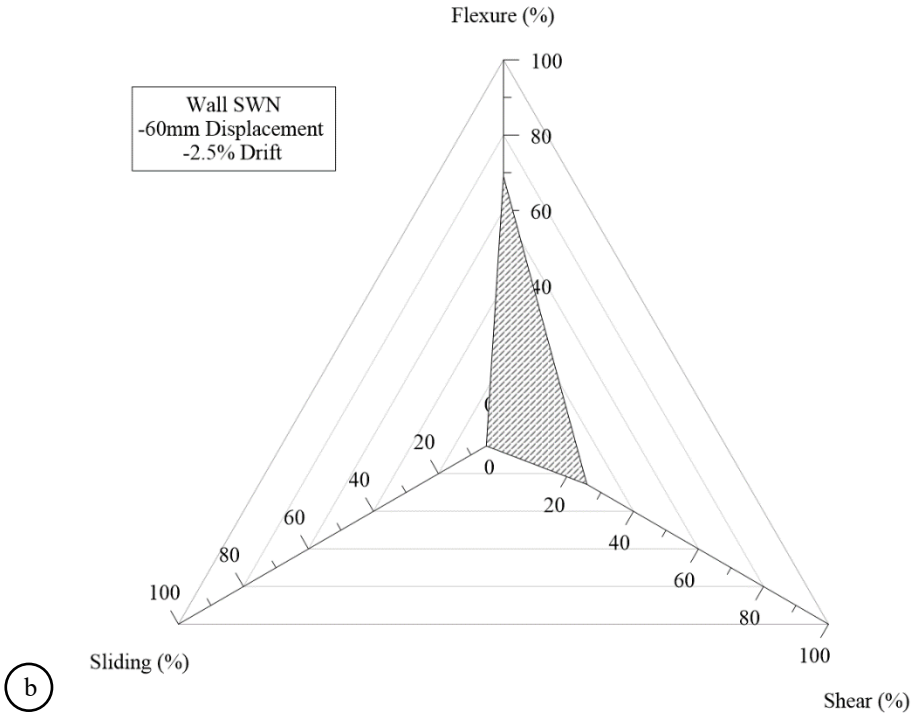

Figure 6.18. Distribution of flexure, shear, and sliding deformation in Wall SWN under: (a) positive loading; and (b) negative loading.

6.2.8 Failure Mechanisms

The damaged experienced by each wall was distinct and varied in intensity at each drift level. The conventional wall quickly accumulated severe damage and was deemed to have failed at the conclusion of cycling at 3% drift. In contrast, Wall SWN presented significantly less severe damage which became apparent at 2.5% drift and had moderately increased at 4.5% drift, prior to the completion of testing at 5% drift. Both walls shared common damage including major flexural cracks, sliding, toe crushing, and buckling and rupturing of longitudinal reinforcement.

Among the network of cracks over the height of each wall were unique flexure cracks running along the base. Wall SWN had additionally developed a secondary major flexural crack at approximately 300mm above the base. As the major flexural cracks progressively widened, they continued to influence the response of each wall. At 2.5% drift, the width of the major flexural crack at the base of Wall SWS-R was approximately 44% smaller than the crack at the base of Wall SWN, and 50% wider than the secondary major flexural crack across the plastic hinge. When unloaded, the major crack of Wall SWS-R was able to close by approximately 78%. The major cracks of Wall SWN were able to close by approximately 31% at the base and 73% across the plastic hinge. The differences in crack width and recovery are related to the lower modulus of elasticity and recovery capacity, respectively, of the superelastic Nitinol longitudinal reinforcing bars in the boundaries, used in place of deformed steel. In the conventional wall, the greatest flexural demand was proportioned linearly to the outermost longitudinal steel reinforcement in the boundary at the cracked section. In the Nitinol-reinforced wall, a higher flexural demand was applied to the stiffer longitudinal steel reinforcing bars in the web. A visual inspection of the strain responses in longitudinal reinforcements for each wall shows that the bars in the web of Wall SWN yielded at approximately half the applied load of Wall SWS-R. The higher strain demand can be visually observed as early as 0.3% drift in Wall SWN as vertical cracks developed in a colinear manner with the longitudinal reinforcement in the web. With increasing drift levels, the elongating web reinforcement had a ratcheting effect at the major flexural cracks, increasingly limiting their recovery. The elongation of the deformed steel reinforcement in the boundaries of Wall SWS-R also limited crack width recovery, however, to significantly lower extent.

The development of vertical cracks over the web of Wall SWN is suspected to be a result of the bond response of deformed steel and Nitinol with the concrete, and the elongation characteristics of both bars. Examining the development of flexural cracks, upon loading it was observed that more cracks appeared to develop outward from the centre of the wall across the web than spread inwards from the tension fiber across the end boundary. Only two cracks were observed to develop from the tension fiber, the first being at the base, and the second being from the left end of the second major flexural crack upon positive loading. The flexural cracks were induced by initial tensile strain in the concrete prior to slippage of the smooth bars. In contrast, the well bonded concrete in the web developed widening flexural cracks as it strained with the elongating longitudinal deformed steel bars under a higher flexural demand. The debonded smooth Nitinol was able to freely elongate without transferring flexural strain to the surrounding concrete. Under flexure, the differential tensile strains in concrete produced a vertical shear path between the segments of bonded concrete in the web and the bulk of debonded concrete towards the boundaries.

The widening major flexural cracks along the base promoted sliding in both walls. The yielded longitudinal steel in the boundaries had a ratcheting effect on Wall SWS-R which gradually minimized contact over in the compression

zone. As the contact pressure gradually diminished between the faces of the fractured concrete, the wall started to slide, and in its path started grinding the rough fracture plane. The damage caused by sliding included dislodging of the loose aggregate and generated debris which further hindered the recovery capacity of the conventional wall. Plastic elongation of the longitudinal bars in the web exasperated the limits of sliding and caused offset settlement. The yielded longitudinal steel bars in the web of Wall SWN had a limited localized ratcheting effect along the base. The axial recovery induced by the longitudinal Nitinol bars in the boundaries produced an improved outcome against sliding by maintaining closer contact over the compression zones at higher drift levels. The elasticity of Nitinol helped to counter the magnitude of sliding and diminish the offset of the structure at rest. At 2.5%, Wall SWS-R had an average recovery of 4% from sliding and had settled at a 3% offset in the positive direction at the completion of the loading cycle. Wall SWN had an average sliding recovery of approximately 42%, and an average settlement offset of 3% in the respective loading direction.

The magnitude of toe crushing in Wall SWS-R is suspected to be enabled by the properties of the self-consolidating concrete (SCC) repair material. Roughly estimating the modulus of elasticity, given a supplier provided density of 2600kg/m^3, using the A23.3 standard, the SCC mix appears to have approximately a 24% greater stiffness than the normal concrete used to cast the wall. This mix also had a maximum aggregate size of 8mm, compared to 14mm. A visual inspection of the damage showed that the SCC mix had good cohesion with the native concrete, however, did not retain the same interlocking characteristics. The fractured concrete at the toes was reduced to fragments and ruble, including complete loss of the cover on all sides at both ends. The native concrete across the web and the remnants in the bounders were not sufficient to mitigate sliding and damage to the longitudinal reinforcement. The combination of higher stiffness and smaller aggregate size proved to be not well suited to resist the vacillating strains produced at the base under cyclic load reversal. Fragmentation at the toes of Wall SWN came apparent much later at 4.5% drift and was limited to small articles, not penetrating beyond the cover.

The final cycle set at 3% drift of Wall SWS-R was concluded with rupturing of the longitudinal reinforcing bars in the boundaries. It was observed that the longitudinal reinforcement in the compression boundary became severely buckled as the reinforcement in the tension boundary ruptured. The footprint of the wall is estimated to have been reduced by approximately 30%, bearing only along the web. Some buckling in the longitudinal reinforcement of the web was also discovered once the concrete was removed for inspection. The buckled length did not exceed 100mm from the base on all bars. The damaged longitudinal reinforcement along the base of Wall SWS-R is illustrated in Figure 6.19. At the severe drift level of 5%, the Nitinol bars in the boundaries of Wall SWN continued to recover the wall, which caused the elongated bars in the web to buckle, prior to rupturing when reloaded. The conditions of the longitudinal reinforcement at the base of Wall SWN are presented in Figure 6.20.

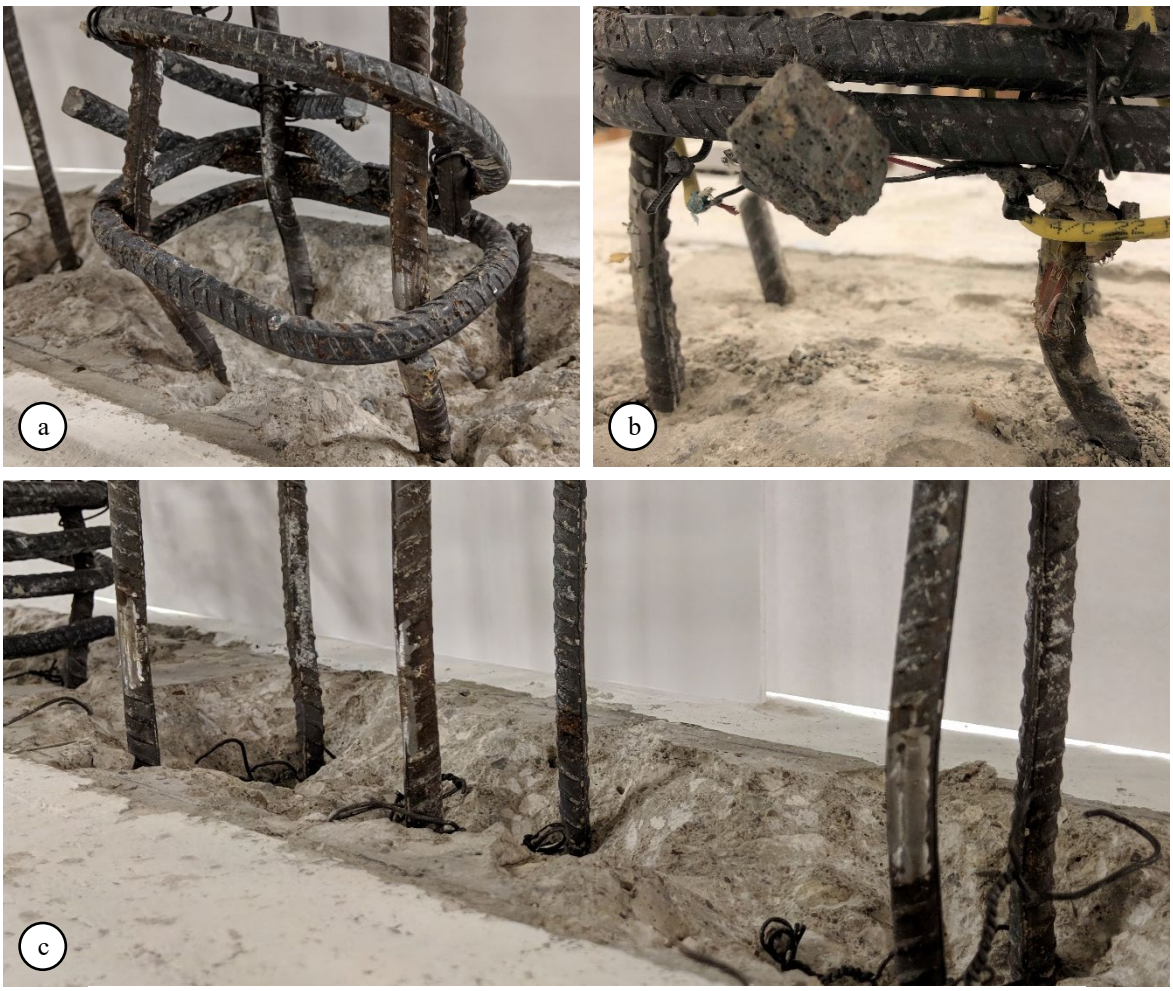

Figure 6.19. Buckled and ruptured longitudinal reinforcement at the base of Wall SWS-R: (a) right boundary; (b) left boundary; and (c) web.

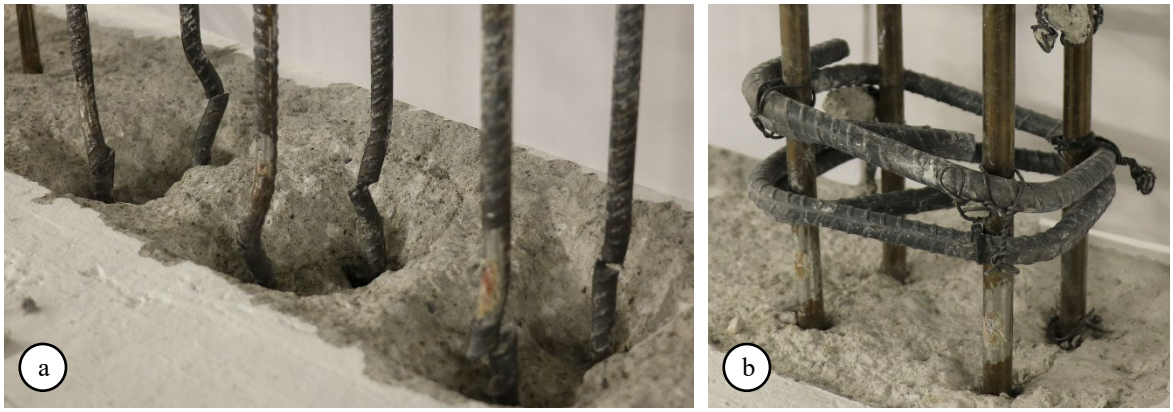

Figure 6.20. Post-testing condition of longitudinal reinforcement at the base of Wall SWN: (a) deformed steel in the web; and (b) Nitinol in the right boundary.

6.3 Behaviour of Nitinol

Cyclic tensile testing of the superelastic Nitinol shape memory alloy (SE-SMA) produced a recovery trend greater than the expected outcomes when using predictive polynomial expressions. The residual plastic strain (ε_p) for Nitinol, from a given maximum strain (ε_m) target, was determined using the relationship in Equation 6.7 by numerical analysis software VecTor2 (2013). The strain values are measured in millimeter per meter.

$$\varepsilon_p = 0.001 \cdot {\varepsilon_m}^2 - 0.005 \cdot \varepsilon_m + 0.4323 \qquad \text{[Eq. 6.7]}$$

Abdulridha et al. (2013) defined the residual plastic strain of Nitinol by the relationship in Equation 6.8.

$$\varepsilon_p = 0.0013 \cdot {\varepsilon_m}^2 - 0.025 \cdot \varepsilon_m + 0.71 \qquad \text{[Eq. 6.8]}$$

Recovery trends were drawn from the predictive expressions using the cyclic strain targets discussed in Section 3.4.1 of Chapter 3. Both numerical models conservatively predicted the values of residual plastic strain, resulting in recovery responses at 3% to 4% lower than the actual performance of superelastic Nitinol.

The experimental recovery trend is drawn from the results of cyclic tensile testing of a superelastic Nitinol coupon, as presented in Section 5.2 of Chapter 5 (Experimental Results). At the first target of 0.5% axial strain, the actual recovery was 94%, compared to 91% for Equation 6.7 and 87% for Equation 6.8. The actual recovery trend peaked at 3% axial strain with 99% recovery, whereas both predictive expressions peaked at 2% axial strain with 96% recovery. At the onset of strain hardening at 6% strain, the Nitinol coupon was able to recover by 97%, in contrast to an averaged prediction of 94% recovery for the numerical recovery models. The experimental and predicted recovery trends for cyclic testing of Nitinol are presented in Figure 6.21.

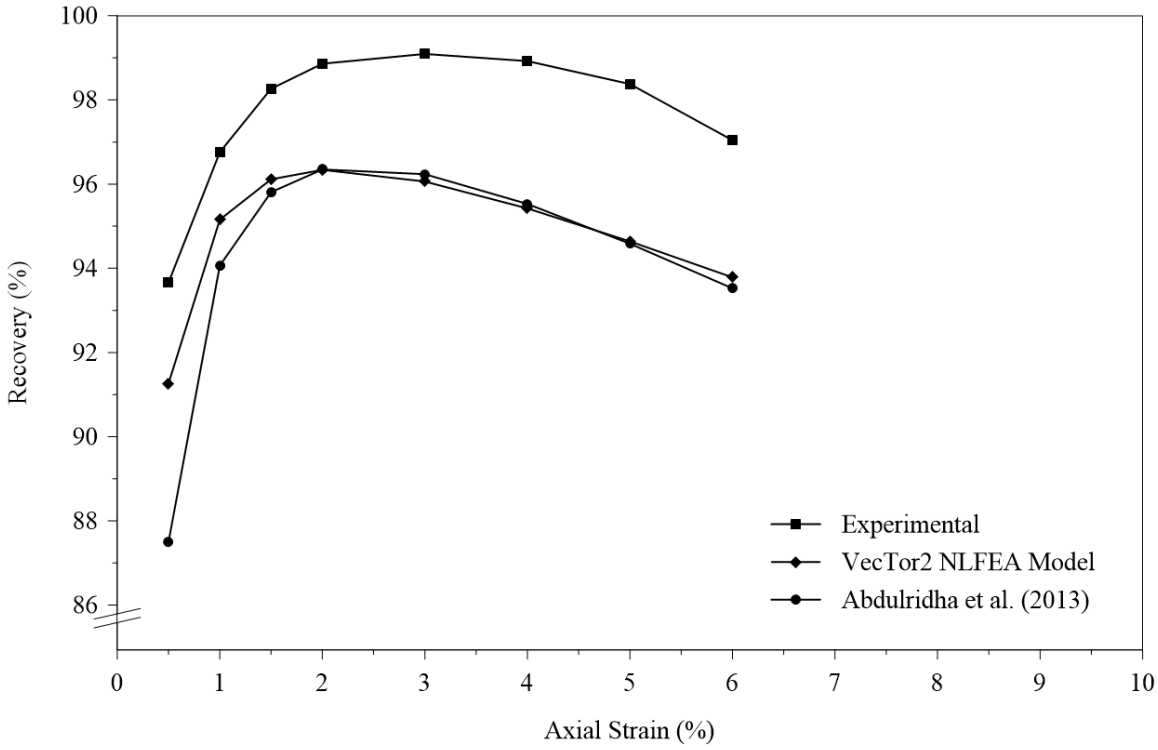

Figure 6.21. Strain recovery trends of superelastic Nitinol under cyclic testing.

Plotting the experimental residual plastic strains against the maximum strain targets from cyclic loading produced the relationship given in Equation 6.9.

$$\varepsilon_p = 0.001 \cdot {\varepsilon_m}^2 - 0.0436 \cdot \varepsilon_m + 0.6188 \qquad \text{[Eq. 6.9]}$$

The affect of the presented recovery capacity of superelastic Nitinol was observed in Wall SWN when studying crack development and widths. Most flexural cracks were noted to appear to develop from the center of the wall and propagate outwards towards the boundaries. Where a measurable crack width was presented across the web, the crack appeared to terminate as it approached the boundaries. The high recovery capacity of Nitinol enabled cracks spreading across the boundaries to completely close, while the elongation of longitudinal steel in the web retained an opening in the bonded concrete.

6.3.1 Decay of the Upper and Lower Plateaus

The upper and lower plateau strengths decayed under cyclic loading.

The decay of the upper plateau strength (σ_u), relative to 3% axial strain, as per ASTM F2516, can be estimated for the desired axial strain level (ε) by the expression:

$$\sigma_u = -15561 \cdot \varepsilon^2 + 311 \cdot \varepsilon + 416.5 \qquad \text{[Eq. 6.10]}$$

The decay of the lower plateau strength (σ_l), relative to 2.5% axial strain, as per ASTM F2516, can be estimated for the desired axial strain level (ε) by the expression:

$$\sigma_l = -100185 \cdot \varepsilon^2 - 14942 \cdot \varepsilon + 662 \qquad \text{[Eq. 6.11]}$$

6.3.2 Performance of Couplers

A post-testing inspection of the couplers embedded within the boundaries of Wall SWN revealed that they were well anchored within the concrete. No visible damage or loose components were noted for all couplers. The post-testing condition of the couplers is provided in Figure 6.22.

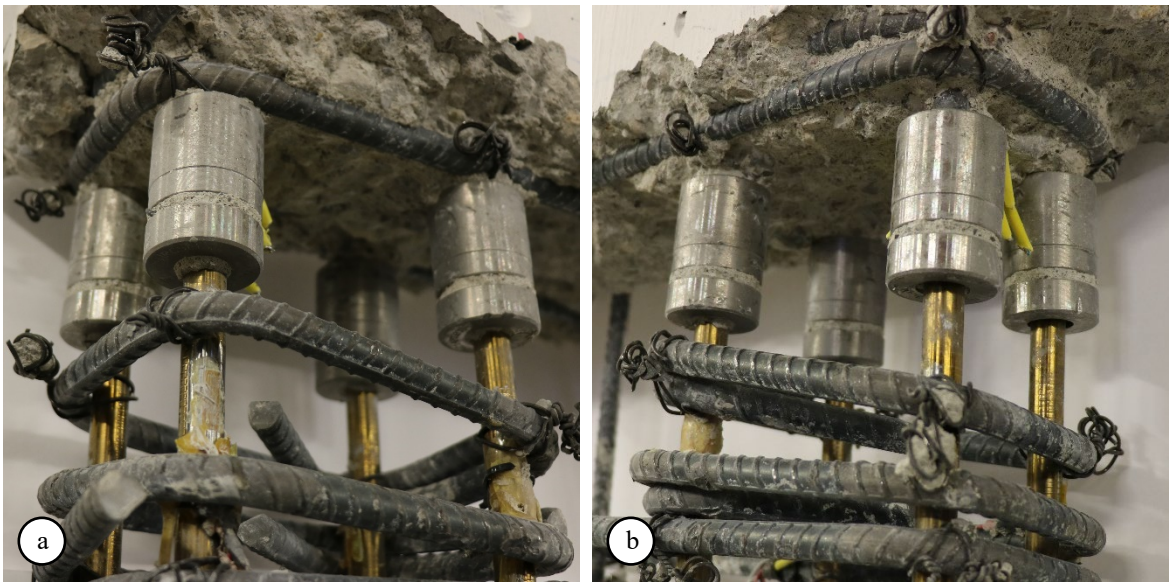

Figure 6.22. Post-testing condition of headed couplers: (a) top of left boundary; and (b) top of right boundary.

CHAPTER 7

Conclusions and Recommendations

7.1 Conclusions

Two slender reinforced concrete shear walls were studied to assess the capacity to self-center from lateral displacement using superelastic (SE) Nitinol shape memory alloy (SMA) longitudinal reinforcement. One wall was reinforced with SE Nitinol while the control wall was conventionally reinforced. The large-scale walls were subjected to experimental testing under a quasi-static load reversal protocol to simulate seismic loading. The results of the study indicate that the use of SE Nitinol significantly reduces the residual displacements retained by drifted walls. The Nitinol reinforced wall also produced a lower degree of damage with finer residual crack widths. Although Nitinol is more costly than traditional deformed steel reinforcement, it could provide substantial savings over the lifetime of a structure, specifically in zones with high seismic activity.

7.1.1 Shear Walls

The following conclusions are drawn from the experimental testing of the walls:

1. The walls were assessed using a loading protocol achieving 5% drift to ensure severe strength and stiffness deterioration. Both walls surpassed the 2.5% drift threshold signifying a collapsed structure. Wall SWS-R terminated at 3.5% drift. Wall SWN completed testing at 5% drift.

2. The lower stiffness of the superelastic Nitinol bars used as longitudinal reinforcement in the boundaries of Wall SWN promoted a series of performance outcomes:

    a. Wall SWN had an initial secant stiffness that is 57% of the steel-reinforced Wall SWS-R.

    b. Wall SWN had a yield displacement that is about five times larger than the conventional Wall SWS-R, but at a lateral load that is approximately 4% lower.

    c. The yield secant stiffness of Wall SWN was proportionally lower at about 5.5 times less than Wall SWS-R.

3. Wall SWN had compatible strength to its conventional counterpart. Both walls presented similar strength capacities under positive and negative loading, ultimately achieving the same average peak load of 118kN.

4. Wall SWN reached an ultimate displacement that is 72% greater than the steel-reinforced wall, at a 12% greater load. However, Wall SWN appeared to have one-third the ductility of the conventional steel-reinforced wall relative to a lower yield secant stiffness.

5. Wall SWN maintained similar lateral displacement profiles under positive and negative loading at 2.5% drift. Wall SWS-R presented asymmetrical profiles.

    a. Under positive displacement, Wall SWN presented a linear profile influenced by rocking and some traces of shear distortion and minor sliding. The linearity of the negative displacement profile was due to rocking as a dominant response, including expressions of flexure and sliding.

    b. The positive profile of Wall SWS-R was concaved, influenced by rocking, shear distortion, and sliding. The convexity of the negative profile was produced by a combination of rocking, some flexure, and base sliding limited by a rightward offset.

6. At 2.5% drift, Wall SWN had nearly complete strength retention, whereas Wall SWS-R had about 91% retention.

7. Wall SWS-R maintained a greater secant stiffness than Wall SWN. The stiffnesses started to converge at 1% drift. Both walls achieved approximately the same secant stiffness at 2.5% drift.

8. Wall SWN had an average lateral displacement recovery of about 58% from 2.5% drift. In comparison, Wall SWS-R recovered by about 25%.

9. Wall SWN sustained an average of 1% residual drift after being subjected to a lateral displacement corresponding to 2.5% drift. Based on this, the average probability of demolition for Wall SWN is projected to be about 15% compared to a probability of 77% for Wall SWS-R.

10. The superelastic Nitinol was able to promote self-centering against the ratcheting of elongated steel reinforcement in the web. At 2.5% drift, the average energy dissipation of Wall SWN was approximately 48% of the energy dissipated by Wall SWS-R. Wall SWN stored the equivalent of about 38% of the dissipated energy as elastic potential energy towards self-centering, in comparison to about 10% stored by Wall SWS-R.

11. At 2.5% drift, Wall SWN had an average overall rotation of about 30% greater than Wall SWS-R, however recovered by 59% compared to 28% by the conventional wall. At rest, Wall SWN retained 37% less rotation than Wall SWS-R.

12. Wall SWN had approximately 54% less average shear distortion than Wall SWS-R at 2.5% drift.

13. Without shear starter bars at the base, each wall developed a dominant flexural crack along the base which promoted rocking and a reduced resistance to sliding.

14. At 2.5% drift, the distribution of lateral deformation to Wall SWN comprised of a 14% greater average flexural response, 19% greater average shear response, and an average of 61% less sliding.

15. At 2.5% drift, Wall SWN presented improved cracking characteristics over Wall SWS-R.

    a. Wall SWN had fewer cracks with an average width of 0.08mm, in comparison to about 3mm in the control wall.

    b. Most cracks in Wall SWN recovered by approximately 82%, compared to about 36% for Wall SWS-R.

    c. The major flexural cracks in Wall SWN were able to recover by about 31% at the base and 73% across the plastic hinge. The major flexural crack of Wall SWS-R was able to recover by about 78%.

16. The failure mechanism of Wall SWN presented a significantly reduced degree of damage.

    a. Two major horizontal flexural cracks developed along the base and at 300mm above the foundation, which can be easily repaired. In contrast, the major flexural crack along the base of Wall SWS-R was surrounded by crushed concrete and an elaborate network of cracks.

    b. Wall SWN was able to recover from base sliding by 42% compared to 4% for Wall SWS-R.

    c. Light toe crushing occurred in Wall SWN at 4.5% drift. By 3% drift, the toes of Wall SWS-R were severely fragmented. The cross section of Wall SWS-R was reduced by approximately 30% at the base.

    d. At the conclusion of 5% drift, the Nitinol bars in the boundaries of Wall SWN remained functional. The deformed steel bars in the web were buckled and eventually ruptured. At the completion of 3% drift, the longitudinal deformed steel reinforcement in the boundaries of Wall SWS-R were buckled and ruptured. The longitudinal steel bars in the web were elongated and severely buckled.

7.1.2 Superelastic Nitinol Reinforcement

The following specific conclusions about superelastic Nitinol reinforcement are drawn from this study:

1. A peak recovery capacity of 99% was achieved at 3% axial strain during cyclic tensile testing of coupon samples. The initial recovery was about 94% at 0.5% axial strain. The recovery at 6% axial strain was about 97%.

2. Tensile testing of a coupled coupon resulted in rupturing at 7% axial strain under monotonic loading at the transition of the bar diameter and the conical head at the end of the bar.

3. Cyclic tensile loading of a Nitinol coupon to 6% axial strain resulted in a residual elongation of approximately 0.19%. The coupon subsequently ruptured at approximately 7% strain.

7.2 Recommendations

The following recommendations are suggested for future research to continue the study of superelastic Nitinol reinforced slender concrete shear walls:

1. Experimental testing of shear walls under in-plane dynamic lateral loading.

   A dynamic loading setup would be constructed using two hydraulic actuators capable of applying a dynamic load to drive a low friction platform, riding on rails, along an in-plane trajectory. Loading would be from a controlled sequence of load reversal cycles or a ground motion record. The specimen would be laterally braced against out-of-plane displacement. The same walls used in this study would be reproduced for dynamic testing.

2. Match bar quantity and length to the seismic energy being delivered to the structure, considering modal responses.

   A reference building would be specified for a seismic region and the seismic energy delivered to it would be quantified from actual ground motion records for common events and rare intense events. Based on the energy demand, the Nitinol reinforcing bars would be sized to provide the structure with adequate capacity for self-centering. A numerical expression can be produced as a design tool.

3. Refine the material constitutive model for non-linear finite element analysis to include functions for the decay of the upper and lower plateau strengths.

   The Nitinol numerical model would be updated to consider the decays of the upper and lower plateau strengths relative to load cycle count and maximum strain, given an assumed stable ambient temperature. The update can be extended to consider performance variations throughout the operational temperature range.

4. Experimental testing of full-sized shear walls equivalent to a single or two-story building.

   Full-scale shear walls would be constructed using superelastic Nitinol reinforcing bars in the end boundaries to demonstrate the application of the technology in a low-rise building. Experimental testing is intended to produce insight into the response of a life-sized structure without the hazard, cost, and risk associated with a seismic event.

5. Combine scaled axial loading to reverse cyclic lateral displacements.

An axial load, representing a tributary gravity load, would be applied to the wall specimen in conjunction with the reverse cyclic loading protocol presented in this study. The same walls used in this study would be reproduced for testing. The influence of gravity loads on the capacity to self-centre would be assessed.

6. Parametric study of SMA length requirement to optimize self-centering.

   A target performance level and residual drift would be defined to benchmark the capacity of different lengths and configurations of Nitinol bars to rectify a drifted structure.

7. Study the lifecycle cost of maintaining a structure reinforced with superelastic Nitinol in a seismic region.

   The study is intended to quantify the benefits of using superelastic Nitinol reinforcement into a monetary value. A breakdown of the associated cost to new construction and future post-disaster repairs would be projected.

REFERENCES

1. Abdulridha, A. (2013). Performance of superelastic shape memory alloy reinforced concrete elements subjected to monotonic and cyclic loading [Doctoral dissertation, University of Ottawa]. uO Research. http://dx.doi.org/10.20381/ruor-3009

2. Abdulridha, A., and Palermo, D. (2017). Behaviour and modelling of hybrid SMA-steel reinforced concrete slender shear wall. Engineering Structures, 147, 77-89.

3. Abdulridha, A., Palermo, D., Foo, S., and Vecchio, F. J. (2013). Behavior and modeling of superelastic shape memory alloy reinforced concrete beams. Engineering Structures, 49, 893-904.

4. Alam, M. S., Nehdi, M., and Youssef, M. A. (2007). Applications of shape memory alloys in earthquake engineering. Ninth Canadian Conference on Earthquake Engineering, Ottawa, Ontario, Canada, 1468-1477.

5. Alam, M. S., Youssef, M. A., and Nehdi, M. L. (2010). Exploratory investigation on mechanical anchors for connecting SMA bars to steel or FRP bars. Materials and Structures, 43, 91-107.

6. Alaneme, K. K., and Okotete, E. A. (2016). Reconciling viability and cost-effective shape memory alloy options – A review of copper and iron based shape memory metallic systems. Engineering Science and Technology, an International Journal, 19(3), 1582-1592.

7. Ali, A., and Wight, J. K. (1990). Reinforced concrete structural walls with staggered opening configurations under reversed cyclic loading (Report No. UMCE 90-05). Department of Civil Engineering, The University of Michigan. http://hdl.handle.net/2027.42/3175

8. ASTM C31 / C31M-17, Standard Practice for Making and Curing Concrete Test Specimens in the Field, ASTM International, West Conshohocken, Pennsylvania, USA, 2017, DOI: 10.1520/C0031_C0031M-17, www.astm.org

9. ASTM C39 / C39M-17, Standard Test Method for Compressive Strength of Cylindrical Concrete Specimens, ASTM International, West Conshohocken, Pennsylvania, USA, 2017, DOI: 10.1520/C0039_C0039M-17, www.astm.org

10. ASTM C94 / C94M-17, Standard Specification for Ready-Mixed Concrete, ASTM International, West Conshohocken, Pennsylvania, USA, 2017, DOI: 10.1520/C0094_C0094M-17, www.astm.org

11. ASTM C143 / C143M-15a, Standard Test Method for Slump of Hydraulic-Cement Concrete, ASTM International, West Conshohocken, Pennsylvania, USA, 2015, DOI: 10.1520/C0143_C0143M-15A, www.astm.org

12. ASTM C172 / C172M-17, Standard Practice for Sampling Freshly Mixed Concrete, ASTM International, West Conshohocken, Pennsylvania, USA, 2017, DOI: 10.1520/C0172_C0172M-17, www.astm.org

13. ASTM C231 / C231M-17a, Standard Test Method for Air Content of Freshly Mixed Concrete by the Pressure Method, ASTM International, West Conshohocken, Pennsylvania, USA, 2017, DOI: 10.1520/C0231_C0231M-17A, www.astm.org

14. ASTM A370-17, Standard Test Methods and Definitions for Mechanical Testing of Steel Products, ASTM International, West Conshohocken, Pennsylvania, USA, 2017, DOI: 10.1520/A0370-17, www.astm.org

15. ASTM C387 / C387M-17, Standard Specification for Packaged, Dry, Combined Materials for Concrete and High Strength Mortar, ASTM International, West Conshohocken, Pennsylvania, USA, 2017, DOI: 10.1520/C0387_C0387M-17, www.astm.org

16. ASTM A1034 / A1034M-10a(2015), Standard Test Methods for Testing Mechanical Splices for Steel Reinforcing Bars, ASTM International, West Conshohocken, Pennsylvania, USA, 2015, DOI: 10.1520/A1034_A1034M-10AR15, www.astm.org

17. ASTM C1064 / C1064M-17, Standard Test Method for Temperature of Freshly Mixed Hydraulic-Cement Concrete, ASTM International, West Conshohocken, Pennsylvania, USA, 2017, DOI: 10.1520/C1064_C1064M-17, www.astm.org

18. ASTM C1611 / C1611M-14, Standard Test Method for Slump Flow of Self-Consolidating Concrete, ASTM International, West Conshohocken, Pennsylvania, USA, 2014, DOI: 10.1520/C1611_C1611M-14, www.astm.org

19. ASTM C1758 / C1758M-15, Standard Practice for Fabricating Test Specimens with Self-Consolidating Concrete, ASTM International, West Conshohocken, Pennsylvania, USA, 2015, DOI: 10.1520/C1758_C1758M-15, www.astm.org

20. ASTM F2516-14, Standard Test Method for Tension Testing of Nickel-Titanium Superelastic Materials, ASTM International, West Conshohocken, Pennsylvania, USA, 2014, DOI: 10.1520/F2516-14, www.astm.org

21. Applied Technology Council. (1992). Guidelines for cyclic seismic testing of components of steel structures (ATC-24).

22. Applied Technology Council. (2007). Interim testing protocols for determining the seismic performance characteristics of structural and nonstructural components (FEMA 461).

23. Auricchio, F., and Sacco, E. (1997). A superelastic shape-memory-alloy beam model. Journal of Intelligent Material Systems and Structures, 8, 489-501.

24. Auricchio, F., Fugazza, D., and DesRoches, R. (2006). Earthquake performance of steel frames with Nitinol braces. Journal of Earthquake Engineering, 10(S1), 45-66.

25. Ayoub, C., Saiidi, M. S., and Itani, A. (2003). A study of shape-memory-alloy reinforced beams and cubes (Report No. RDT 04-046, CCEER-03-07). Nevada Department of Transportation. http://www.worldcat.org/title/study-of-shape-memory-alloy-reinforced-beams-and-cubes/oclc/55996875

26. Billah, A. H. M. M., and Alam, M. S. (2012). Seismic performance of concrete columns reinforced with hybrid shape memory alloy (SMA) and fiber reinforced polymer (FRP) bars. Construction and Building Materials, 28(1), 730-742.

27. Billah, A. H. M. M., and Alam, M. S. (2016). Bond behavior of smooth and sand-coated shape memory alloy (SMA) rebar in concrete. Structures, 5, 186-195.

28. Buehler, W. J., Gilfrich, J. V., and Wiley, R. C. (1963). Effect of low-temperature phase changes on the mechanical properties of alloys near composition TiNi. Journal of Applied Physics, 34(5), 1475-1477.

29. Canadian Standards Association. (2014). Concrete materials and methods of concrete construction / Test methods and standard practices for concrete (CAN/CSA Standard No. A23.1-14/A23.2-14).

30. Canadian Standards Association. (2014). Design of concrete structures (CAN/CSA Standard No. A23.3-14).

31. Canadian Standards Association. (2014). Design of steel structures (CAN/CSA Standard No. S16-14).

32. Cardone, D., Palermo G., and Dolce, M. (2010). Direct displacement-based design of buildings with different seismic isolation systems. Journal of Earthquake Engineering, 14(2), 163-191.

33. Chang, W., and Araki, Y. (2016). Use of shape-memory alloys in construction: A critical review. Institution of Civil Engineers, 169(CE2), 87-95.

34. Choi, E., Kim, D., Chung, Y., and Nam, T. (2014). Bond–slip characteristics of SMA reinforcing fibers obtained by pull-out test. Materials Research Bulletin, 58, 28-31.

35. Choi, E., Lee, D. H., and Choei, N. Y. (2009). Shape memory alloy bending bars as seismic restrainers for bridges in seismic areas. International Journal of Steel Structures, 9(4), 261-273.

36. Cladera, A., Weber, B., Leinenbach, C., Czaderski, C., Shahverdi, M., and Motavalli, M. (2014). Iron-based shape memory alloys for civil engineering structures: An overview. Construction and Building Materials, 63, 281-293.

37. Clark, P. W., Aiken, I. D., Kelly, J. M., Higashino, M., and Krumme, R. C. (1995). Experimental and analytical studies of shape-memory alloy dampers for structural control. Smart Structures and Materials, Proceedings of SPIE, 2445, 241-251.

38. Corley, W. G., Fiorato, E., and Oesterle, R. G. (1981). Structural walls. Symposium Paper, 72, 77-132.

39. Cortés-Puentes, W. L. (2017). Seismic retrofit of squat reinforced concrete shear walls using shape memory alloys [Doctoral dissertation, University of Ottawa]. uO Research. http://dx.doi.org/10.20381/ruor-20447

40. Cross, W. B., Kariotis, A. H., and Stimler, F. J. (1969). Nitinol characterization study (Report No. GER 14188). National Aeronautics and Space Administration. https://ntrs.nasa.gov/citations/19690026989

41. Czaderski, C., Shahverdi, M., Brönnimann, R., Leinenbach, C., and Motavalli, M. (2014). Feasibility of iron-based shape memory alloy strips for prestressed strengthening of concrete structures. Construction and Building Materials, 56, 94-105.

42. Darjan, C., and Dolinsek, J. (2007). Shape memory alloys. Oddelek Za Fiziko, Fakulteta Za Matematiko In Fiziko, Univerza V Ljubljani, 1-20.

43. Dasgupta, R. (2014). A look into Cu-based shape memory alloys: Present scenario and future prospects. Journal of Materials Research, 29(16), 1681-1698.

44. De la Flor, S., Urbina, C., and Ferrando, F. (2006). Constitutive model of shape memory alloys: Theoretical formulation and experimental validation. Materials Science and Engineering: A, 427, 112-122.

45. Debbarma, S. R., and Saha, S. (2012). Review of shape memory alloys applications in civil structures, and analysis for its potential as reinforcement in concrete flexural members. International Journal of Civil and Structural Engineering, 2(3), 924-942.

46. Deng, Z., Li, Q., and Sun, H. (2006). Behavior of concrete beam with embedded shape memory alloy wires. Engineering Structures, 28(12), 1691-1697.

47. DesRoches, R., and Delemont, M. (2002). Seismic retrofit of simply supported bridges using shape memory alloys. Engineering Structures, 24(3), 325-332.

48. DesRoches, R., McCormick, J., and Delemont, M. (2004). Cyclic properties of superelastic shape memory alloy wires and bars. Journal of Structural Engineering, 130(1), 38-46.

49. Dolce, M., Cardone, D., and Ponzo, F. C. (2006). Shaking-table tests on reinforced concrete frames with different isolation systems. Earthquake Engineering and Structural Dynamics, 36(5), 573-596.

50. Effendy, E., Liao, W. I., Song, G., Mo, Y. L., and Loh, C. H. (2006). Seismic behavior of low-rise shear walls with SMA bars. Earth & Space 2006: Engineering, Construction, and Operations in Challenging Environment, American Society of Civil Engineers, Houston, Texas, USA, 1-8.

51. Elnashai A. S., and Pinho, R. (1998). Repair and retrofitting of RC Walls using selective techniques. Journal of Earthquake Engineering, 2(4), 525-568,

52. El-Tawil, S., and Ortega-Rosales, J. (2004). Prestressing concrete using shape memory-alloy tendons. Structural Journal, 846-851.

53. Fintel, M. (1991). Shearwalls – An answer for seismic resistance?. Concrete International, 13(7), 48-53.

54. Ghassemieh, M., Bahaari, M., Ghodratian, S., and Nojoumi, S. (2012). Improvement of concrete shear wall structures by smart materials. Open Journal of Civil Engineering, 2(3), 87-95.

55. Huang, W. M., Ding, Z., Wang, C. C., Wei, J., Zhao, Y., and Purnawali, H (2010). Shape memory materials. Materials Today, 13(7-8), 54-61.

56. Janke, L., Czaderski, C., Motavalli, M., and Ruth, J. (2005). Applications of shape memory alloys in civil engineering structures - Overview, limits and new ideas. Materials and Structures, 38(5), 578-592.

57. Johnson, R., Padgett, J. E., Maragakis, M. E., DesRoches, R., and Saiidi, M. S. (2008). Large scale testing of Nitinol shape memory alloy devices for retrofitting of bridges. Smart Materials and Structures, 17(3), 1-10.

58. Kheirikhah, M. M., Rabiee, S., and Edalat M. E. (2011). A Review of Shape Memory Alloy Actuators in Robotics. In: Ruiz-del-Solar J., Chown E., Plöger P.G. (eds) RoboCup 2010: Robot Soccer World Cup XIV. RoboCup 2010. Lecture Notes in Computer Science, vol 6556. Springer, Berlin, Heidelberg.

59. Krawinkler, H., (2009). Loading histories for cyclic tests in support of performance assessment of structural components. 3rd International conference on advances in experimental structural engineering, 1-10.

60. Kuang, Y., and Ou, J. (2008). Self-repairing performance of concrete beams strengthened using superelastic SMA wires in combination with adhesives released from hollow fibers. Smart Materials and Structures, 17, 1-7.

61. Kurdyumov, G. V., and Khandros, L. G. (1949). On the “thermoelastic” equilibrium on martensitic transformations. Doklady Akademii Nauk SSSR, 66(2), 211-214.

62. Lafortune, P., McCormick, J., DesRoches, R., and Terriault, P. (2007). Testing of superelastic re-centering prestrained braces for seismic resistant design. Journal of Earthquake Engineering, 11(3), 383-399.

63. Lagoudas, D. C. (2008). Shape memory alloys: Modeling and engineering applications. Springer Science & Business Media.

64. Li, X., Li, M., and Song, G. (2015). Energy-dissipating and self-repairing SMA-ECC composite material system. Smart Materials and Structures, 24(2), 1-15.

65. Maji, A. K., and Negret, I. (1998). Smart prestressing with shape memory alloy. Journal of Engineering Mechanics, 1121-1128.

66. Massone, L. M., and Wallace, J. W. (2004). Load-Deformation Responses of Slender Reinforced Concrete Walls. Structural Journal, 101(1), 103-113.

67. McCormick, J., Tyber, J., DesRoches, R., Gall, K., and Maier, H. J. (2007). Structural engineering with NiTi. II: Mechanical behavior and scaling. Journal of Engineering Mechanics, 133(9), 1019-1029.

68. Menna, C., Aurricchio, F., and Asprone, D. (2015). Chapter 13 - Applications of shape memory alloys in structural engineering. In Lecce, L., and Concilio, A. (Eds.), Shape Memory Alloy Engineering (369-403). Butterworth-Heinemann.

69. Mitchell, D., Paultre, P., Tinawi, R., Saatcioglu, M., Tremblay, R., Elwood, K., Adams, J., and DeVall, R. (2010). Evolution of seismic design provisions in the national building code of Canada. Canadian Journal of Civil Engineering, 37(9), 1157-1170.

70. Nakashoji, B. A. (2014). Seismic performance of square nickel-titanium reinforced ECC columns with headed couplers [Master's thesis, University of Nevada, Reno]. ScholarWorks. http://hdl.handle.net/11714/2943

71. Nehdi, M., Alam, M. S., and Youssef, M. A. (2010). Development of corrosion-free concrete beam–column joint with adequate seismic energy dissipation. Engineering Structures, 32(9), 2518-2528.

72. Ocel, J., DesRoches, R., Leon, R. T., Hess, G., Krumme, R., Hayes, J., and Sweeney, S. (2004). Steel Beam-Column Connections Using Shape Memory Alloys. Journal of Structural Engineering, 130(5), 732-740.

73. Oesterle, R. G., Fiorato, A. E., Johal, L. S., Carpenter, J. E., and Russell, H. G. (1976). Earthquake resistant structural walls - Tests of isolated walls (Report No. NSF/RA-760815). National Science Foundation, Washington, D.C., Research Applied to National Needs. https://nehrpsearch.nist.gov/article/PB-271%20467/3/XAB

74. Ozbulut, O. E., Hurlebaus, S., and Desroches, R. (2011). Seismic Response Control Using Shape Memory Alloys: A Review. Journal of Intelligent Material Systems and Structures, 22(14), 1531-1549.

75. Paiva, A., and Savi, M. A. (2006). An overview of constitutive models for shape memory alloys. Mathematical Problems in Engineering, 2006, 1-30.

76. Palermo, D., Youssef, M. A., and Alam, M. S. (2013). Pushing the envelope in structural concrete design: Applications of superelastic shape memory alloys. Canadian Civil Engineer, 26-29.

77. Park, R. (1989). Evaluation of ductility of structures and structural assemblages from laboratory testing. Bulletin of the New Zealand Society for Earthquake Engineering, 22(3), 155-166.

78. Paulay, T. (1975). Design aspects of shear walls for seismic areas. Canadian Journal of Civil Engineering, 2(3), 321-344.

79. Paulay, T. (1980). Earthquake-Resisting Shearwalls – New Zealand Design Trends. Journal Proceedings, 77(3), 144-152.

80. Piedboeuf, M. C., Gauvin, R., and Thomas, M. (1998). Damping behaviour of shape memory alloys: strain amplitude, frequency and temperature effects. Journal of Sound and Vibration, 214(5), 885-901.

81. Pilakoutas, K., and Elnashai, A. (1995). Cyclic behaviour of reinforced concrete cantilever walls, Part I: Experimental results. Structural Journal, 92(3), 271-281.

82. Priestley, M. J. N. (1993). Myths and fallacies in earthquake engineering. Bulletin of the New Zealand Society for Earthquake Engineering, 26(3), 329-341.

83. Priestley, M. J. N. (2000). Performance based seismic design. 12th World Conference on Earthquake Engineering, Auckland, New Zealand, 2831, 1-22.

84. Ramirez, C. M., and Miranda, E. (2012). Significance of residual drifts in building earthquake loss estimation. Earthquake Engineering & Structural Dynamics, 41, 1477-1493.

85. Rojob, H., and El-Hacha, R. (2018). Performance of RC beams strengthened with self-prestressed Fe-SMA bars exposed to freeze-thaw cycles and sustained load. Engineering Structures, 169, 107-118.

86. Saiidi, M. S., and Wang, H. (2006). Exploratory study of seismic response of concrete columns with SMA reinforcement. Structural Journal, 103(3), 436-443.

87. Saiidi, M. S., Sadrossadat-Zadeh, M., Ayoub, C., and Itani, A (2007). Pilot study of behavior of concrete beams reinforced with shape memory alloys. Journal of Materials in Civil Engineering, 19(6), 454-461.

88. Saiidi, M. S., Tazarv, M., Nakashoji, B., Varela, S., and Kavianipour, F. (2015). Resilient and sustainable bridges of the future. International Journal of Bridge Engineering, 3(2), 37-48.

89. Shahin, A. R., Meckl, P. H., and Jones, J. D. (1997). Modeling of SMA tendons for active control of structures. Journal of Intelligent Material Systems and Structures, 8, 51-70.

90. Shin, M., and Andrawes, B. (2010). Experimental investigation of actively confined concrete using shape memory alloys. Engineering Structures, 32(3), 656-664.

91. Sittipunt, W., and Wood, S. L. (1995). Influence of web reinforcement on the cyclic response of structural walls. Structural Journal, 92(6), 745-756.

92. Song, G., Ma, N., and Li, H.-N. (2006). Applications of shape memory alloys in civil structures. Engineering Structures, 28(9), 1266-1274.

93. Speicher, M. S., DesRoches, R., and Leon, R. T. (2010). Behaviour of SMA-based partially restrained beam-column connection. 9th U.S. National and 10th Canadian Conference on Earthquake Engineering, Toronto, Ontario, Canada, 982, 1-10.

94. Suhail, R., Amato, G., Chen, J., and Mccrum, D. (2015). Shape memory alloy features for seismic retrofitting of external RC beam-column joint. Anidis Conference, Italian National Association of Earthquake Engineering, L'Aquila, Italy, 1-9.

95. Sutou, Y., Omori, T., Wang, J. J., Kainuma, R., and Ishida, K. (2004). Characteristics of Cu–Al–Mn-based shape memory alloys and their applications. Materials Science and Engineering A, 378, 278-282.

96. Tanaka, K., Kobayashi, S., and Sato, Y. (1986). Thermomechanics of transformation pseudoelasticity and shape memory effect in alloys. International Journal of Plasticity, 2, 59-72.

97. Tazarv, M., and Saiidi, M. S. (2017). Analysis, design, and construction of SMA-reinforced FRP-confined concrete columns. Fourth Conference on Smart Monitoring, Assessment and Rehabilitation of Civil Structures, Zurich, Switzerland, 39, 1-8.

98. Thomsen IV, J. H., and Wallace, J. W. (2004). Displacement-based design of slender reinforced concrete structural walls - Experimental verification. Journal of Structural Engineering, 130(4), 618-630.

99. Tyber, J., McCormick, J., Gall, K., DesRoches, R., Maier, H. J., and Abdel Maksoud, A. E. (2007). Structural engineering with NiTi. I: Basic materials characterization. Journal of Engineering Mechanics, 133(9), 1009-1018.

100. Van Humbeeck, J. (1991). Cycling effects, fatigue and degradation of shape memory alloys. Journal de Physique IV, 01(C4), 189-197.

101. Vecchio, F. J., Haro de la Peña, O. A., Bucci, F., and Palermo, D. (2002). Behavior of repaired cyclically loaded shearwalls. Structural Journal, 99(3), 327-334.

102. Wang, B., and Zhu, S. (2018). Seismic behavior of self-centering reinforced concrete wall enabled by superelastic shape memory alloy bars. Bull Earthquake Eng, 16, 479-502.

103. Wierschem, N., and Andrawes, B. (2010). Superelastic SMA–FRP composite reinforcement for concrete structures. Smart Materials and Structures, 19, 1-13.

104. Wong, P. S., Vecchio, F. J., and Trommels, H. (2013). VecTor2 & FormWorks user's manual. [User's Manual, University of Toronto]. VecTor Analysis Group. http://vectoranalysisgroup.com/user_manuals/manual1.pdf

105. Yam, M. C. H., Fang, C., Lam, A. C. C., and Zhang, Y. (2015). Numerical study and practical design of beam-to-column connections with shape memory alloys. Journal of Constructional Steel Research, 104, 177-192.

106. Yazgan, U., and Dazio, A. (2011). The use of post-earthquake residual displacements as a performance indicator in seismic assessment. Georisk: Assessment and Management of Risk for Engineered Systems and Geohazards, 5(1), 59-76.

107. Youssef, M. A., Alam, M. S., and Nehdi, M. (2008). Experimental investigation on the seismic behavior of beam-column joints reinforced with superelastic shape memory alloys. Journal of Earthquake Engineering, 12, 1205-1222.

108. Zafar, A., and Andrawes, B. (2013). Experimental flexural behavior of SMA-FRP reinforced concrete beam. Frontiers of Structural and Civil Engineering, 7(4), 341-355.

109. Zaidi, M., Palermo, D., and Dragomirescu, E. (2017). Performance of repaired sma shear wall. 16th World Conference on Earthquake Engineering, Santiago, Chile, 3304, 1-11.

110. Zuo, X., Chang, W., Li, A., and Chen, Q. (2006). Design and experimental investigation of a superelastic SMA damper. Material Science and Engineering: A, 438-440, 1150-1153.

Material Properties

Steel Reinforcement

Figure A.1. Coupon batches of deformed steel reinforcing bars.

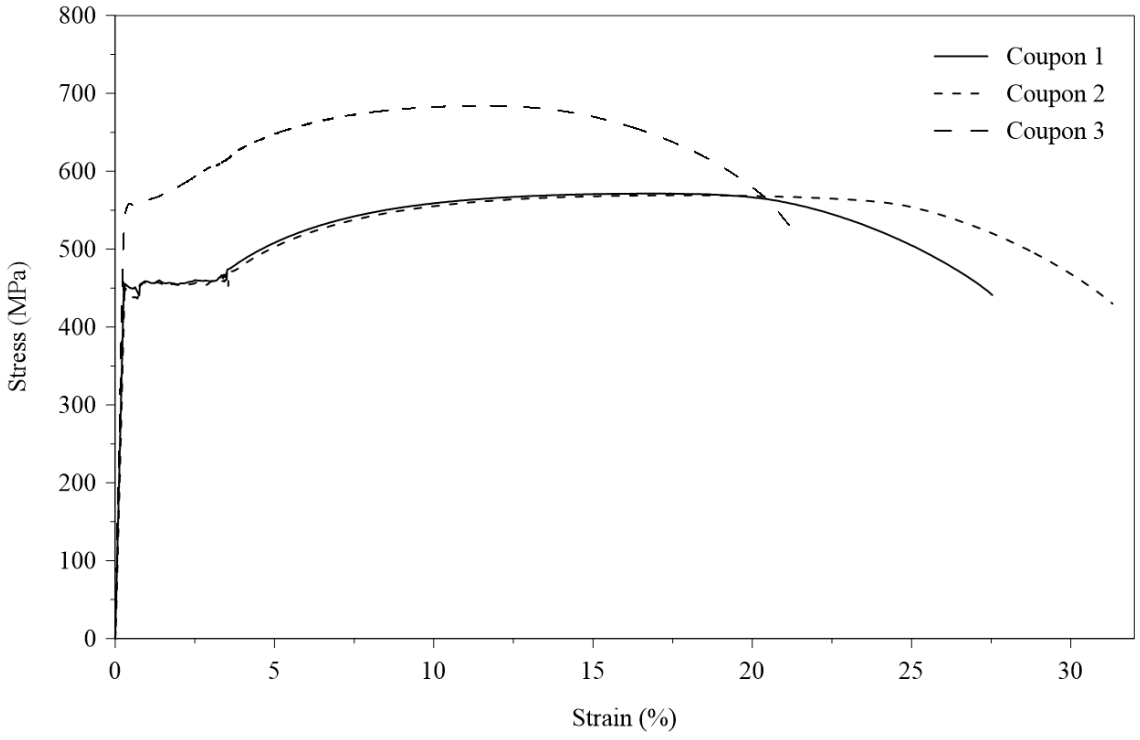

Figure A.2. Monotonic stress-strain response of 10M reinforcing bars from Supplier A.

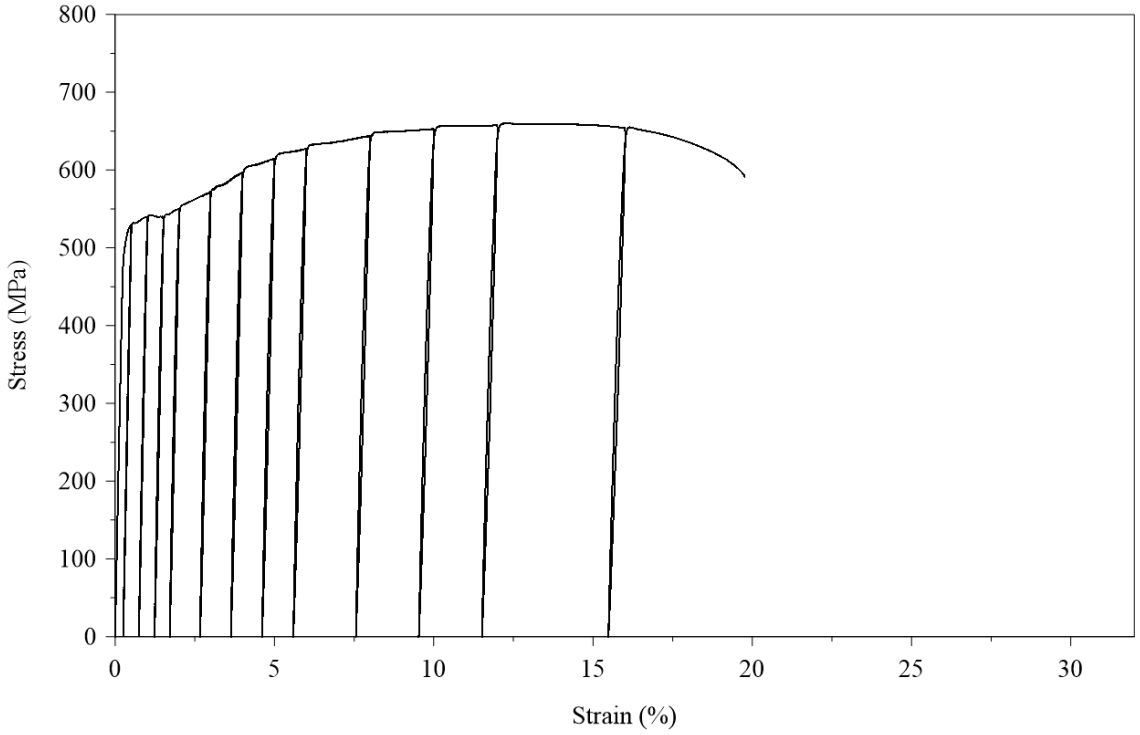

Figure A.3. Cyclic stress-strain response of a 10M reinforcing bar from Supplier A.

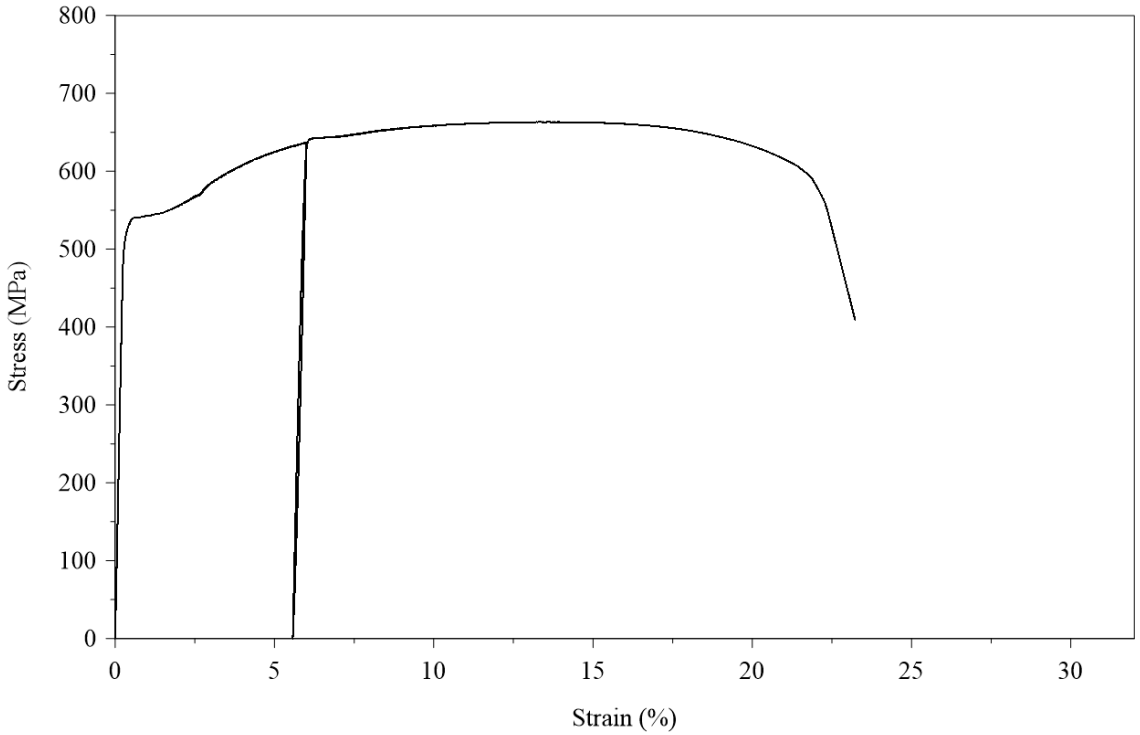

Figure A.4. Monotonic stress-strain response with 6% strain cycle of a 10M reinforcing bar from Supplier A.

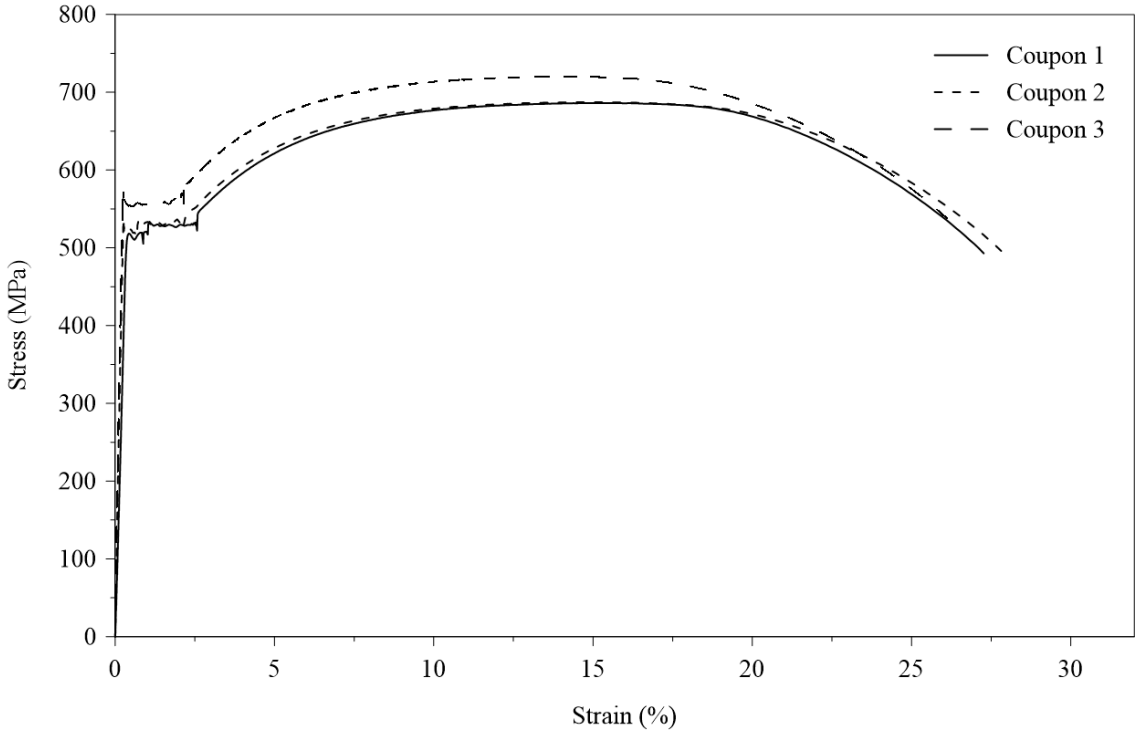

Figure A.5. Monotonic stress-strain response of 10M reinforcing bars from Supplier B.

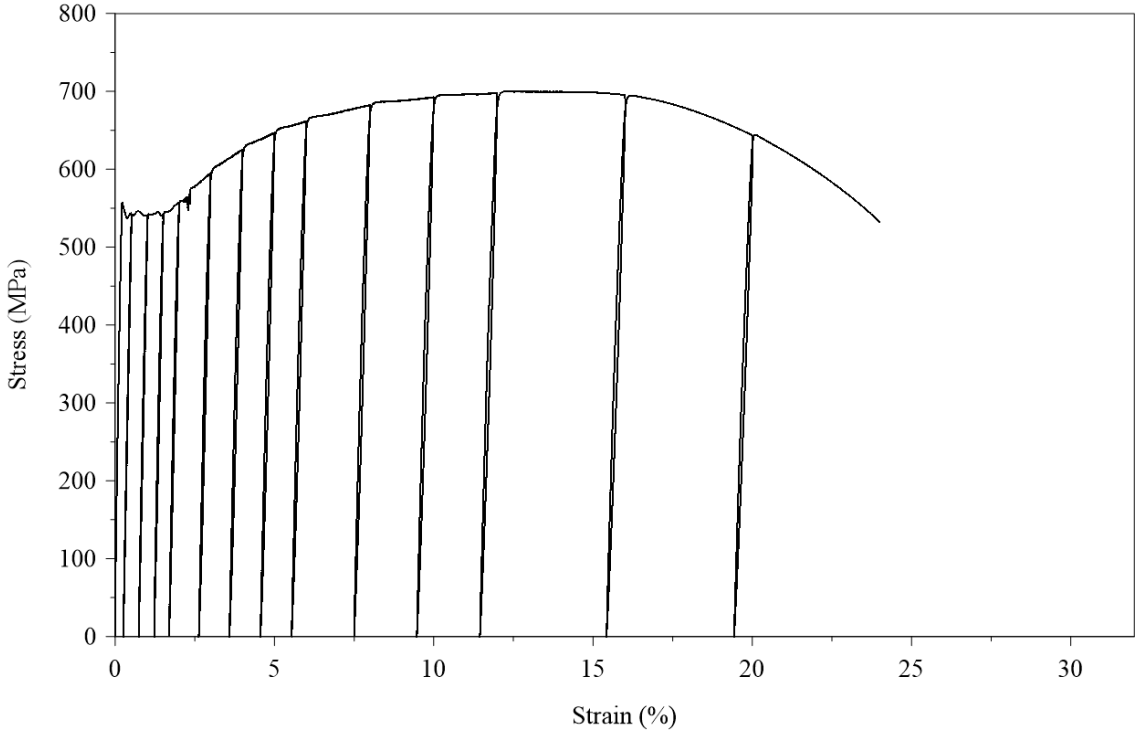

Figure A.6. Cyclic stress-strain response of a 10M reinforcing bar from Supplier B.

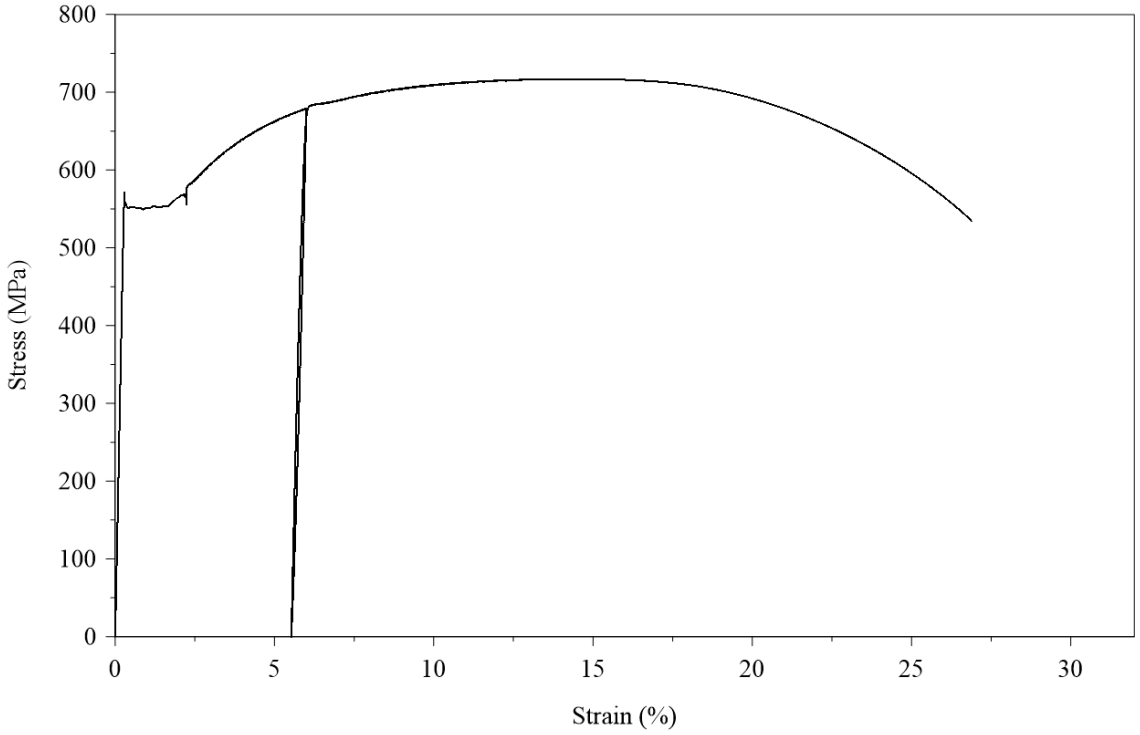

Figure A.7. Monotonic stress-strain response with 6% strain cycle of a 10M reinforcing bar from Supplier B.

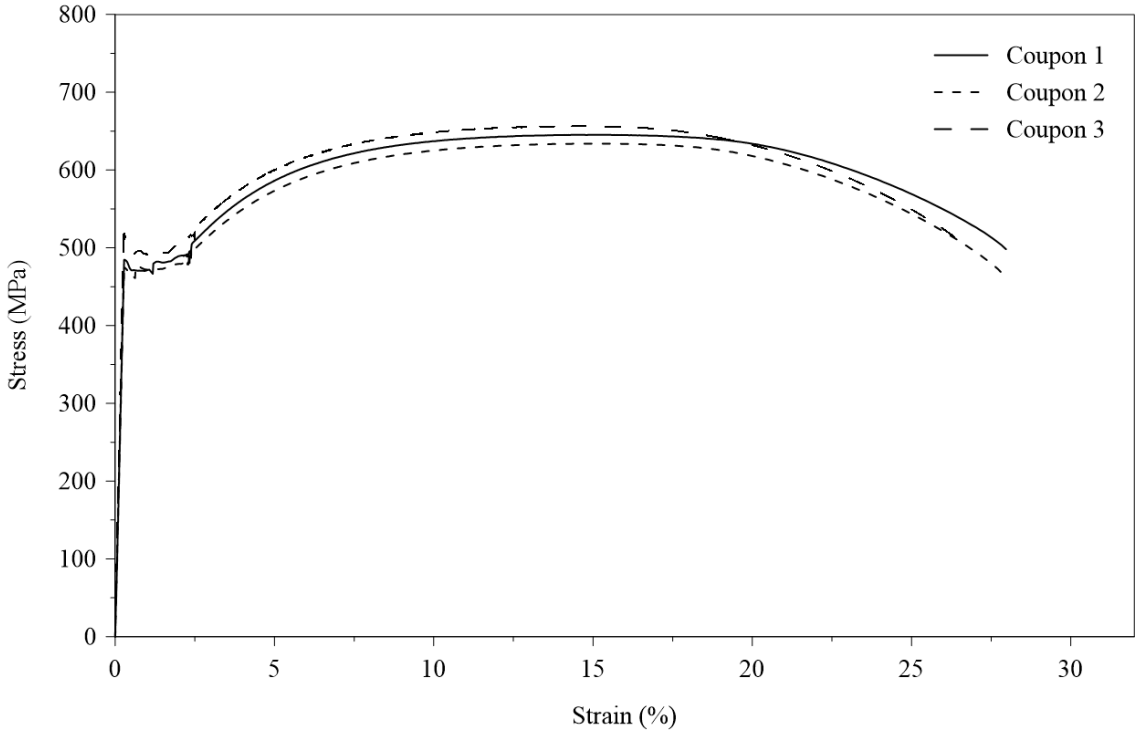

Figure A.8. Monotonic stress-strain response of #13 reinforcing bars.

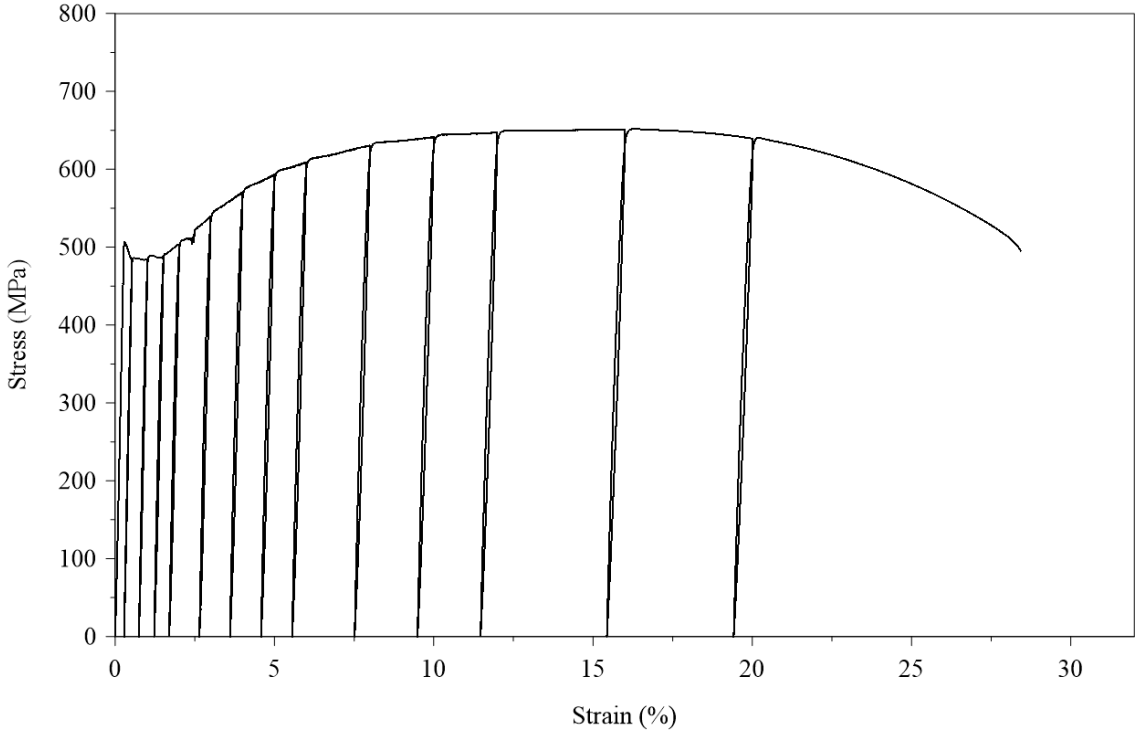

Figure A.9. Cyclic stress-strain response of a #13 reinforcing bar.

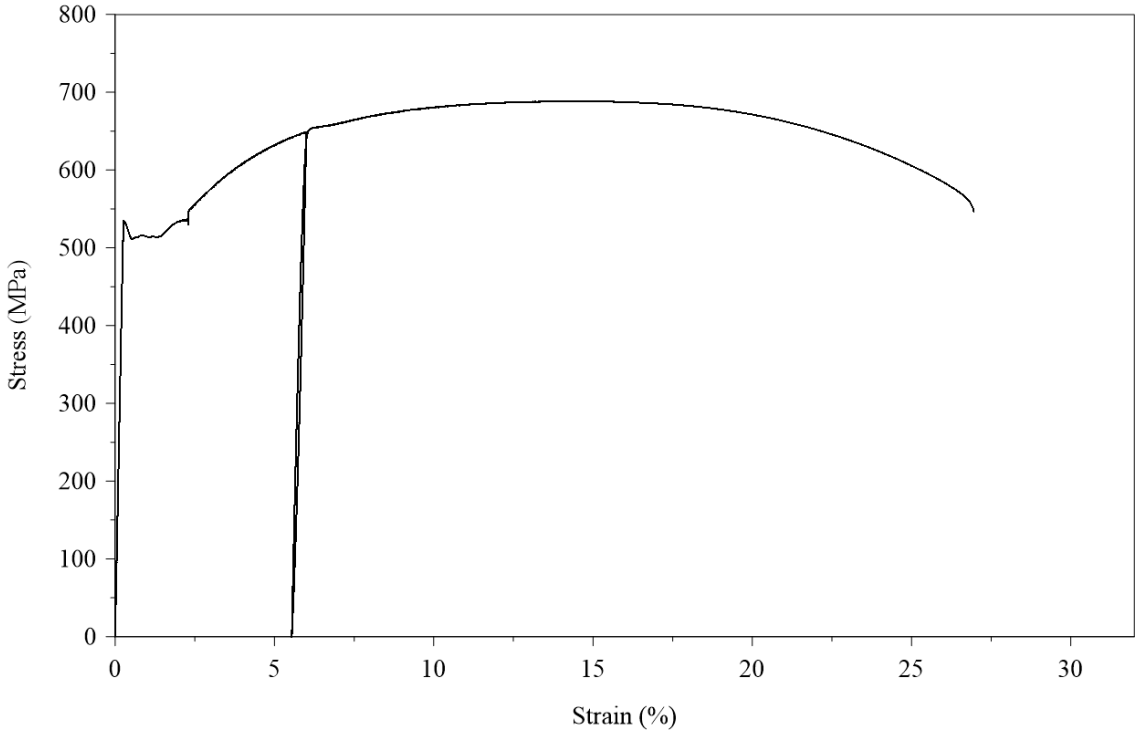

Figure A.10. Monotonic stress-strain response with 6% strain cycle of a #13 reinforcing bar.

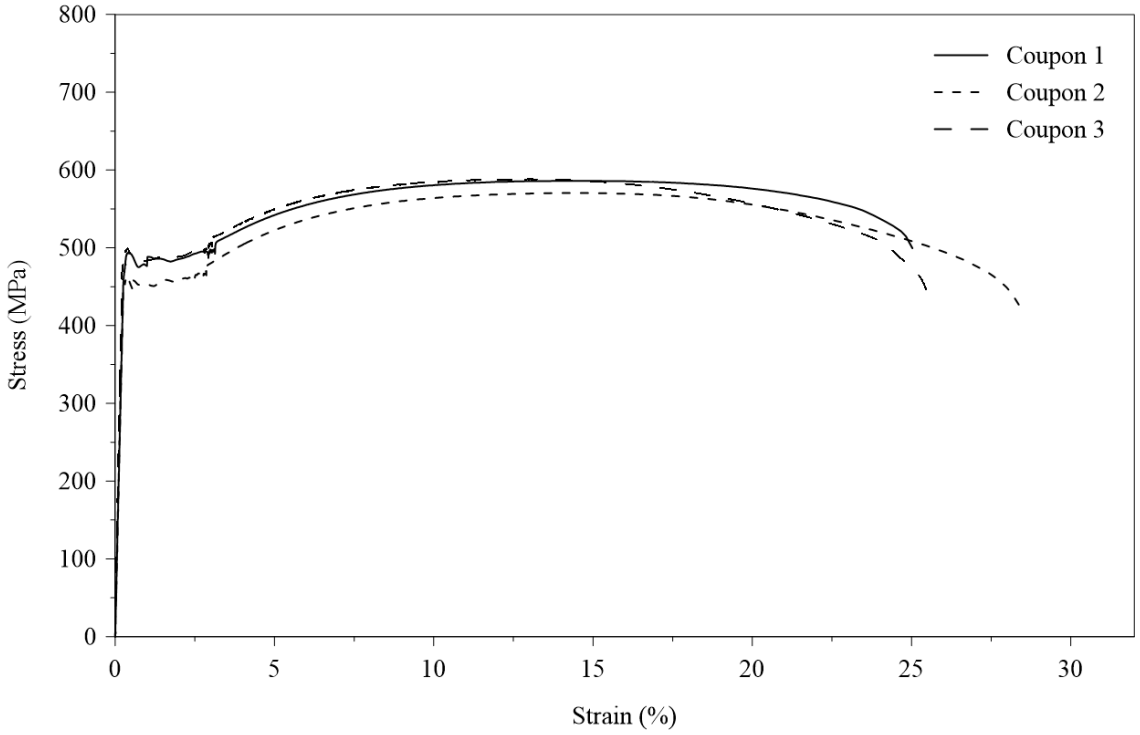

Figure A.11. Monotonic stress-strain response of 15M reinforcing bars.

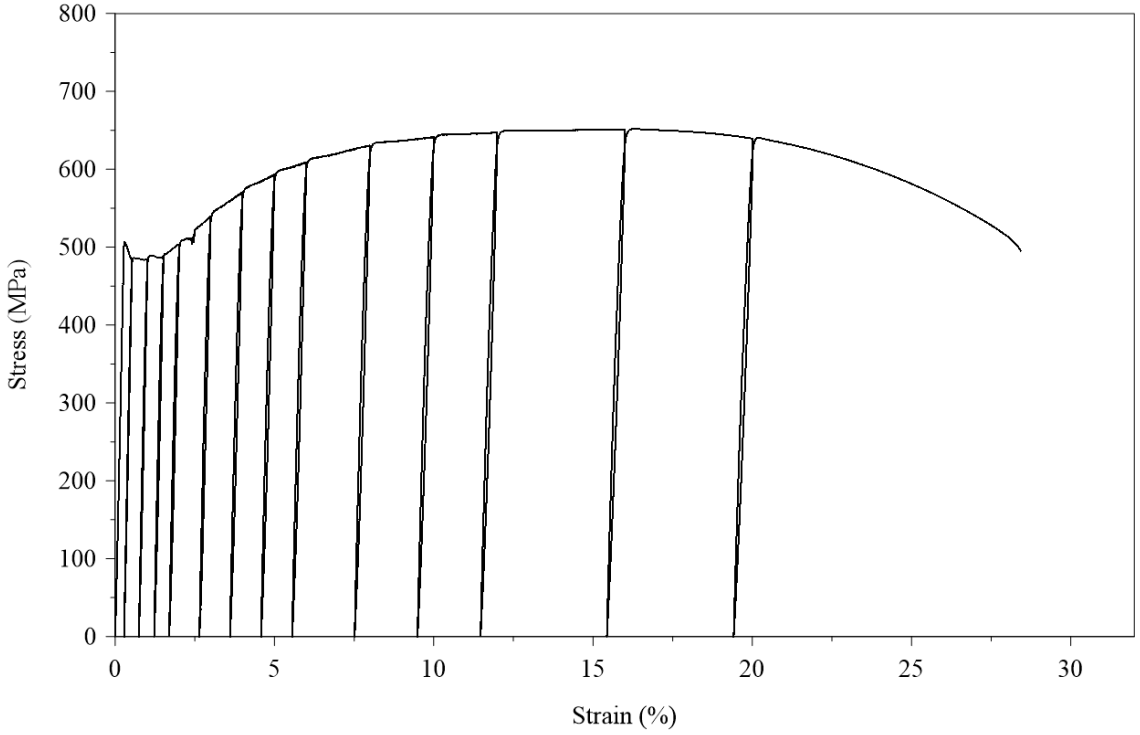

Figure A.12. Cyclic stress-strain response of a 15M reinforcing bar.

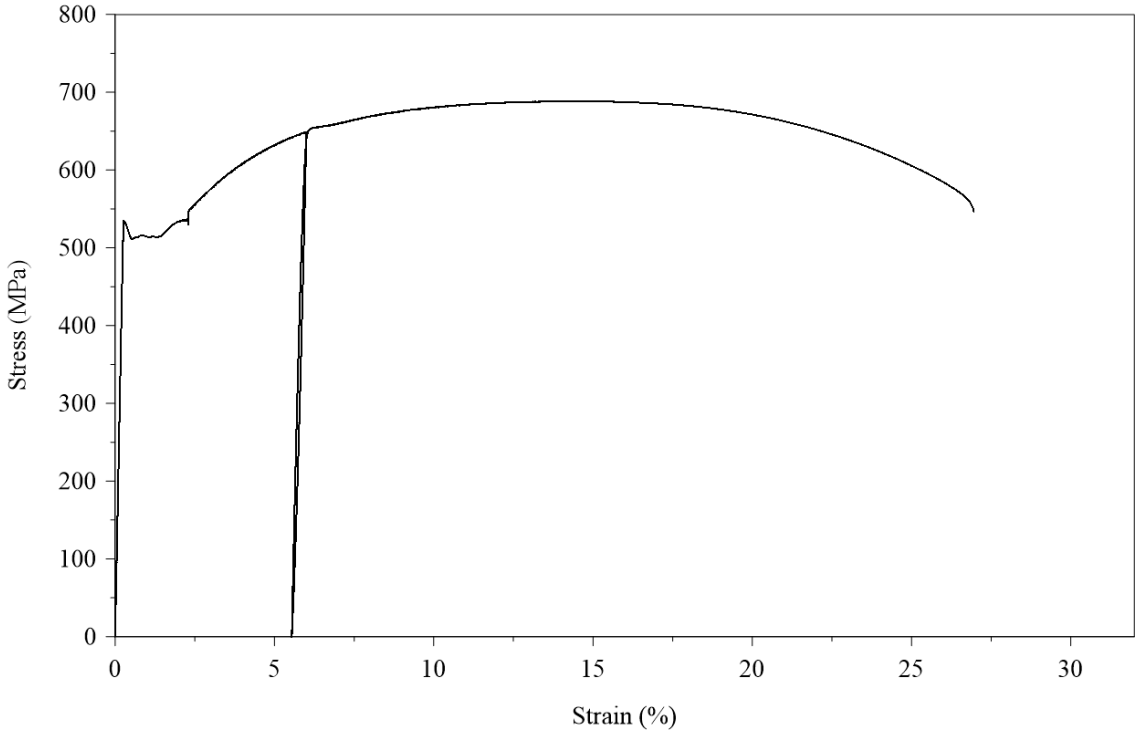

Figure A.13. Monotonic stress-strain response with 6% strain cycle of a 15M reinforcing bar.

Nitinol Reinforcement

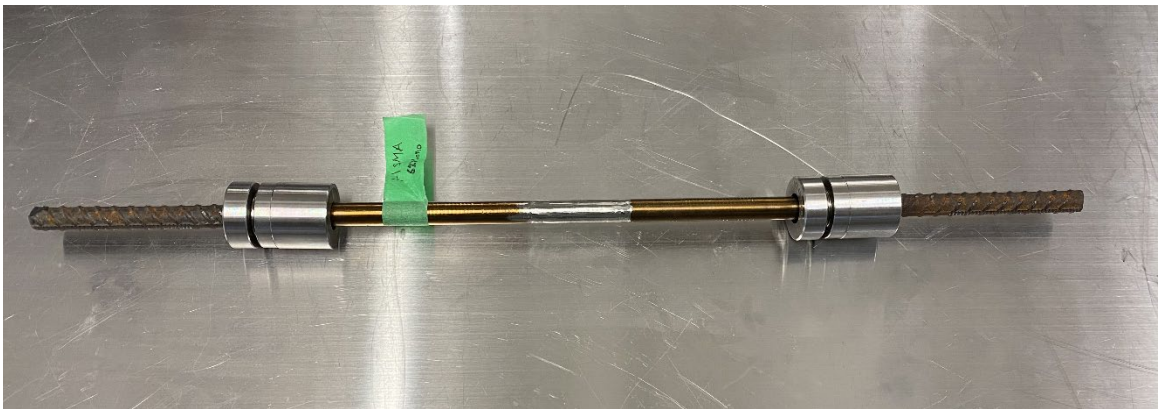

Figure A.14. Nitinol tension test Coupon 1 assembly with deformed steel end grips.

Figure A.15. Nitinol tension test Coupon 2 assembly with coupler end grips.

Figure A.16. Nitinol tension test Coupon 3 with bare end grips.

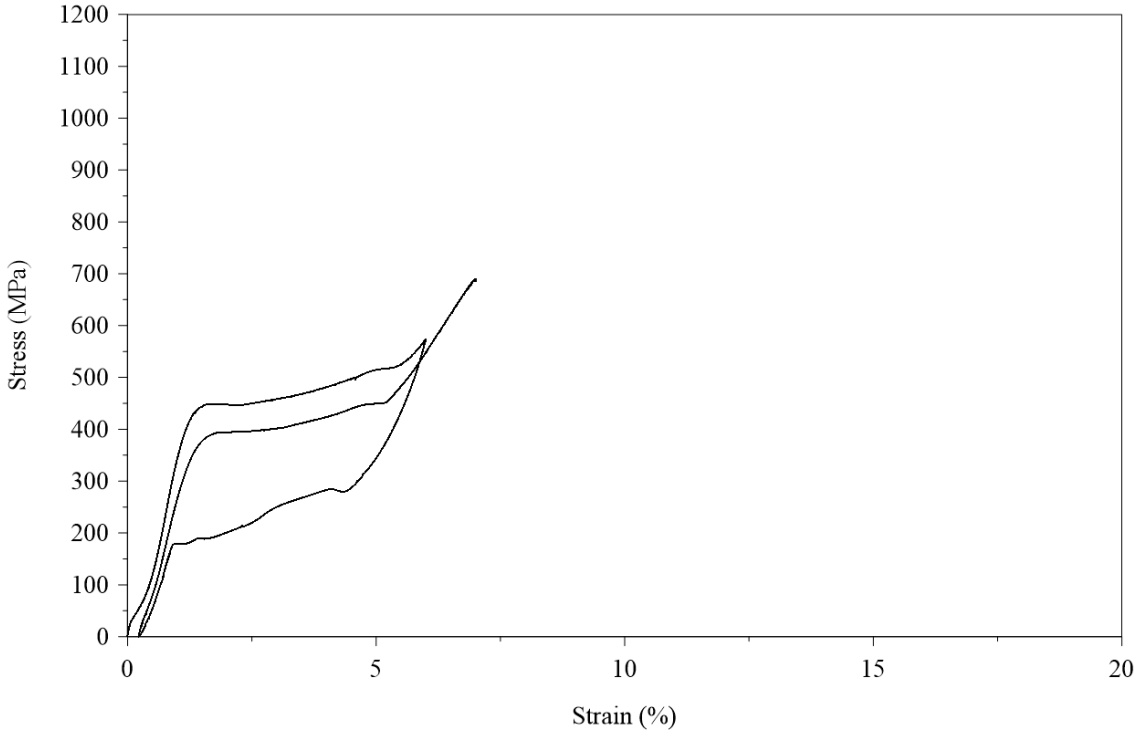

Figure A.17. Monotonic stress-strain response with 6% strain cycle of Nitinol Coupon 1.

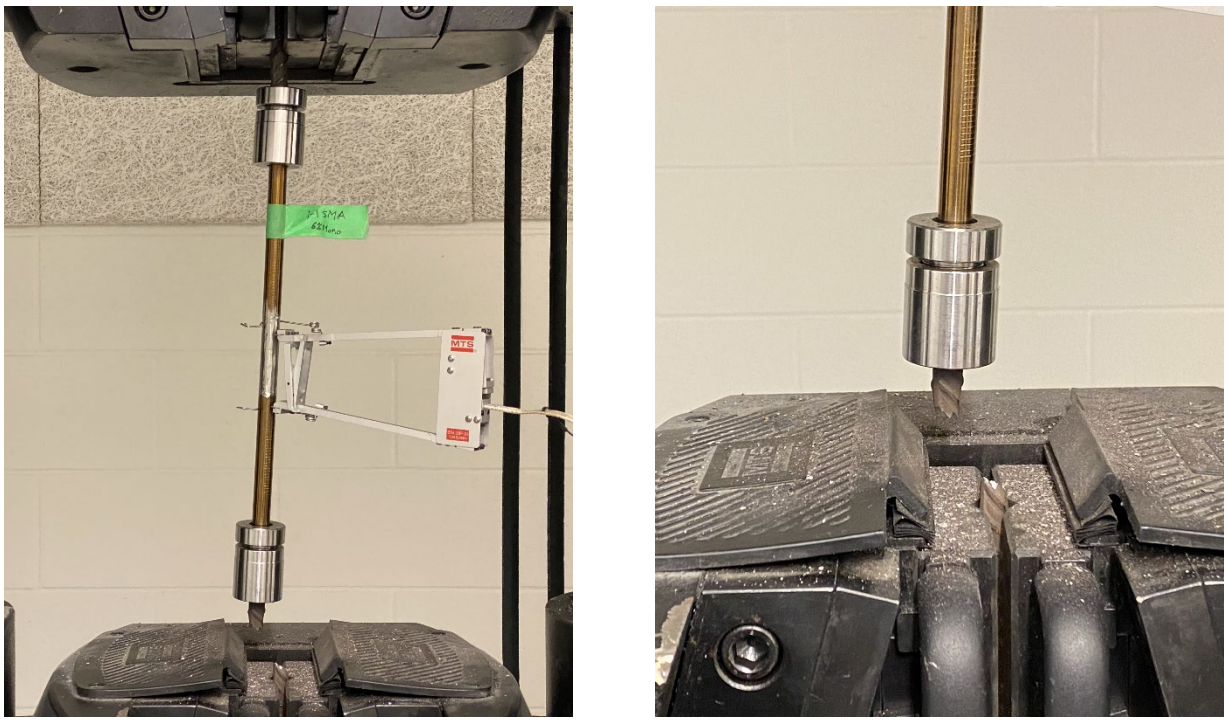

Figure A.18. Failure of Coupon 1 under tension: test setup (left); rupture of bottom steel grip (right).

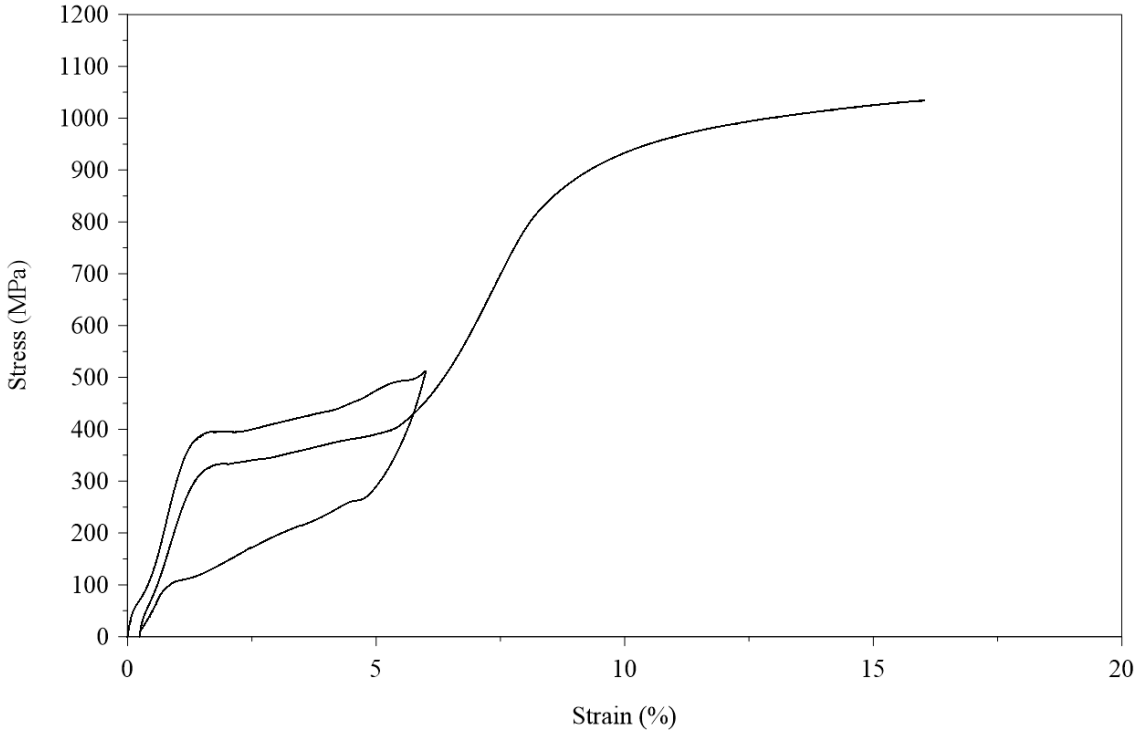

Figure A.19. Monotonic stress-strain response with 6% strain cycle of Nitinol Coupon 2.

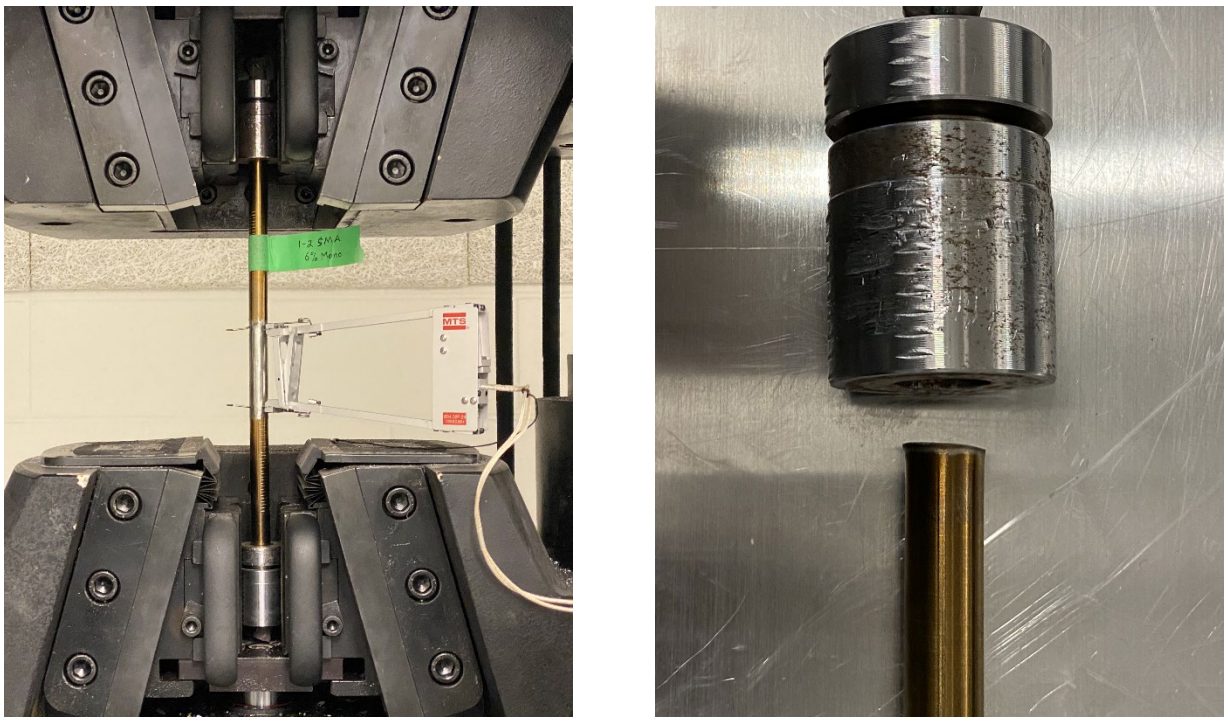

Figure A.20. Initial failure of Coupon 2 under tension: test setup (left); rupture of top conical head in coupler (right).

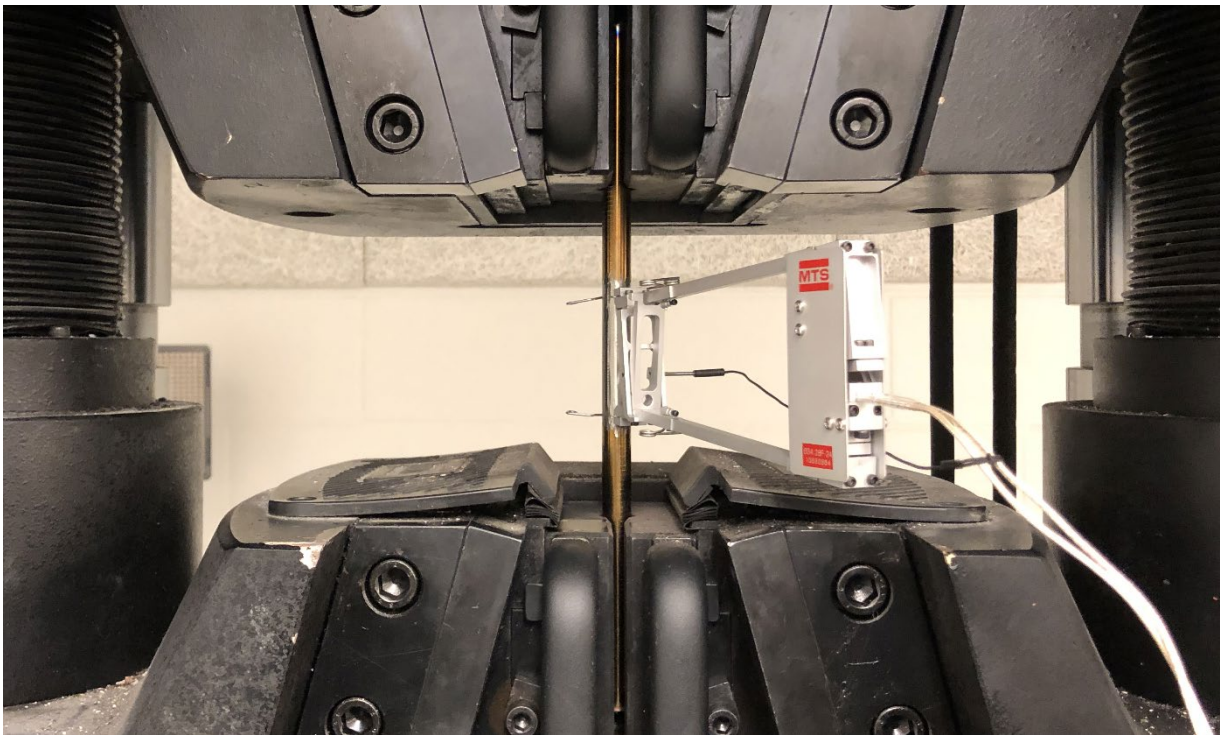

Figure A.21. Modified tension test setup of Coupon 2 with bare end grips.

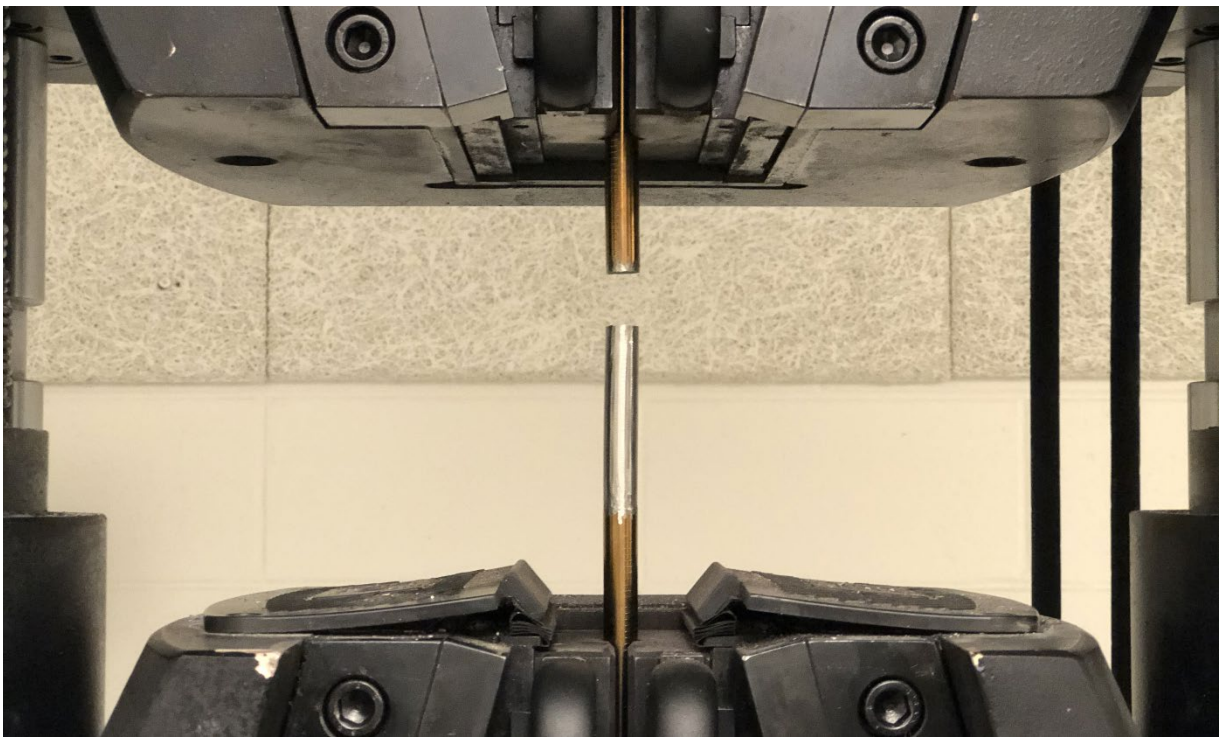

Figure A.22. Final failure of Coupon 2 under tension: rupture within reduced cross-section.

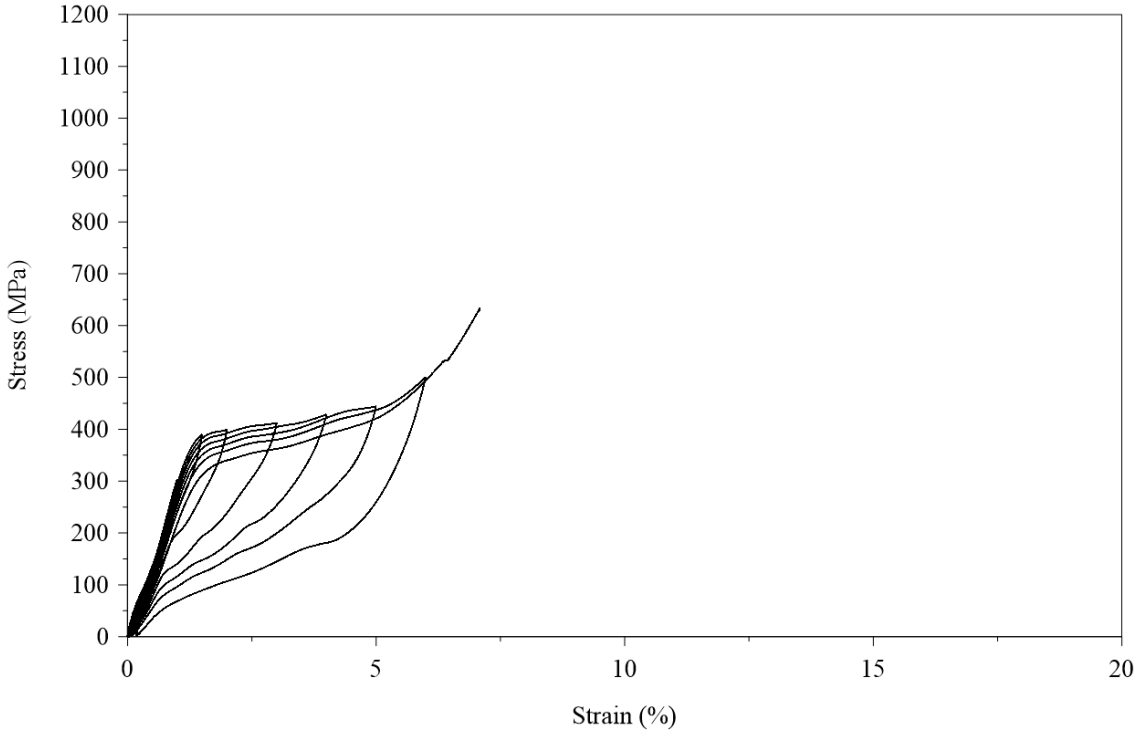

Figure A.23. Cyclic stress-strain response of Nitinol Coupon 3.

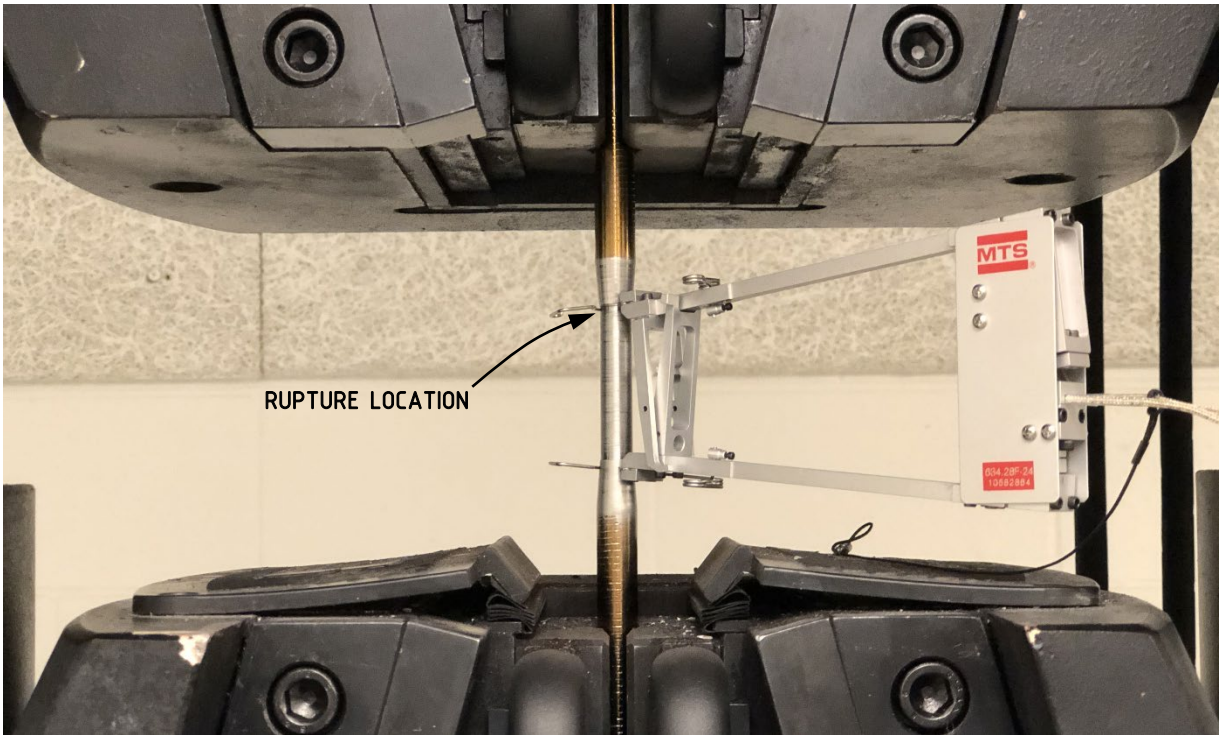

Figure A.24. Cyclic tension test setup of Coupon 3, indicating rupture at the top of the reduced cross-section.

Normal Concrete

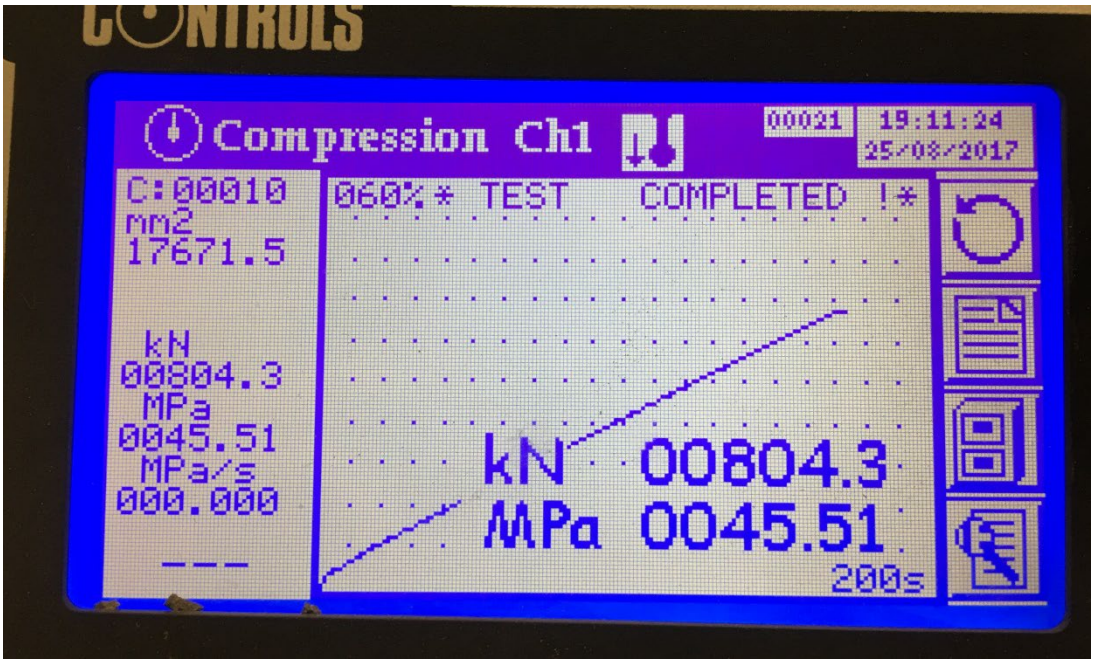

Figure A.25. Sample normal concrete cylinder strength at 28 days for steel-reinforced wall.

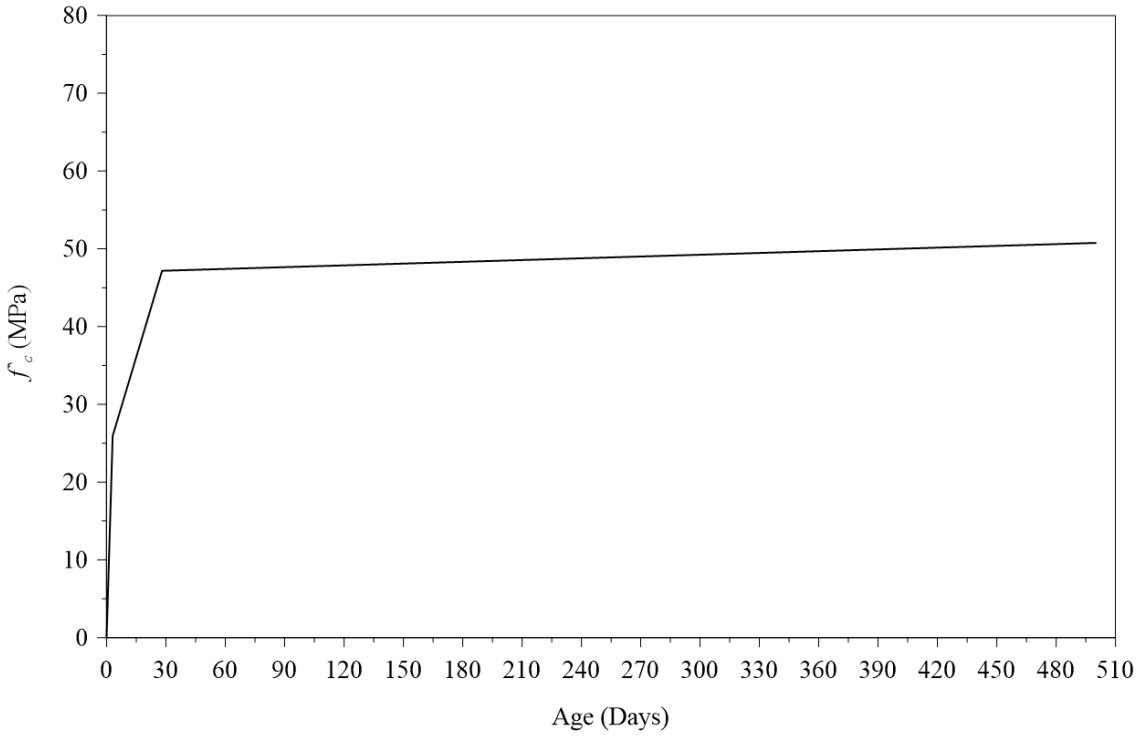

Figure A.26. Concrete strength development to test day of steel-reinforced wall; age is 500 days.

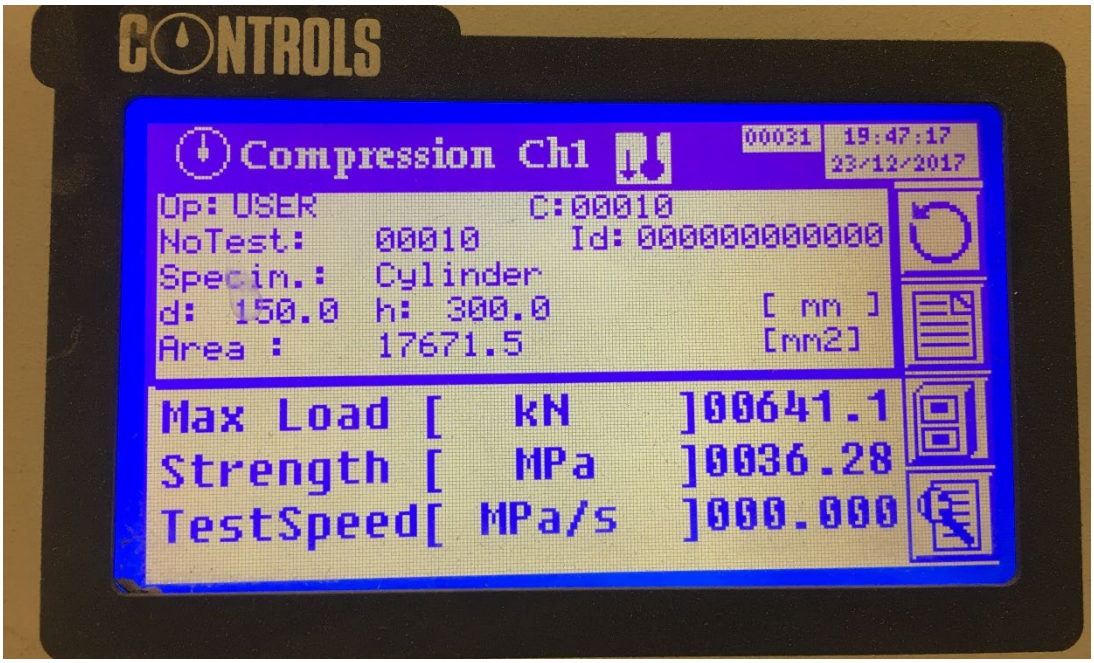

Figure A.27. Sample normal concrete cylinder strength at 28 days for Nitinol-reinforced wall.

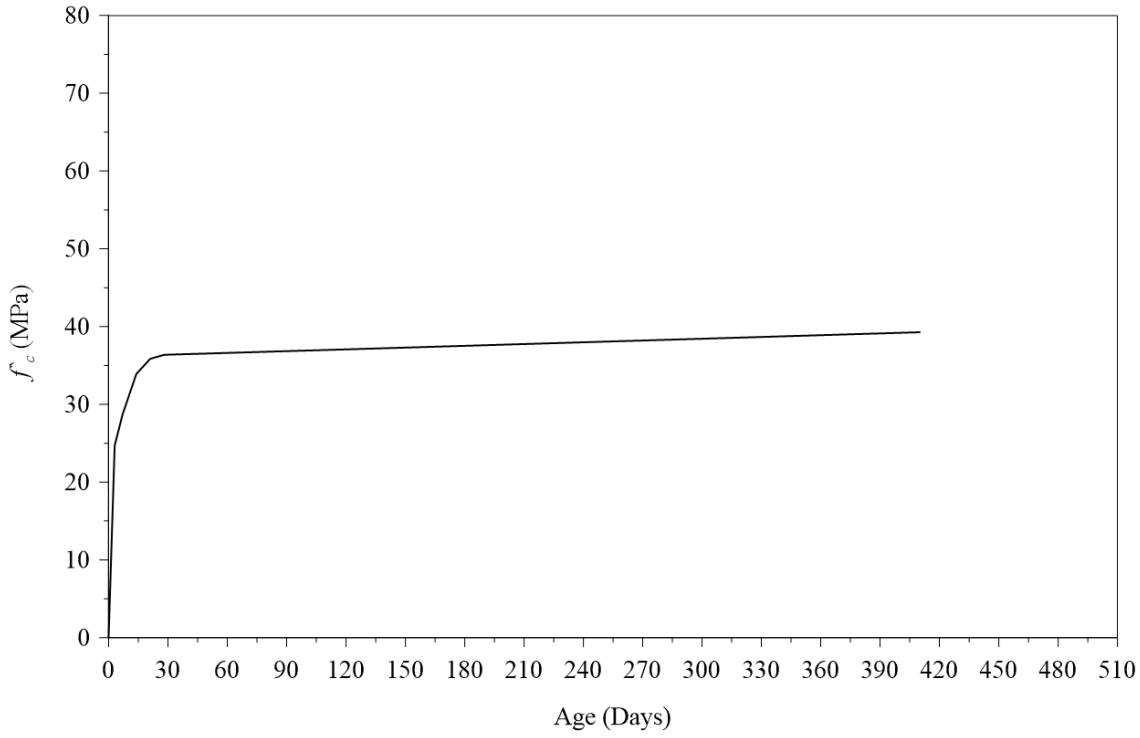

Figure A.28. Concrete strength development up to test day of Nitinol-reinforced wall; age is 410 days.

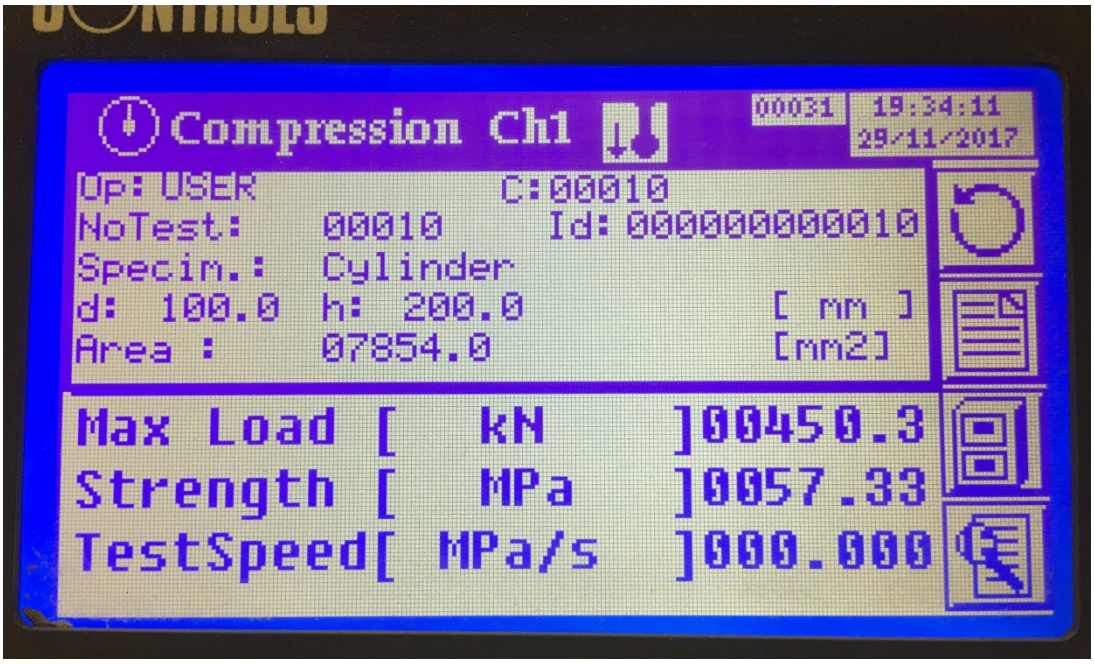

Figure A.29. Sample self-consolidating concrete cylinder strength at 28 days for repair of steel-reinforced wall.

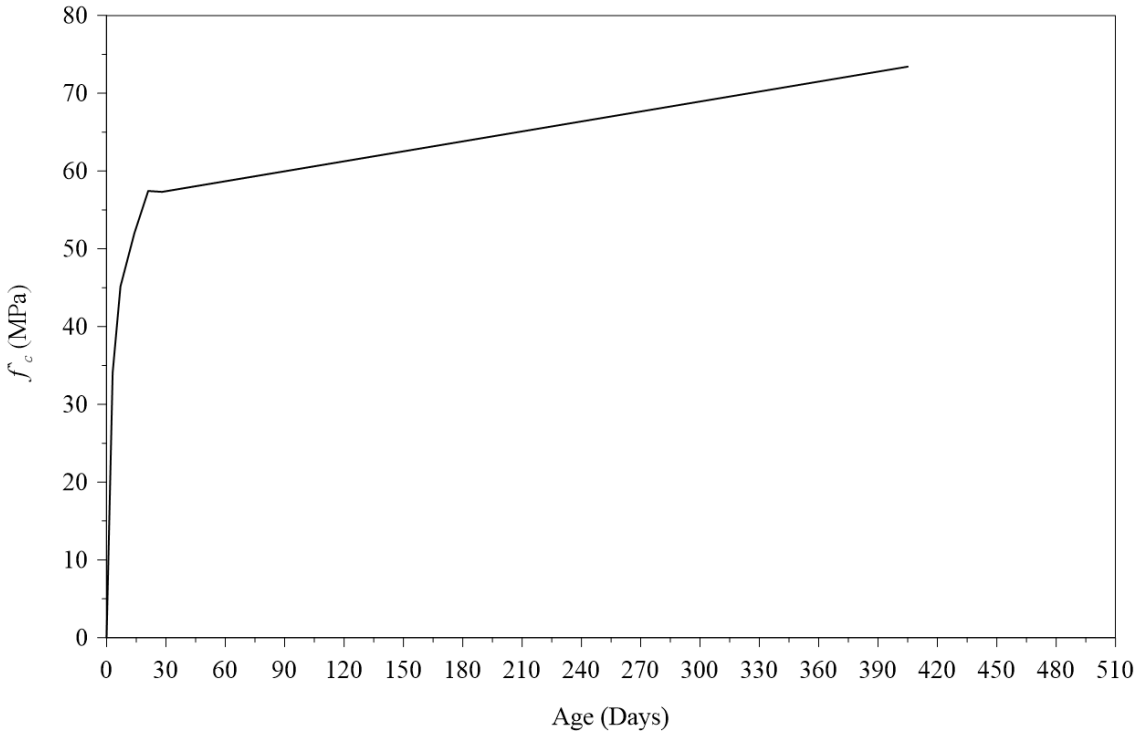

Figure A.30. Concrete strength development up to test day of steel-reinforced wall; age is 405 days.

APPENDIX B

Construction of Shear Walls

Figure B.1. Assembled formwork for foundation block.

Figure B.2. Panel components of foundation block formwork.

Figure B.3. Assembly process of foundation block formwork panels.

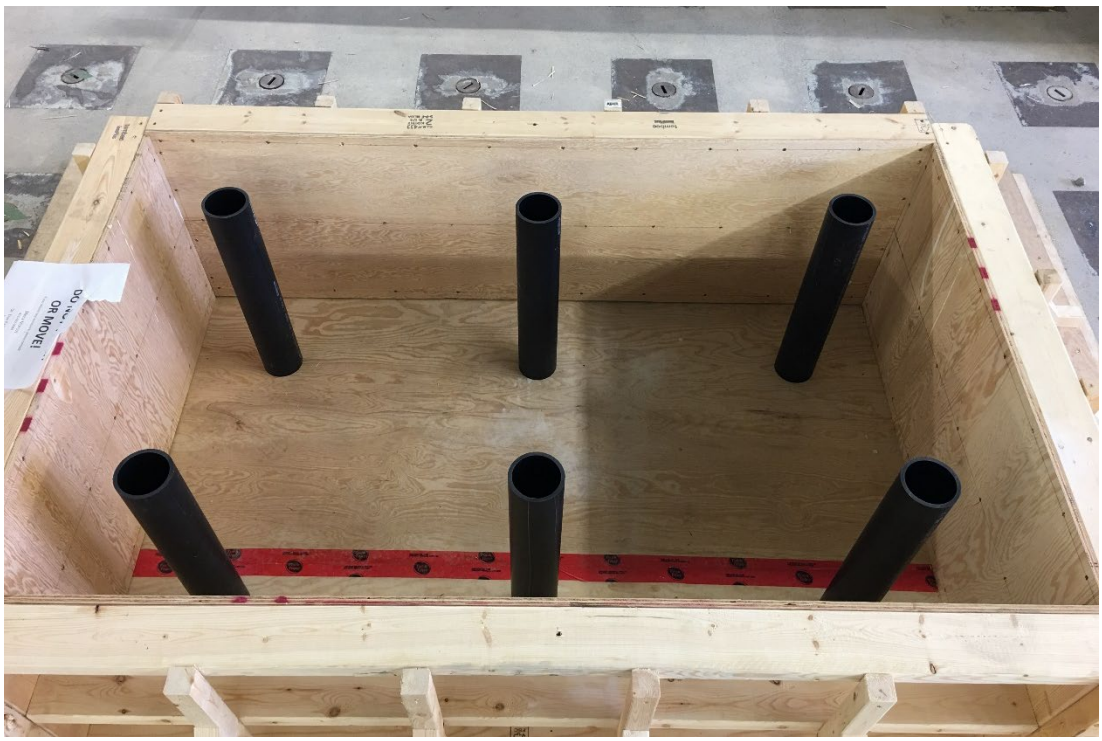

Figure B.4. Anchor rod sleeves in foundation block formwork.

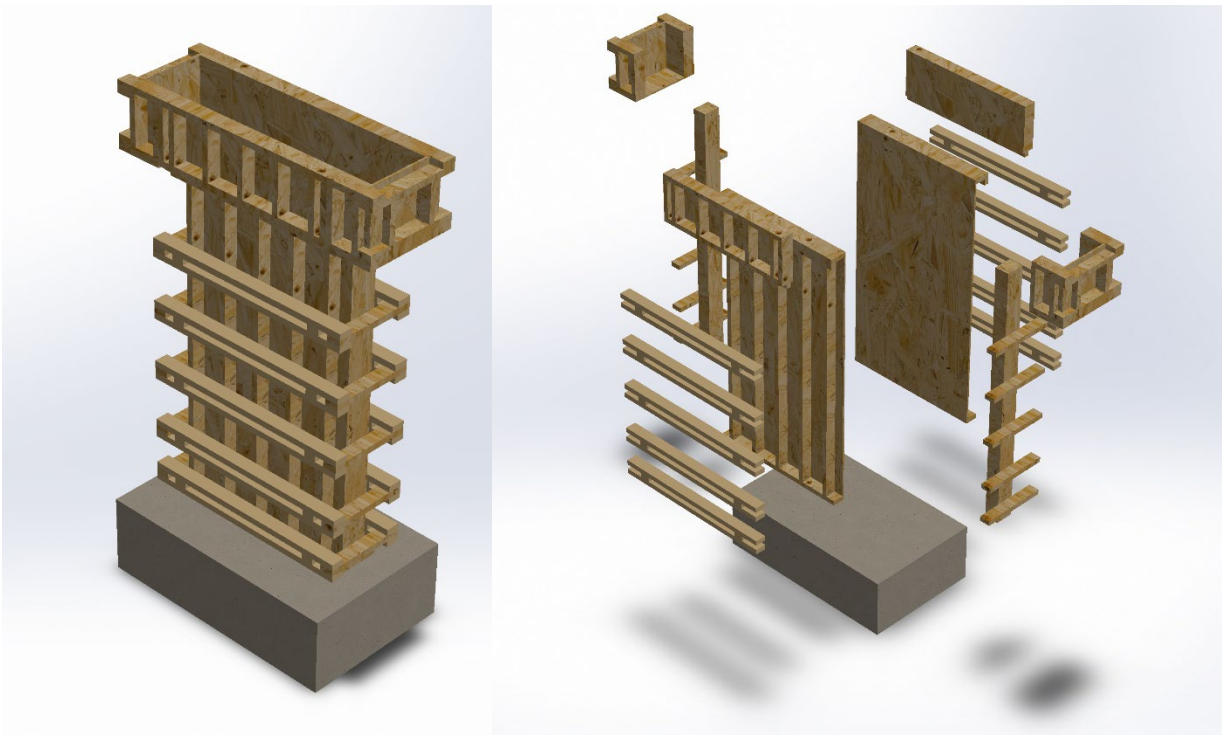

Figure B.5. Design model of shear wall and cap beam formwork.

Figure B.6. Shear wall formwork panel.

Figure B.7. Construction of shear wall formwork side panels.

Figure B.8. Fitting of shear wall formwork panels.

Figure B.9. Assembled cap beam formwork.

Figure B.10. Threaded rod sleeves through cap beam formwork.

Figure B.11. Assembly of foundation block reinforcement cage.

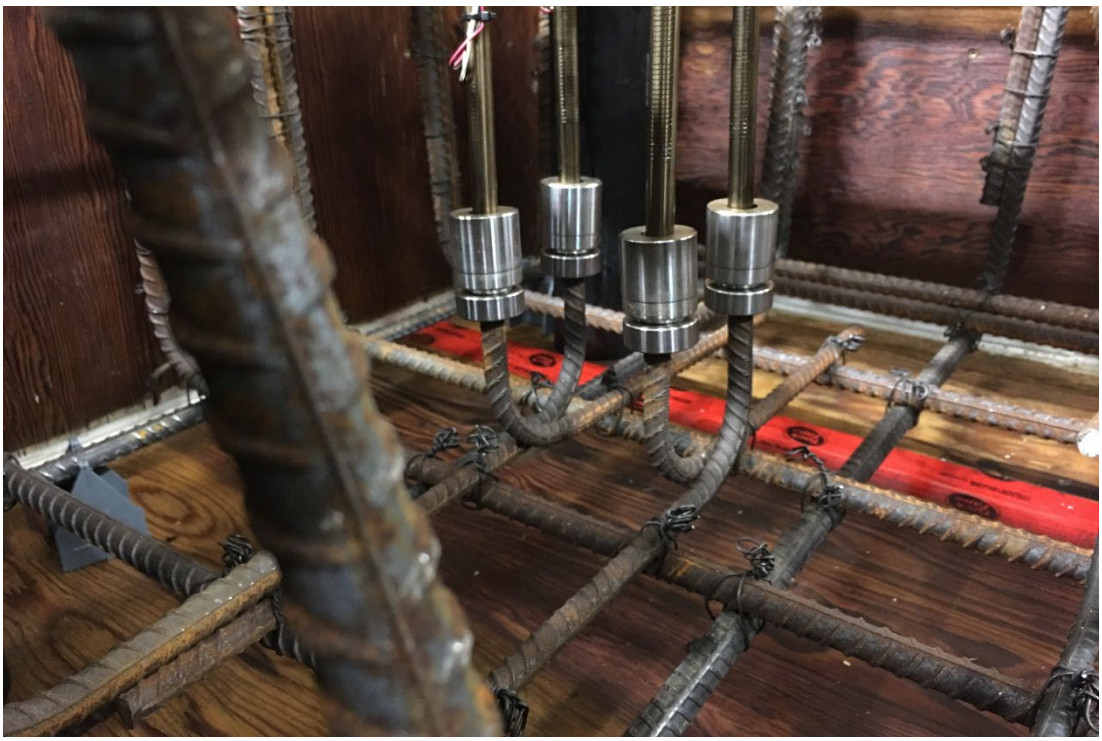

Figure B.12. Assembly of boundary element longitudinal reinforcement through foundation block.

Figure B.13. Shear wall longitudinal reinforcement curtains projecting from foundation block.

Figure B.14. Completed construction of concrete foundation block.

Figure B.15. Assembly of shear wall reinforcement cage.

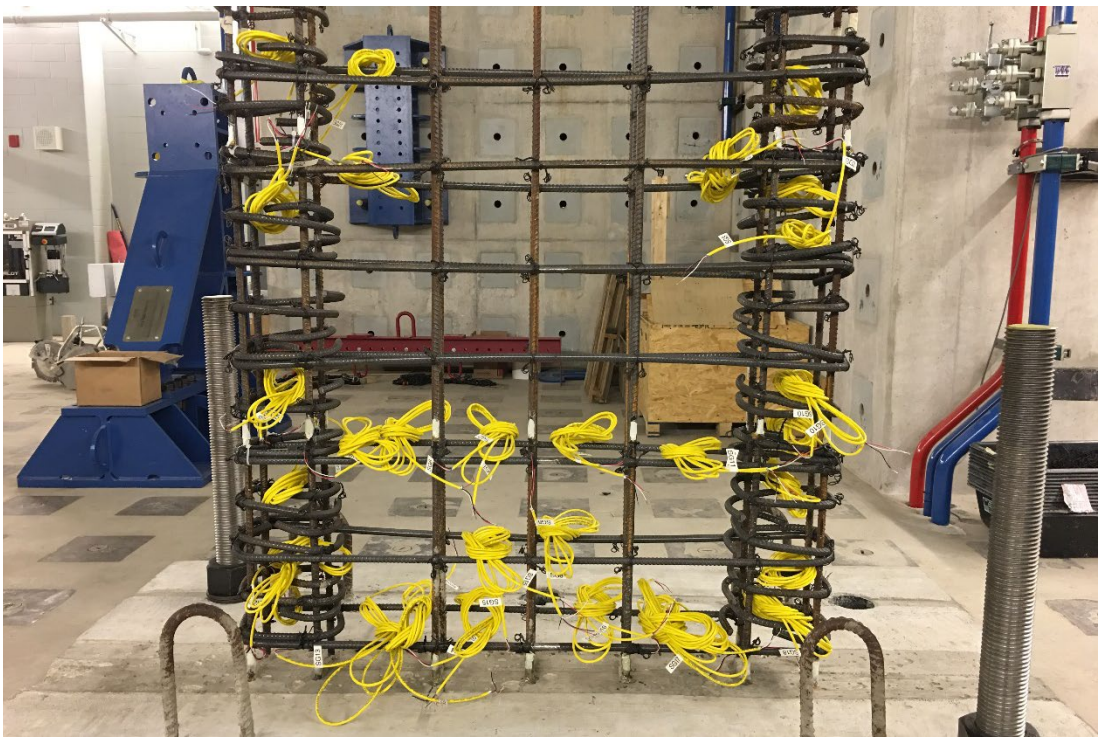

Figure B.16. Application of strain gauges to reinforcement bars within plastic hinge region.

Figure B.17. Wall ties to maintain profile of shear wall under pressure of wet concrete.

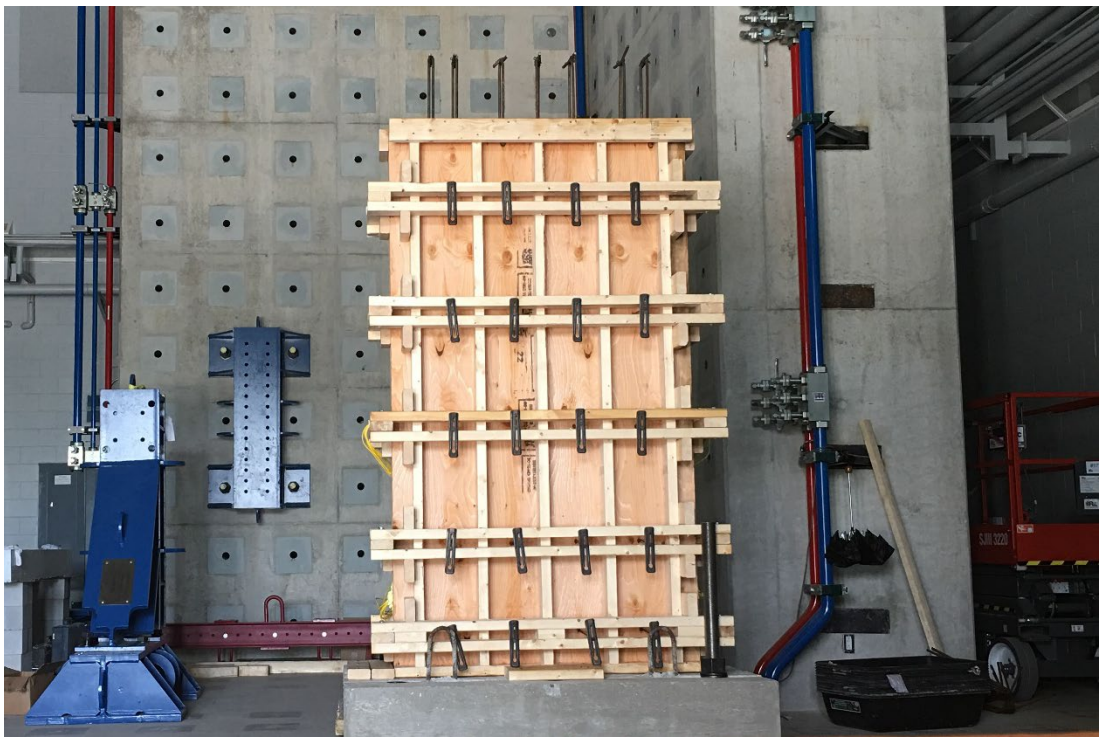

Figure B.18. Assembly of shear wall formwork.

Figure B.19. Project of shear wall longitudinal reinforcement into cap beam.

Figure B.20. Observation of cover clearance around boundary element.

Figure B.21. Placement of cap beam reinforcement cage.

Figure B.22. Top of assembled of shear wall and cap beam formwork and reinforcement cages.

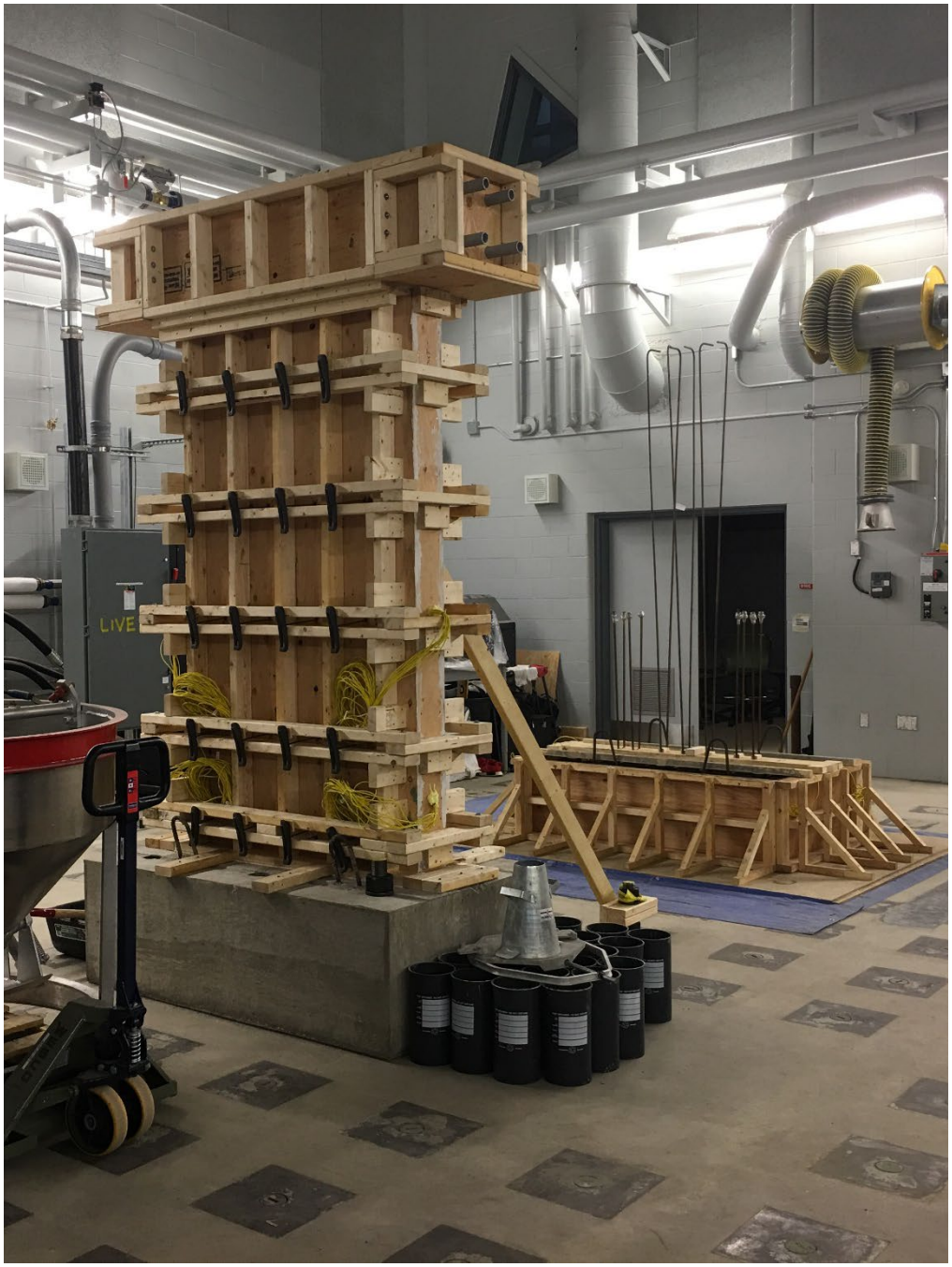

Figure B.23. Preparation for casting of concrete.

Figure B.24. Demoulded steel-reinforced shear wall specimen and assembled reinforcement cage of SMA wall.

Figure B.25. Poor consolidation of concrete along base length of steel shear wall; Side A (top); Side B (bottom) .

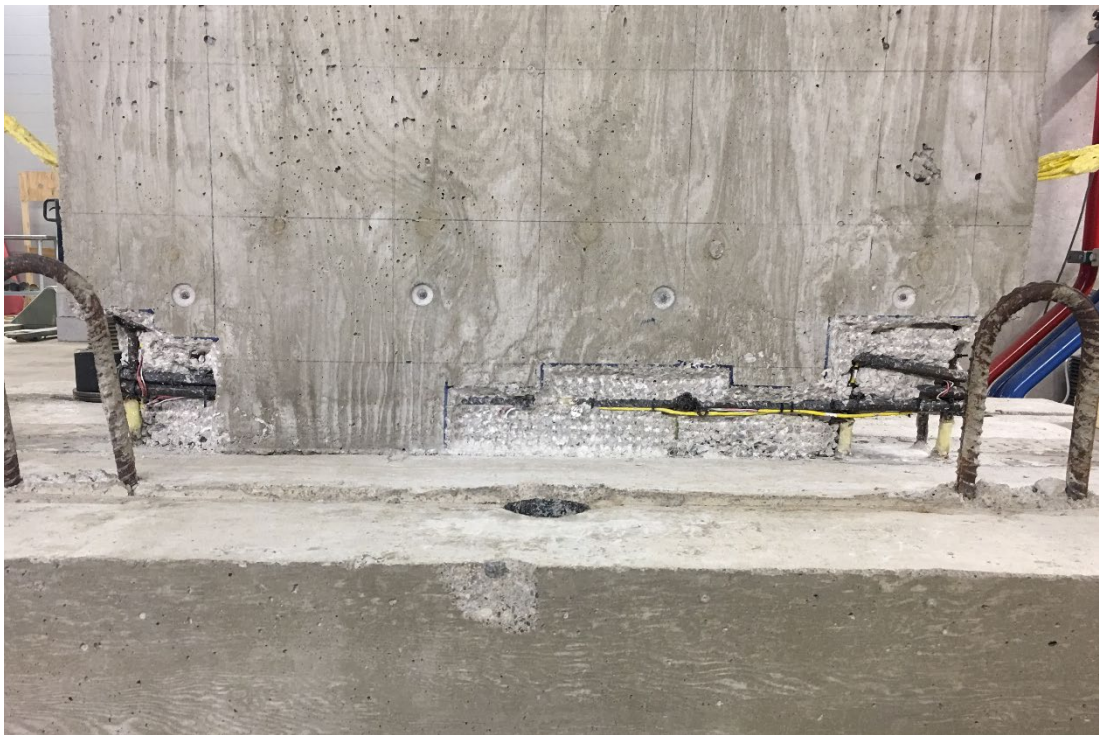

Figure B.26. Removal of poorly consolidated concrete along base of Side A on steel shear wall.

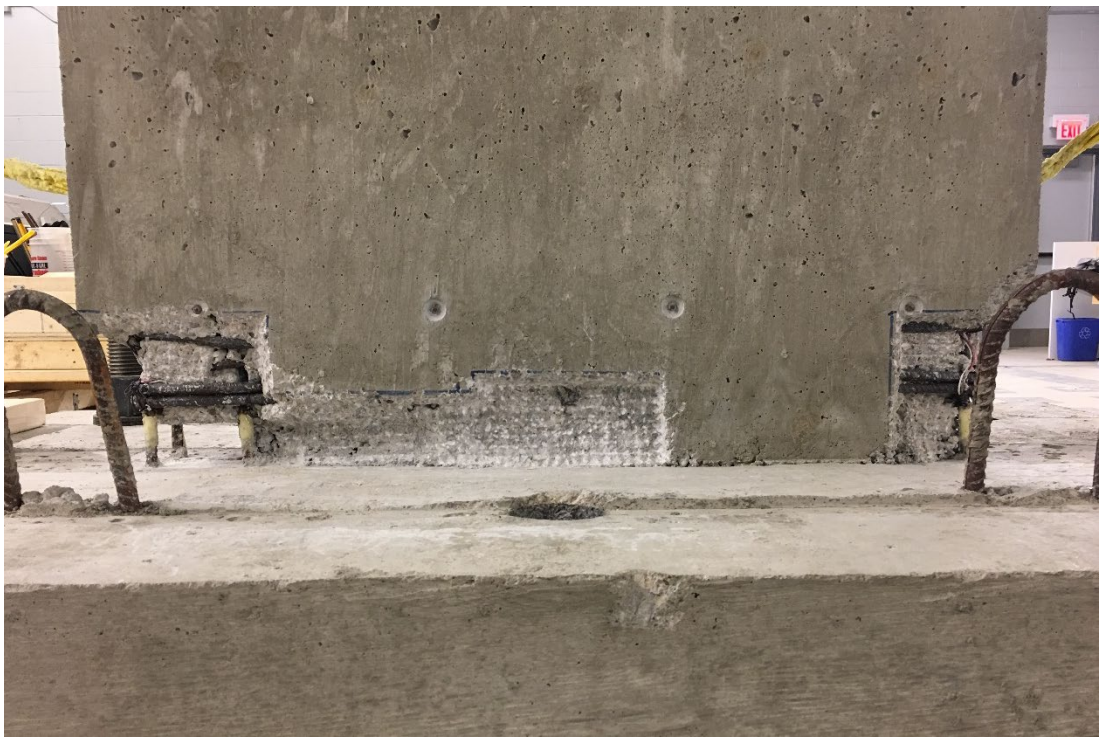

Figure B.27. Removal of poorly consolidated concrete along base of Side B on steel shear wall.

Figure B.28. Formation of fill ports for local repair.

Figure B.29. Assembly of formwork for repair along base of steel shear wall.

Figure B.30. Repair on Side A of steel shear wall.

Figure B.31. Repair on Side B of steel shear wall.

Figure B.32. Prepared shear wall specimens: steel wall (left), and Nitinol wall (right).

APPENDIX C

Instrumentation Data

Wall SWS–R Measurements and Raw Data

Table C.1. Steel wall instrumentation identification and status

No.	Instrument	Type	Capacity	Purpose	Reference	Status
1	CP–A–300	CP	300mm	Sliding	Foundation Block	Active
2	CP–B–300	CP	300mm	Slip	Test Frame	Active
3	CP–C–300	CP	300mm	Vertical Displacement	Foundation Block	Active
4	CP–D–300	CP	300mm	Vertical Displacement	Foundation Block	Active
5	CP–A–600	CP	600mm	Lateral Displacement	Test Frame	Active
6	CP–B–600	CP	600mm	Lateral Displacement	Instrumentation Frame	Active
7	CP–C–600	CP	600mm	Lateral Displacement	Instrumentation Frame	Active
8	CP–D–600	CP	600mm	Vertical Displacement	Foundation Block	Active
9	CP–E–600	CP	600mm	Vertical Displacement	Foundation Block	Active
10	CP–A–1250	CP	1250mm	Shear	Plastic Hinge	Active
11	CP–B–1250	CP	1250mm	Shear	Plastic Hinge	Active
12	CP–C–1250	CP	1250mm	Shear	Plastic Hinge	Active
13	CP–D–1250	CP	1250mm	Shear	Plastic Hinge	Active
14	CP–E–1250	CP	1250mm	Lateral Displacement	Instrumentation Frame	Active
15	LP–A–100	LP	100mm	Uplift	Strong Floor	Active
16	LP–B–100	LP	100mm	Uplift	Strong Floor	Active
17	Actuator–P	Load Cell	±250kN	Force	Strong Wall	Active
18	Actuator–δ	LVDT	±250mm	Displacement	Strong Wall	Active

CP denotes Cable Potentiometer

LP denotes Linear Potentiometer

Table C.2. Steel wall strain gauges identification and status

No.	Instrument	Strain Capacity	Location	Notes	Status
1	SG1	2 – 4% max.	Side A – Left Boundary		Active
2	SG2	2 – 4% max.	Side A – Left Boundary	Work Damage	Inactive
3	SG3	2 – 4% max.	Side A – Right Boundary		Active
4	SG4	2 – 4% max.	Side A – Right Boundary		Active
5	SG5	2 – 4% max.	Side A – Left Boundary		Active
6	SG6	2 – 4% max.	Side A – Left Boundary		Active
7	SG7	2 – 4% max.	Side A – Web		Active
8	SG8	2 – 4% max.	Side A – Web		Active
9	SG9	2 – 4% max.	Side A – Web	Faulty	Inactive
10	SG10	2 – 4% max.	Side A – Right Boundary		Active
11	SG11	2 – 4% max.	Side A – Right Boundary		Active
12	SG12	2 – 4% max.	Side A – Left Boundary	Work Damage	Inactive
13	SG13	2 – 4% max.	Side A – Left Boundary	Work Damage	Inactive
14	SG14	2 – 4% max.	Side A – Web		Active
15	SG15	2 – 4% max.	Side A – Web	No Room	Disconnected
16	SG16	2 – 4% max.	Side A – Web		Active
17	SG17	2 – 4% max.	Side A – Right Boundary	Work Damage	Inactive
18	SG18	2 – 4% max.	Side A – Right Boundary	Work Damage	Inactive
19	SG19	2 – 4% max.	Side B – Right Boundary		Active
20	SG20	2 – 4% max.	Side B – Right Boundary		Active
21	SG21	2 – 4% max.	Side B – Left Boundary		Active
22	SG22	2 – 4% max.	Side B – Left Boundary		Active
23	SG23	2 – 4% max.	Side B – Right Boundary		Active
24	SG24	2 – 4% max.	Side B – Right Boundary		Active
25	SG25	2 – 4% max.	Side B – Left Boundary		Active
26	SG26	2 – 4% max.	Side B – Left Boundary		Active
27	SG27	2 – 4% max.	Side B – Right Boundary		Active

28	SG28	2 – 4% max.	Side B – Right Boundary		Active
29	SG29	2 – 4% max.	Side B – Left Boundary		Active
30	SG30	2 – 4% max.	Side B – Left Boundary		Active
31	SG31	2 – 4% max.	Side A – Top Stirrup		Active
32	SG32	2 – 4% max.	Side A – Middle Stirrup		Active
33	SG33	2 – 4% max.	Side A – Bottom Stirrup	Work Damage	Inactive

SG denotes Standard Strain Gauge

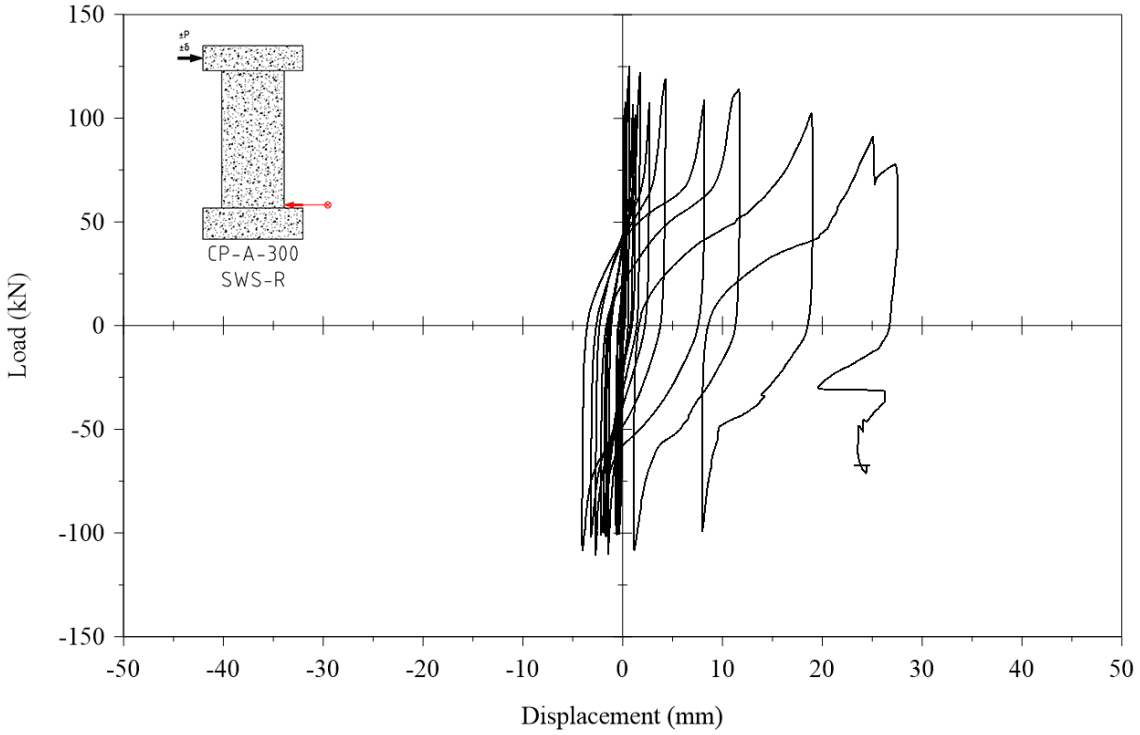

Figure C.1. Cyclic displacement response from CP-A-300.

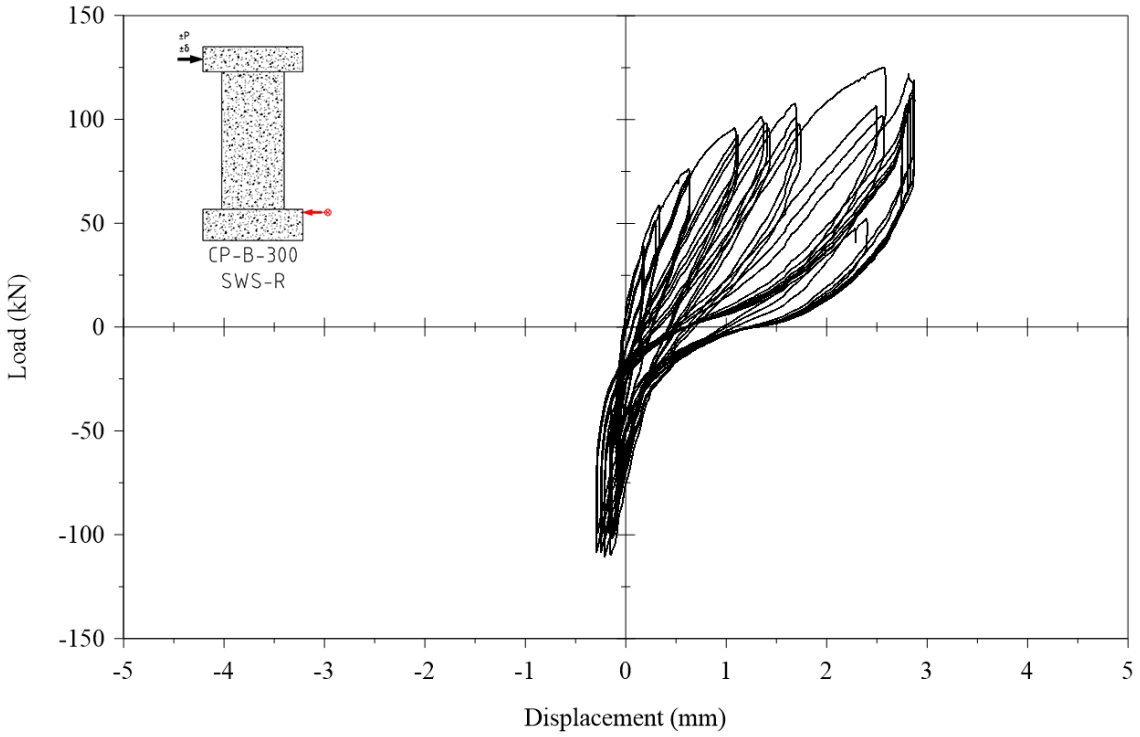

Figure C.2. Cyclic displacement response from CP-B-300.

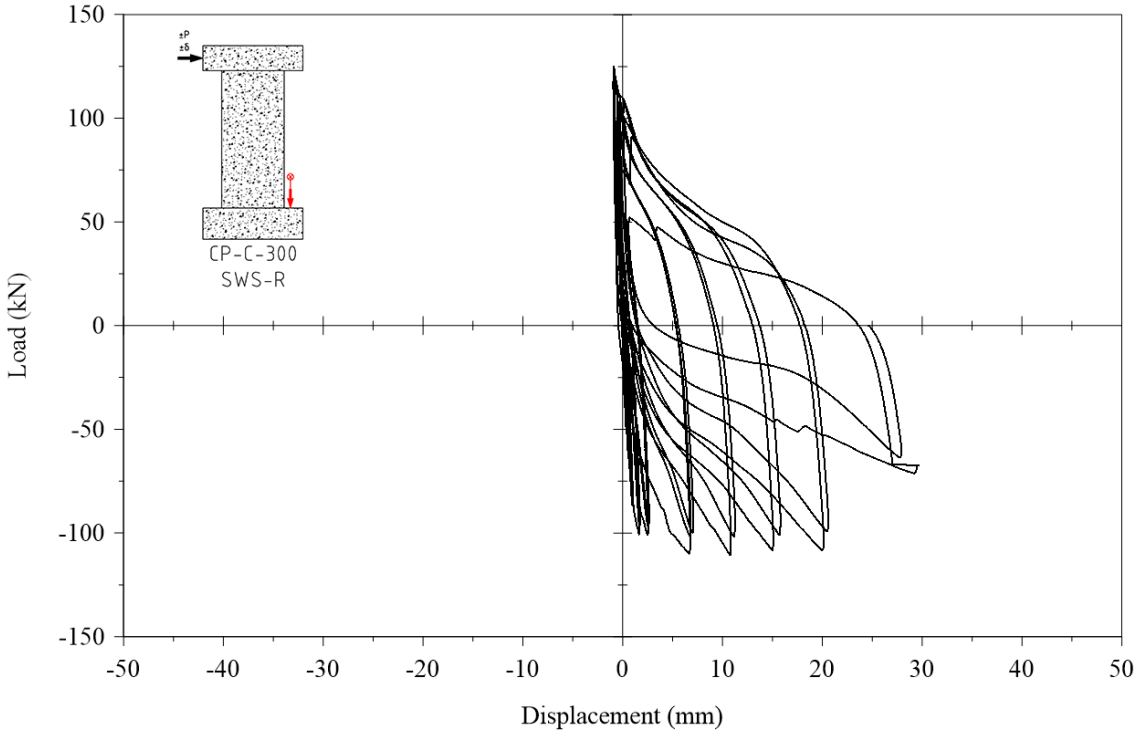

Figure C.3. Cyclic displacement response from CP-C-300.

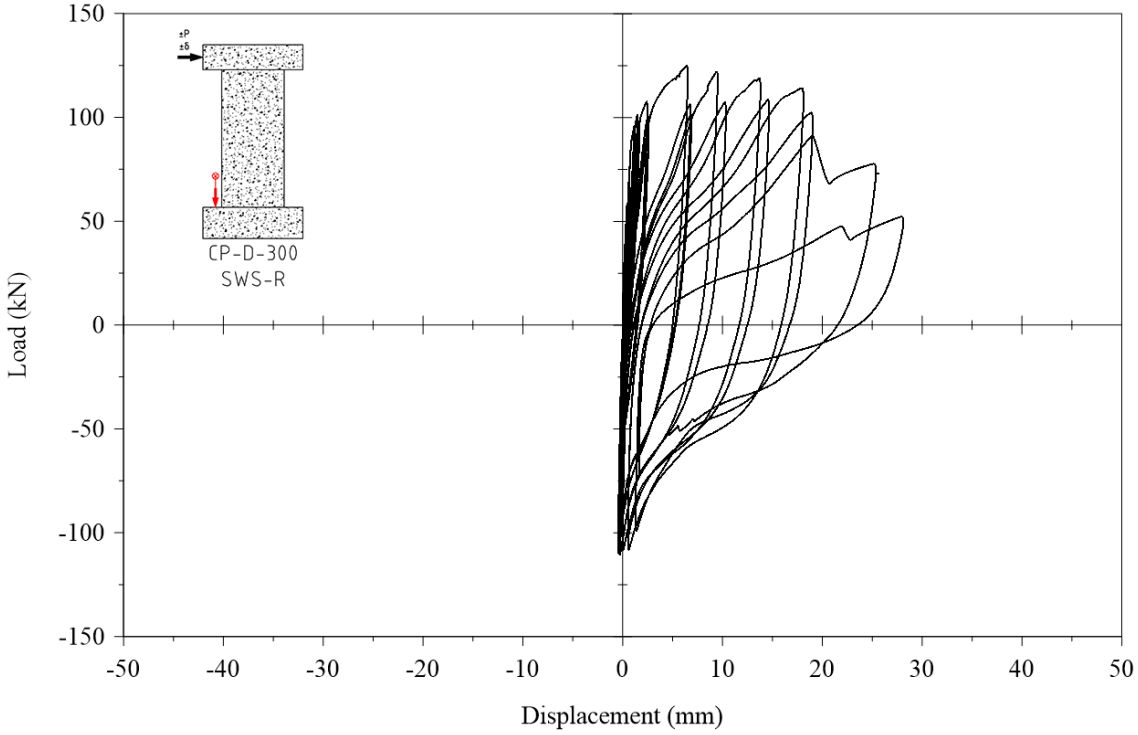

Figure C.4. Cyclic displacement response from CP-D-300.

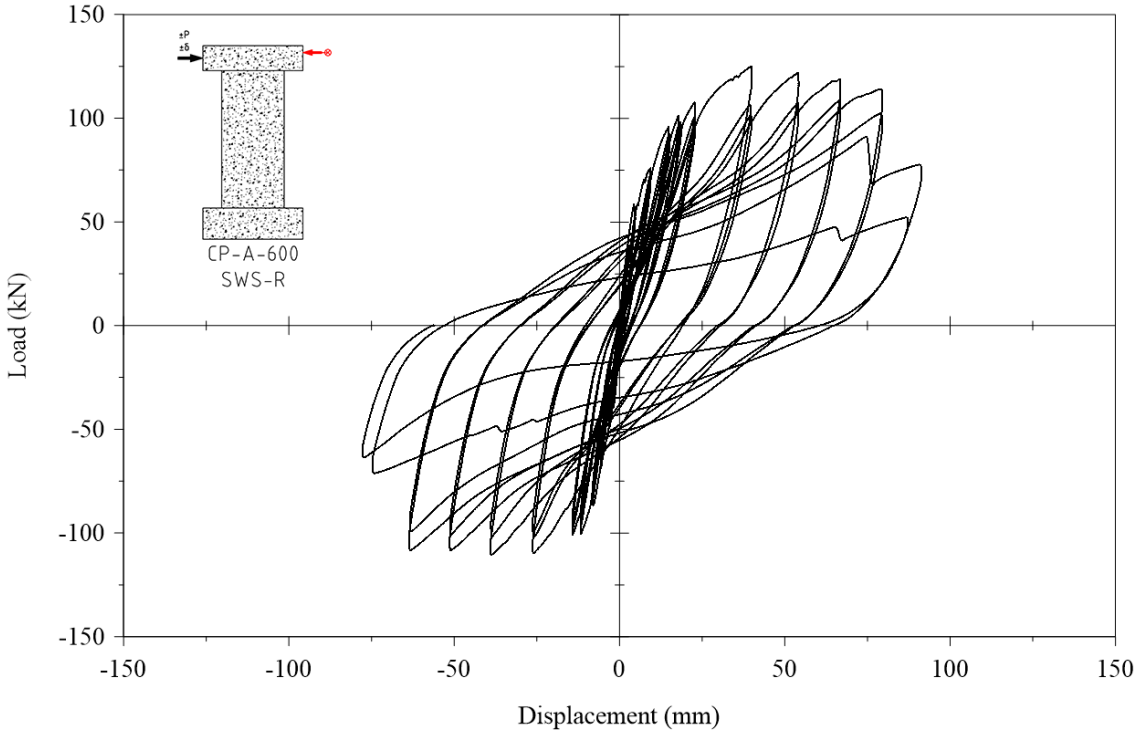

Figure C.5. Cyclic displacement response from CP-A-600.

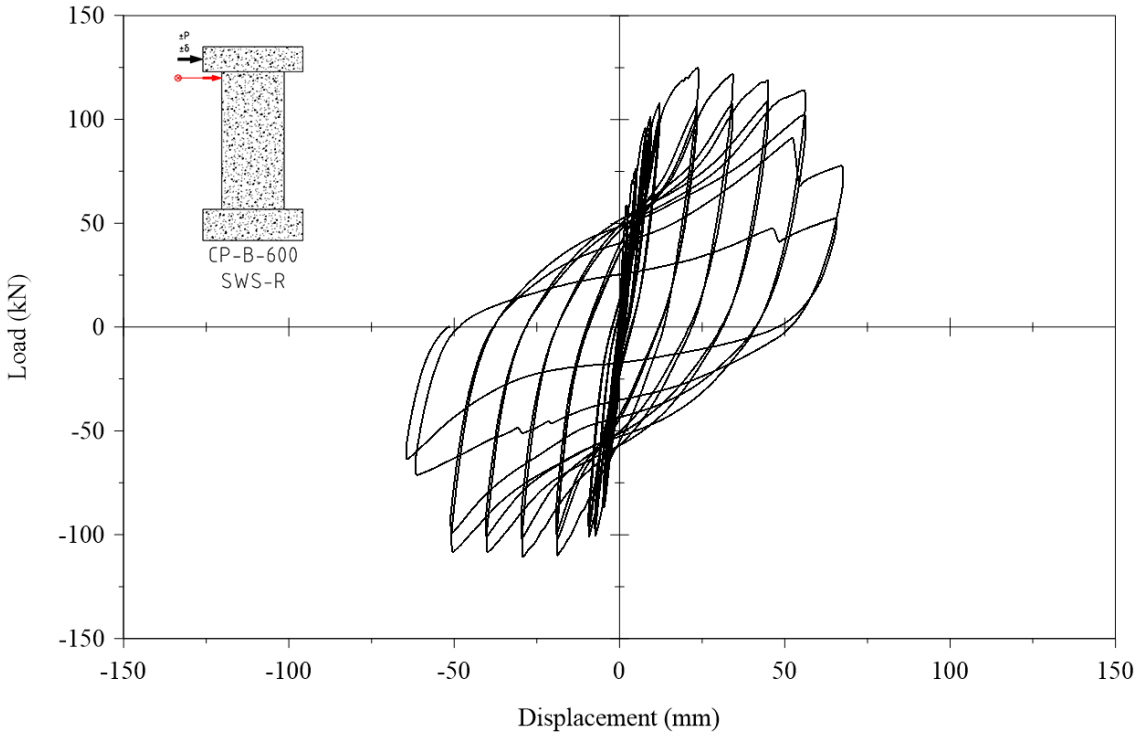

Figure C.6. Cyclic displacement response from CP-B-600.

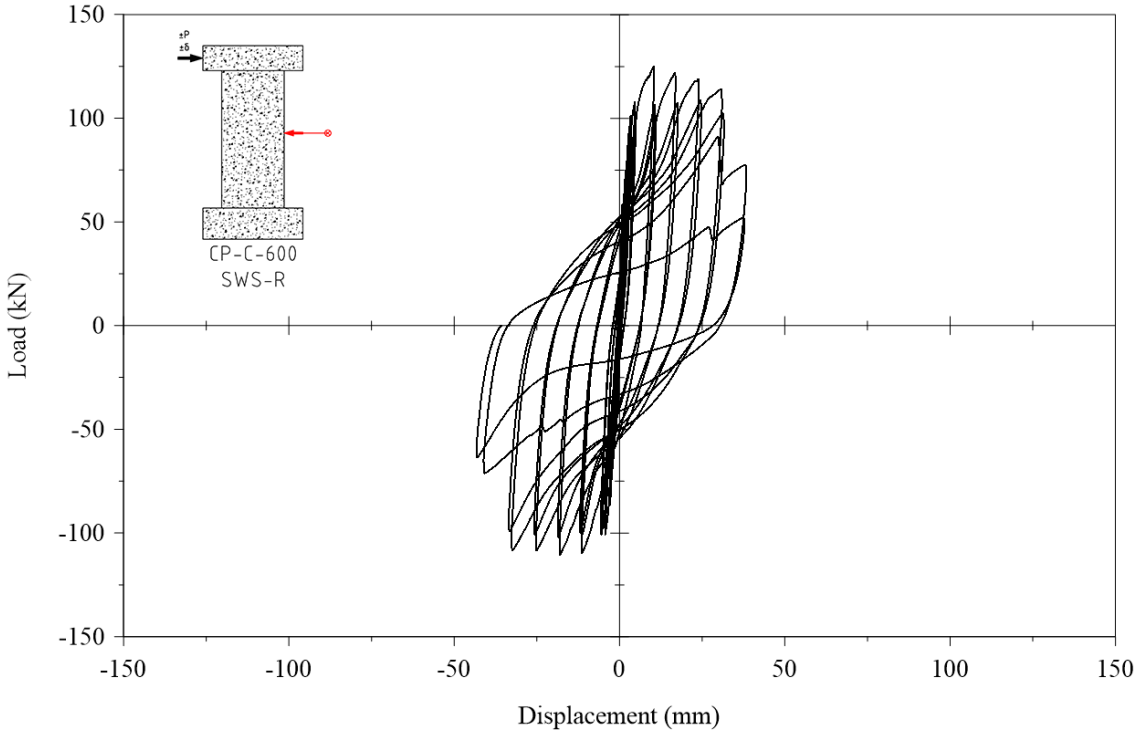

Figure C.7. Cyclic displacement response from CP-C-600.

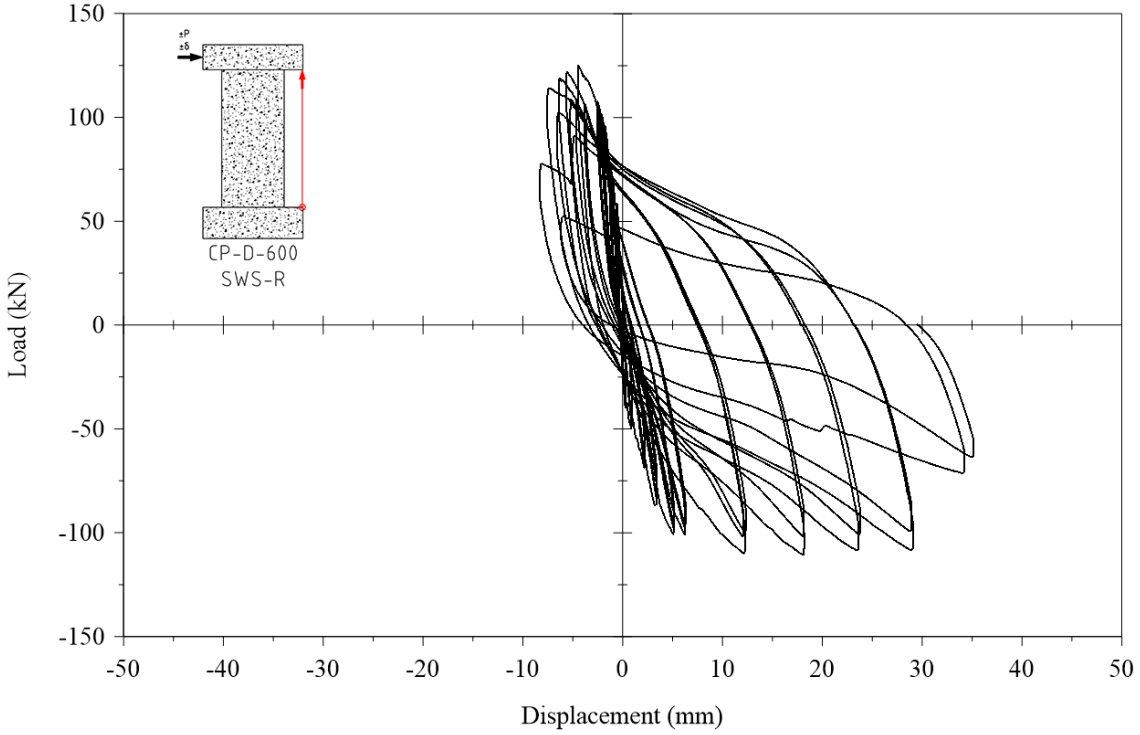

Figure C.8. Cyclic displacement response from CP-D-600.

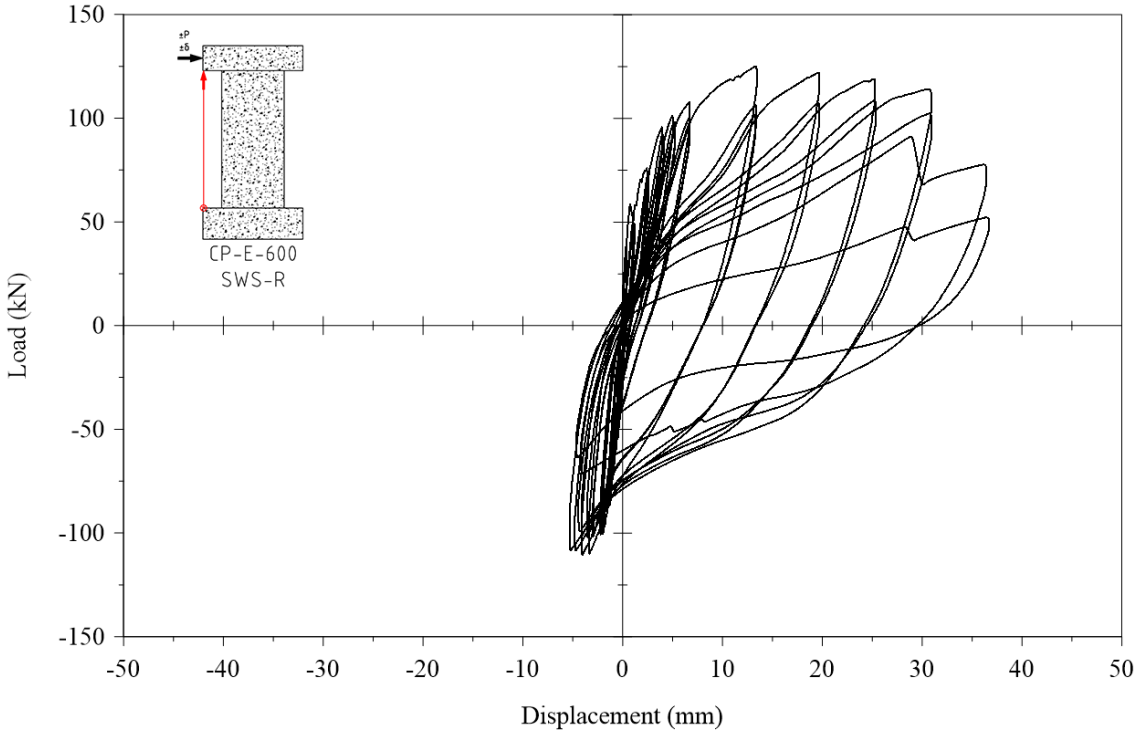

Figure C.9. Cyclic displacement response from CP-E-600.

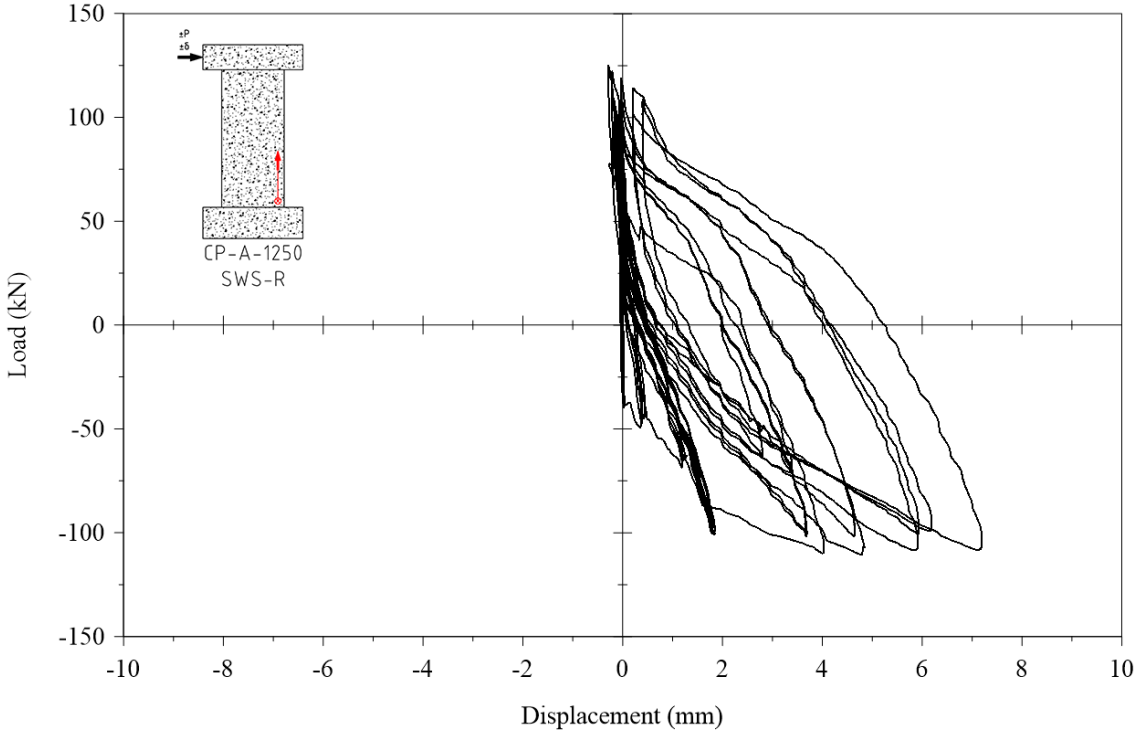

Figure C.10. Cyclic displacement response from CP-A-1250.

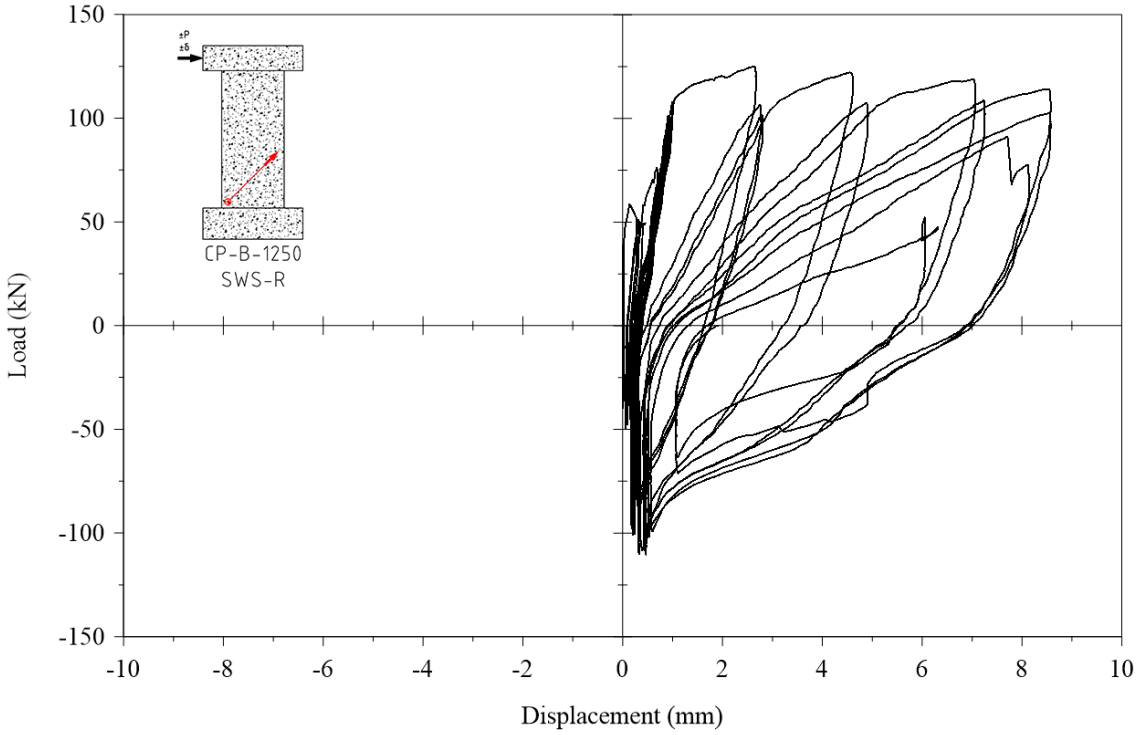

Figure C.11. Cyclic displacement response from CP-B-1250.

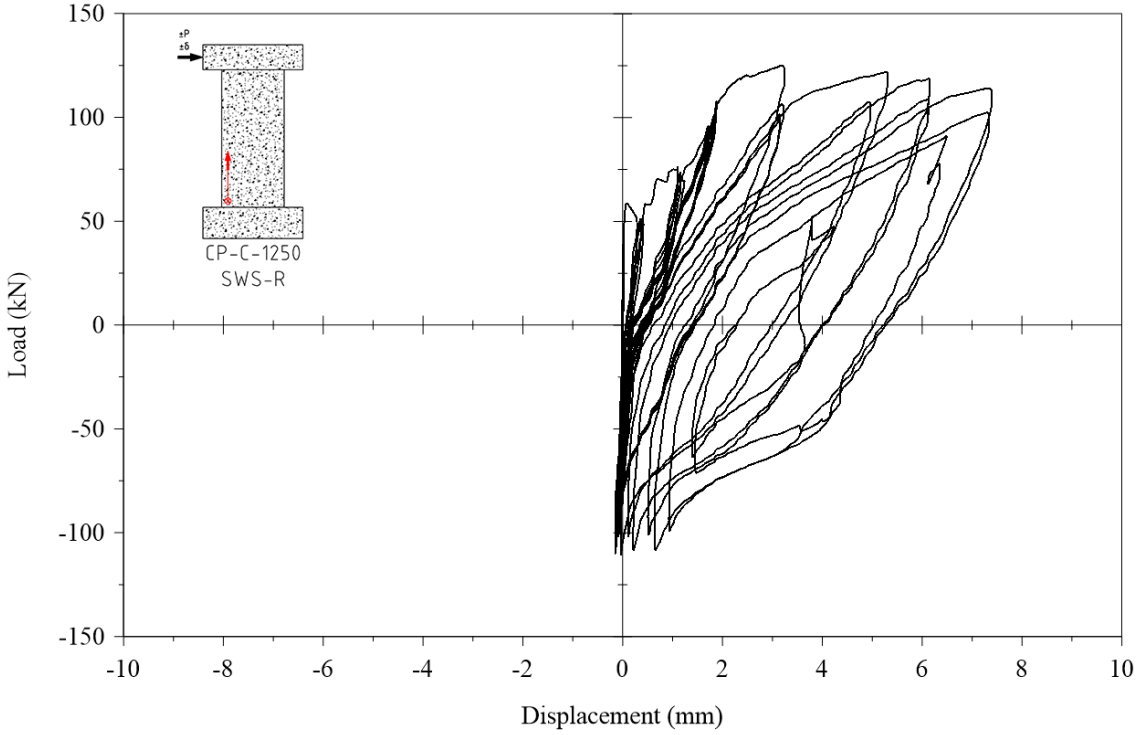

Figure C.12. Cyclic displacement response from CP-C-1250.

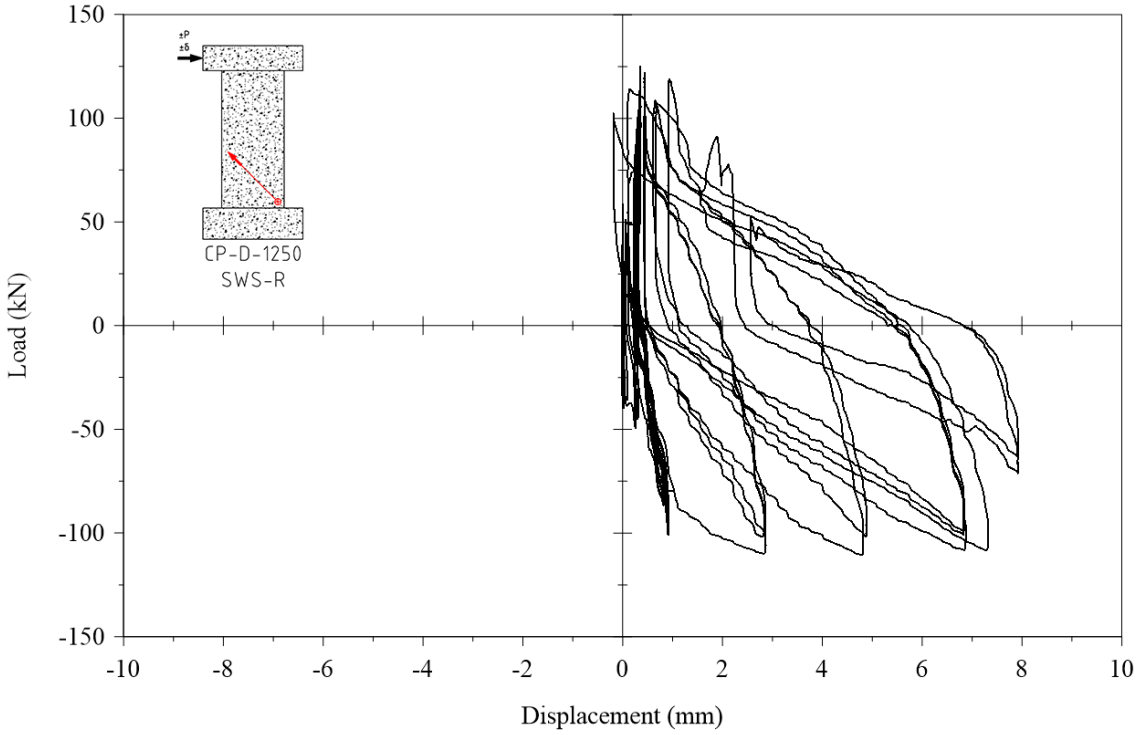

Figure C.13. Cyclic displacement response from CP-D-1250.

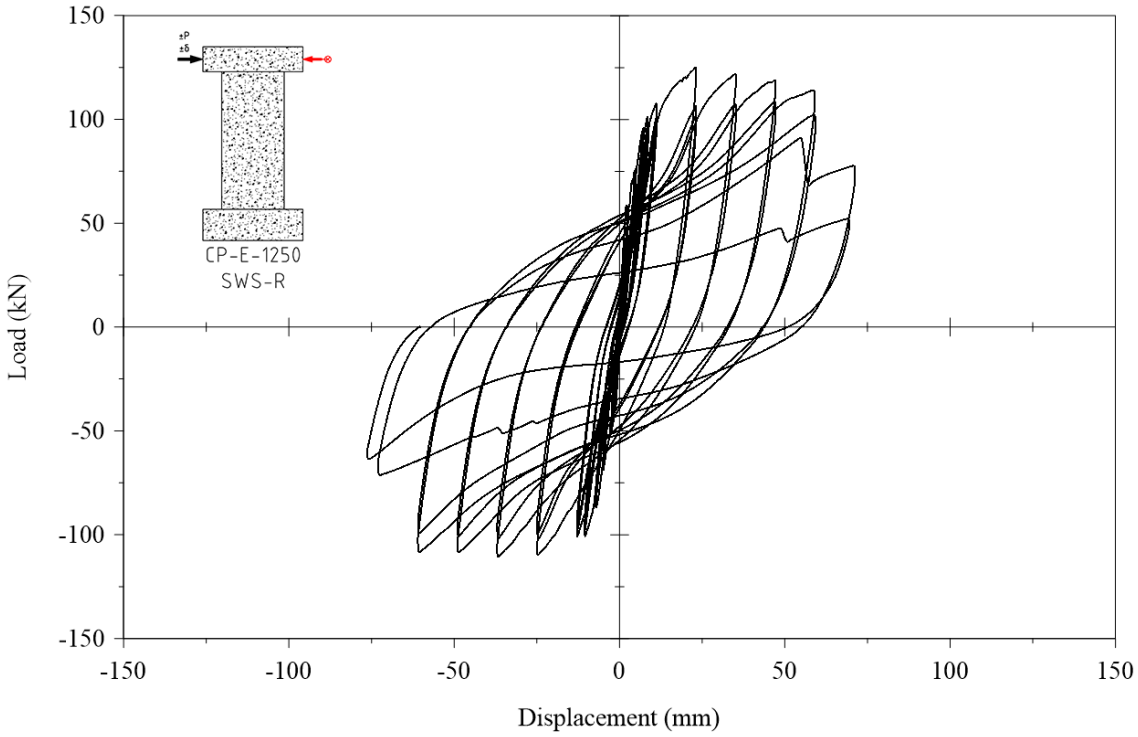

Figure C.14. Cyclic displacement response from CP-E-1250.

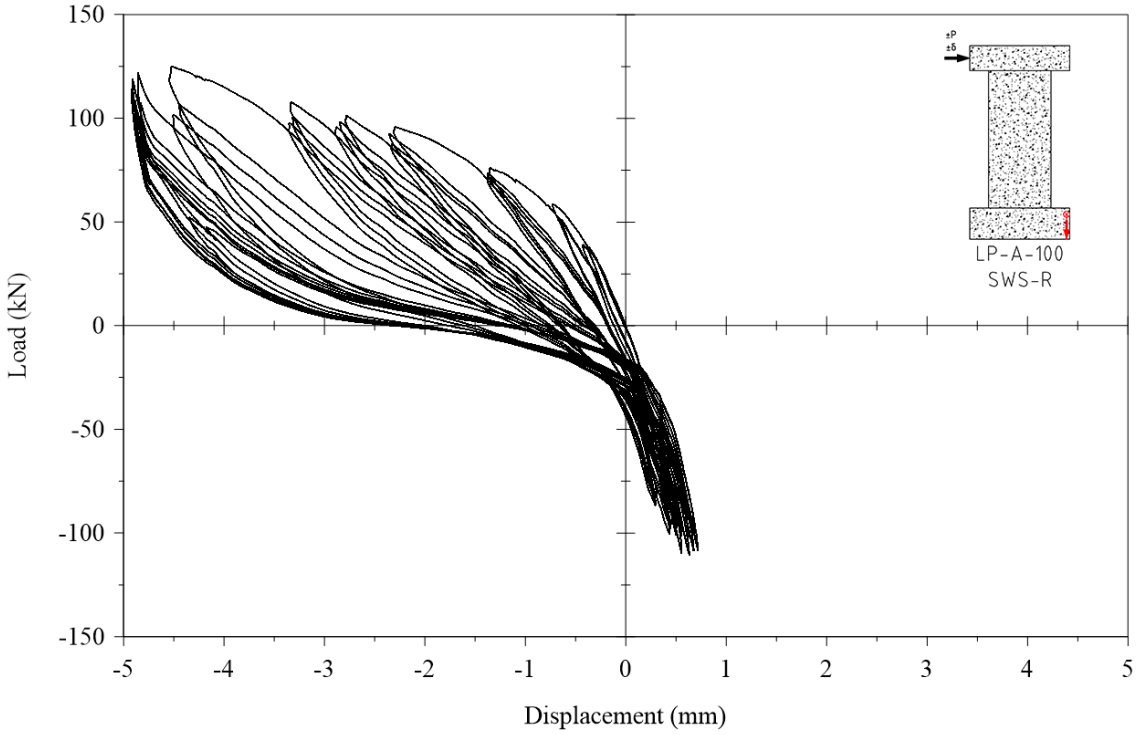

Figure C.15. Cyclic displacement response from LP-A-100.

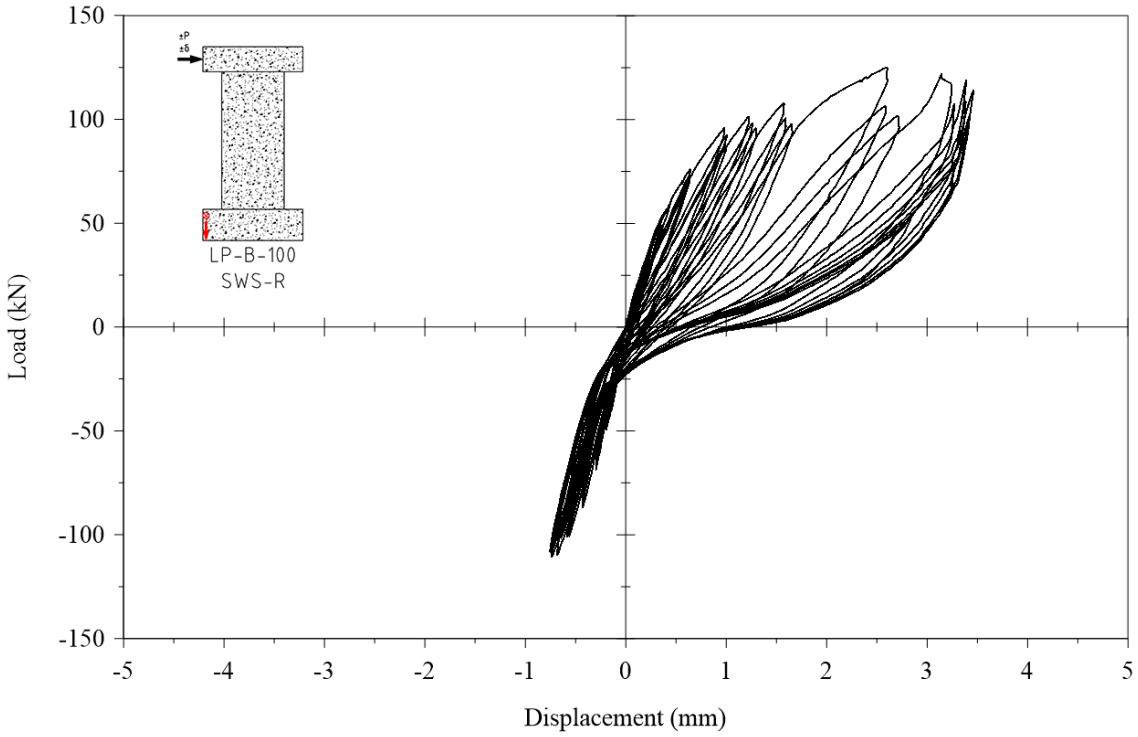

Figure C.16. Cyclic displacement response from LP-B-100.

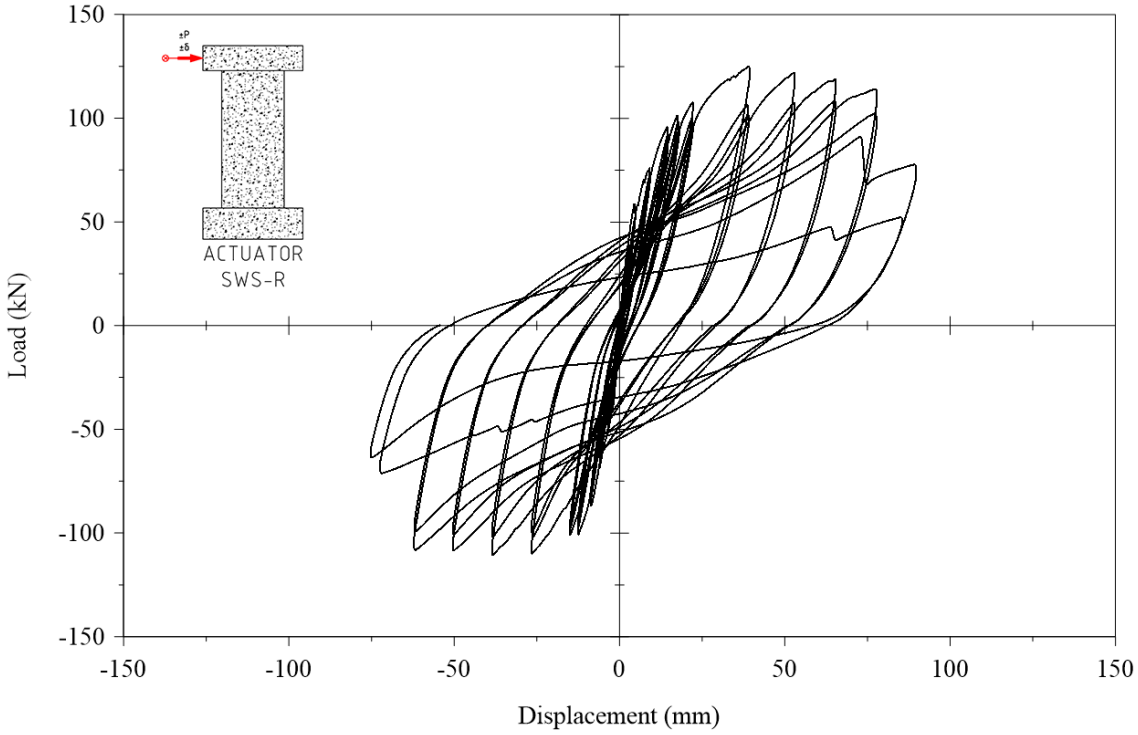

Figure C.17. Cyclic displacement response from hydraulic actuator.

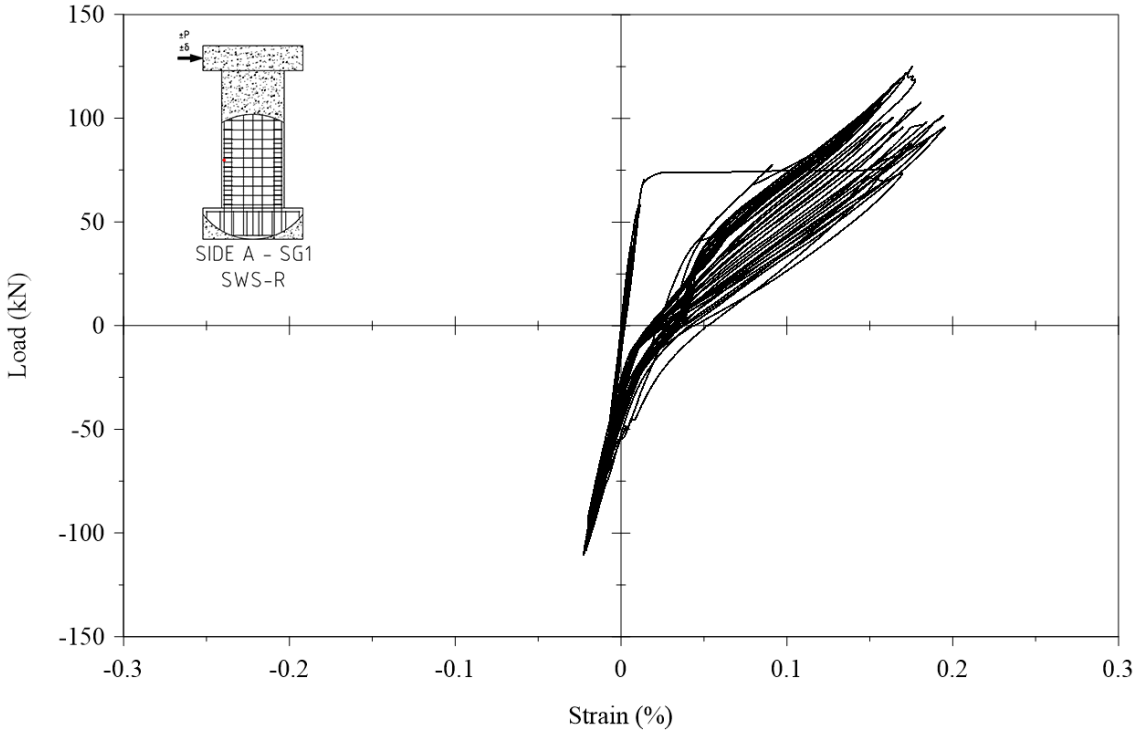

Figure C.18. Cyclic strain response from Strain Gauge 1.

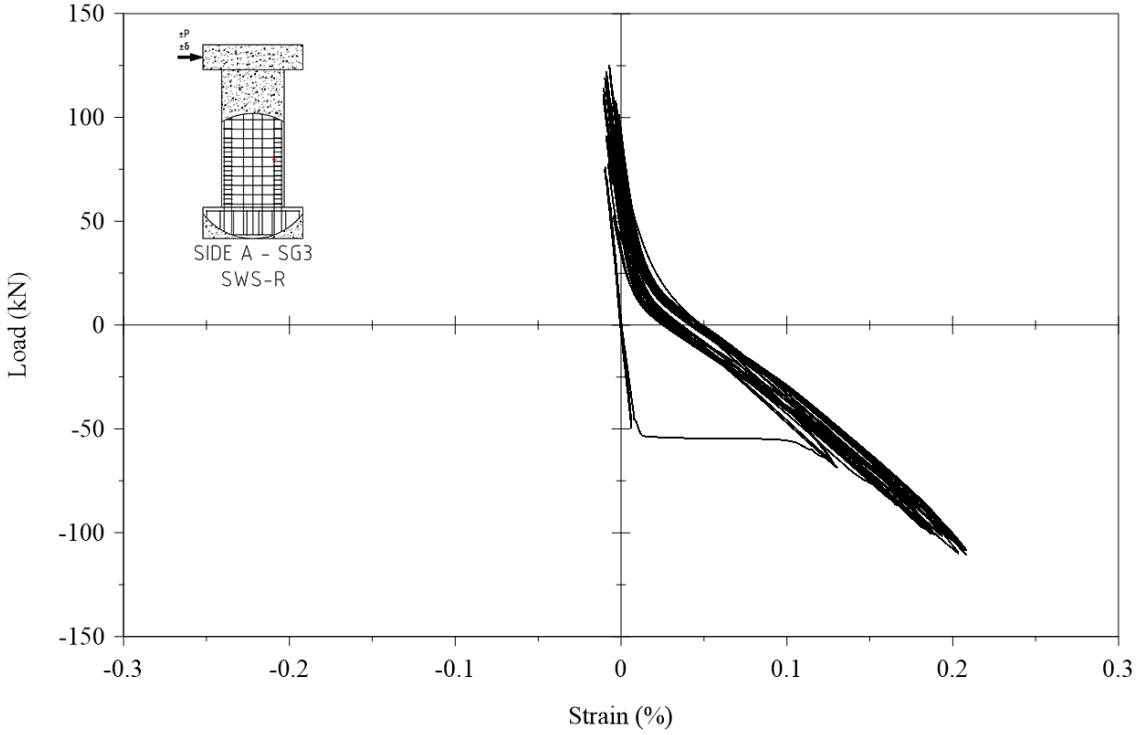

Figure C.19. Cyclic strain response from Strain Gauge 3.

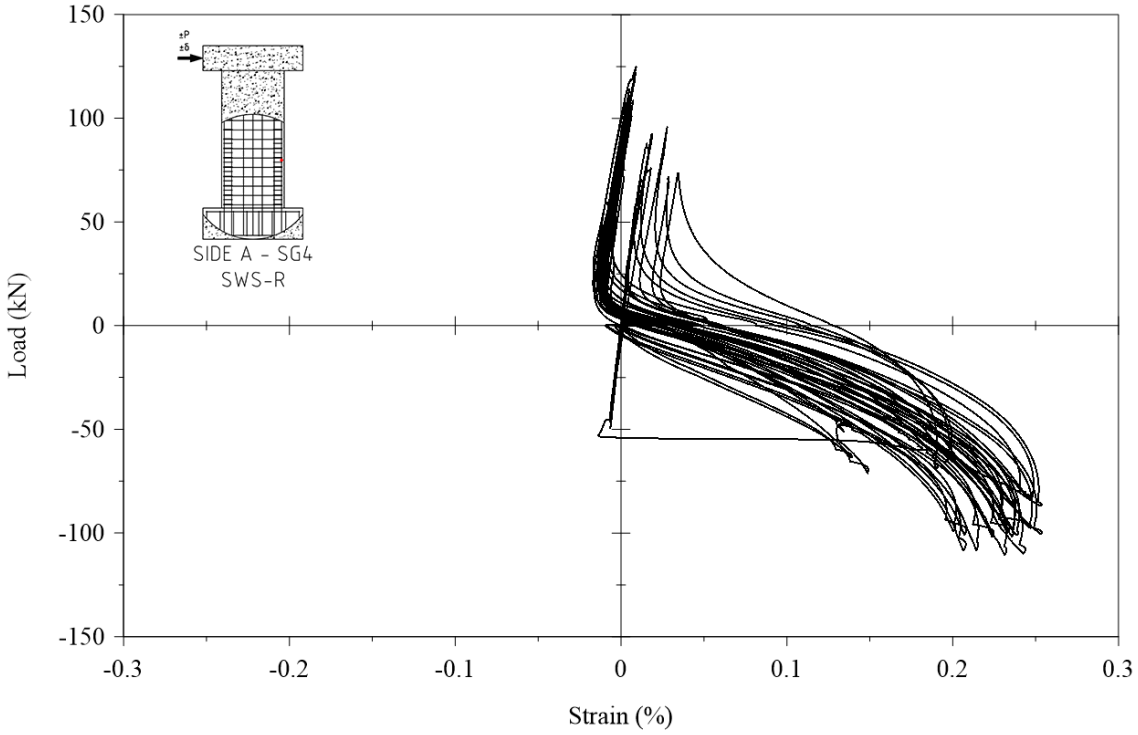

Figure C.20. Cyclic strain response from Strain Gauge 4.

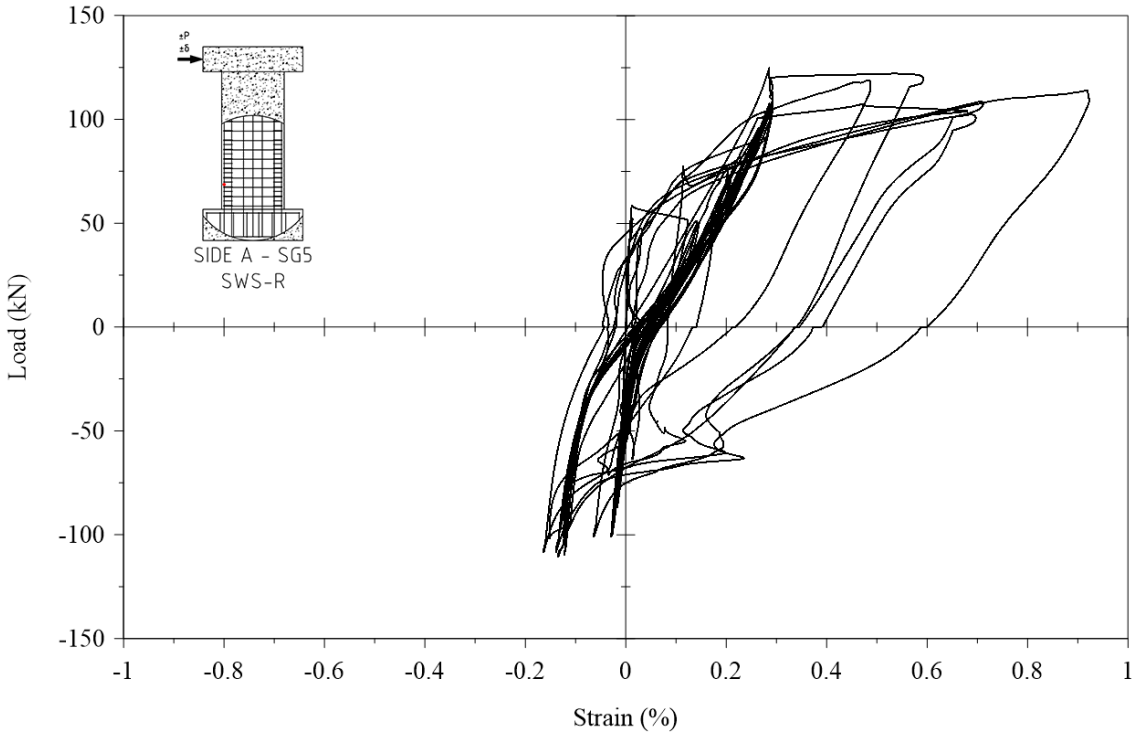

Figure C.21. Cyclic strain response from Strain Gauge 5.

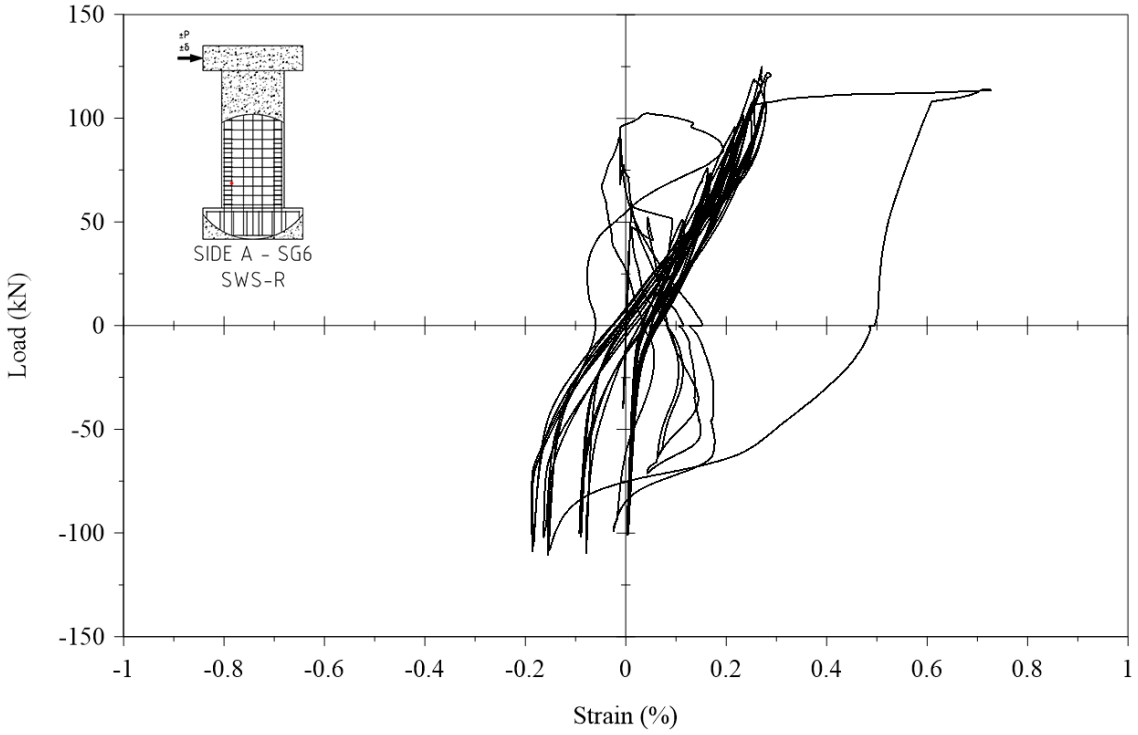

Figure C.22. Cyclic strain response from Strain Gauge 6.

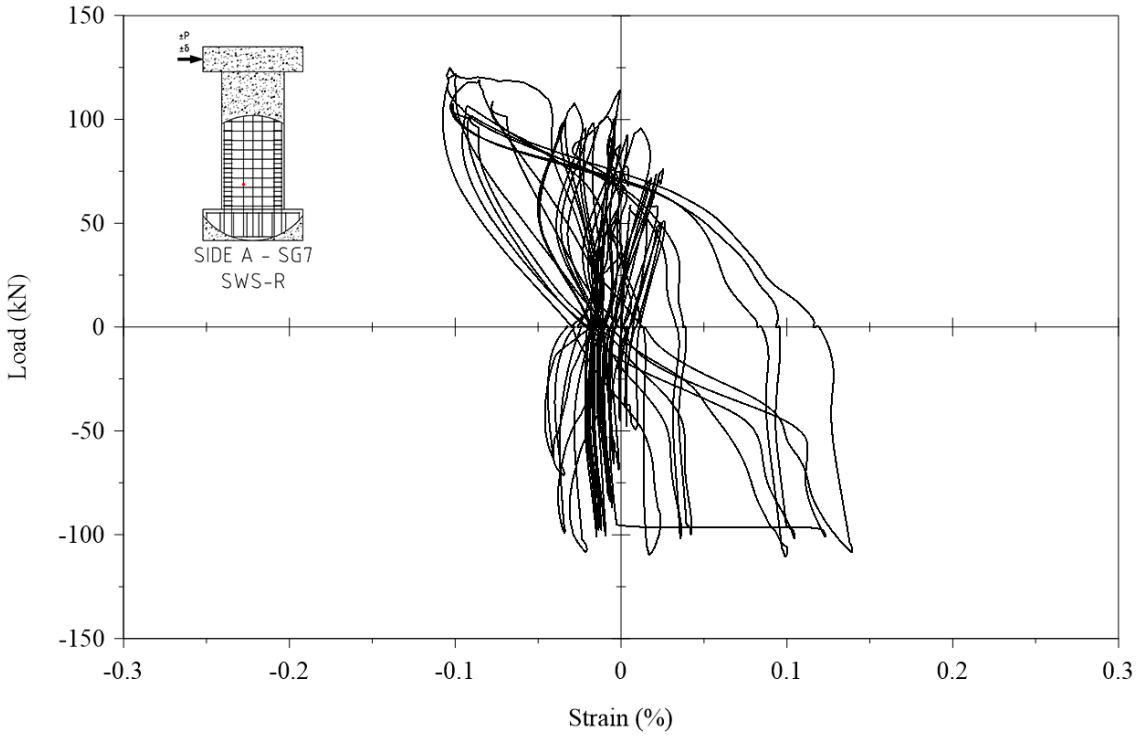

Figure C.23. Cyclic strain response from Strain Gauge 7.

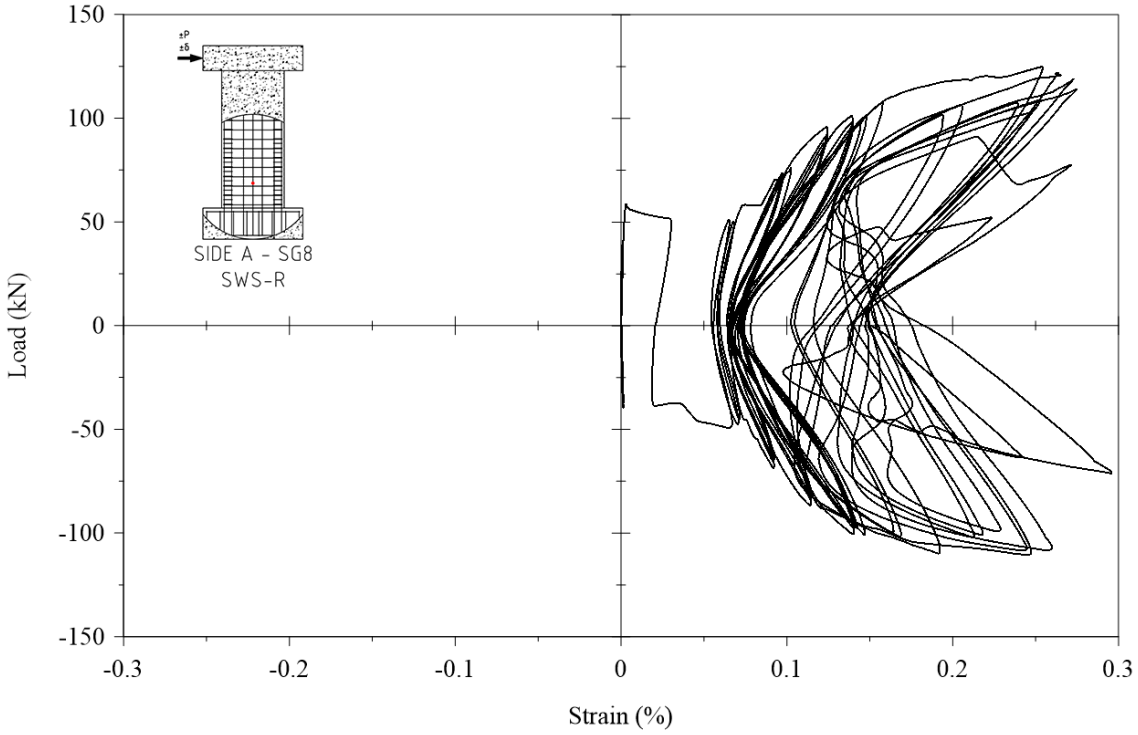

Figure C.24. Cyclic strain response from Strain Gauge 8.

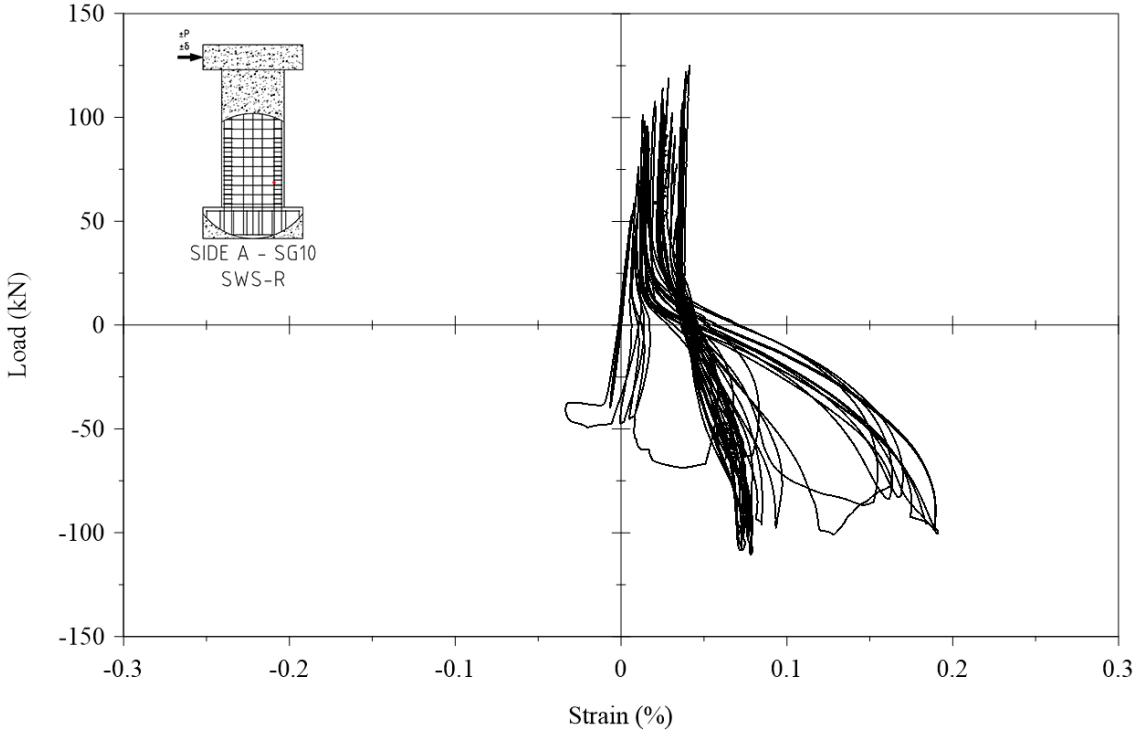

Figure C.25. Cyclic strain response from Strain Gauge 10.

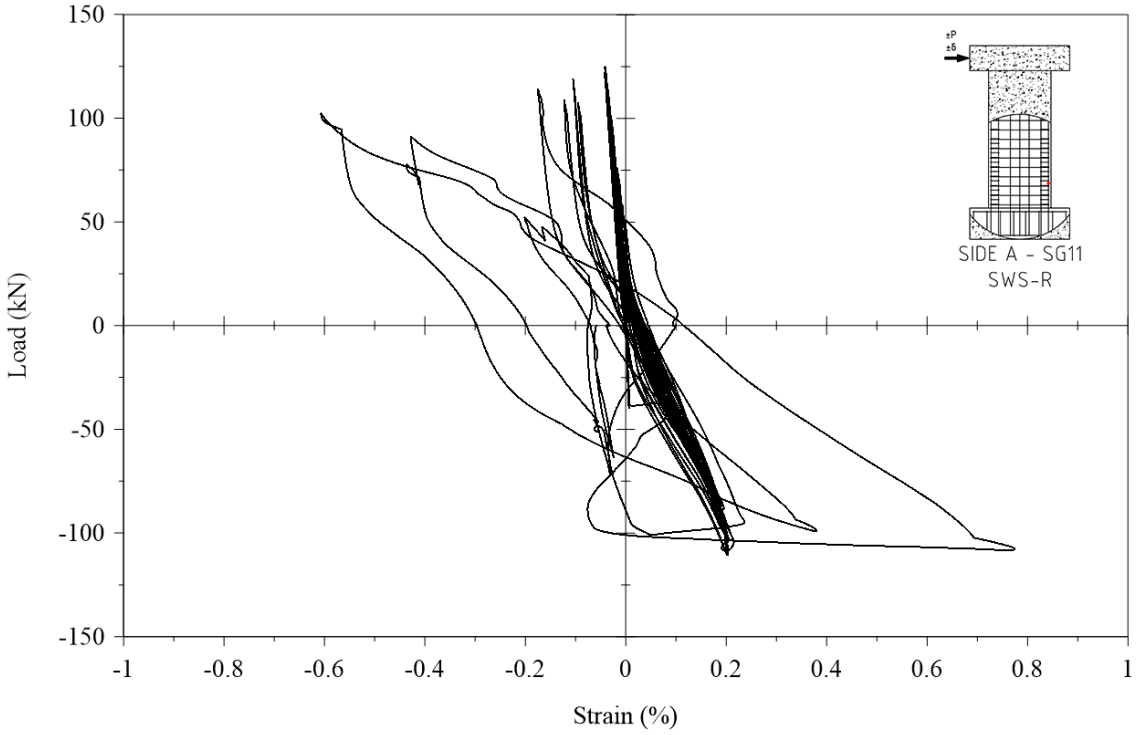

Figure C.26. Cyclic strain response from Strain Gauge 11.

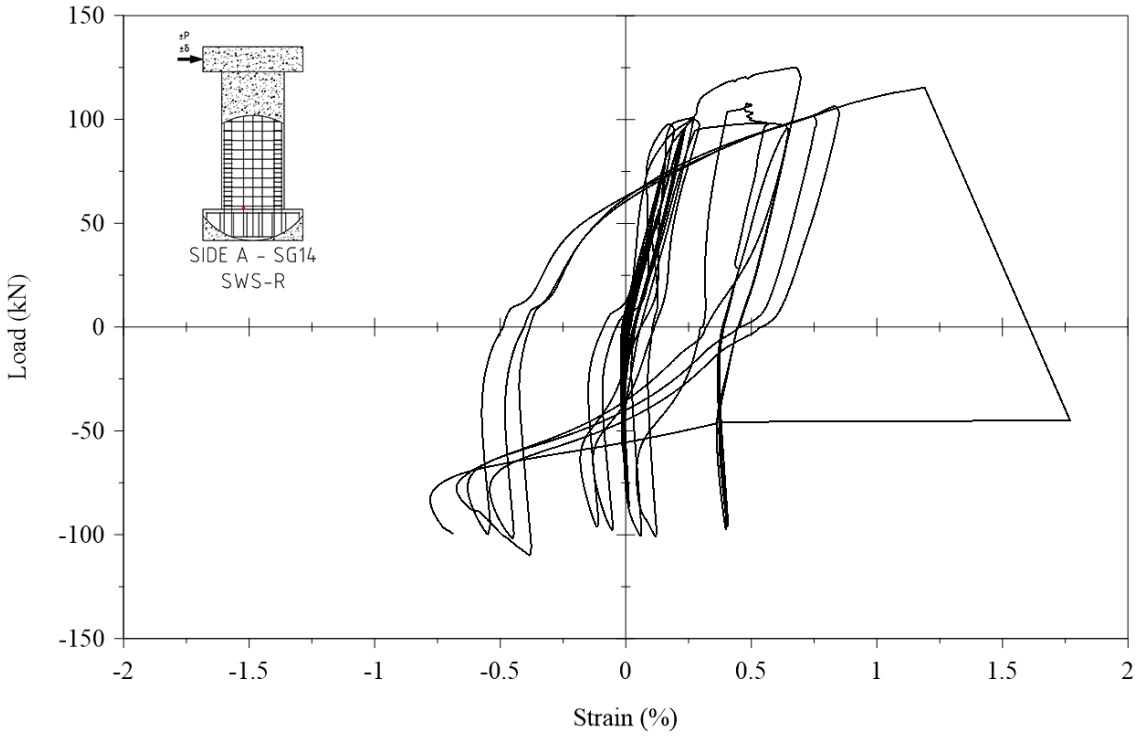

Figure C.27. Cyclic strain response from Strain Gauge 14.

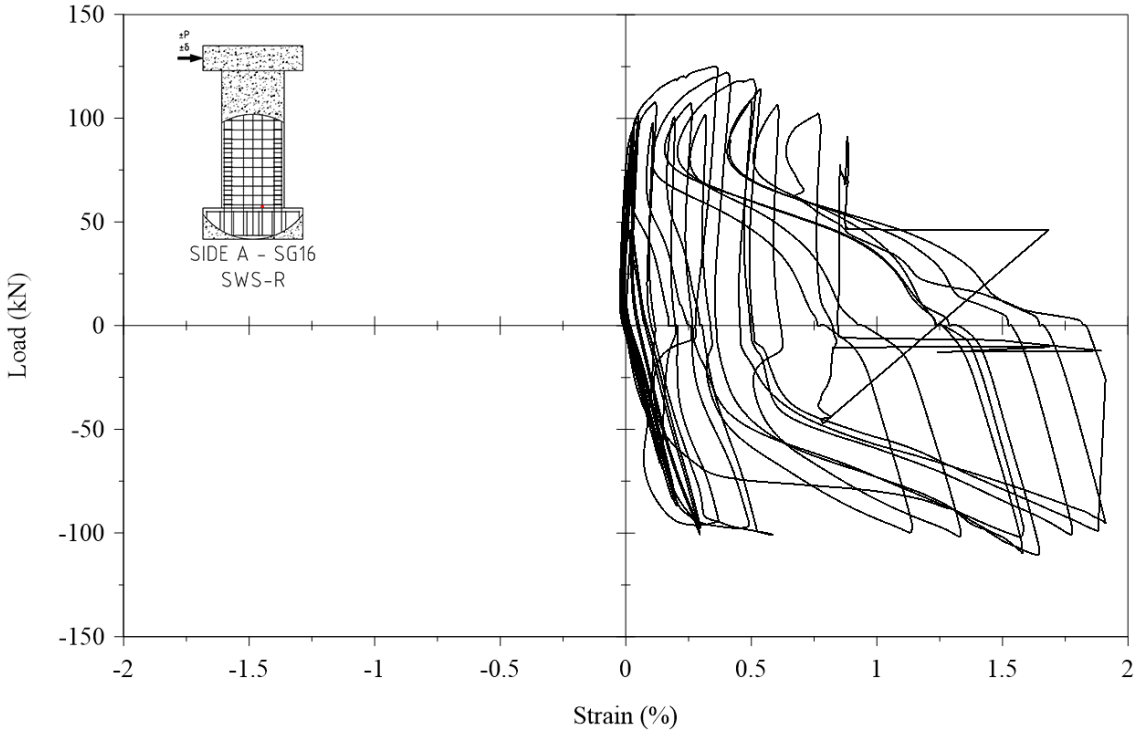

Figure C.28. Cyclic strain response from Strain Gauge 16.

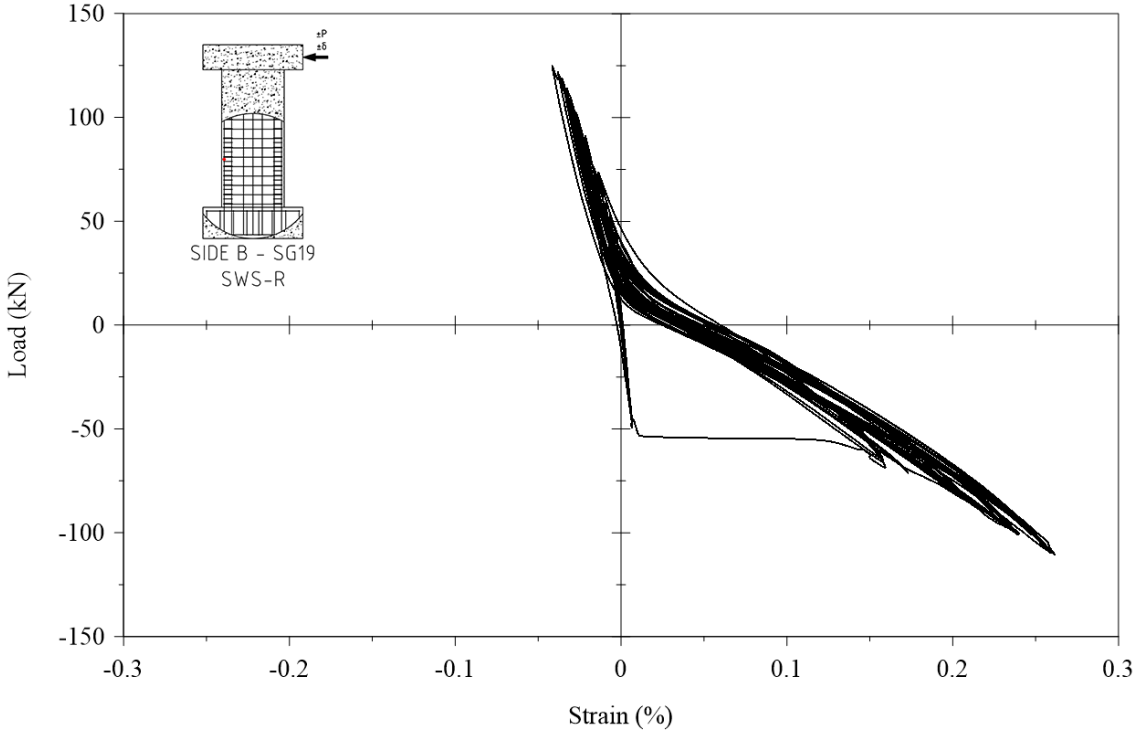

Figure C.29. Cyclic strain response from Strain Gauge 19.

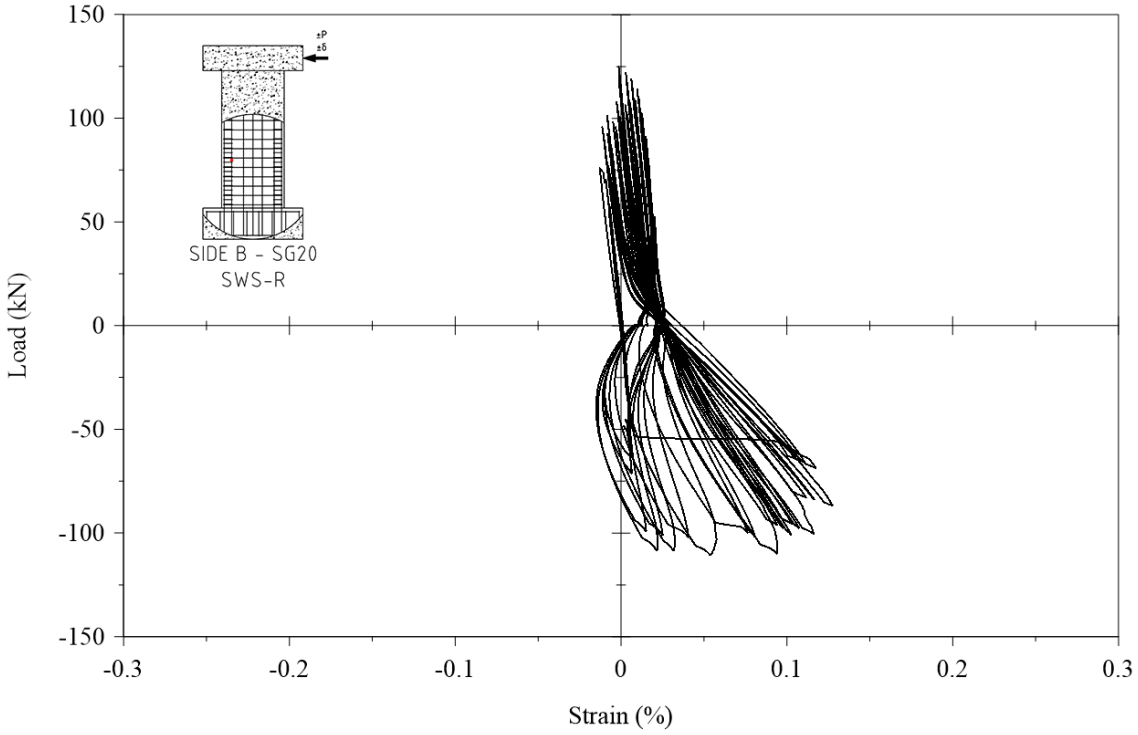

Figure C.30. Cyclic strain response from Strain Gauge 20.

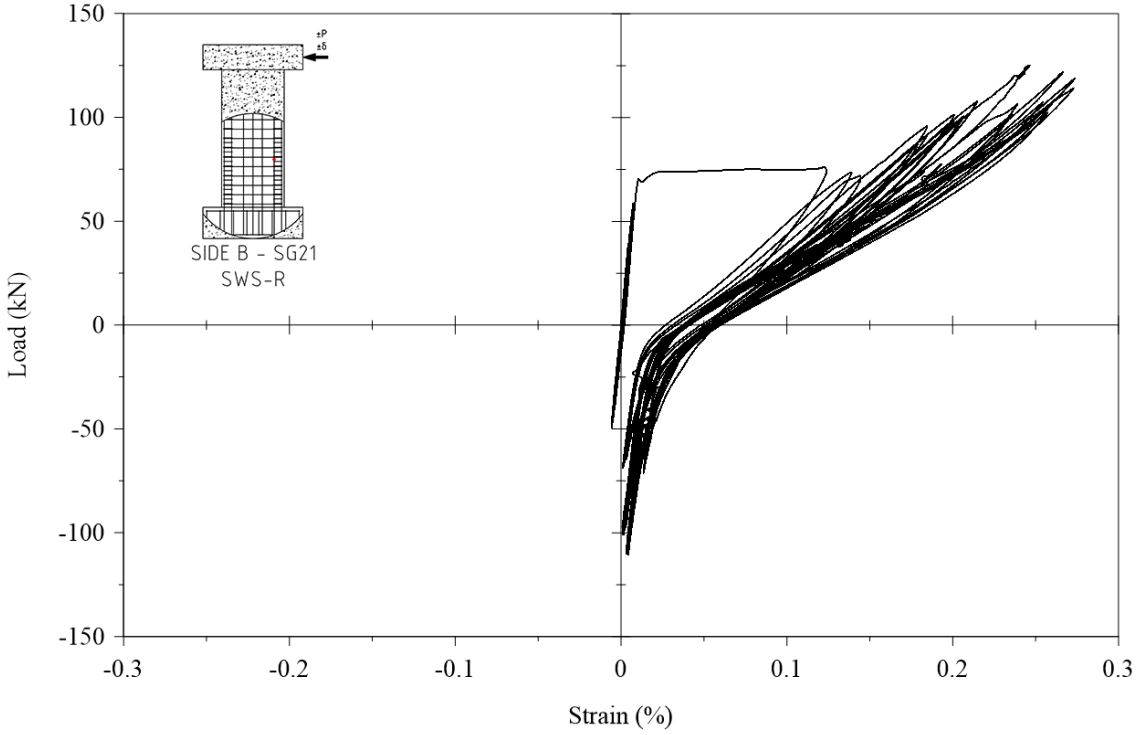

Figure C.31. Cyclic strain response from Strain Gauge 21.

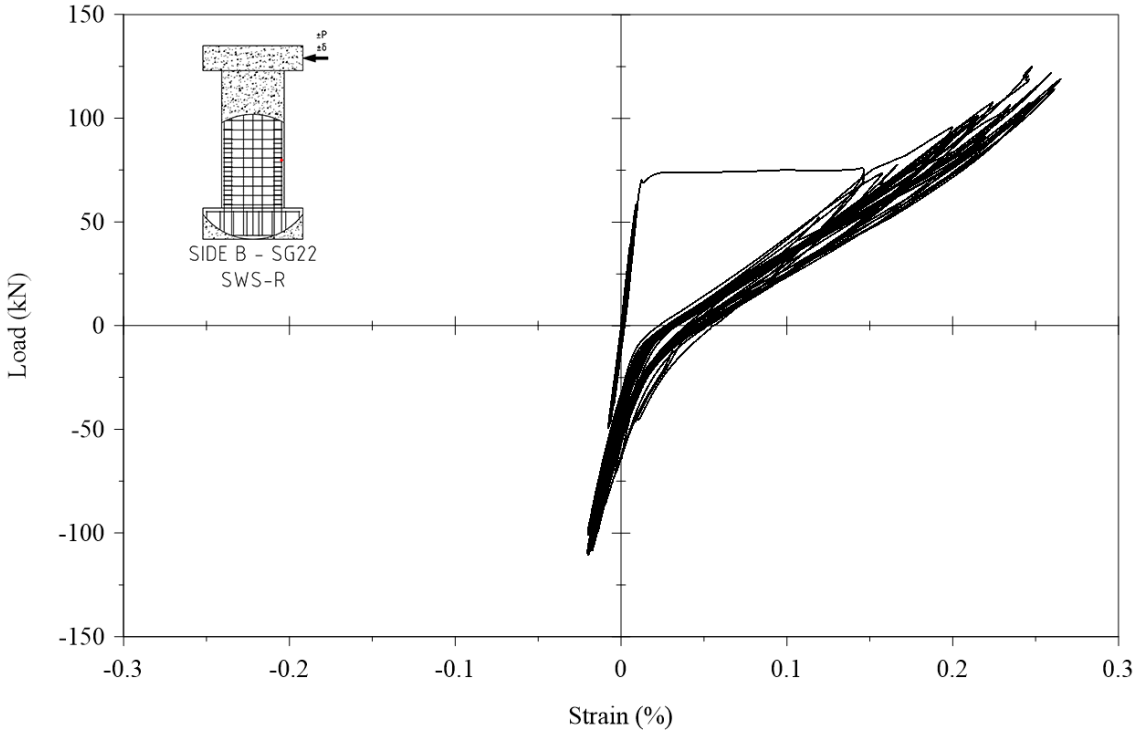

Figure C.32. Cyclic strain response from Strain Gauge 22.

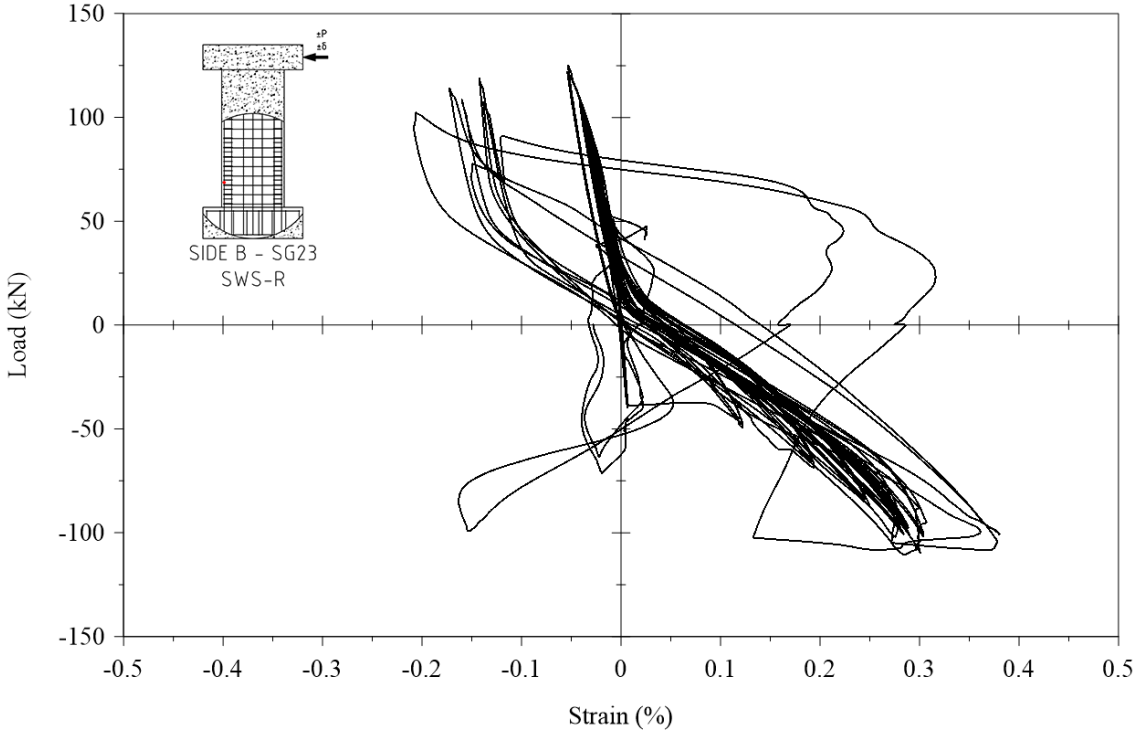

Figure C.33. Cyclic strain response from Strain Gauge 23.

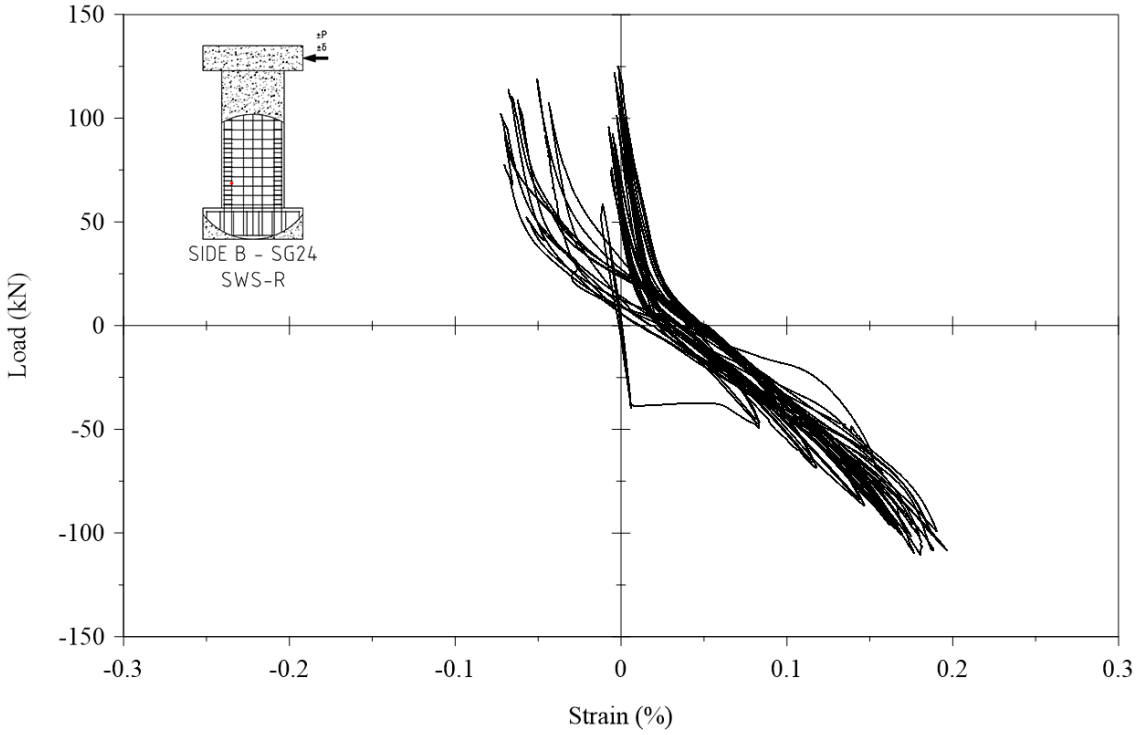

Figure C.34. Cyclic strain response from Strain Gauge 24.

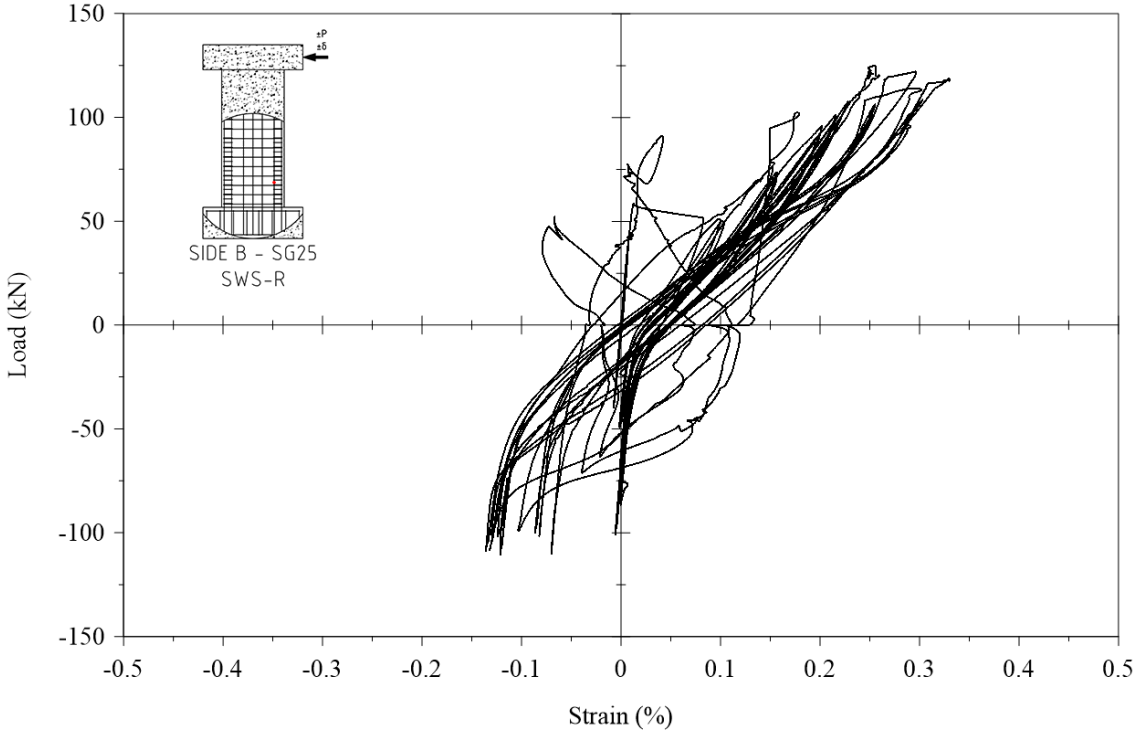

Figure C.35. Cyclic strain response from Strain Gauge 25.

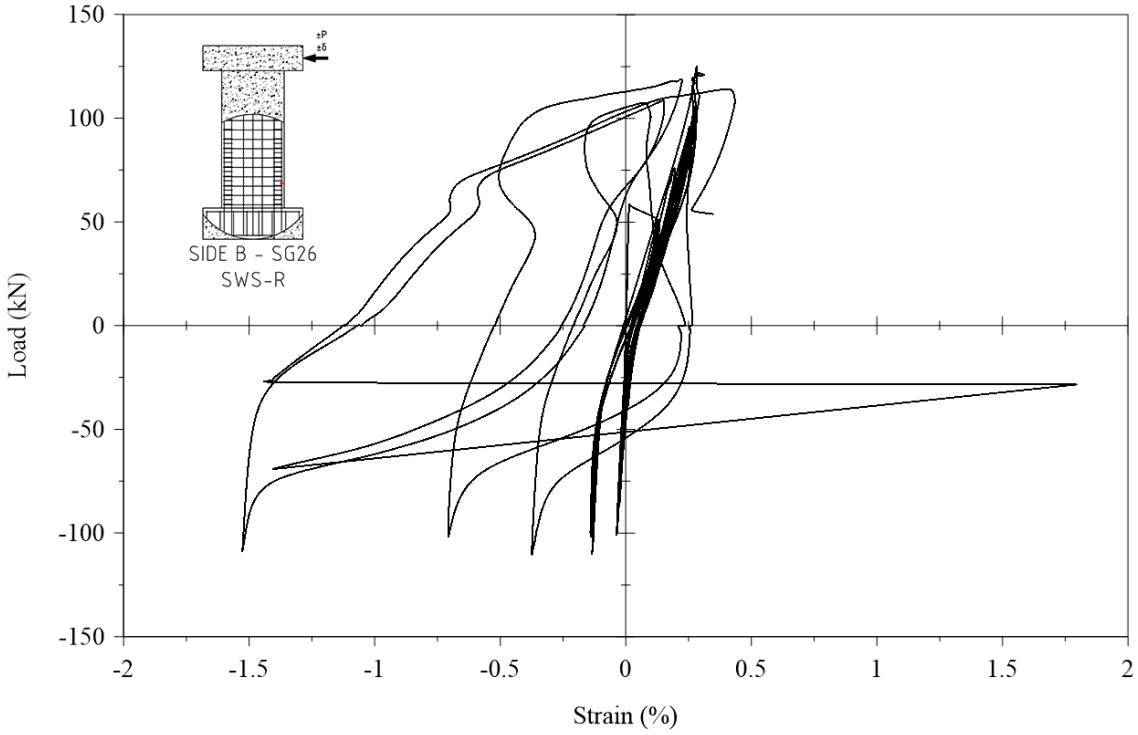

Figure C.36. Cyclic strain response from Strain Gauge 26.

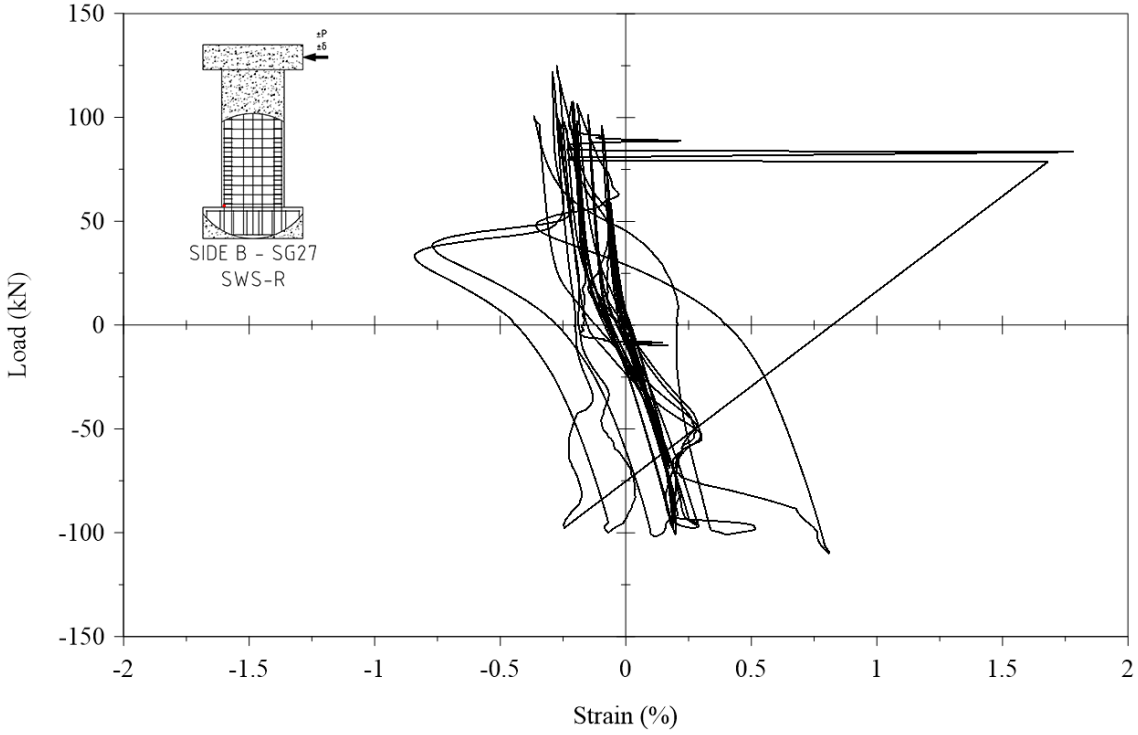

Figure C.37. Cyclic strain response from Strain Gauge 27.

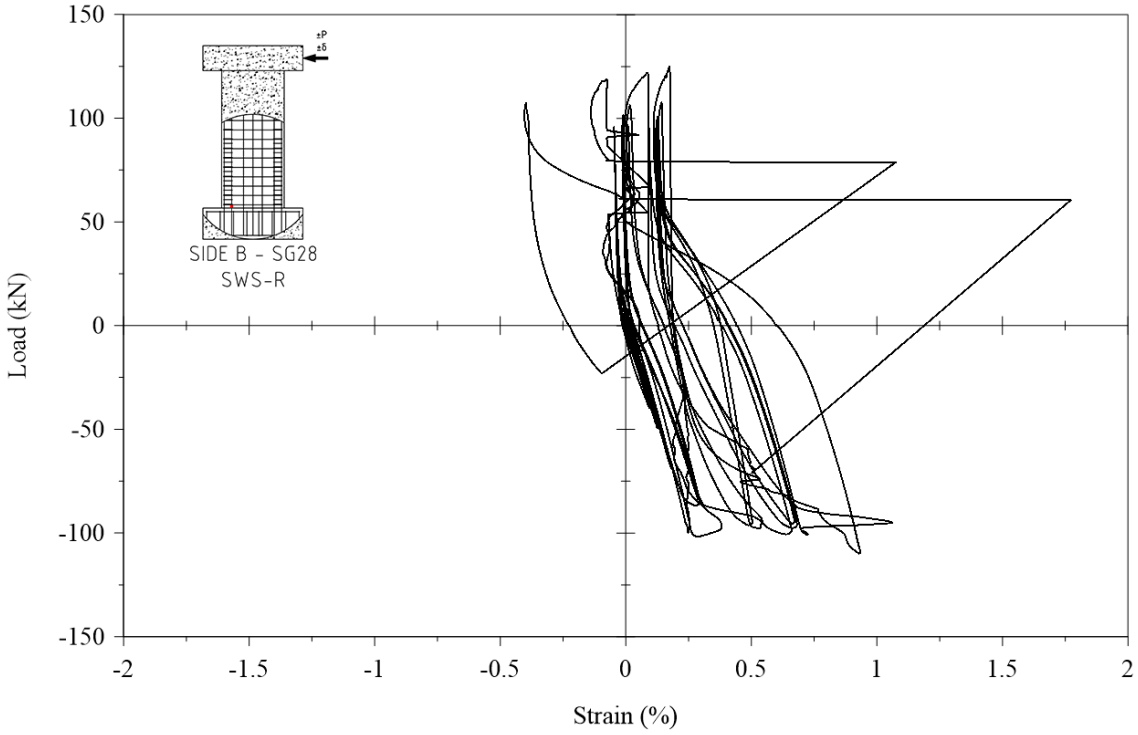

Figure C.38. Cyclic strain response from Strain Gauge 28.

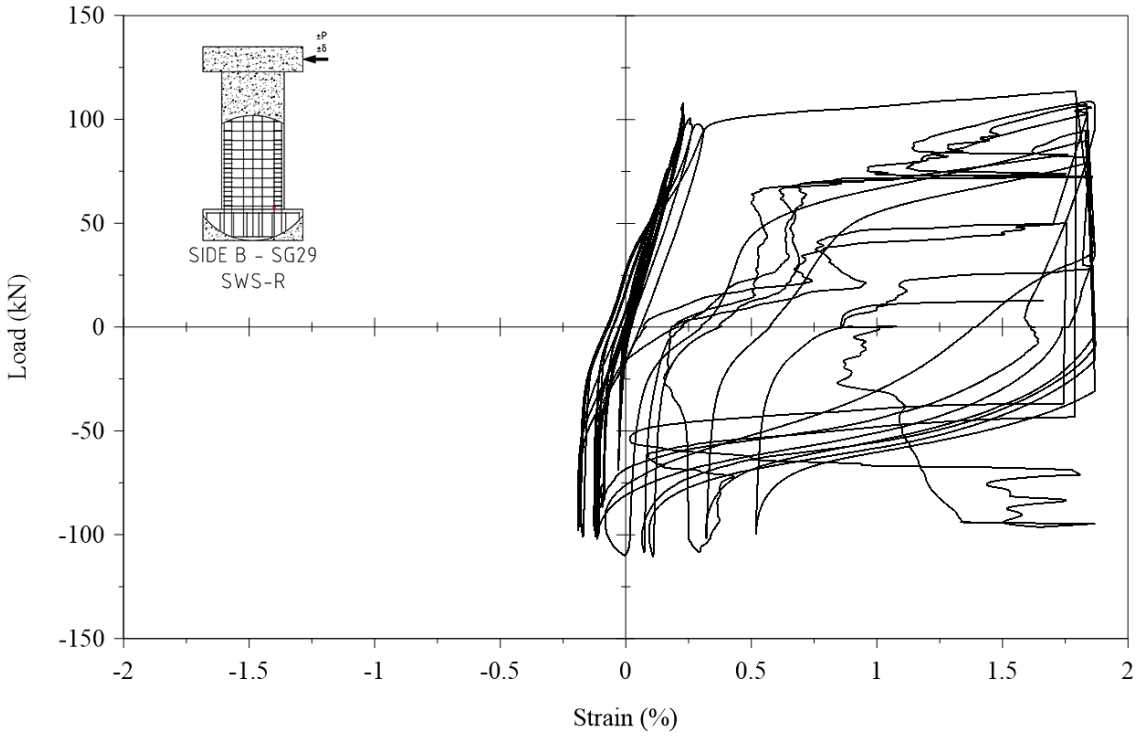

Figure C.39. Cyclic strain response from Strain Gauge 29.

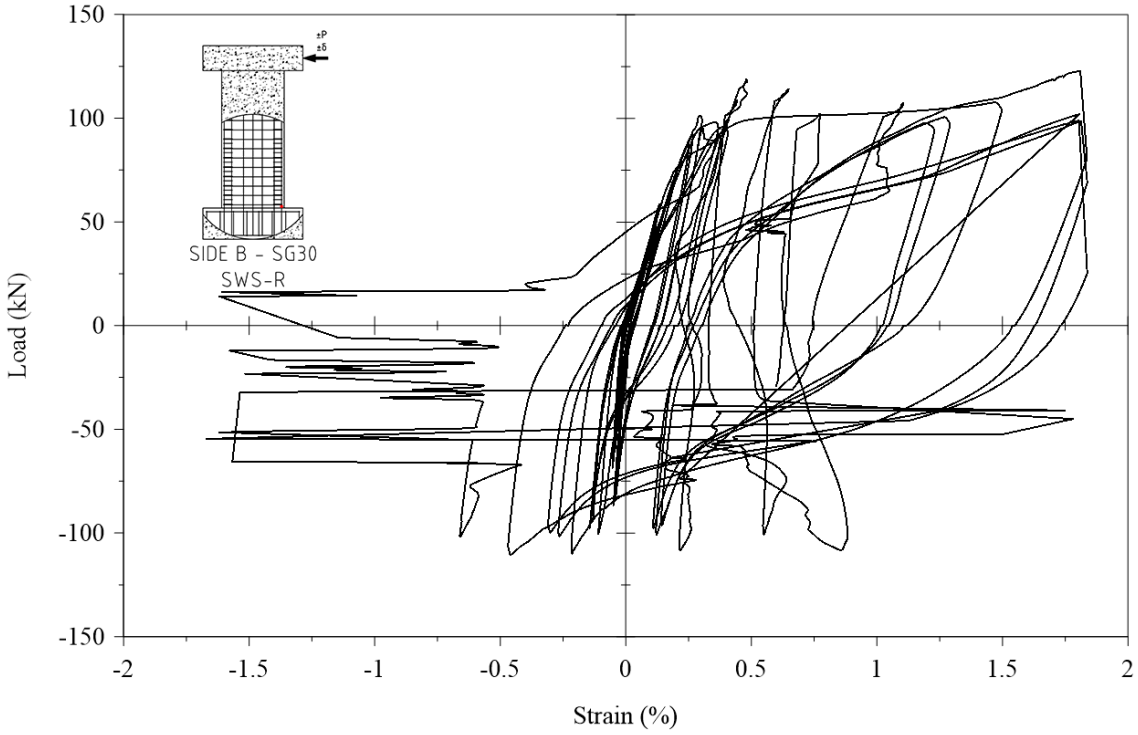

Figure C.40. Cyclic strain response from Strain Gauge 30.

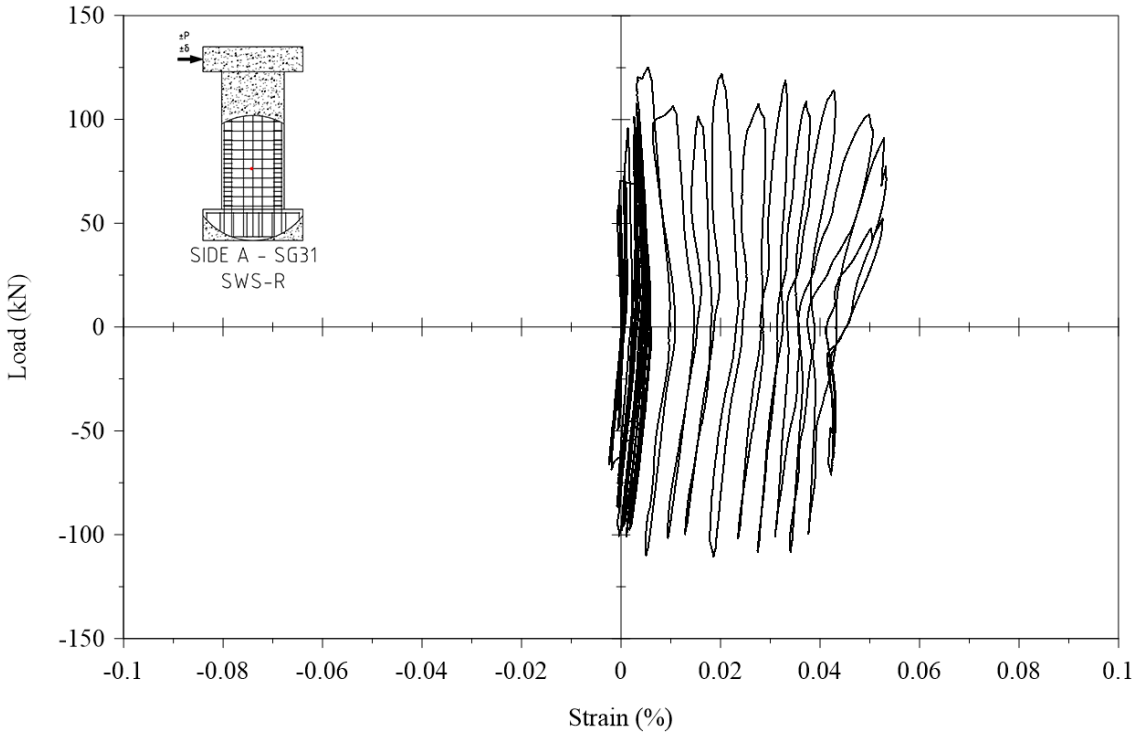

Figure C.41. Cyclic strain response from Strain Gauge 31.

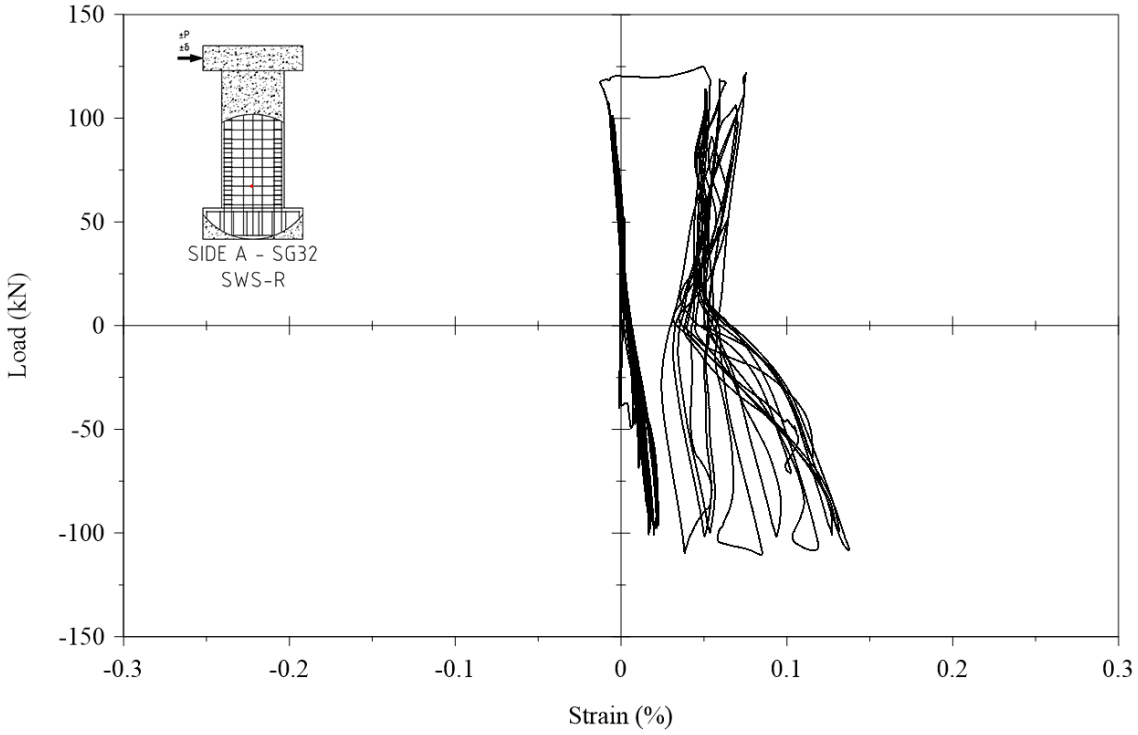

Figure C.42. Cyclic strain response from Strain Gauge 32.

Wall SWN Measurements and Raw Data

Table C.3. Nitinol SMA wall instrumentation identification and status

No.	Instrument	Type	Capacity	Purpose	Reference	Status
1	CP–A–300	CP	300mm	Sliding	Foundation Block	Active
2	CP–B–300	CP	300mm	Slip	Test Frame	Active
3	CP–C–300	CP	300mm	Vertical Displacement	Foundation Block	Active
4	CP–D–300	CP	300mm	Vertical Displacement	Foundation Block	Active
5	CP–A–600	CP	600mm	Lateral Displacement	Test Frame	Active
6	CP–B–600	CP	600mm	Lateral Displacement	Instrumentation Frame	Active
7	CP–C–600	CP	600mm	Lateral Displacement	Instrumentation Frame	Active
8	CP–D–600	CP	600mm	Vertical Displacement	Foundation Block	Active
9	CP–E–600	CP	600mm	Vertical Displacement	Foundation Block	Active
10	CP–A–1250	CP	1250mm	Shear	Plastic Hinge	Active
11	CP–B–1250	CP	1250mm	Shear	Plastic Hinge	Active
12	CP–C–1250	CP	1250mm	Shear	Plastic Hinge	Active
13	CP–D–1250	CP	1250mm	Shear	Plastic Hinge	Active
14	CP–E–1250	CP	1250mm	Lateral Displacement	Instrumentation Frame	Active
15	LP–A–100	LP	100mm	Uplift	Strong Floor	Active
16	LP–B–100	LP	100mm	Uplift	Strong Floor	Active
17	Actuator–P	Load Cell	±250kN	Force	Strong Wall	Active
18	Actuator–δ	LVDT	±250mm	Displacement	Strong Wall	Active

CP denotes Cable Potentiometer

LP denotes Linear Potentiometer

Table C.4. Nitinol SMA wall strain gauges identification and status

No.	Instrument	Strain Capacity	Location	Notes	Status
1	SGY1	15 – 20% max.	Side A – Left Boundary		Active
2	SGY2	15 – 20% max.	Side A – Left Boundary		Active
3	SGY3	15 – 20% max.	Side A – Right Boundary		Active
4	SGY4	15 – 20% max.	Side A – Right Boundary		Active
5	SGY5	15 – 20% max.	Side A – Left Boundary		Active
6	SGY6	15 – 20% max.	Side A – Left Boundary		Active
7	SG7	2 – 4% max.	Side A – Web	No Room	Disconnected
8	SG8	2 – 4% max.	Side A – Web	No Room	Disconnected
9	SG9	2 – 4% max.	Side A – Web	No Room	Disconnected
10	SGY10	15 – 20% max.	Side A – Right Boundary		Active
11	SGY11	15 – 20% max.	Side A – Right Boundary		Active
12	SGY12	15 – 20% max.	Side A – Left Boundary		Active
13	SGY13	15 – 20% max.	Side A – Left Boundary	No Room	Disconnected
14	SG14	2 – 4% max.	Side A – Web		Active
15	SG15	2 – 4% max.	Side A – Web		Active
16	SG16	2 – 4% max.	Side A – Web		Active
17	SGY17	15 – 20% max.	Side A – Right Boundary		Active
18	SGY18	15 – 20% max.	Side A – Right Boundary		Active
19	SG19	2 – 4% max.	Side B – Right Boundary		Active
20	SG20	2 – 4% max.	Side B – Right Boundary		Active
21	SG21	2 – 4% max.	Side B – Left Boundary		Active
22	SG22	2 – 4% max.	Side B – Left Boundary		Active
23	SG23	2 – 4% max.	Side B – Right Boundary		Active
24	SG24	2 – 4% max.	Side B – Right Boundary		Active
25	SG25	2 – 4% max.	Side B – Left Boundary		Active
26	SG26	2 – 4% max.	Side B – Left Boundary		Active
27	SG27	2 – 4% max.	Side B – Right Boundary		Active

28	SG28	2 – 4% max.	Side B – Right Boundary		Active
29	SG29	2 – 4% max.	Side B – Left Boundary		Active
30	SG30	2 – 4% max.	Side B – Left Boundary		Active
31	SG31	2 – 4% max.	Side A – Top Stirrup		Active
32	SG32	2 – 4% max.	Side A – Middle Stirrup		Active
33	SG33	2 – 4% max.	Side A – Bottom Stirrup		Active
34	SG–A	2 – 4% max.	Side A – Left Boundary		Active
35	SG–B	2 – 4% max.	Side A – Right Boundary		Active
36	SG–C	2 – 4% max.	Side B – Right Boundary	No Room	Disconnected
37	SG–D	2 – 4% max.	Side B – Left Boundary		Active

SG denotes Standard Strain Gauge

SGY denotes Post Yield Strain Gauge

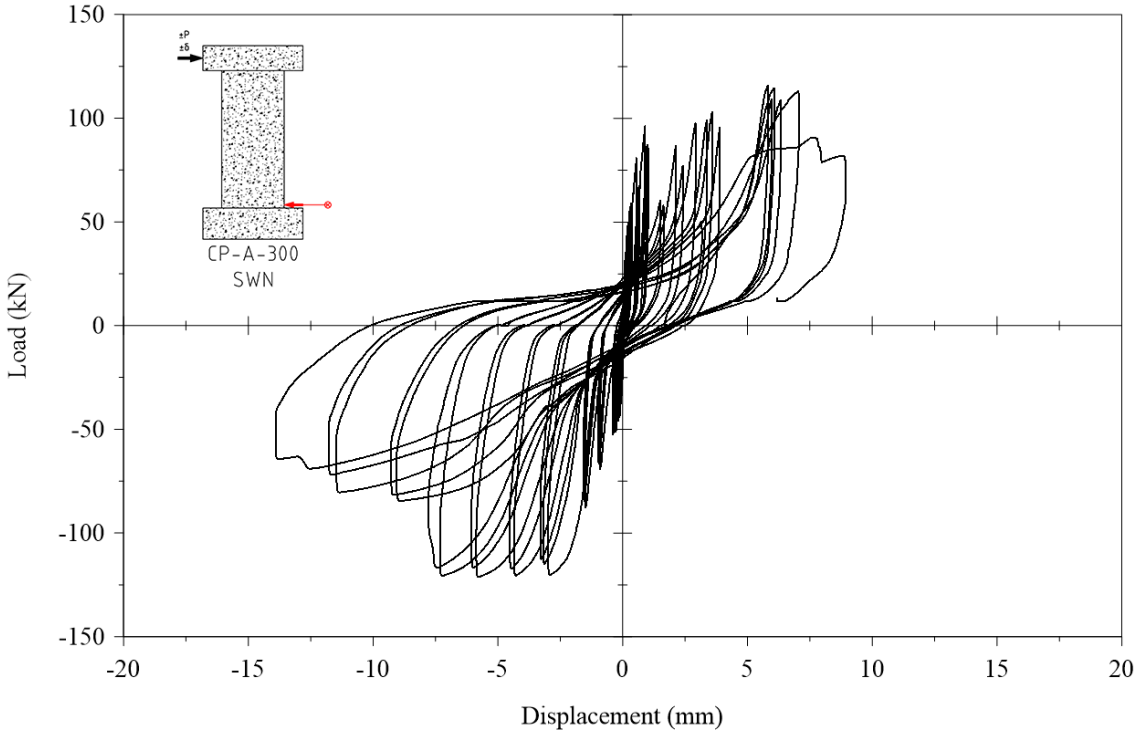

Figure C.43. Cyclic displacement response from CP-A-300.

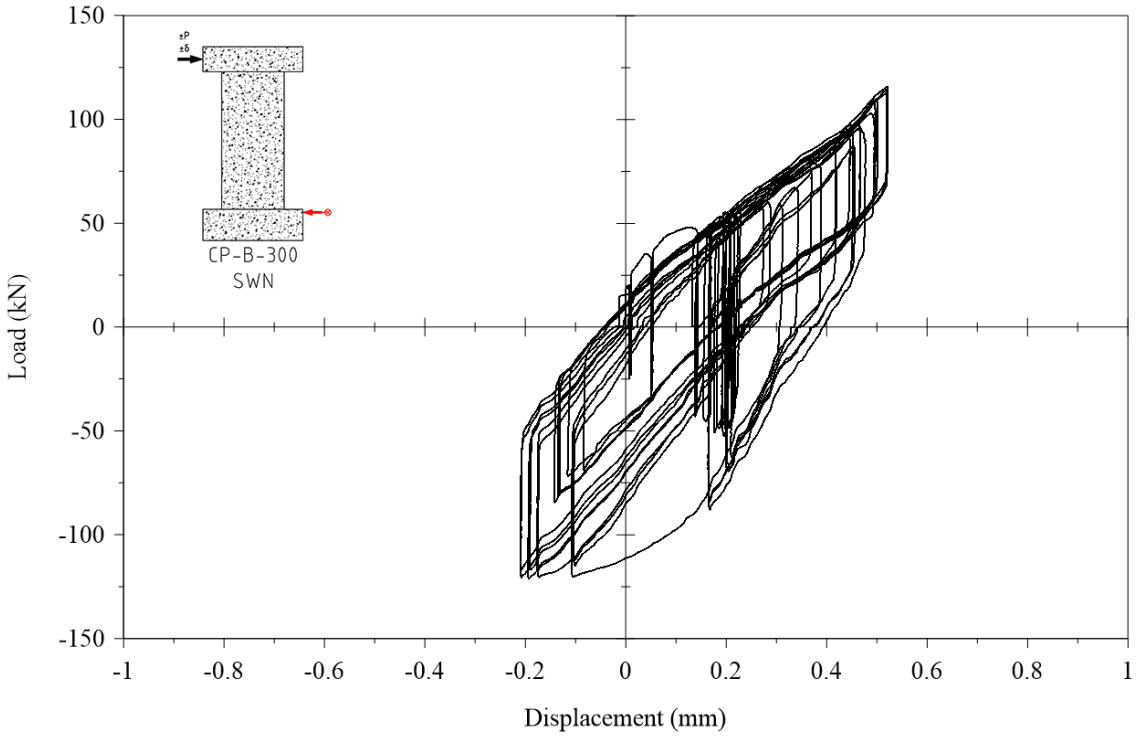

Figure C.44. Cyclic displacement response from CP-B-300.

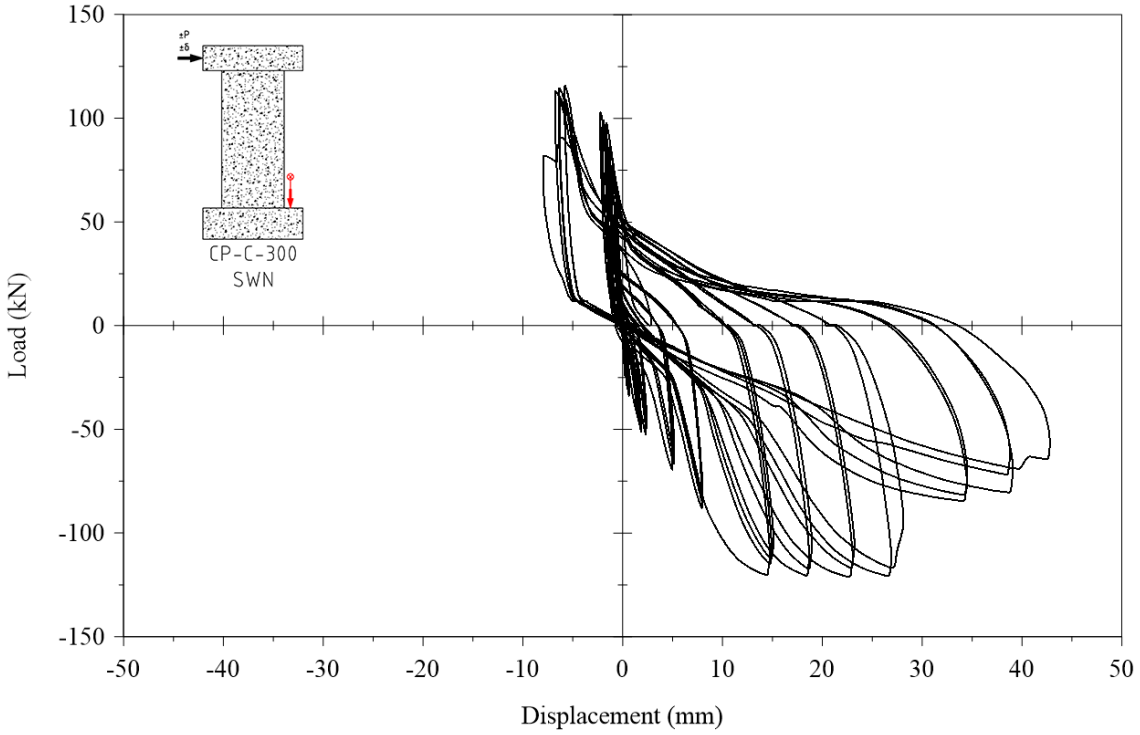

Figure C.45. Cyclic displacement response from CP-C-300.

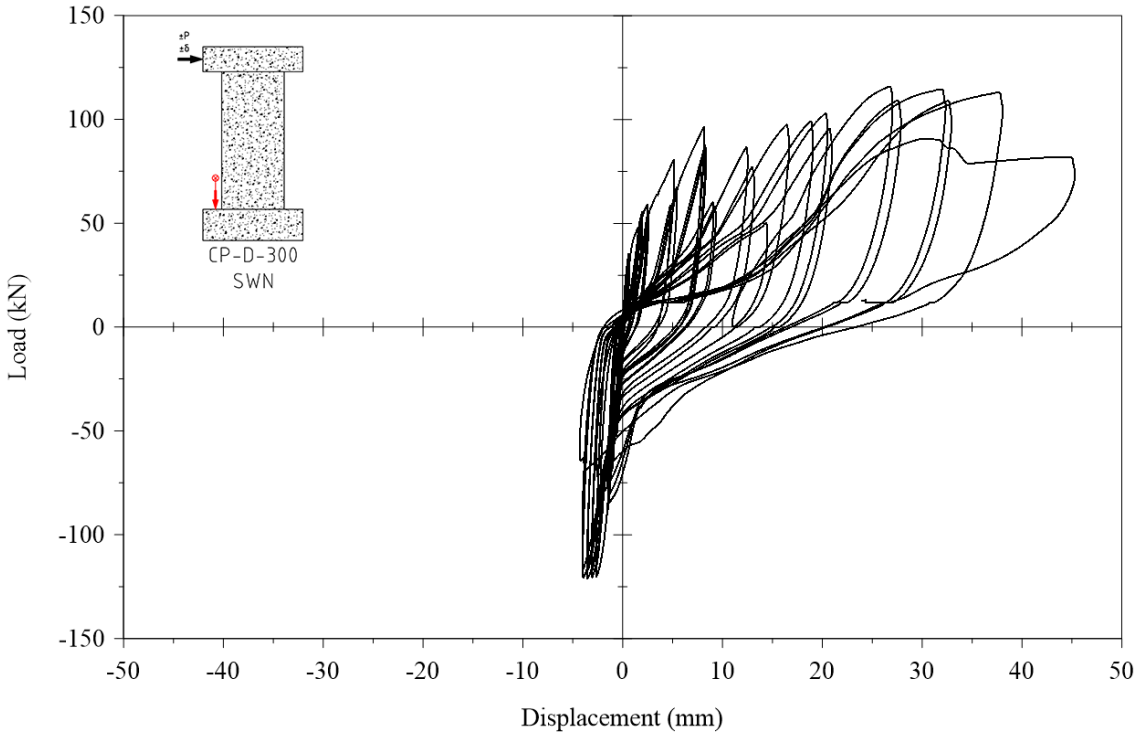

Figure C.46. Cyclic displacement response from CP-D-300.

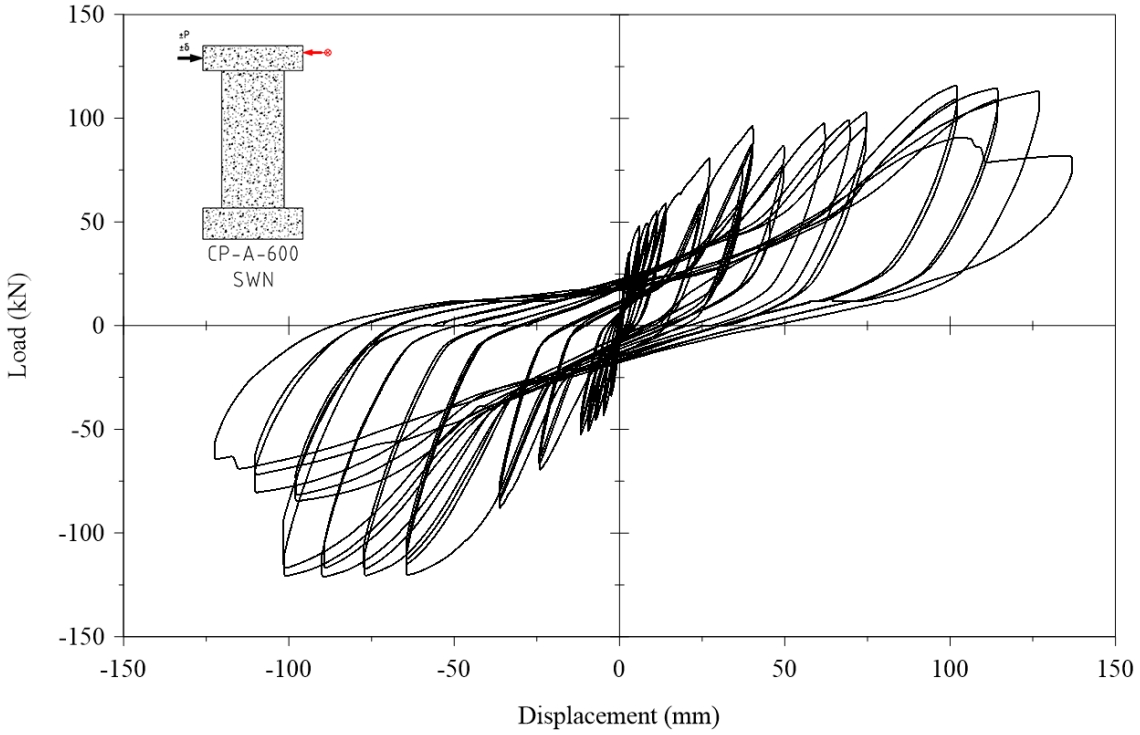

Figure C.47. Cyclic displacement response from CP-A-600.

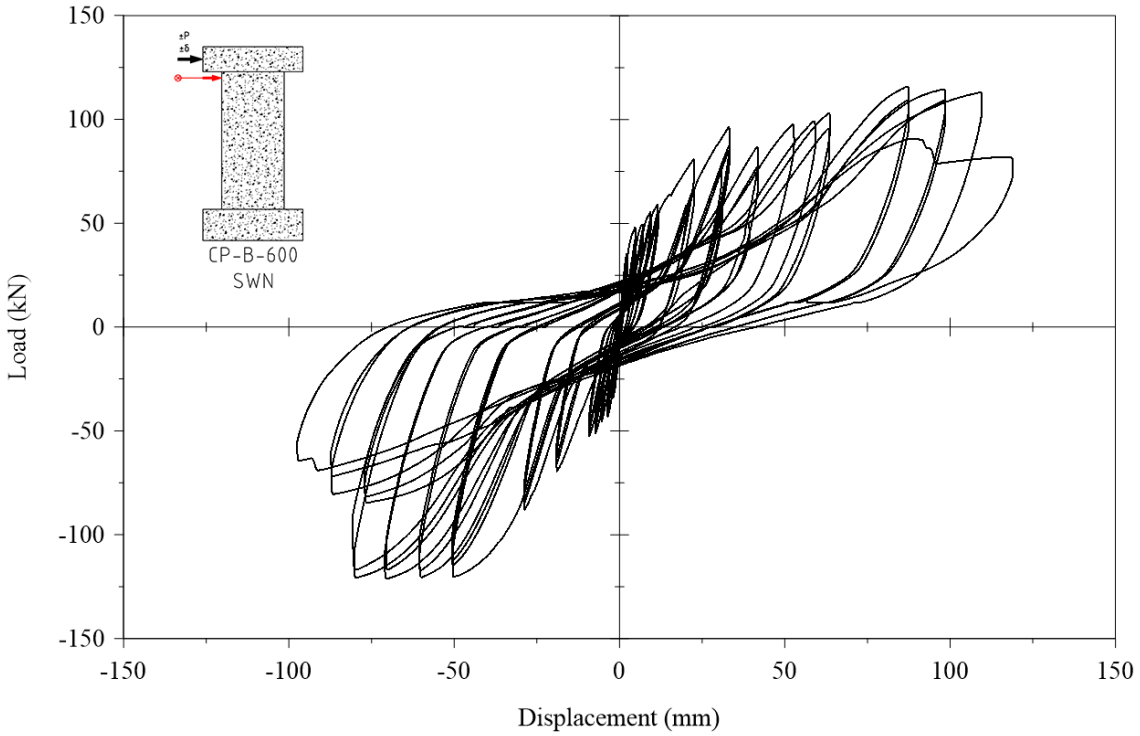

Figure C.48. Cyclic displacement response from CP-B-600.

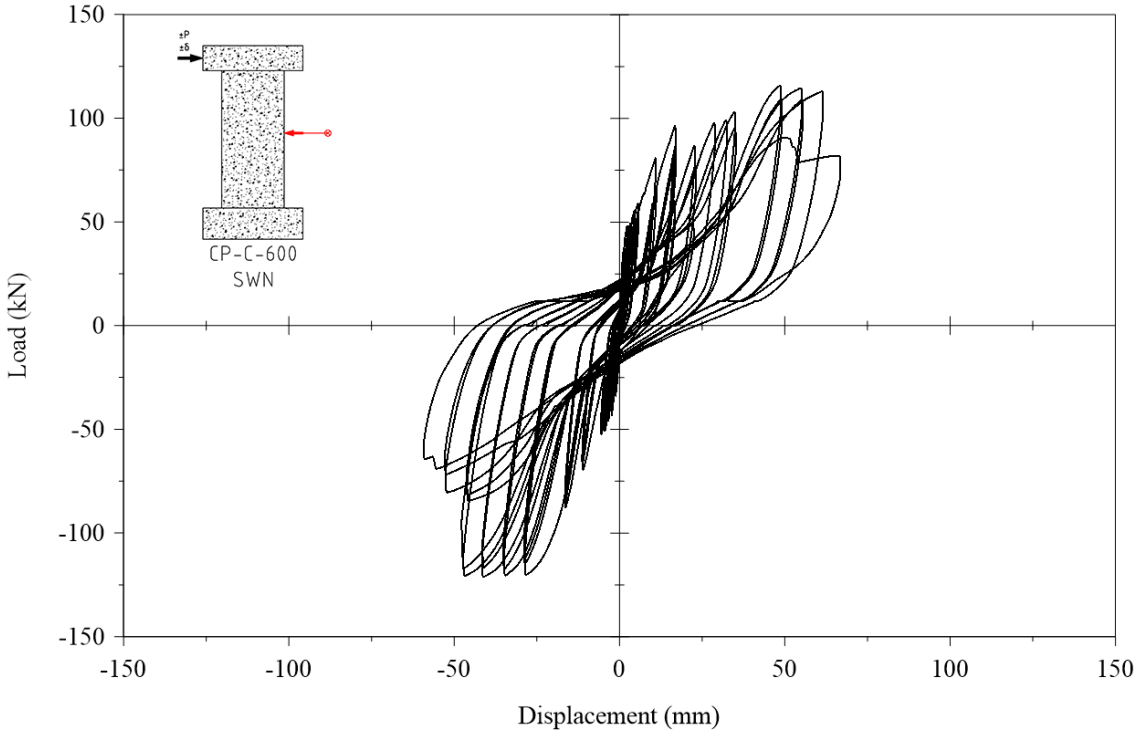

Figure C.49. Cyclic displacement response from CP-C-600.

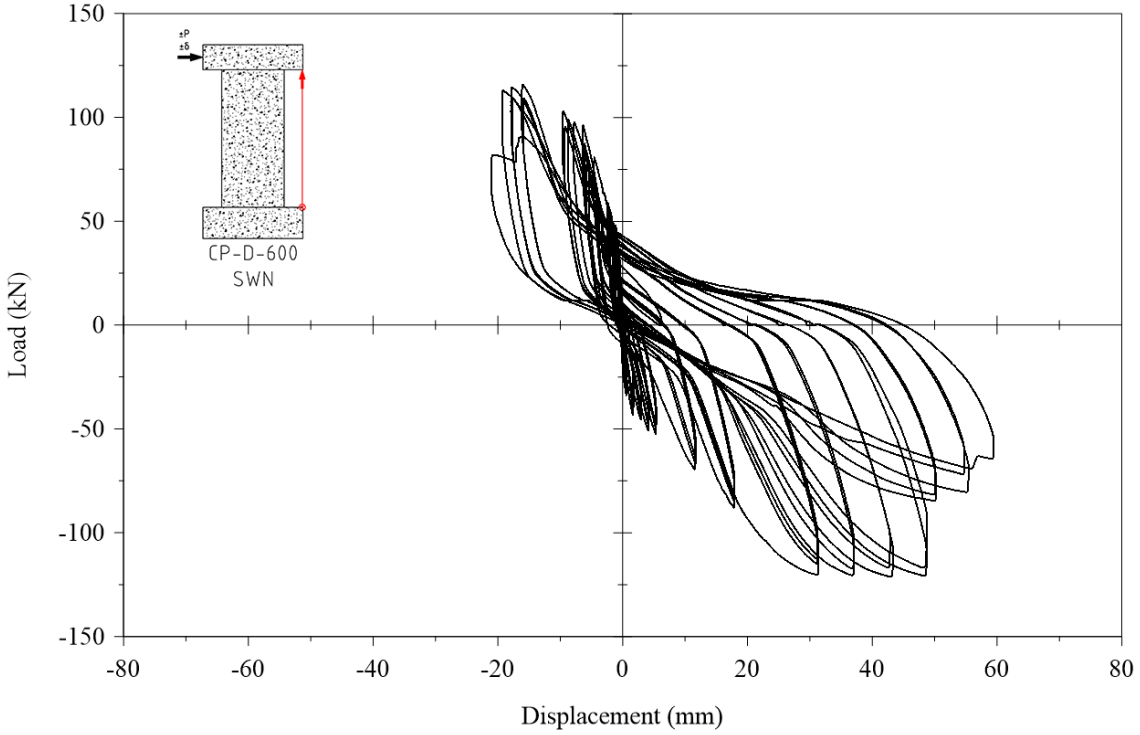

Figure C.50. Cyclic displacement response from CP-D-600.

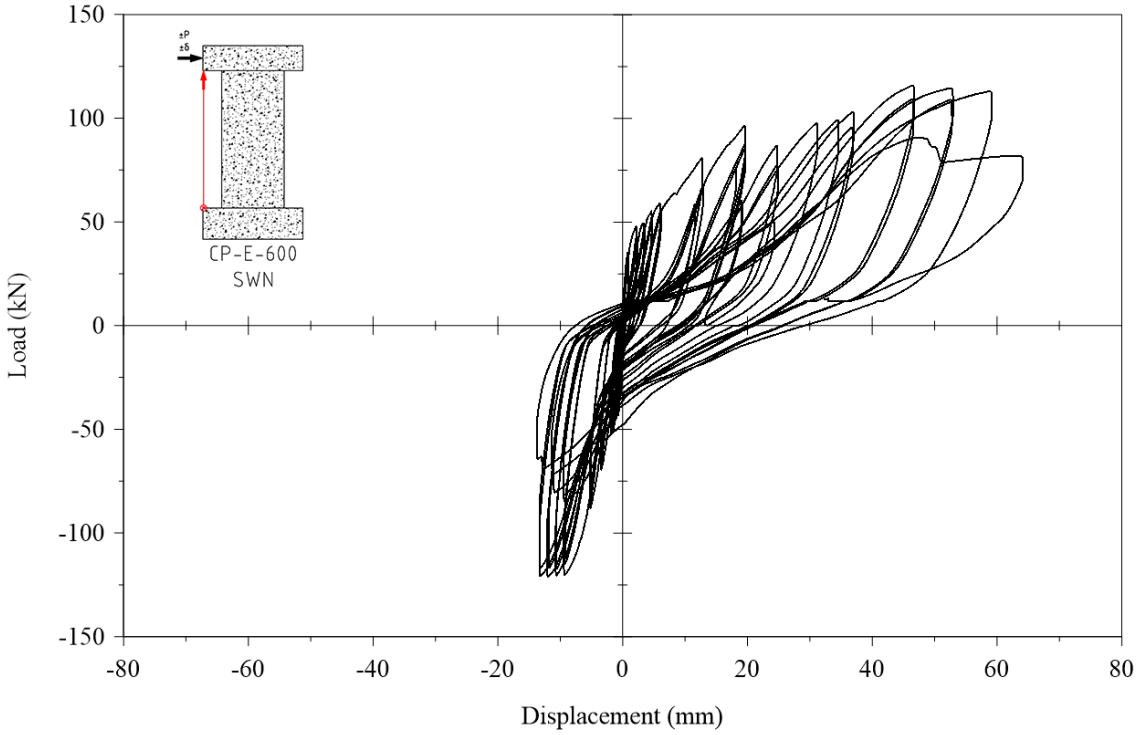

Figure C.51. Cyclic displacement response from CP-E-600.

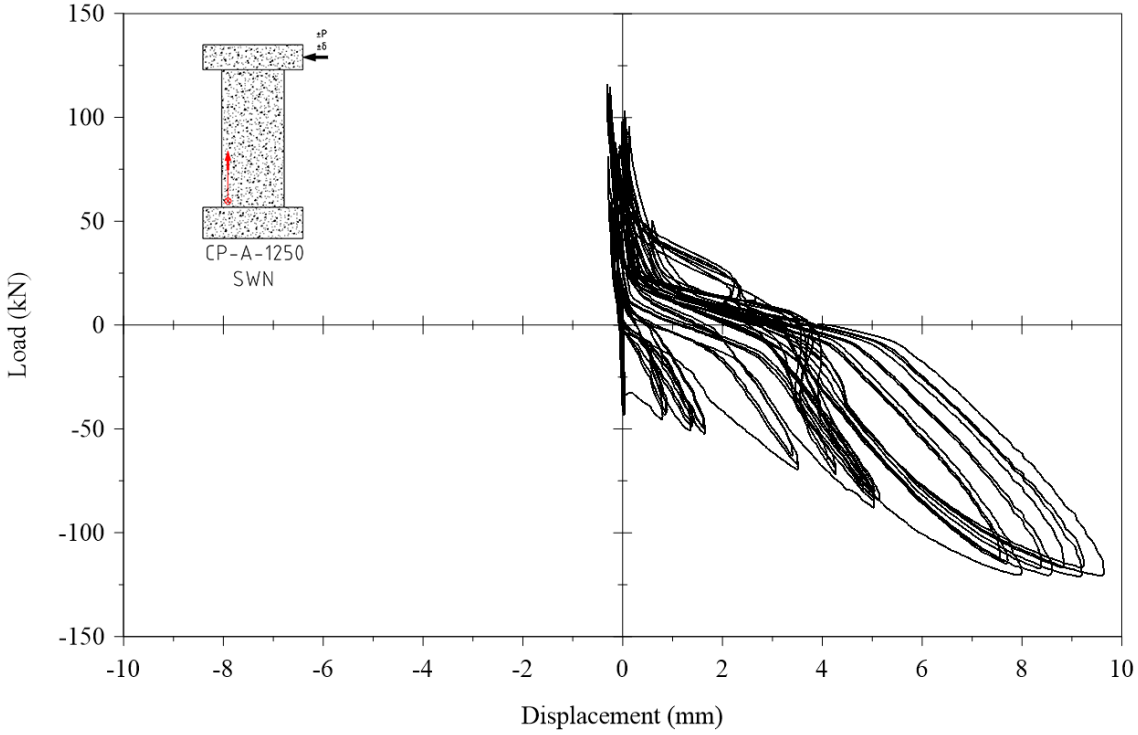

Figure C.52. Cyclic displacement response from CP-A-1250.

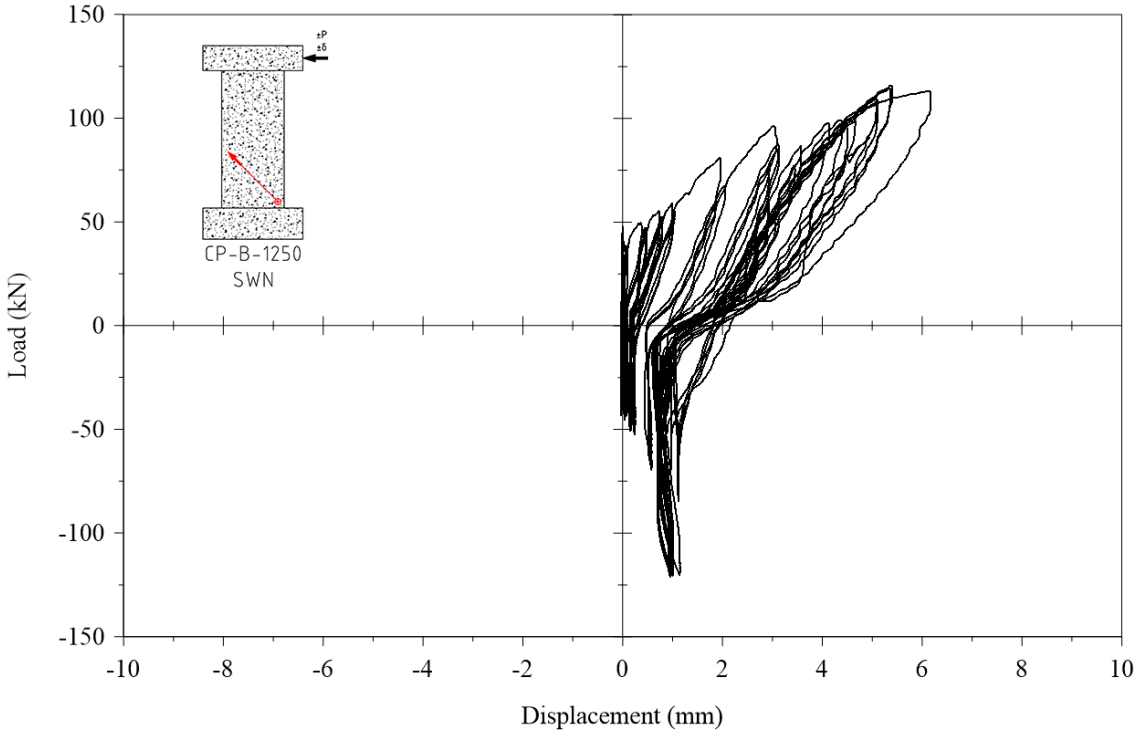

Figure C.53. Cyclic displacement response from CP-B-1250.

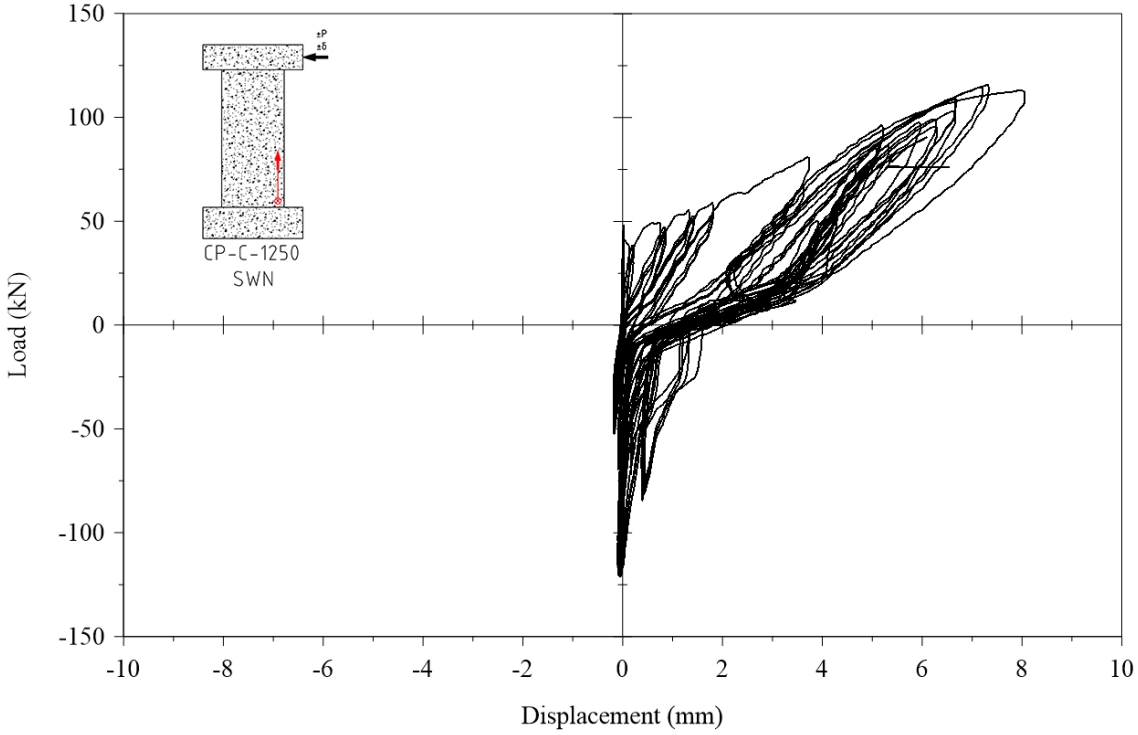

Figure C.54. Cyclic displacement response from CP-C-1250.

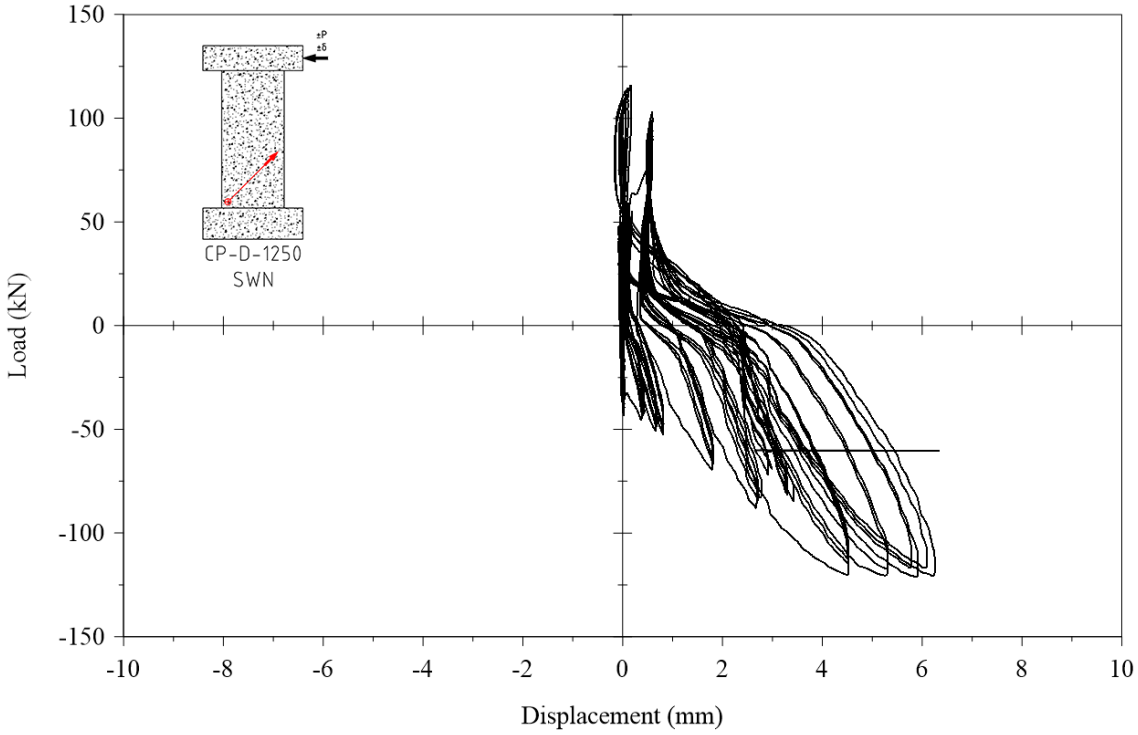

Figure C.55. Cyclic displacement response from CP-D-1250.

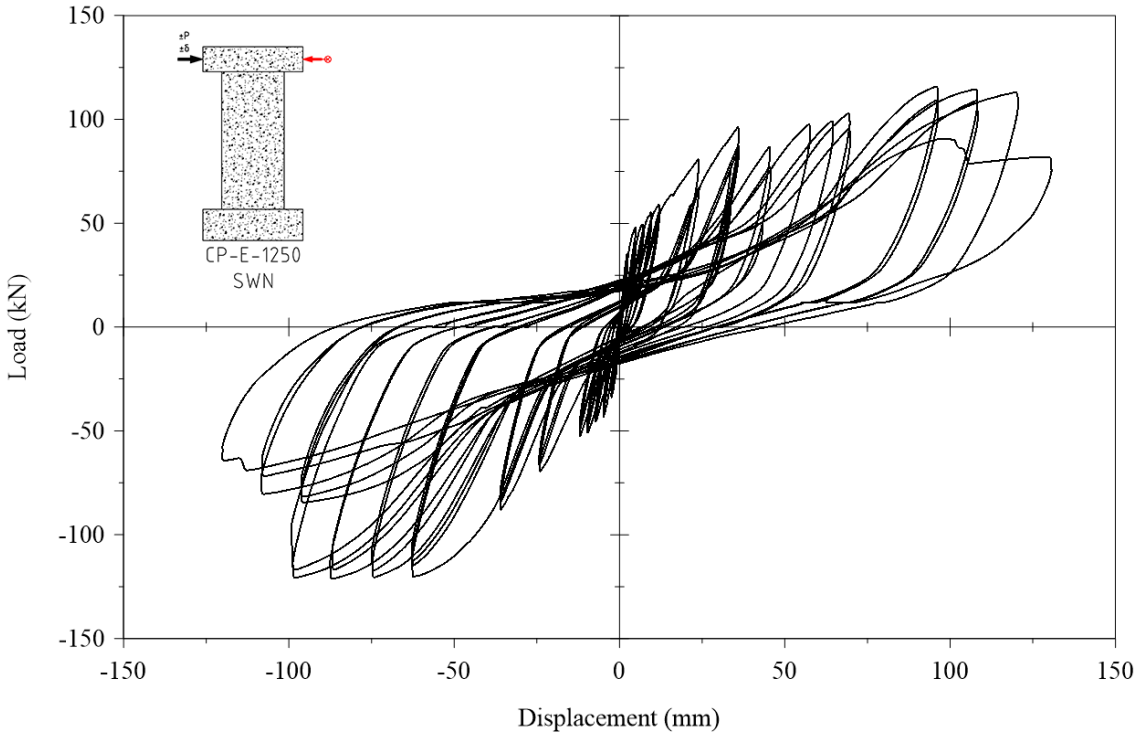

Figure C.56. Cyclic displacement response from CP-E-1250.

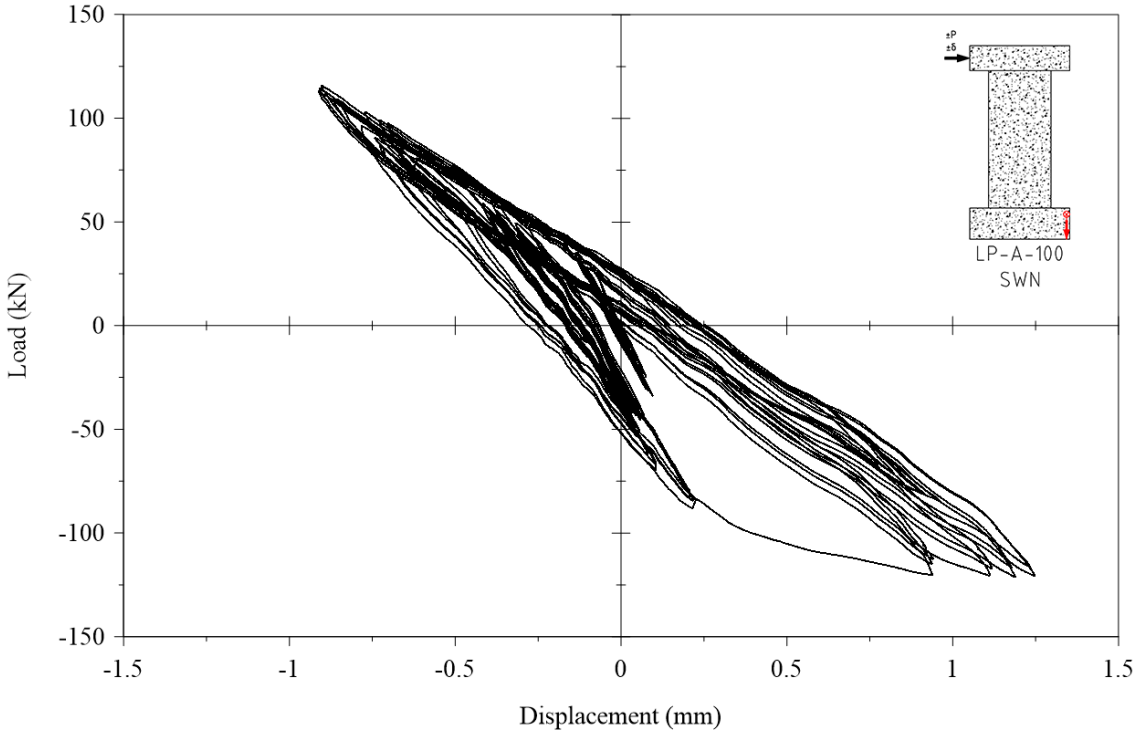

Figure C.57. Cyclic displacement response from LP-A-100.

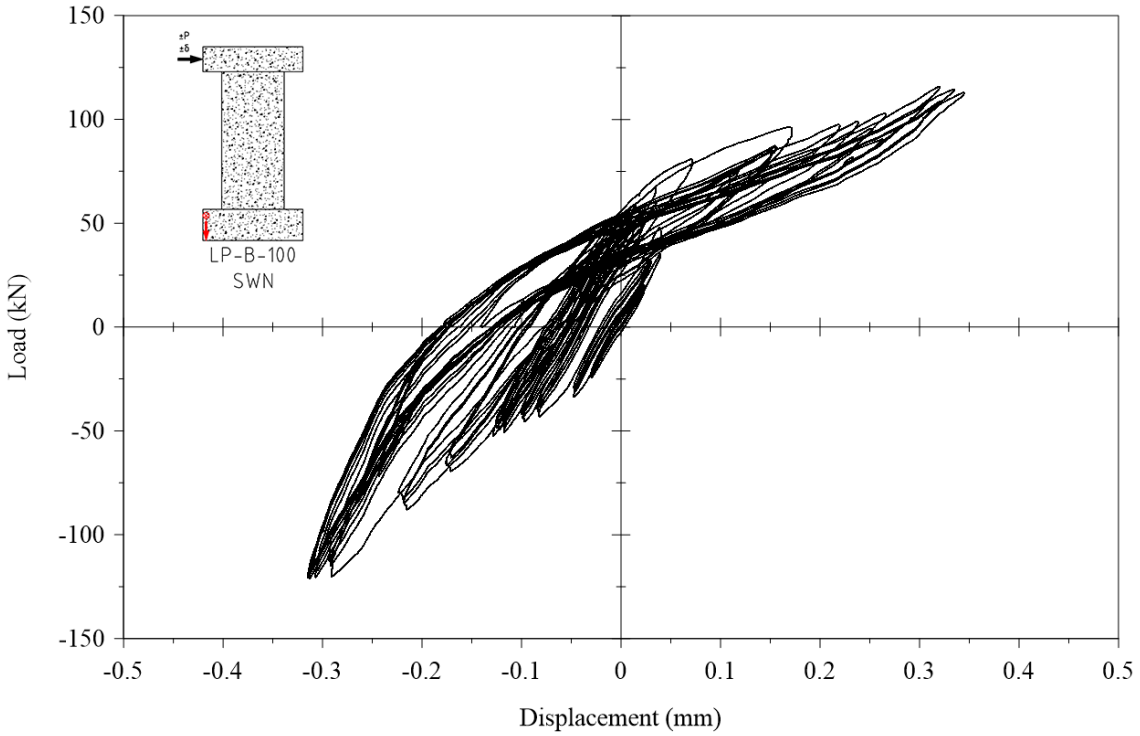

Figure C.58. Cyclic displacement response from LP-B-100.

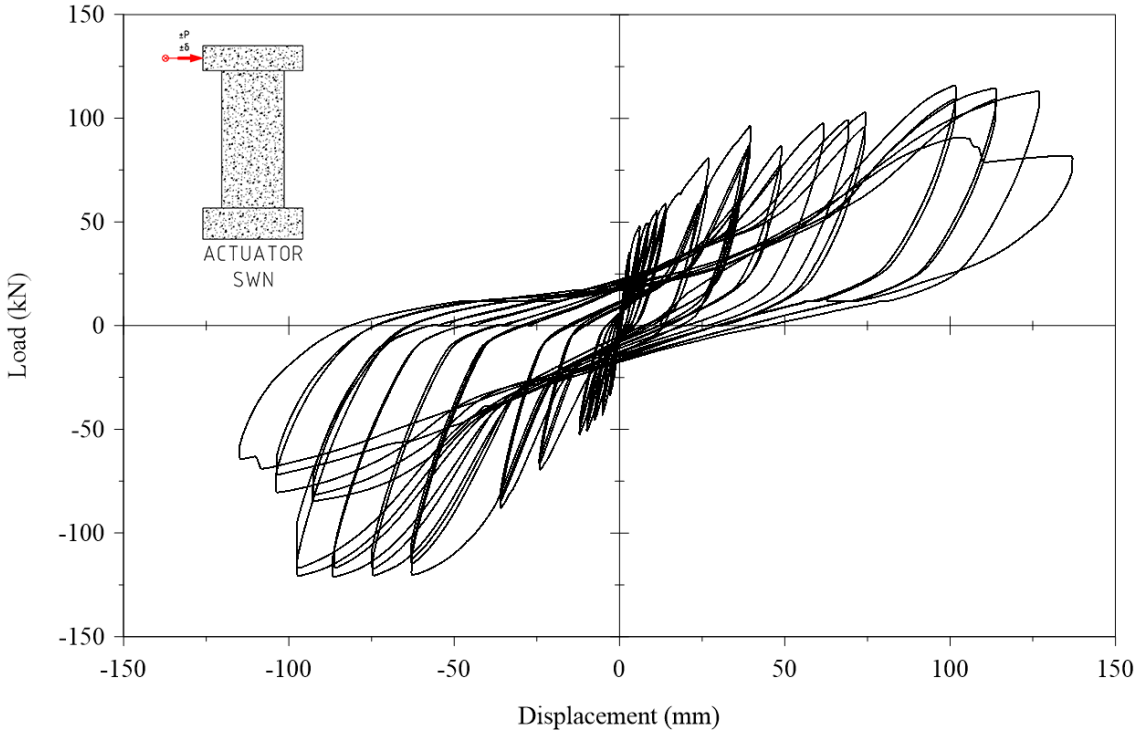

Figure C.59. Cyclic displacement response from hydraulic actuator.

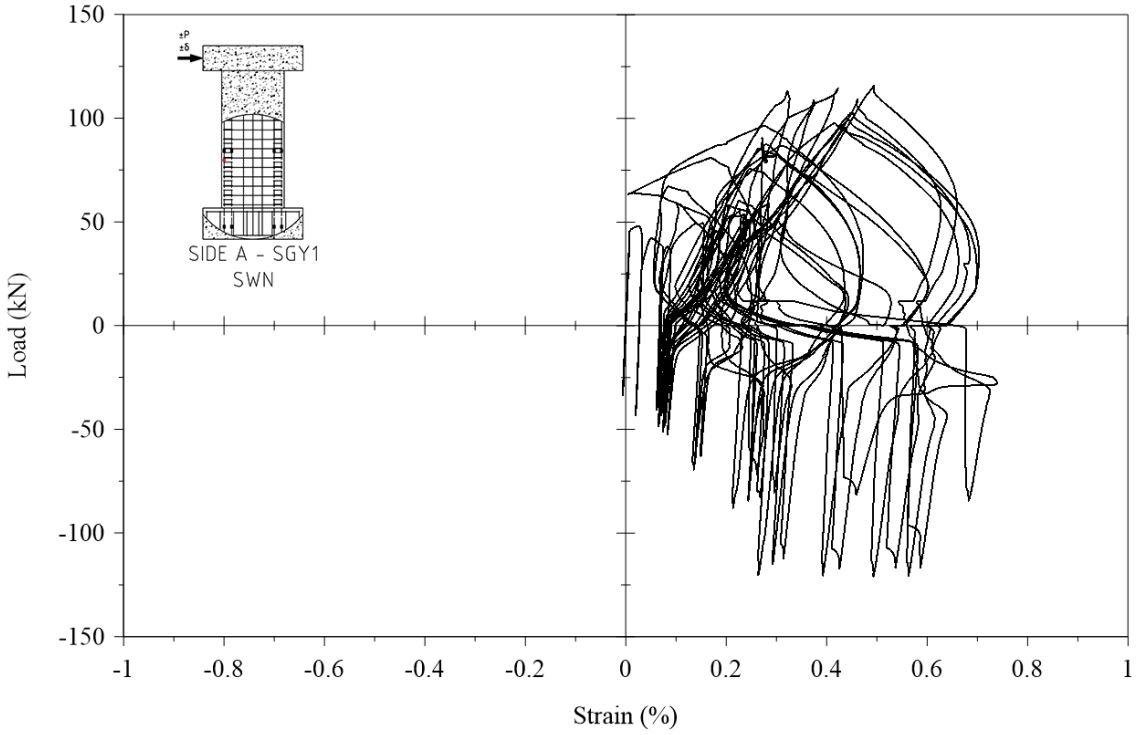

Figure C.60. Cyclic strain response from Strain Gauge 1.

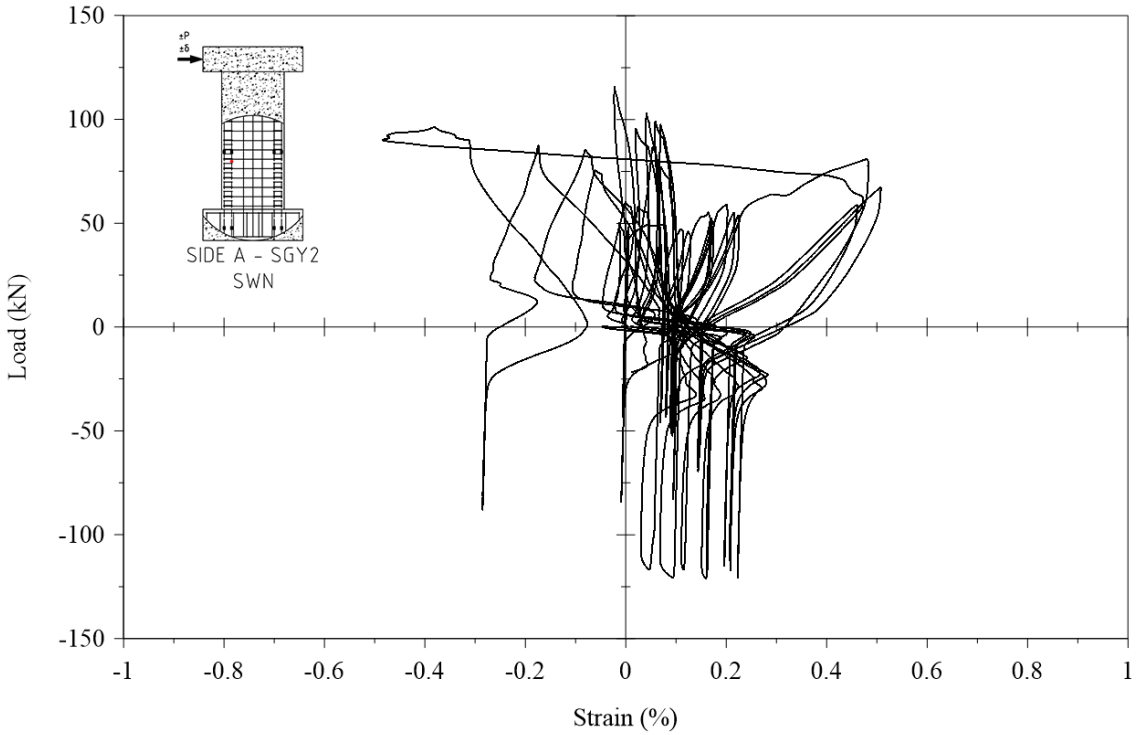

Figure C.61. Cyclic strain response from Strain Gauge 2.

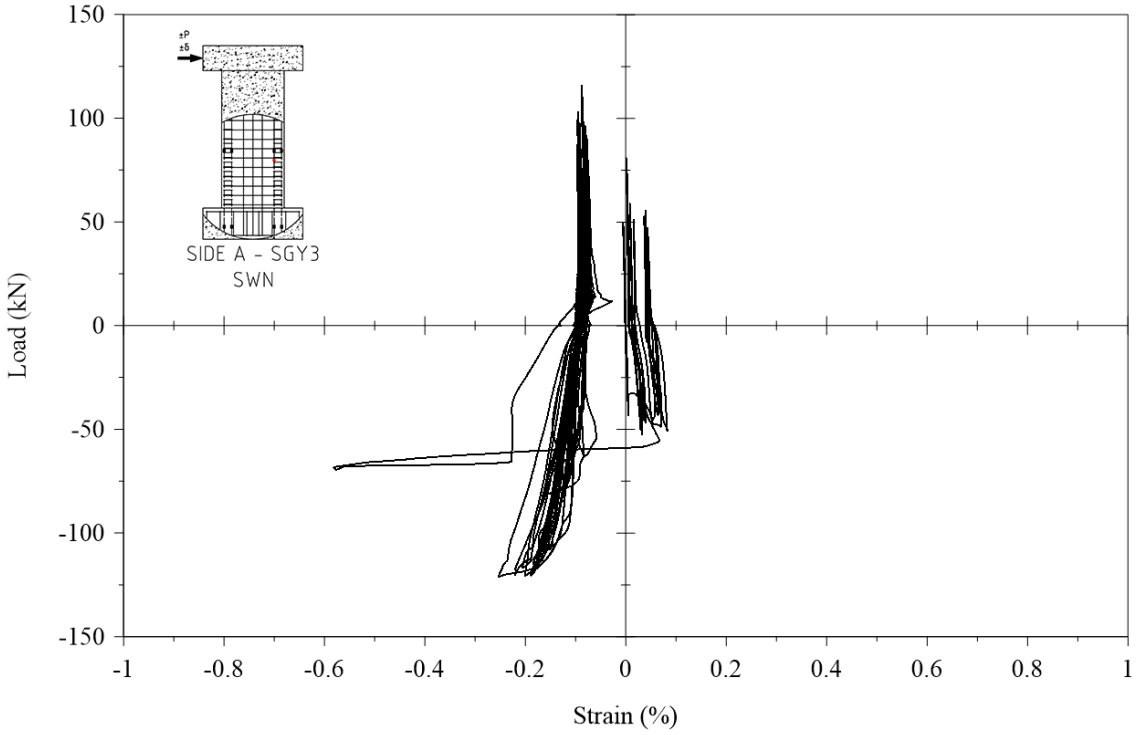

Figure C.62. Cyclic strain response from Strain Gauge 3.

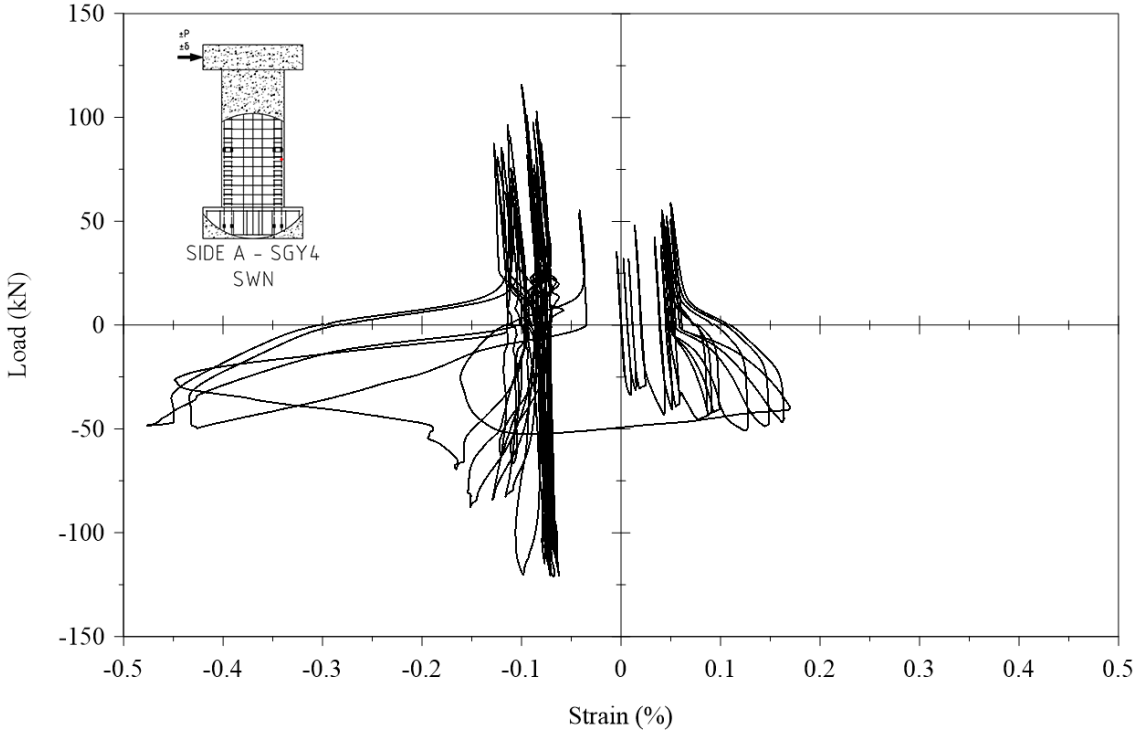

Figure C.63. Cyclic strain response from Strain Gauge 4.

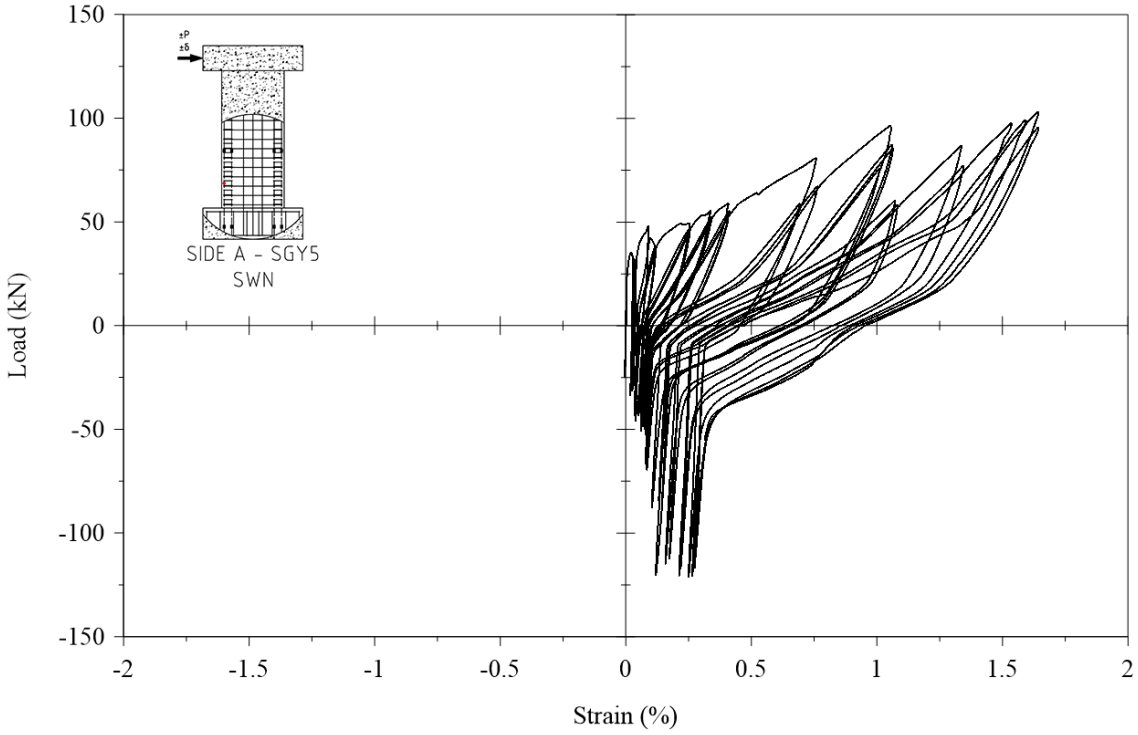

Figure C.64. Cyclic strain response from Strain Gauge 5.

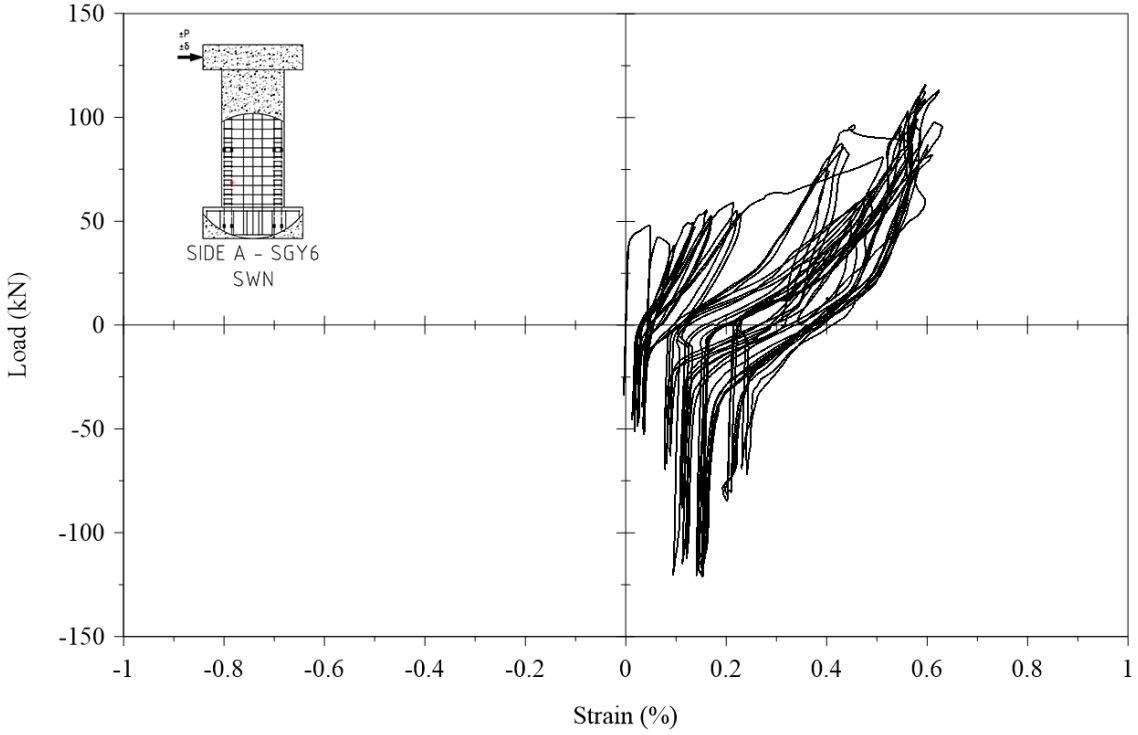

Figure C.65. Cyclic strain response from Strain Gauge 6.

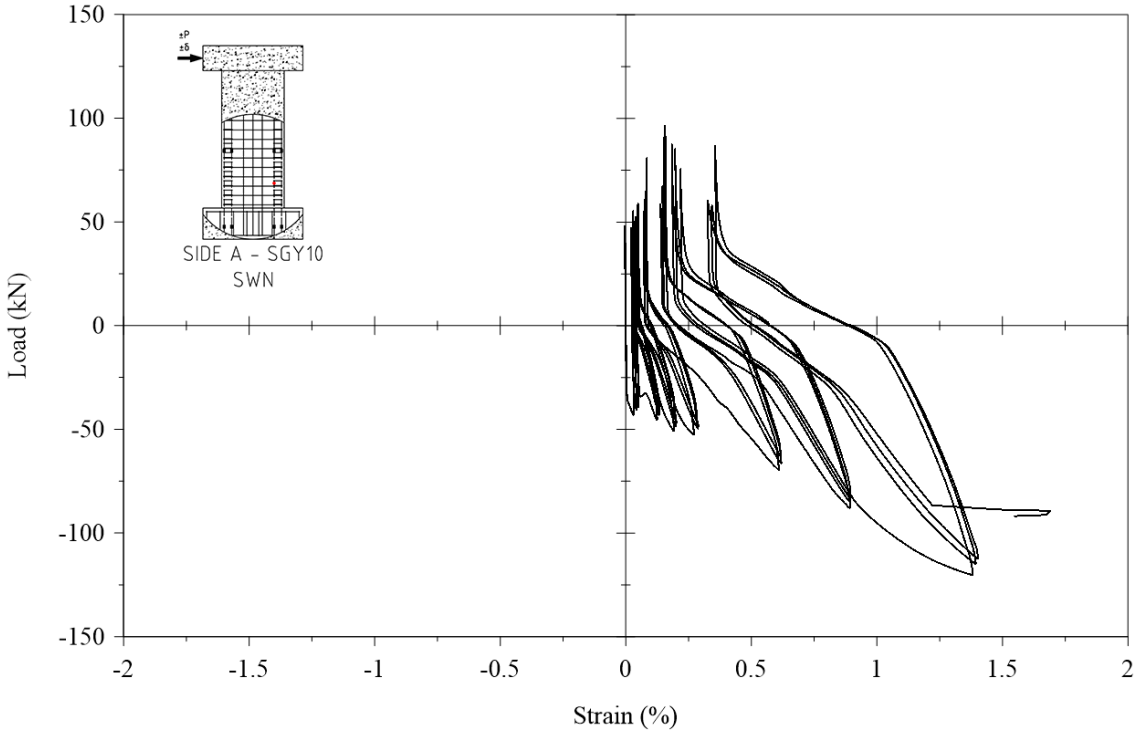

Figure C.66. Cyclic strain response from Strain Gauge 10.

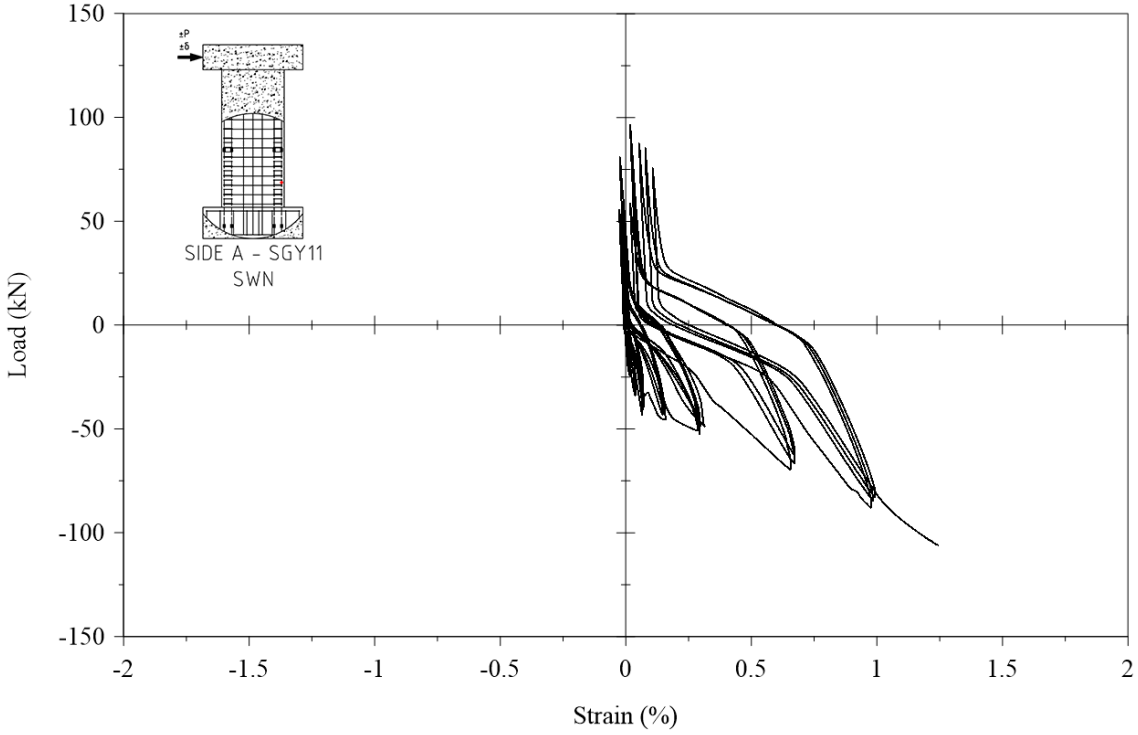

Figure C.67. Cyclic strain response from Strain Gauge 11.

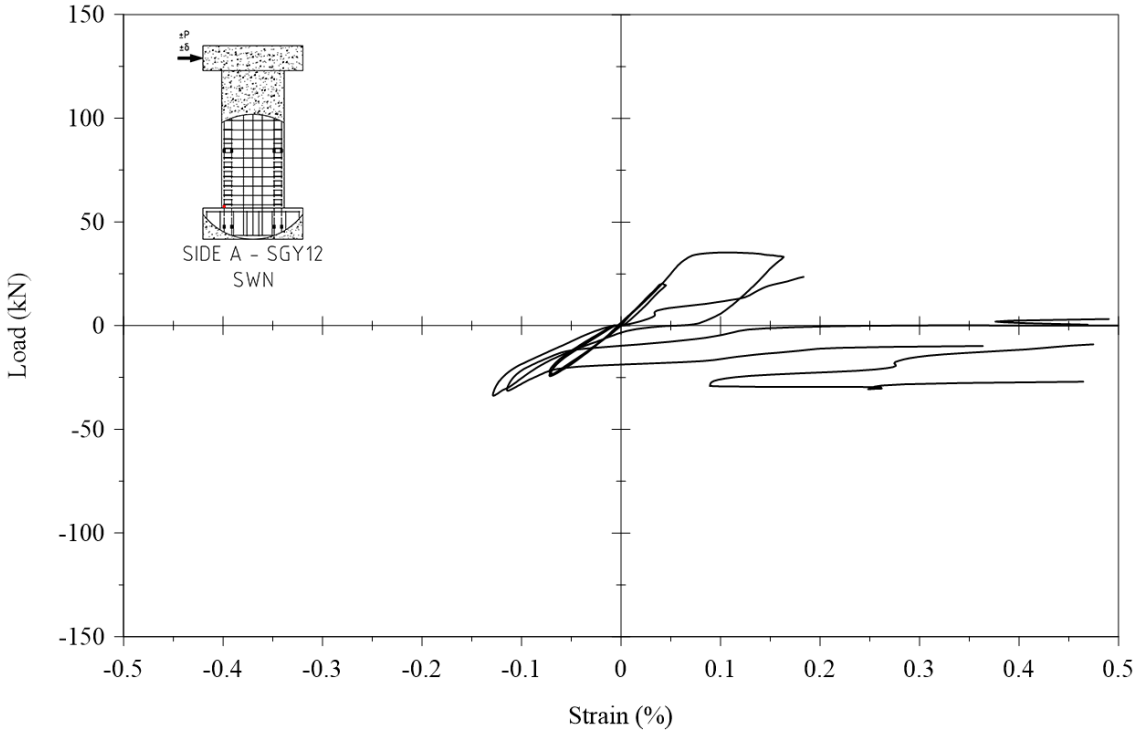

Figure C.68. Cyclic strain response from Strain Gauge 12.

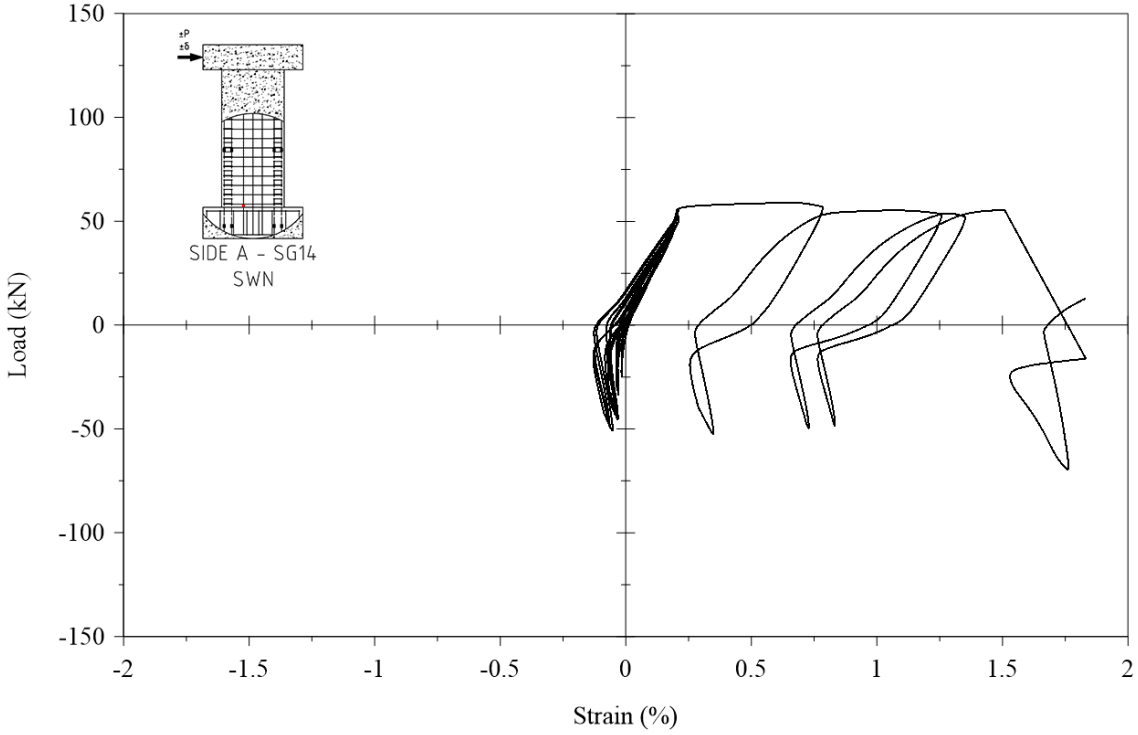

Figure C.69. Cyclic strain response from Strain Gauge 14.

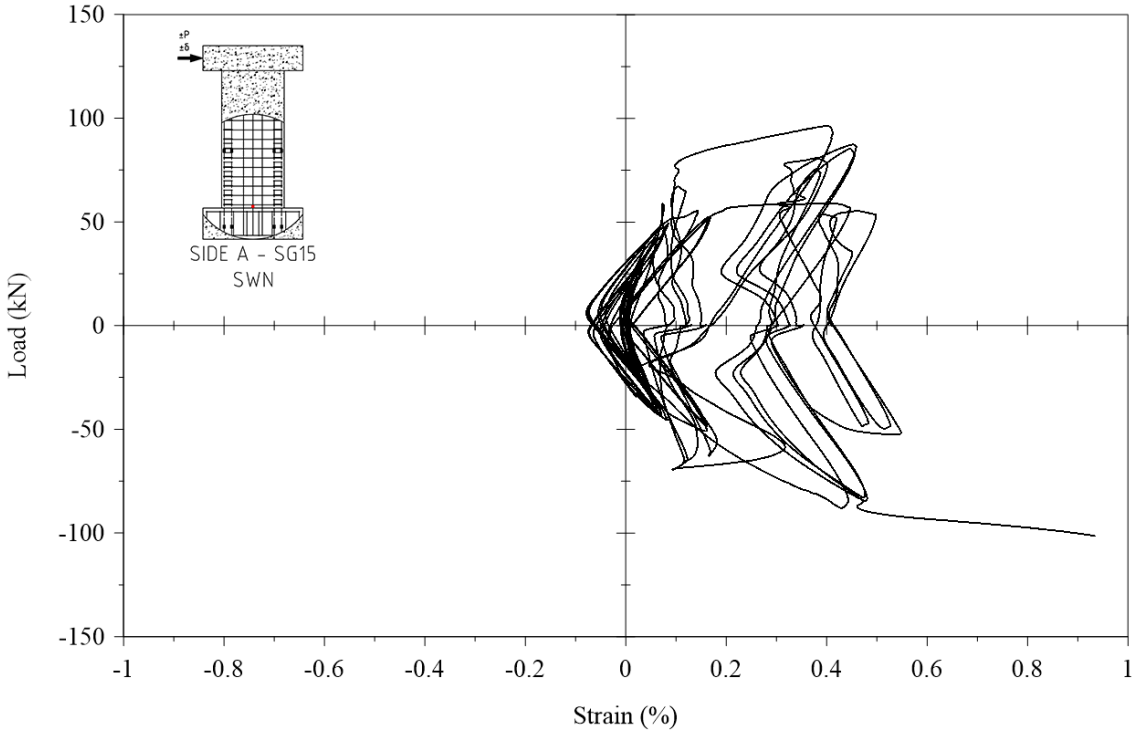

Figure C.70. Cyclic strain response from Strain Gauge 15.

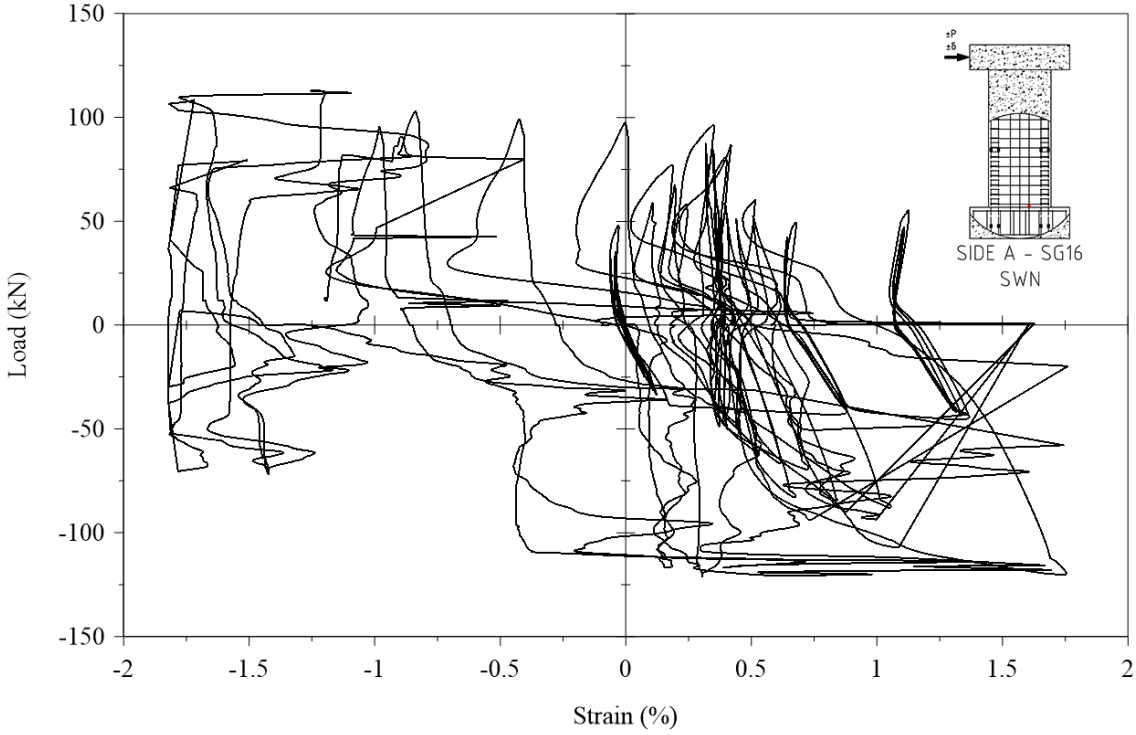

Figure C.71. Cyclic strain response from Strain Gauge 16.

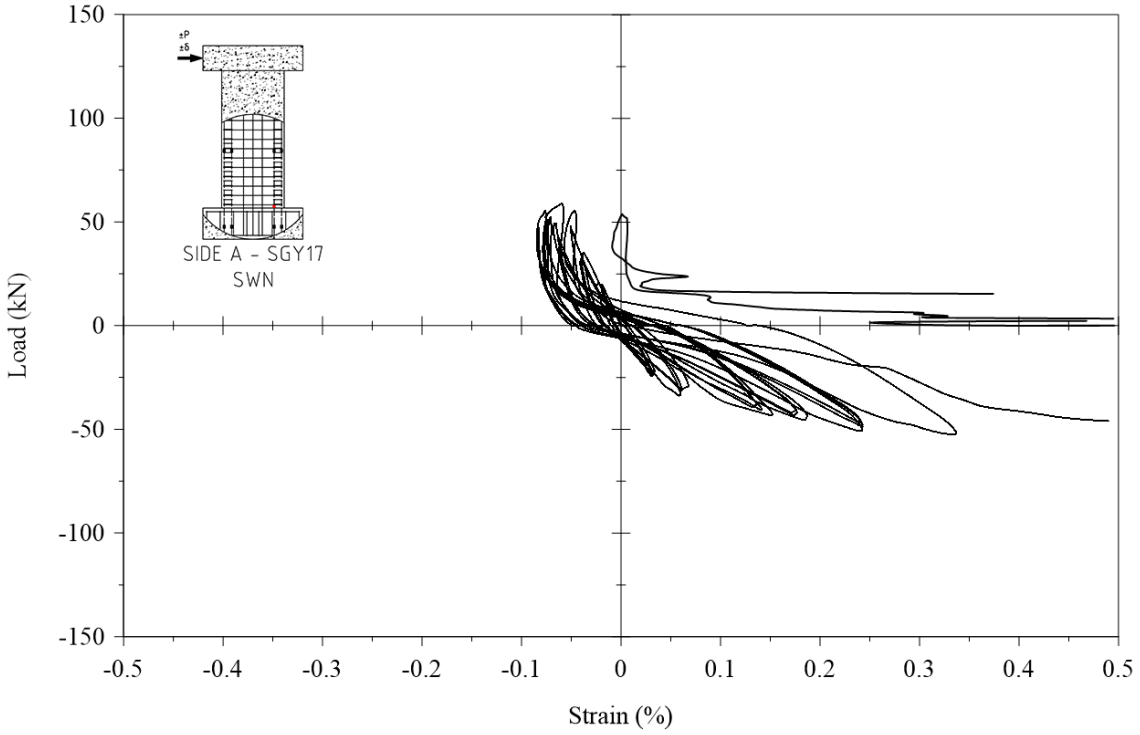

Figure C.72. Cyclic strain response from Strain Gauge 17.

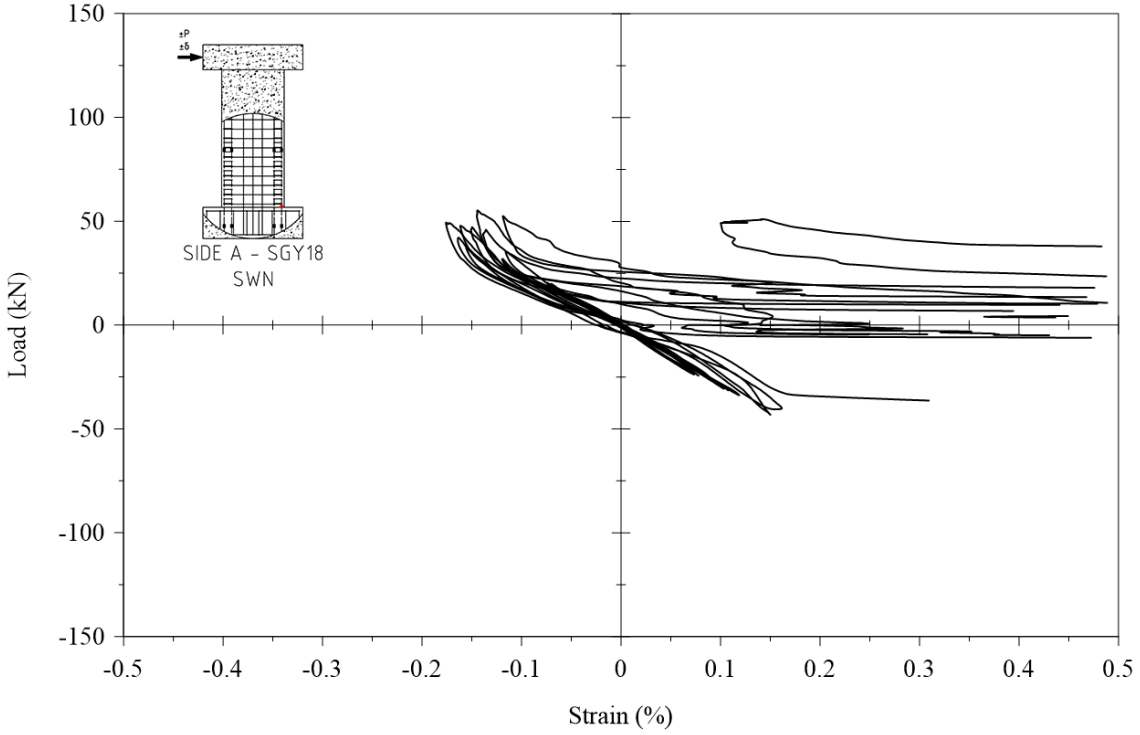

Figure C.73. Cyclic strain response from Strain Gauge 18.

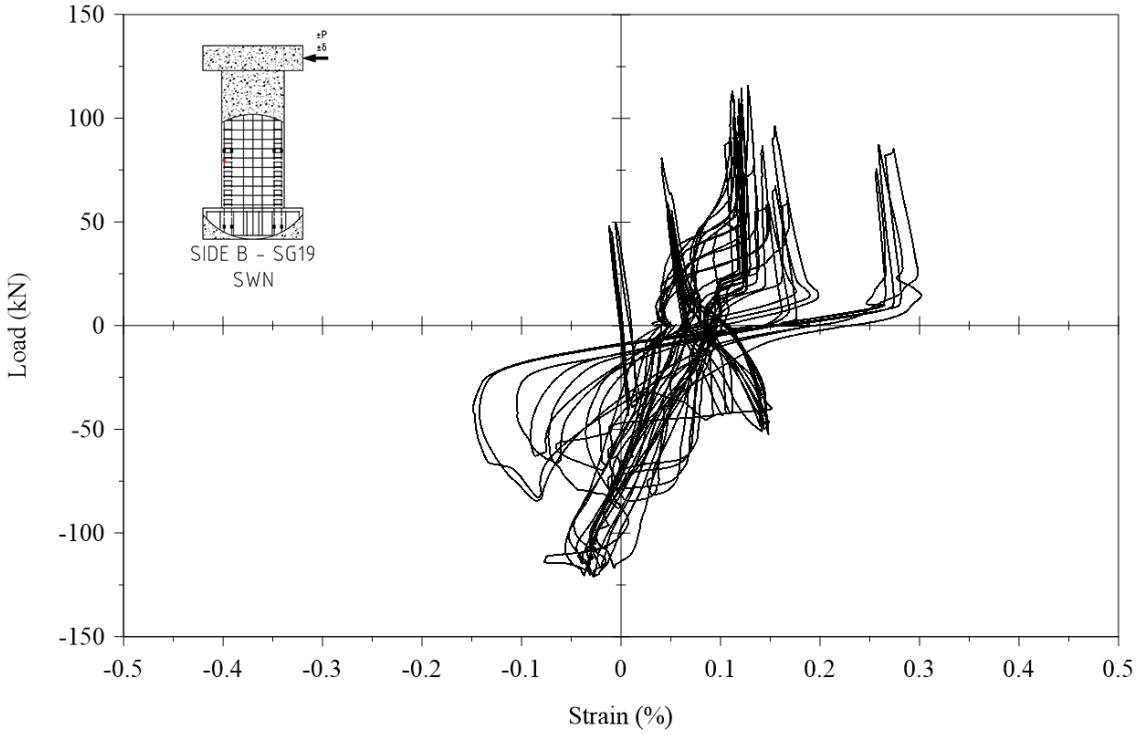

Figure C.74. Cyclic strain response from Strain Gauge 19.

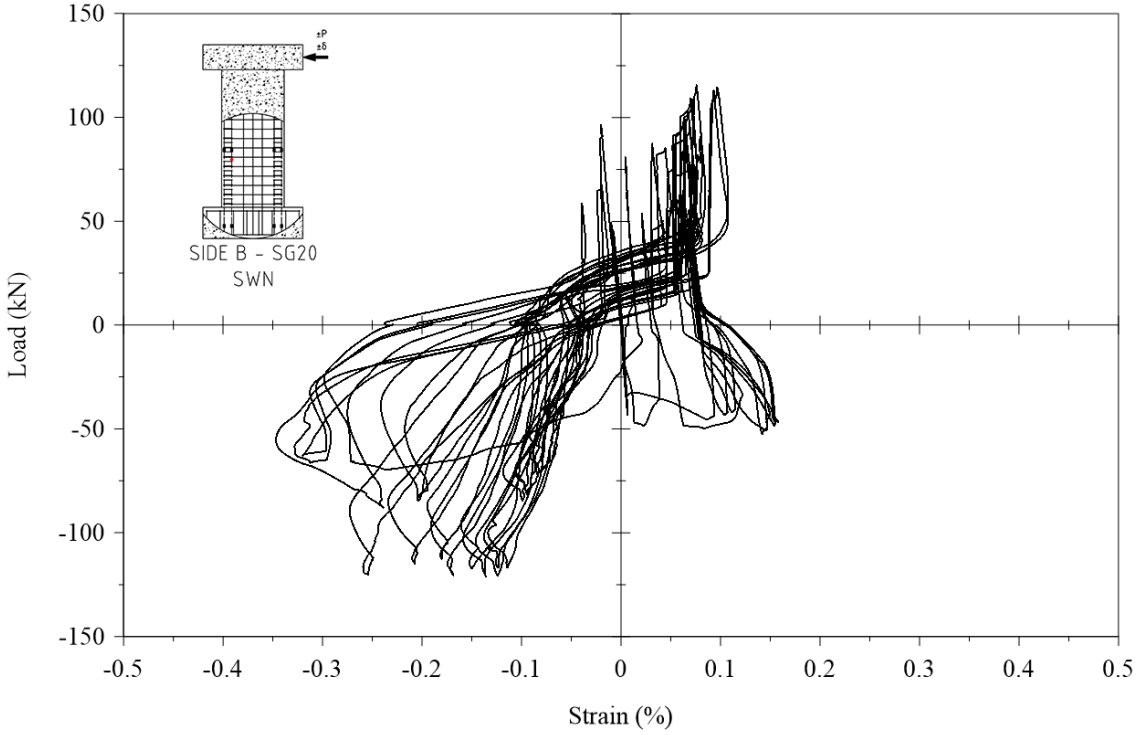

Figure C.75. Cyclic strain response from Strain Gauge 20.

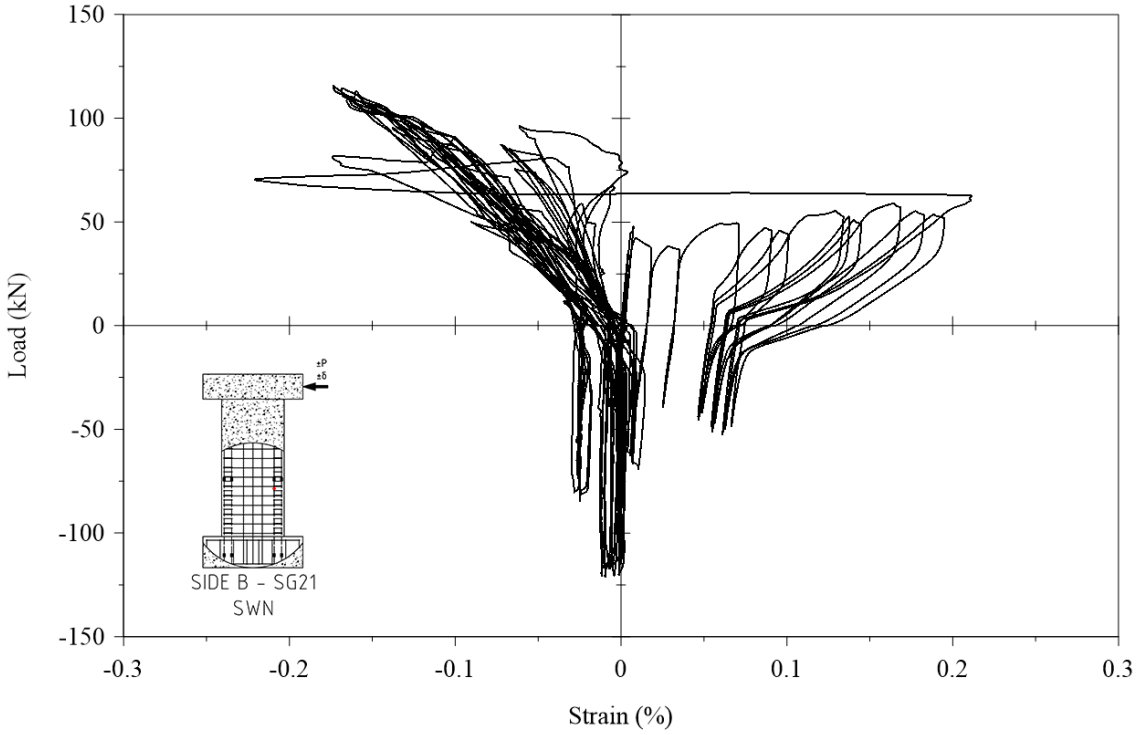

Figure C.76. Cyclic strain response from Strain Gauge 21.

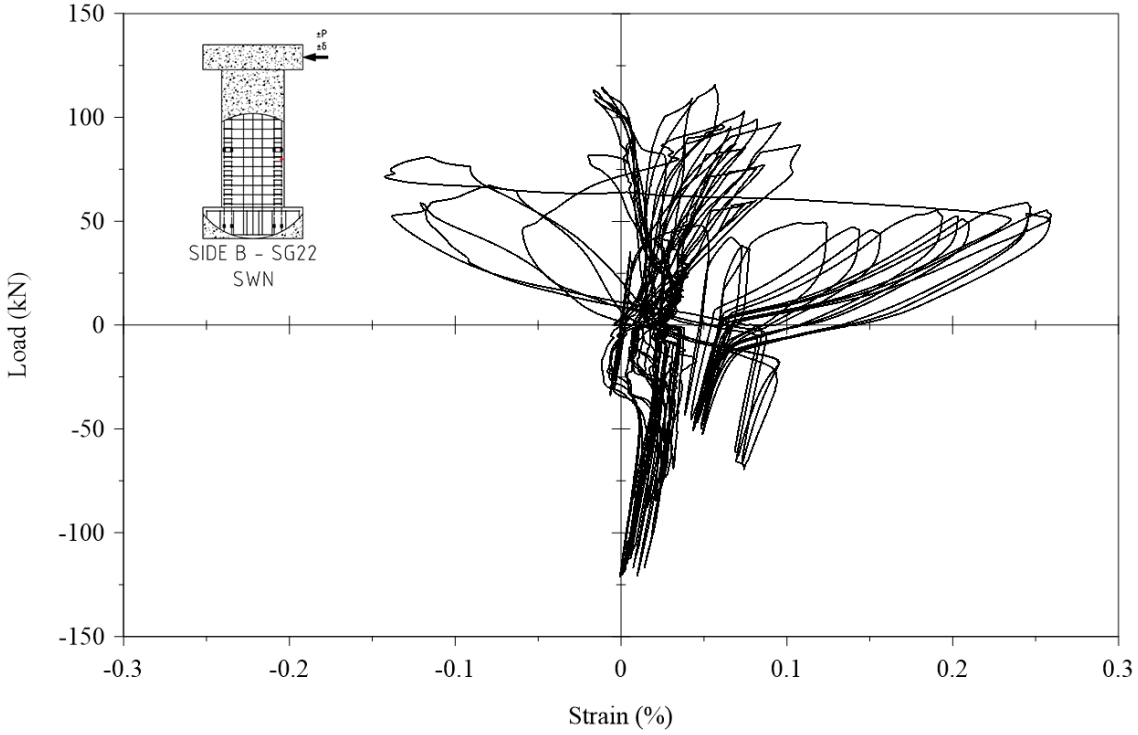

Figure C.77. Cyclic strain response from Strain Gauge 22.

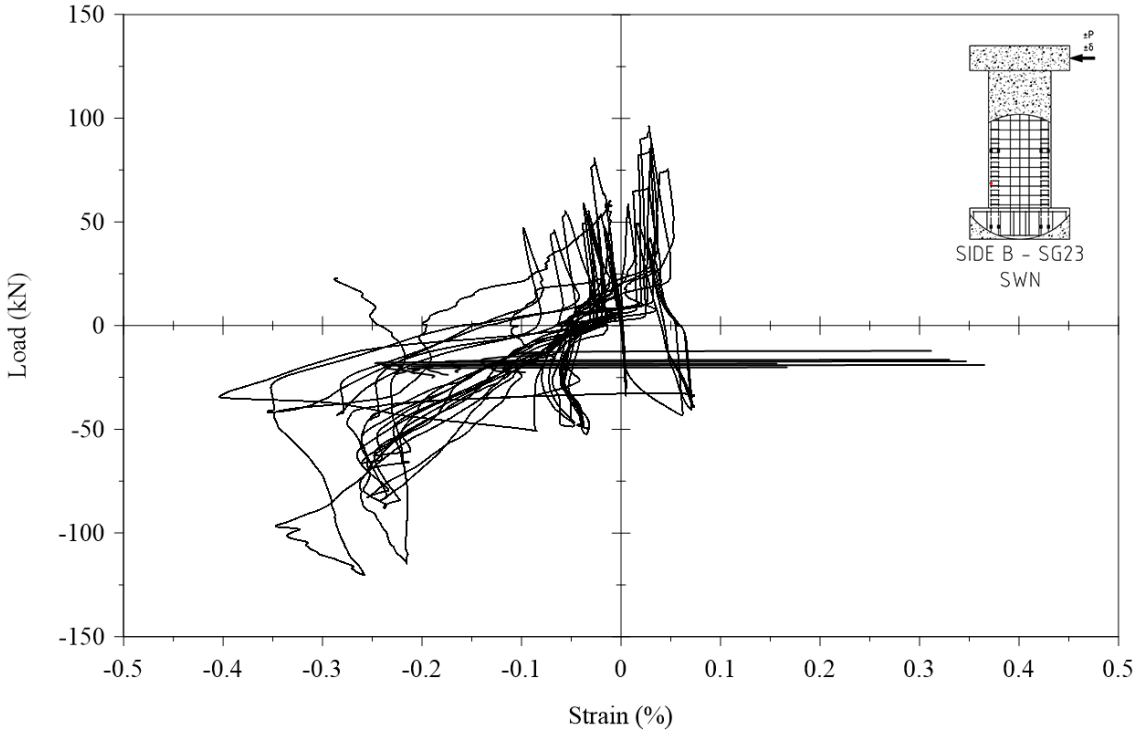

Figure C.78. Cyclic strain response from Strain Gauge 23.

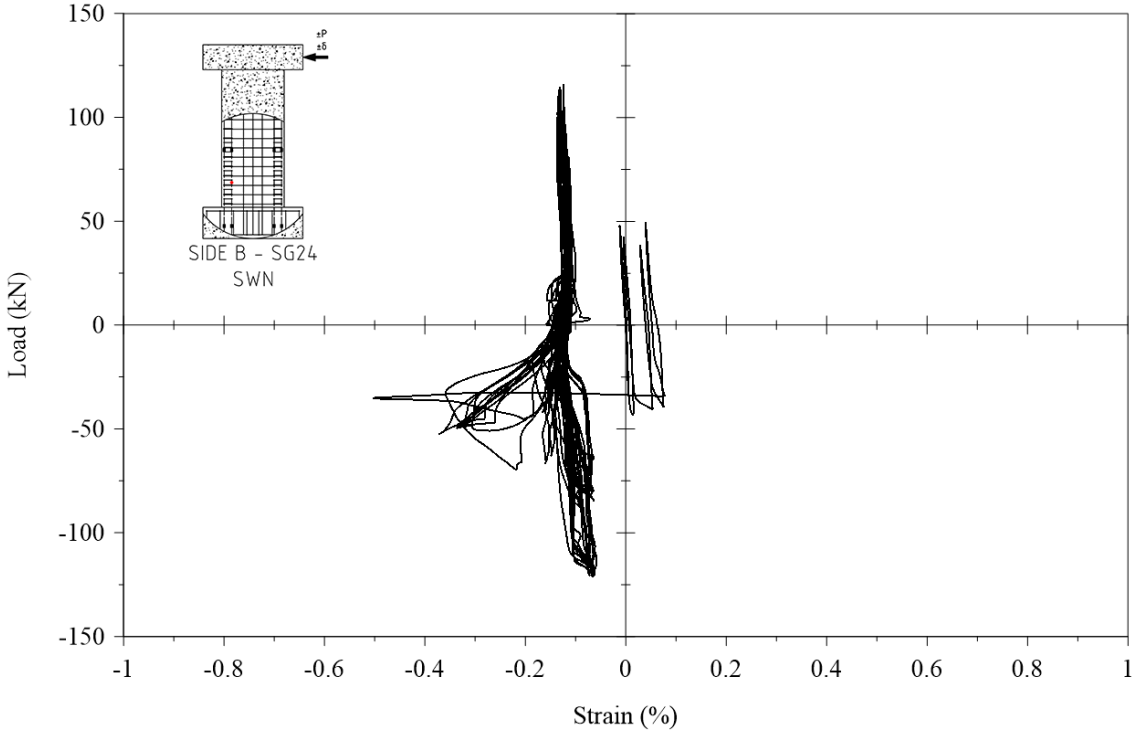

Figure C.79. Cyclic strain response from Strain Gauge 24.

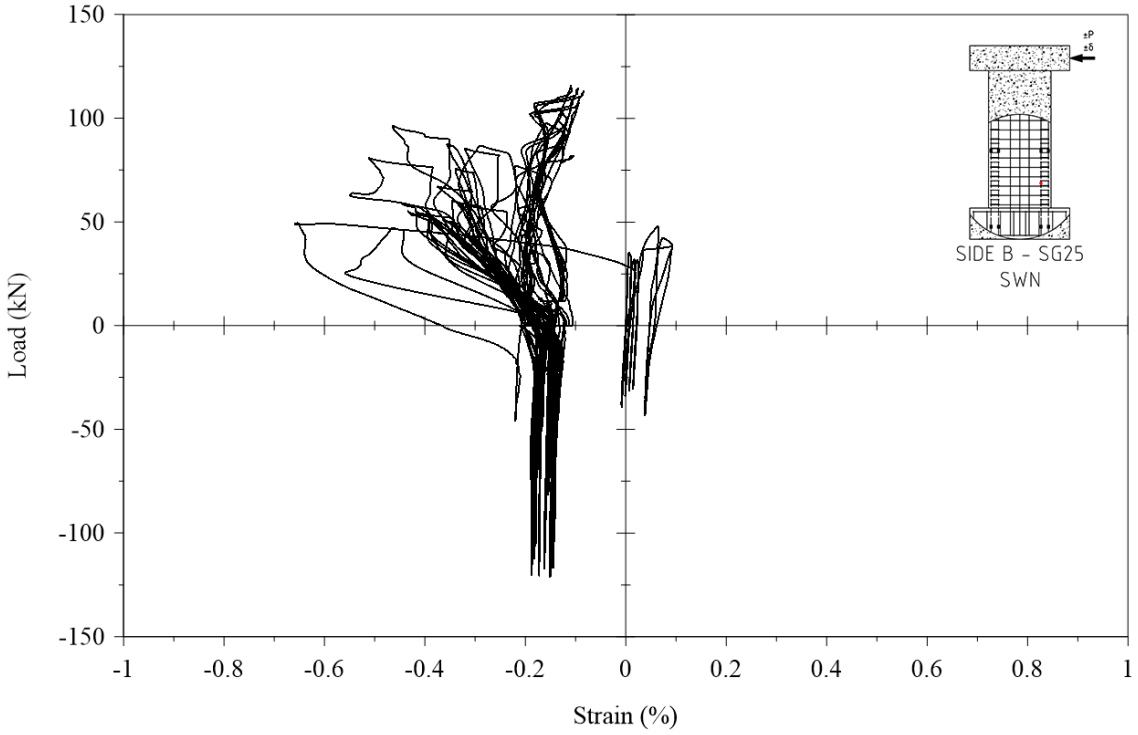

Figure C.80. Cyclic strain response from Strain Gauge 25.

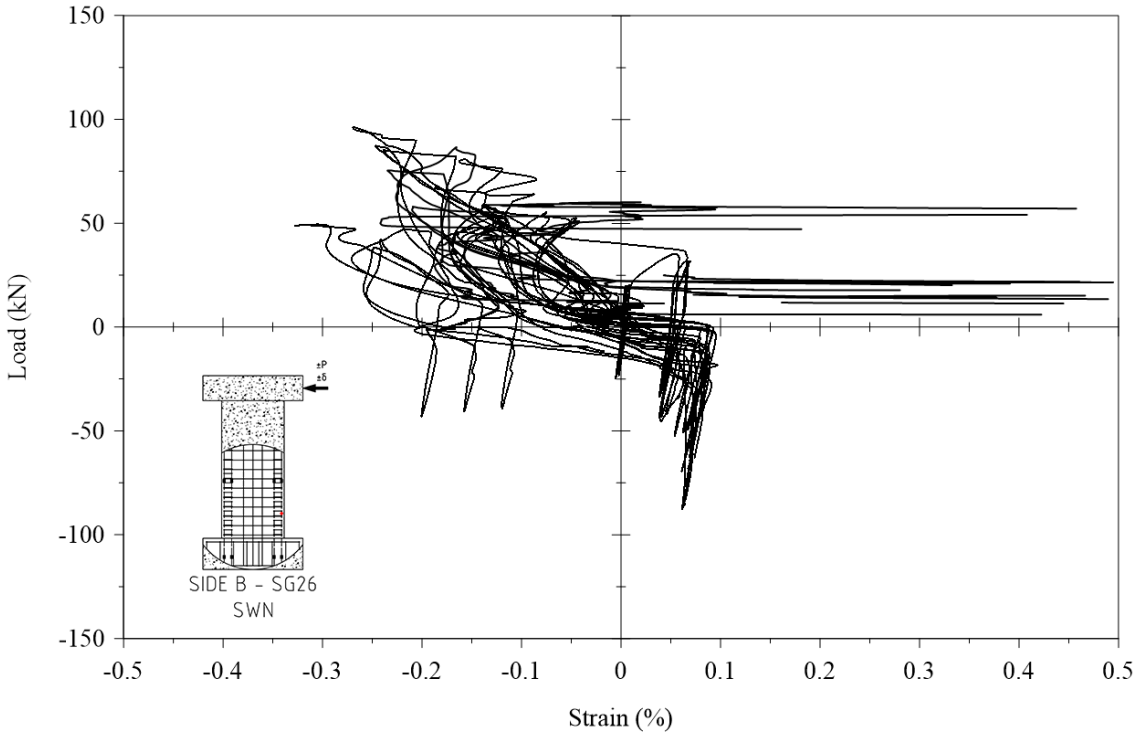

Figure C.81. Cyclic strain response from Strain Gauge 26.

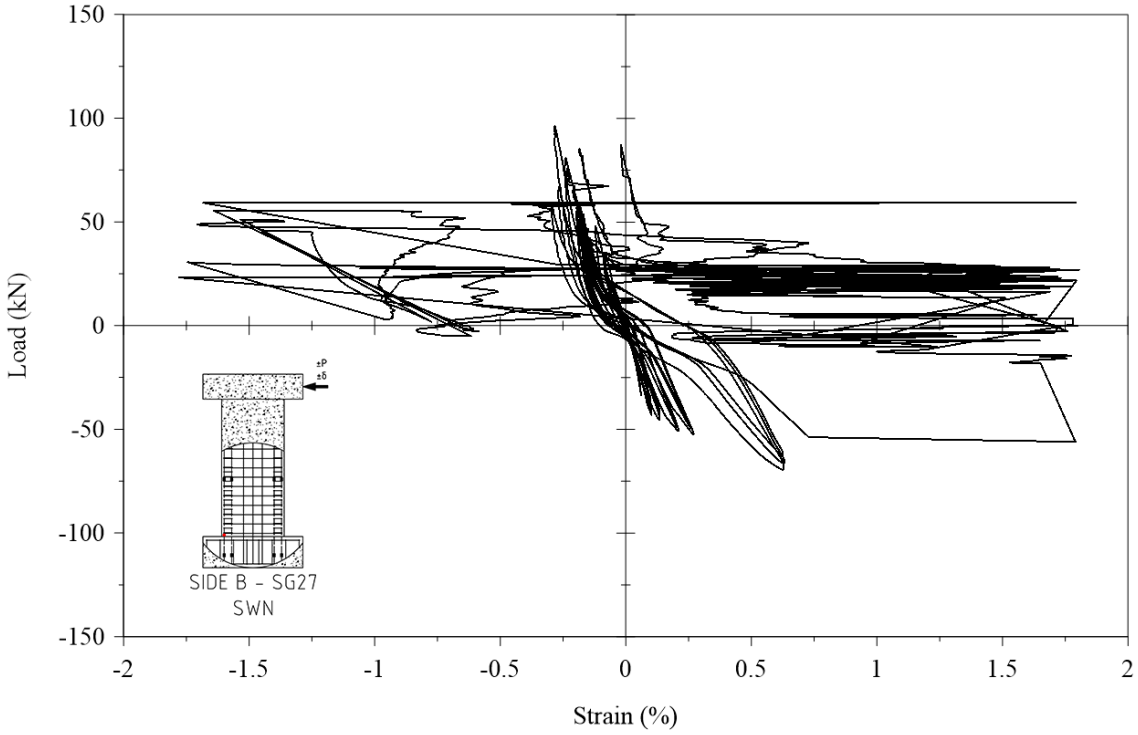

Figure C.82. Cyclic strain response from Strain Gauge 27.

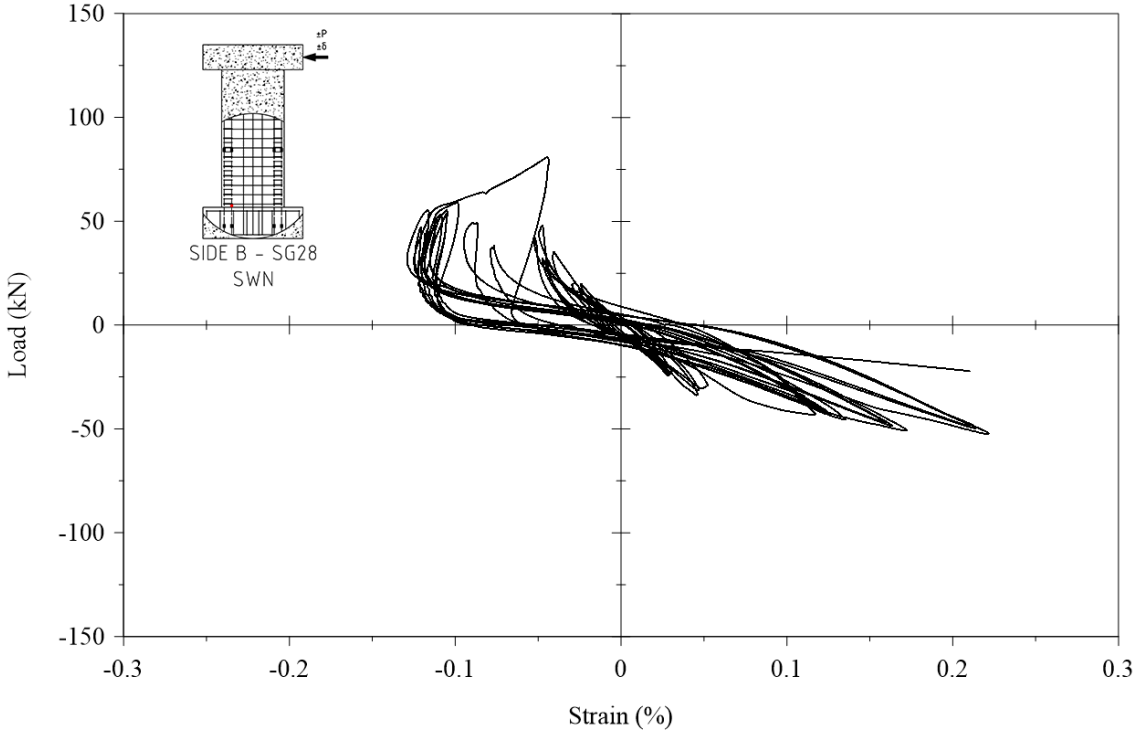

Figure C.83. Cyclic strain response from Strain Gauge 28.

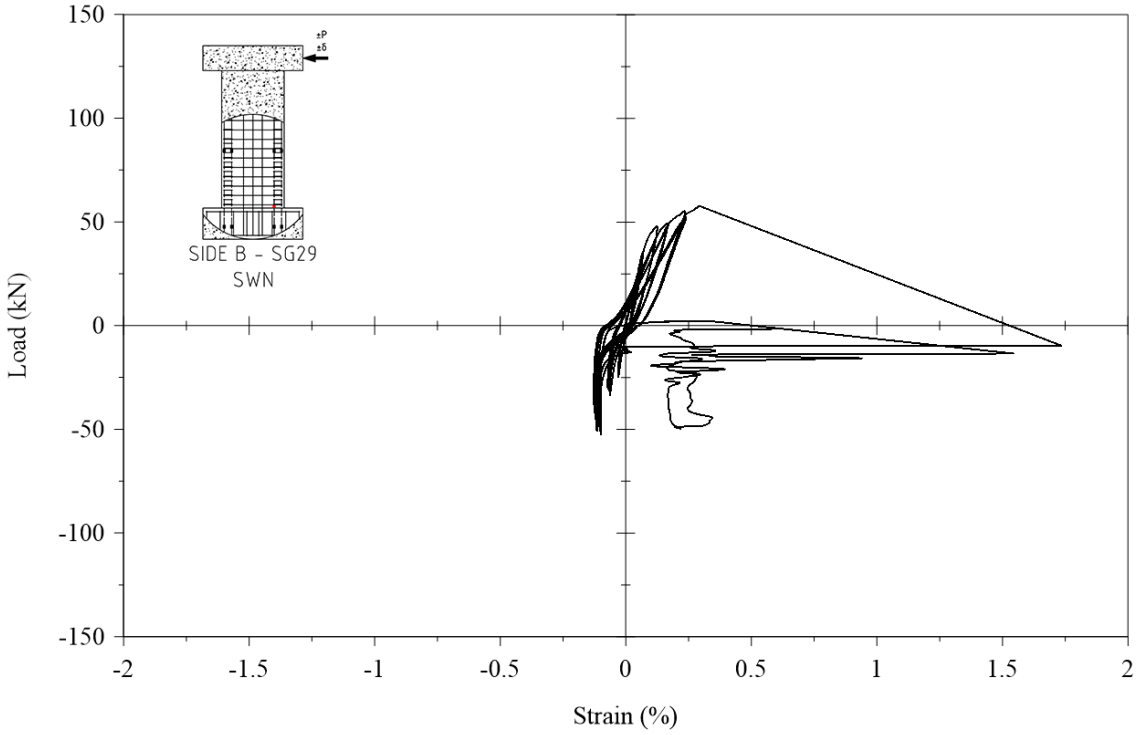

Figure C.84. Cyclic strain response from Strain Gauge 29.

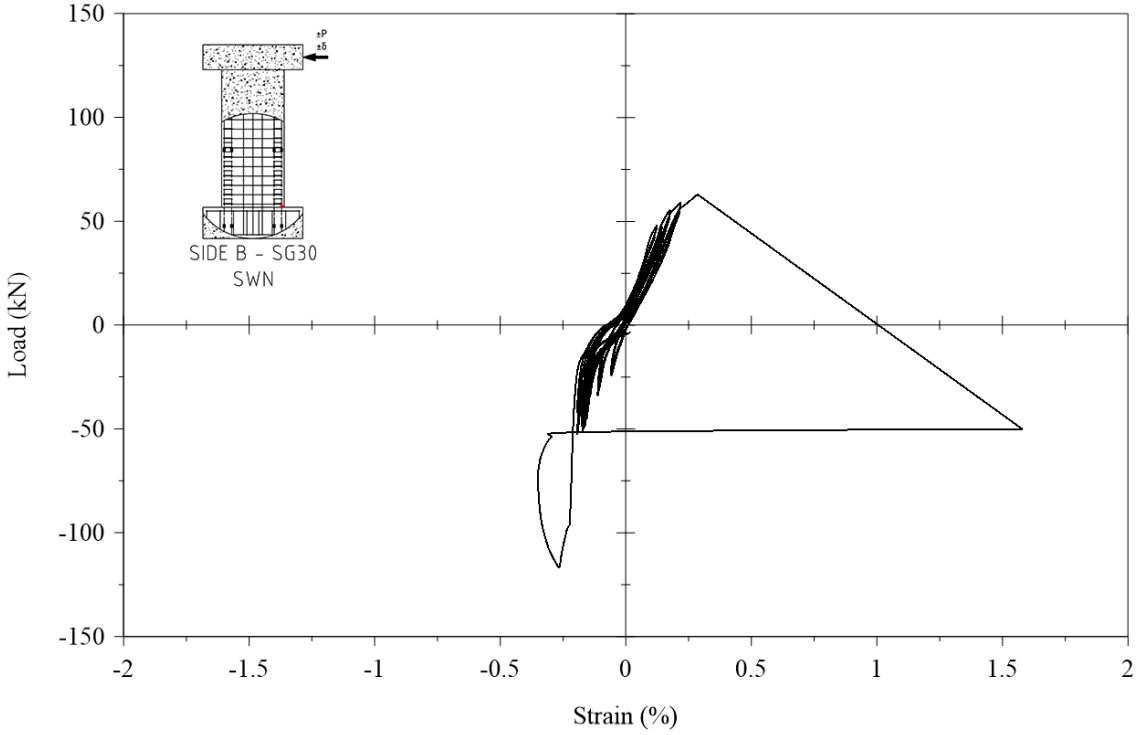

Figure C.85. Cyclic strain response from Strain Gauge 30.

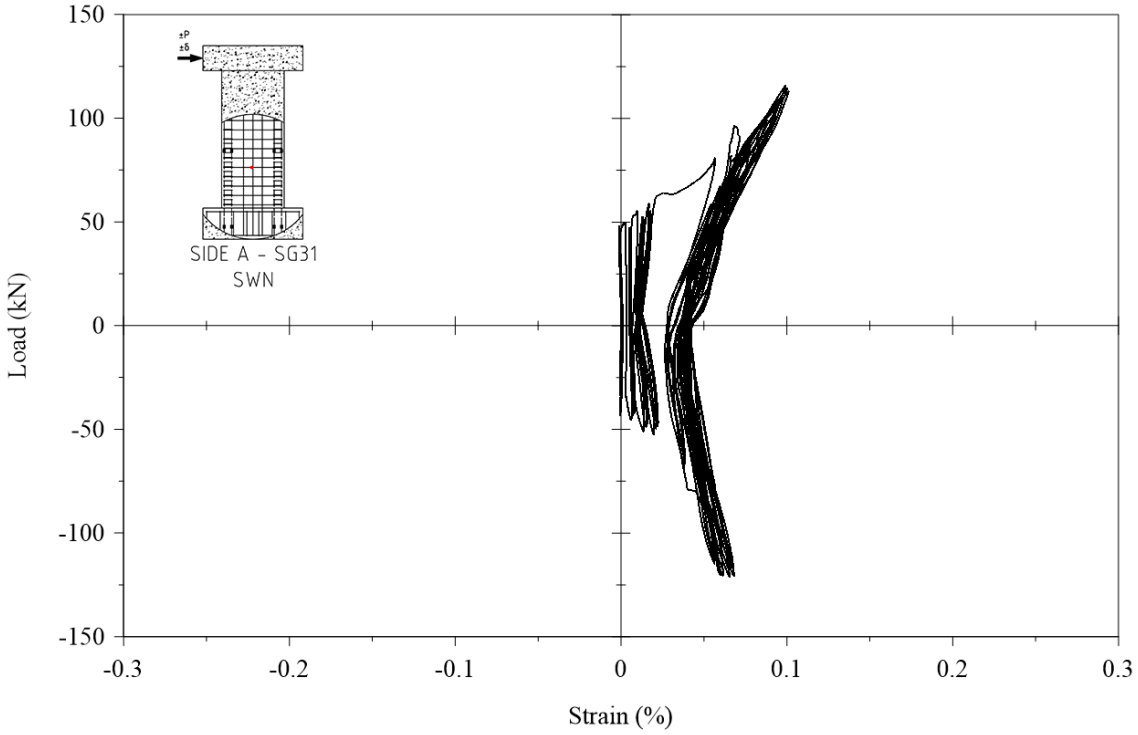

Figure C.86. Cyclic strain response from Strain Gauge 31.

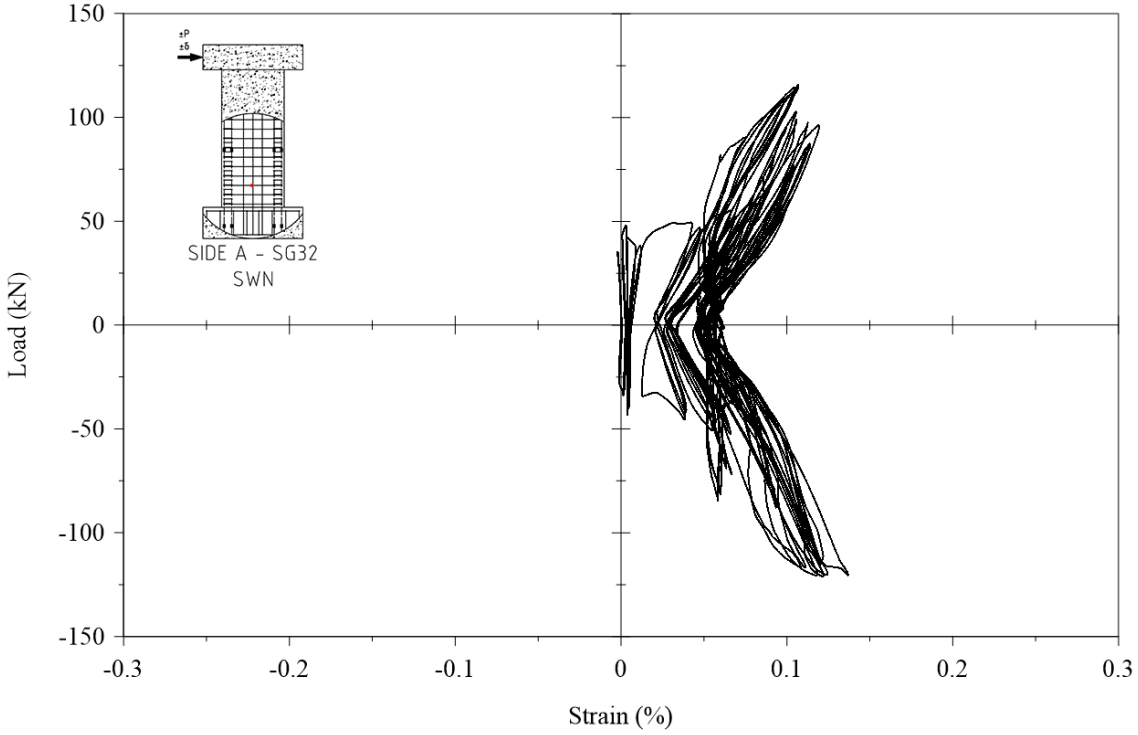

Figure C.87. Cyclic strain response from Strain Gauge 32.

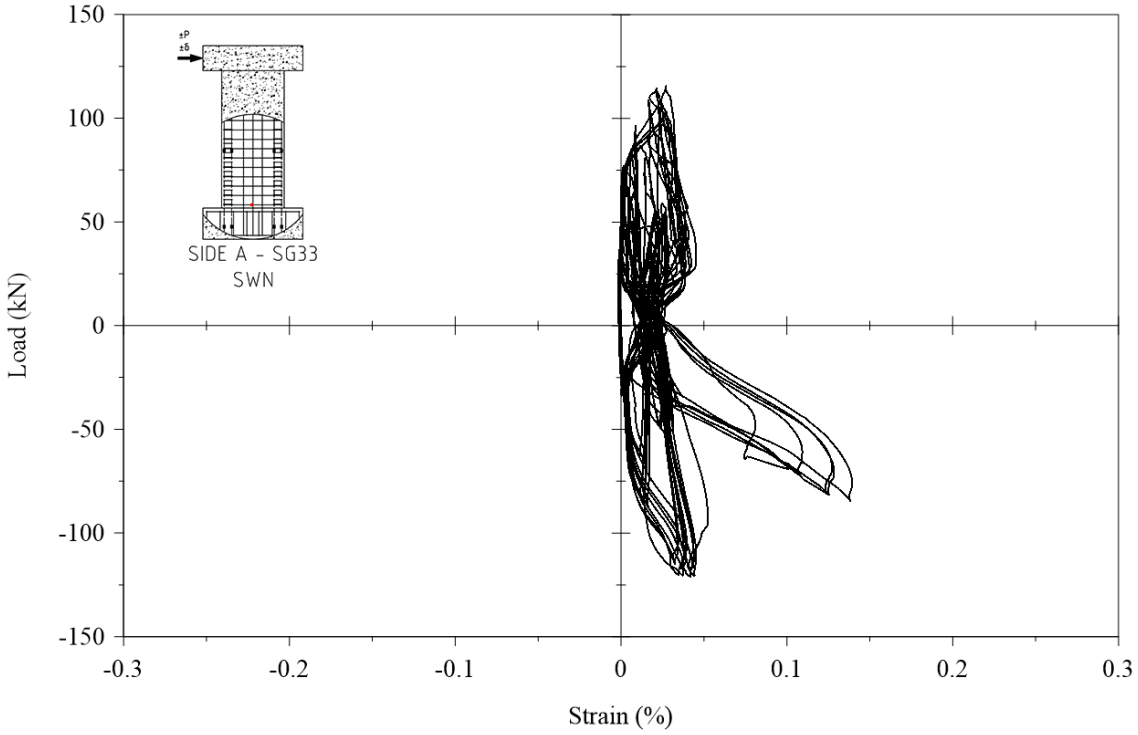

Figure C.88. Cyclic strain response from Strain Gauge 33.

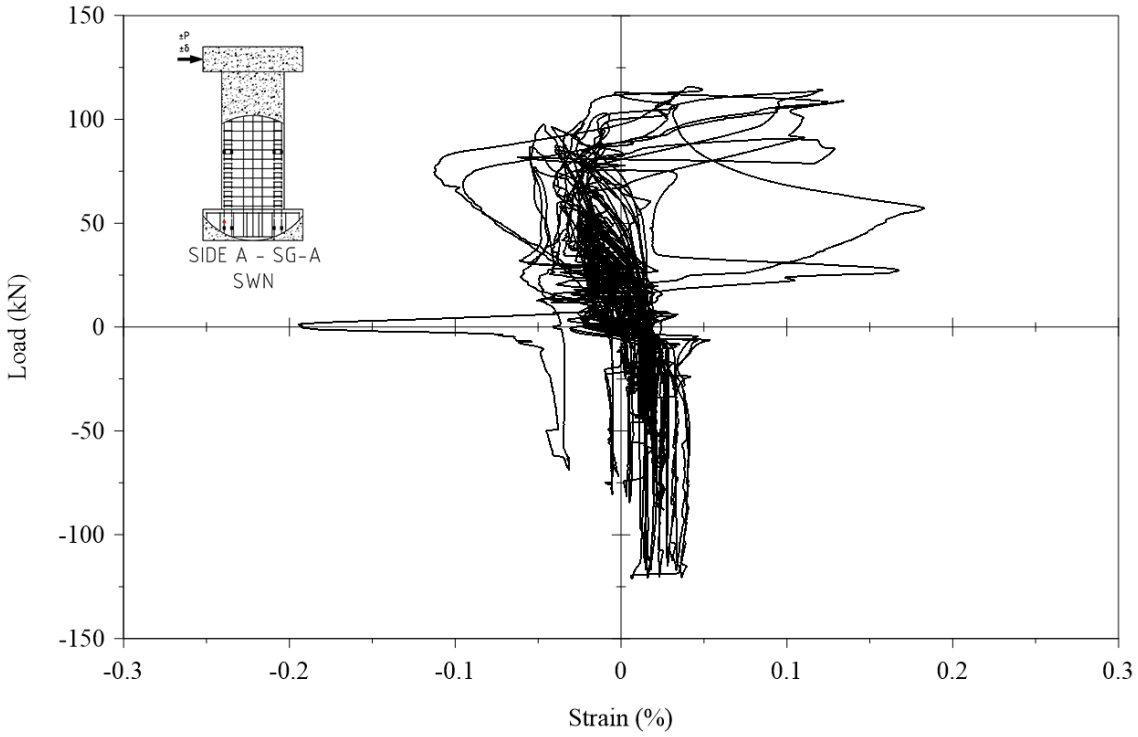

Figure C.89. Cyclic strain response from Strain Gauge A.

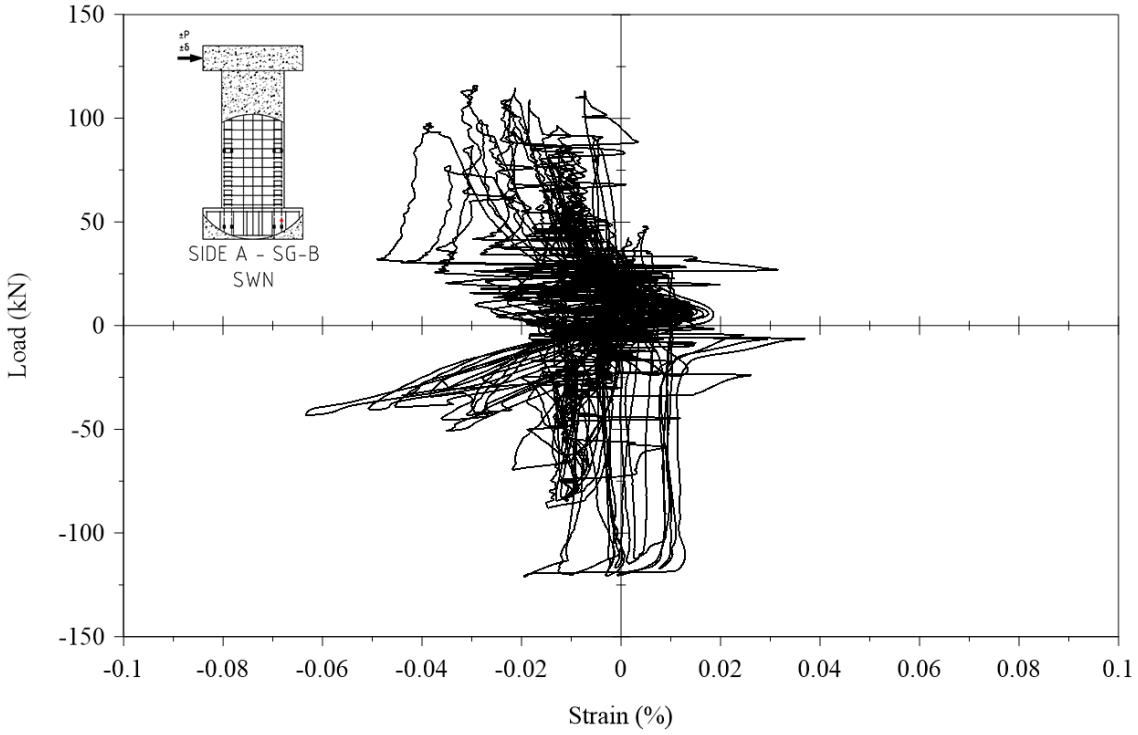

Figure C.90. Cyclic strain response from Strain Gauge B.

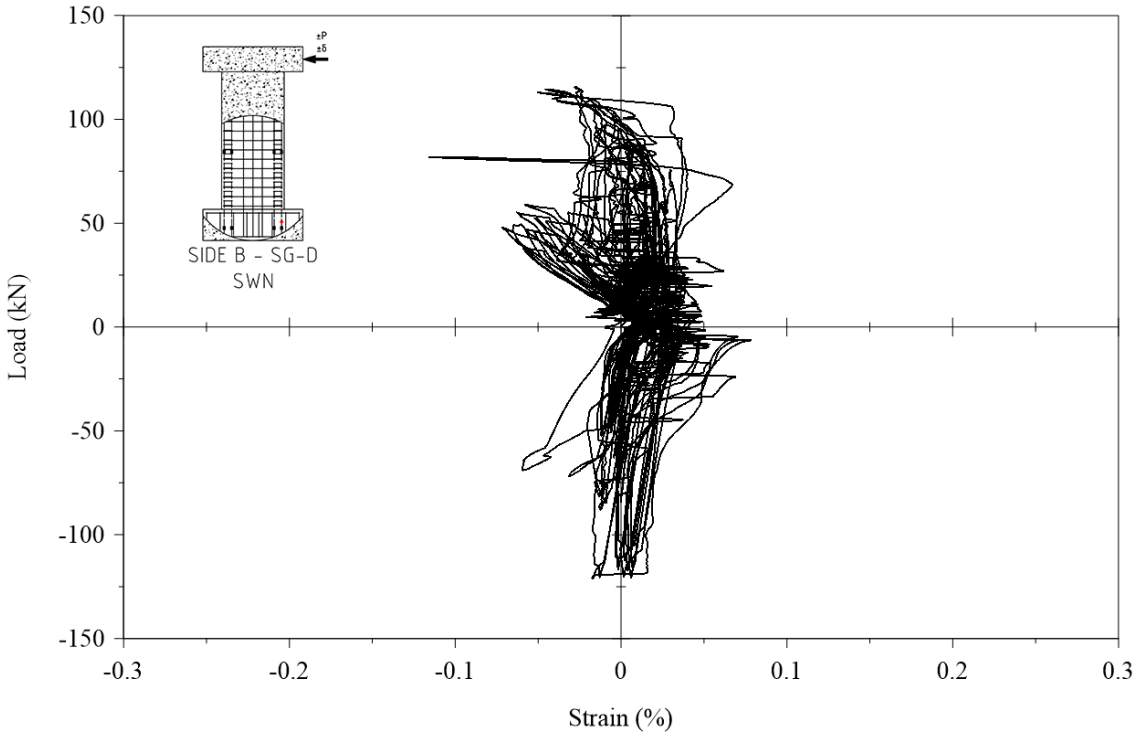

Figure C.91. Cyclic strain response from Strain Gauge D.

APPENDIX D

Instrumentation Frame

Design Drawings

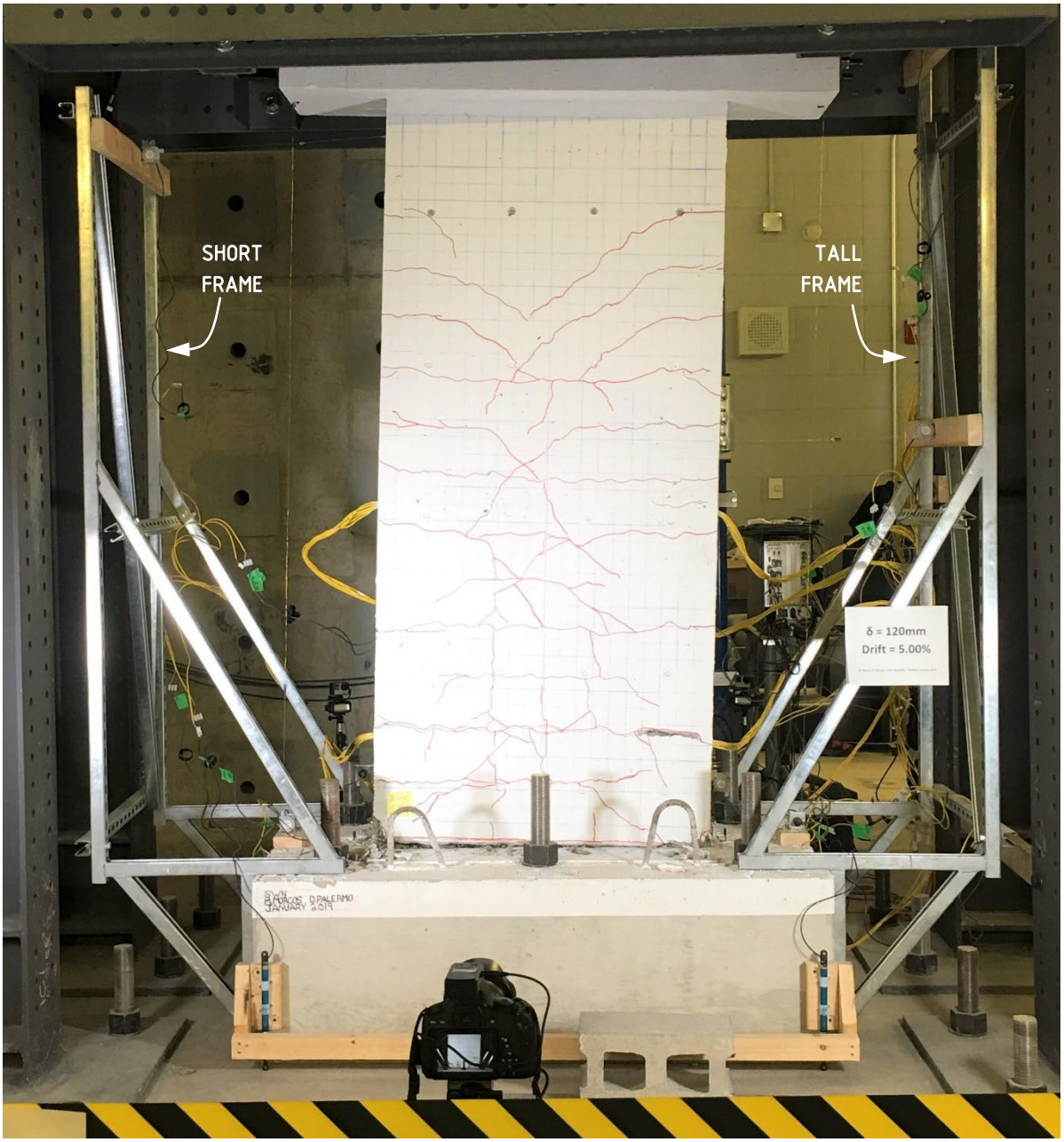

Figure D.1. Instrumentation frame installed on shear wall specimen with mounted instruments.

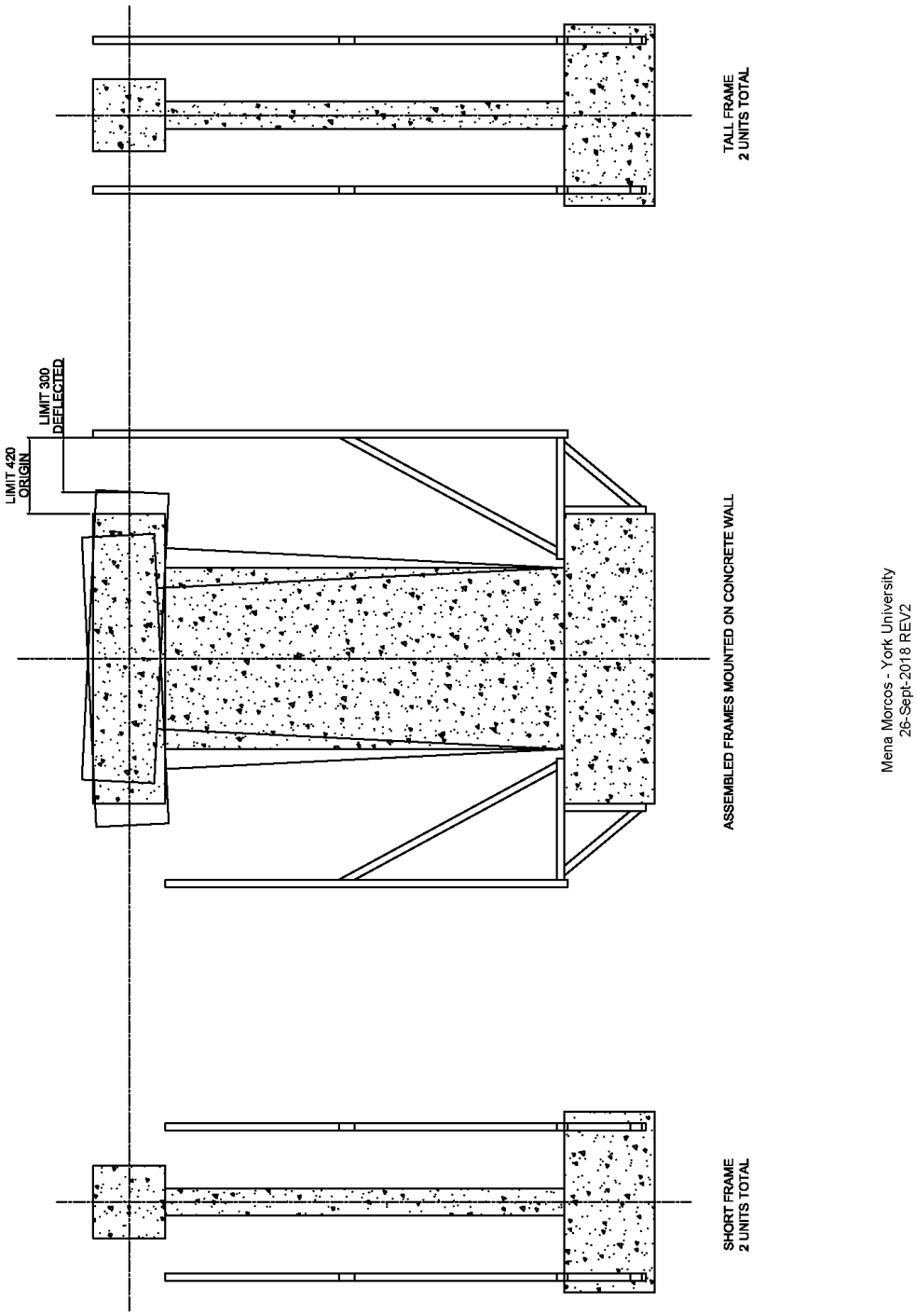

Figure D.2. Instrumentation frame design detail – Drawing 1.

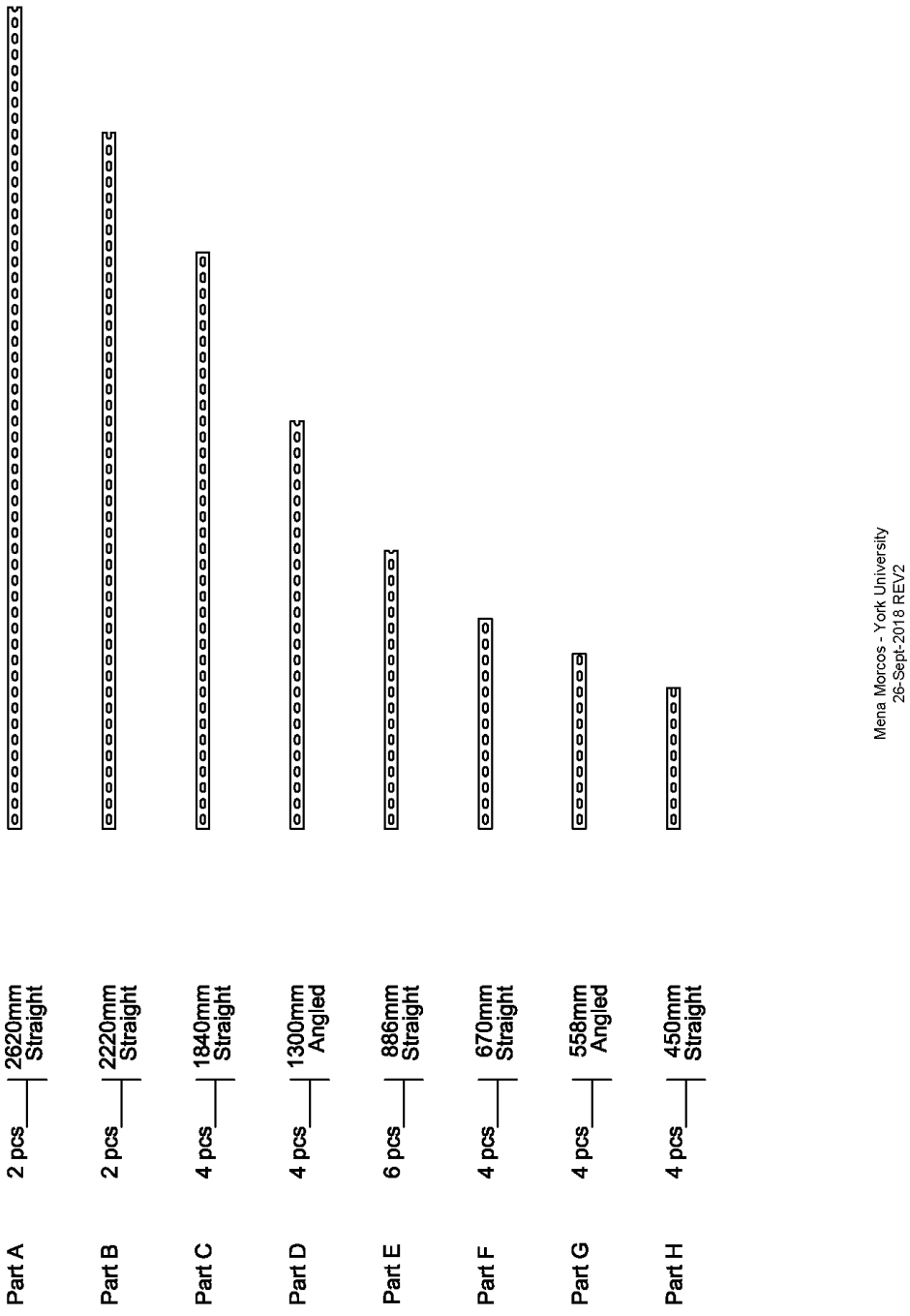

Figure D.3. Instrumentation frame design detail – Drawing 2.

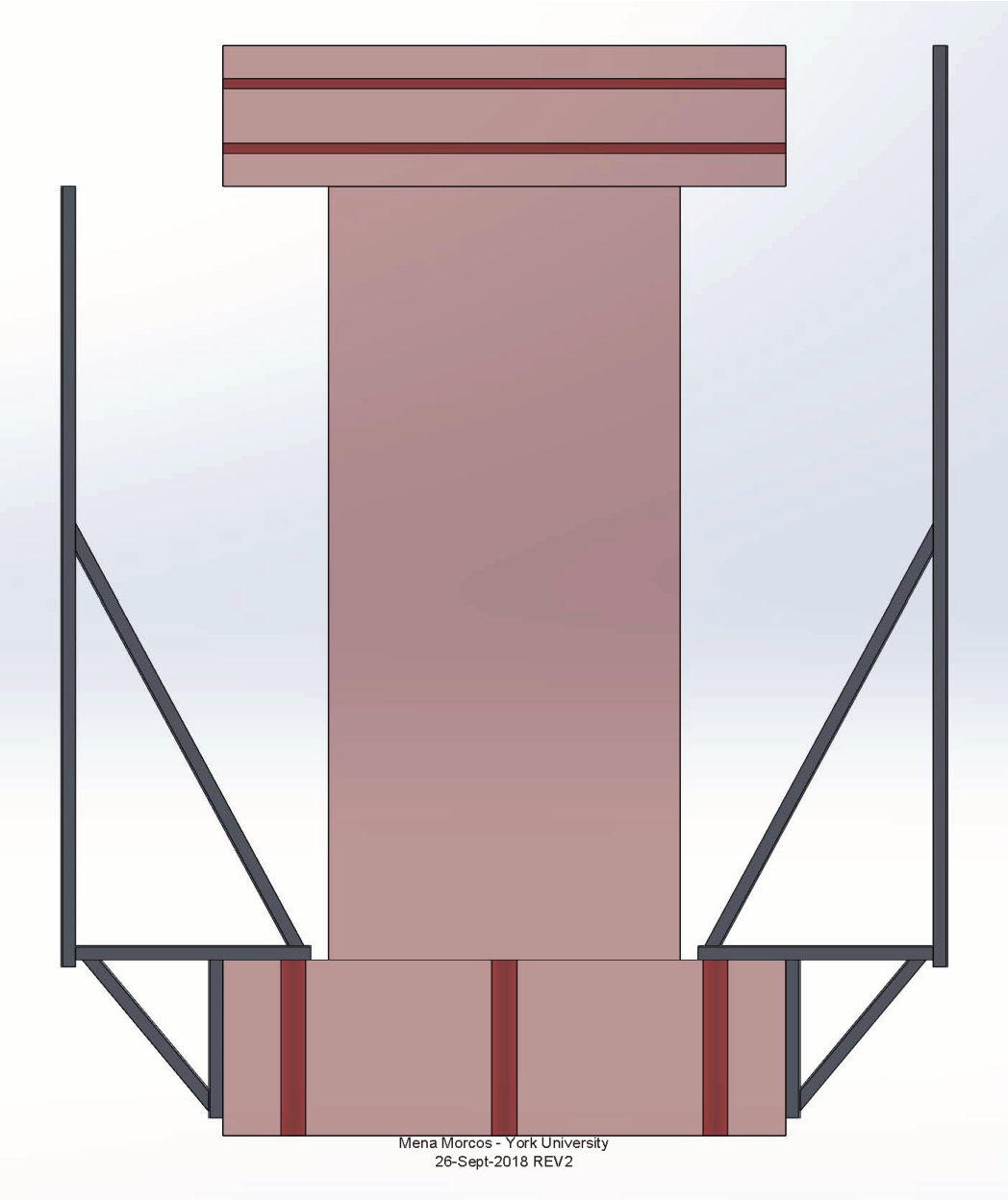

Figure D.4. Instrumentation frame design detail – Drawing 3.

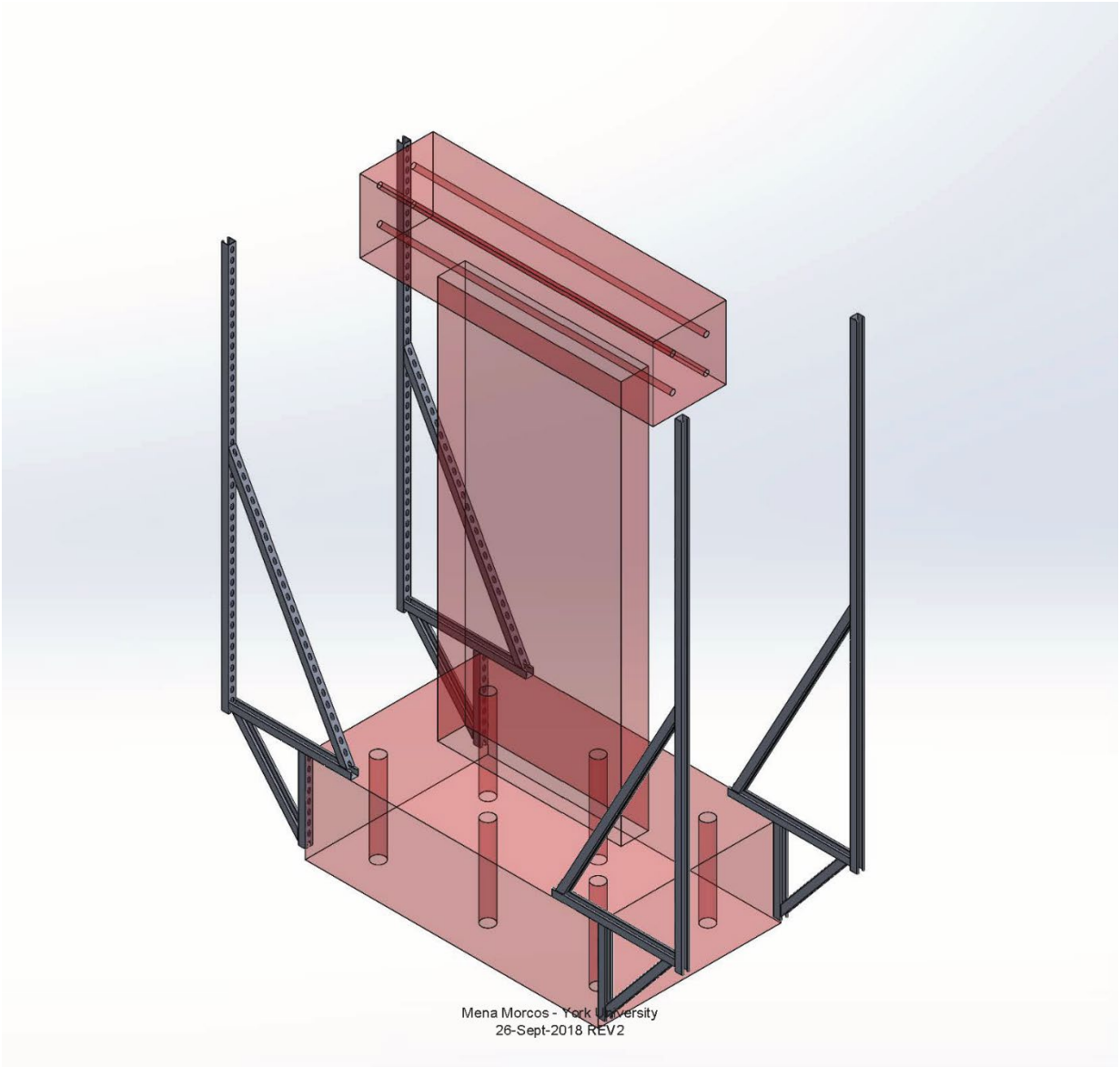

Figure D.5. Instrumentation frame design detail – Drawing 4.

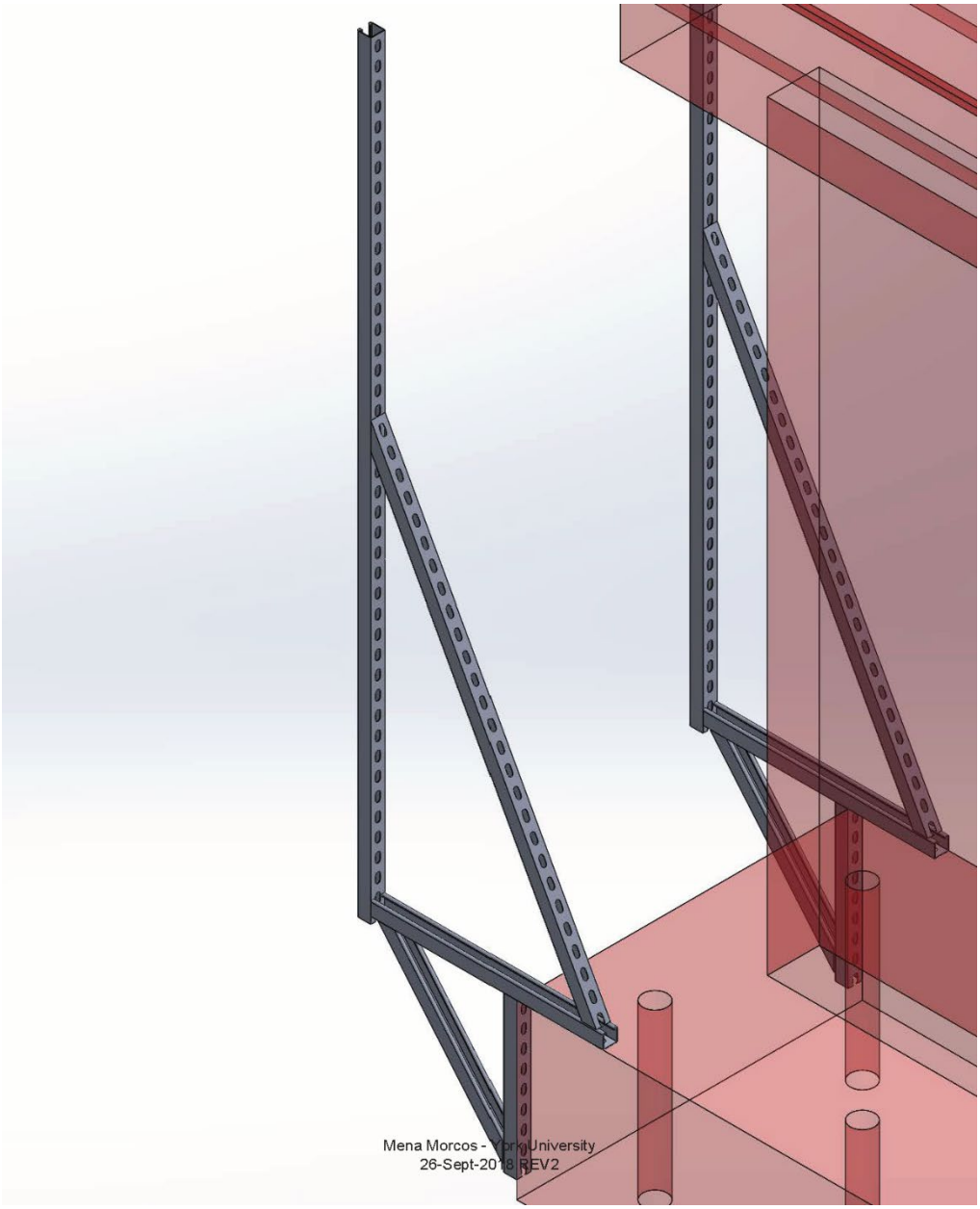

Figure D.6. Instrumentation frame design detail – Drawing 5.

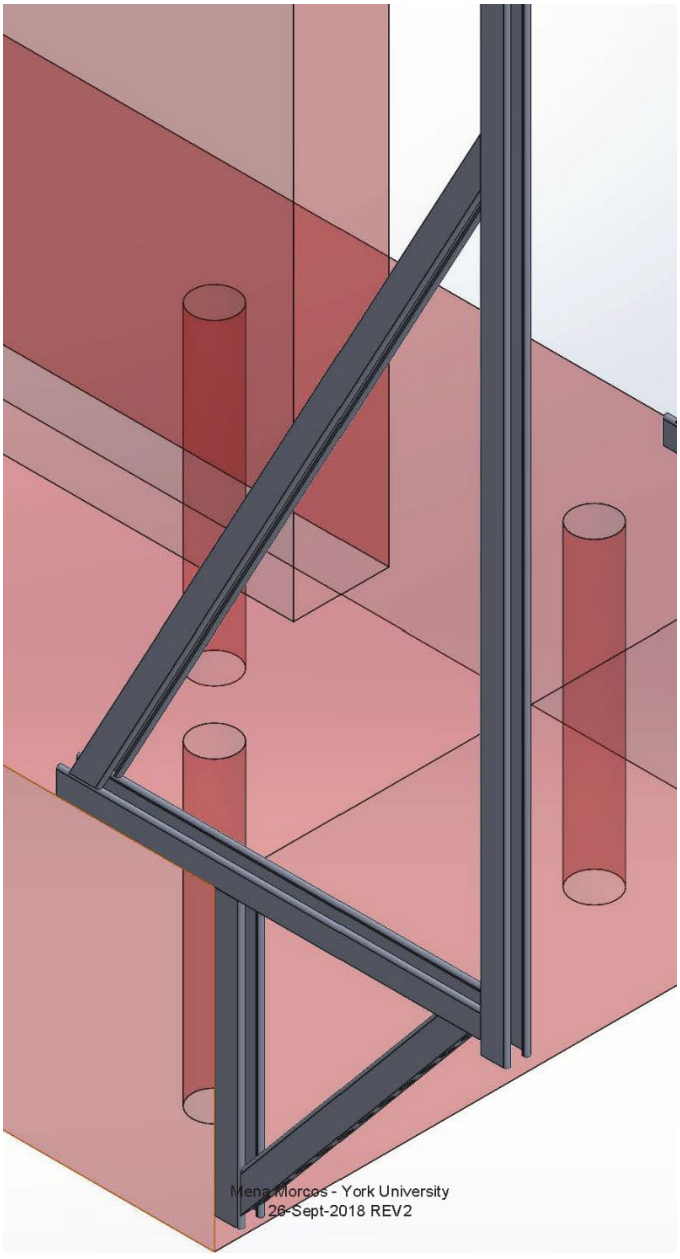

Figure D.7. Instrumentation frame design detail – Drawing 6.

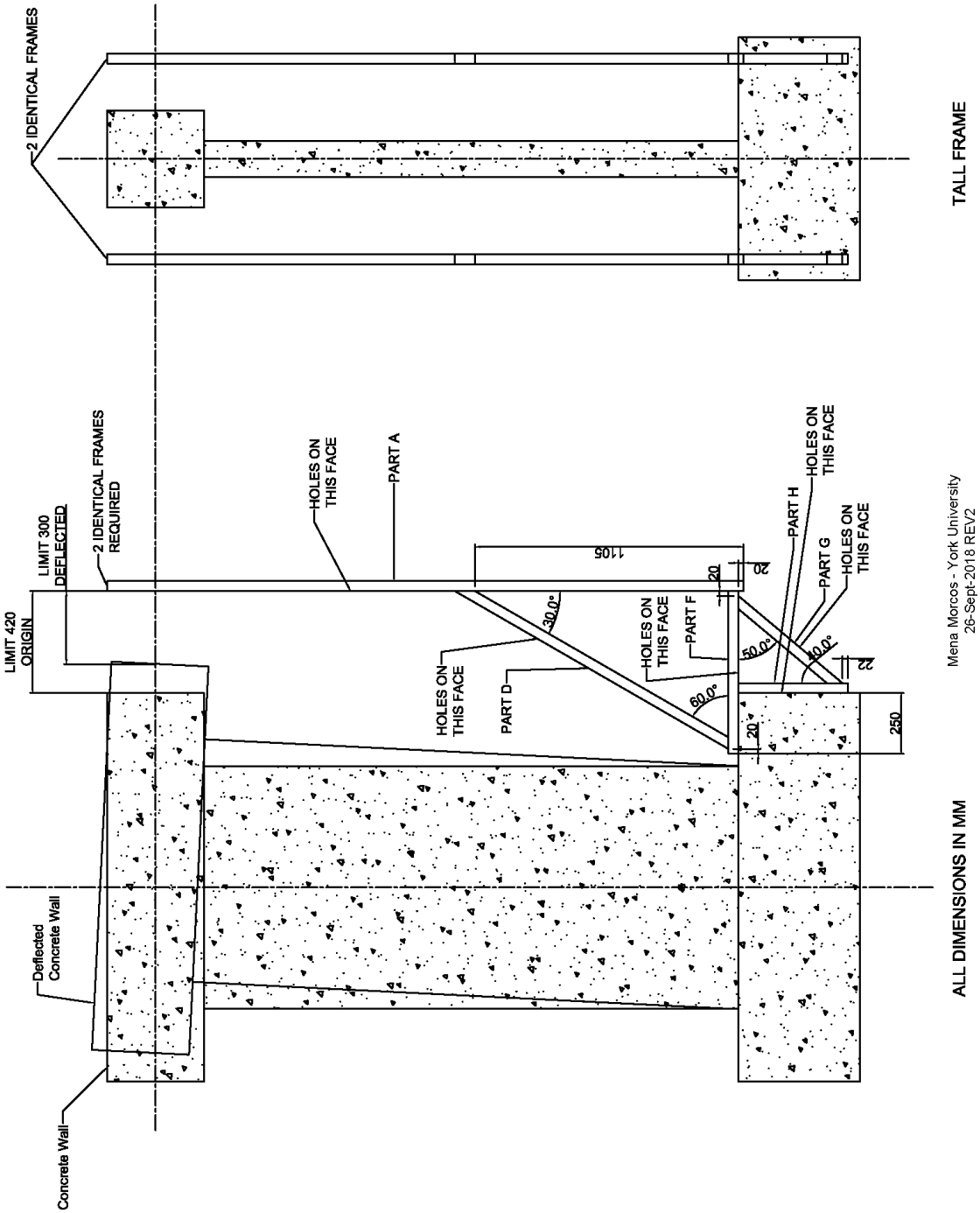

Figure D.8. Instrumentation frame design detail – Drawing 7.

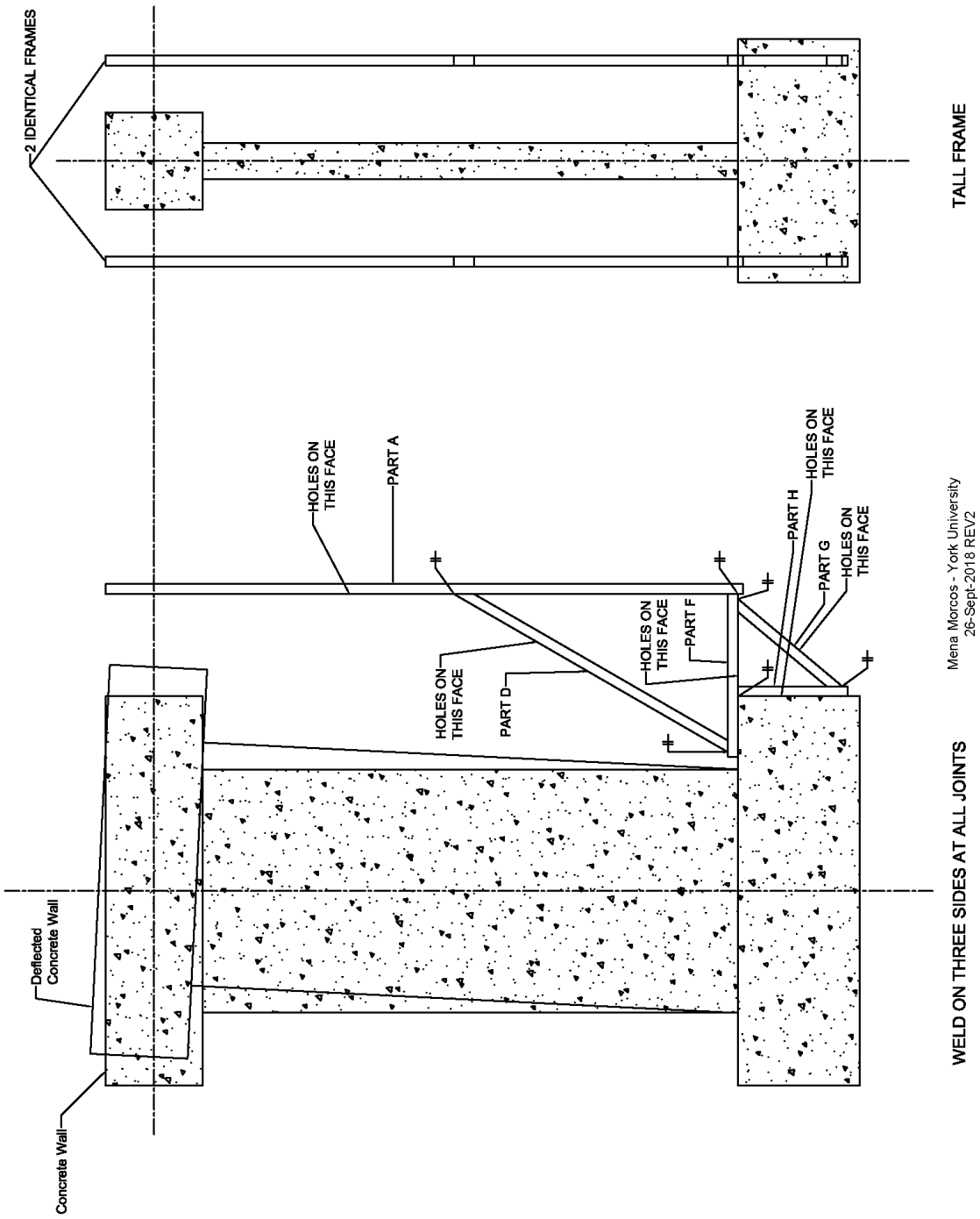

Figure D.9. Instrumentation frame design detail – Drawing 8.

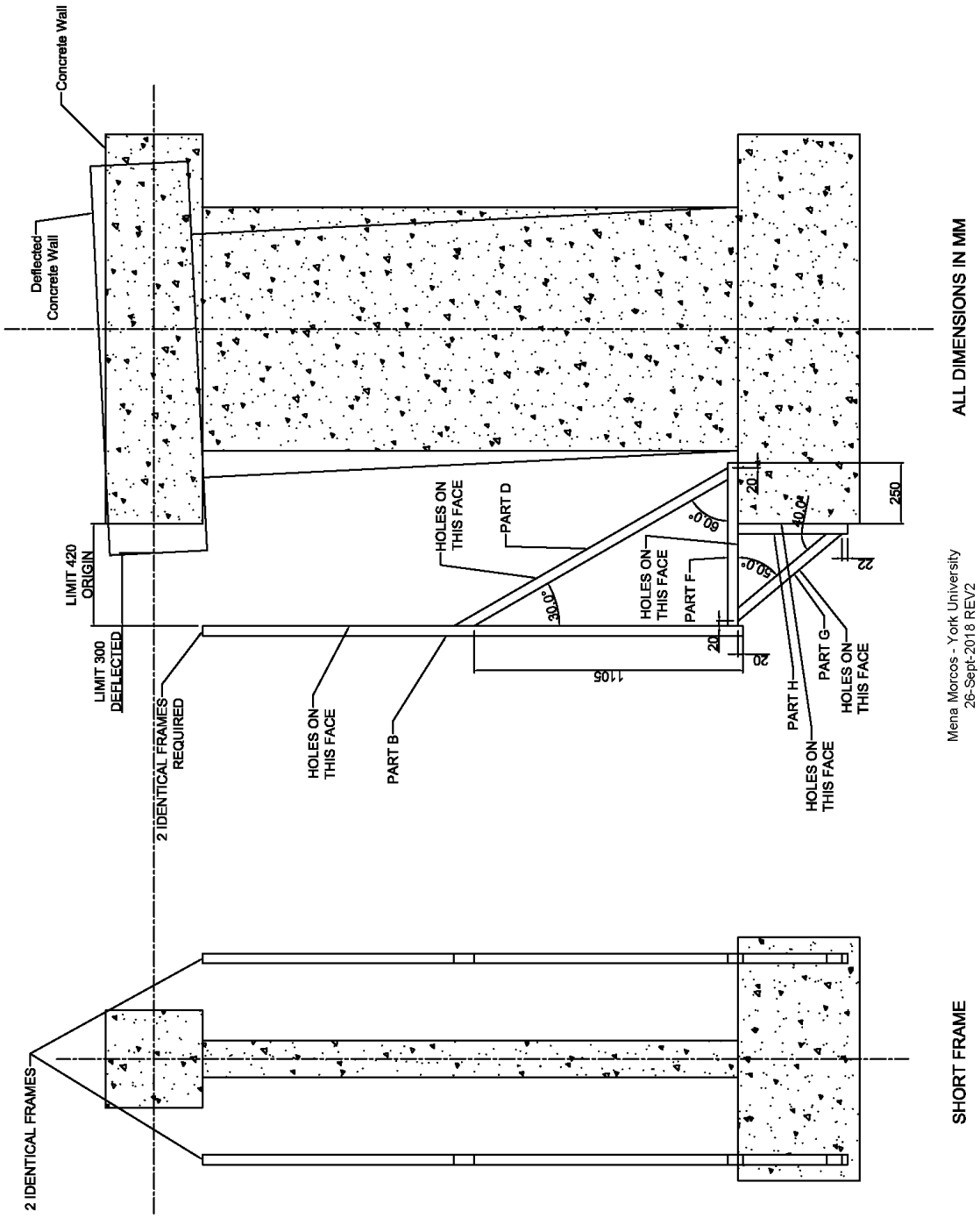

Figure D.10. Instrumentation frame design detail – Drawing 9.

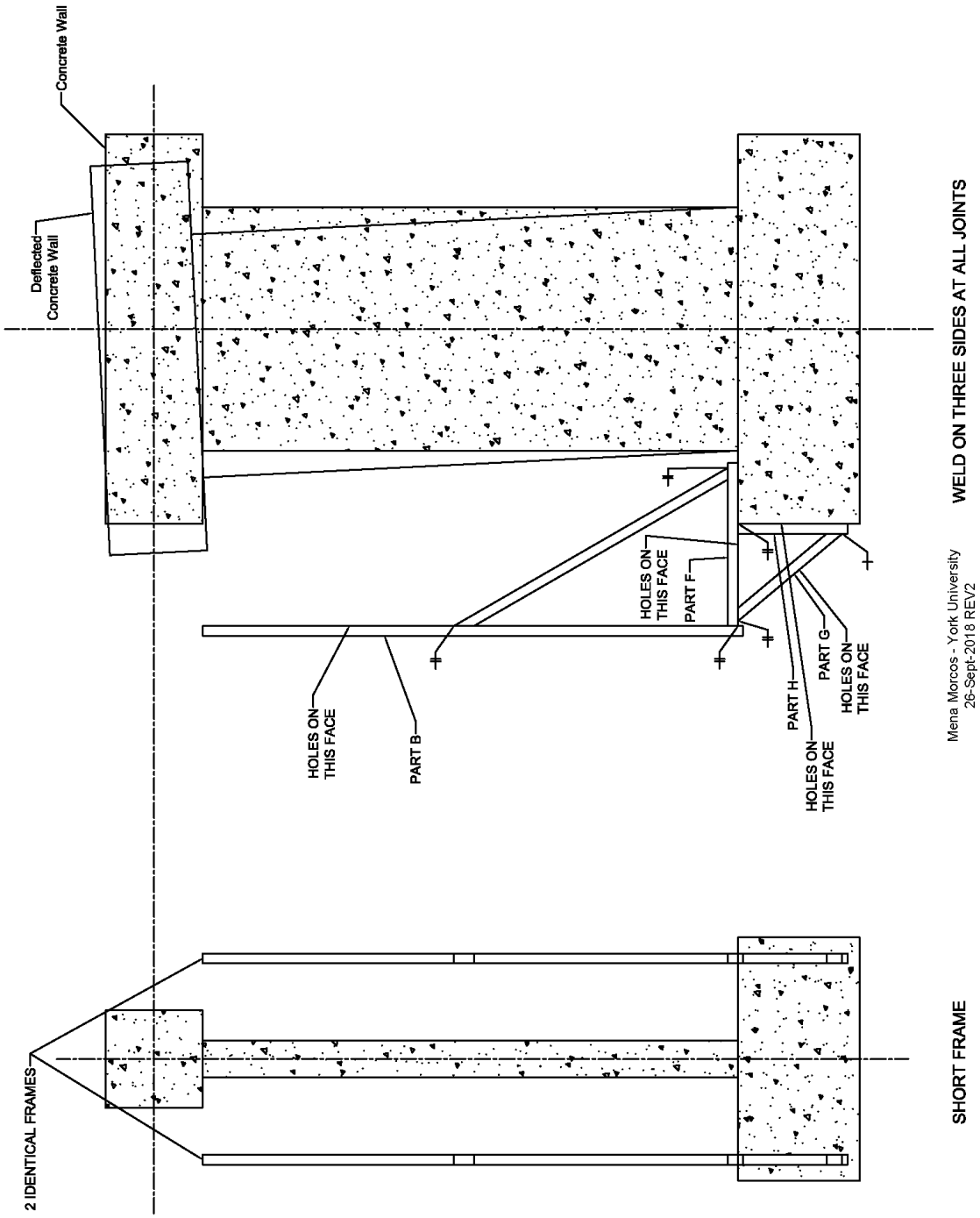

Figure D.11. Instrumentation frame design detail – Drawing 10.

Lateral Bracing System

Design Calculations and Design Drawings

Design of Lateral Brace System

Date: 27-November-2017 Designed according to CSA S16-14

Wall Dimensions

$t := 150mm$ Thickness

$l := 1000mm$ Length

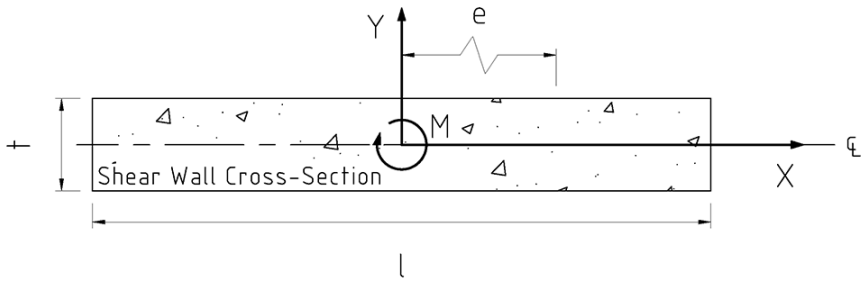

Determine out-of-plane lateral forces.

Assume: Accidental eccentricity inherent in structure.

$D_X := 1m$ Eccentricity reference dimension - length of wall

$e := 0.1 \cdot D_X$ Accidental Eccentricity

$e = 0.1\,m$ Eccentricity

Assume: Max. lateral load estimate is 120kN based on NFLEA simulation.

$F_X := 120kN$ Maximum in-plane lateral load

$M := e \cdot F_X$

$M = 12 \cdot kN \cdot m$ Accidental torsion

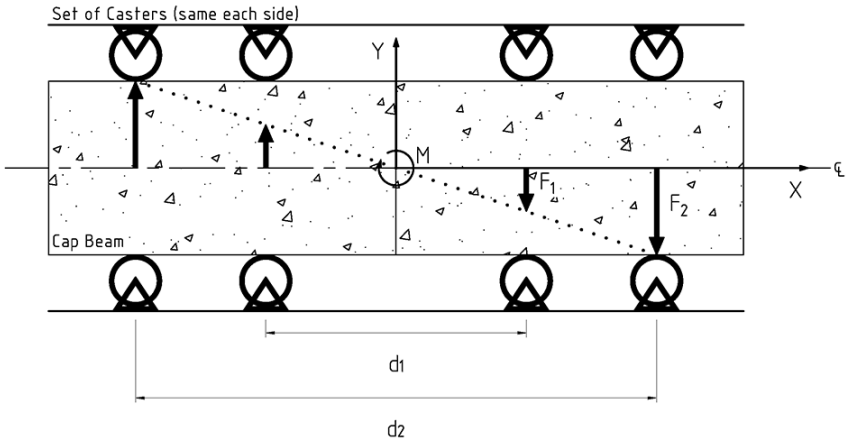

Given

$F_1 := 0kN$ $F_2 := 0kN$ Magnitude of out-of-plane lateral forces is unknown.

$d_1 := 0.6m$ $d_2 := 1.2m$ Assumed spacing of casters along length of cap beam. Symmetrical about 'Y' centerline.

Variable solution parameters.

$(F_1 \cdot d_1) + (F_2 \cdot d_2) = M$ Eqn 1

$F_1 \cdot d_2 = F_2 \cdot d_1$ Eqn 2

$$\text{Find}(F_1, F_2) \rightarrow \begin{pmatrix} 4.0 \cdot kN \\ 8.0 \cdot kN \end{pmatrix}$$

Design values for out-of-plane lateral forces.

$F_1 := 4kN$ Force 1

$F_2 := 8kN$ Force 2

Design Requirements:

- Castors that support min. 10kN.
- Lateral brace sufficiently resists out-of-plane rotation

Modified Channel Weak Axis Flexure Check

Structural Steel Section: C150x19

Dimensions

$d := 152mm$ Depth

$w := 11.1mm$ Web Thickness

$b := 54mm$ Flange Width

$t := 8.7mm$ Flange Thickness

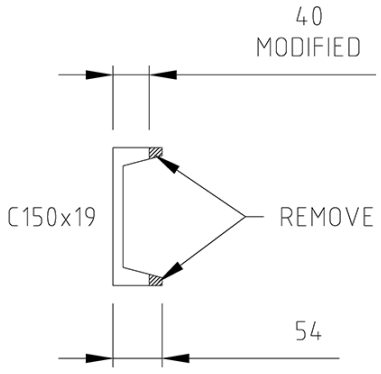

Material Properties

$f_y := 350MPa$ Steel Yield Strength - G40.21-350W

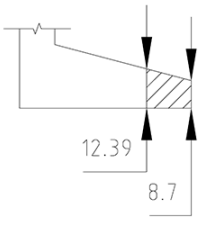

Modification (to allow for clamping adjustment of lateral brace along cap beam)

$b := 40mm$ Flange Width

$t := 12.4mm$ Flange Thickness

Geometric Properties

$A := d \cdot w + 2 \cdot (b - w) \cdot t$

$A = 2.404 \times 10^{3} \cdot mm^{2}$ Cross-Section Area

$x := \frac{1}{2 \cdot A} \cdot \left[(d - 2 \cdot t) \cdot w^{2} + 2 \cdot t \cdot b^{2} \right]$

$x = 11.5 \cdot mm$ Distance to elastic neutral axis from back of channel

$I_y := \frac{1}{3} \cdot \left[d \cdot x^{3} + 2 \cdot t \cdot (b - x)^{3} - (d - 2 \cdot t) \cdot (x - w)^{3} \right]$

$I_y = 268420.651 \cdot mm^{4}$ Moment of Inertia about y-axis (weak axis)

Mechanical Properties

$S_1 := \frac{I_y}{x}$

$S_1 = 2.331 \times 10^{4} \cdot mm^{3}$ Elastic Section Modulus (below neutral axis)

$S_2 := \frac{I_y}{b - x}$

$S_2 = 9.423 \times 10^{3} \cdot mm^{3}$ Elastic Section Modulus (above neutral axis)

Elastic Flexural Capacity Check

$M_r := 0.9 \cdot f_y \cdot \min(S_1, S_2)$ Elastic Flexural Moment Capacity (based on first yield)

$M_r = 2.97 \cdot kN \cdot m$ Elastic Flexural Moment Capacity

Moment Due to Applied Load

$l_c := 1650mm$ Channel Length

$F_1 = 4 \cdot kN$ First Point Load

$x_1 := 1125mm$ Position of First Point Load from Left Support

$F_2 = 8 \cdot kN$ Second Point Load

$x_2 := 225mm$ Position of Second Point Load from Right Support

$$R_A := \frac{F_1 \cdot (l_c - x_1) + F_2 \cdot x_2}{l_c}$$

$R_A = 2.36 \cdot kN$ Support Reaction at Point A

$$R_B := \frac{F_1 \cdot x_1 + F_2 \cdot (l_c - x_2)}{l_c}$$

$R_B = 9.64 \cdot kN$ Support Reaction Point B

Location	Shear	Moment
Point A	$V_A := R_A = 2.36 \cdot kN$	$M_A := 0kN \cdot m$
Point B	$V_B := R_A - F_1 = -1.64 \cdot kN$	$M_B := M_A + V_A \cdot 1.125m = 2.66 \cdot kN \cdot m$
Point C	$V_C := V_B - F_2 = -9.64 \cdot kN$	$M_C := M_B + V_B \cdot 0.3m = 2.17 \cdot kN \cdot m$
Point D	$V_D := R_B = 9.64 \cdot kN$	$M_D := M_C + V_C \cdot 0$

$M_{max} := \max(M_A, M_B, M_C, M_D)$

$M_{max} = 2.66 \cdot kN \cdot m$ Maximum Moment

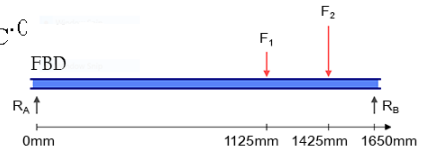

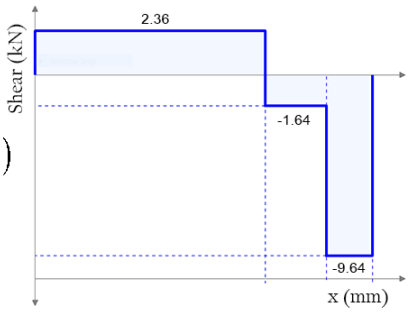

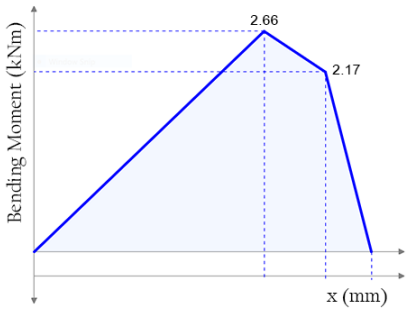

Flexure Check

$M_{check} := \text{if}(M_r > M_{max}, \text{"Sufficient Capacity"}, \text{"Insufficient Capacity"})$

$M_{check} = \text{"Sufficient Capacity"}$ Moment Capacity Check

Assume: Limit out-of-plane deflection at location of load F_2 (at 1425mm from left support) to below 10mm, with consideration to cost of material and fabrication.

$\delta_{limit} := 10mm$

Deflection at F2 was determined by online software SkyCiv.

$\delta_{F2} := 5.77mm$

$\delta_{check} := \text{if}(\delta_{F2} < \delta_{limit}, \text{"Sufficient Capacity"}, \text{"Insufficient Capacity"})$

$\delta_{check} = \text{"Sufficient Capacity"}$ Deflection Check

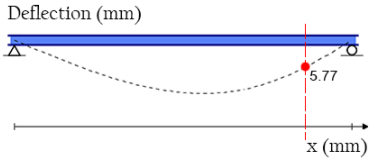

Therefore, section C150x19 is sufficient for lateral bracing.

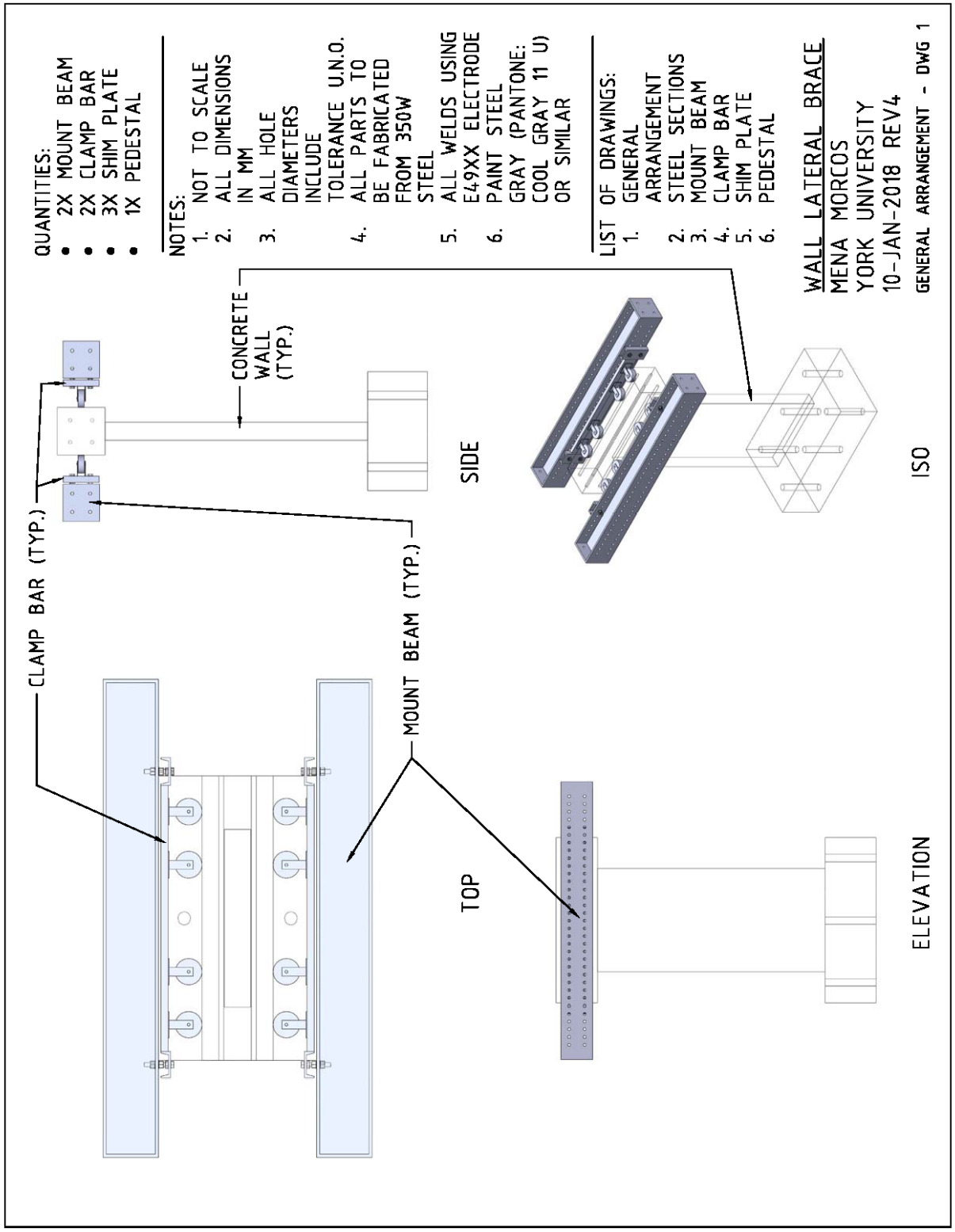

Figure E.1. Lateral brace design detail – Drawing 1.

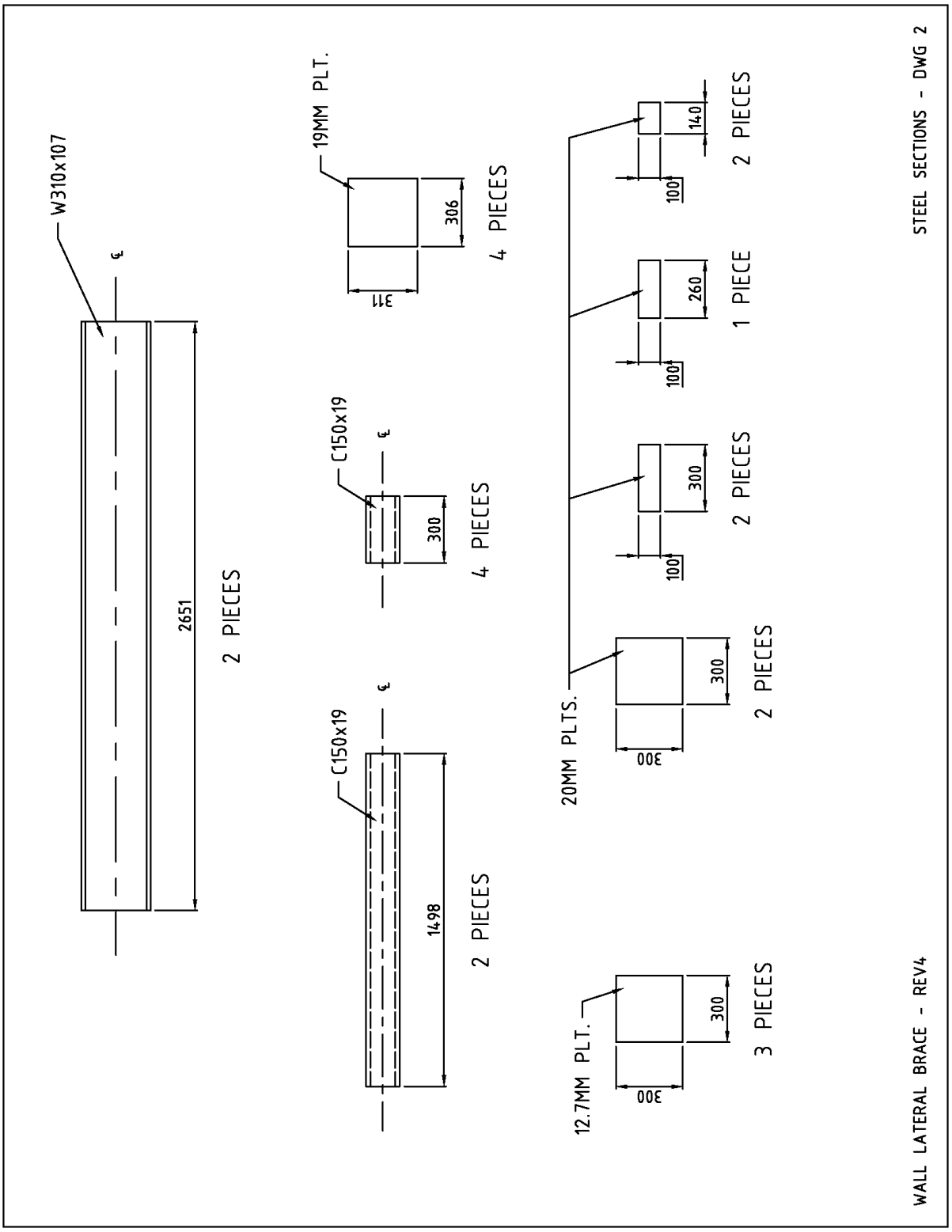

Figure E.2. Lateral brace design detail – Drawing 2.

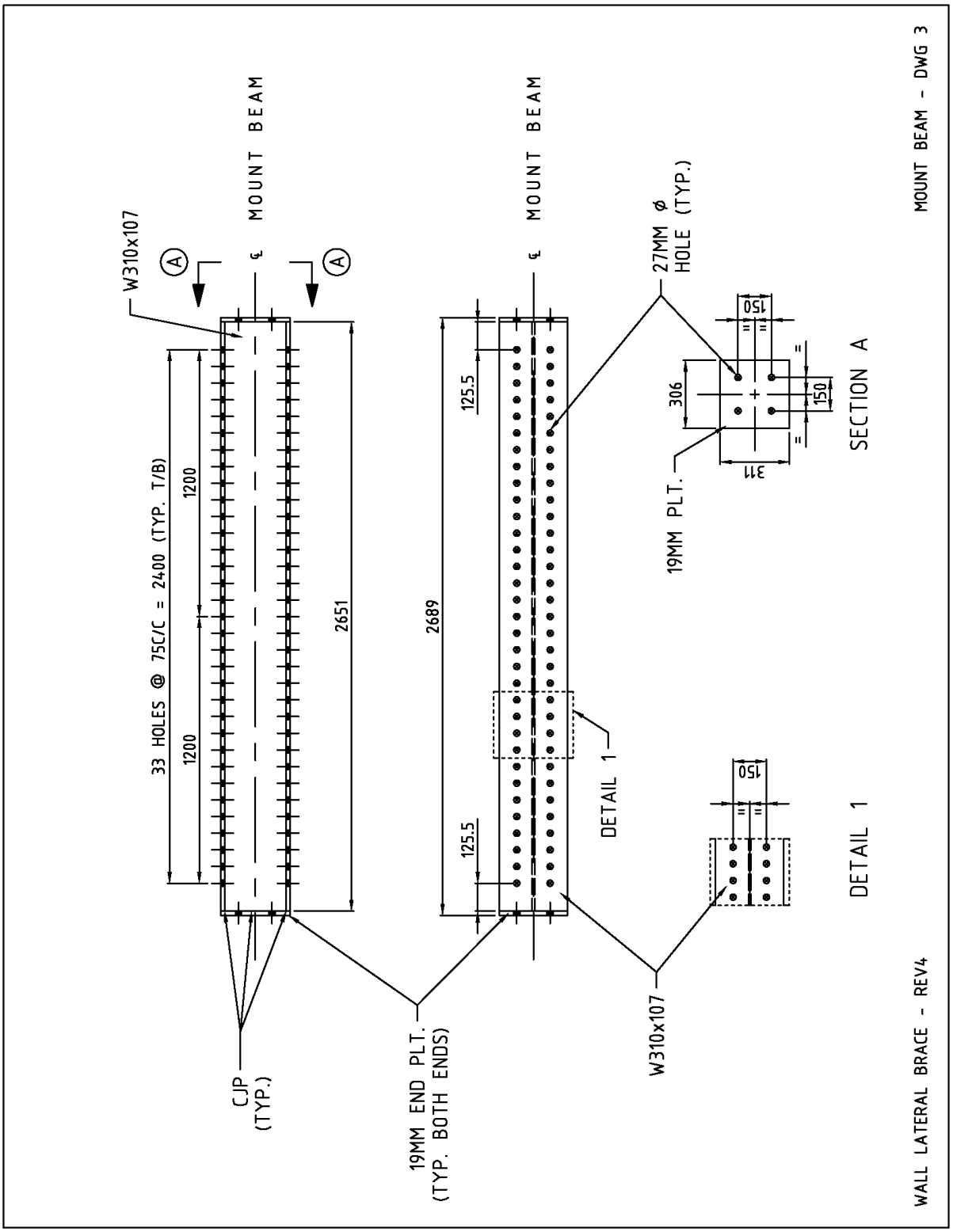

Figure E.3. Lateral brace design detail – Drawing 3.

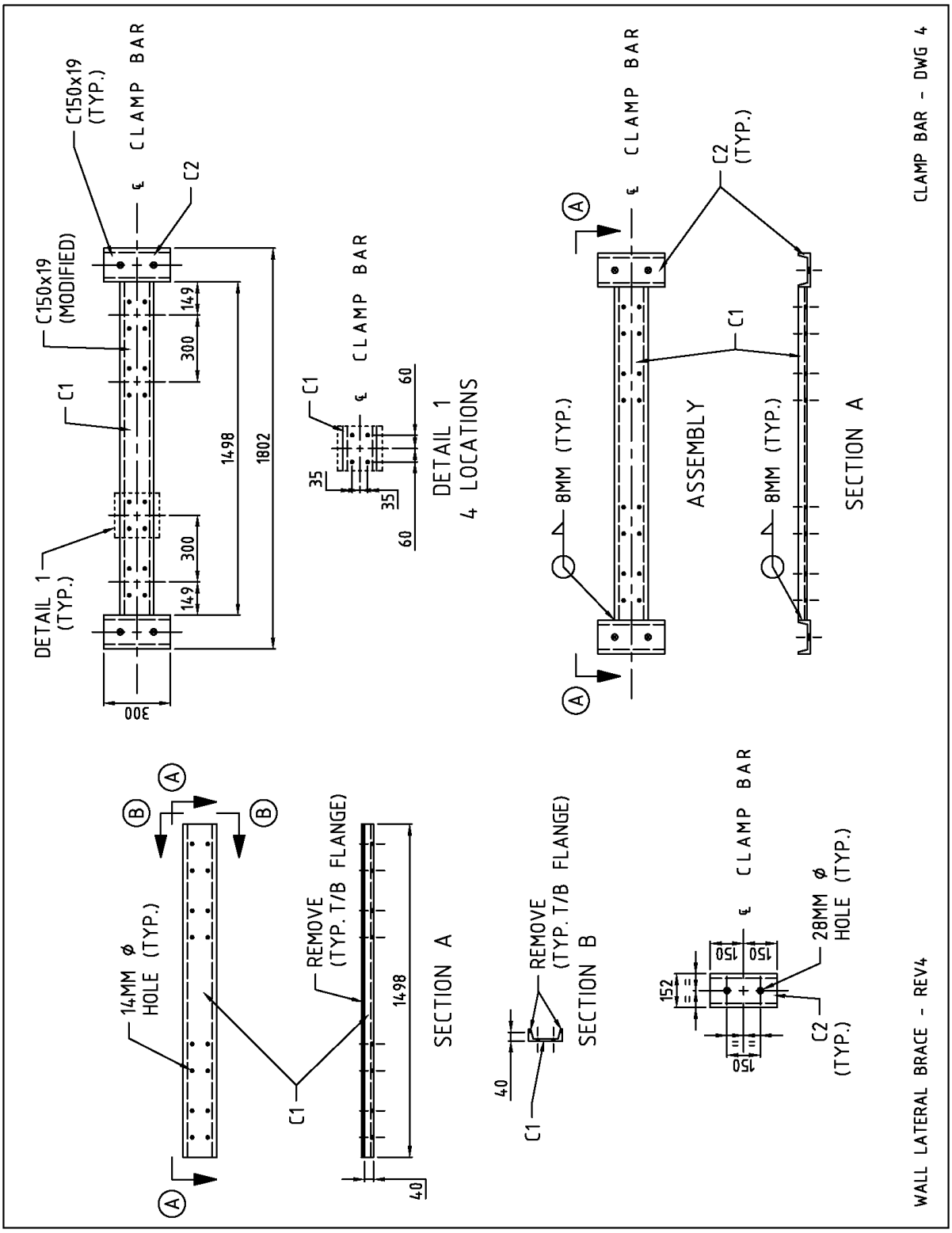

Figure E.4. Lateral brace design detail – Drawing 4.

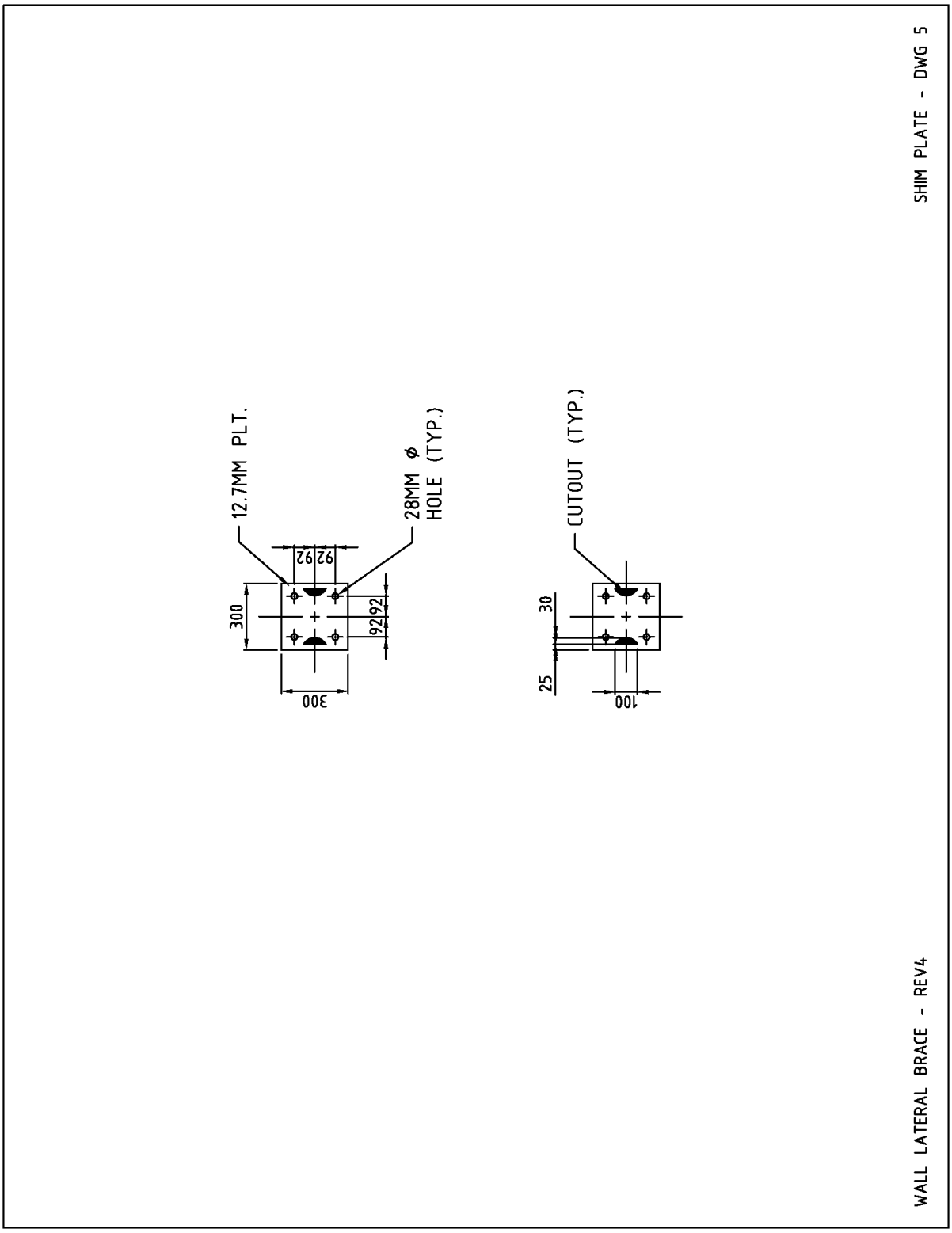

Figure E.5. Lateral brace design detail – Drawing 5.

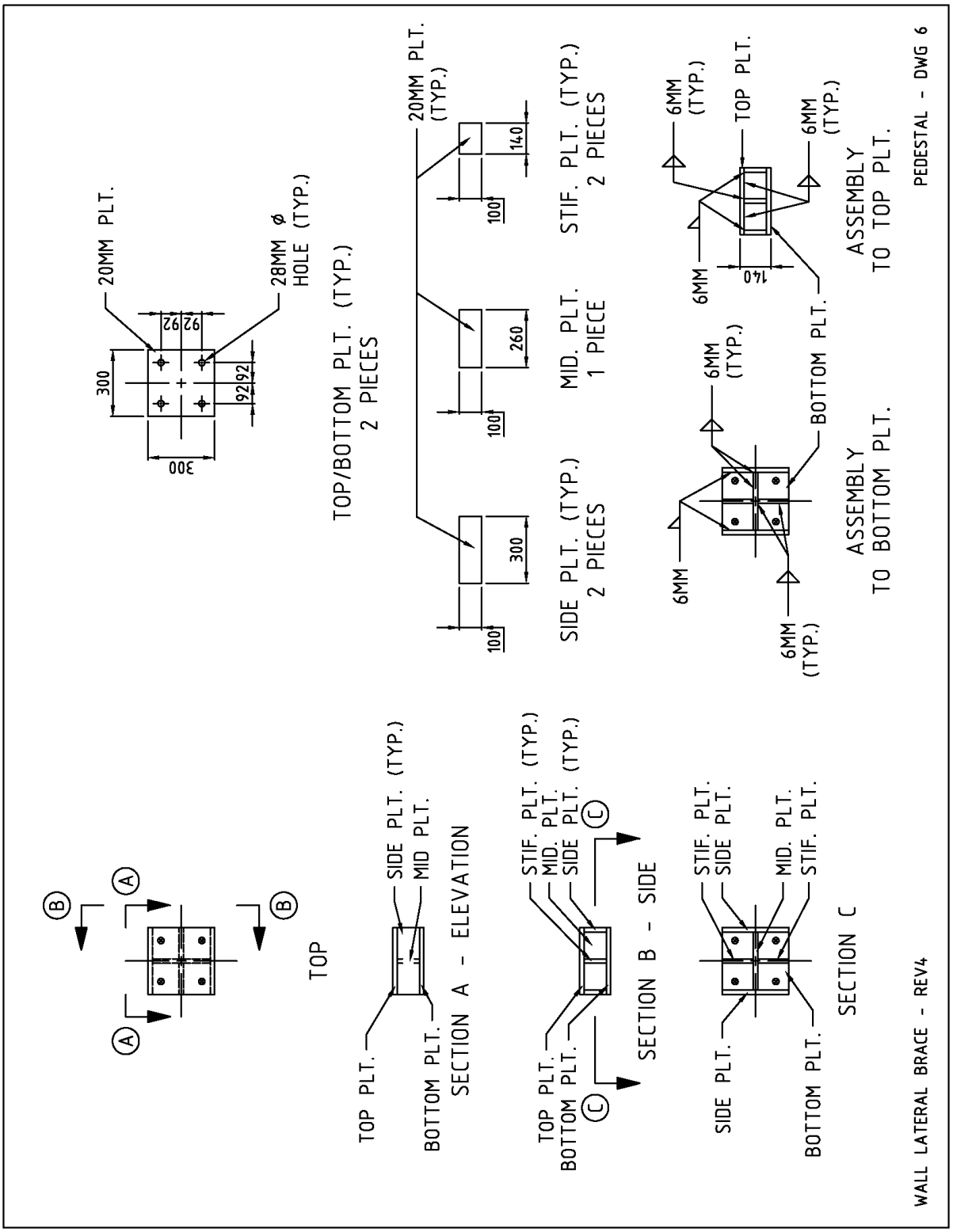

Figure E.6. Lateral brace design detail – Drawing 6.

Loading System

Simplified Design Check and Fabrication Drawings

Steel Loading Bracket Simplified Design Check

Date: 10-March-2016 Designed according to CSA S16-14

Loading Bracket - REV1.sdb

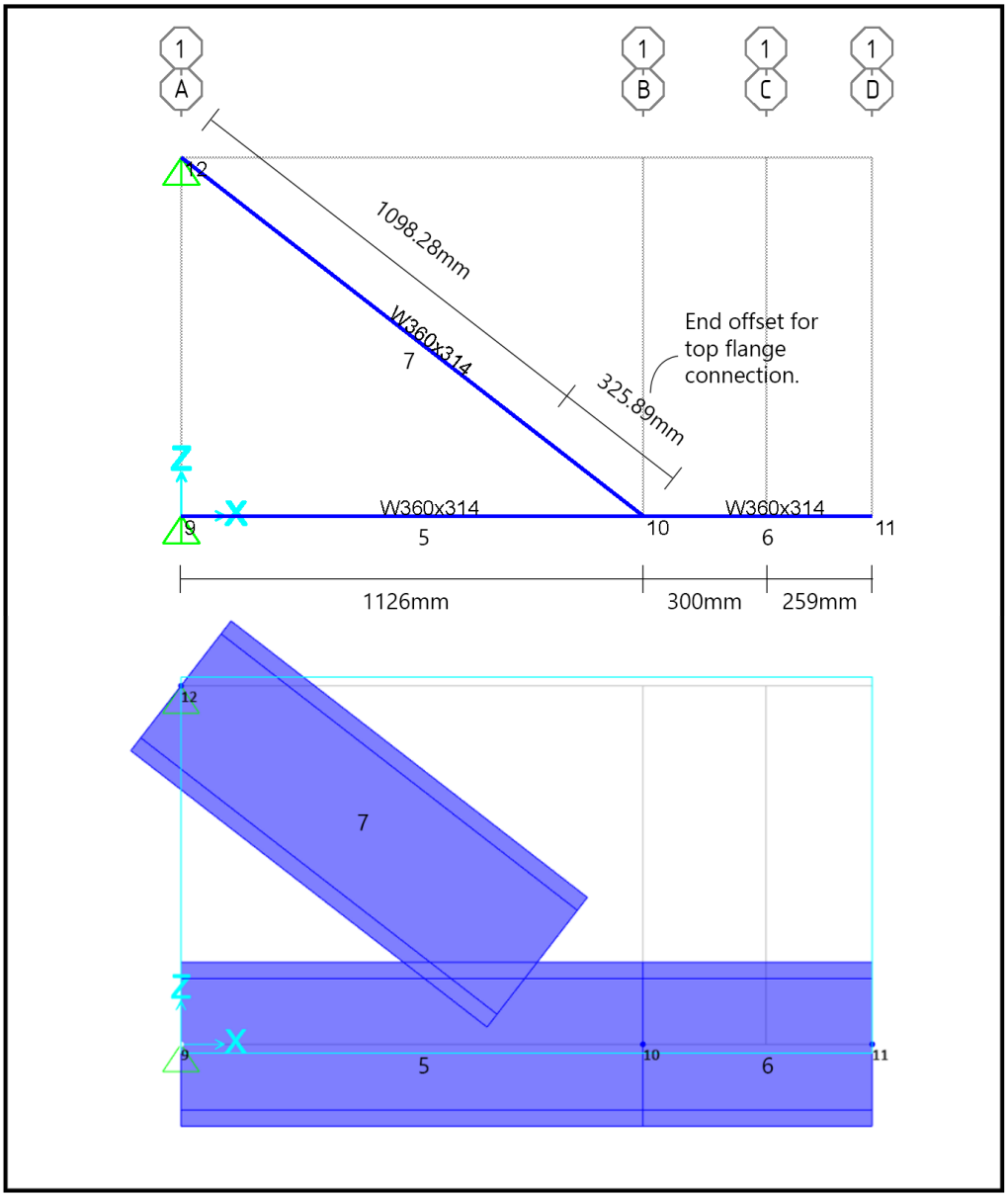

Loading Bracket - REV1.sdb

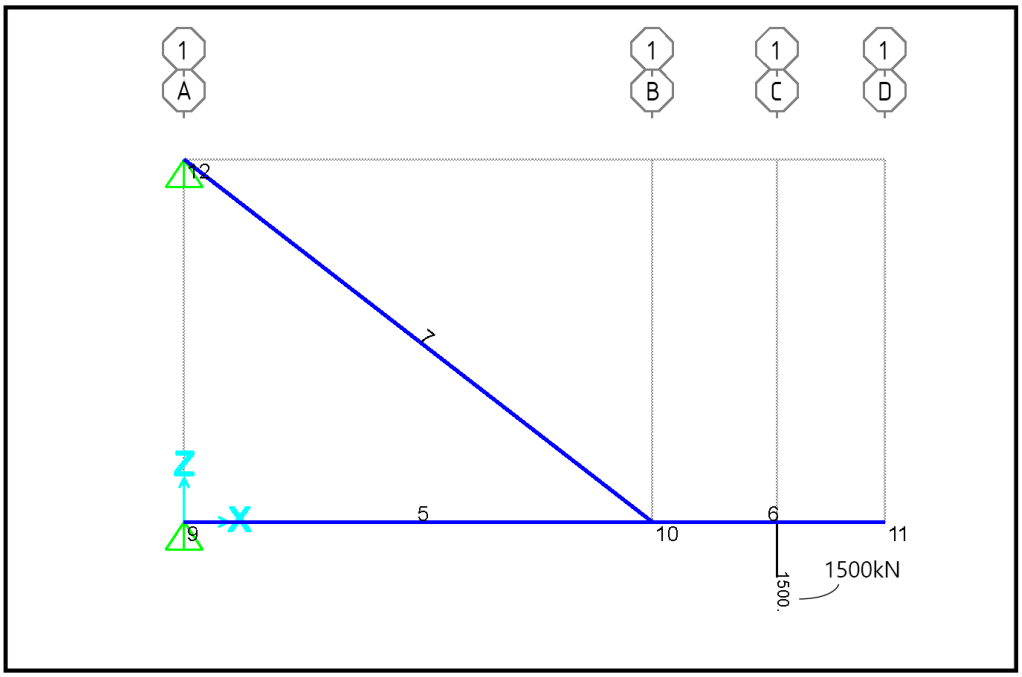

SAP2000 22.0.0 Frame Span Loads (ACT-C-1500kN) (GLOBAL CSys) KN, mm, C

Loading Bracket - REV1.sdb

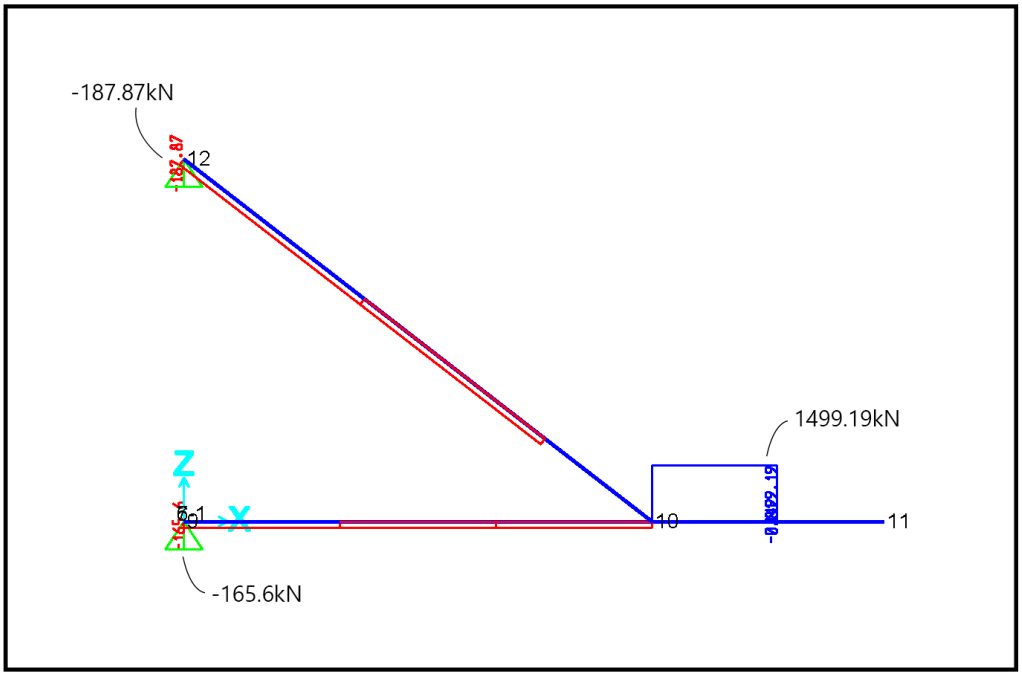

SAP2000 22.0.0 Shear Force 2-2 Diagram (COMB4 - SW + 1xACT-COM) KN, mm, C

Loading Bracket - REV1.sdb

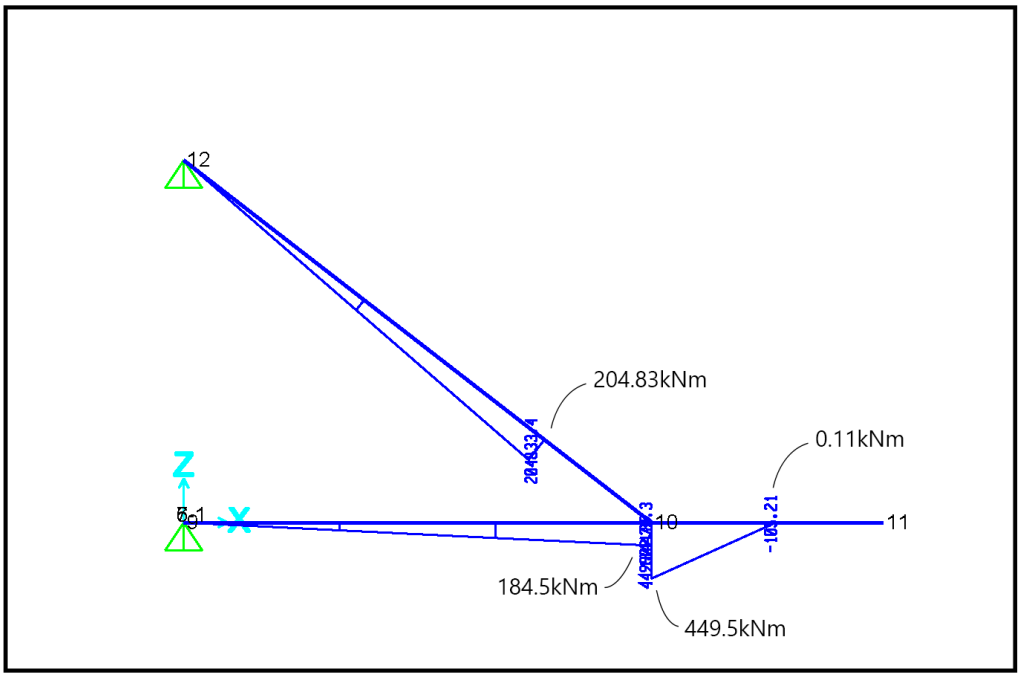

SAP2000 22.0.0 Moment 3-3 Diagram (COMB4 - SW + 1xACT-COM) KN, mm, C

Loading Bracket - REV1.sdb

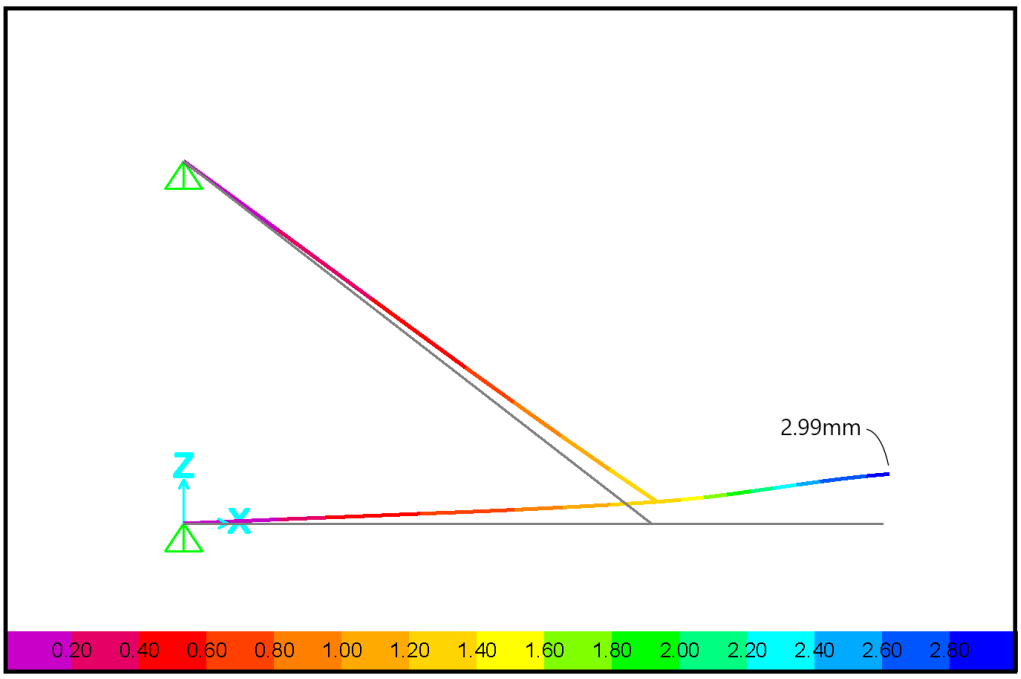

SAP2000 22.0.0 Deformed Shape (COMB4 - SW + 1xACT-COM) - Contours for Uz KN, mm, C

Loading Bracket - REV1.sdb

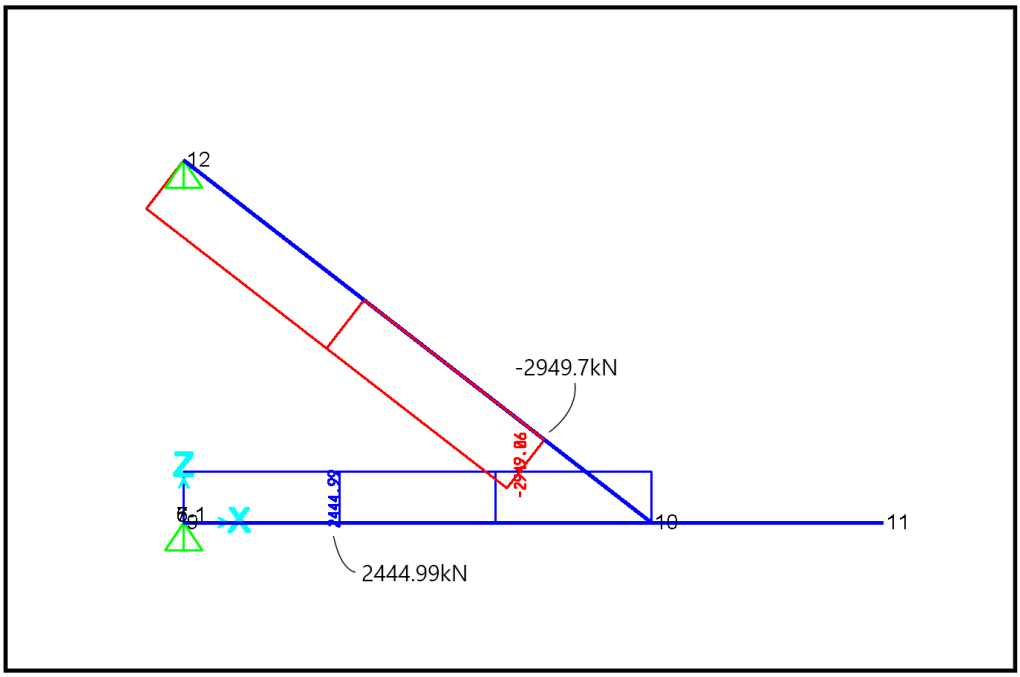

SAP2000 22.0.0 Axial Force Diagram (COMB4 - SW + 1xACT-COM) KN, mm, C

Loading Bracket - REV1.sdb

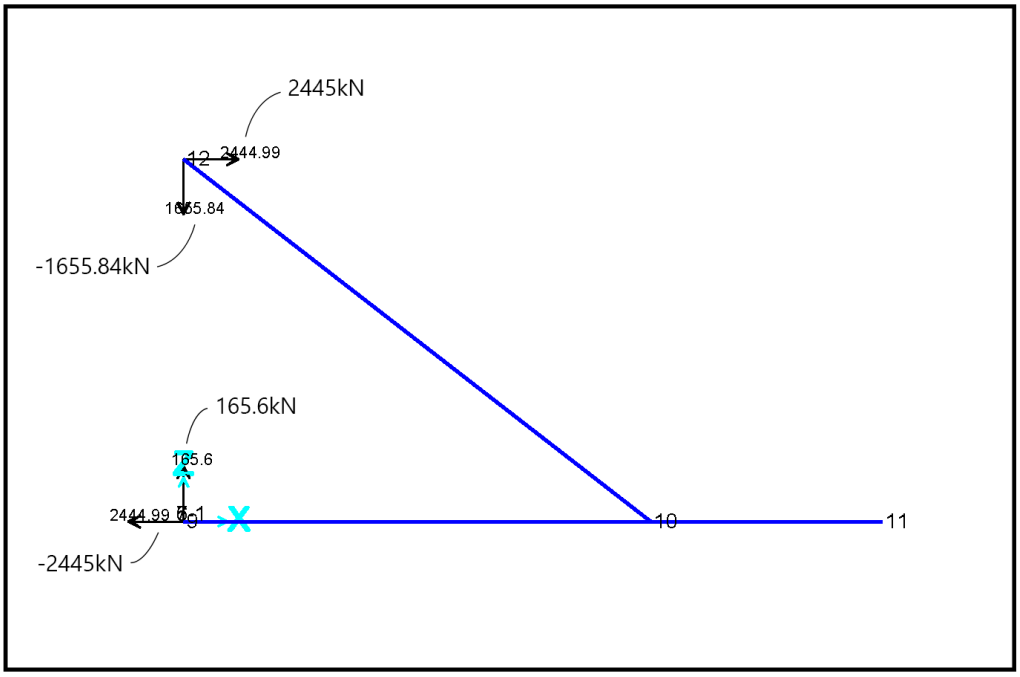

SAP2000 22.0.0 Joint Reactions (COMB4 - SW + 1xACT-COM) KN, mm, C

Loading Bracket - REV1.sdb

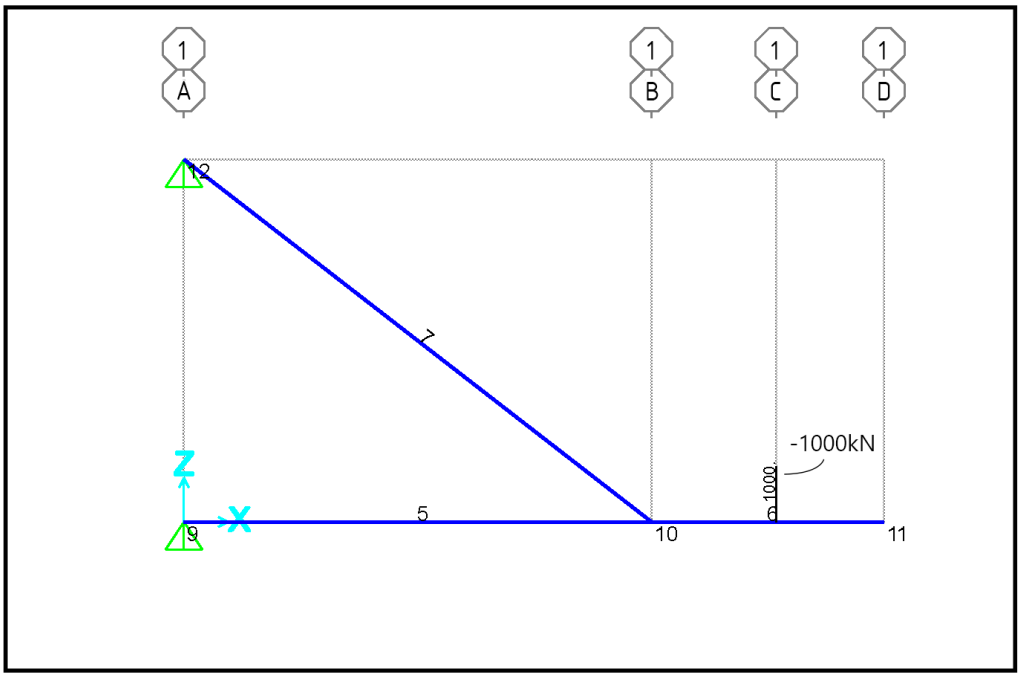

SAP2000 22.0.0 Frame Span Loads (ACT-T-1000kN) (GLOBAL CSys) KN, mm, C

Loading Bracket - REV1.sdb

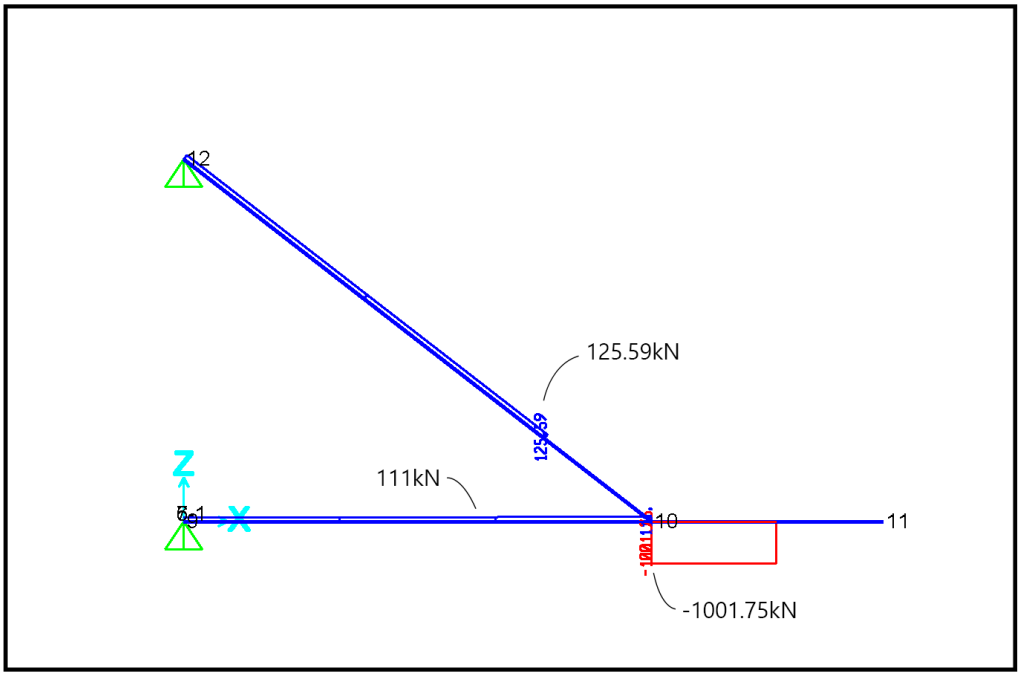

SAP2000 22.0.0 Shear Force 2-2 Diagram (COMB11 - SW + 1xACT-TEN) KN, mm, C

Loading Bracket - REV1.sdb

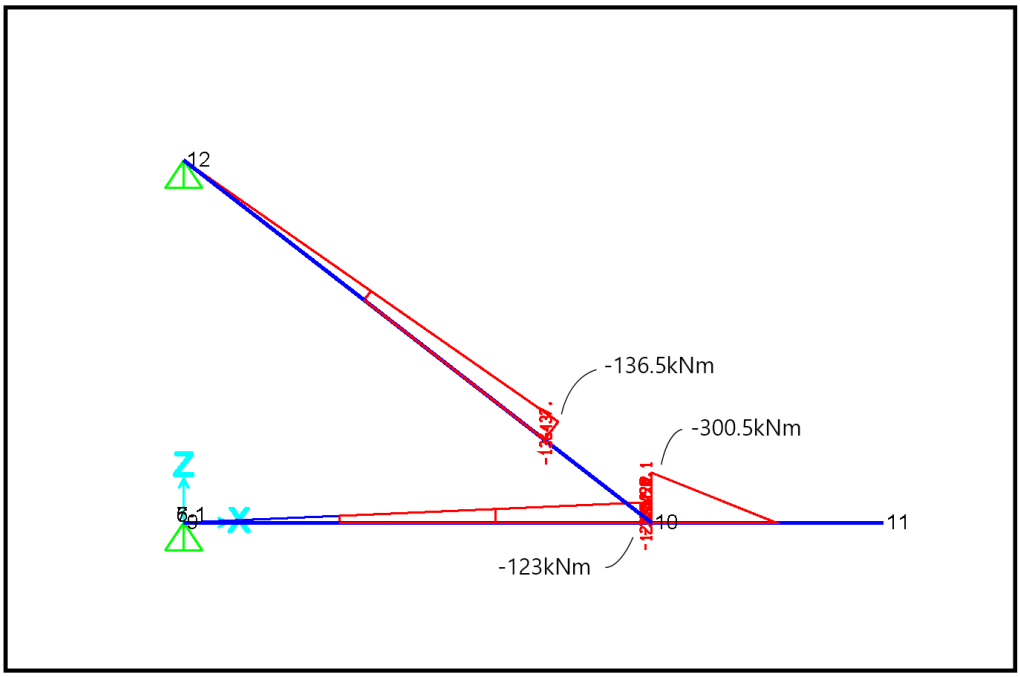

SAP2000 22.0.0 Moment 3-3 Diagram (COMB11 - SW + 1xACT-TEN) KN, mm, C

Loading Bracket - REV1.sdb

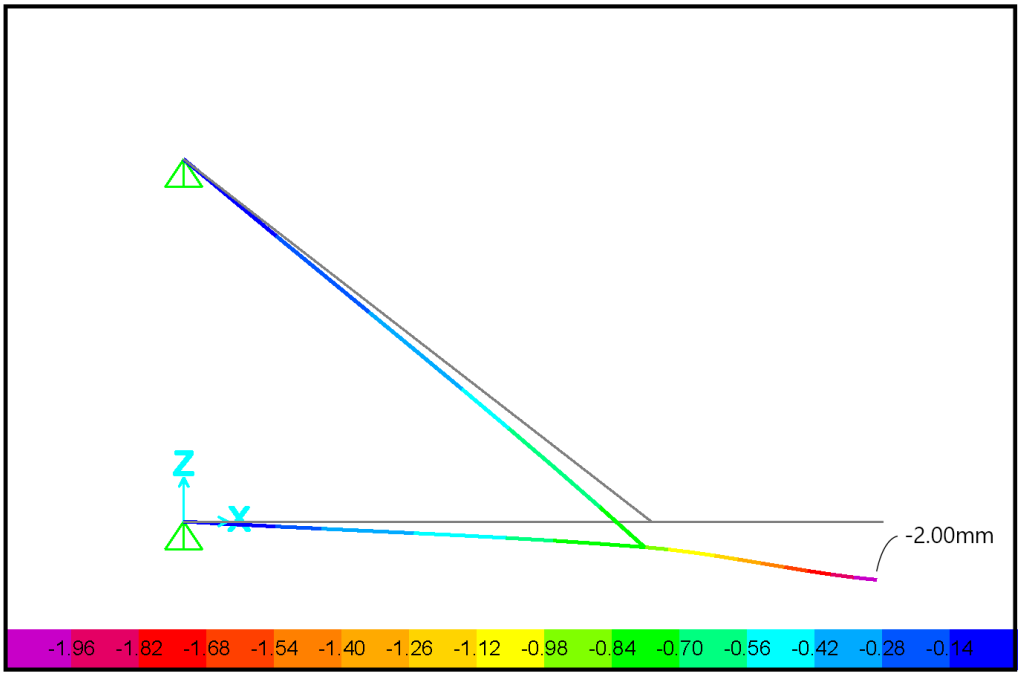

SAP2000 22.0.0 Deformed Shape (COMB11 - SW + 1xACT-TEN) - Contours for Uz KN, mm, C

Loading Bracket - REV1.sdb

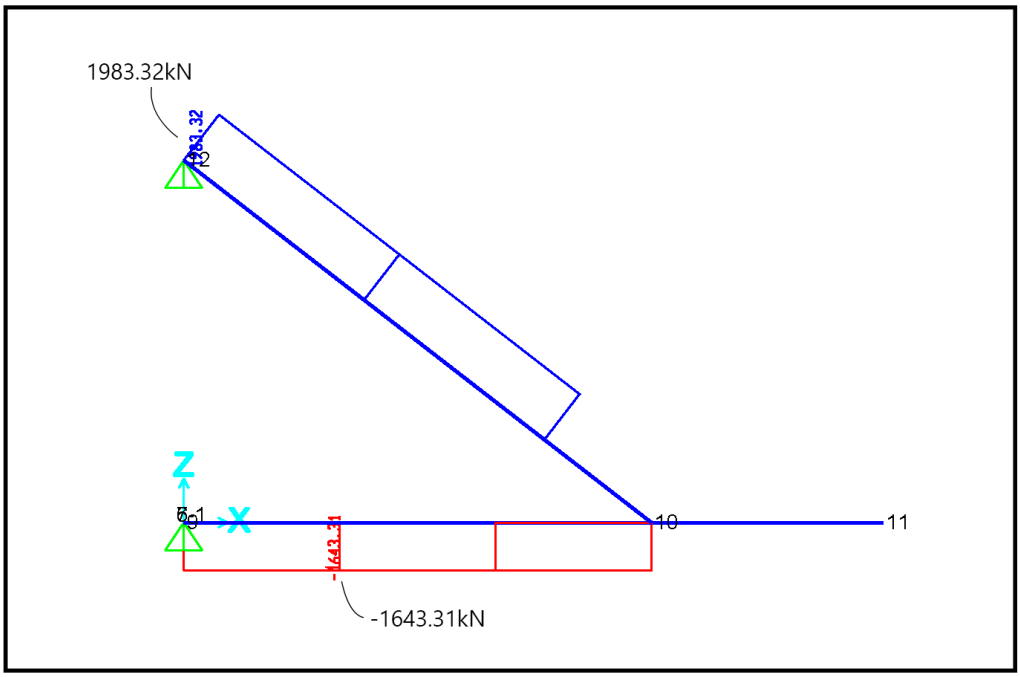

SAP2000 22.0.0 Axial Force Diagram (COMB11 - SW + 1xACT-TEN) KN, mm, C

Loading Bracket - REV1.sdb

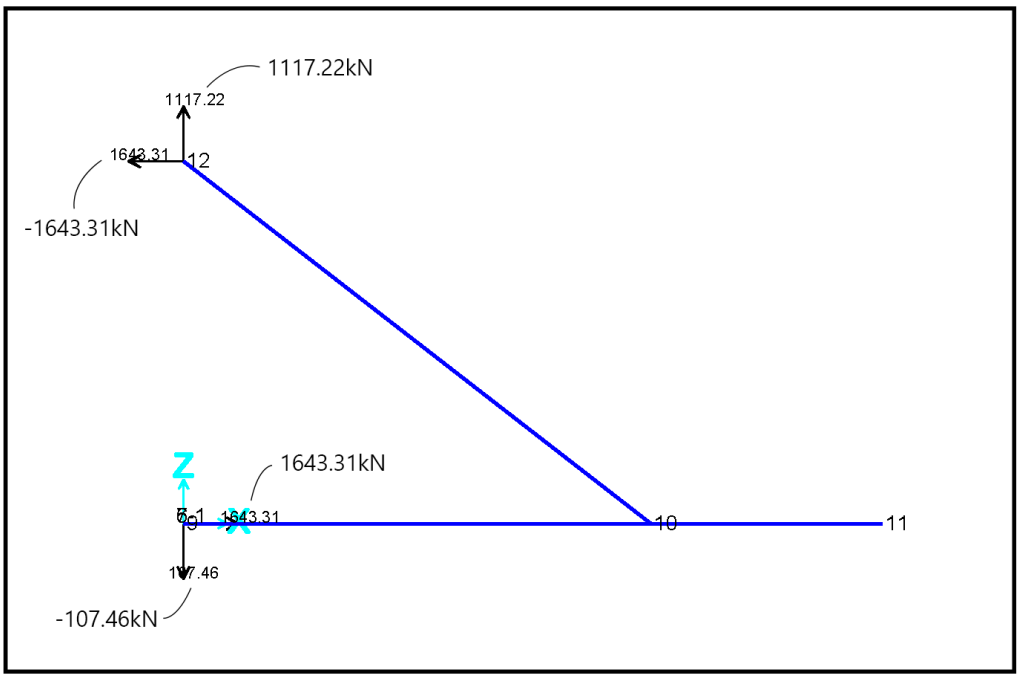

SAP2000 22.0.0 Joint Reactions (COMB11 - SW + 1xACT-TEN) KN, mm, C

Section: W360x314

Dimensions

$d := 399mm$ Depth

$b := 401mm$ Width

$t := 39.6mm$ Flange Thickness

$w := 24.9mm$ Web Thickness

$L := 1685mm$ Length (longest member)

Section Properties

$I_x := 1100 \cdot 10^6 mm^4$ Moment of inertia about x-axis

$S_x := 5530 \cdot 10^3 mm^3$ Elastic modulus about x-axis

$Z_x := 6370 \cdot 10^3 mm^3$ Plastic modulus about x-axis

$r_x := 166mm$ Radius of gyration about x-axis

$I_y := 426 \cdot 10^6 mm^4$ Moment of inertia about y-axis

$S_y := 2120 \cdot 10^3 mm^3$ Elastic modulus about y-axis

$Z_y := 3240 \cdot 10^3 mm^3$ Plastic modulus about y-axis

$r_y := 103mm$ Radius of gyration about y-axis

$A := 39900mm^2$ Cross-sectional Area

$J := 18500 \cdot 10^3 mm^4$ Torsional Constant

$C_w := 13800 \cdot 10^9 mm^6$ Warping Constant

Steel Section Strength

$F_y := 345 MPa$ Yield Stress

$F_u := 450 MPa$ Ultimate Stress

Steel Properties

$\rho := 8050 \frac{kg}{m^3}$ Density

$E := 200GPa$ Young's Modulus

$G := 77000MPa$ Shear Modulus

$\upsilon := 0.3$ Poisson's Ratio

$\phi := 0.9$ Yield Resistance Factor

$\phi_u := 0.75$ Ultimate Resistance Factor

Design Loads

Internal forces developed by application of actuator model: 201.70 (1000kN Compression & 1500kN Tension)
Absolute rounded-up load values for design.

Compressive Axial Force

From Analysis: -2950kN

$C_f := 3000kN$ Design Compressive Axial Force

Shear

From Analysis: 1499kN

$V_f := 1500kN$ Design Shear Force

Tensile Axial Force

From Analysis: 2445kN

$T_f := 2500kN$ Design Tensile Axial Force

Moment

From Analysis: 450kNm

$M_f := 500kN \cdot m$ Design Bending Moment

Section Resistance Check

Axial Tension - Clause 13.2.a

$A_g := d \cdot w$

$A_g = 9935.1 \cdot mm^2$ Gross tension area

$A_{ne} := A_g$

$A_{ne} = 9935.1 \cdot mm^2$ Effective Net area (Clause 12.3.3.3)

$A_n := A_{ne}$ Net Area (Clause 13.11.b)

$A_{gv} := A_{ne}$ Gross Shear Area (Clause 13.11.c)

$U_t := 1.0$ Efficiency Factor (Clause 13.11.a)

$T_{r1} := \phi \cdot A_g \cdot F_y \cdot MPa$

$T_{r1} = 3085 \cdot kN$ Clause 13.2.a.i

$T_{r2} := \phi_u \cdot \left[U_t \cdot A_n \cdot F_u \cdot MPa + 0.6 \cdot A_{gv} \cdot \frac{(F_y + F_u)}{2} \cdot MPa \right]$

$T_{r2} = 5130 \cdot kN$ Clause 13.2.a.ii & Clause 13.11

$T_{r3} := \phi_u \cdot A_{ne} \cdot F_u \cdot MPa$

$T_{r3} = 3353 \cdot kN$ Clause 13.2.a.iii

$T_r := \min(T_{r1}, T_{r2}, T_{r3})$ Tensile Resistance

$T_r = 3085 \cdot kN$

OK

Axial Compression - Clause 13.3.1 & 13.3.2

Flexural Buckling of Doubly Symmetric Shapes

$K := 1$ Effective Length Factor

$n := 1.34$ For hot-rolled sections

$F_e := \frac{\pi^2 \cdot E}{\left(\frac{K \cdot L}{r_x}\right)}$ $\lambda := \sqrt{\frac{F_y}{\frac{F_e}{MPa}}}$

$F_e = 194463 \cdot MPa$ $\lambda = 0.042$

$C_r := \phi \cdot A \cdot F_y \cdot MPa \cdot \left(1 + \lambda^{2 \cdot n}\right)^{\frac{-1}{n}}$ Compressive Resistance (Clause 13.3.1)

$C_r = 12387 \cdot kN$

OK

Flexural-Torsional Buckling

$r_o := r_x^2 + r_y^2$

$\Omega := 1$

$F_{ex} := \frac{\pi^2 \cdot E}{\left(\frac{K \cdot L}{r_x}\right)}$ $F_{ey} := \frac{\pi^2 \cdot E}{\left(\frac{K \cdot L}{r_y}\right)}$

$F_{ex} = 194463 \cdot MPa$ $F_{ey} = 120661 \cdot MPa$

$F_{ez} := \left[\frac{\pi^2 \cdot E \cdot C_w}{(K \cdot L)^2} + G \cdot J \right] \cdot \frac{1}{A \cdot r_o}$

$F_{ez} = 7236 \cdot MPa$

$F_e := \min(F_{ex}, F_{ey}, F_{ez})$ $F_e = 7236 \cdot MPa$ Redefined

$\lambda := \sqrt{\frac{F_y}{\frac{F_e}{MPa}}}$ $\lambda = 0.218$ Redefined

$C_r := \phi \cdot A \cdot F_y \cdot MPa \cdot \left(1 + \lambda^{2 \cdot n}\right)^{\frac{-1}{n}}$ Compressive Resistance (Clause 13.3.2)

$C_r = 12235 \cdot kN$

OK

Section Class - Table 2

$$Class_{web} := \begin{cases} h \leftarrow d - 2 \cdot t & \\ 3 \text{ if } \frac{h}{w} \le \left(1 - 0.65 \cdot \frac{C_f}{C_r}\right) \cdot \frac{1900}{\sqrt{F_y}} & \\ 2 \text{ if } \frac{h}{w} \le \left(1 - 0.61 \cdot \frac{C_f}{C_r}\right) \cdot \frac{1700}{\sqrt{F_y}} & \\ 1 \text{ if } \frac{h}{w} \le \left(1 - 0.39 \cdot \frac{C_f}{C_r}\right) \cdot \frac{1100}{\sqrt{F_y}} & \\ 4 \text{ otherwise} & \end{cases}$$

$$Class_{flng} := \begin{cases} b_{el} \leftarrow 0.5 \cdot b & \\ 3 \text{ if } \frac{b_{el}}{t} \le \frac{200}{\sqrt{F_y}} & \\ 2 \text{ if } \frac{b_{el}}{t} \le \frac{170}{\sqrt{F_y}} & \\ 1 \text{ if } \frac{b_{el}}{t} \le \frac{145}{\sqrt{F_y}} & \\ 4 \text{ otherwise} & \end{cases}$$

$Class_{web} = 1$

$Class_{flng} = 1$

Section: Class 1

Shear Resistance - Clause 13.4

Shear Height

$h_w := d$ $h_w = 399 \cdot mm$

Shear Area

$A_w := h_w \cdot w$ $A_w = 9935 \cdot mm^2$

$$F_s := \begin{cases} 0.66 \cdot F_y \cdot MPa & \text{if } \frac{h_w}{w} \le \frac{1014}{\sqrt{F_y}} \\ \frac{670 \cdot \sqrt{F_y}}{\frac{h_w}{w}} \cdot MPa & \text{if } \frac{1014}{\sqrt{F_y}} < \frac{h_w}{w} \le \frac{1435}{\sqrt{F_y}} \\ \frac{961200}{\left(\frac{h_w}{w}\right)^2} \cdot MPa & \text{if } \frac{h_w}{w} > \frac{1435}{\sqrt{F_y}} \end{cases}$$

$F_s = 227.7 \cdot MPa$

$V_r := \phi \cdot A_w \cdot F_s$ $V_r = 2036 \cdot kN$ Shear Resistance

OK

Bending - Laterally Supported - Clause 13.5

$M_{r1} := \phi \cdot Z_x \cdot F_y \cdot MPa$ Braced Moment Resistance

$M_{r1} = 1978 \cdot kN \cdot m$

OK

Bending - Laterally Unsupported - Clause 13.6.a.i

$M_p := \frac{M_{r1}}{\phi}$ Plastic Moment

$M_p = 2198 \cdot kN \cdot m$

$\omega_2 := 1$ Moment Resistance Coefficient

$L_u := 1.4 \cdot L$ Effective Unbraced Length

$L_u = 2359 \cdot mm$

$$M_u := \frac{\omega_2 \cdot \pi}{L_u} \cdot \sqrt{E \cdot I_y \cdot G \cdot J + \left(\frac{\pi \cdot E}{L_u}\right)^2 \cdot I_y \cdot C_w}$$ Critical Elastic Moment

$M_u = 30902 \cdot kN \cdot m$

$$check := \begin{cases} \text{"Yes"} & \text{if } M_u > 0.67 \cdot M_p \\ \text{"No"} & \text{otherwise} \end{cases}$$

$check = \text{"Yes"}$

$$M_{r2} := 1.15 \cdot \phi \cdot M_p \cdot \left(1 - \frac{0.28 \cdot M_p}{M_u}\right)$$ Unbraced Moment Resistance

$M_{r2} = 2229 \cdot kN \cdot m$

OK

Governing Moment: Mr1 Governs

$$M_r := \begin{cases} M_{r1} & \text{if } M_{r1} < M_{r2} \\ M_{r2} & \text{otherwise} \end{cases}$$ Moment Resistance

$M_r = 1978 \cdot kN \cdot m$

OK

Axial Tension and Bending - Clause 13.9.1

$$Utility_{TM} := \frac{T_f}{T_r} + \frac{M_f}{M_r}$$

$Utility_{TM} = 1.063$ Combined Utility ≤1.0

Fail

Note:
Actuator must not be loaded to
full tension capacity at 1500kN.
At 90% load, utility is 0.918.
(Mf=405kNm, Tf=2200kN)

Web Crippling - Clause 14.3.2

Interior Loads

$\phi_{bi} := 0.8$

$N_{br} := 400mm$ Length of Bearing

$B_{ri1} := \phi_{bi} \cdot w \cdot (N_{br} + 10 \cdot t) \cdot F_y \cdot MPa$ $B_{ri1} = 5470 \cdot kN$

$B_{ri2} := 1.45 \cdot \phi_{bi} \cdot w^2 \cdot \sqrt{E \cdot F_y \cdot MPa}$ $B_{ri2} = 5974 \cdot kN$

$B_{ri} := \min(B_{ri1}, B_{ri2})$ $B_{ri} = 5470 \cdot kN$ Bearing Resistance

OK

End Reactions

$\phi_{be} := 0.75$

$B_{re1} := \phi_{be} \cdot w \cdot (N_{br} + 4 \cdot t) \cdot F_y \cdot MPa$ $B_{re1} = 3598 \cdot kN$

$B_{re2} := 0.6 \cdot \phi_{be} \cdot w^2 \cdot \sqrt{E \cdot F_y \cdot MPa}$ $B_{re2} = 2318 \cdot kN$

$B_{re} := \min(B_{re1}, B_{re2})$ $B_{re} = 2318 \cdot kN$ Bearing Resistance

OK

Combined Shear and Moment - Clause 14.6

$$Utility_{VM} := 0.727 \cdot \frac{M_f}{M_r} + 0.455 \cdot \frac{V_f}{V_r}$$

$Utility_{VM} = 0.519$ Combined Utility ≤1.0

OK

Mounting:
Only use SAE Grade 8 material for all fasteners.

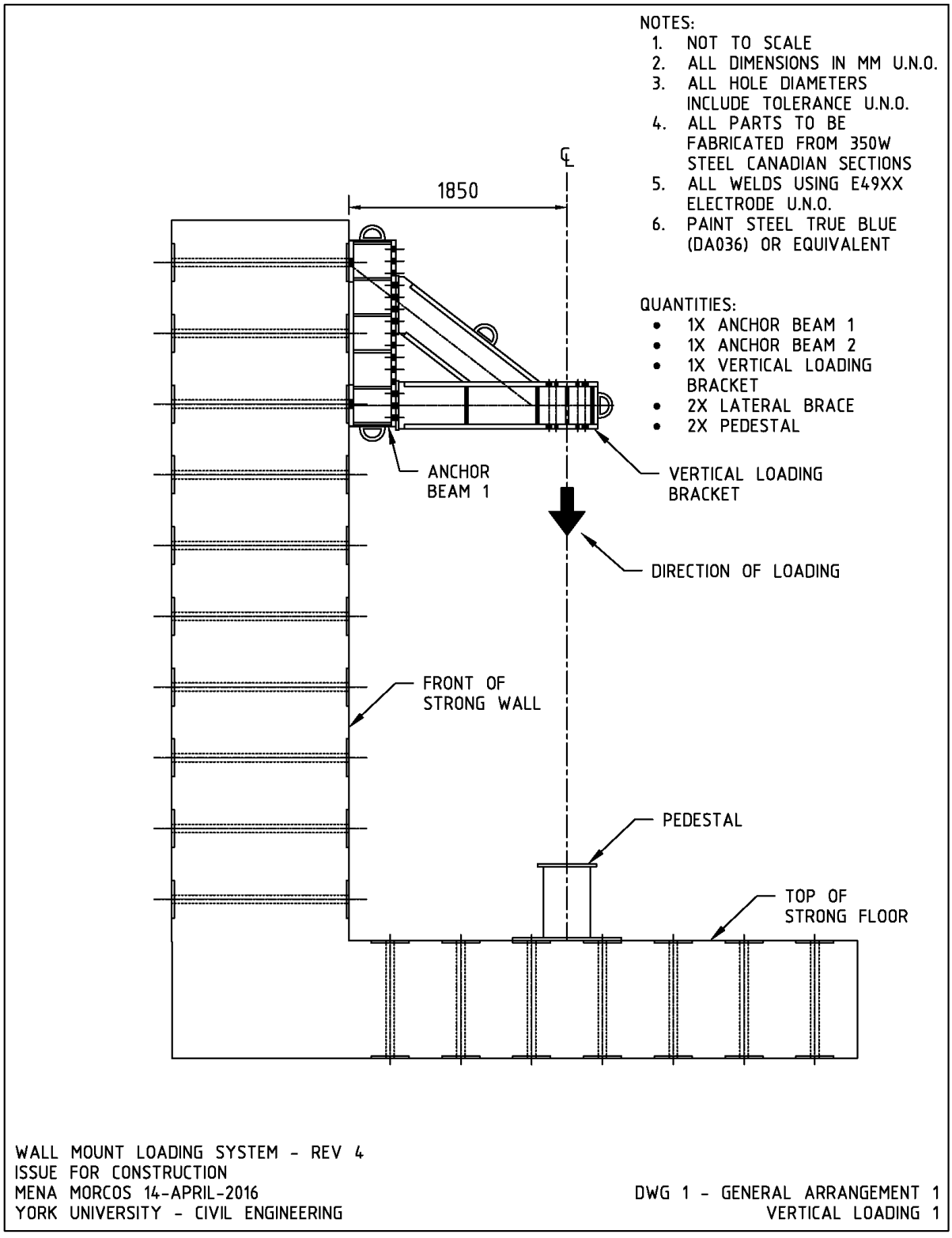

Figure F.1. Wall mount loading system design and fabrication drawing – Drawing 1.

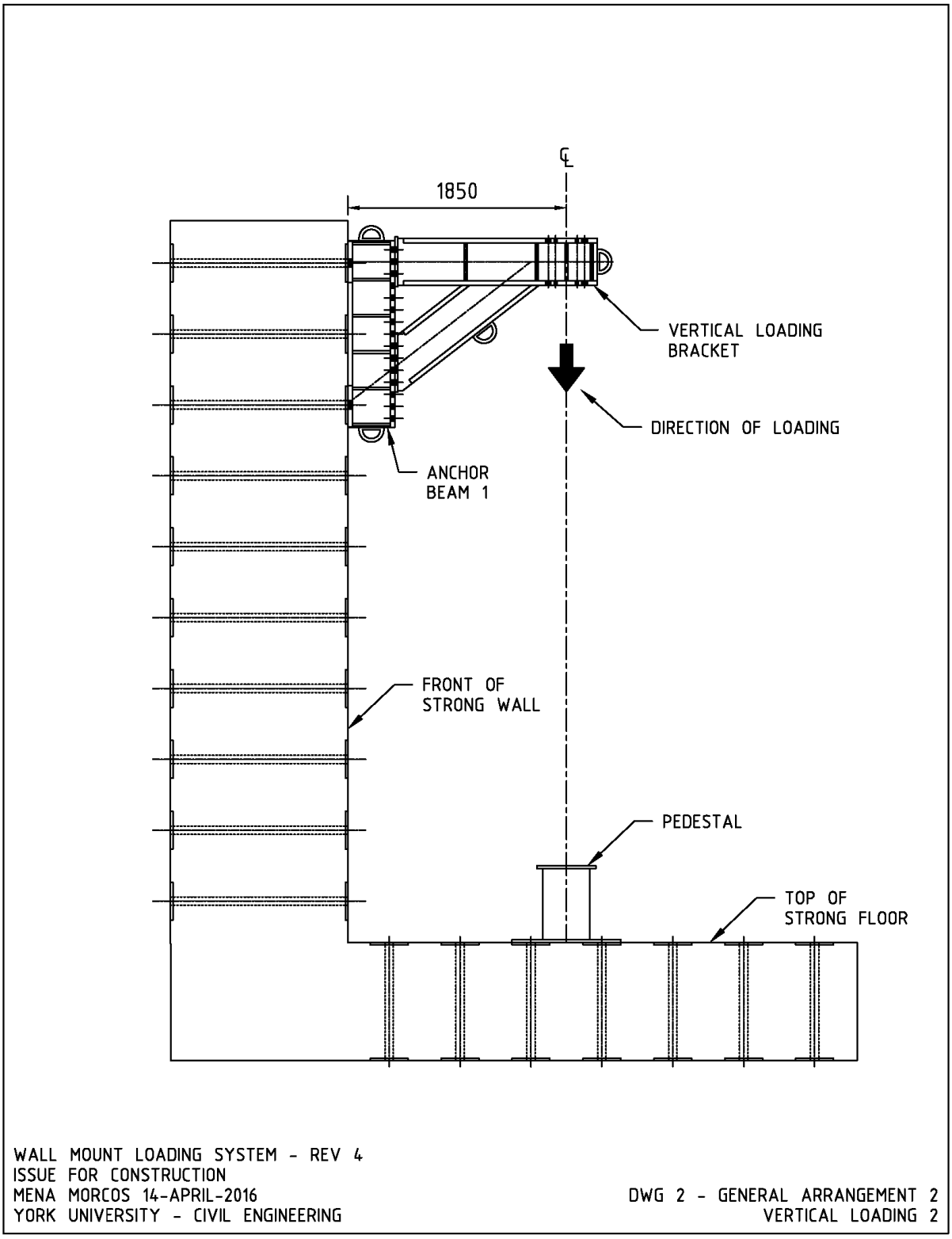

Figure F.2. Wall mount loading system design and fabrication drawing – Drawing 2.

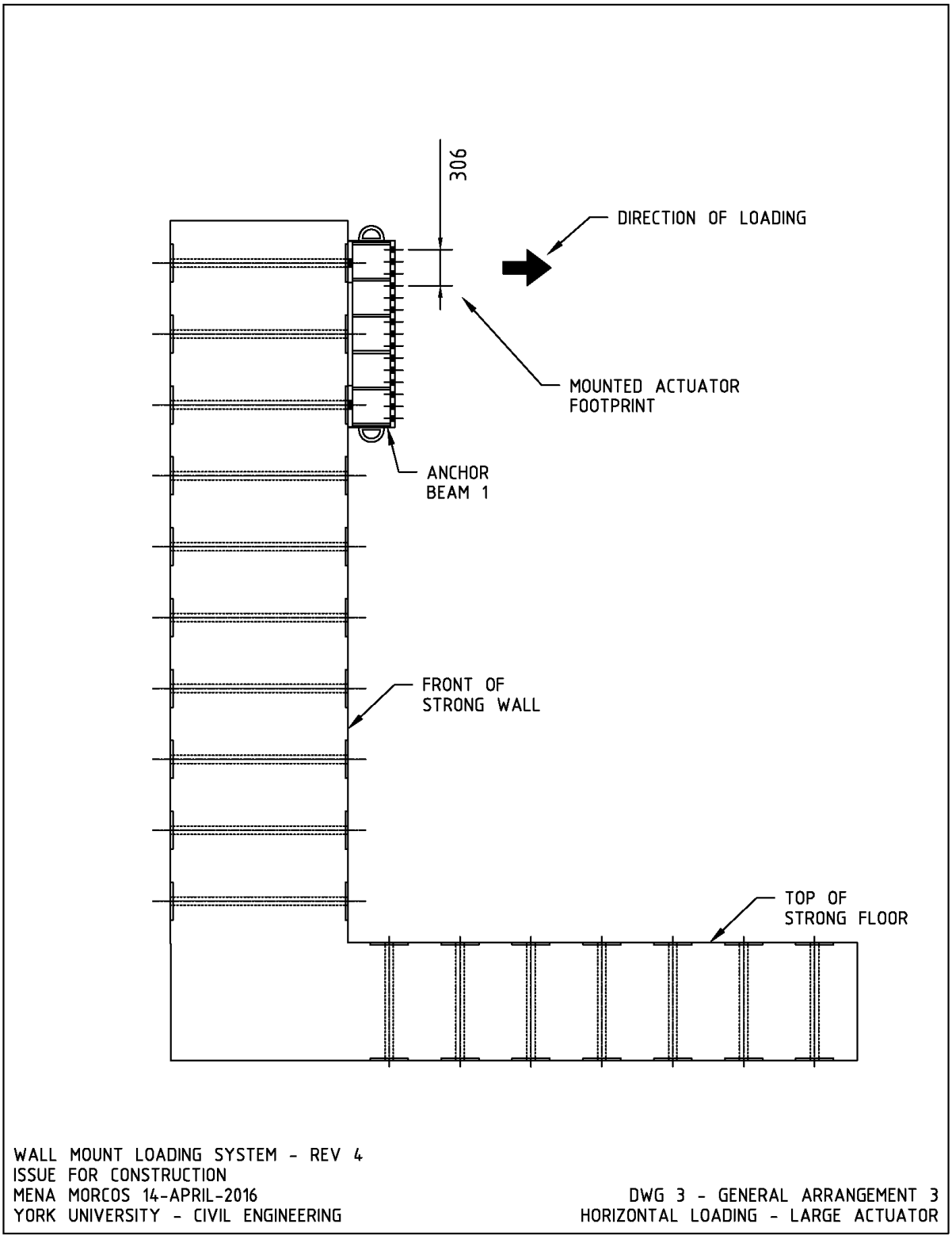

Figure F.3. Wall mount loading system design and fabrication drawing – Drawing 3.

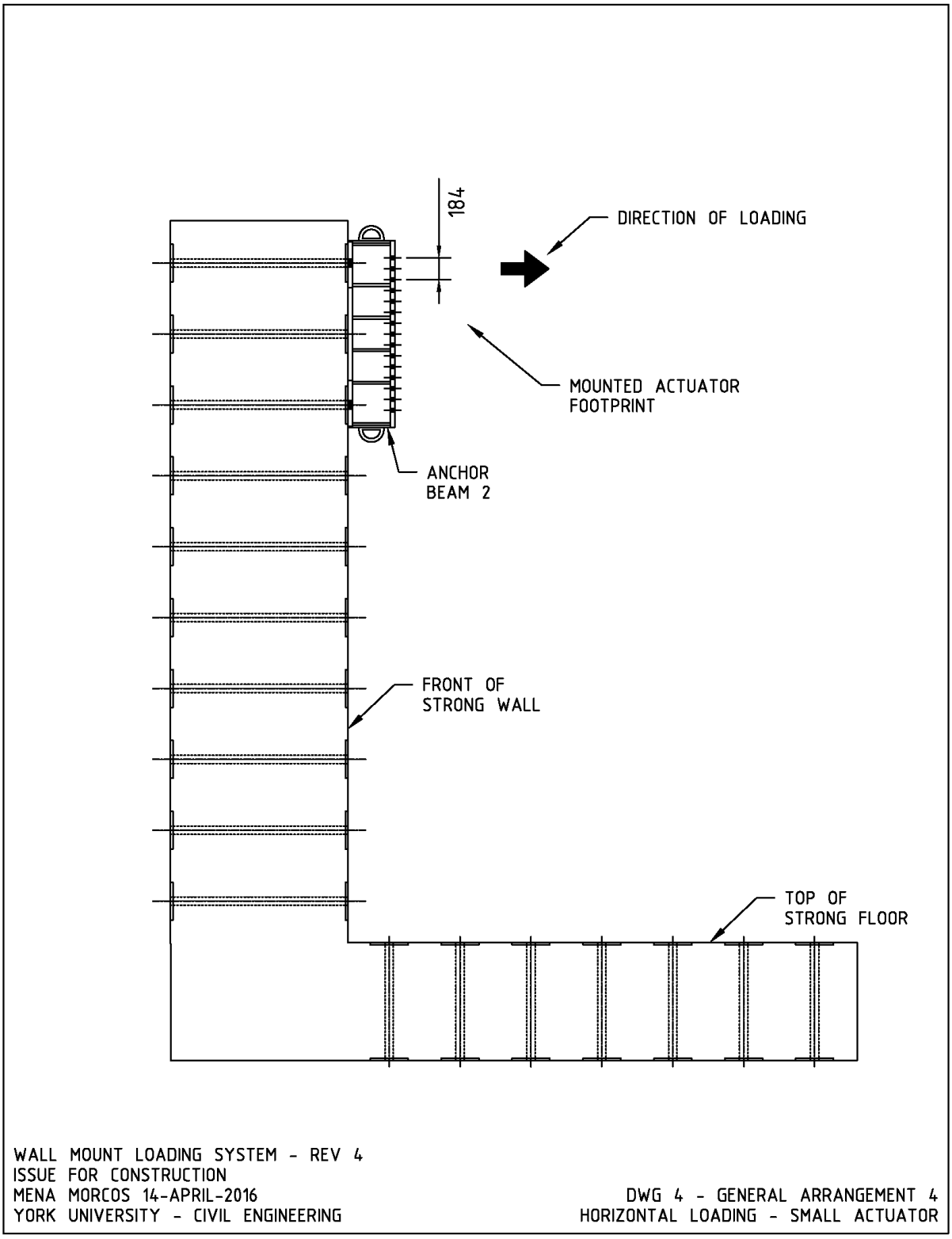

Figure F.4. Wall mount loading system design and fabrication drawing – Drawing 4.

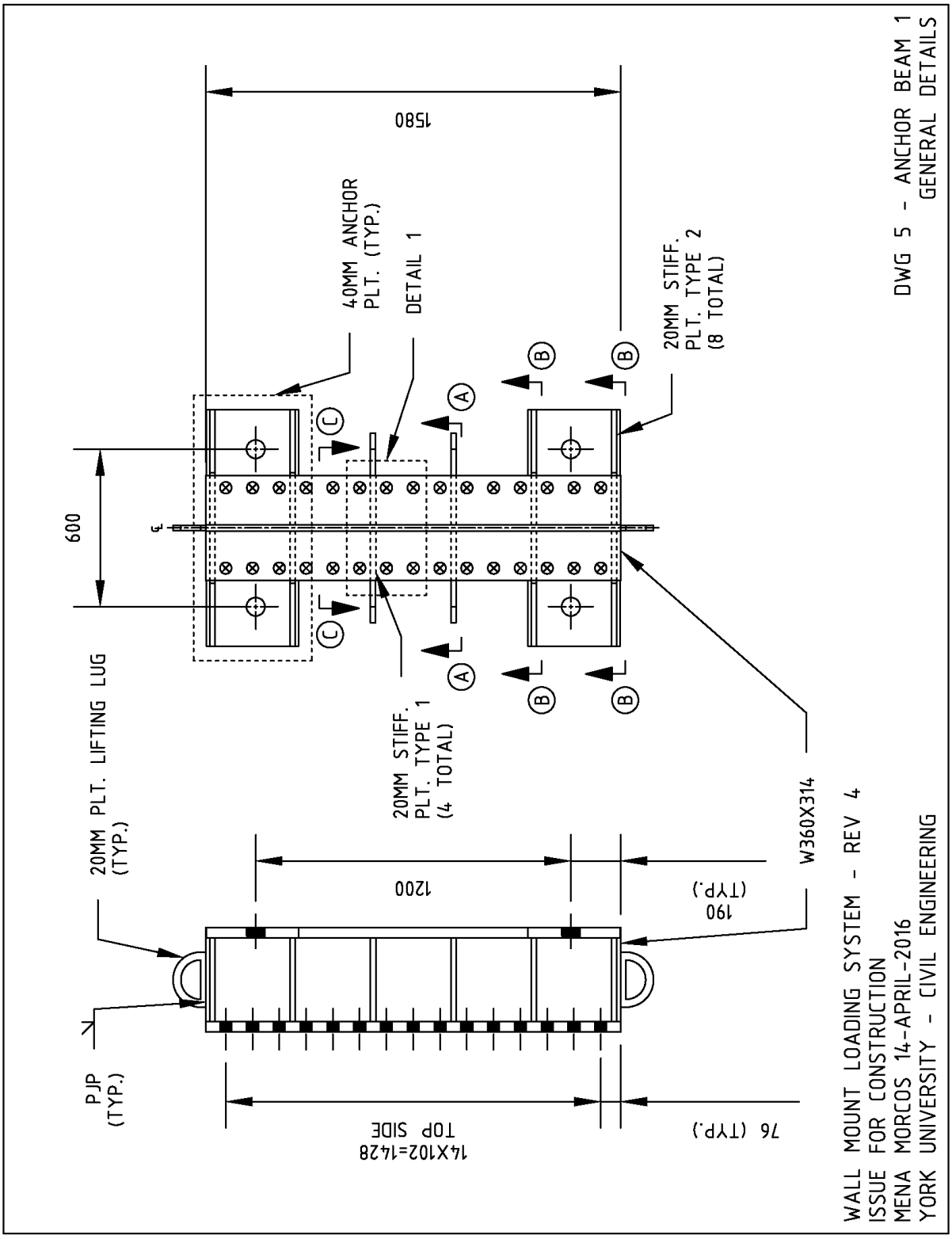

Figure F.5. Wall mount loading system design and fabrication drawing – Drawing 5.

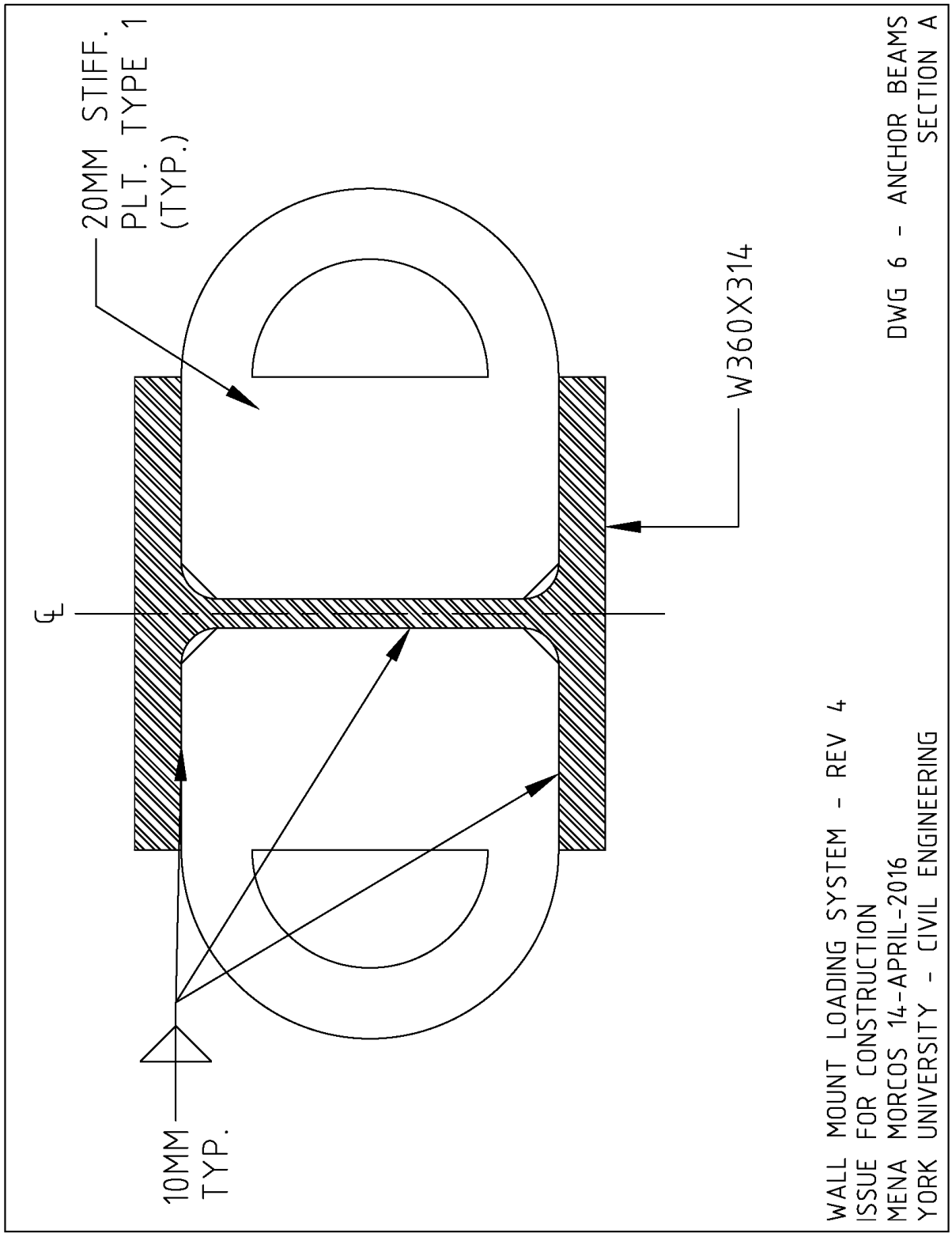

Figure F.6. Wall mount loading system design and fabrication drawing – Drawing 6.

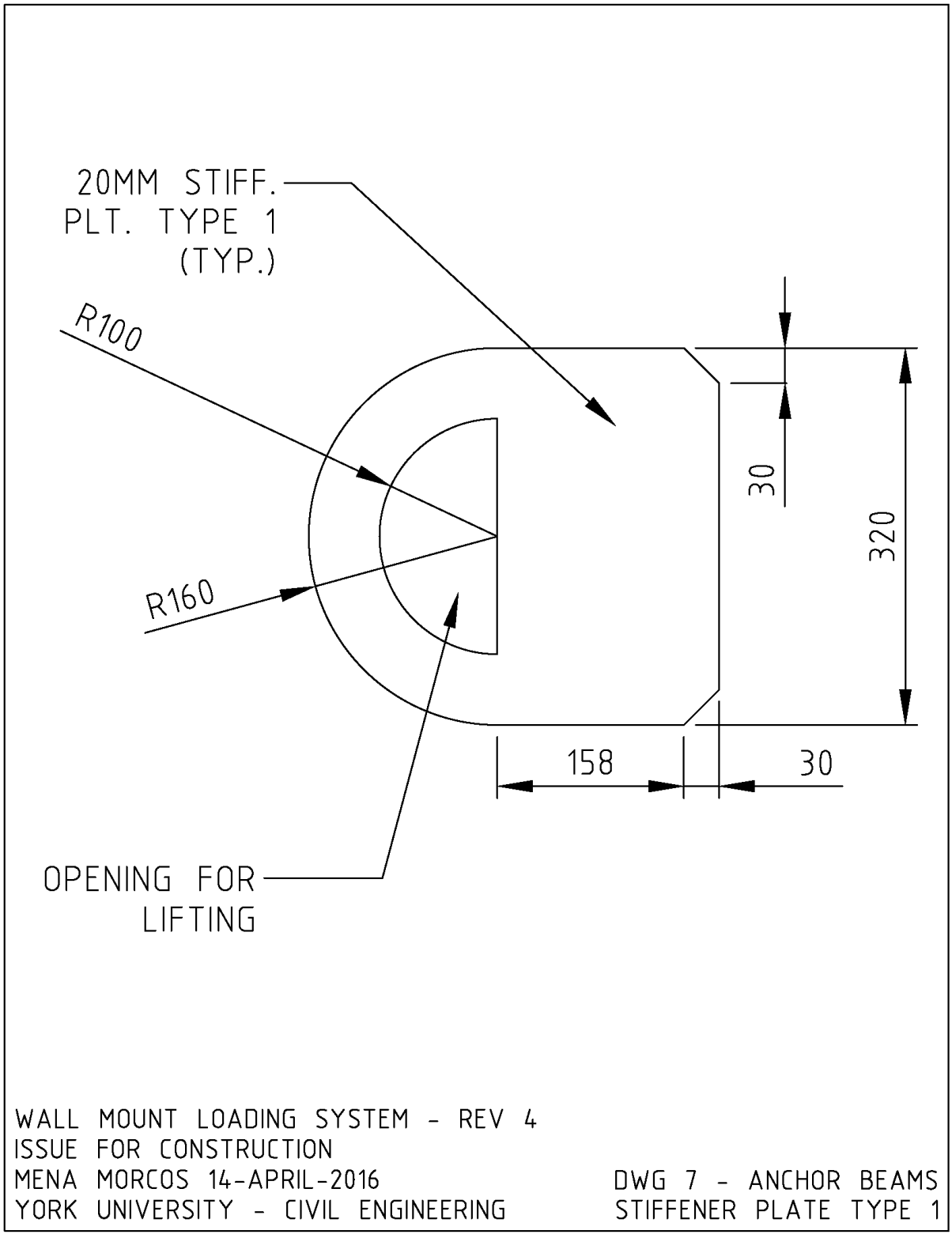

Figure F.7. Wall mount loading system design and fabrication drawing – Drawing 7.

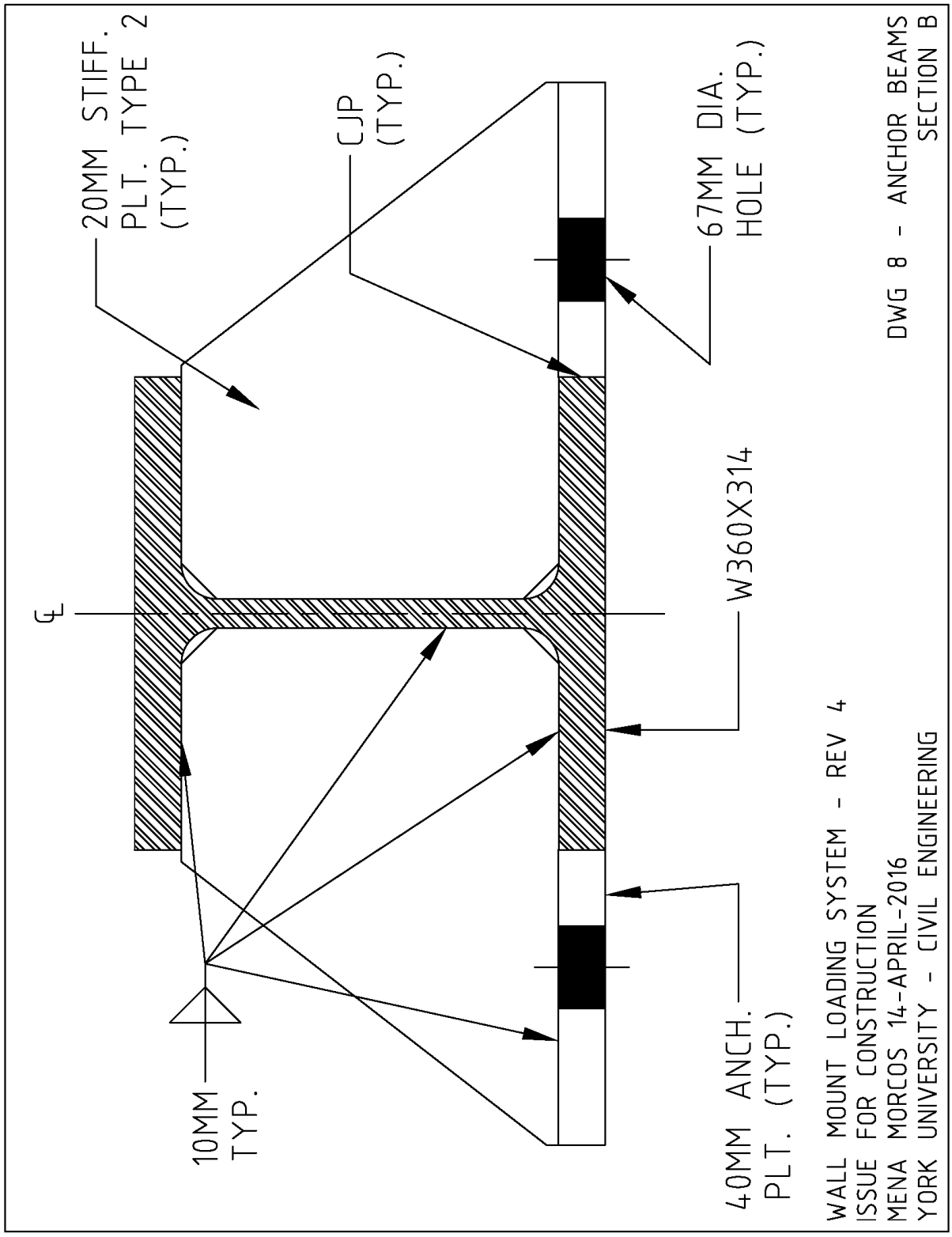

Figure F.8. Wall mount loading system design and fabrication drawing – Drawing 8.

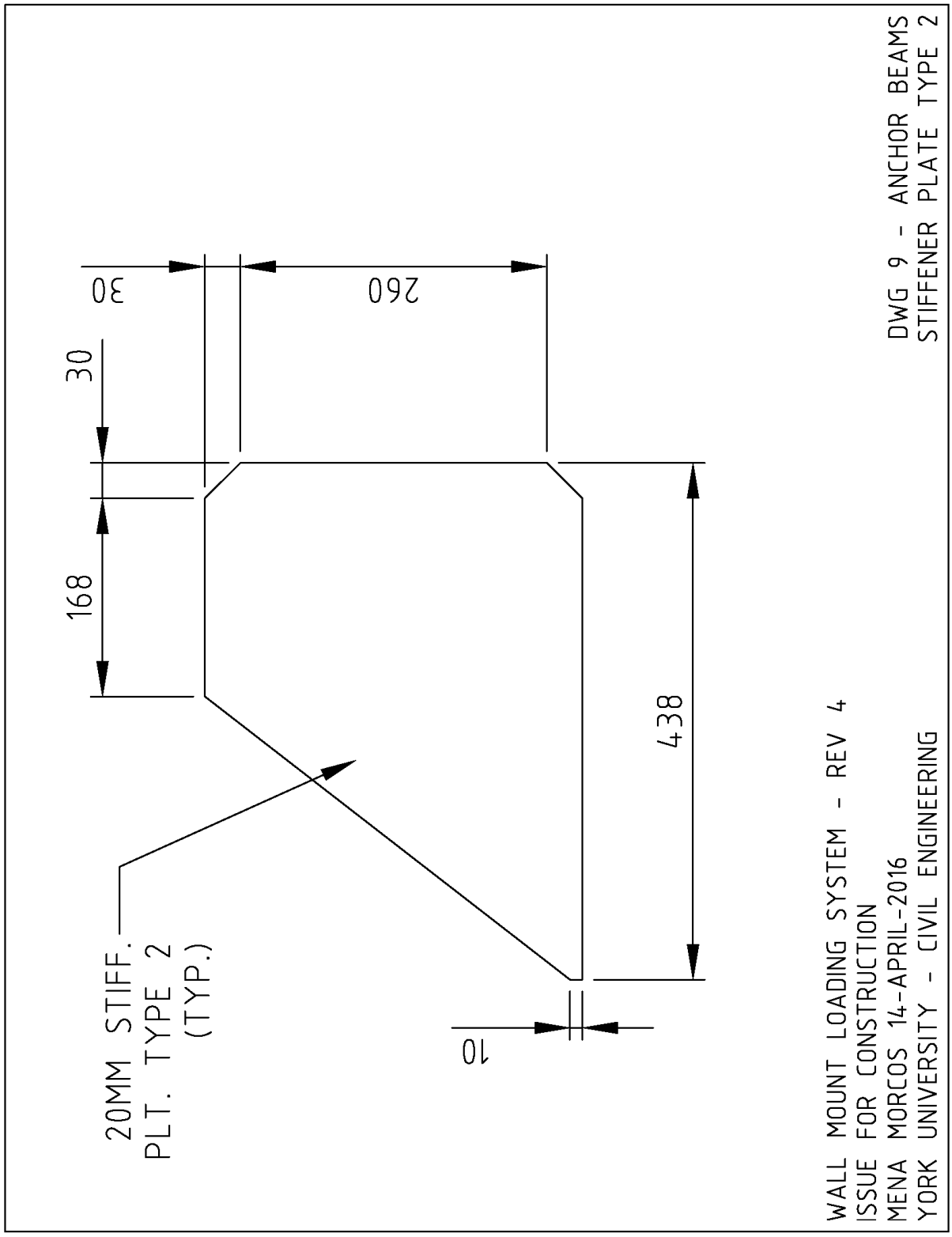

Figure F.9. Wall mount loading system design and fabrication drawing – Drawing 9.

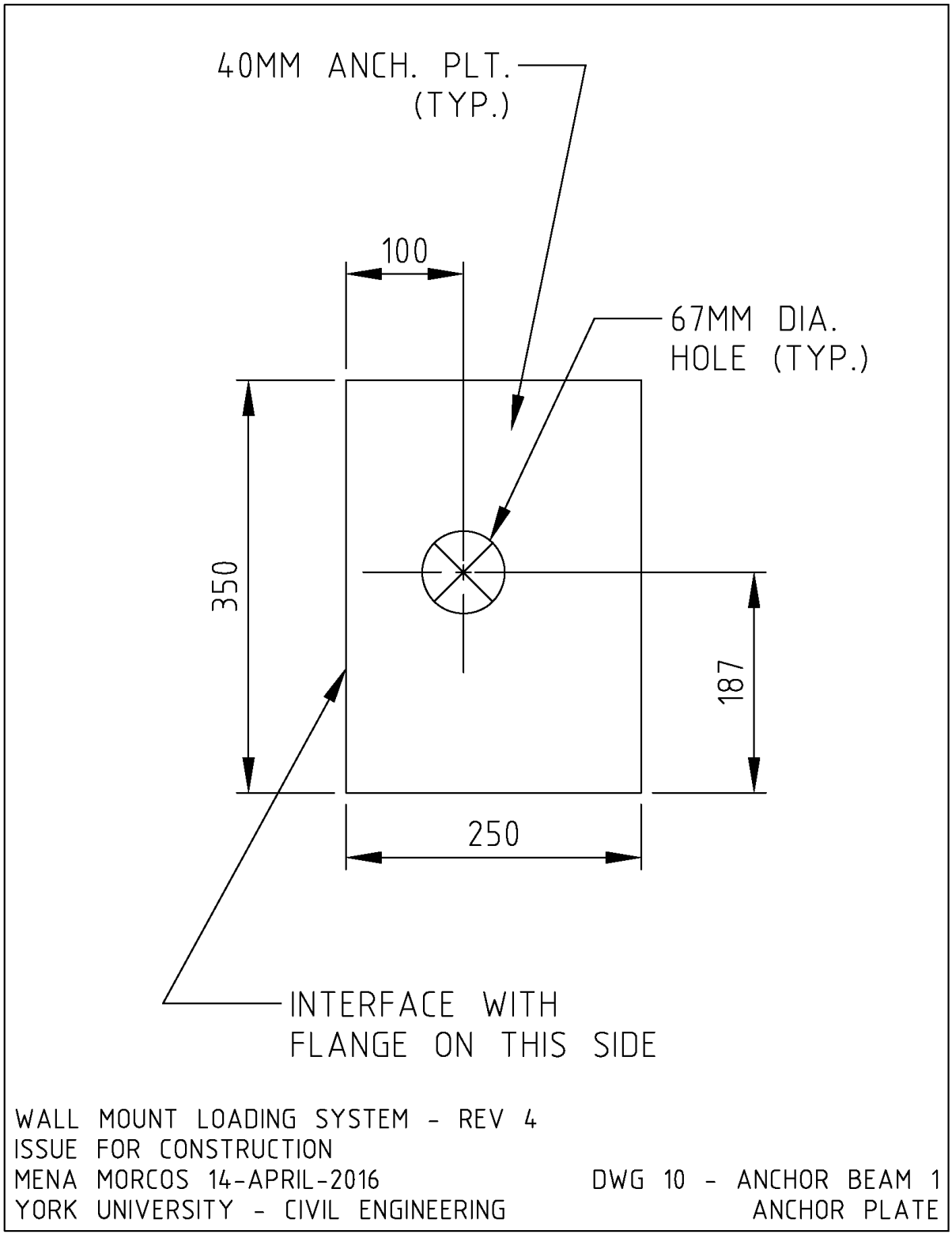

Figure F.10. Wall mount loading system design and fabrication drawing – Drawing 10.

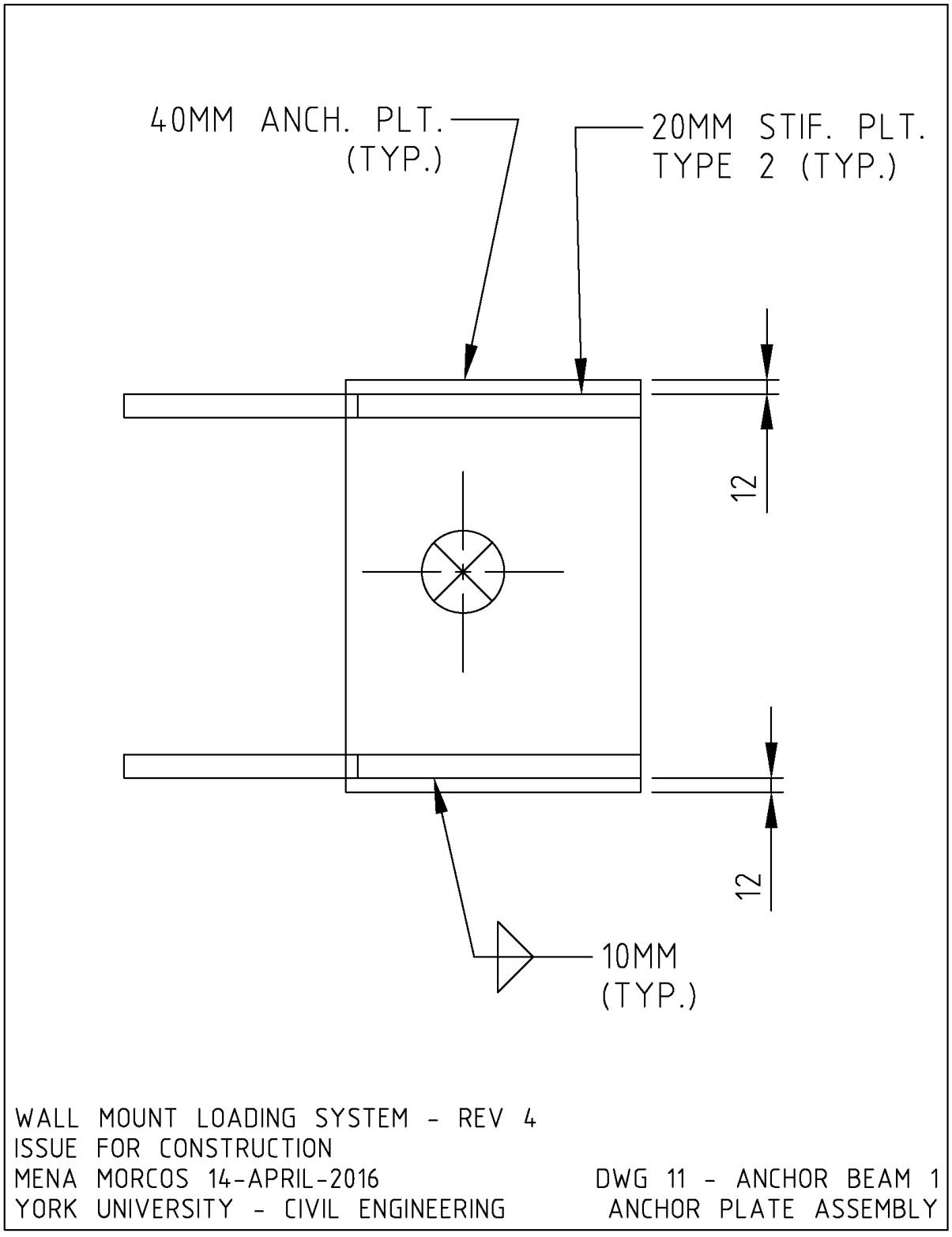

Figure F.11. Wall mount loading system design and fabrication drawing – Drawing 11.

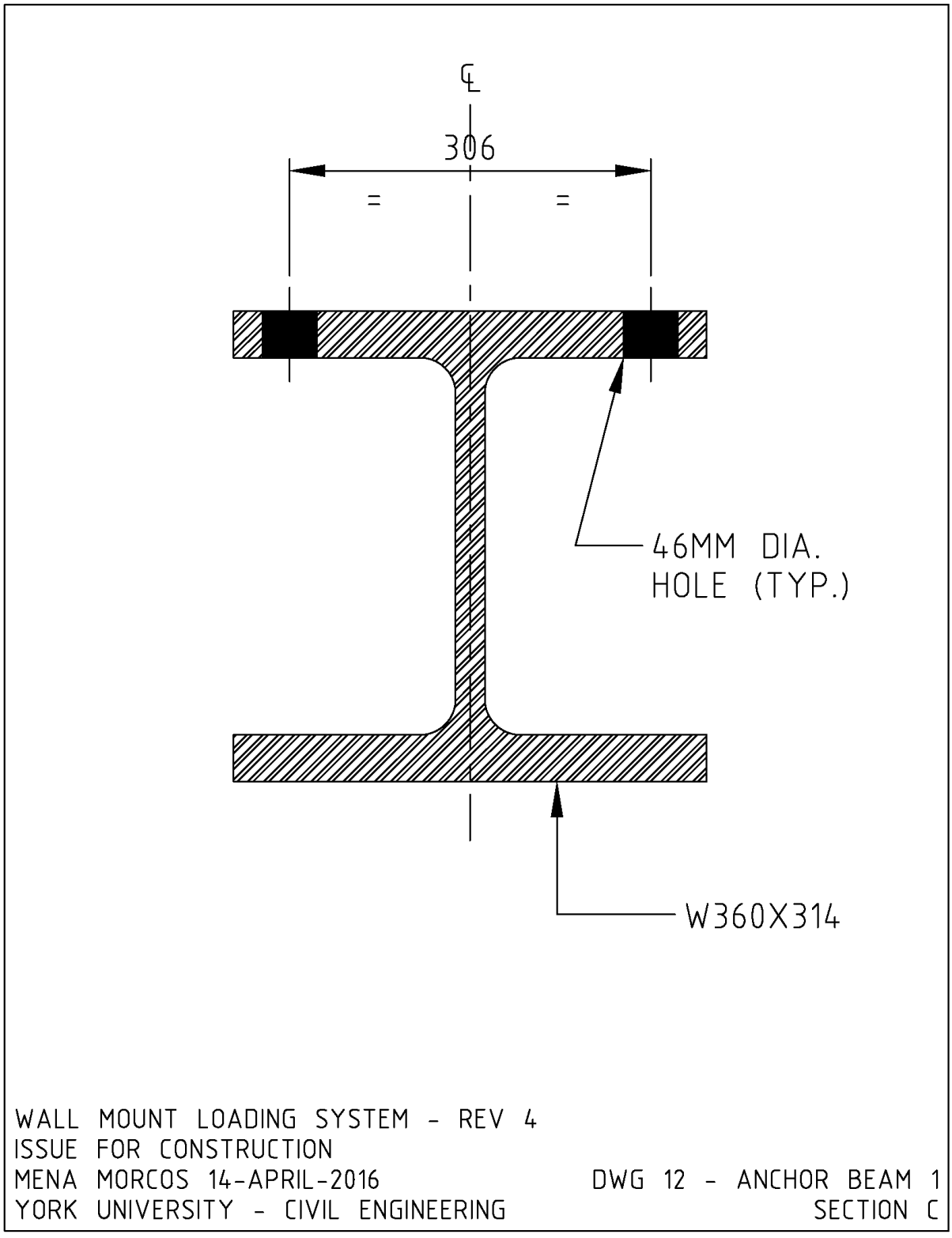

Figure F.12. Wall mount loading system design and fabrication drawing – Drawing 12.

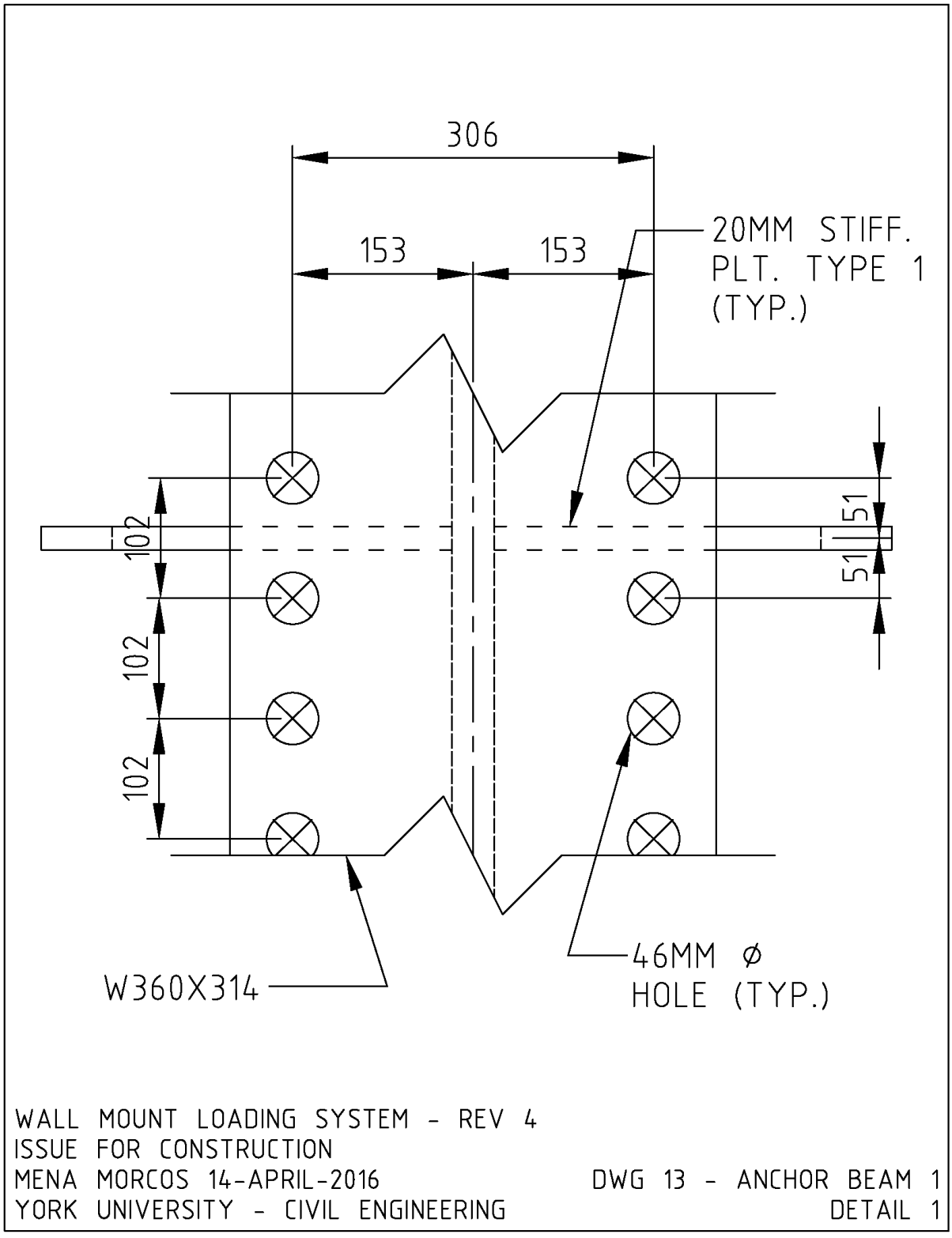

Figure F.13. Wall mount loading system design and fabrication drawing – Drawing 13.

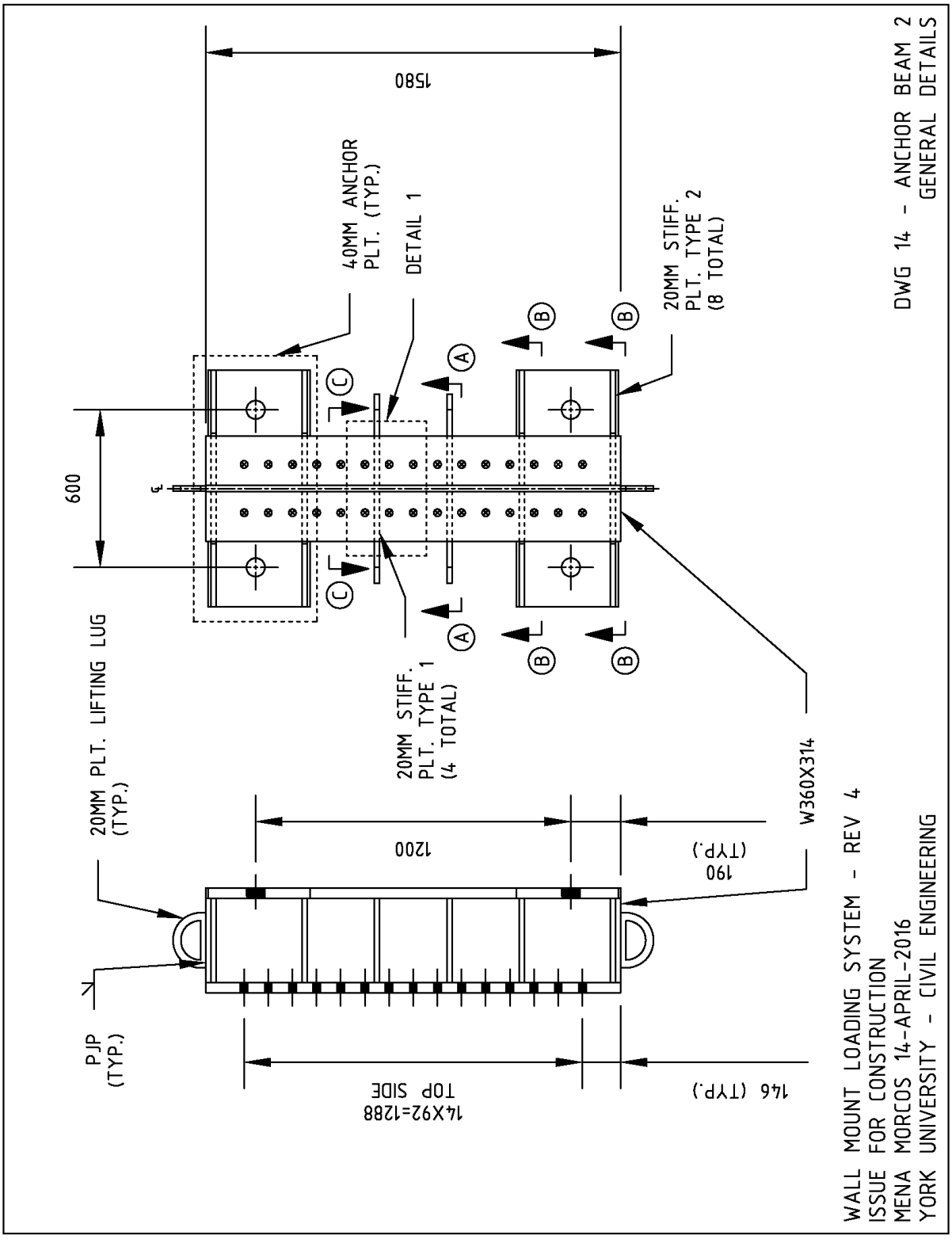

Figure F.14. Wall mount loading system design and fabrication drawing – Drawing 14.

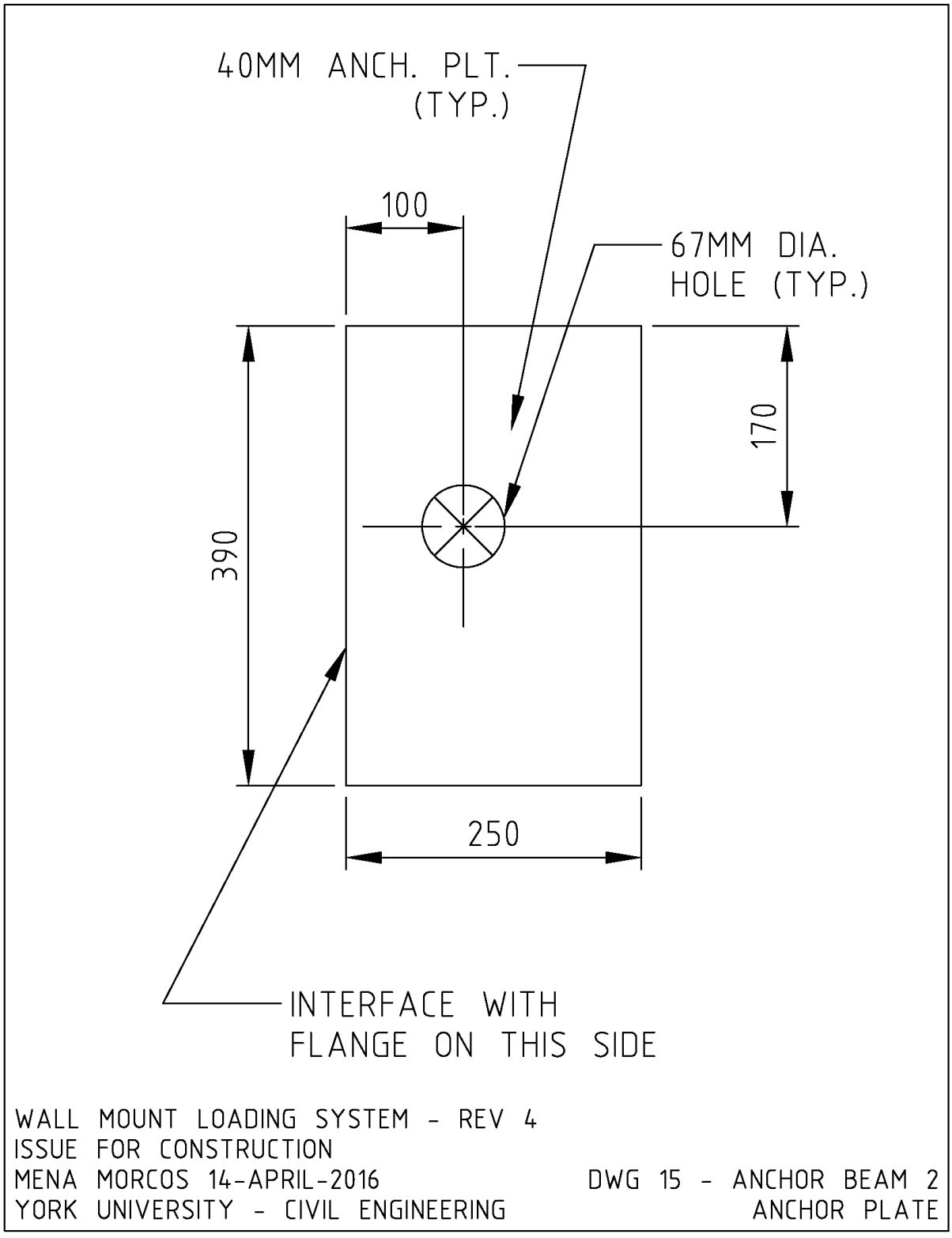

Figure F.15. Wall mount loading system design and fabrication drawing – Drawing 15.

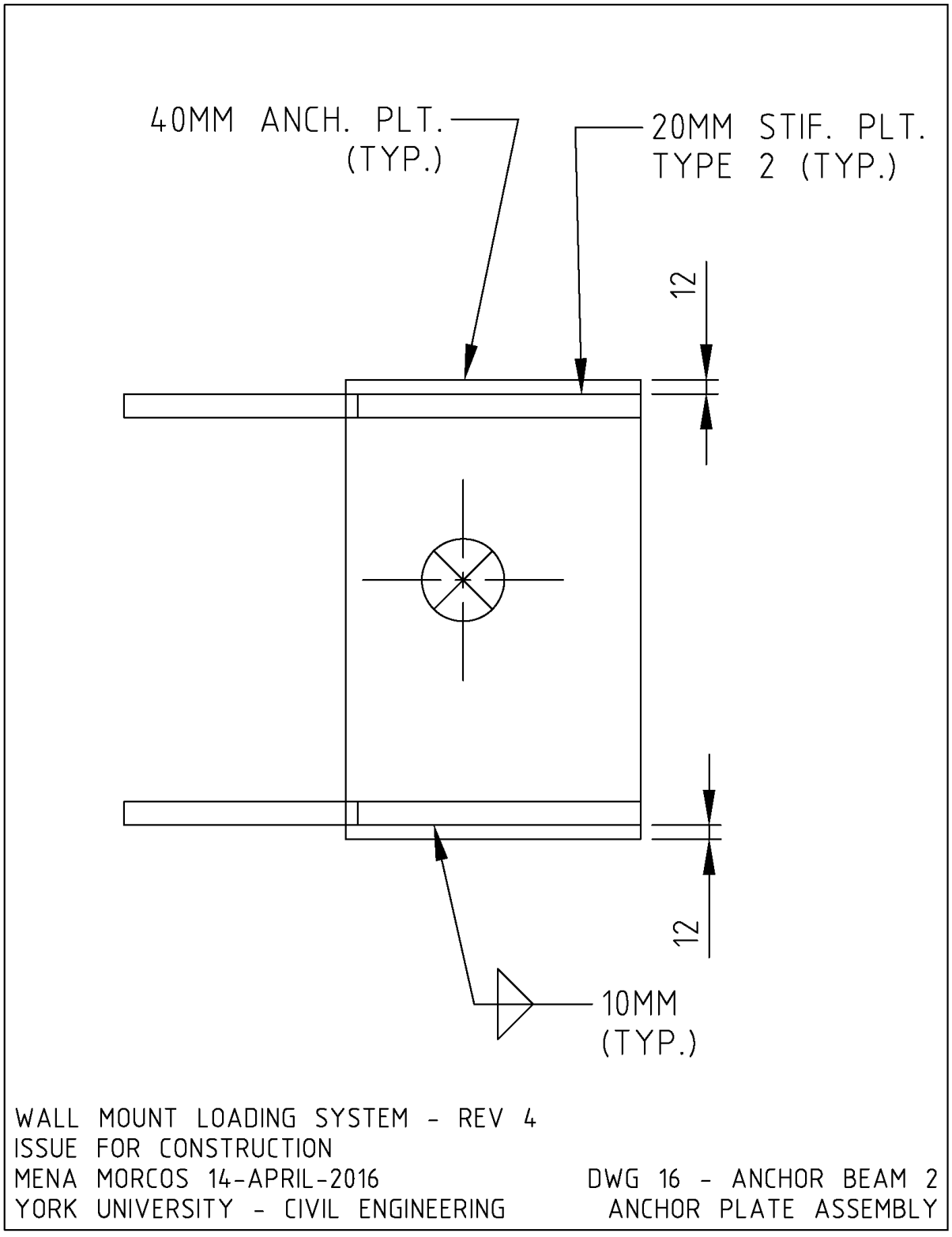

Figure F.16. Wall mount loading system design and fabrication drawing – Drawing 16.

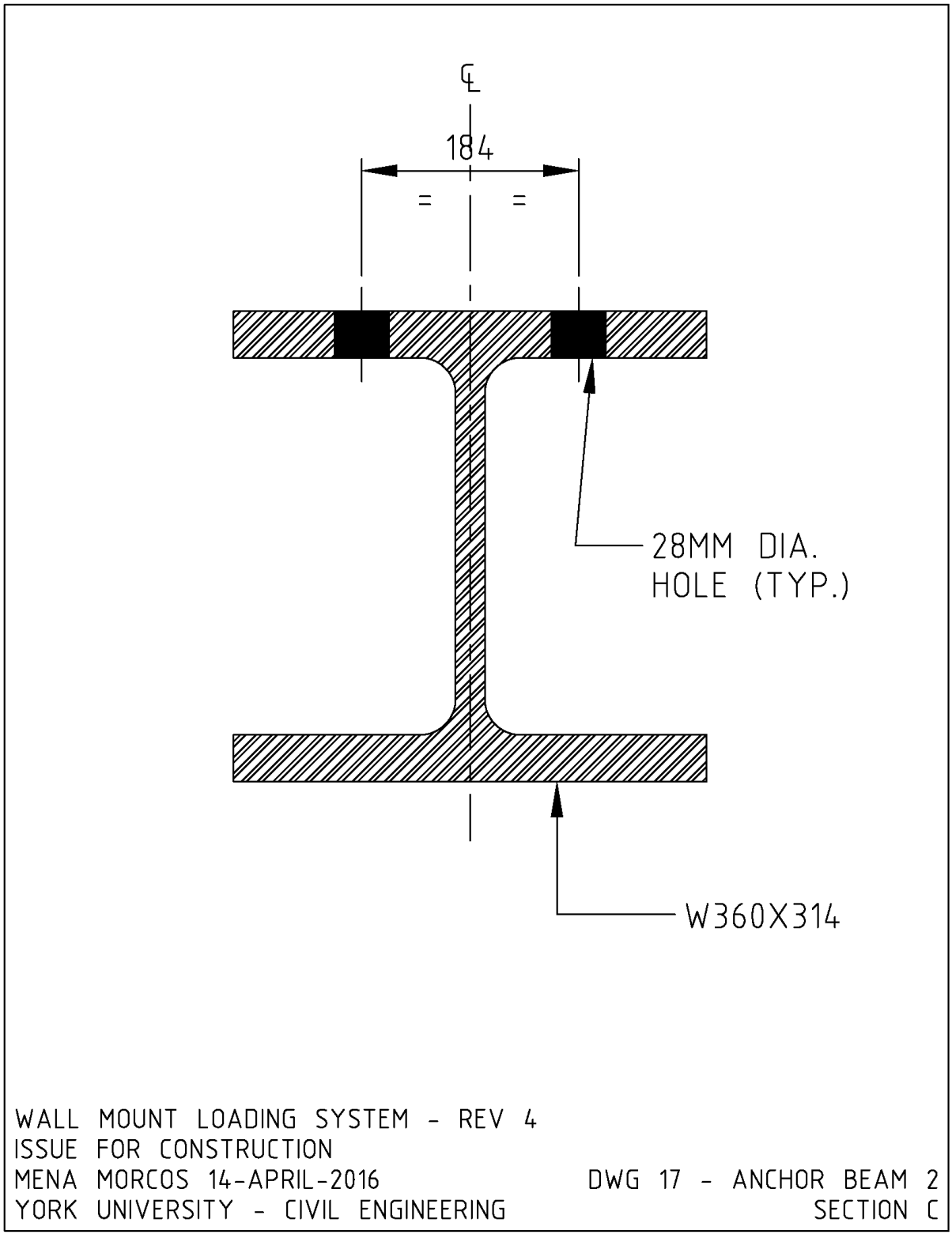

Figure F.17. Wall mount loading system design and fabrication drawing – Drawing 17.

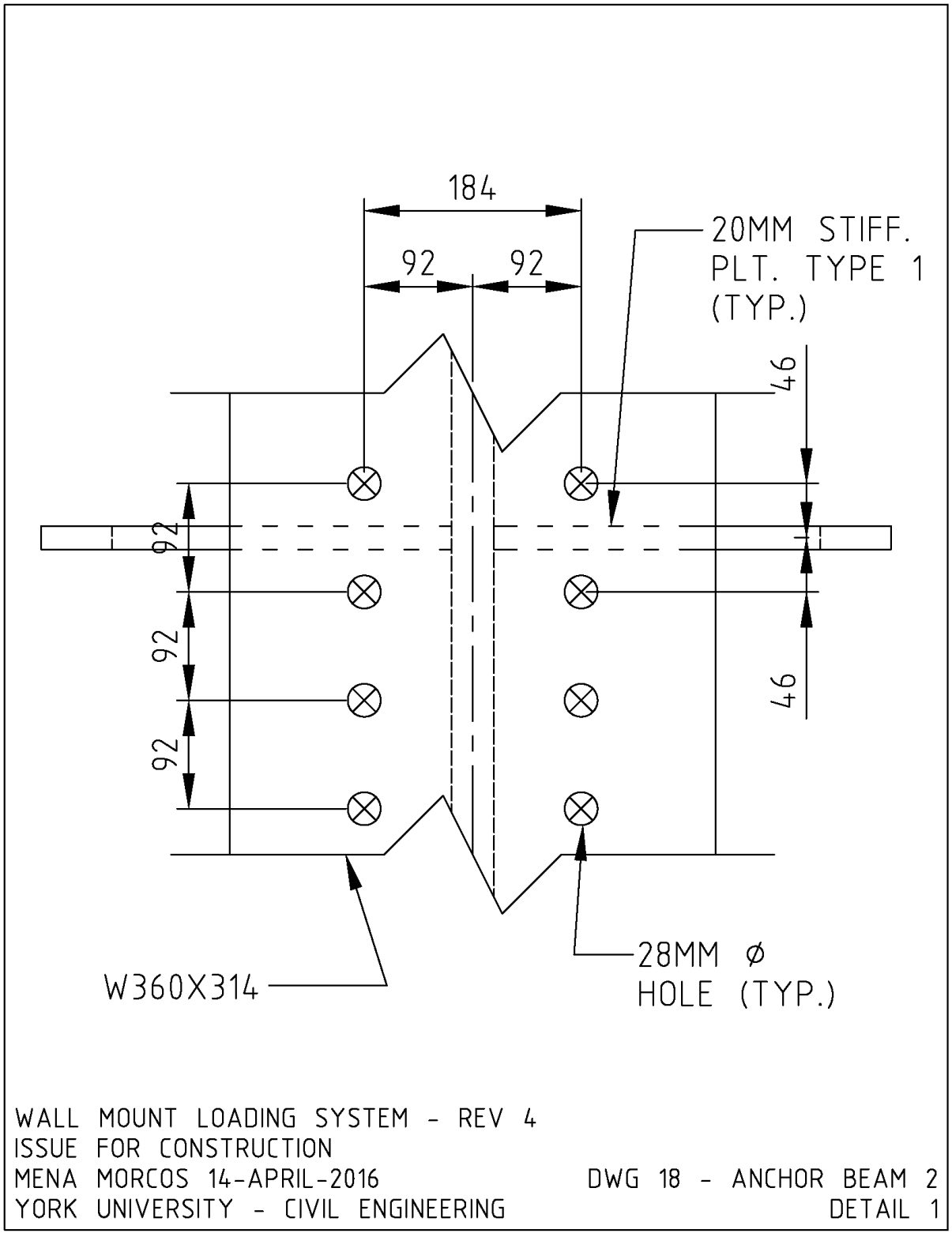

Figure F.18. Wall mount loading system design and fabrication drawing – Drawing 18.

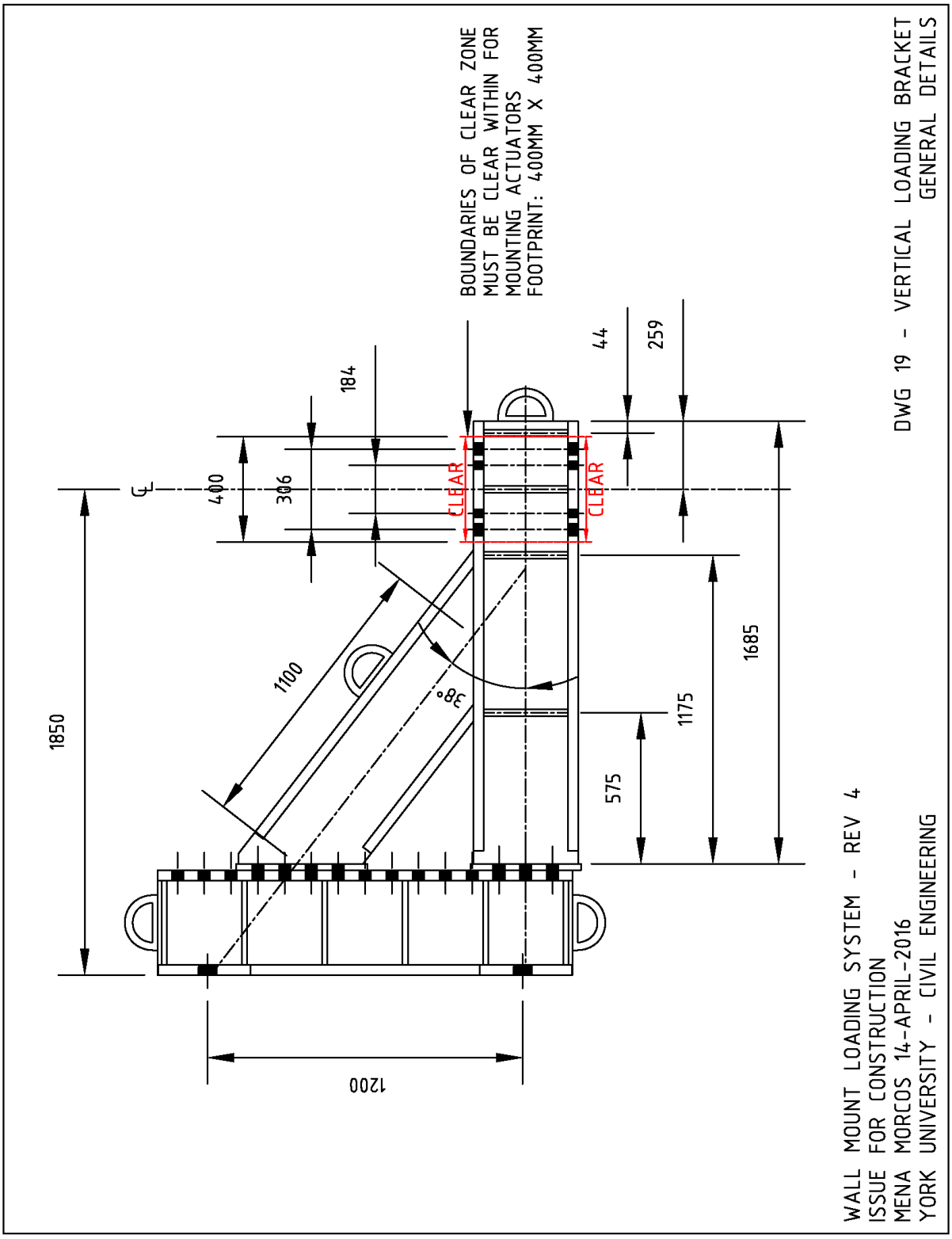

Figure F.19. Wall mount loading system design and fabrication drawing – Drawing 19.

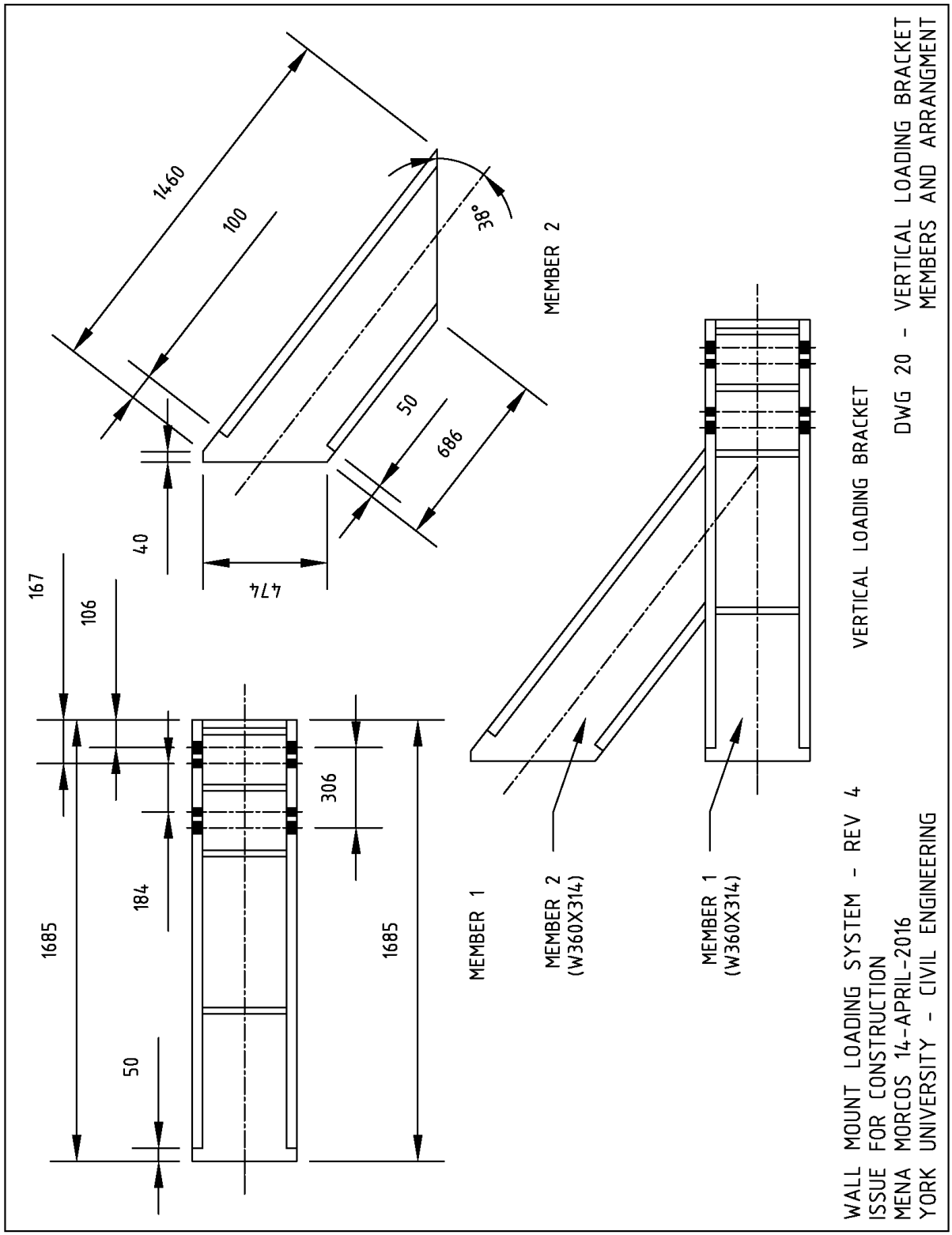

Figure F.20. Wall mount loading system design and fabrication drawing – Drawing 20.

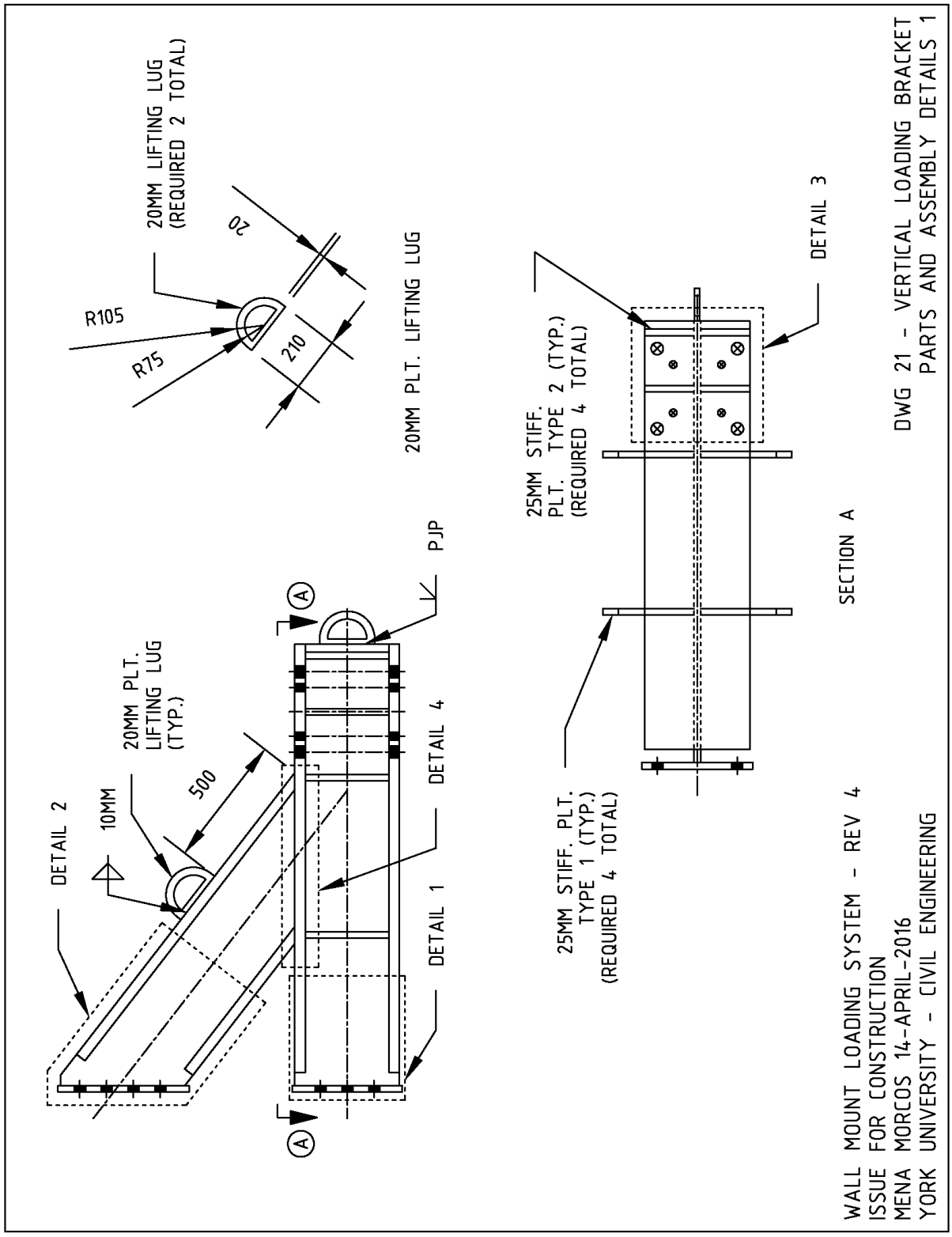

Figure F.21. Wall mount loading system design and fabrication drawing – Drawing 21.

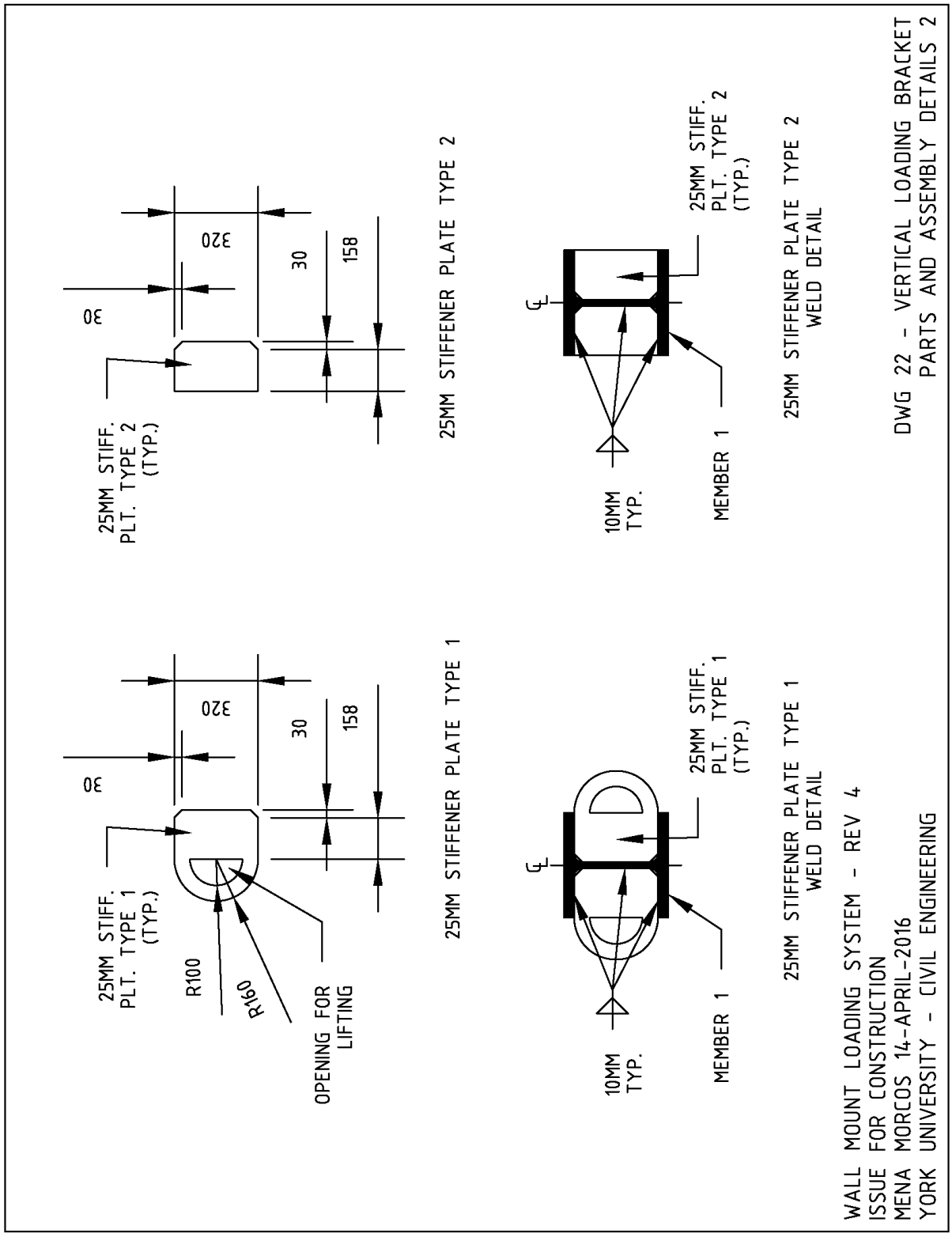

Figure F.22. Wall mount loading system design and fabrication drawing – Drawing 22.

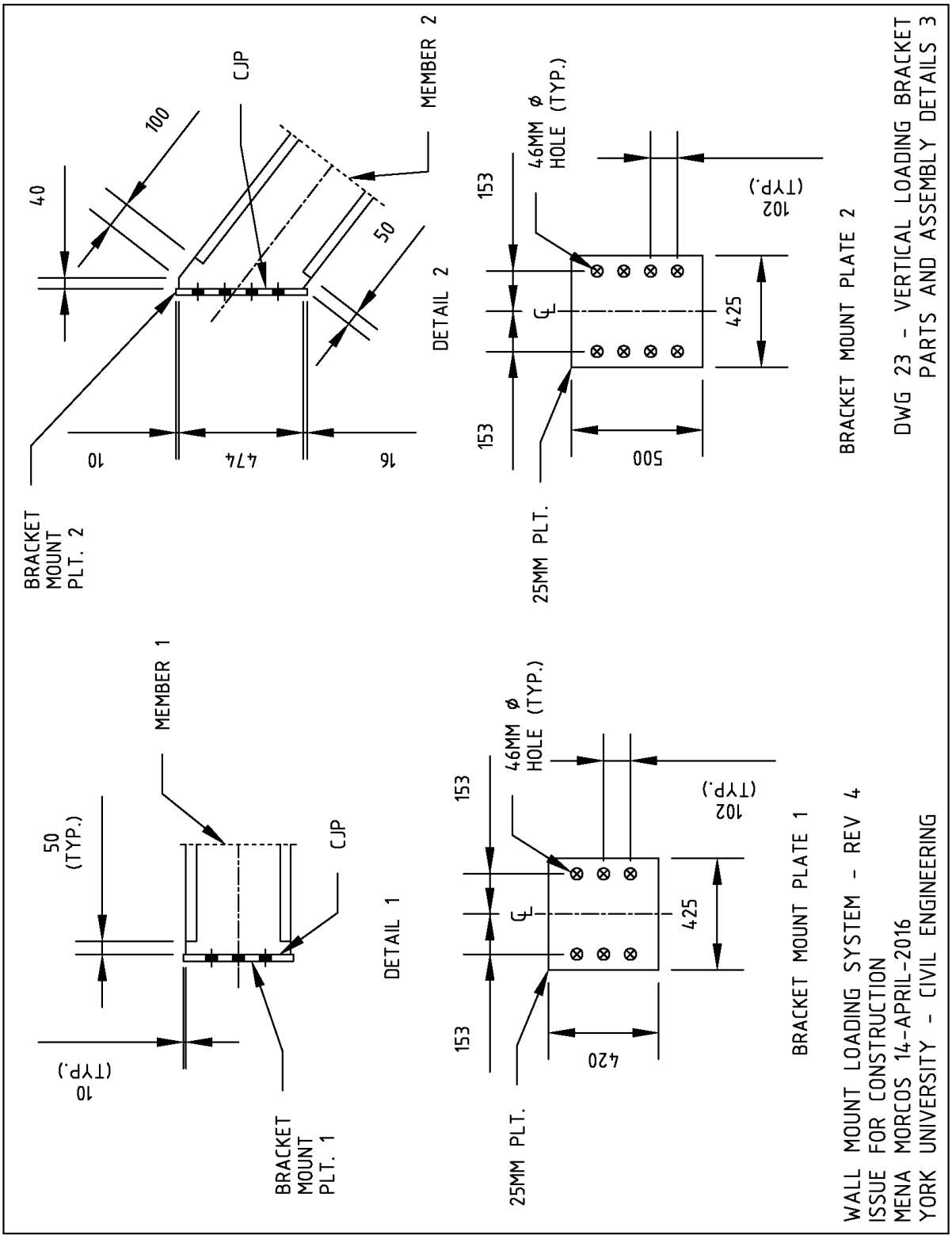

Figure F.23. Wall mount loading system design and fabrication drawing – Drawing 23.

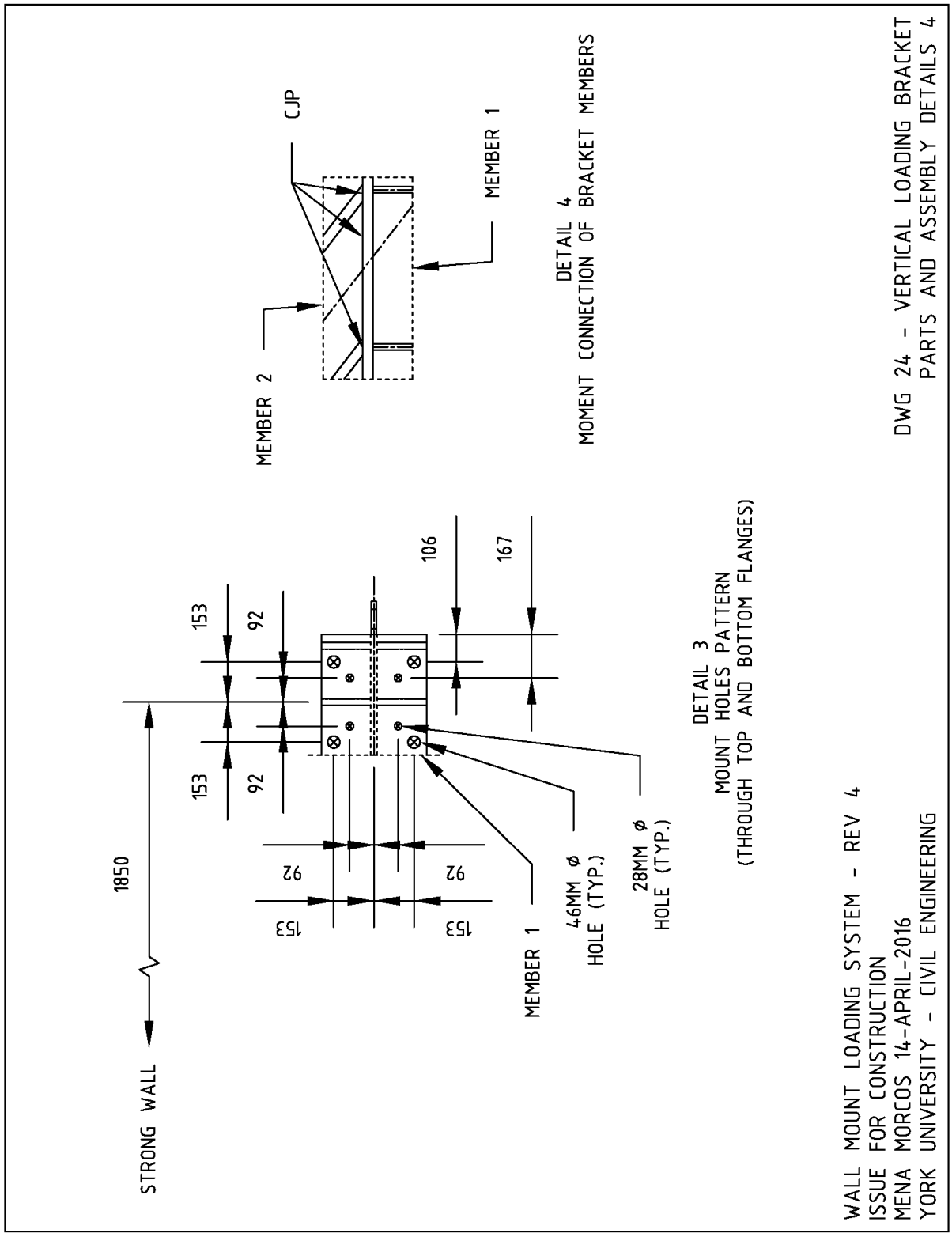

Figure F.24. Wall mount loading system design and fabrication drawing – Drawing 24.

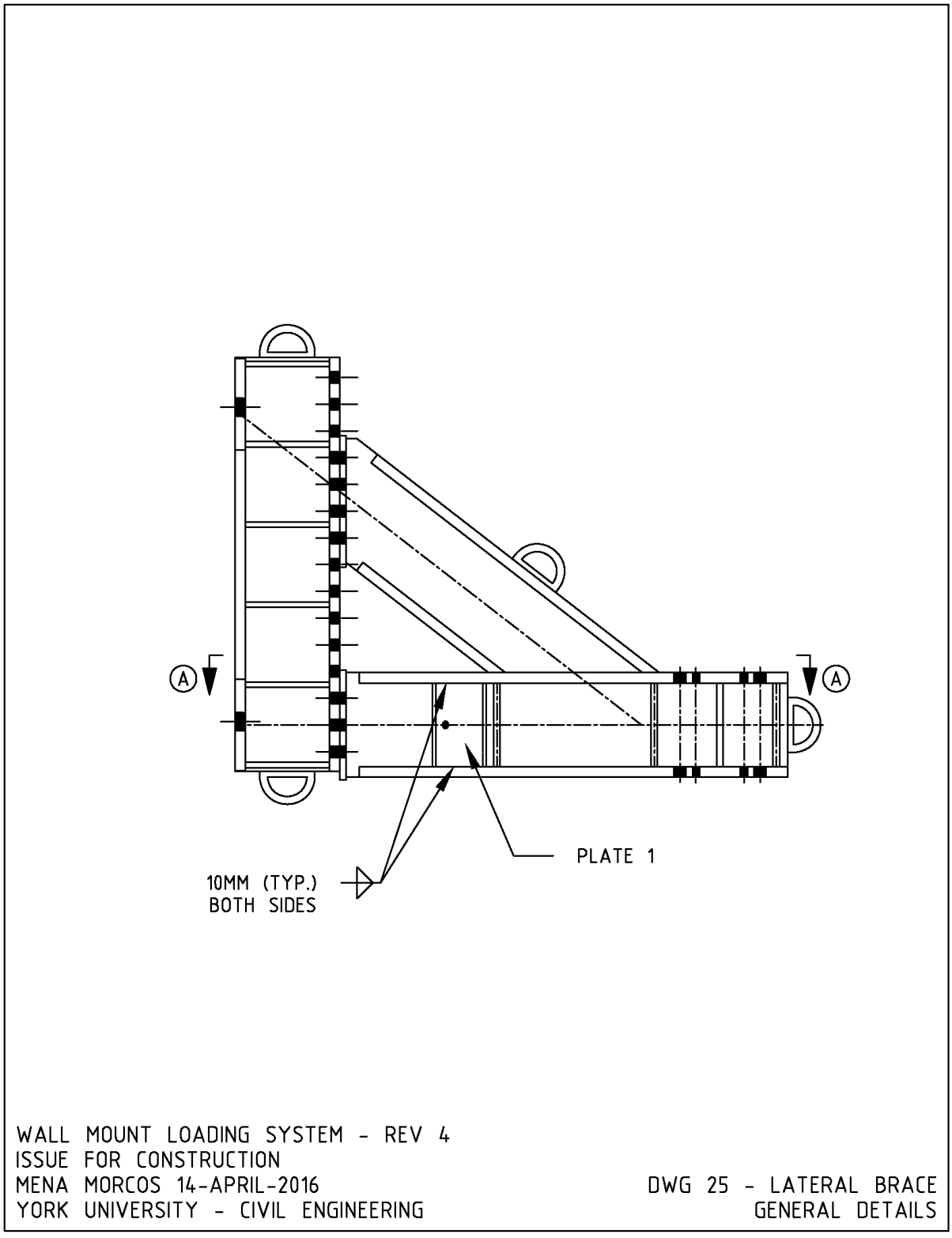

Figure F.25. Wall mount loading system design and fabrication drawing – Drawing 25.

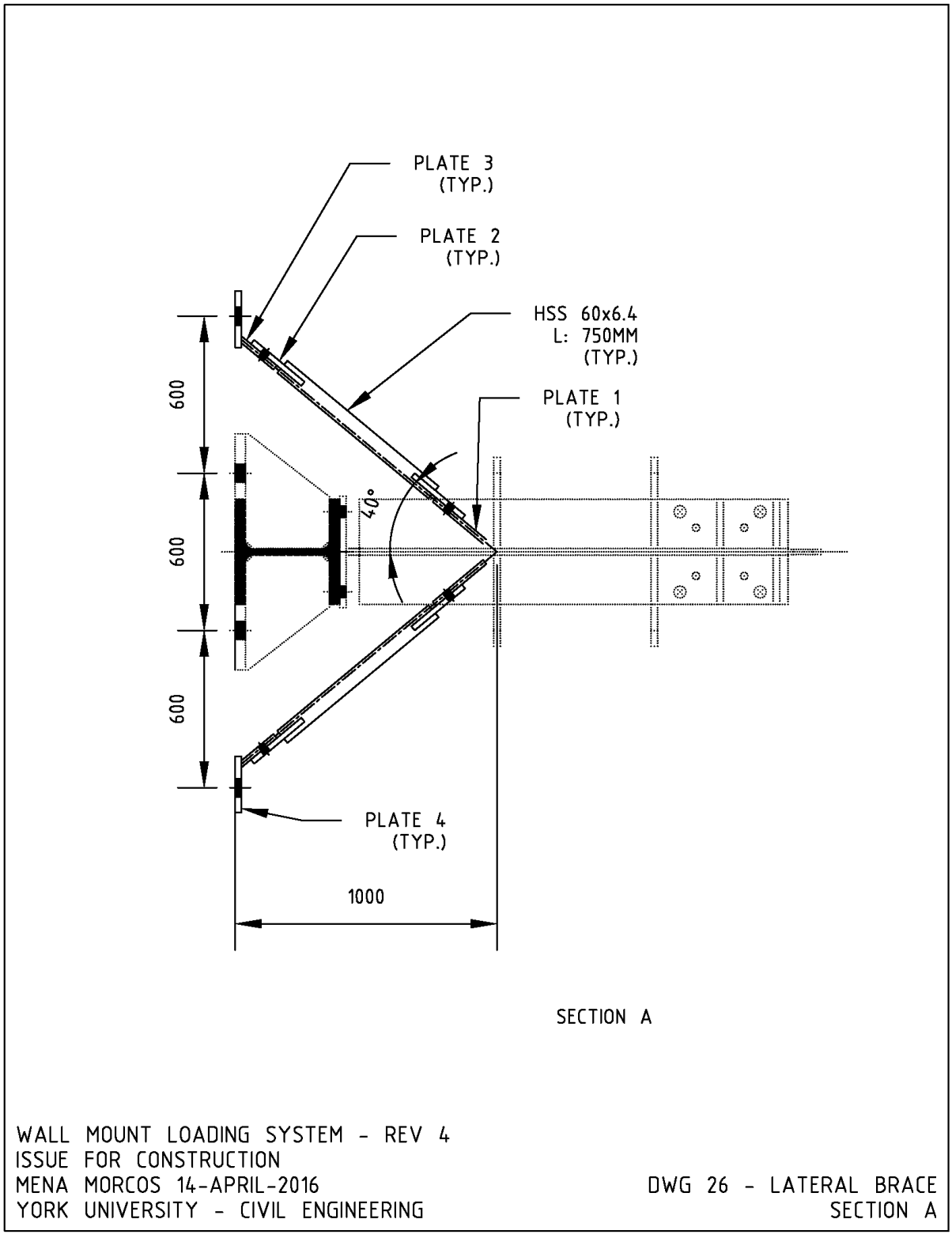

Figure F.26. Wall mount loading system design and fabrication drawing – Drawing 26.

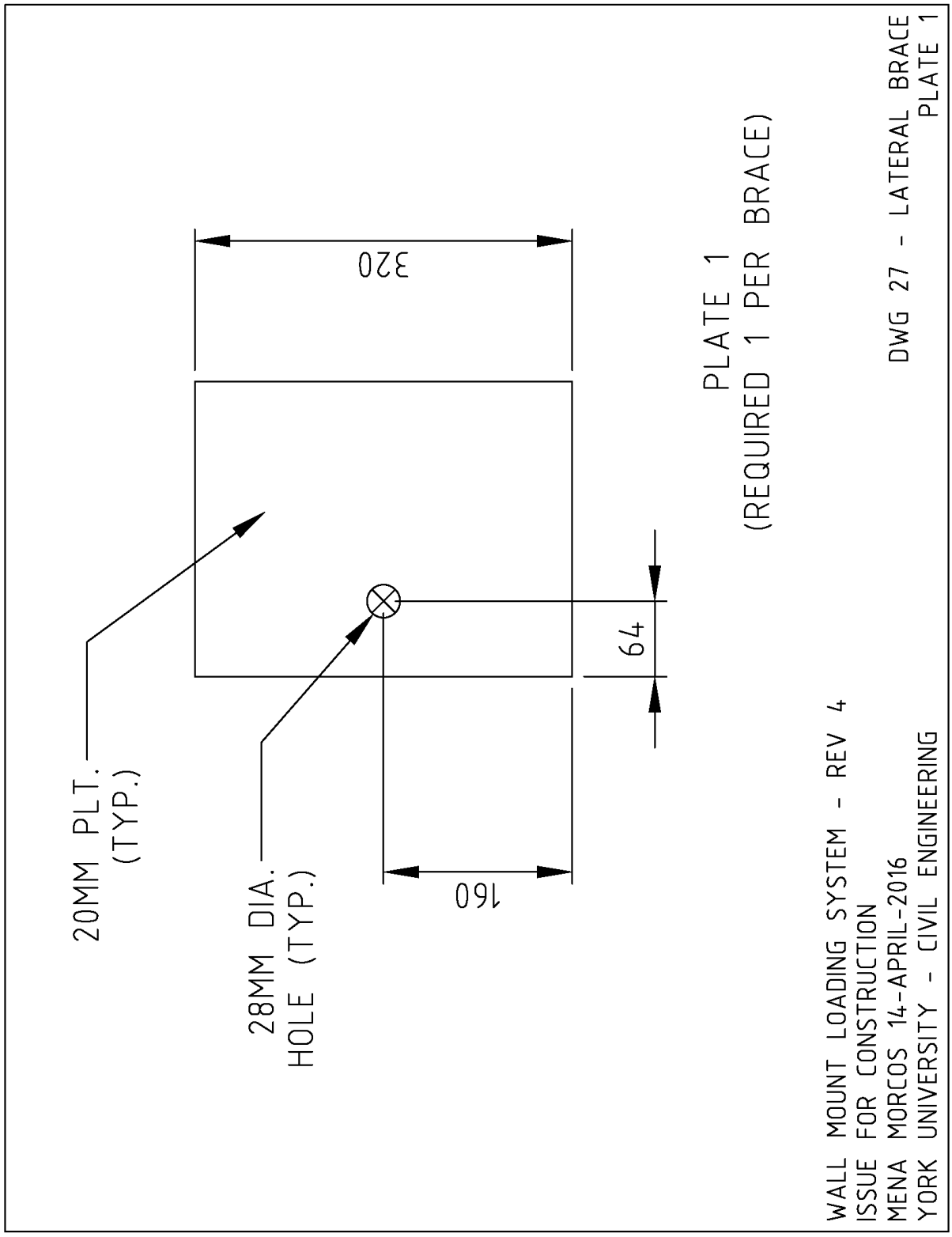

Figure F.27. Wall mount loading system design and fabrication drawing – Drawing 27.

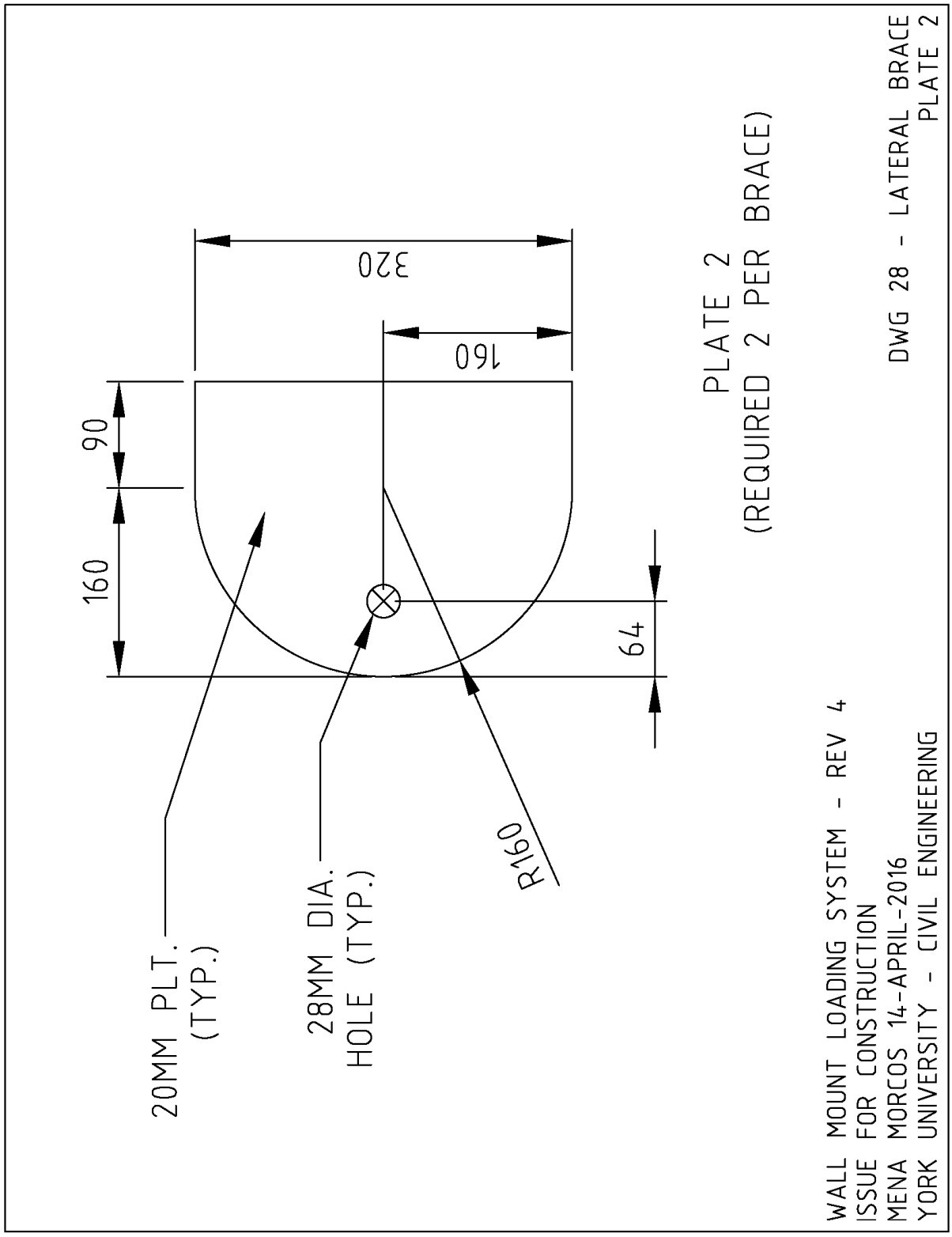

Figure F.28. Wall mount loading system design and fabrication drawing – Drawing 28.

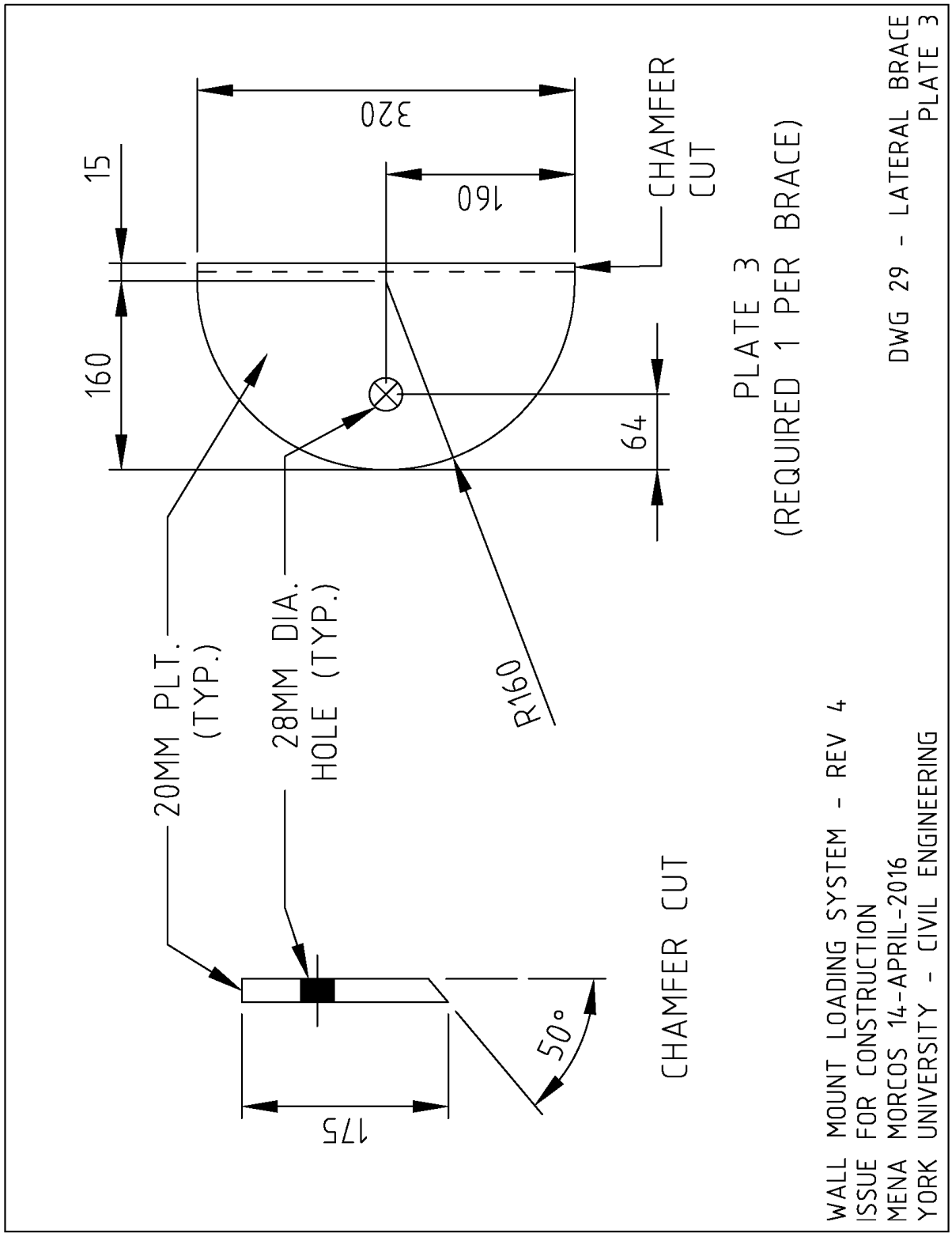

Figure F.29. Wall mount loading system design and fabrication drawing – Drawing 29.

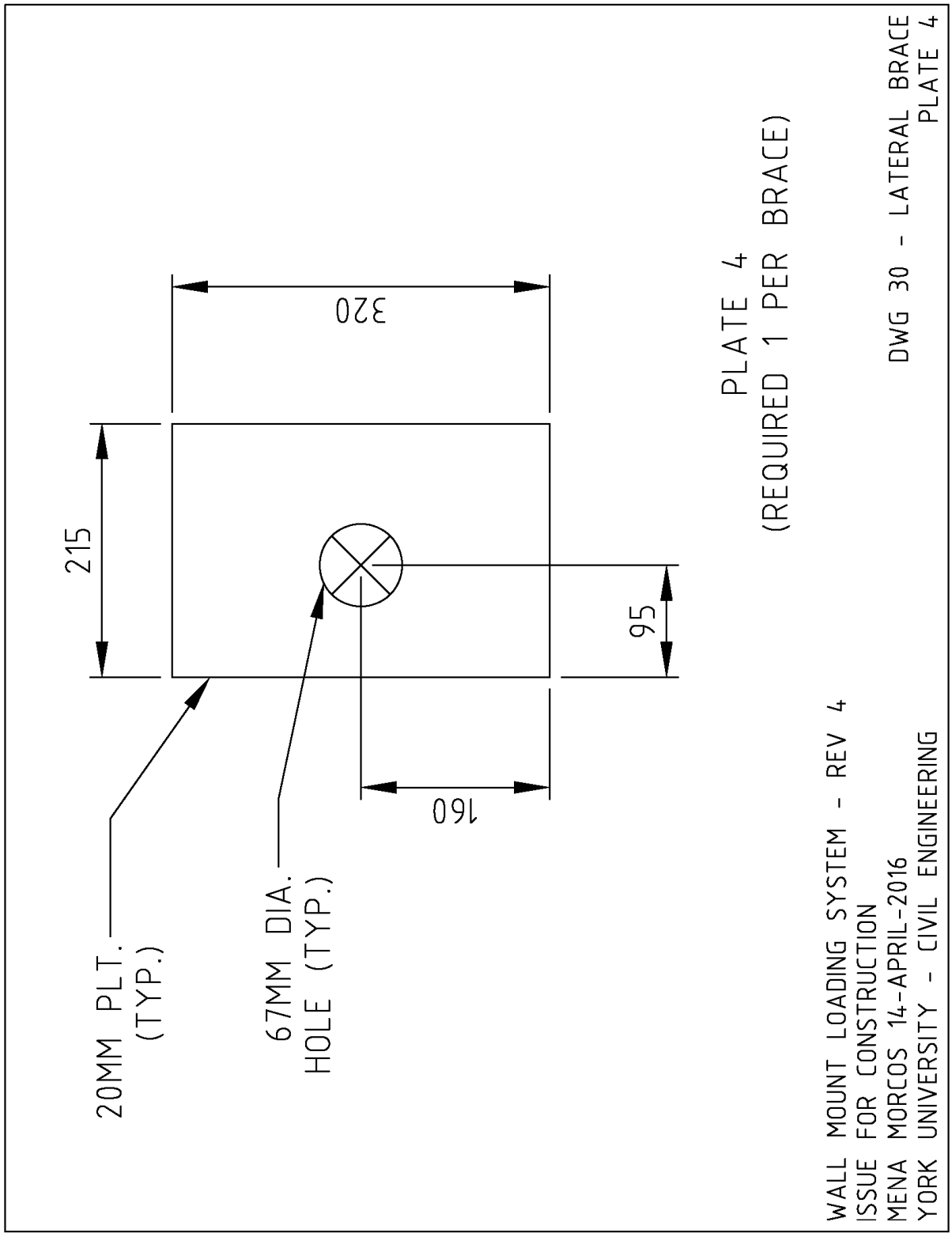

Figure F.30. Wall mount loading system design and fabrication drawing – Drawing 30.

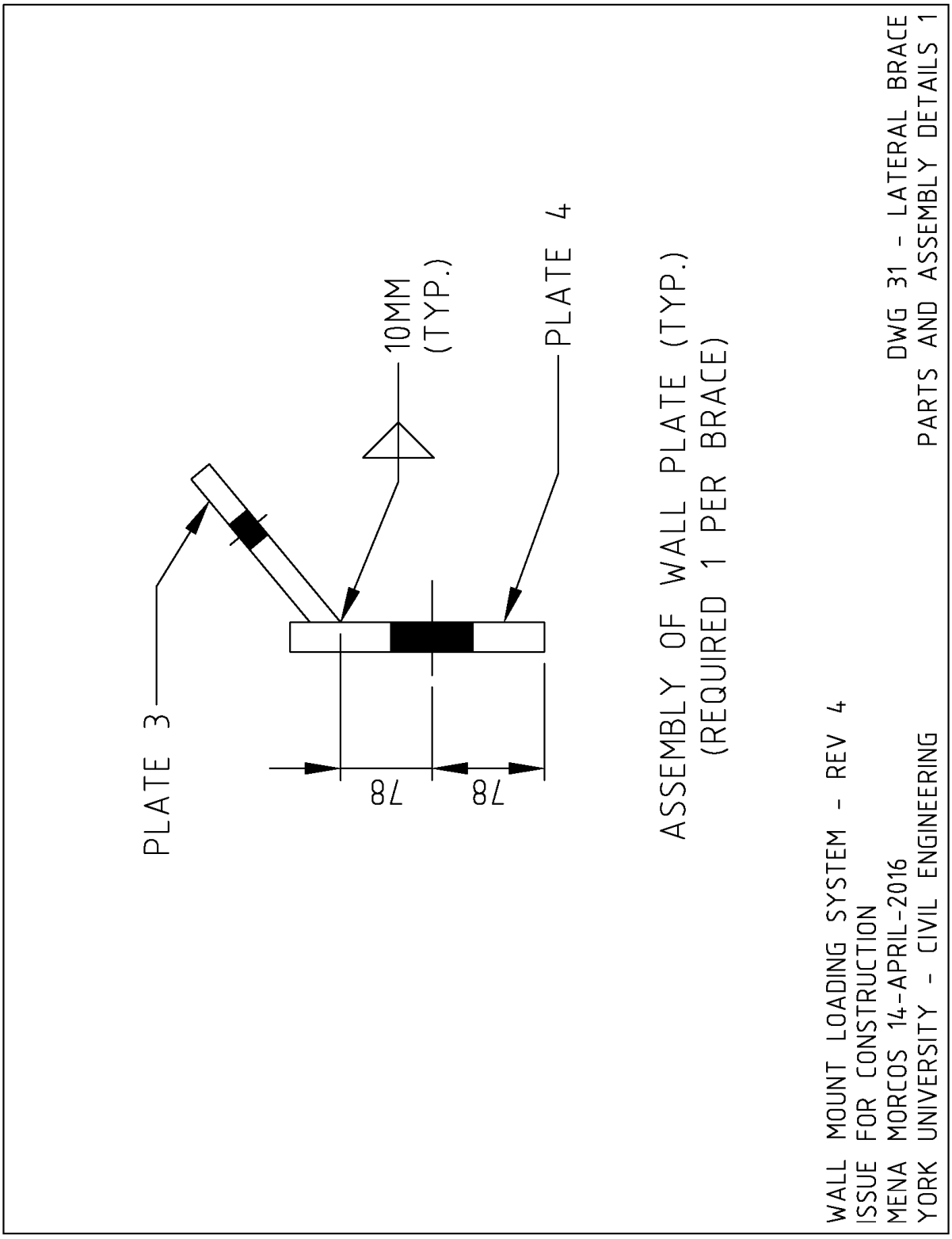

Figure F.31. Wall mount loading system design and fabrication drawing – Drawing 31.

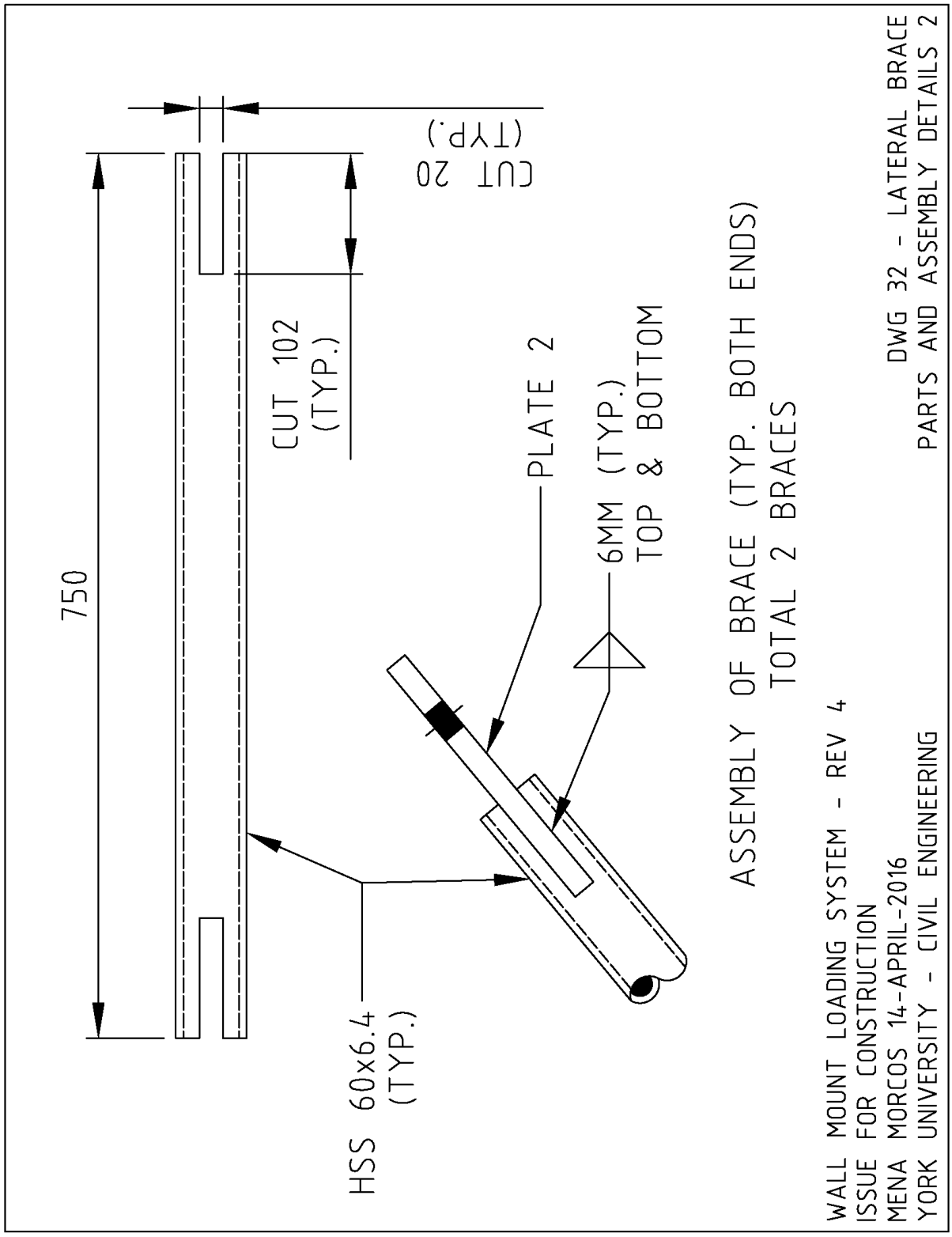

Figure F.32. Wall mount loading system design and fabrication drawing – Drawing 32.

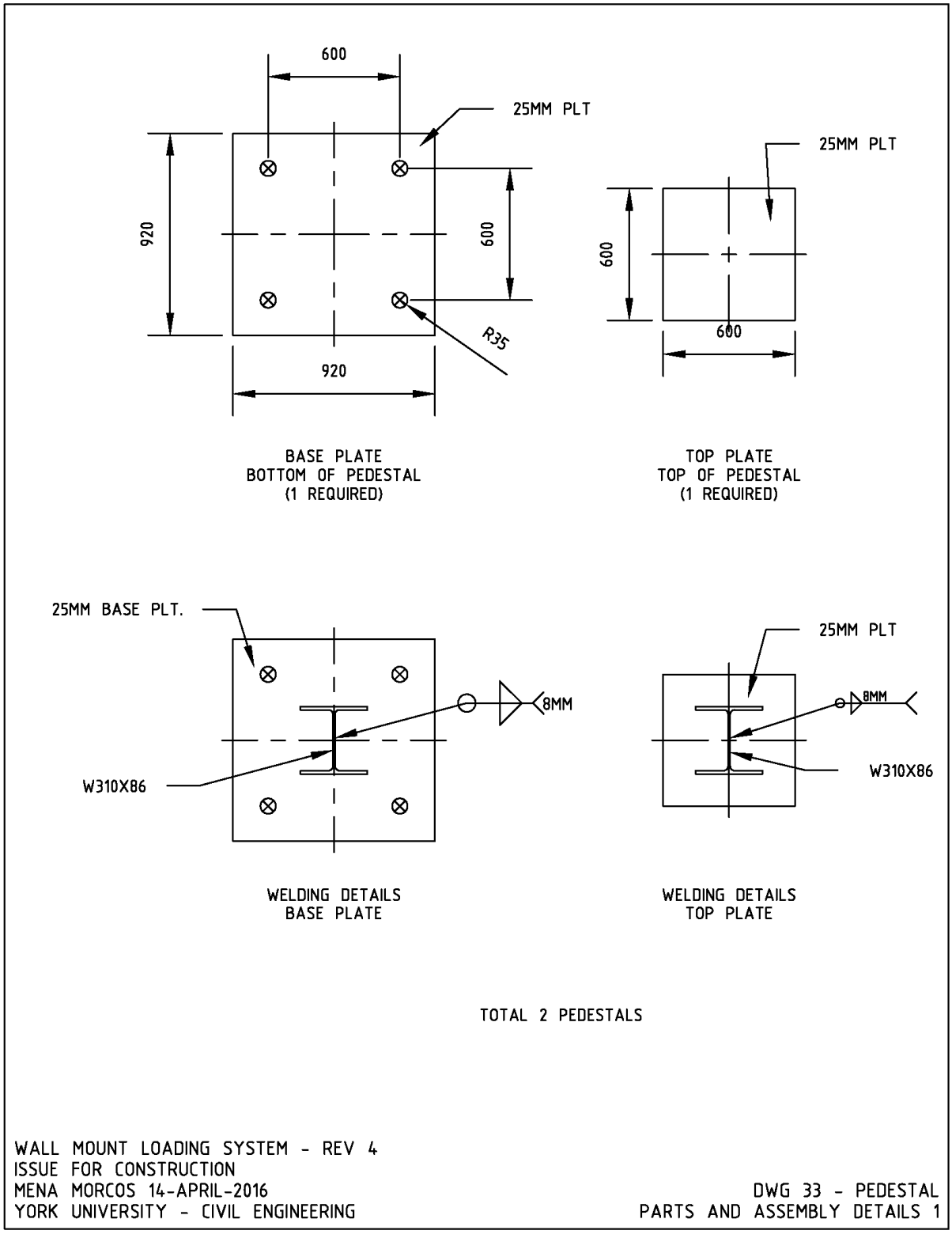

Figure F.33. Wall mount loading system design and fabrication drawing – Drawing 33.

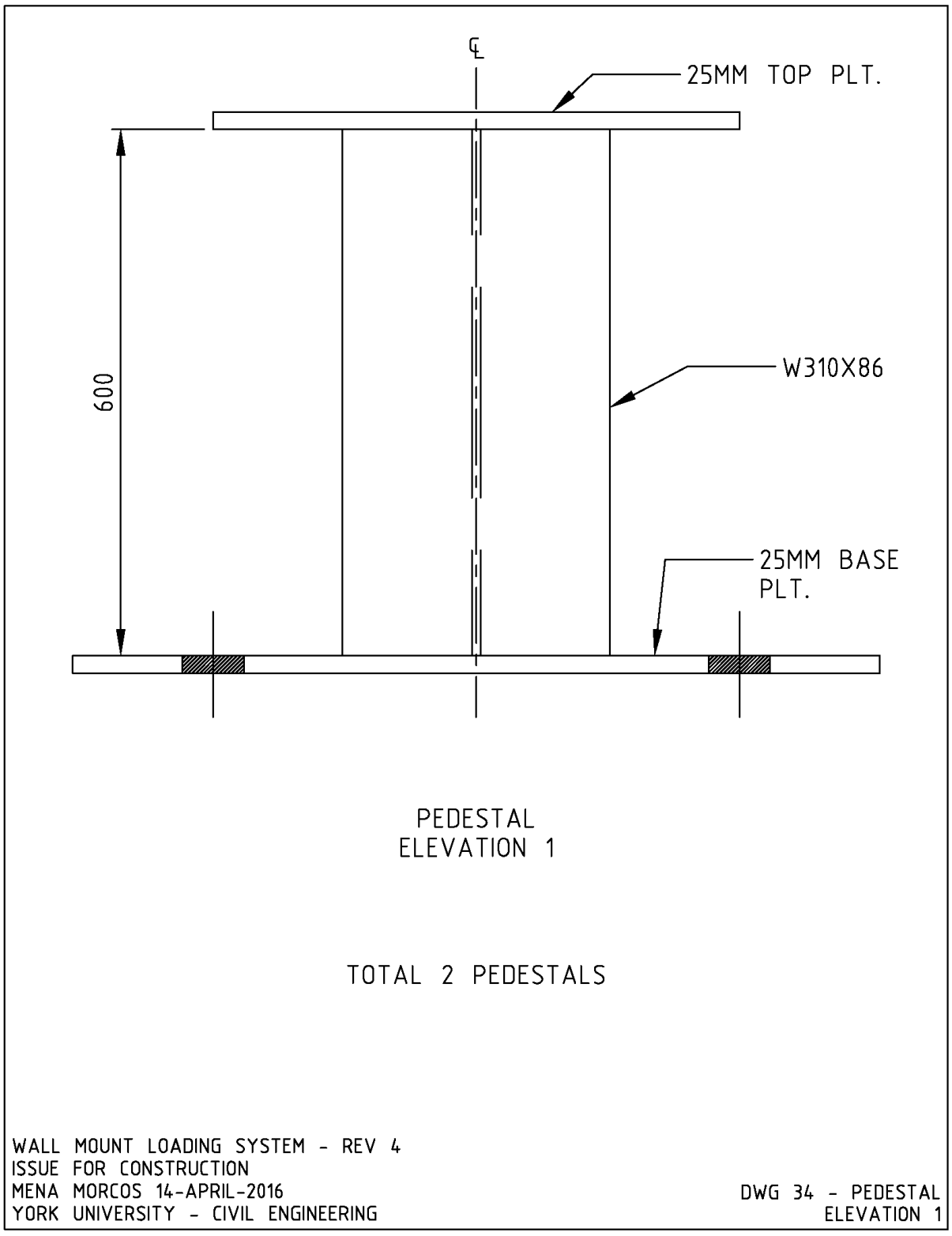

Figure F.34. Wall mount loading system design and fabrication drawing – Drawing 34.

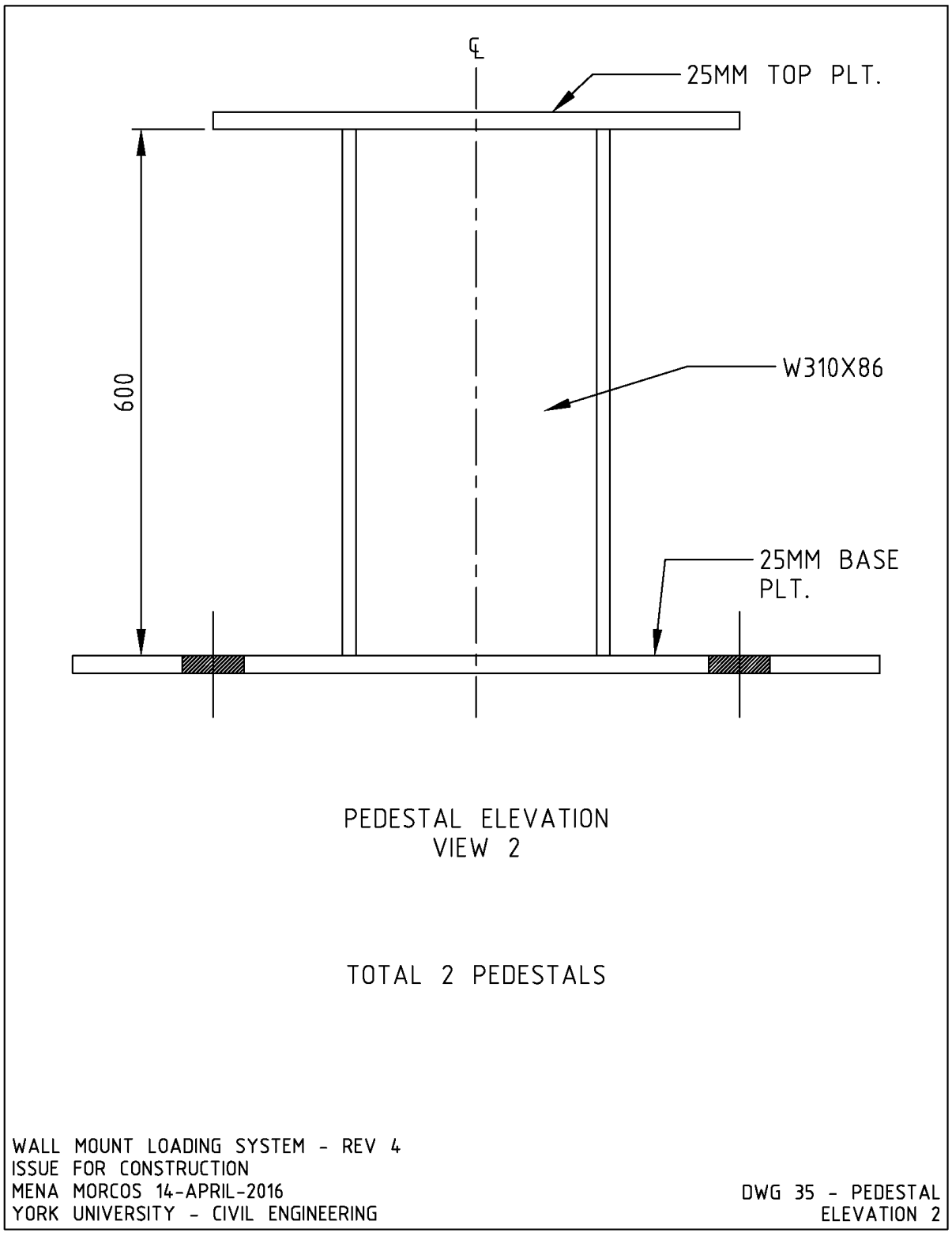

Figure F.35. Wall mount loading system design and fabrication drawing – Drawing 35.

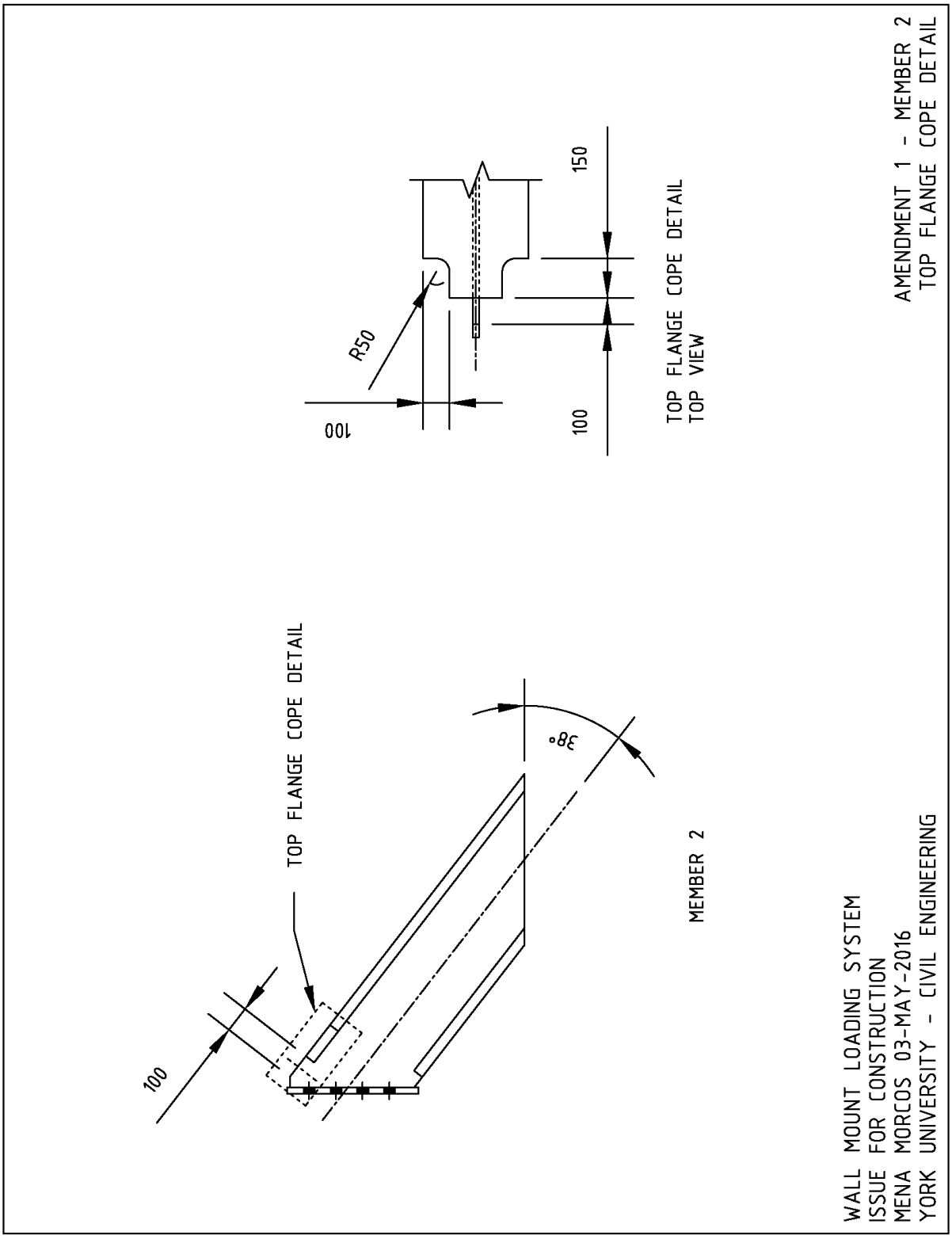

Figure F.36. Wall mount loading system design and fabrication drawing – Amendment 1.

Programming of Loading Protocol

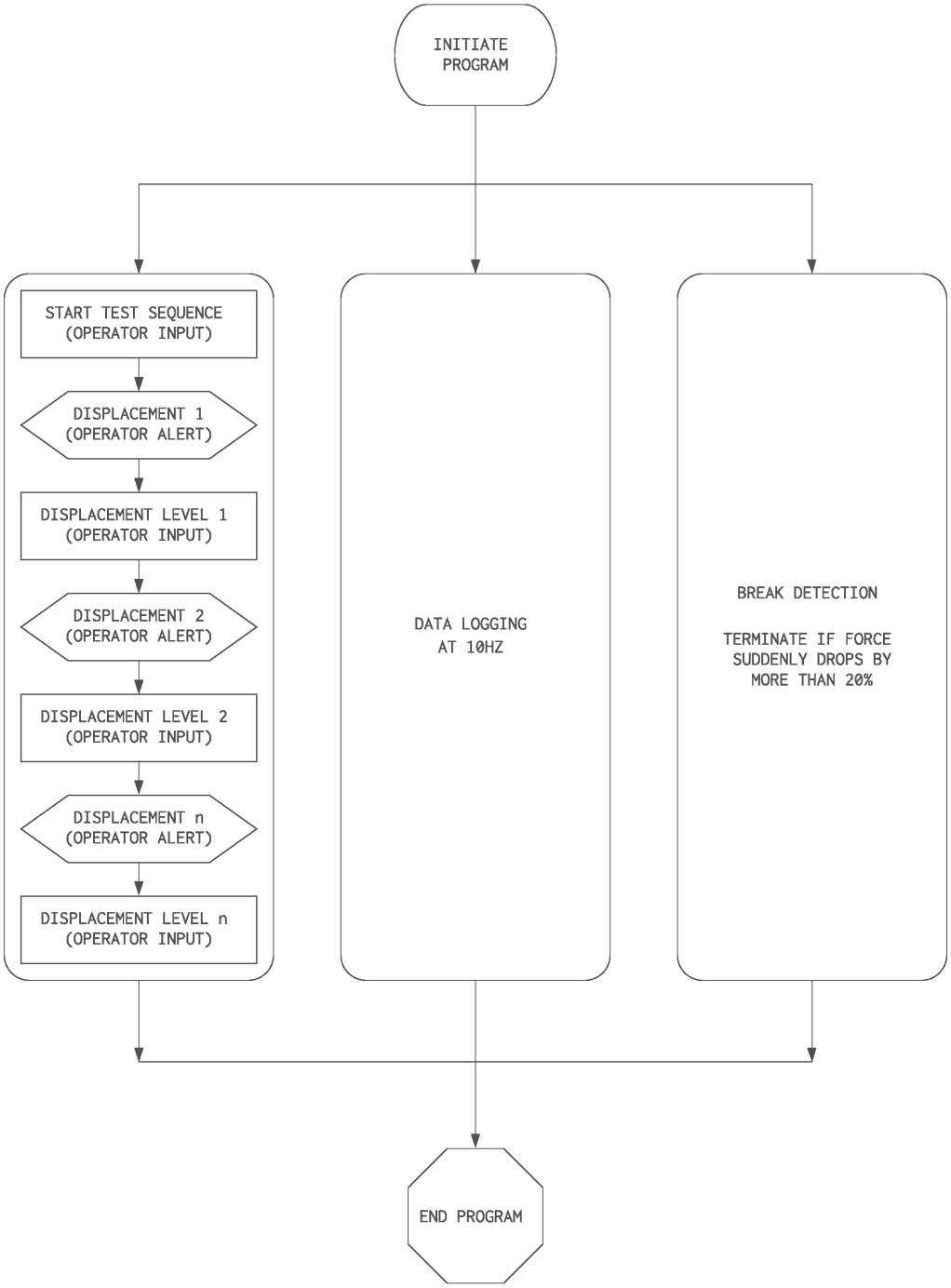

Figure G.1. Loading protocol parallel paths.

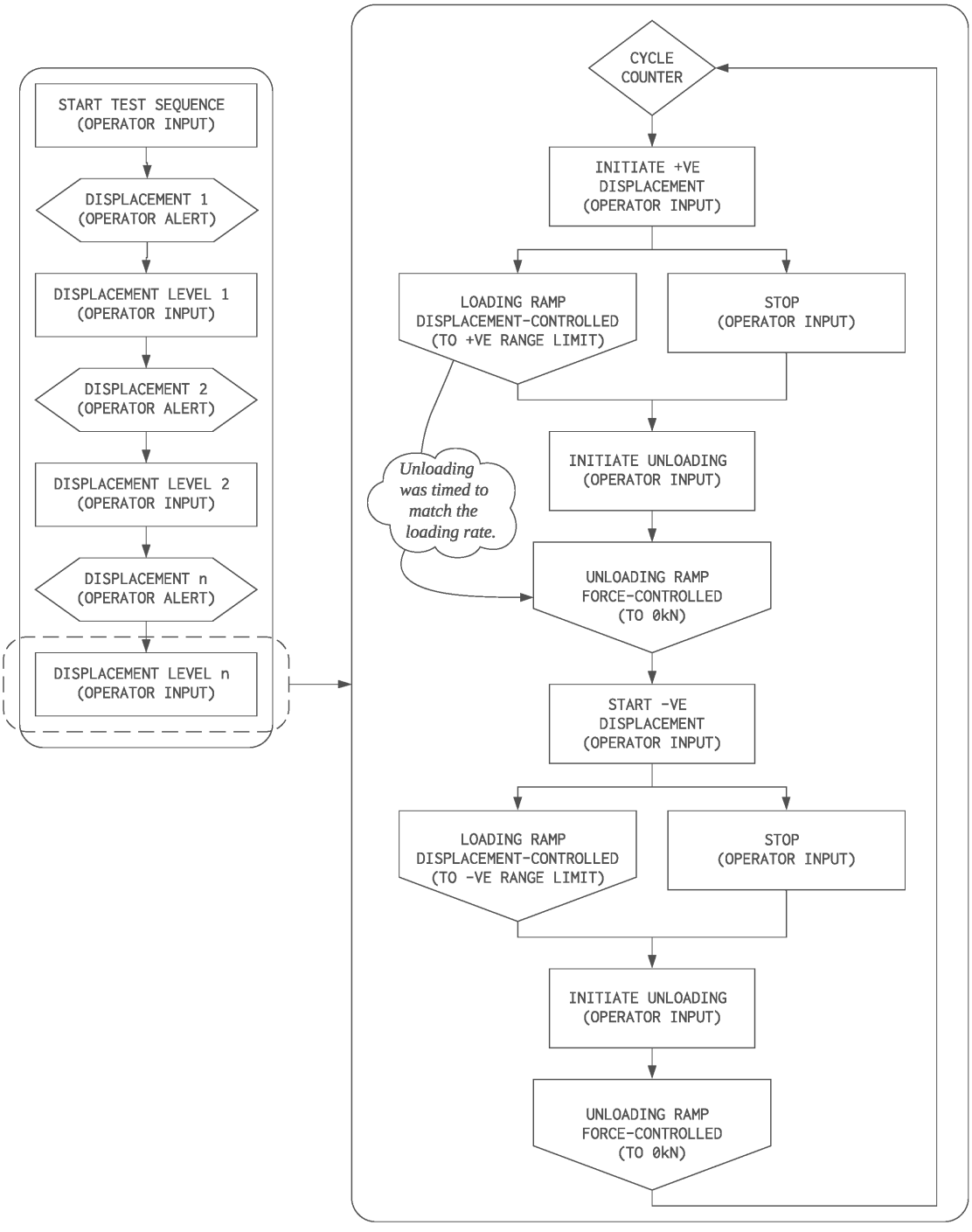

Figure G.2. Cyclic loading and unloading sequence.

APPENDIX H

Crack Widths

The crack width tables provided in Appendix H are only for failure mechanisms where a distinct crack pattern was present, new cracks had developed, or crack widths had significantly changed. The tables provided for both walls are for the yield displacements, peak loads, at the 2.5% drift threshold, and at the ultimate (final) displacement.

Yield Displacement Cracks

Table H.1. Crack widths at yield displacement of wall SWS-R

Left End			Right End		
Elevation (mm)	Open Width (mm)	Closed Width (mm)	Elevation (mm)	Open Width (mm)	Closed Width (mm)
1400	Hairline	Hairline	1400	0.1	Hairline
1300	0.1	Hairline	1250	0.1	Hairline
1150	0.1	Hairline	1100	0.1	Hairline
950	0.1	Hairline	950	0.1	Hairline
800	0.1	Hairline	800	0.1	Hairline
650	0.1	Hairline	650	Hairline	Hairline
500	0.1	Hairline	500	0.3	Hairline
350	Hairline	Hairline	350	0.25	Hairline
200	Hairline	Hairline	200	Hairline	Hairline
0	1	Hairline	0	1	Hairline

Table H.2. Crack widths at yield displacement of wall SWN

Left End			Right End		
Elevation (mm)	Open Width (mm)	Closed Width (mm)	Elevation (mm)	Open Width (mm)	Closed Width (mm)
1700	Hairline	Hairline	1900	Hairline	Hairline
1550	0.1	Hairline	1700	0.1	Hairline
1400	0.1	Hairline	1550	0.18	Hairline
1250	0.1	Hairline	1400	0.1	Hairline
1100	0.15	0.1	1250	0.25	Hairline
950	0.15	0.1	1100	0.2	Hairline
600	0.1	Hairline	950	0.18	Hairline
350	5	1.5	650	0.6	Hairline
0	9	6	300	6	0.5
			0	14	9

Peak Load Cracks

Table H.3. Crack widths at peak load of wall SWS-R

Left End			Right End		
Elevation (mm)	Open Width (mm)	Closed Width (mm)	Elevation (mm)	Open Width (mm)	Closed Width (mm)
1650	Hairline	Hairline	1450	Hairline	Hairline
1550	0.2	Hairline	1400	0.15	Hairline
1400	Hairline	Hairline	1250	0.18	Hairline
1300	0.18	Hairline	1100	0.15	Hairline
1150	0.15	Hairline	950	0.3	Hairline
950	0.3	Hairline	800	0.25	Hairline
800	0.4	Hairline	650	0.18	Hairline
650	0.2	Hairline	500	0.3	Hairline
500	0.3	Hairline	350	0.8	0.4
350	1	0.8	200	0.5	0.25
200	1	Hairline	150	1.5	0.4
0	8	3	50	0.5	0.18
			0	5	1

Table H.4. Crack widths at peak load of wall SWN

Left End			Right End		
Elevation (mm)	Open Width (mm)	Closed Width (mm)	Elevation (mm)	Open Width (mm)	Closed Width (mm)
1850	Hairline	Hairline	1900	Hairline	Hairline
1700	Hairline	Hairline	1700	Hairline	Hairline
1550	0.1	Hairline	1550	0.1	Hairline
1400	0.1	Hairline	1350	0.15	Hairline
1250	0.18	Hairline	1250	0.15	0.1
1100	0.2	Hairline	1100	0.18	Hairline
950	0.25	0.15	950	0.2	0.1
600	0.18	Hairline	650	Hairline	Hairline
350	8	1.25	300	5	2
150	0.1	Hairline	0	38	12
0	35	12			

2.5% Drift Cracks

Table H.5. Crack widths at 2.5% drift of wall SWS-R

Left End			Right End		
Elevation (mm)	Open Width (mm)	Closed Width (mm)	Elevation (mm)	Open Width (mm)	Closed Width (mm)
1650	Hairline	Hairline	1450	Hairline	Hairline
1550	Hairline	Hairline	1400	0.15	Hairline
1400	Hairline	Hairline	1250	0.18	Hairline
1300	Hairline	Hairline	1100	0.15	Hairline
1150	Hairline	Hairline	950	0.3	Hairline
950	Hairline	Hairline	800	0.25	Hairline
800	Hairline	Hairline	650	0.18	Hairline
650	Hairline	Hairline	500	0.3	Hairline
500	Hairline	Hairline	350	0.9	0.6
350	1.5	1	200	2	1
300	1.25	0.9	150	-	-
250	1.5	0.8	50	4	3
200	1.25	0.8	0	7	1
0	10	3			

Table H.6. Crack widths at 2.5% drift of wall SWN

Left End			Right End		
Elevation (mm)	Open Width (mm)	Closed Width (mm)	Elevation (mm)	Open Width (mm)	Closed Width (mm)
1700	Hairline	Hairline	1900	Hairline	Hairline
1550	0.1	Hairline	1700	0.1	Hairline
1400	0.1	Hairline	1550	0.15	Hairline
1250	0.1	Hairline	1350	Hairline	Hairline
1100	0.1	Hairline	1250	0.18	0.1
950	0.15	0.1	1100	0.18	Hairline
600	H	Hairline	950	0.15	0.1
350	5	1.25	650	0.4	Hairline
0	12	9	300	7	2
			0	19	13

Ultimate Displacement Cracks

Table H.7. Crack widths at the final displacement of wall SWS-R

Left End			Right End		
Elevation (mm)	Open Width (mm)	Closed Width (mm)	Elevation (mm)	Open Width (mm)	Closed Width (mm)
1650	Hairline	Hairline	1450	Hairline	Hairline
1550	Hairline	Hairline	1400	0.15	Hairline
1400	Hairline	Hairline	1250	0.18	Hairline
1300	Hairline	Hairline	1100	0.15	Hairline
1150	Hairline	Hairline	950	0.3	Hairline
950	Hairline	Hairline	800	0.25	Hairline
800	Hairline	Hairline	650	0.18	Hairline
650	Hairline	Hairline	500	0.3	Hairline
500	Hairline	Hairline	350	0.9	0.6
350	1.5	1	200	2	1
300	1.25	0.9	150	-	-
250	1.5	0.8	50	-	-
200	2	1	0	8	5
0	10	3			

Table H.8. Crack widths at the final displacement of wall SWN

Left End			Right End		
Elevation (mm)	Open Width (mm)	Closed Width (mm)	Elevation (mm)	Open Width (mm)	Closed Width (mm)
1850	Hairline	Hairline	1900	Hairline	Hairline
1700	Hairline	Hairline	1700	Hairline	Hairline
1550	0.1	Hairline	1550	0.1	Hairline
1400	0.15	Hairline	1350	0.15	Hairline
1250	0.1	Hairline	1250	0.15	Hairline
1100	0.15	Hairline	1100	0.15	Hairline
950	0.18	0.1	950	0.2	Hairline
600	0.1	Hairline	650	Hairline	Hairline
350	7	1.25	300	4	1.25
150	0.18	Hairline	0	38	18
0	37	30			

APPENDIX I

Crack Patterns at Target Displacements

Wall SWS-R Crack Patterns

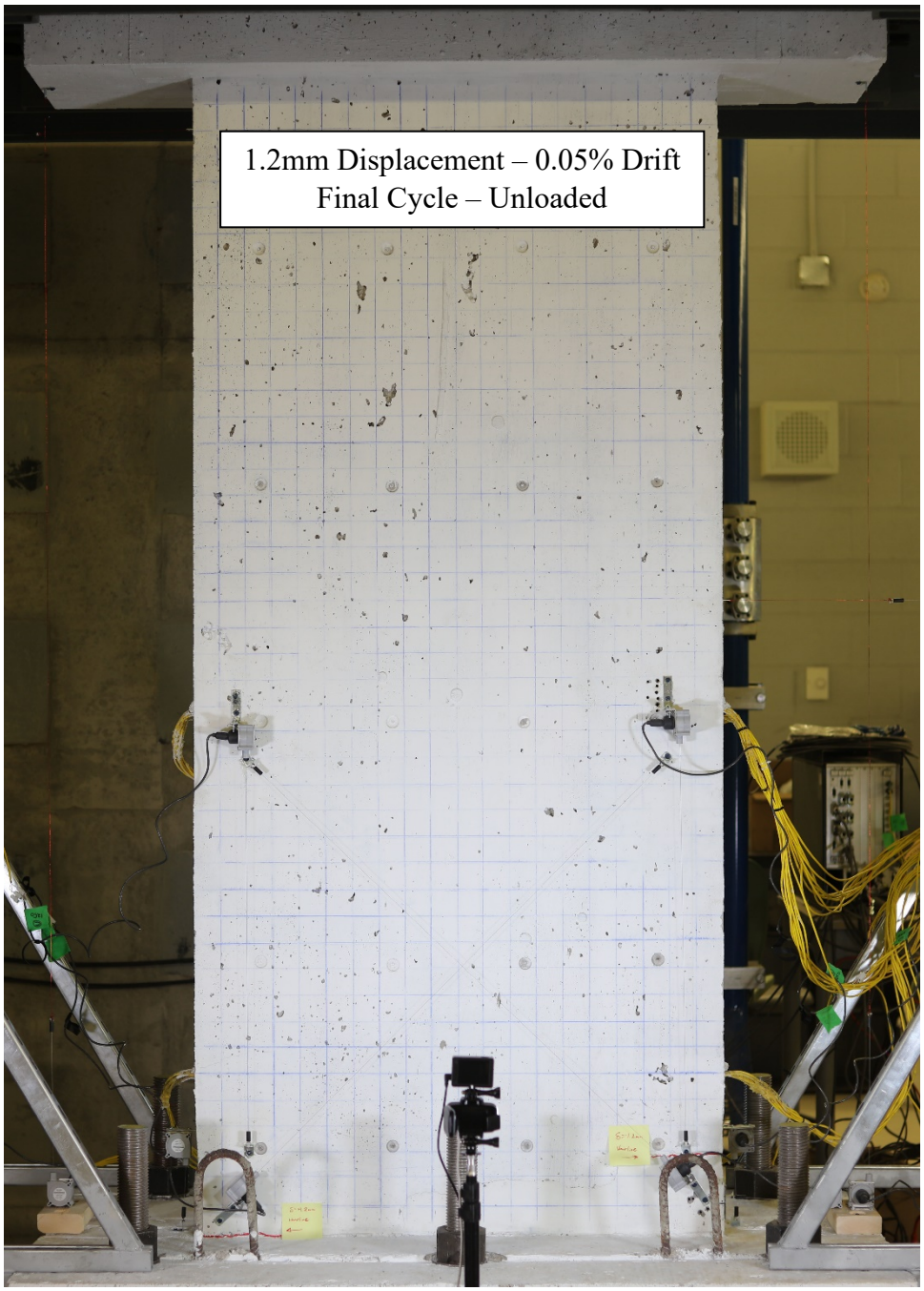

Figure I.1. Crack pattern at 1.2mm displacement of wall SWS-R.

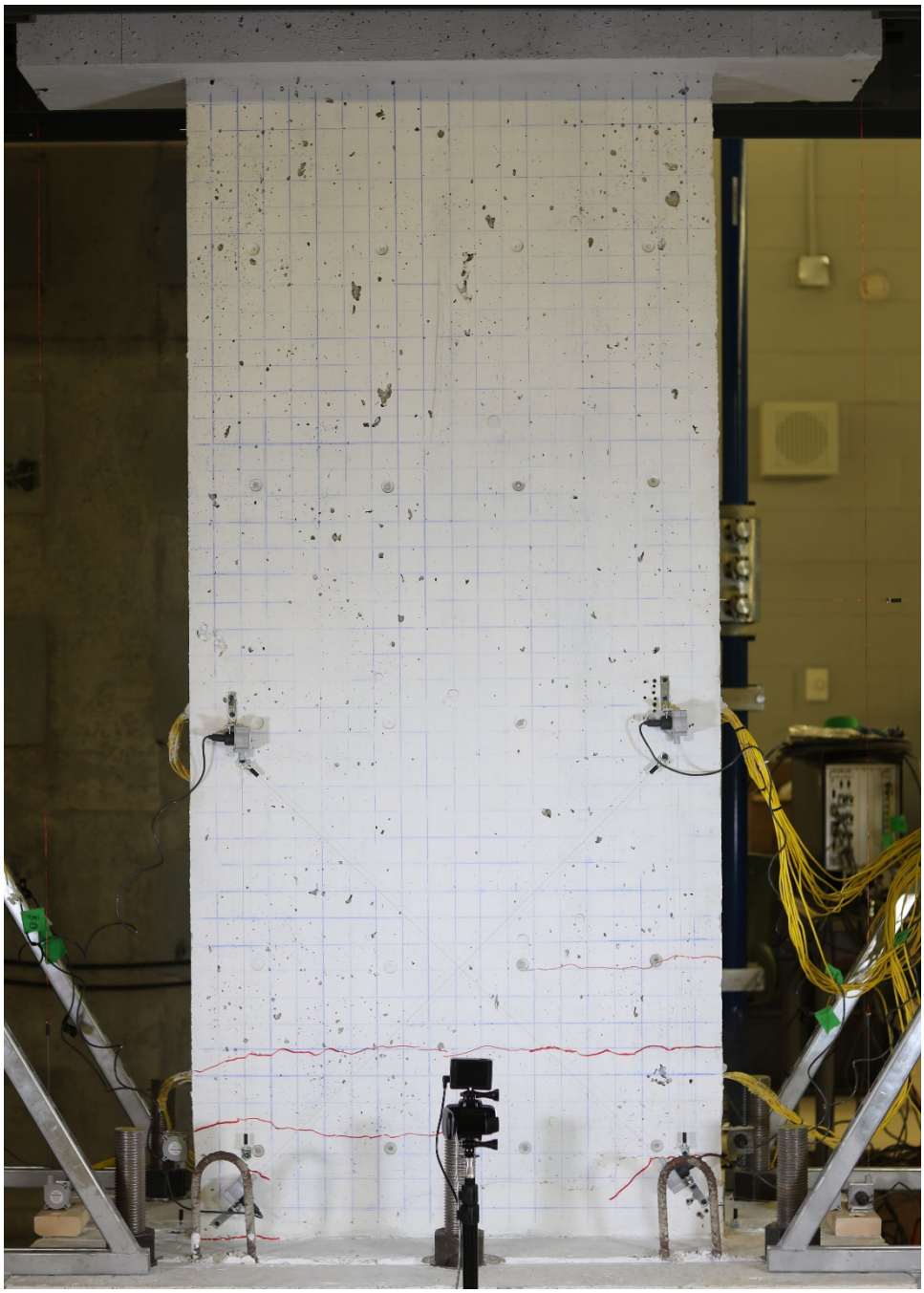

2.4mm Displacement – 0.1% Drift
Final Cycle – Unloaded

Figure I.2. Crack pattern at 2.4mm displacement of wall SWS-R.

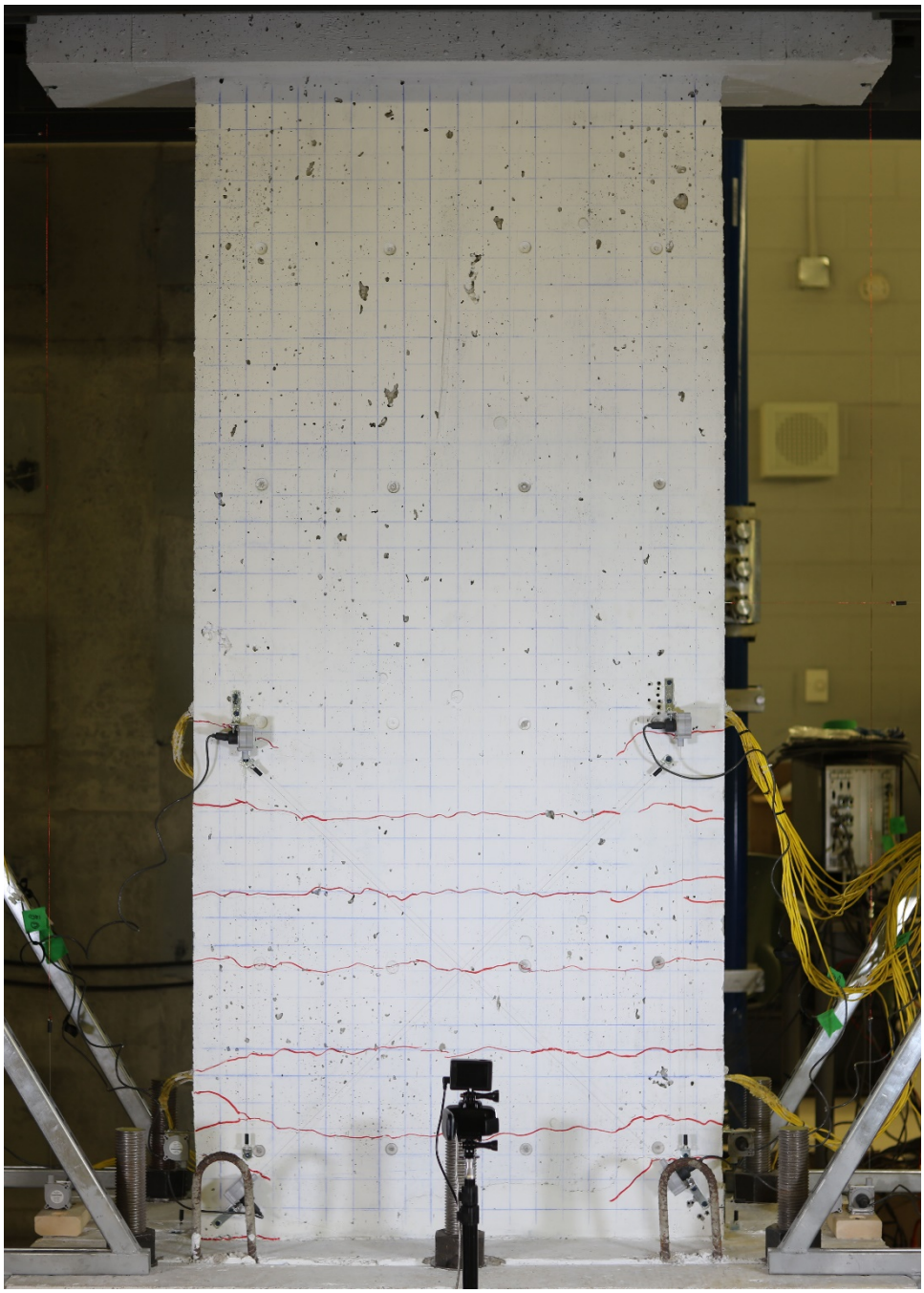

4.8mm Displacement – 0.2% Drift
Final Cycle – Unloaded

Figure I.3. Crack pattern at 4.8mm displacement of wall SWS-R.

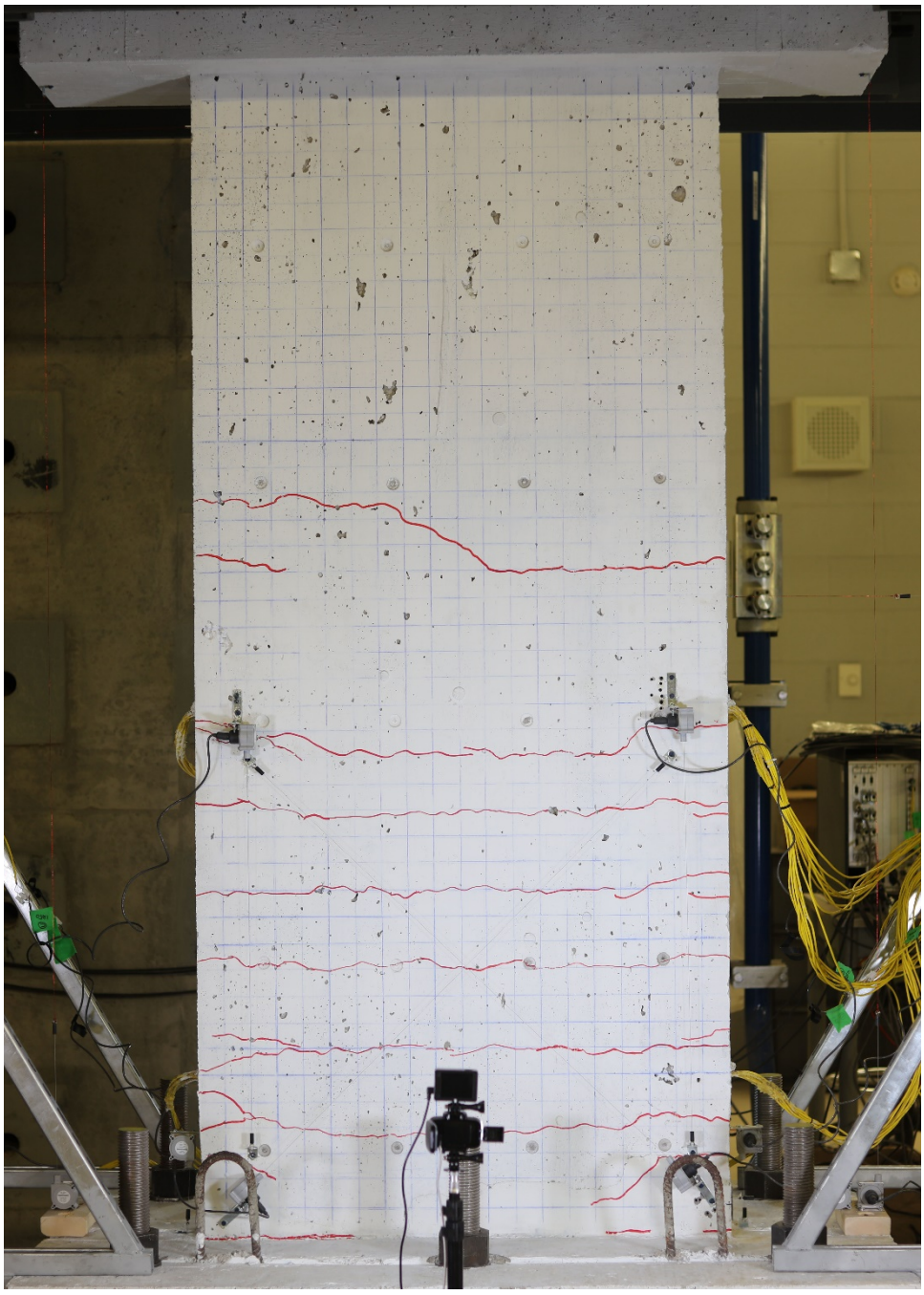

7.2mm Displacement – 0.3% Drift
Final Cycle – Unloaded

Figure I.4. Crack pattern at 7.2mm displacement of wall SWS-R.

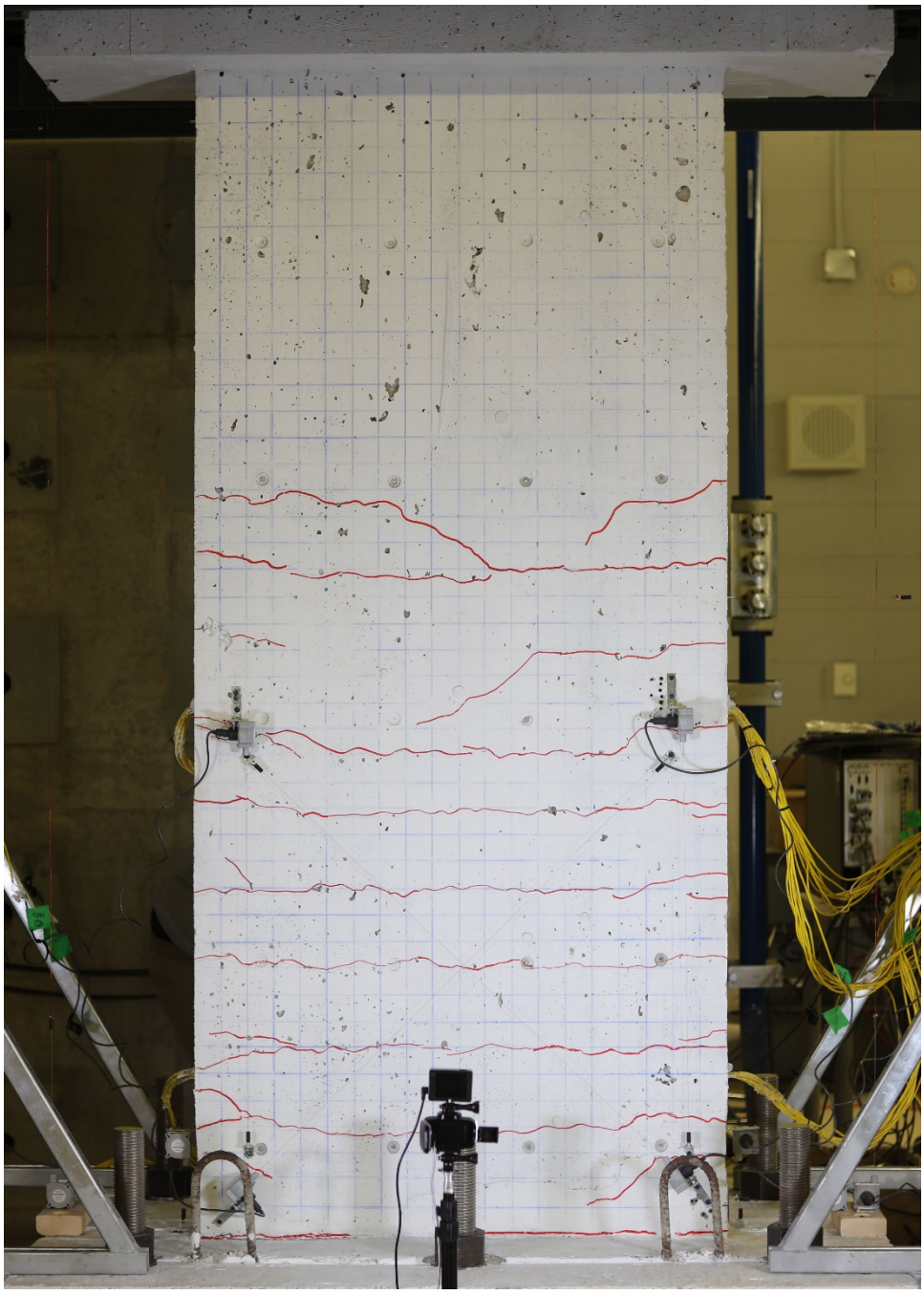

9.6mm Displacement – 0.4% Drift
Final Cycle – Unloaded

Figure I.5. Crack pattern at 9.6mm displacement of wall SWS-R.

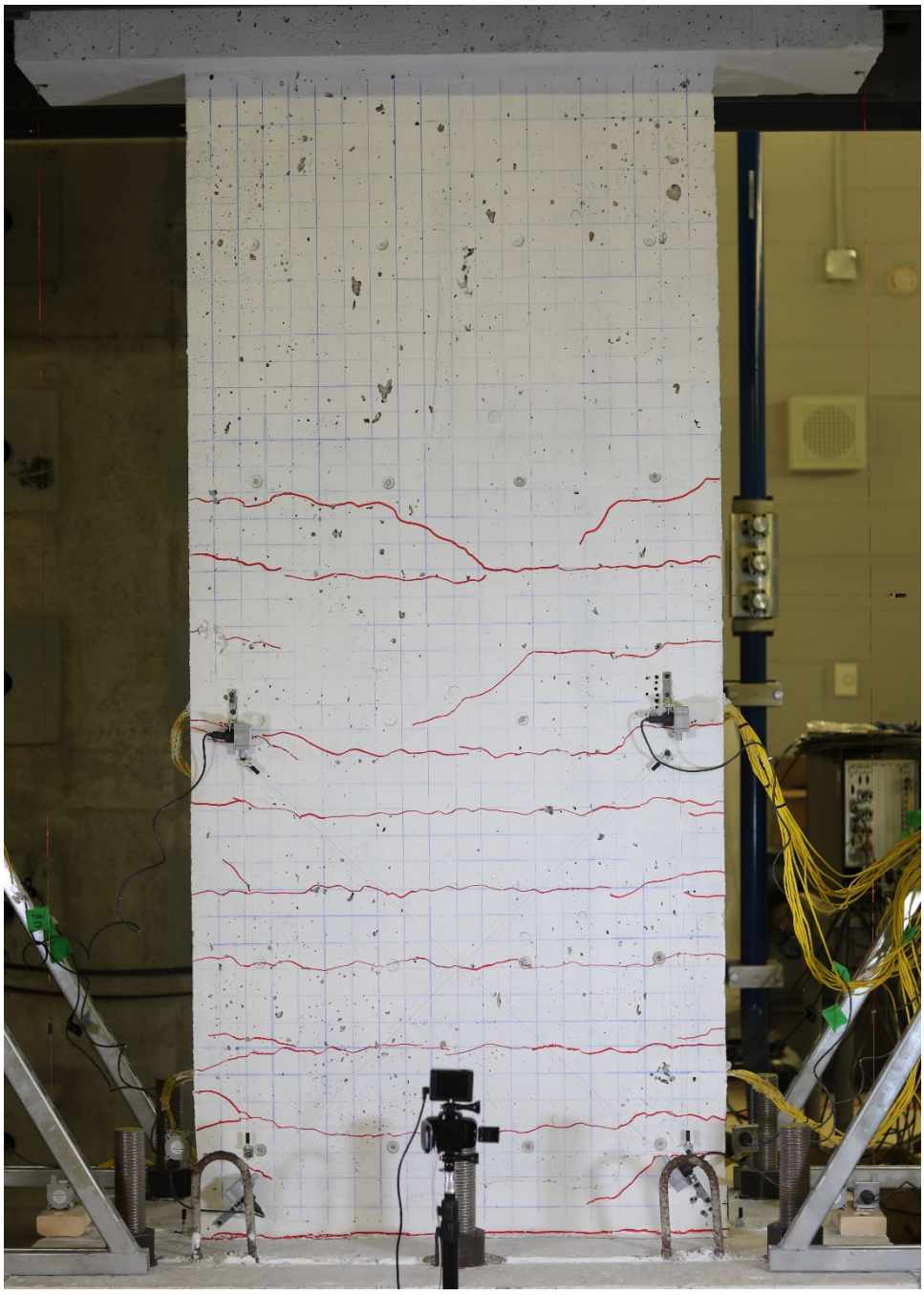

12mm Displacement – 0.5% Drift
Final Cycle – Unloaded

Figure I.6. Crack pattern at 12mm displacement of wall SWS-R.

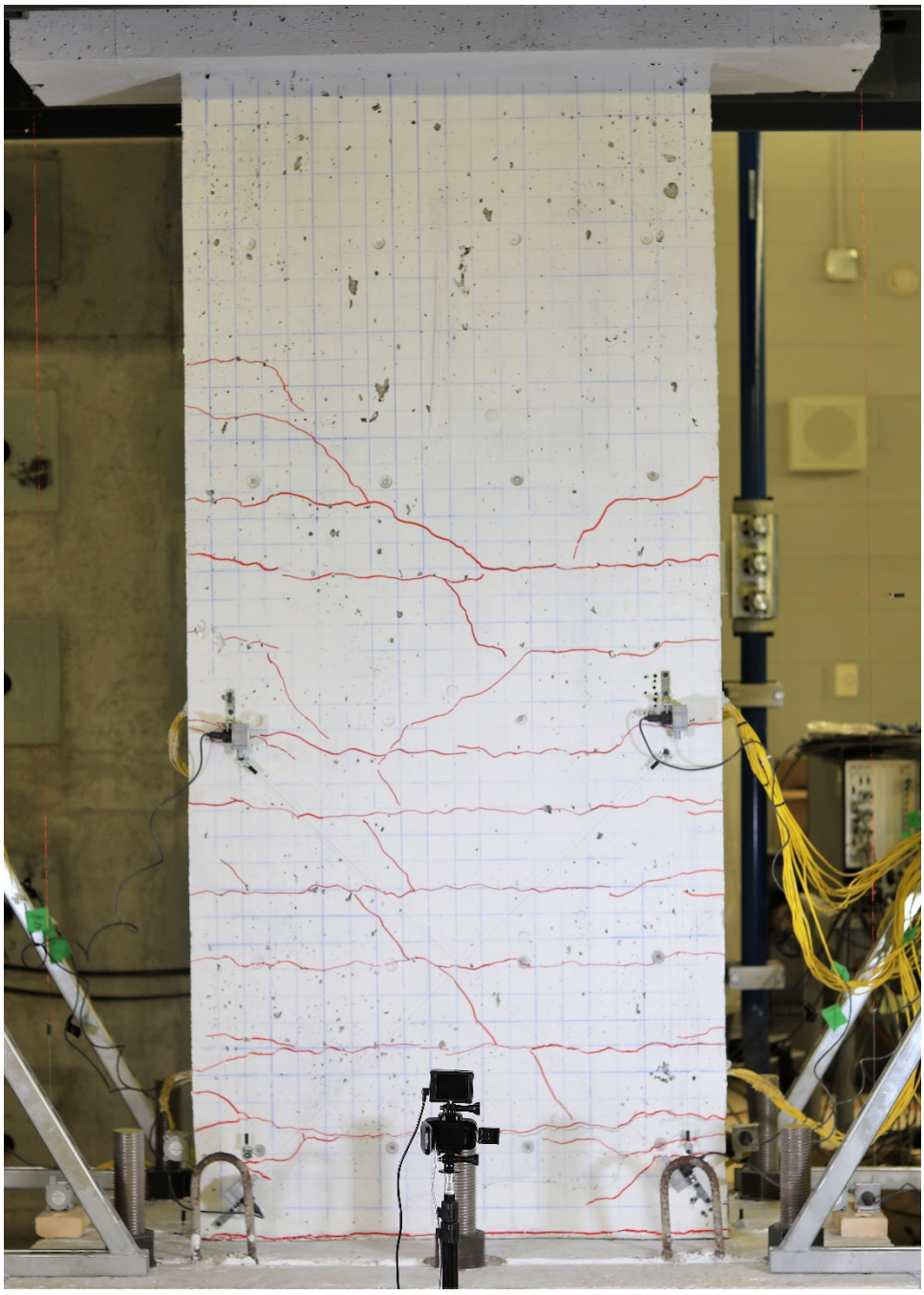

24mm Displacement – 1% Drift
Final Cycle – Unloaded

Figure I.7. Crack pattern at 24mm displacement of wall SWS-R.

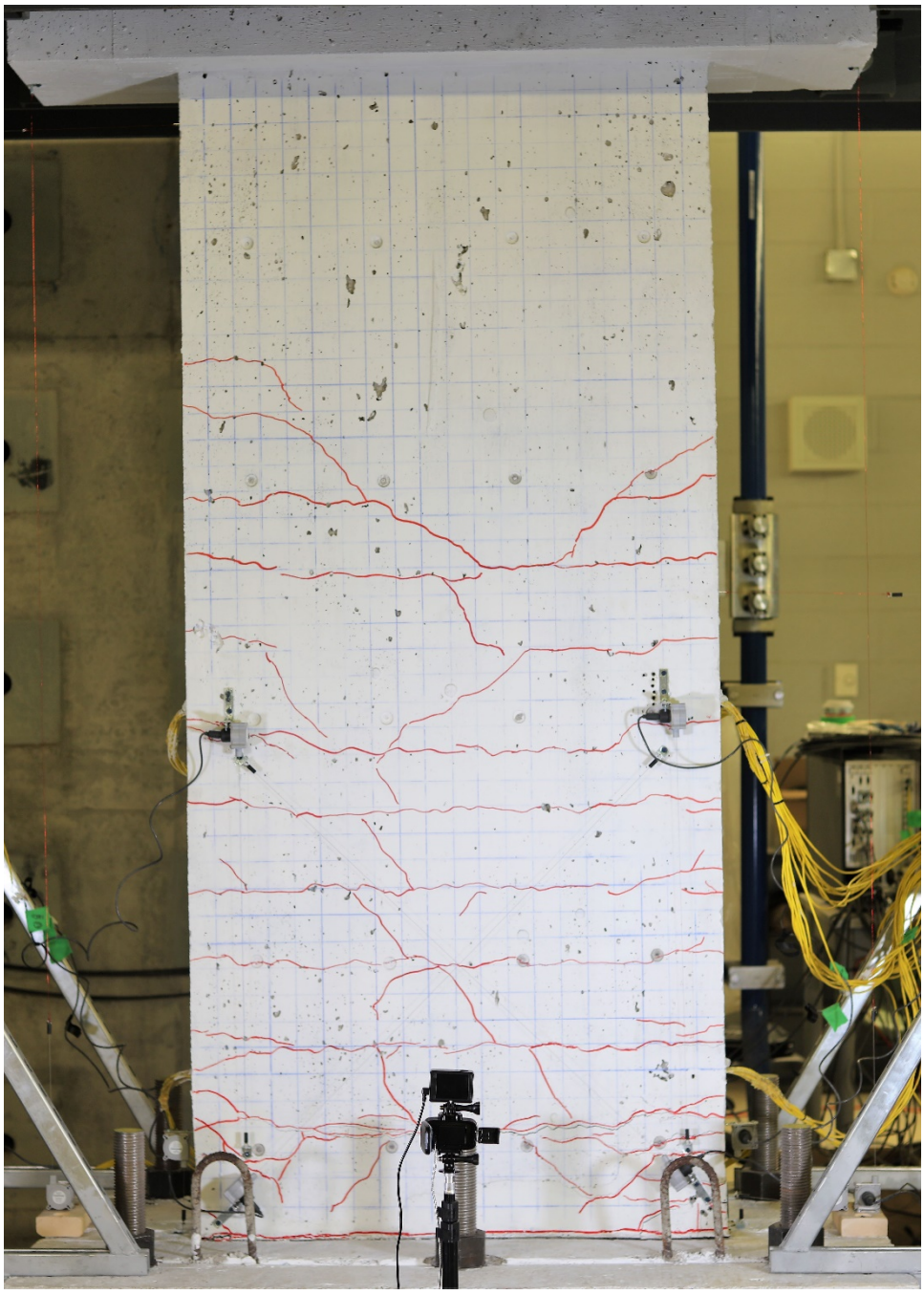

36mm Displacement – 1.5% Drift
Final Cycle – Unloaded

Figure I.8. Crack pattern at 36mm displacement of wall SWS-R.

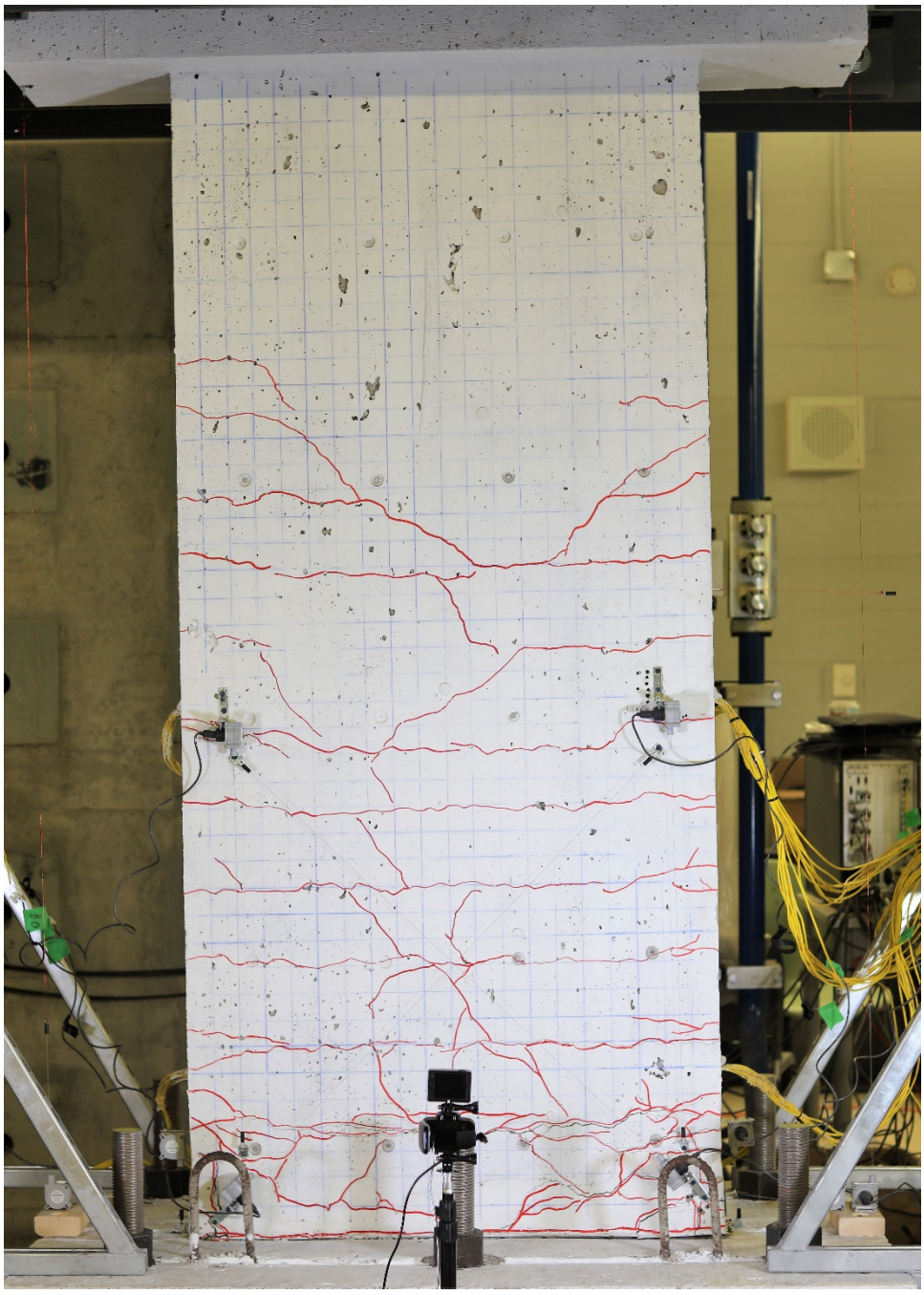

48mm Displacement – 2% Drift
Final Cycle – Unloaded

Figure I.9. Crack pattern at 48mm displacement of wall SWS-R.

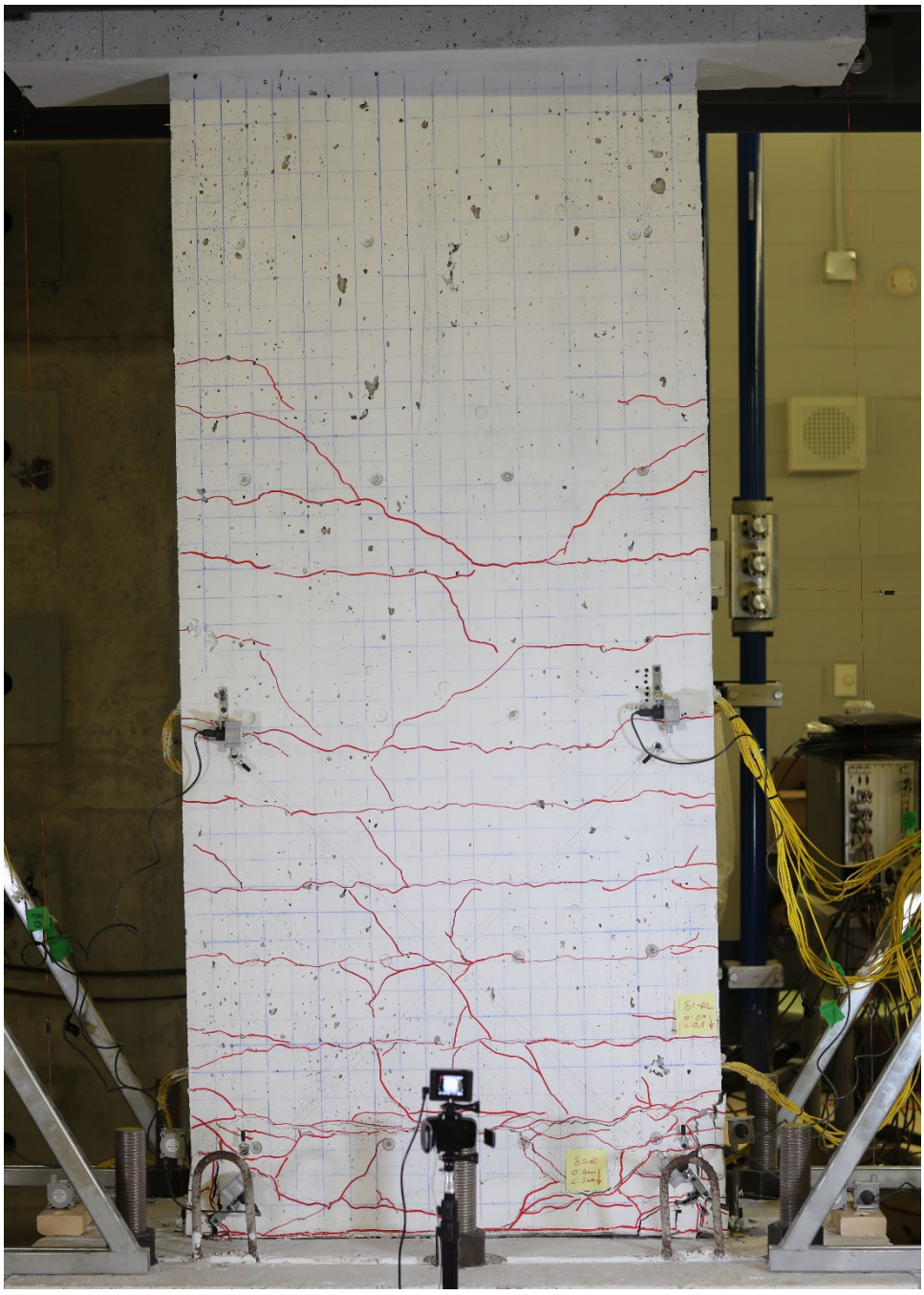

60mm Displacement – 2.5% Drift
Final Cycle – Unloaded

Figure I.10. Crack pattern at 60mm displacement of wall SWS-R.

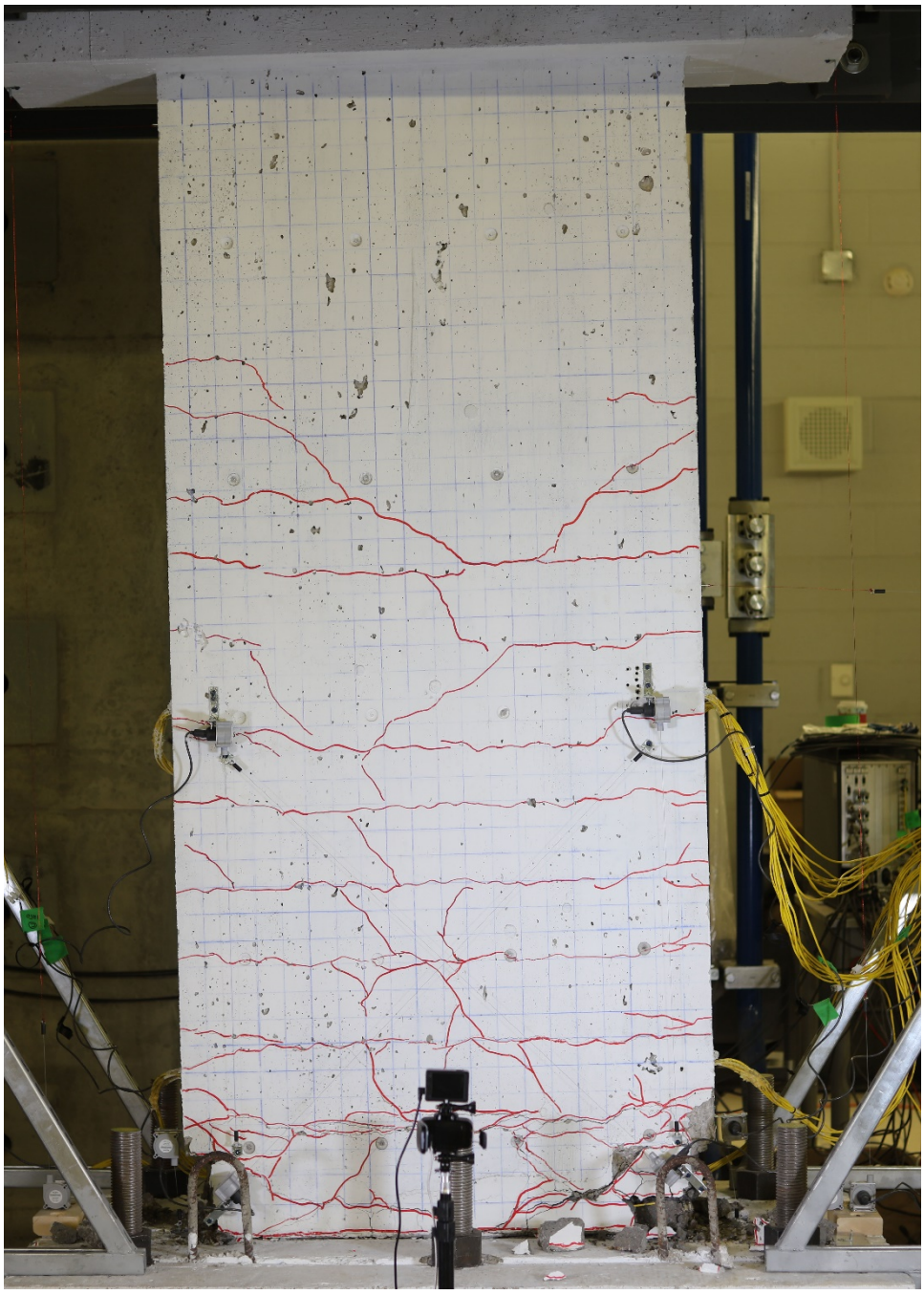

72mm Displacement – 3% Drift
Final Cycle – Unloaded

Figure I.11. Crack pattern at 72mm displacement of wall SWS-R.

Wall SWN Crack Patterns

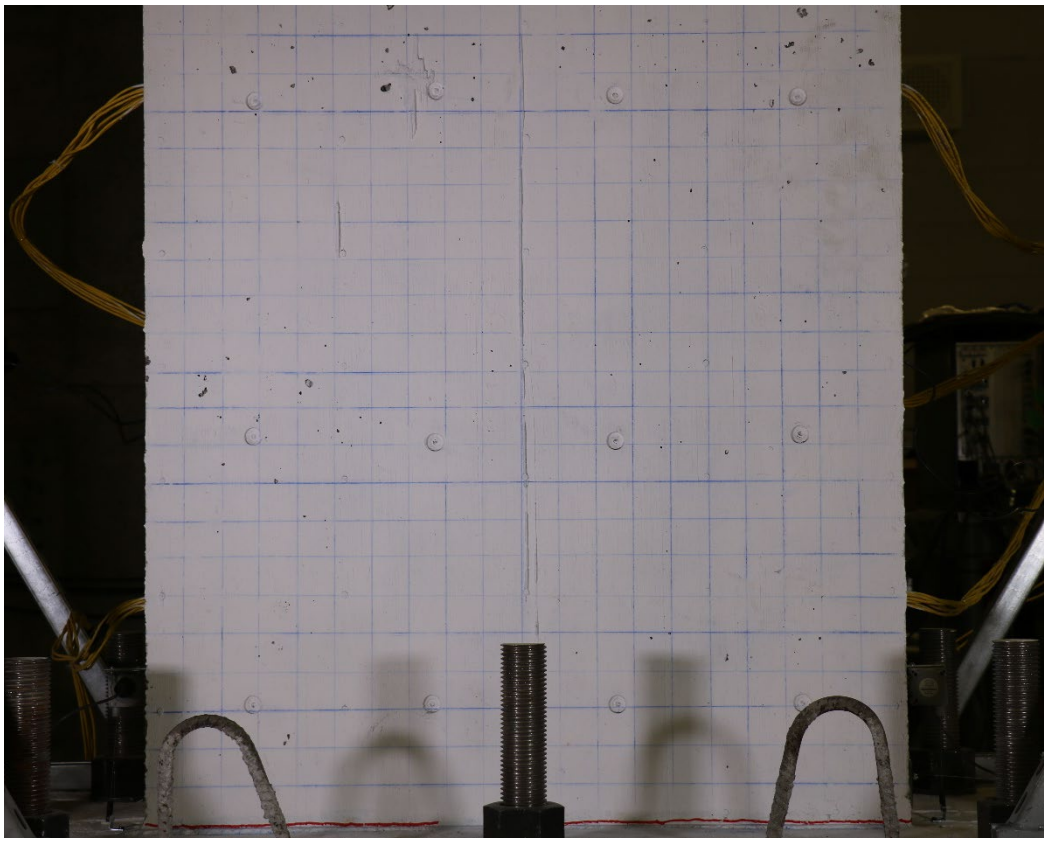

1.2mm Displacement – 0.05% Drift
Final Cycle – Unloaded

Figure I.12. Crack pattern at 1.2mm displacement of wall SWN.

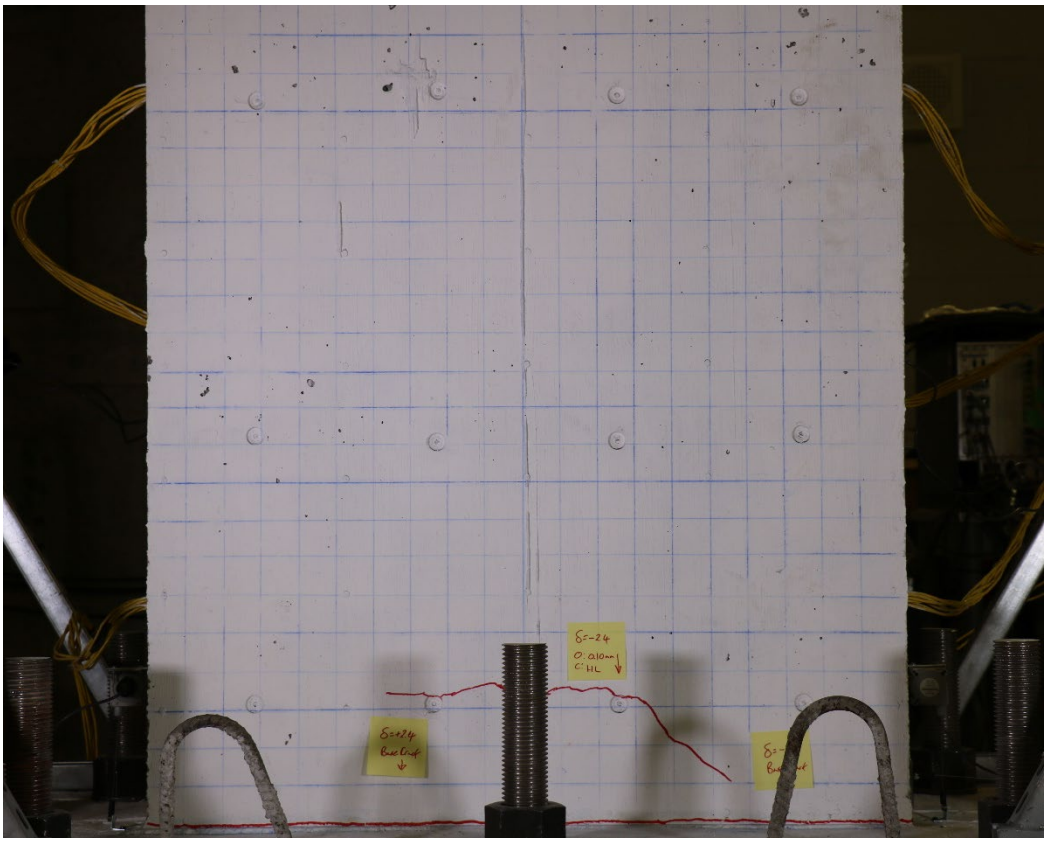

2.4mm Displacement – 0.1% Drift
Final Cycle – Unloaded

Figure I.13. Crack pattern at 2.4mm displacement of wall SWN.

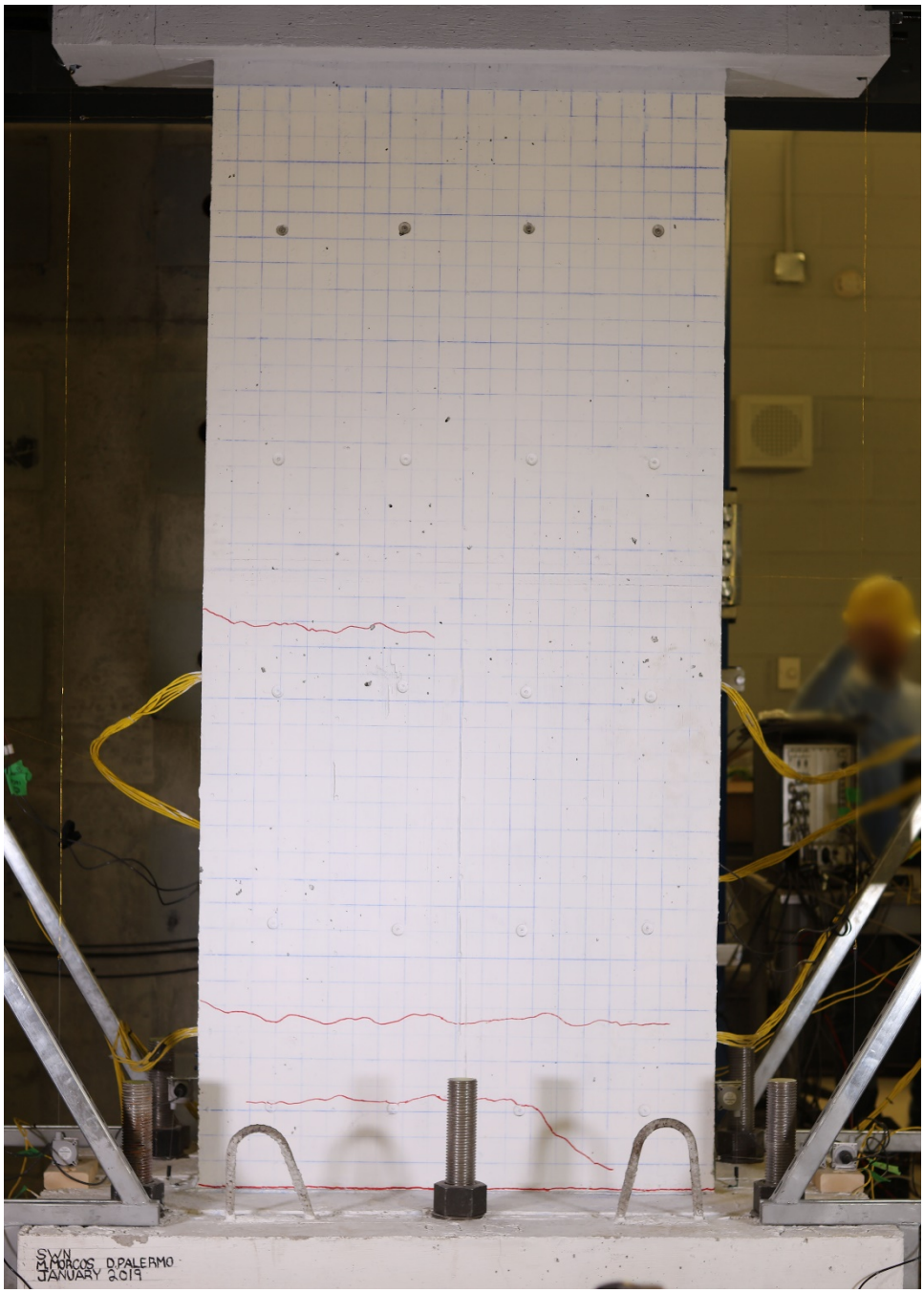

4.8mm Displacement – 0.2% Drift
Final Cycle – Unloaded

Figure I.14. Crack pattern at 4.8mm displacement of wall SWN.

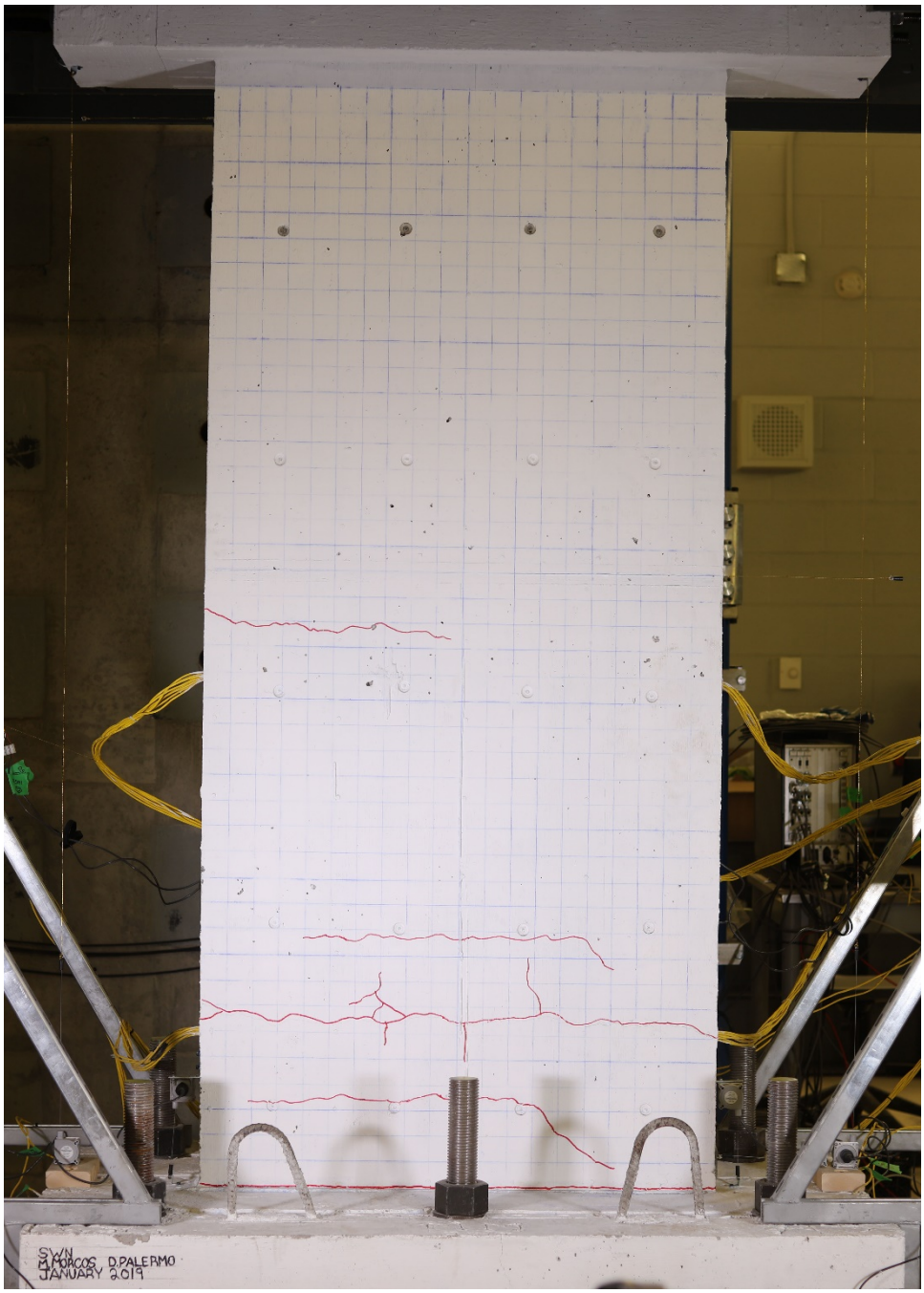

7.2mm Displacement – 0.3% Drift
Final Cycle – Unloaded

Figure I.15. Crack pattern at 7.2mm displacement of wall SWN.

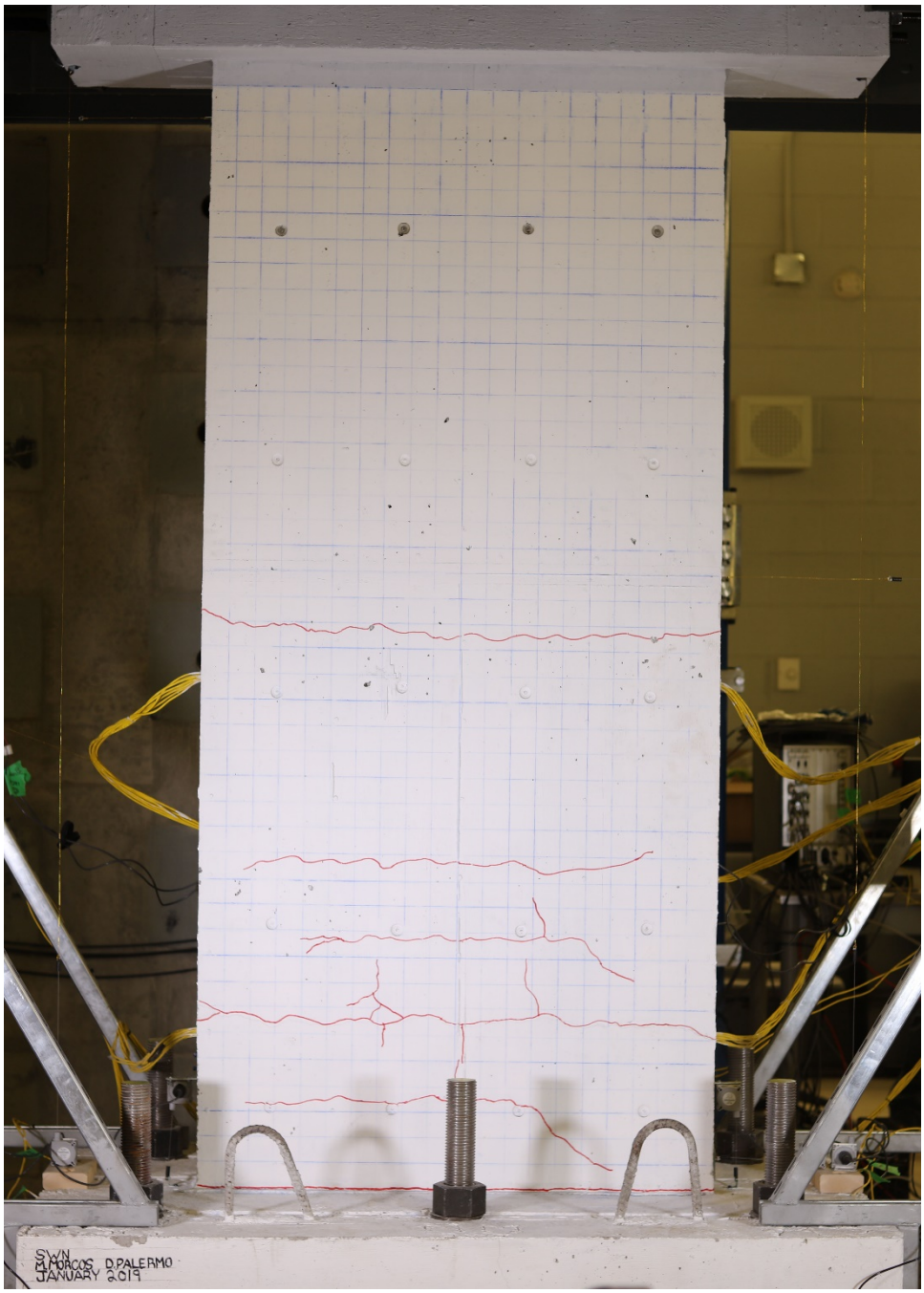

9.6mm Displacement – 0.4% Drift
Final Cycle – Unloaded

Figure I.16. Crack pattern at 9.6mm displacement of wall SWN.

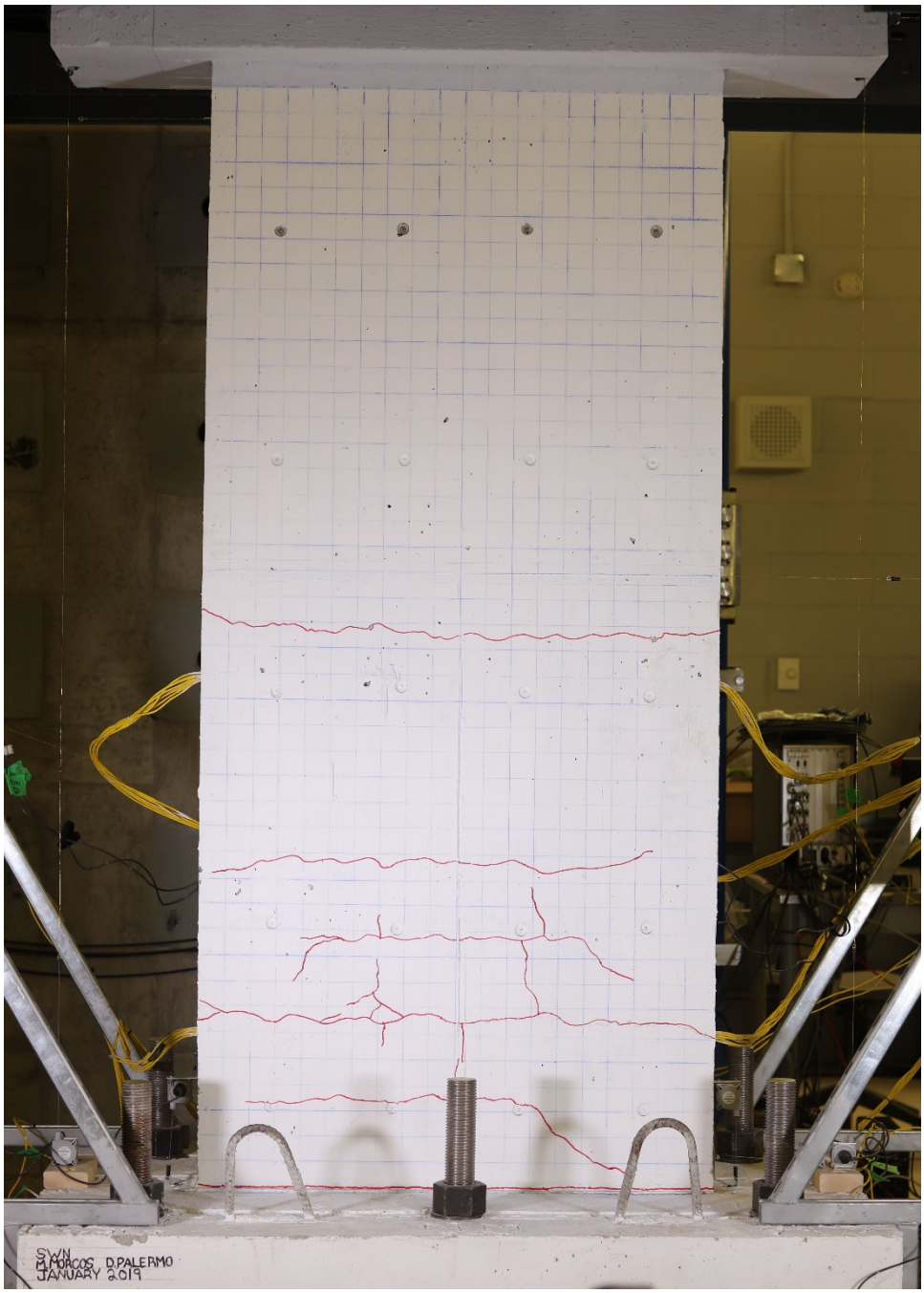

12mm Displacement – 0.5% Drift
Final Cycle – Unloaded

Figure I.17. Crack pattern at 12mm displacement of wall SWN.

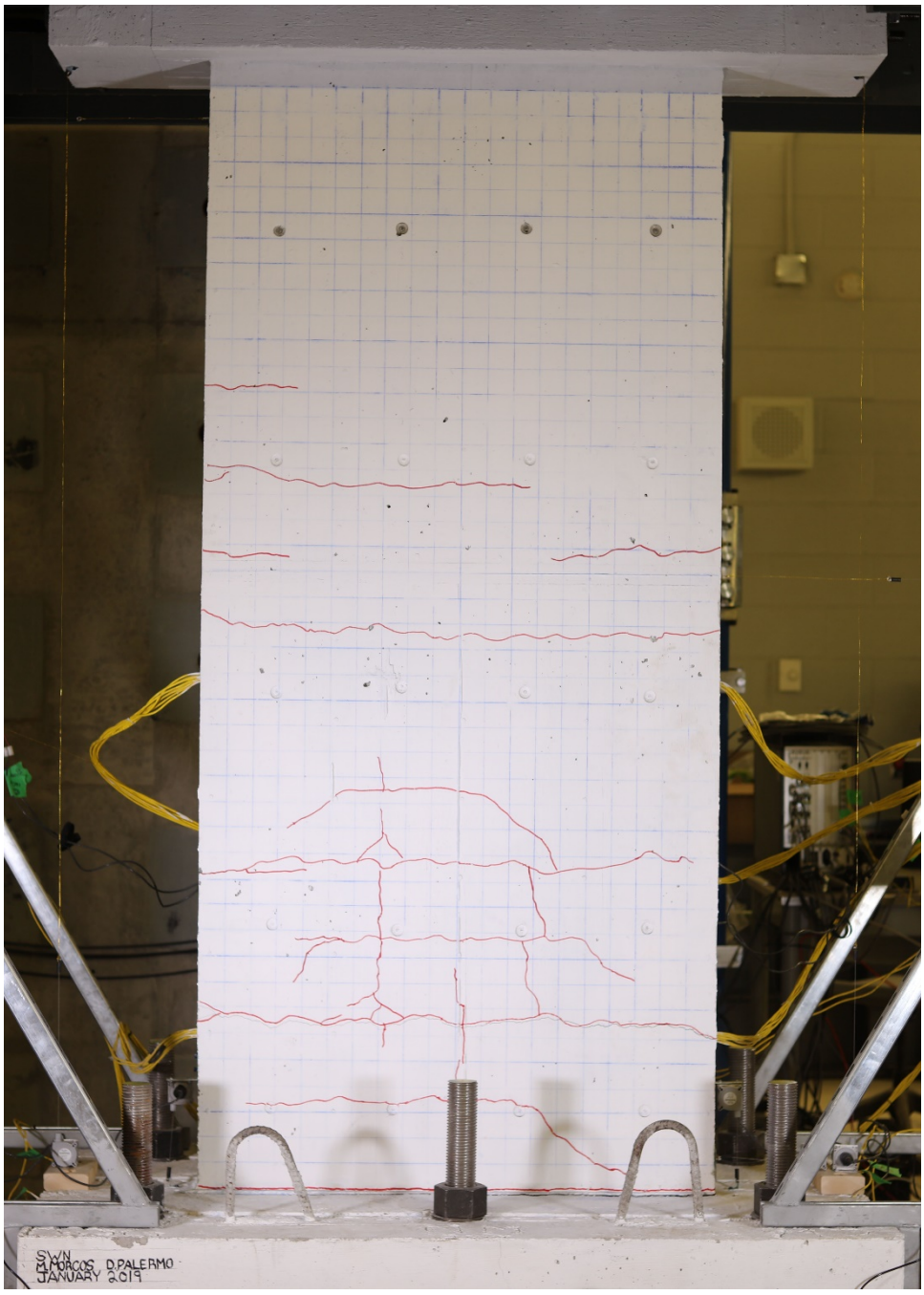

24mm Displacement – 1% Drift
Final Cycle – Unloaded

Figure I.18. Crack pattern at 24mm displacement of wall SWN.

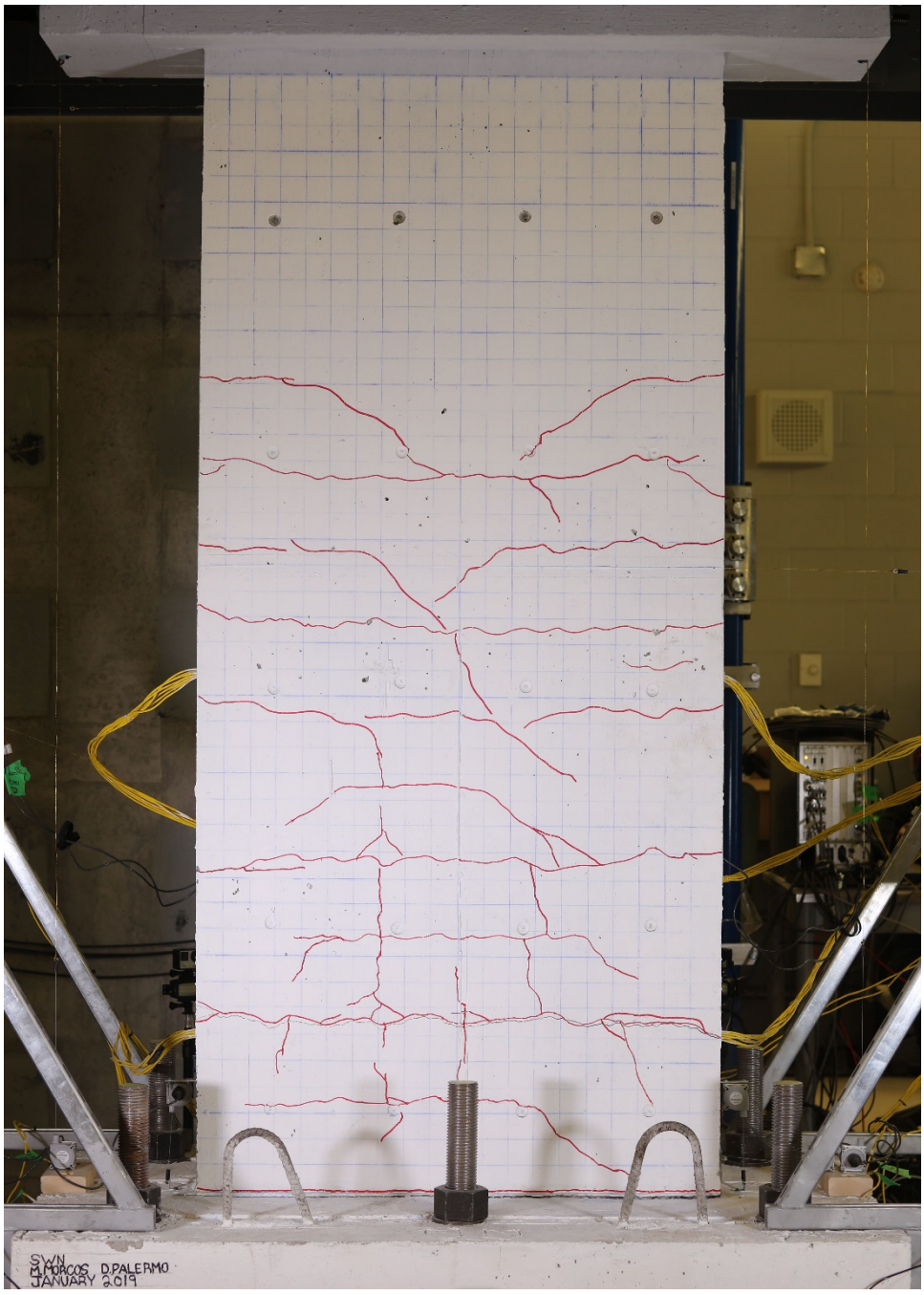

36mm Displacement – 1.5% Drift
Final Cycle – Unloaded

Figure I.19. Crack pattern at 36mm displacement of wall SWN.

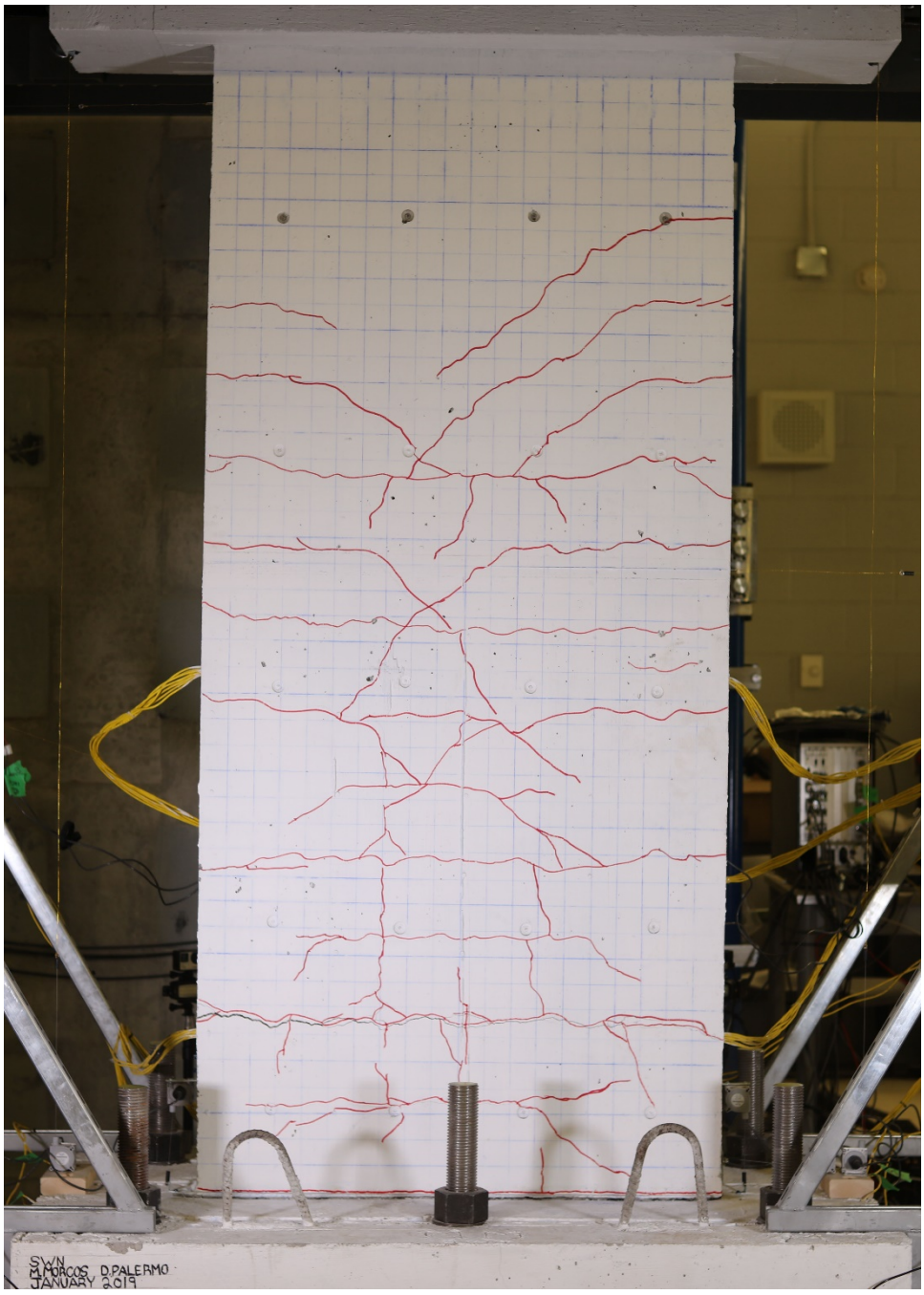

48mm Displacement – 2% Drift
Final Cycle – Unloaded

Figure I.20. Crack pattern at 48mm displacement of wall SWN.

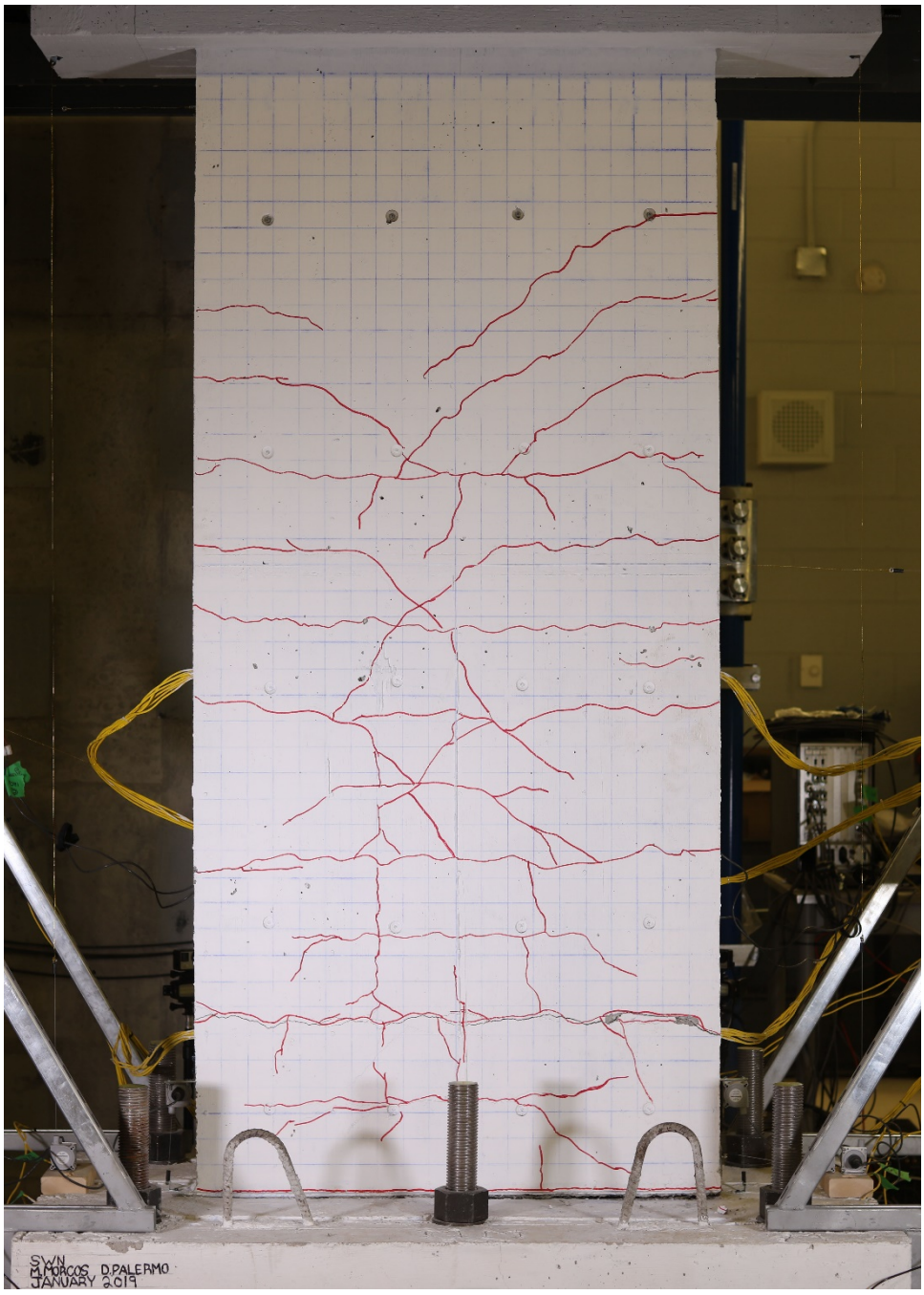

60mm Displacement – 2.5% Drift
Final Cycle – Unloaded

Figure I.21. Crack pattern at 60mm displacement of wall SWN.

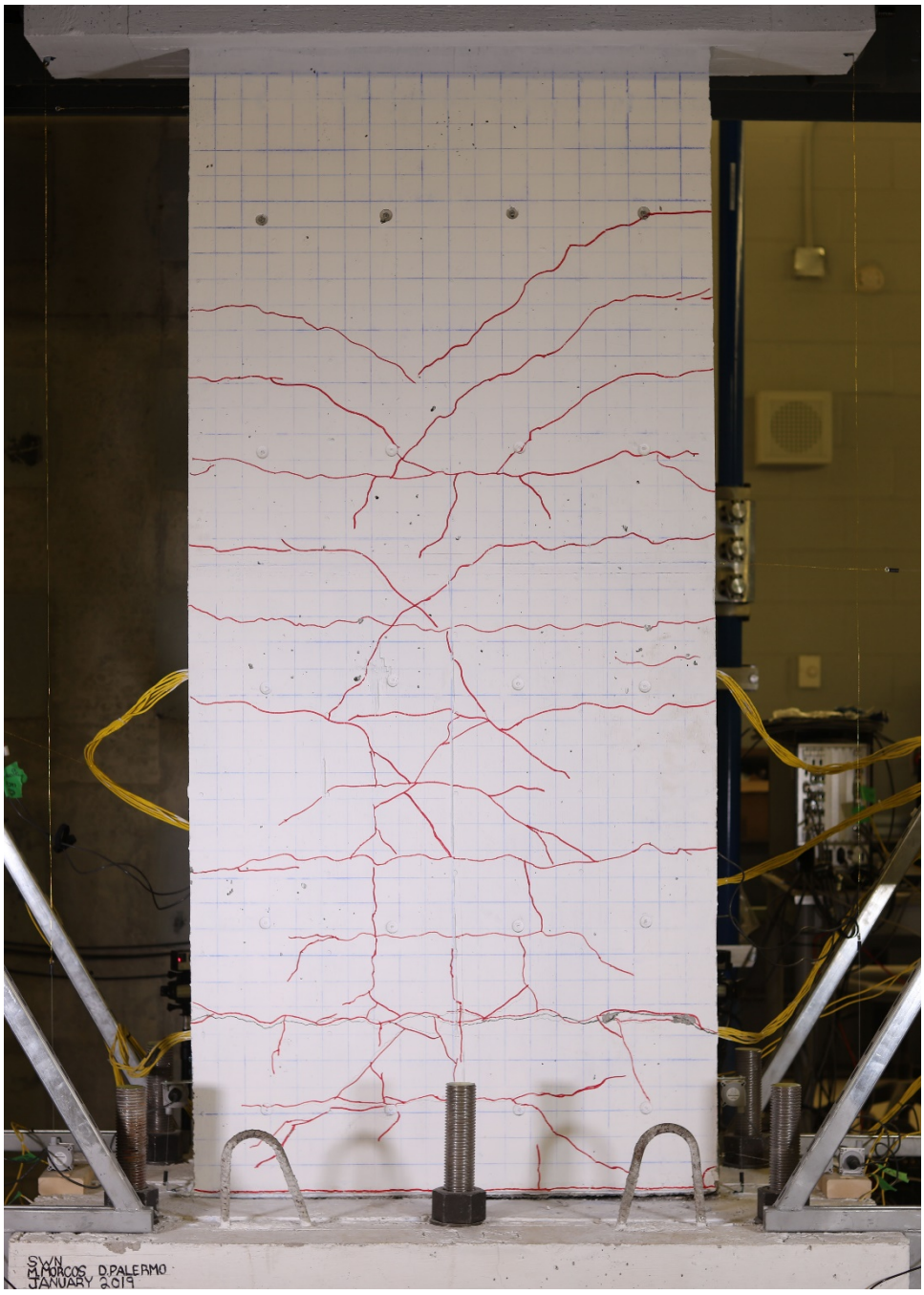

72mm Displacement – 3% Drift
Final Cycle – Unloaded

Figure I.22. Crack pattern at 72mm displacement of wall SWN.

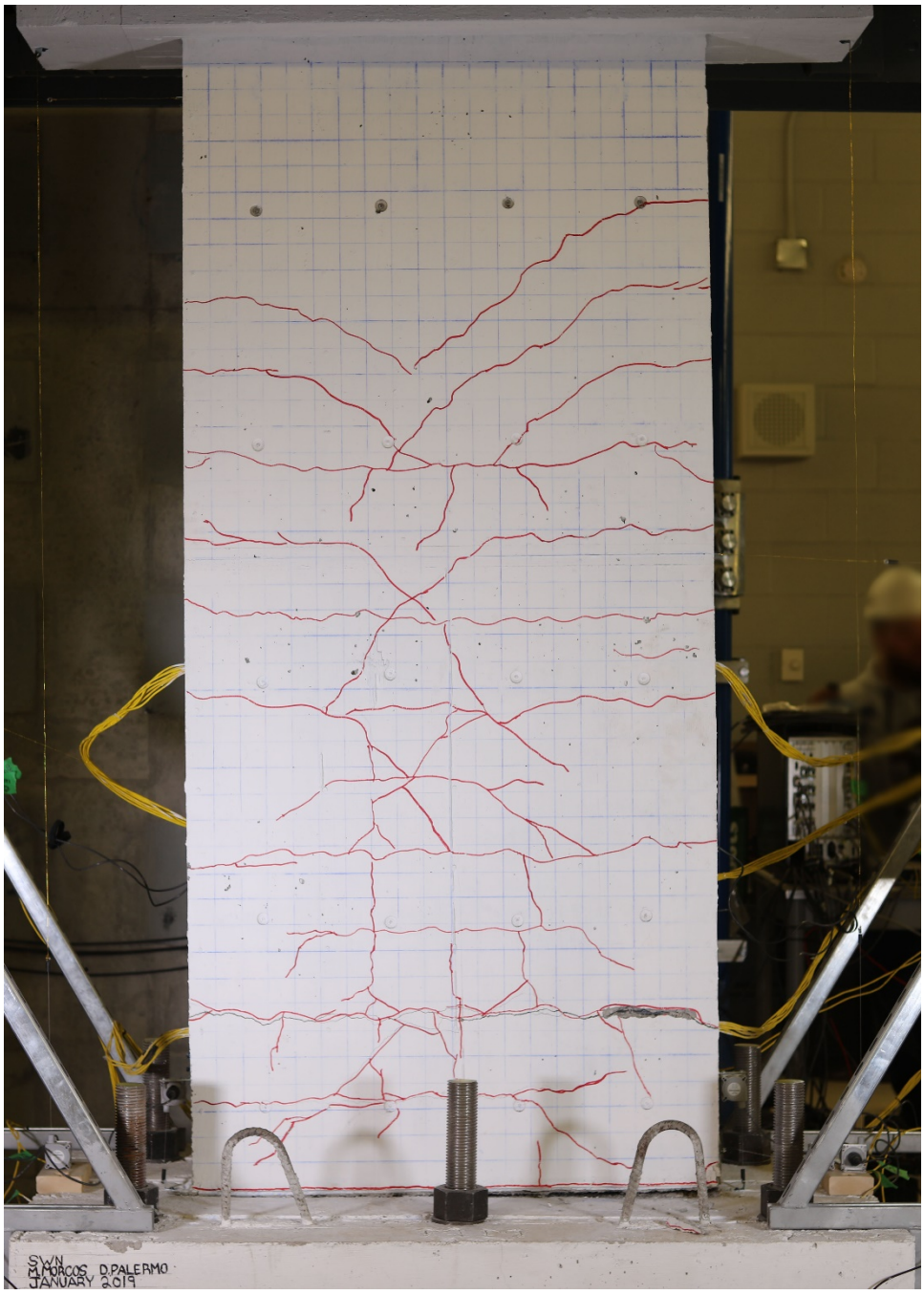

84mm Displacement – 3.5% Drift
Final Cycle – Unloaded

Figure I.23. Crack pattern at 84mm displacement of wall SWN.

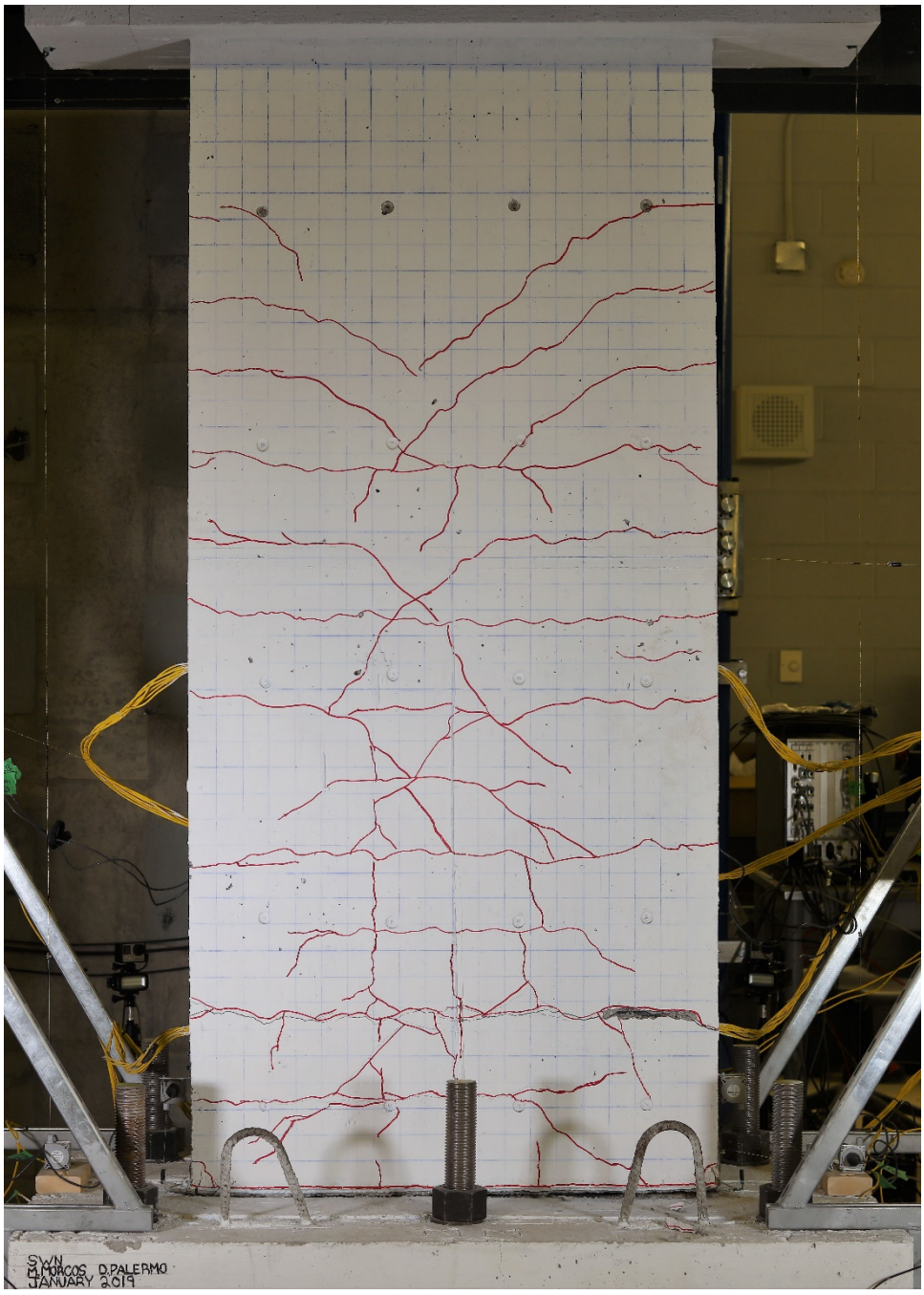

96mm Displacement – 4% Drift
Final Cycle – Unloaded

Figure I.24. Crack pattern at 96mm displacement of wall SWN.

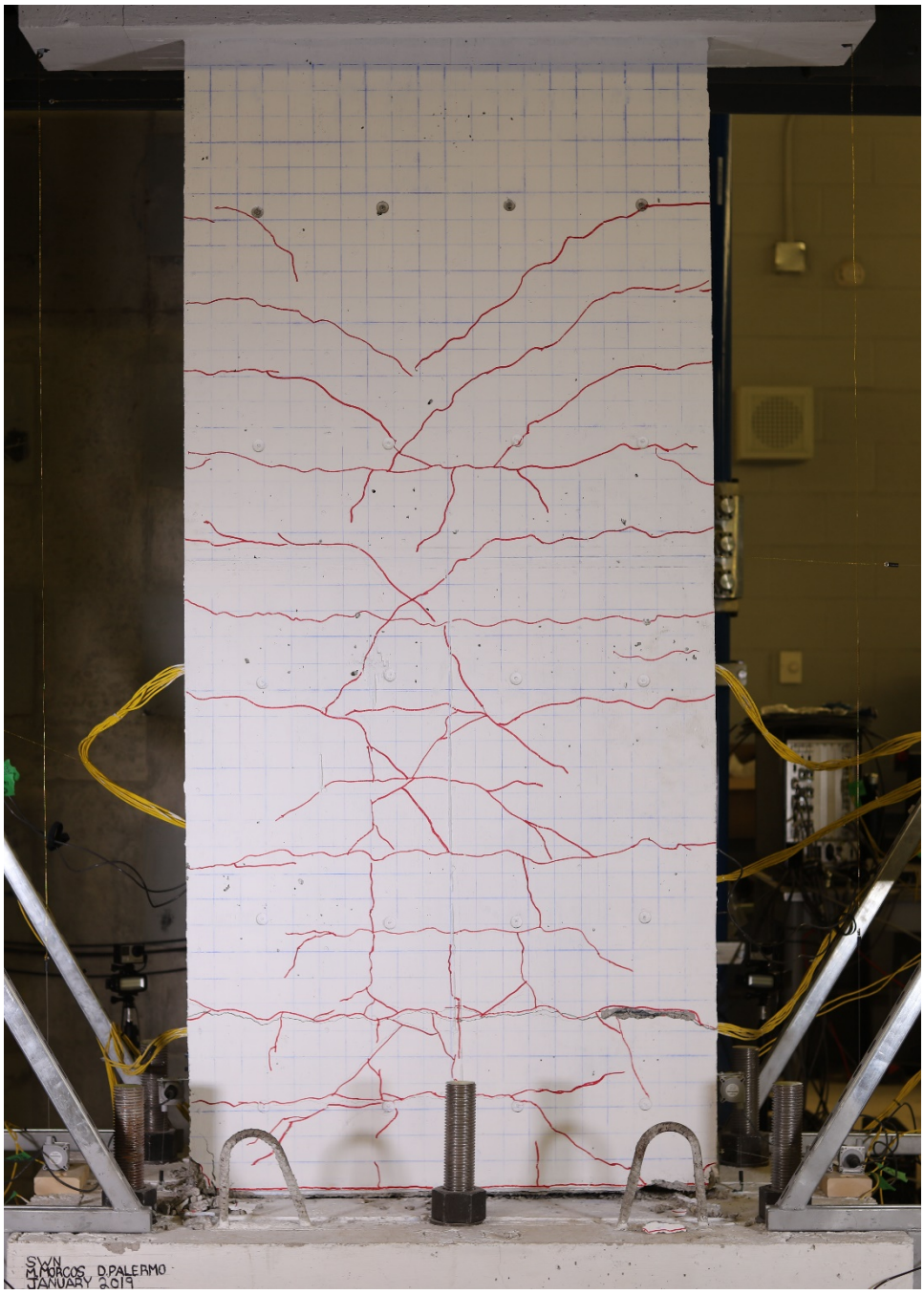

108mm Displacement – 4.5% Drift
Final Cycle – Unloaded

Figure I.25. Crack pattern at 108mm displacement of wall SWN.

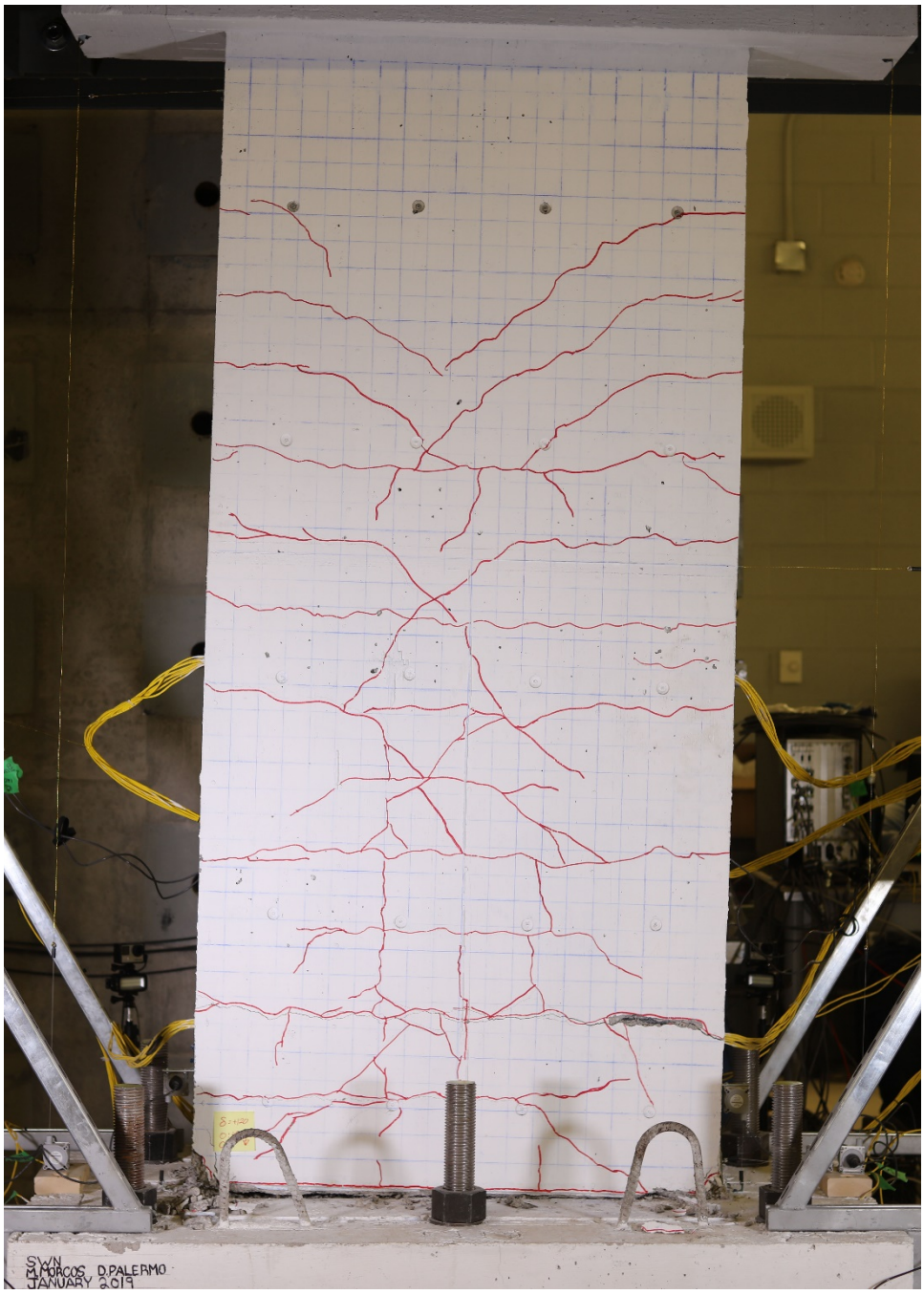

120mm Displacement – 5% Drift
Final Cycle – Unloaded

Figure I.26. Crack pattern at 120mm displacement of wall SWN.

APPENDIX J

Supplementary Performance Data

Wall SWS-R

Supplementary performance results for positive and negative loading of wall SWS-R.

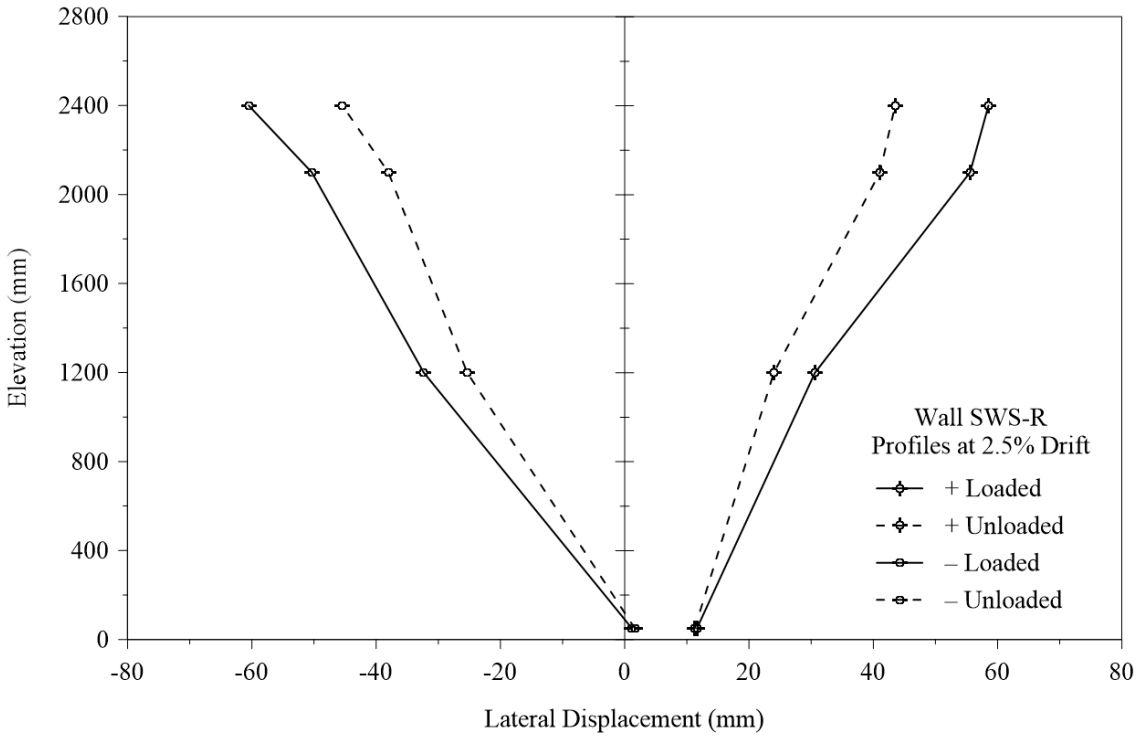

Figure J.1. Loaded and unloaded lateral displacement profiles at 2.5% drift of wall SWS-R.

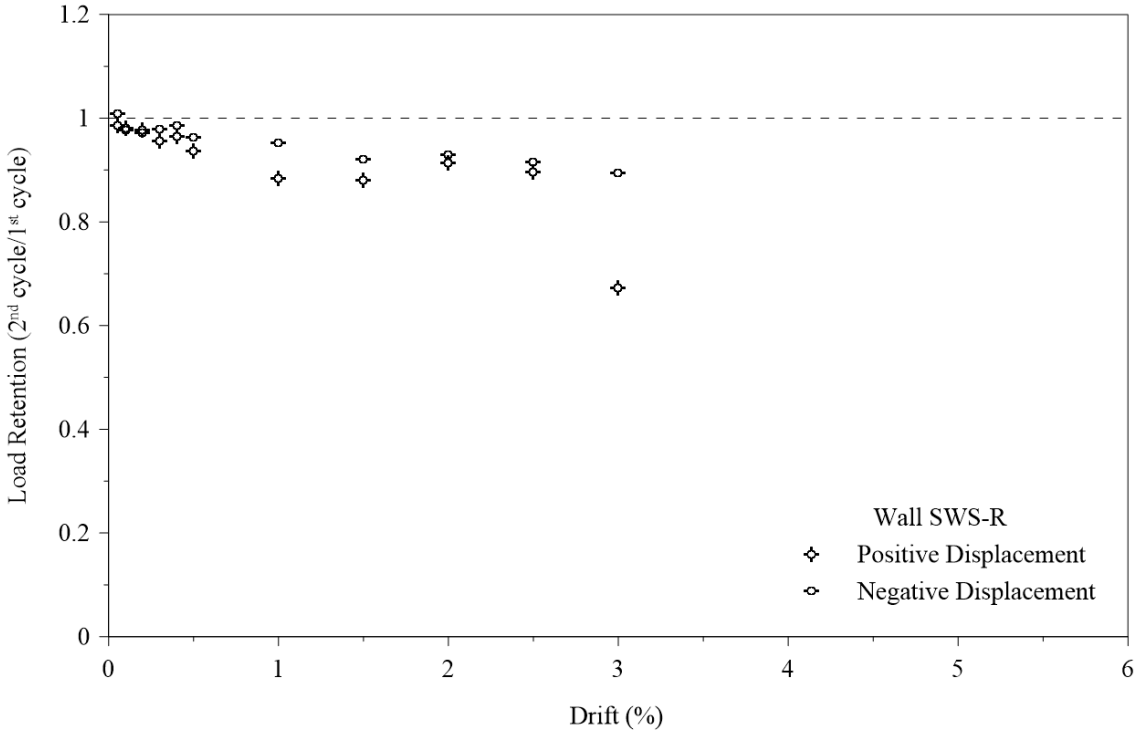

Figure J.2. Load retention of wall SWS-R.

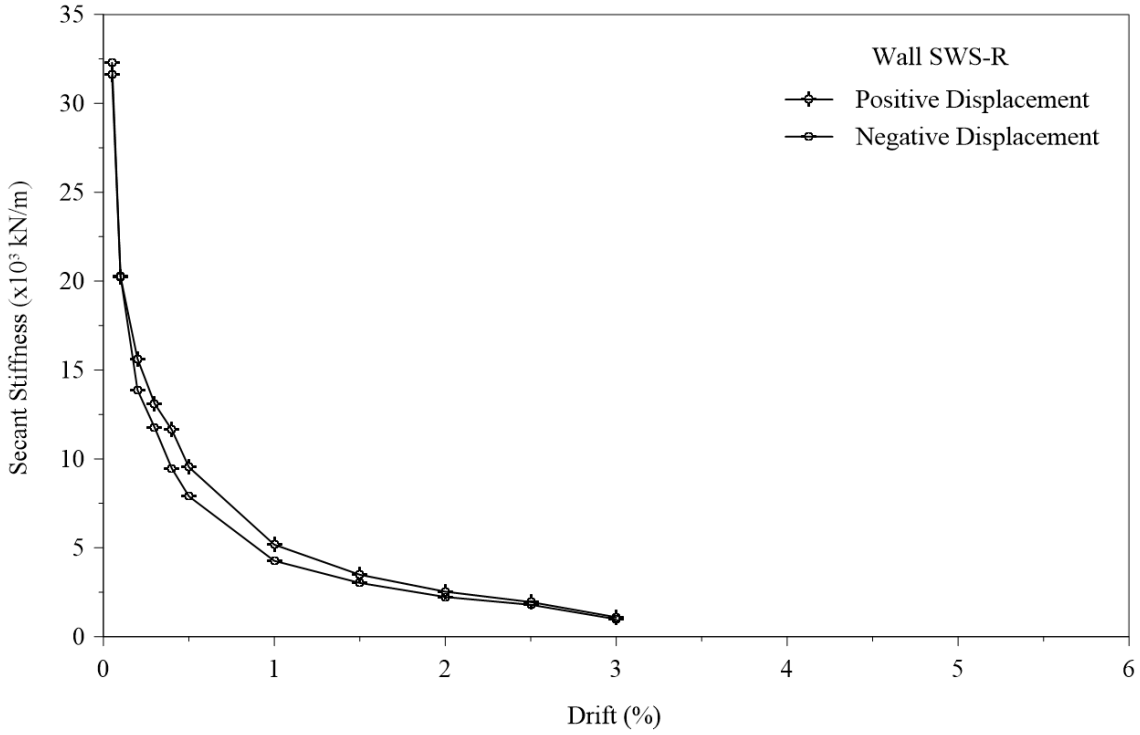

Figure J.3. Stiffness degradation of wall SWS-R.

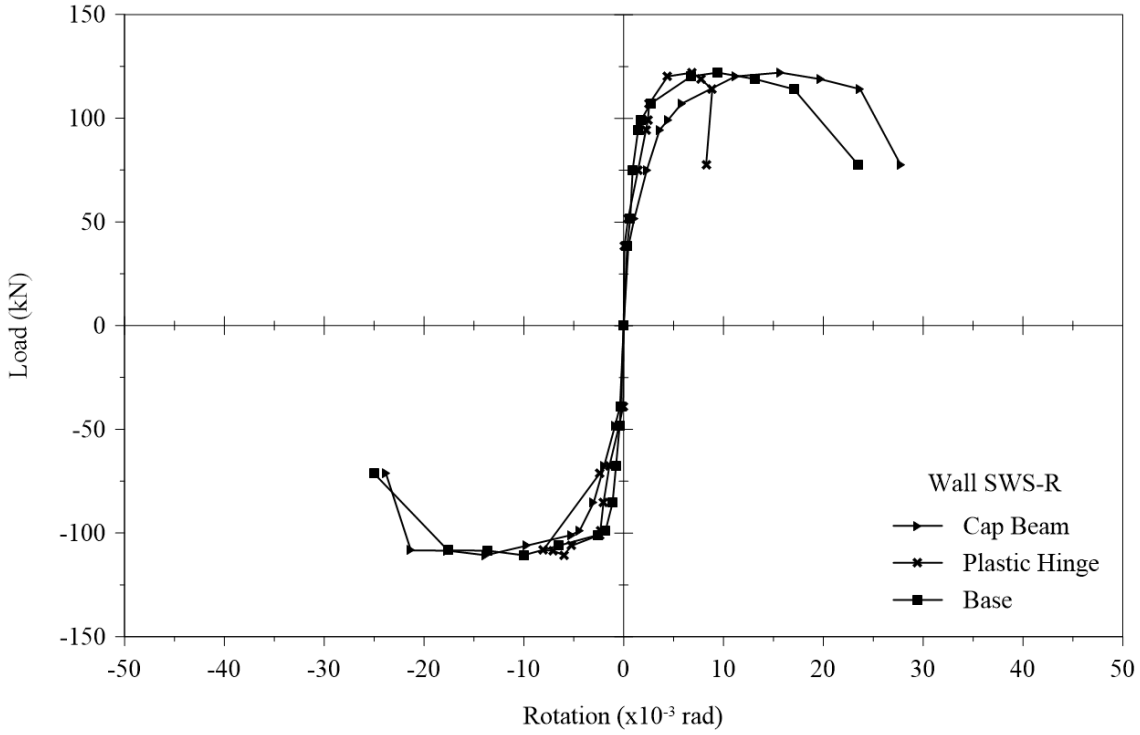

Figure J.4. Load-rotation envelope of wall SWS-R.

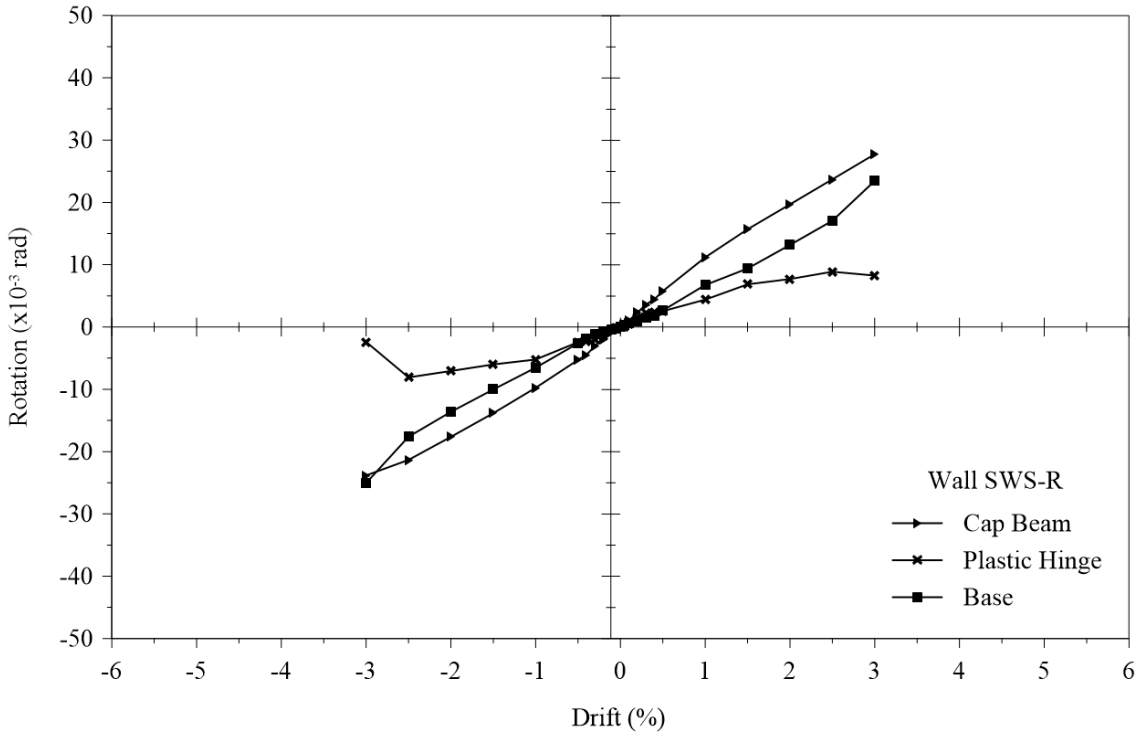

Figure J.5. Rotation-drift relationship of wall SWS-R.

Wall SWN

Supplementary performance results for positive and negative loading of wall SWN.

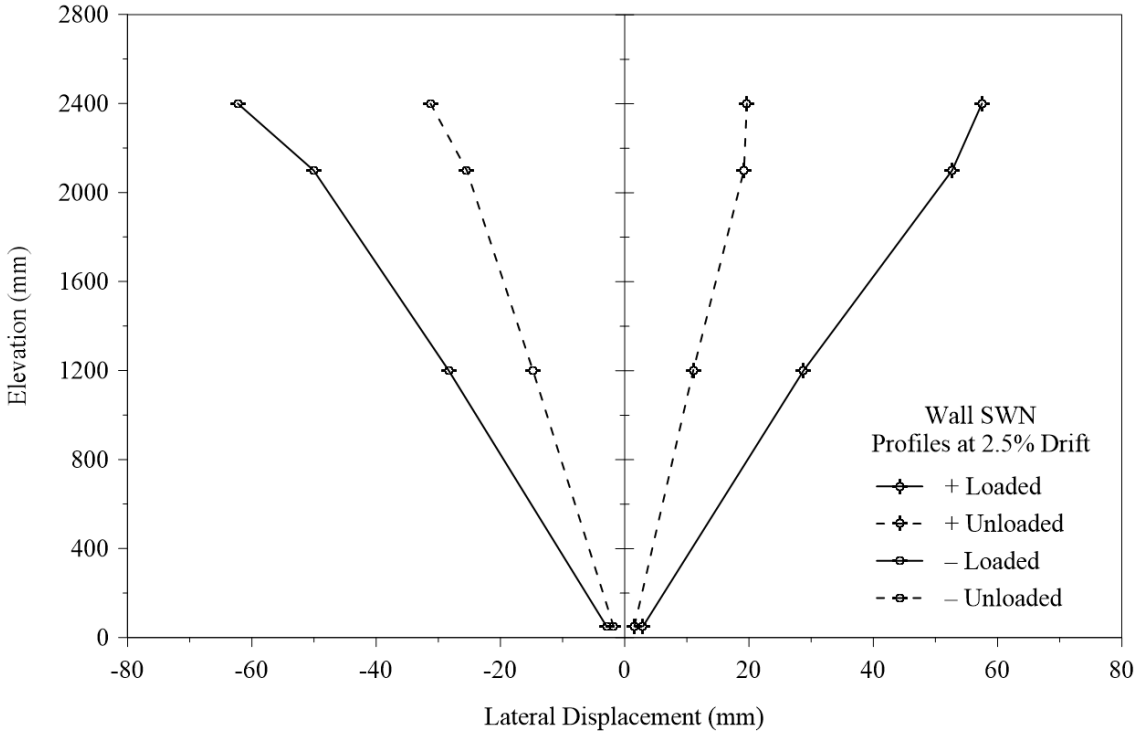

Figure J.6. Loaded and unloaded lateral displacement profiles at 2.5% drift of wall SWN.

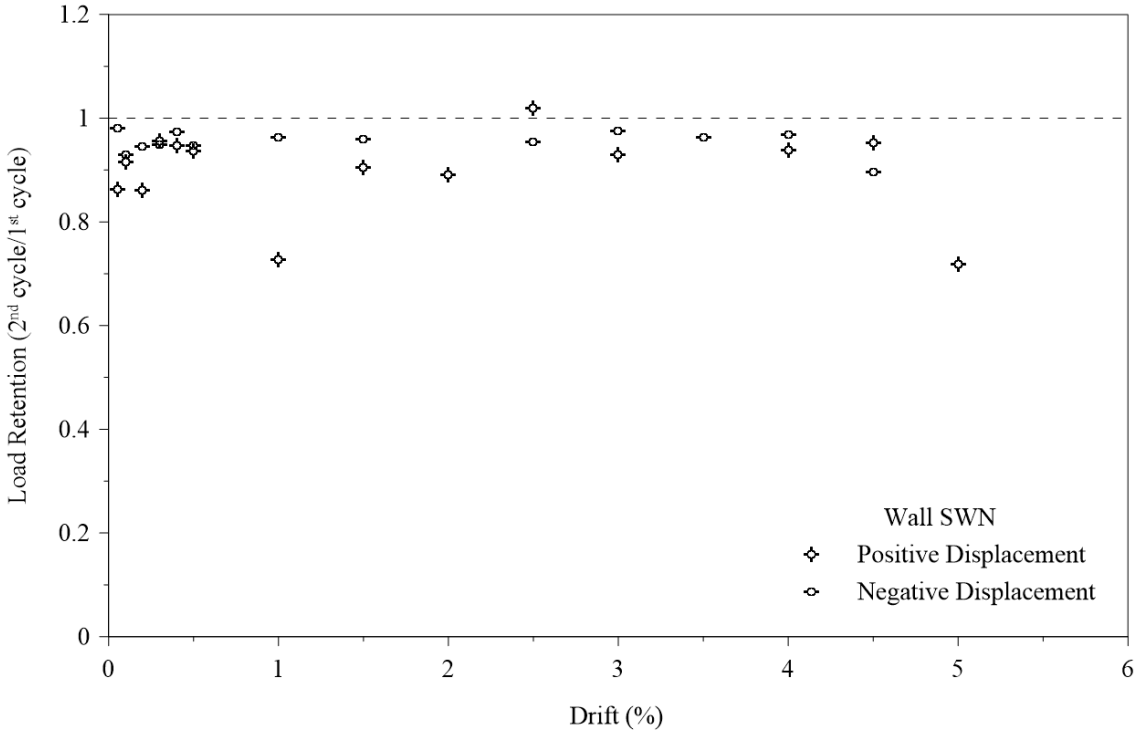

Figure J.7. Load retention of wall SWN.

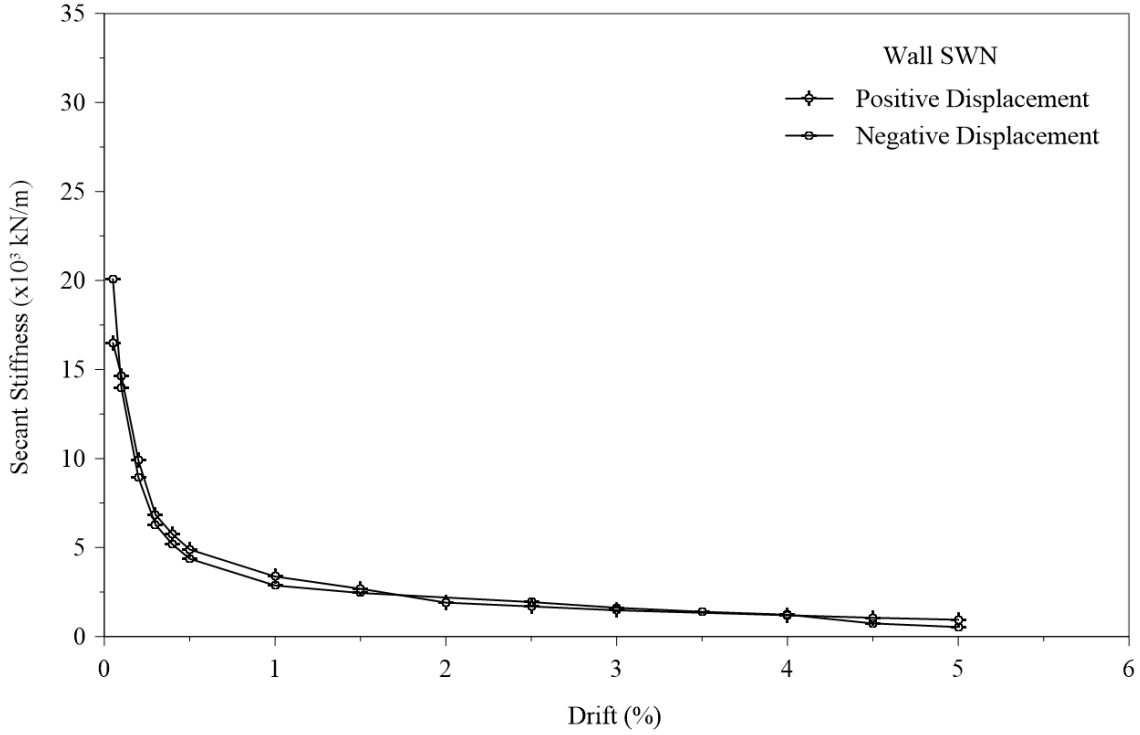

Figure J.8. Stiffness degradation of wall SWN.

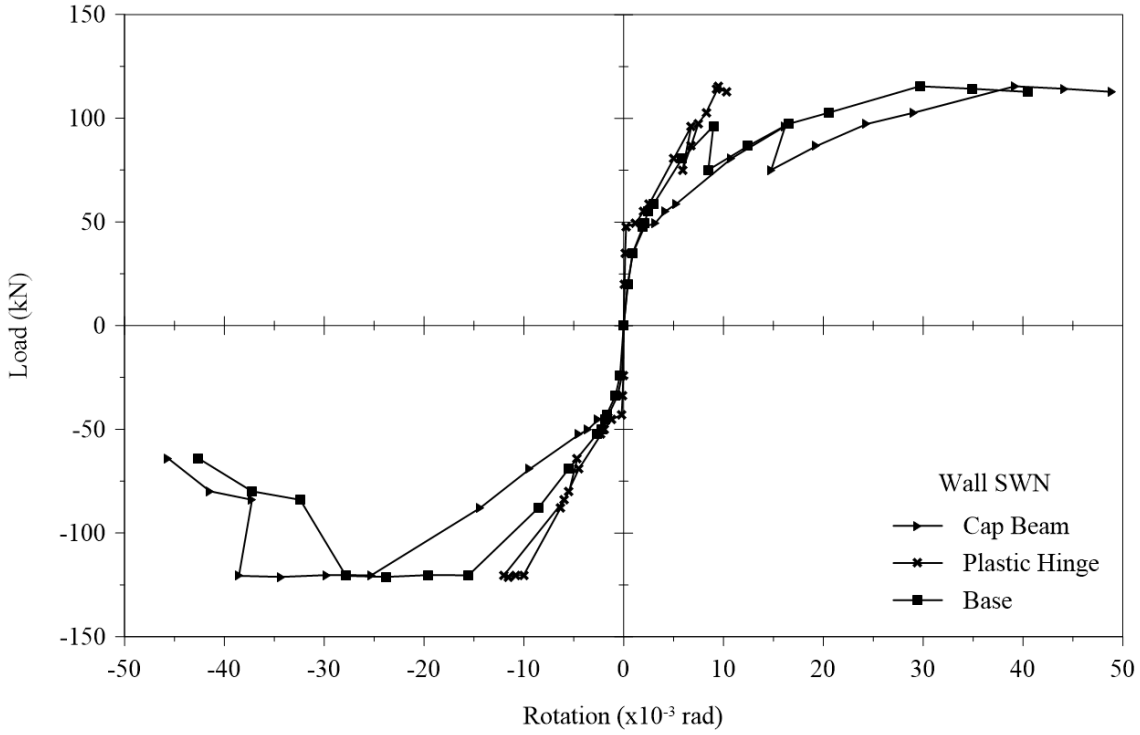

Figure J.9. Load-rotation envelope of wall SWN.

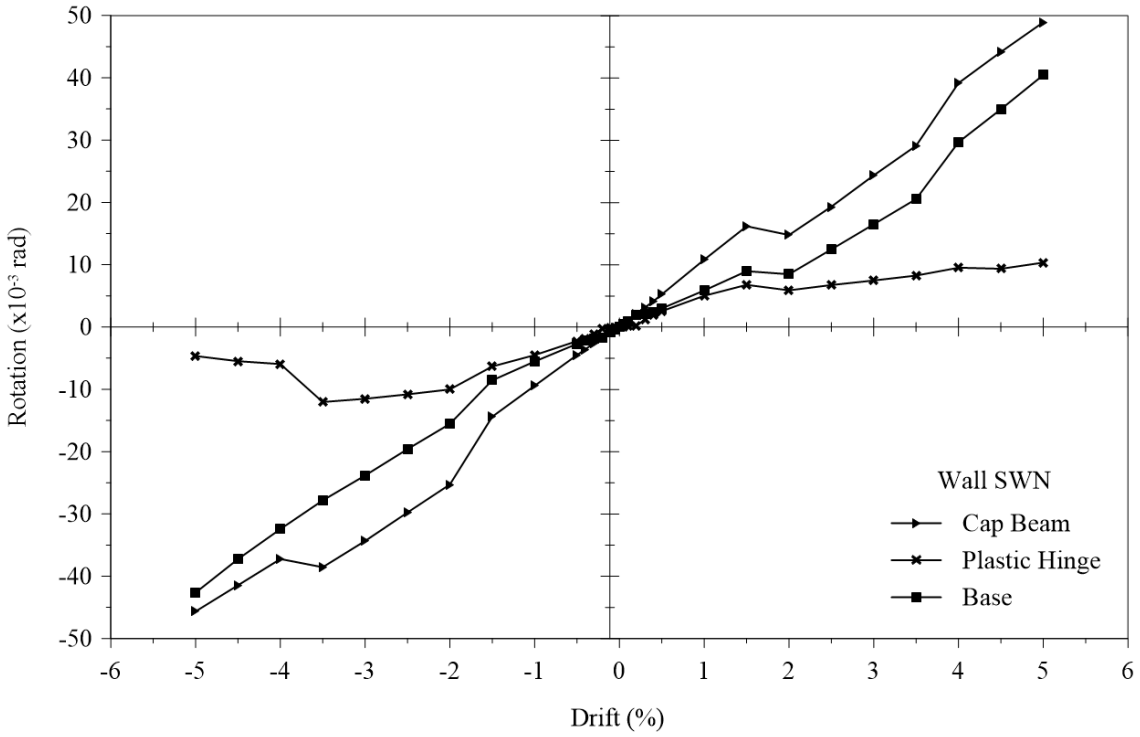

Figure J.10. Rotation-drift relationship of wall SWN.

APPENDIX K

Distribution of Flexure, Shear, and Sliding

Wall SWS-R Distributions – Positive Loading

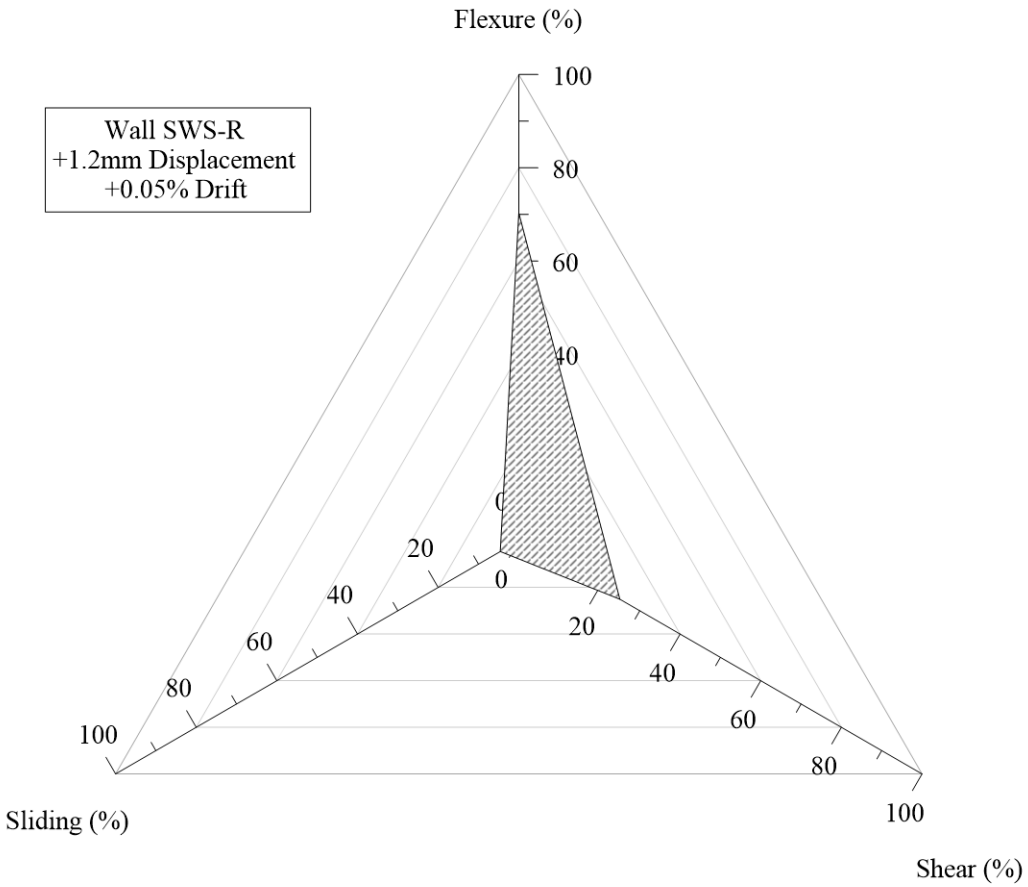

Figure K.1. Distribution of flexure, shear, and sliding of wall SWS-R at positive 1.2mm displacement.

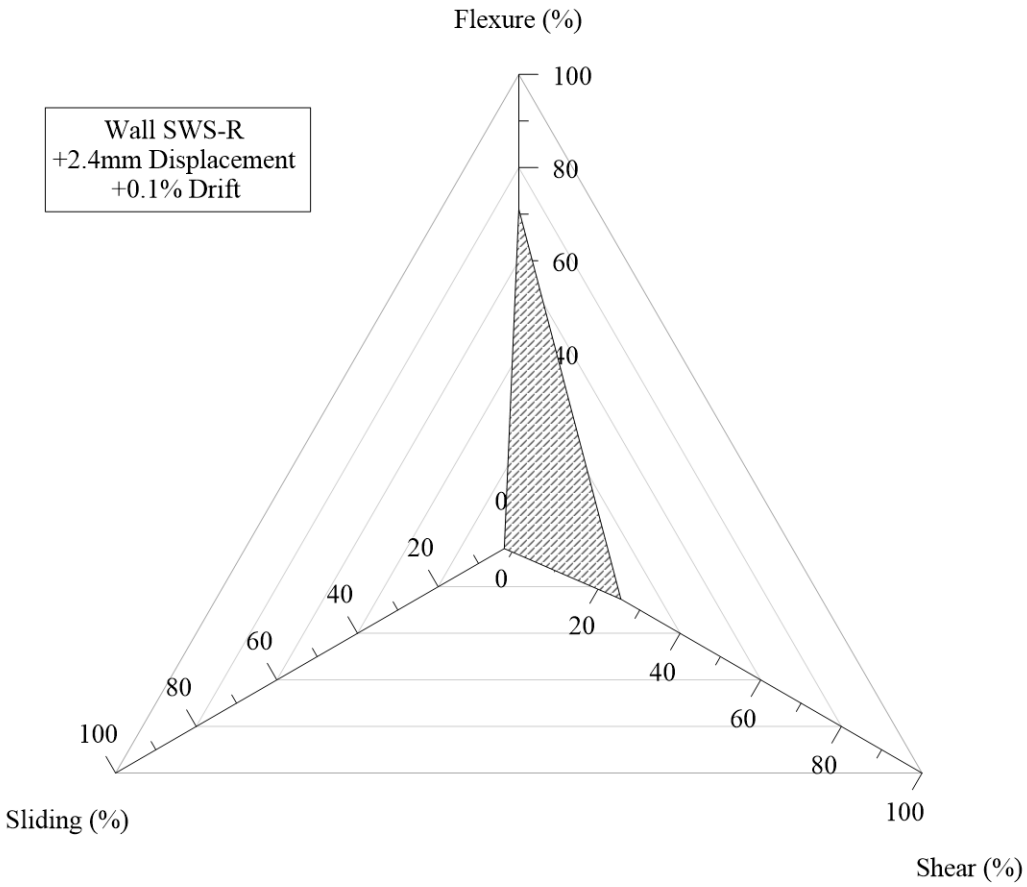

Figure K.2. Distribution of flexure, shear, and sliding of wall SWS-R at positive 2.4mm displacement.

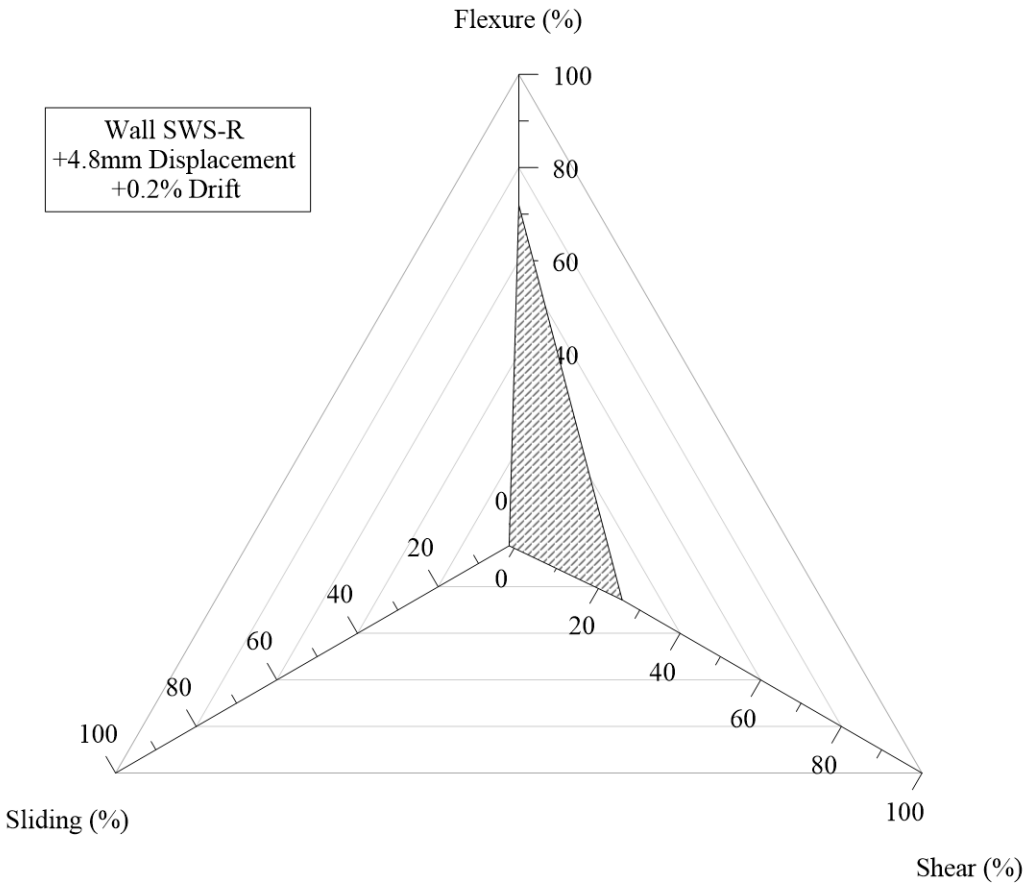

Figure K.3. Distribution of flexure, shear, and sliding of wall SWS-R at positive 4.8mm displacement.

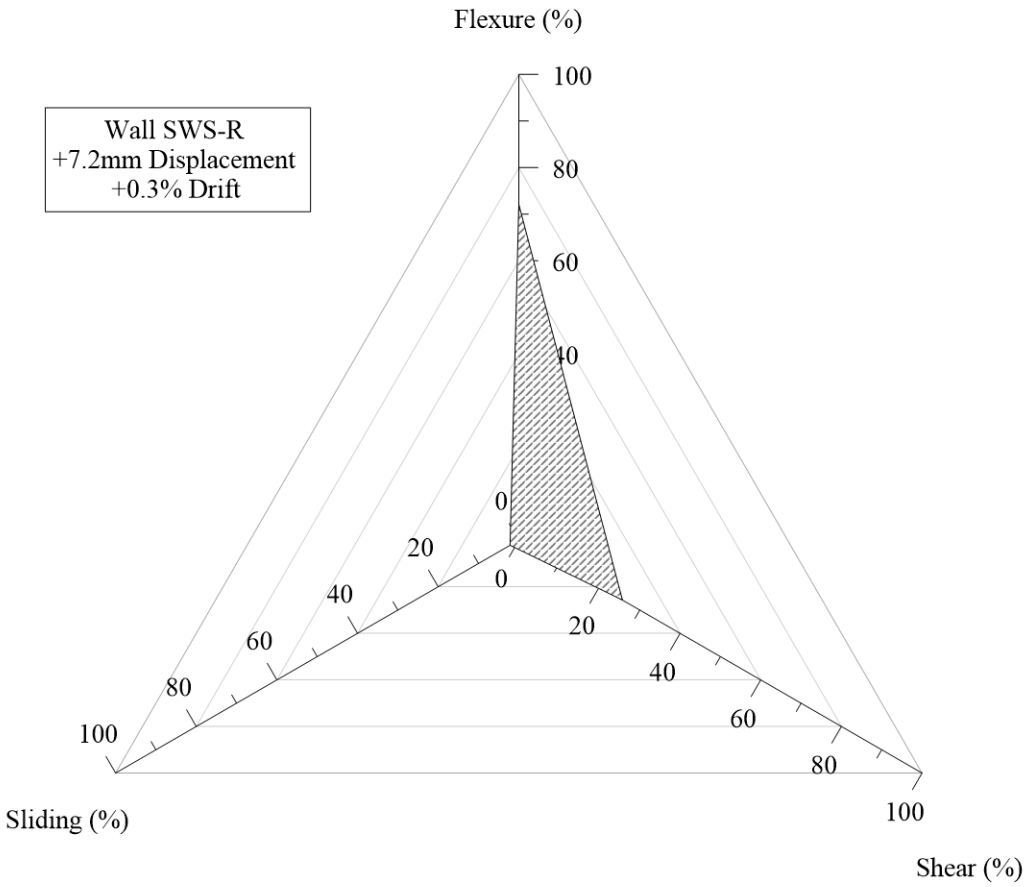

Figure K.4. Distribution of flexure, shear, and sliding of wall SWS-R at positive 7.2mm displacement.

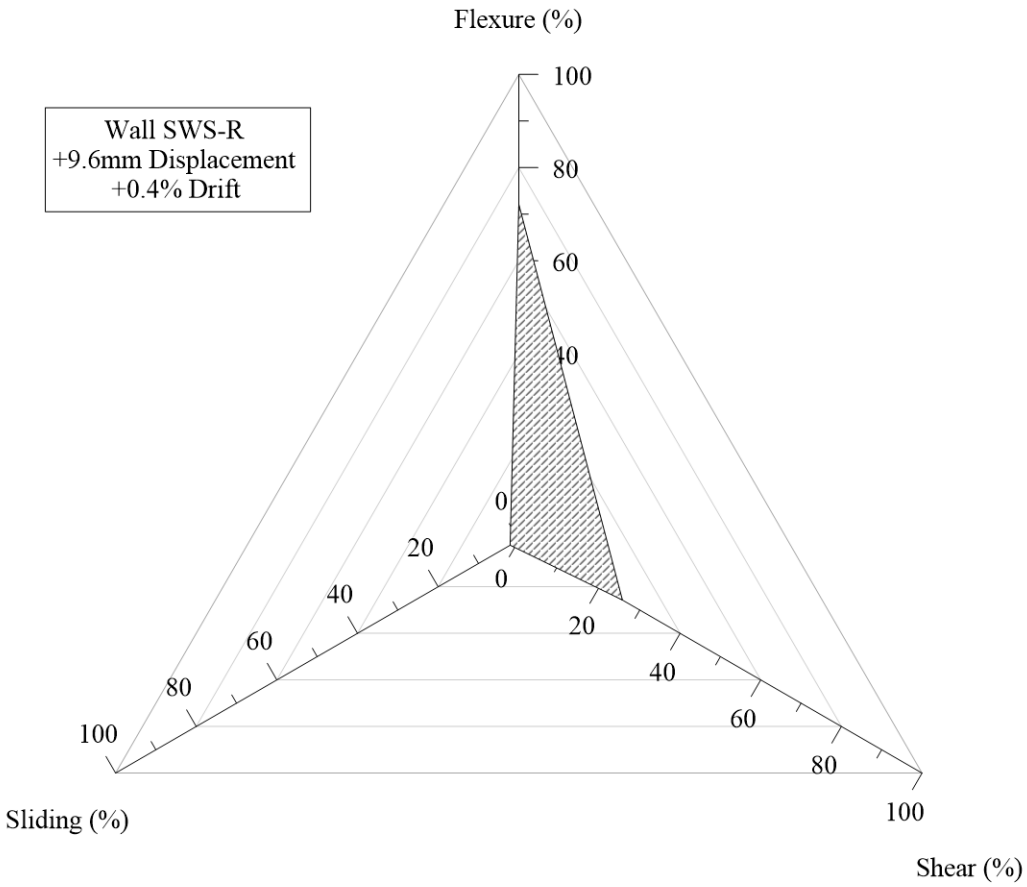

Figure K.5. Distribution of flexure, shear, and sliding of wall SWS-R at positive 9.6mm displacement.

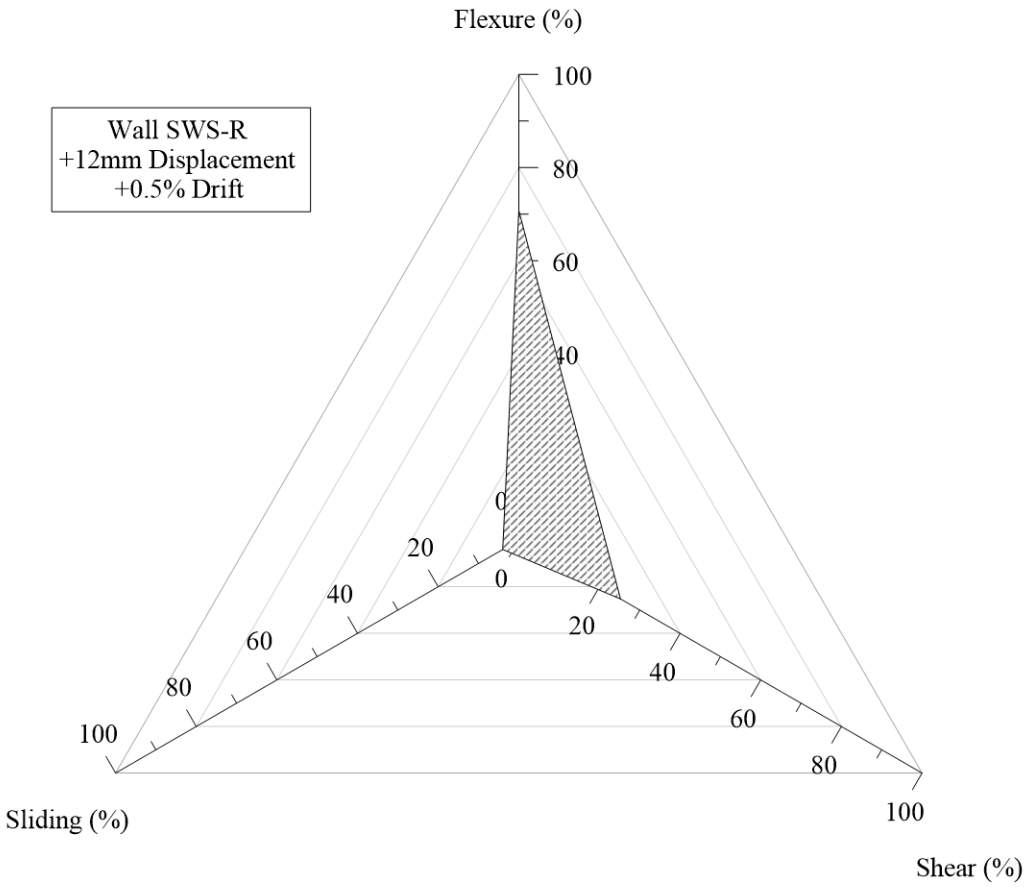

Figure K.6. Distribution of flexure, shear, and sliding of wall SWS-R at positive 12mm displacement.

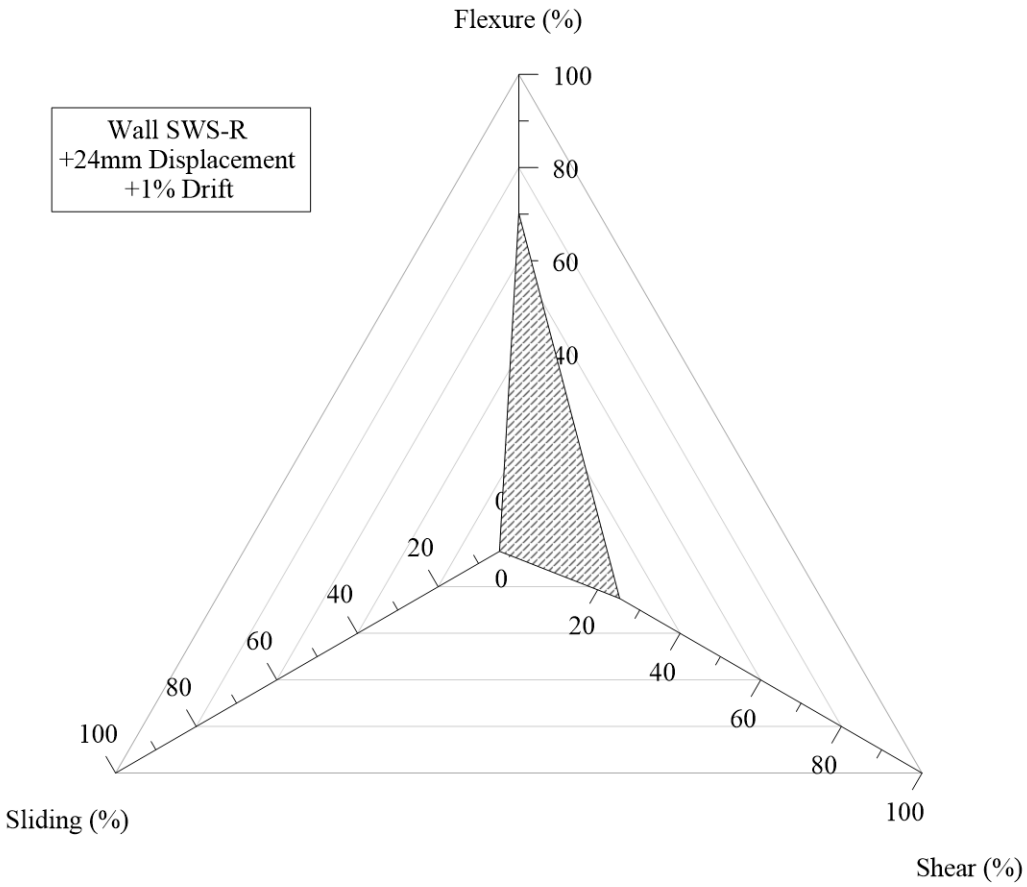

Figure K.7. Distribution of flexure, shear, and sliding of wall SWS-R at positive 24mm displacement.

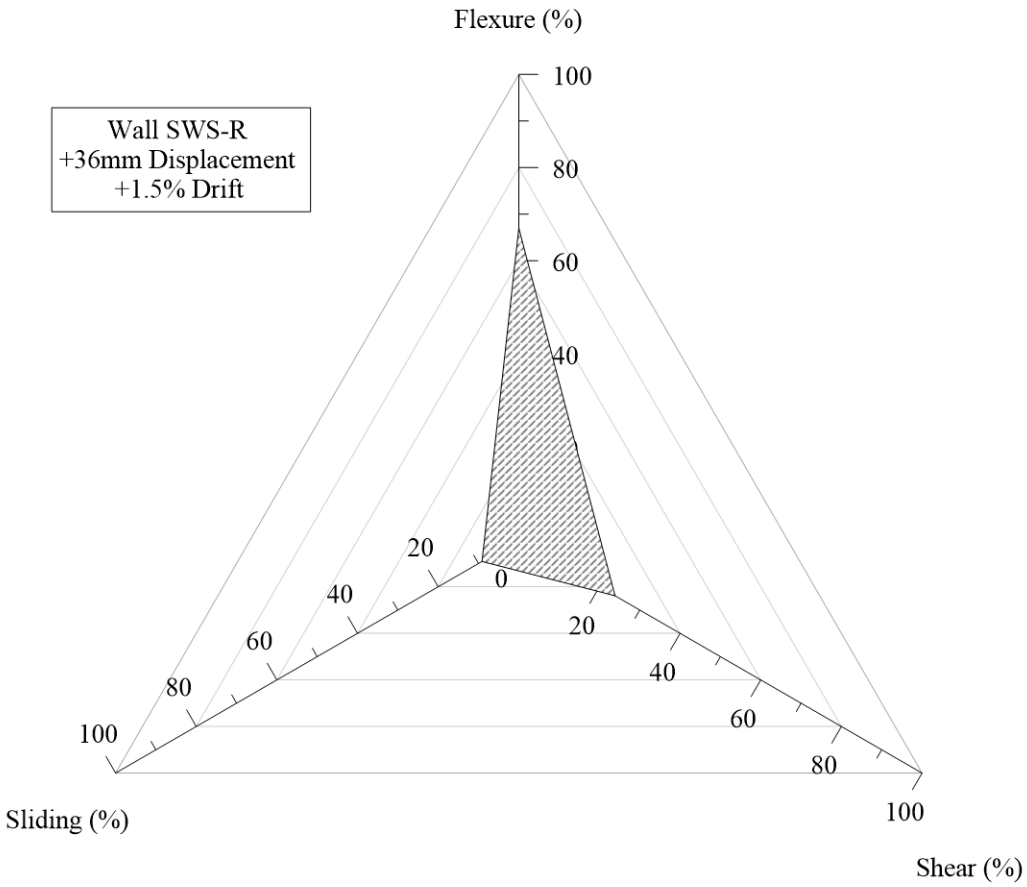

Figure K.8. Distribution of flexure, shear, and sliding of wall SWS-R at positive 36mm displacement.

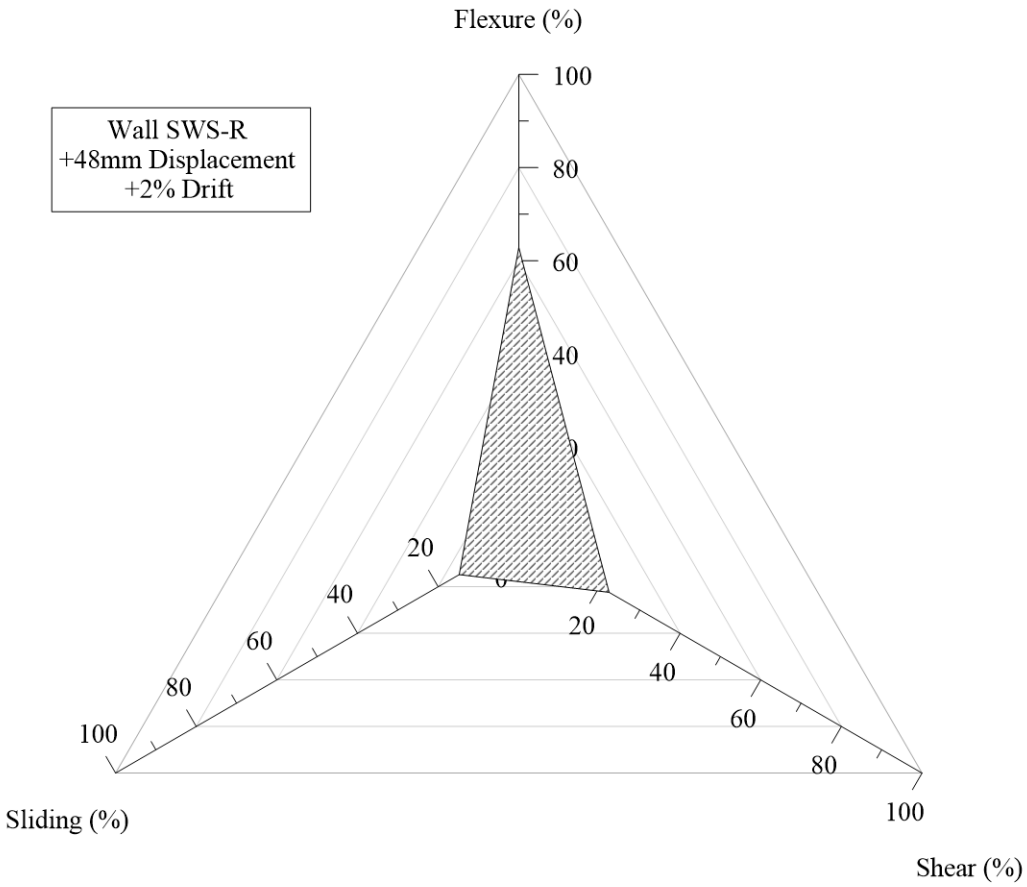

Figure K.9. Distribution of flexure, shear, and sliding of wall SWS-R at positive 48mm displacement.

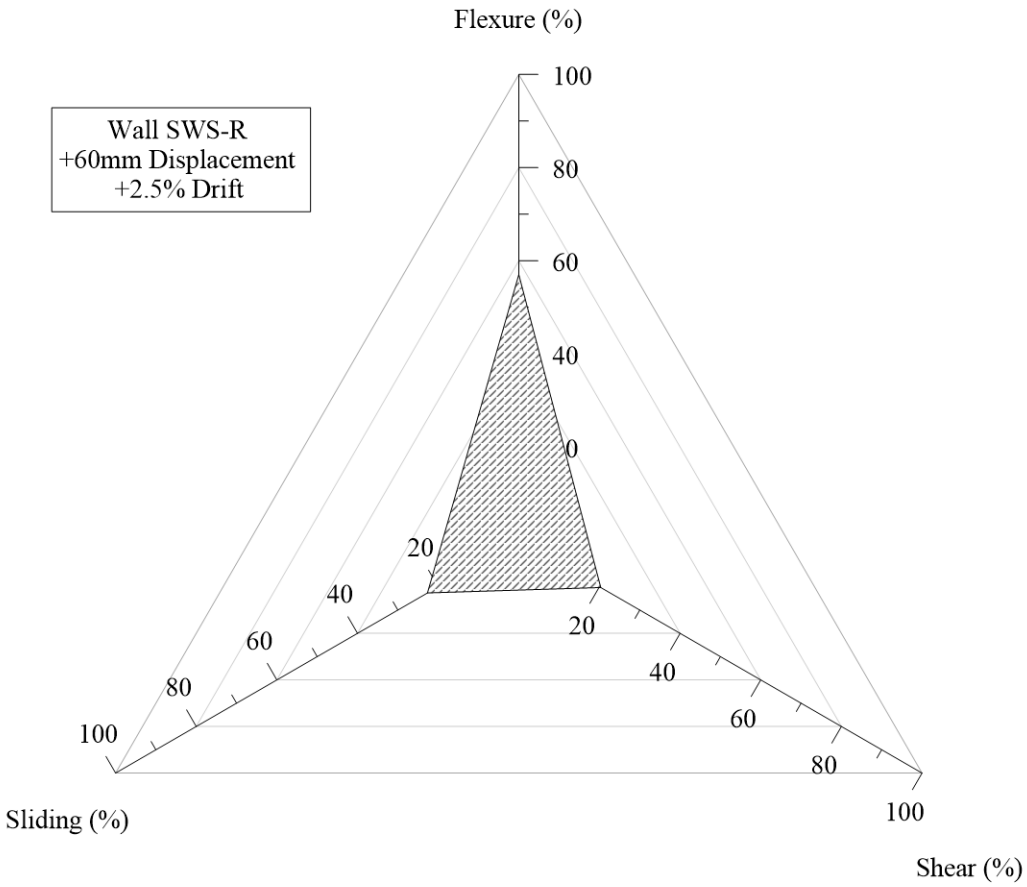

Figure K.10. Distribution of flexure, shear, and sliding of wall SWS-R at positive 60mm displacement.

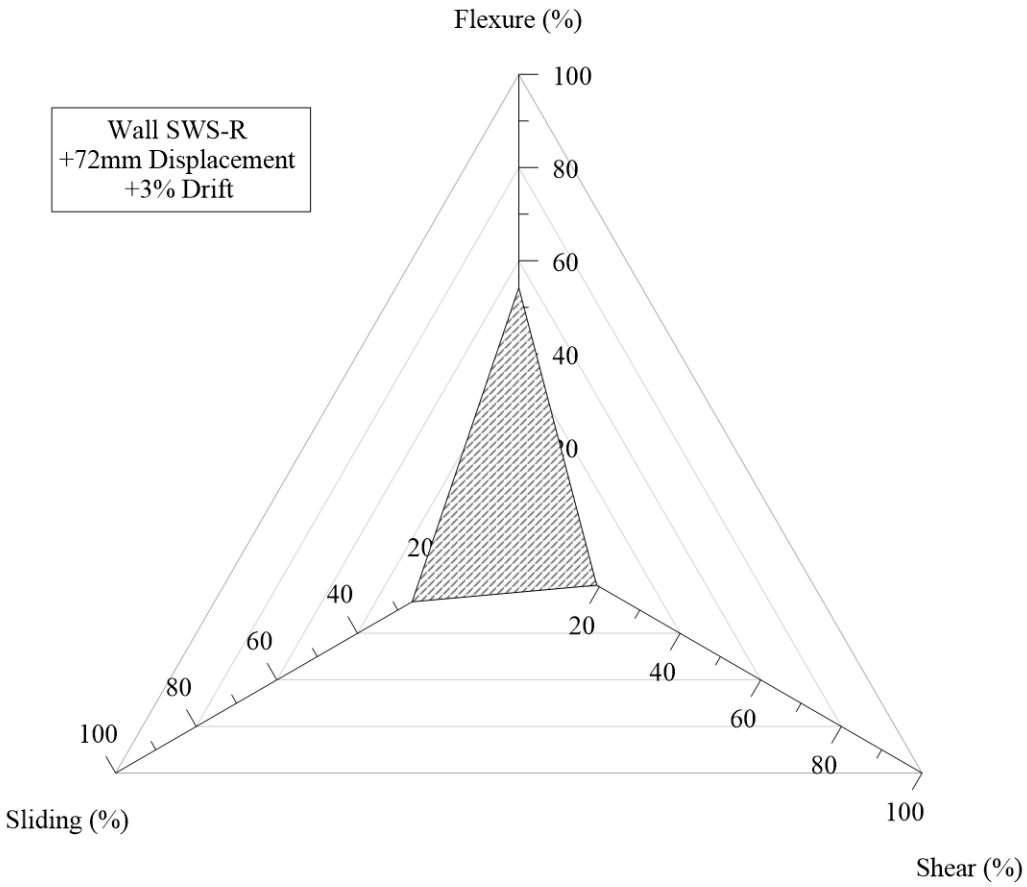

Figure K.11. Distribution of flexure, shear, and sliding of wall SWS-R at positive 72mm displacement.

Wall SWS-R Distributions – Negative Loading

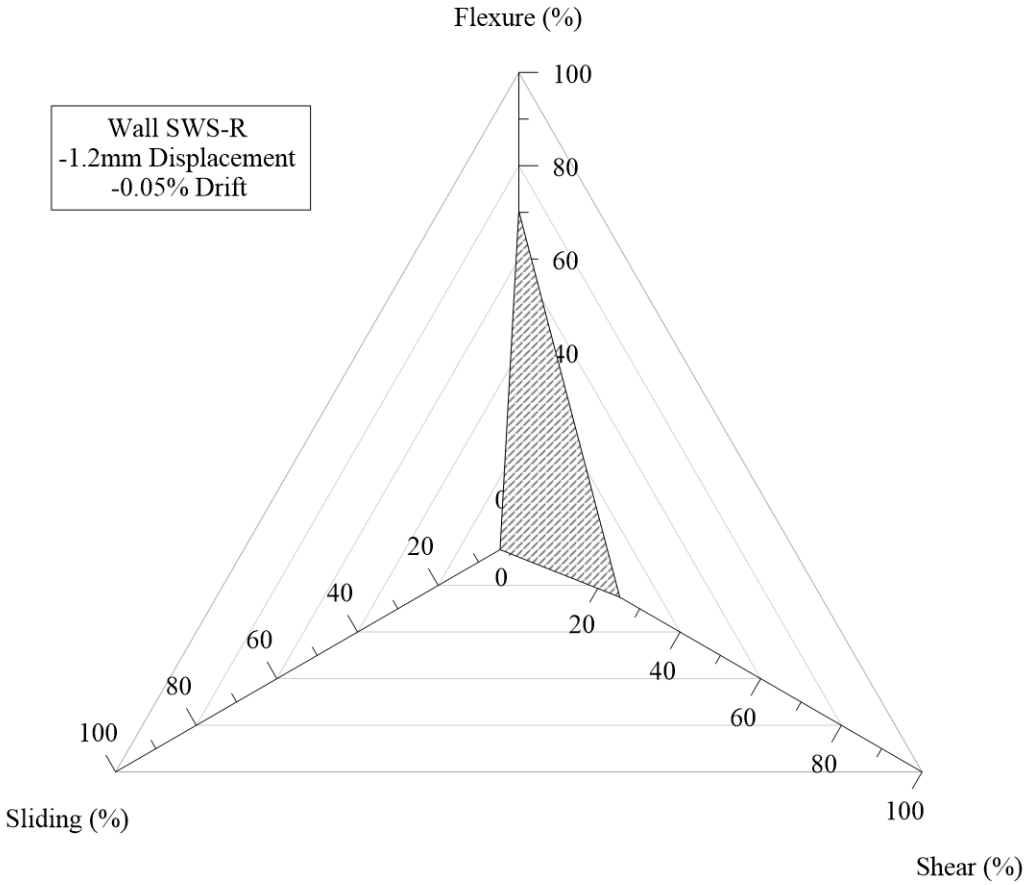

Figure K.12. Distribution of flexure, shear, and sliding of wall SWS-R at negative 1.2mm displacement.

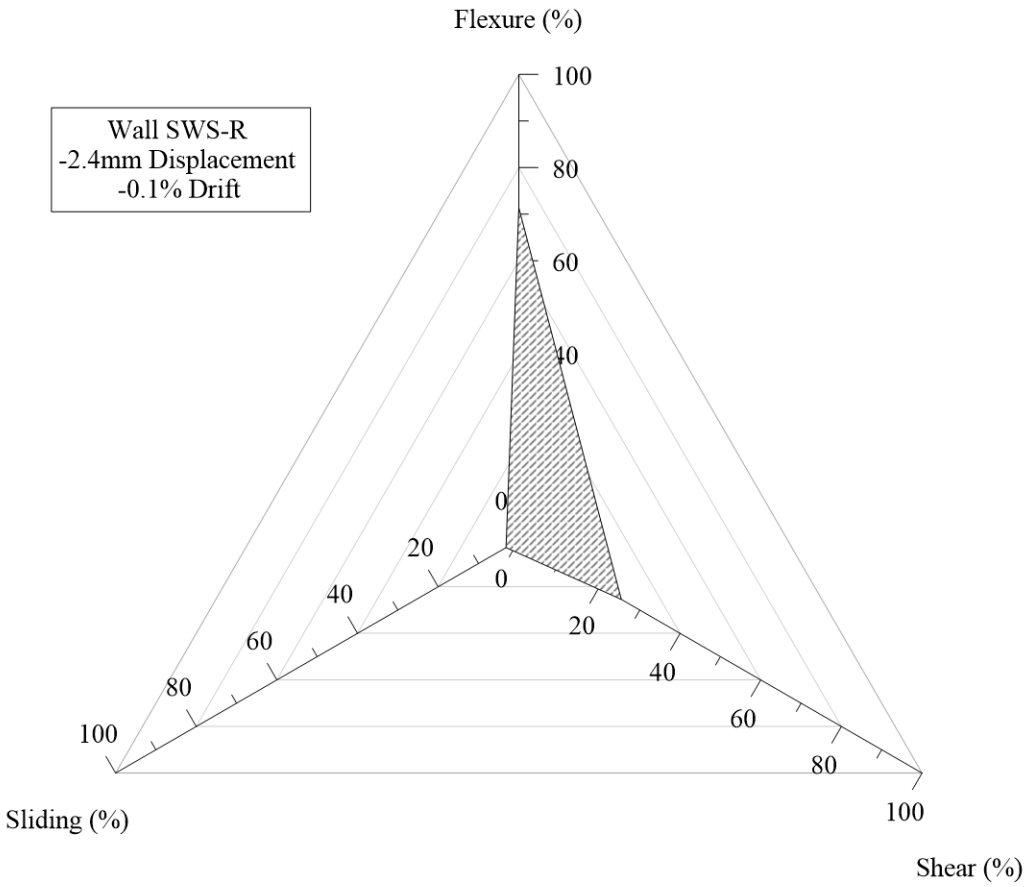

Figure K.13. Distribution of flexure, shear, and sliding of wall SWS-R at negative 2.4mm displacement.

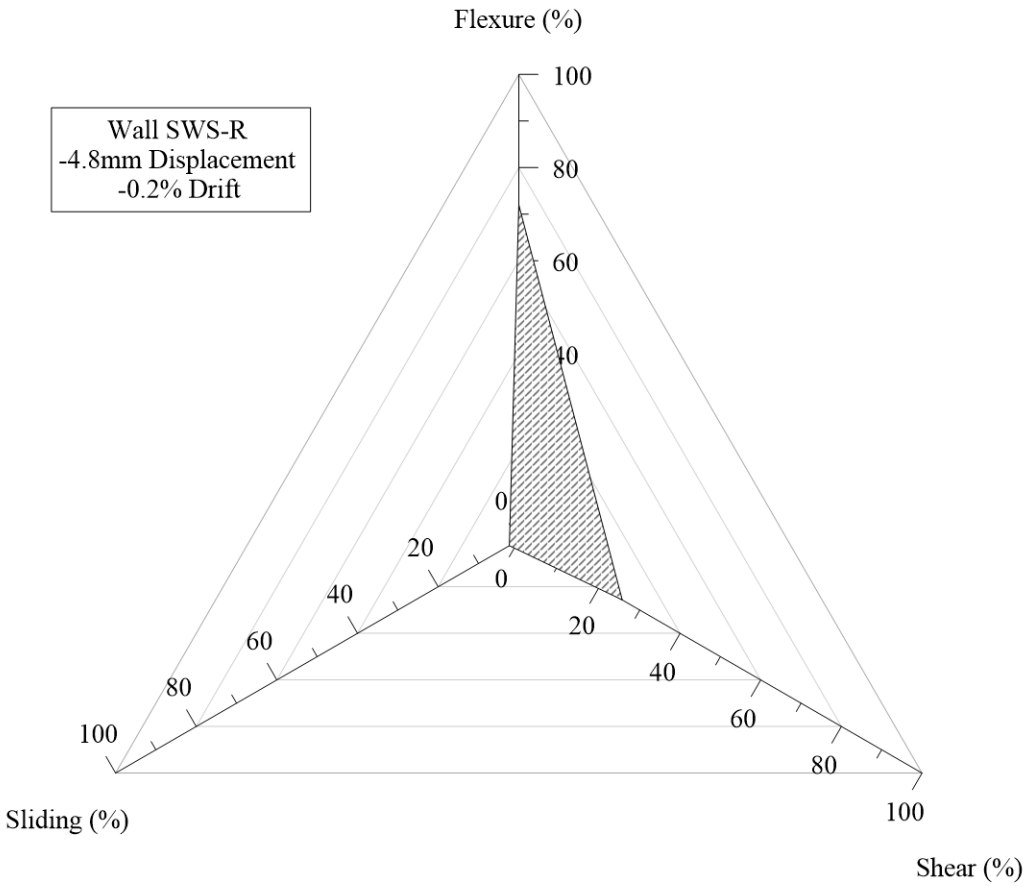

Figure K.14. Distribution of flexure, shear, and sliding of wall SWS-R at negative 4.8mm displacement.

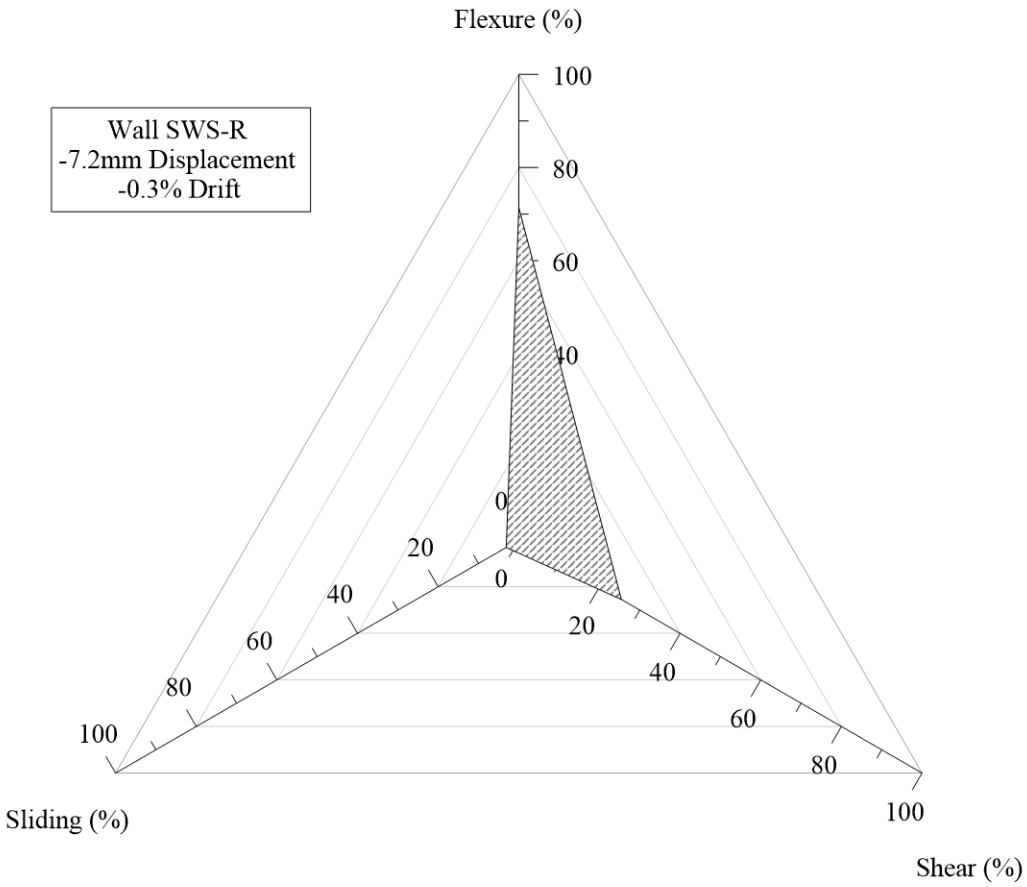

Figure K.15. Distribution of flexure, shear, and sliding of wall SWS-R at negative 7.2mm displacement.

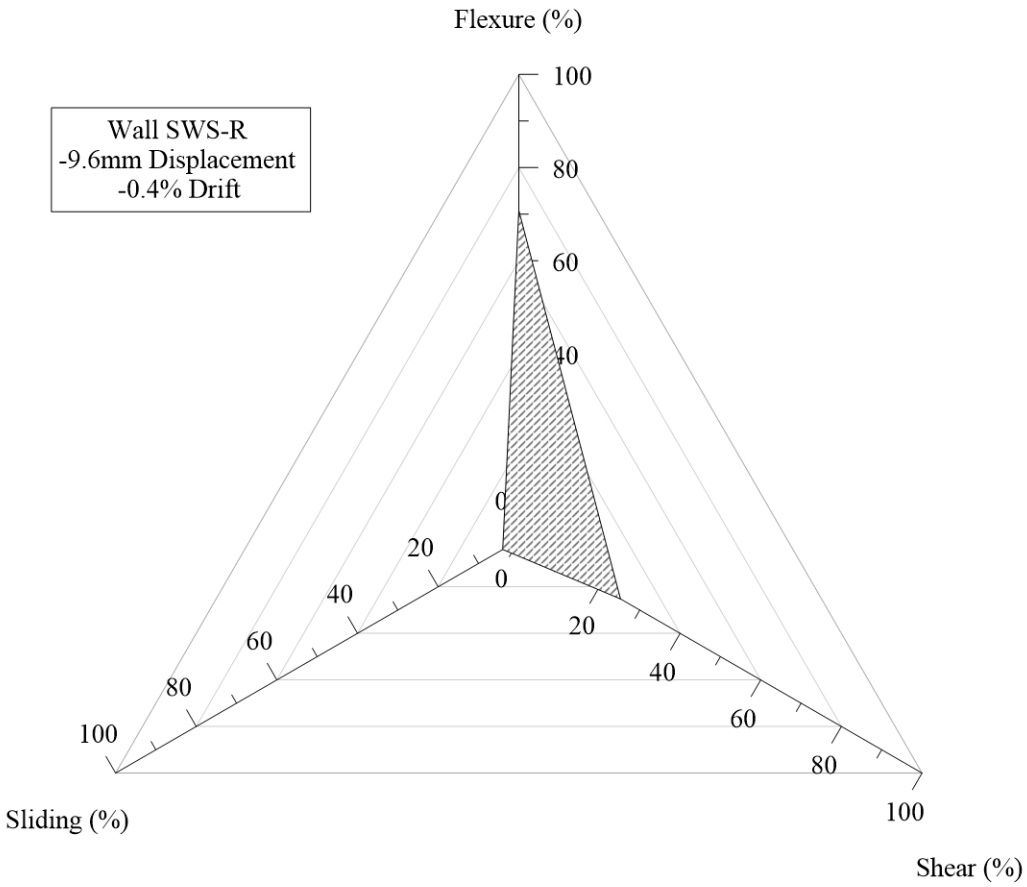

Figure K.16. Distribution of flexure, shear, and sliding of wall SWS-R at negative 9.6mm displacement.

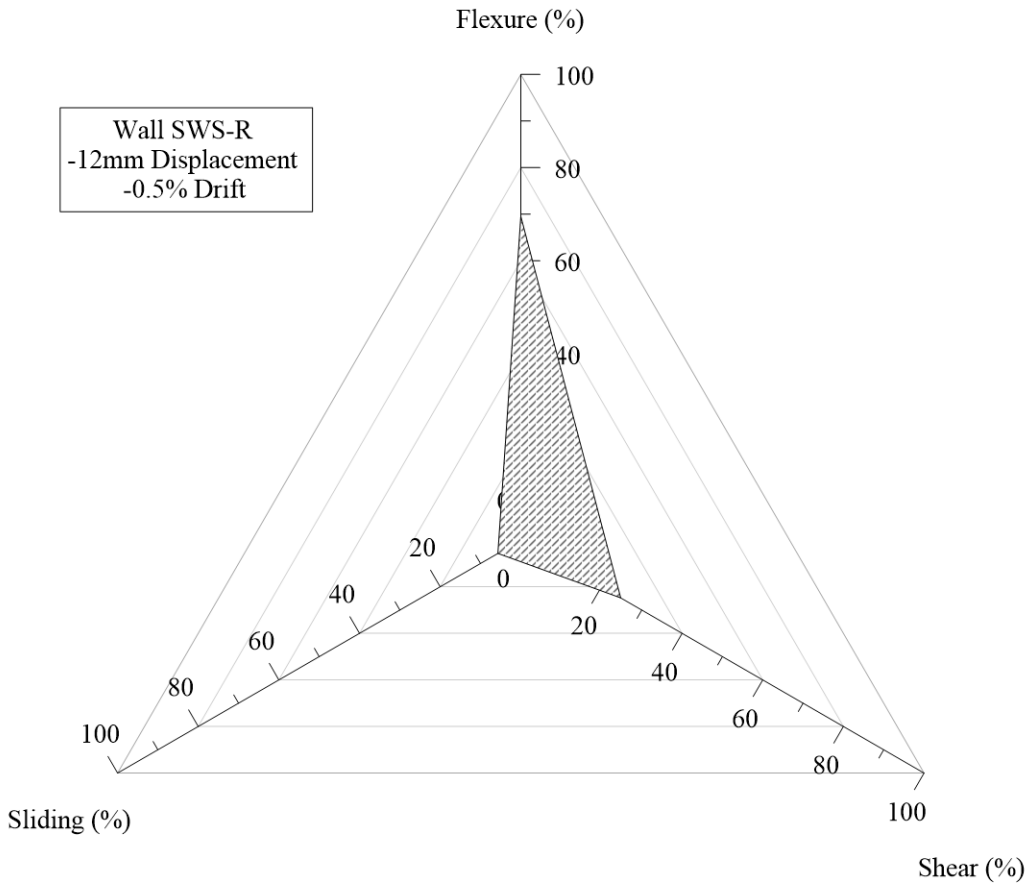

Figure K.17. Distribution of flexure, shear, and sliding of wall SWS-R at negative 12mm displacement.

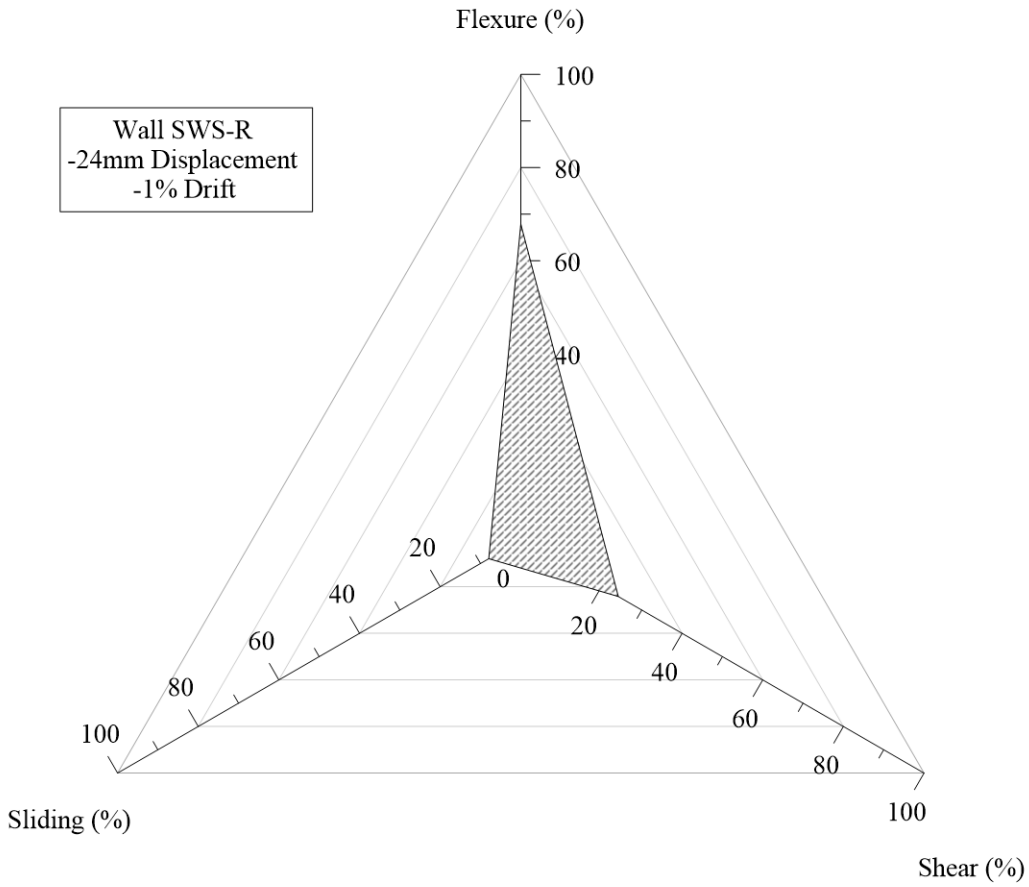

Figure K.18. Distribution of flexure, shear, and sliding of wall SWS-R at negative 24mm displacement.

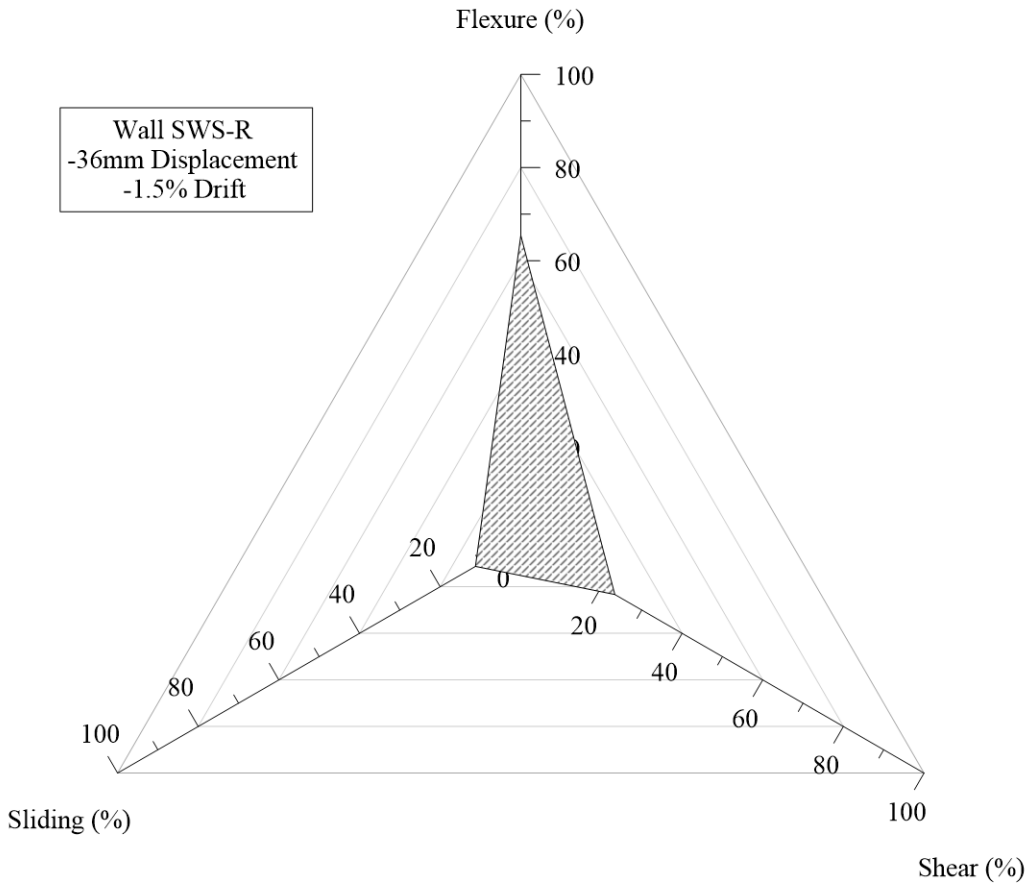

Figure K.19. Distribution of flexure, shear, and sliding of wall SWS-R at negative 36mm displacement.

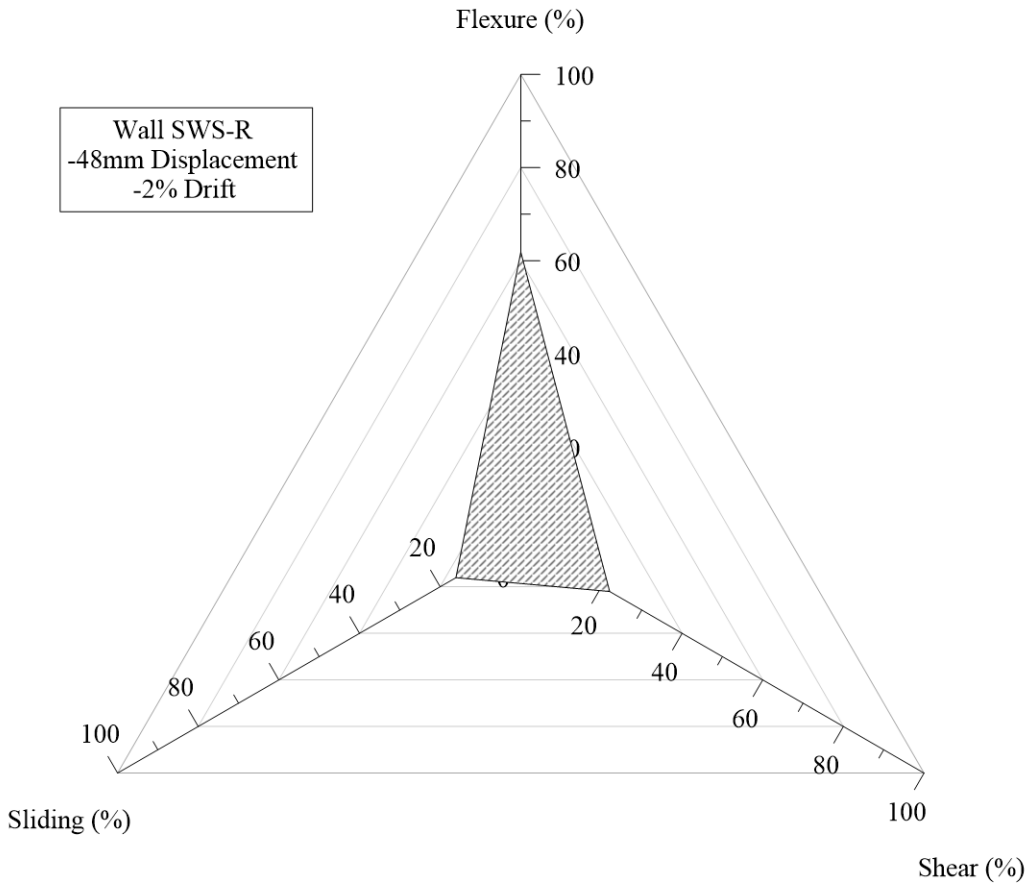

Figure K.20. Distribution of flexure, shear, and sliding of wall SWS-R at negative 48mm displacement.

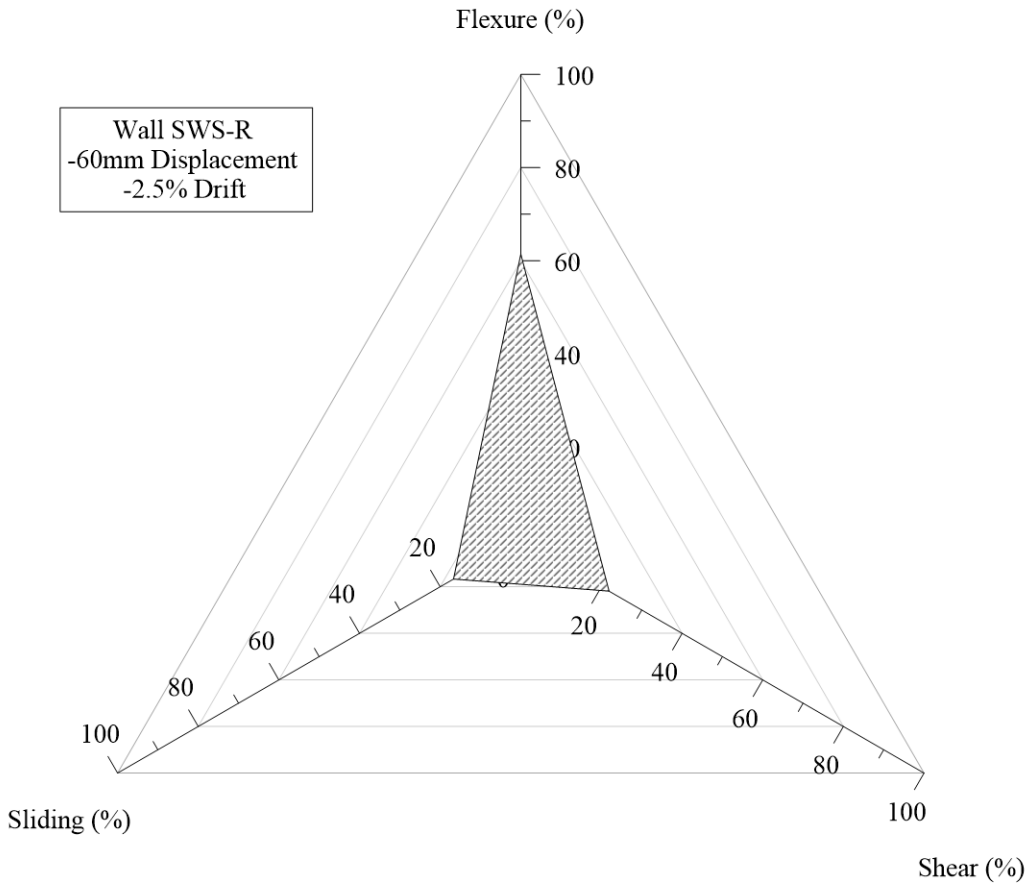

Figure K.21. Distribution of flexure, shear, and sliding of wall SWS-R at negative 60mm displacement.

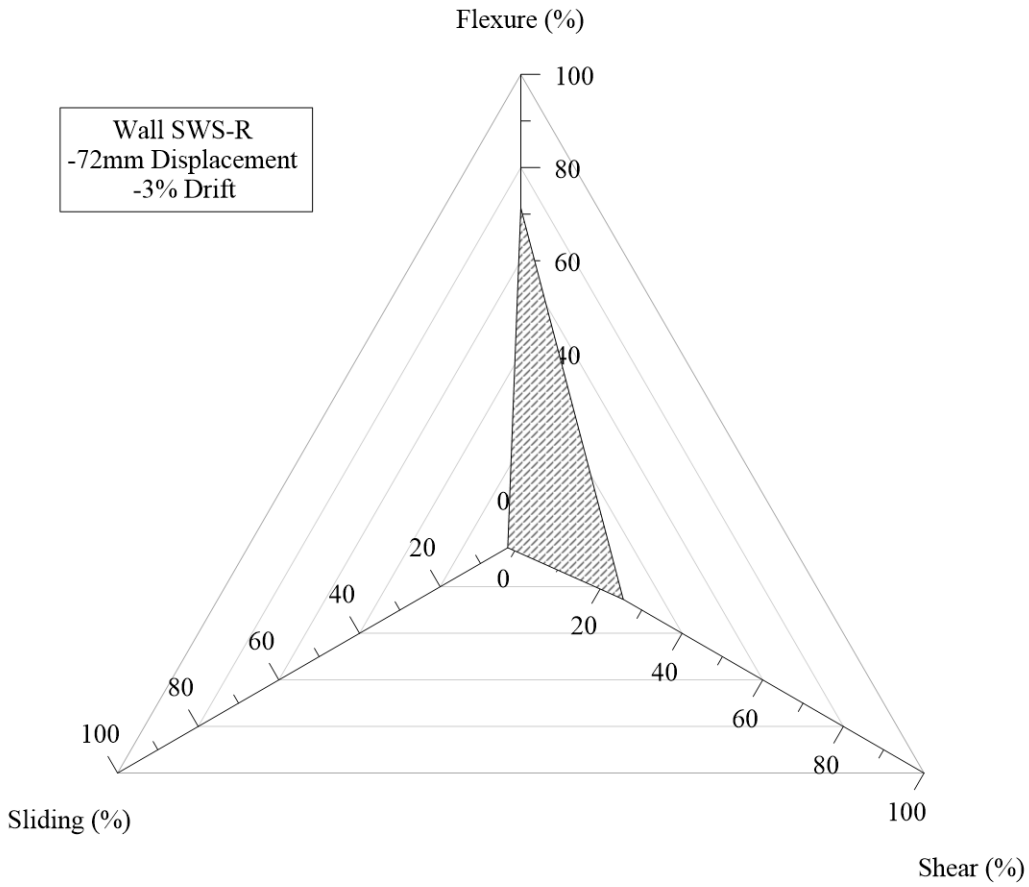

Figure K.22. Distribution of flexure, shear, and sliding of wall SWS-R at negative 72mm displacement.

Wall SWN Distributions – Positive Loading

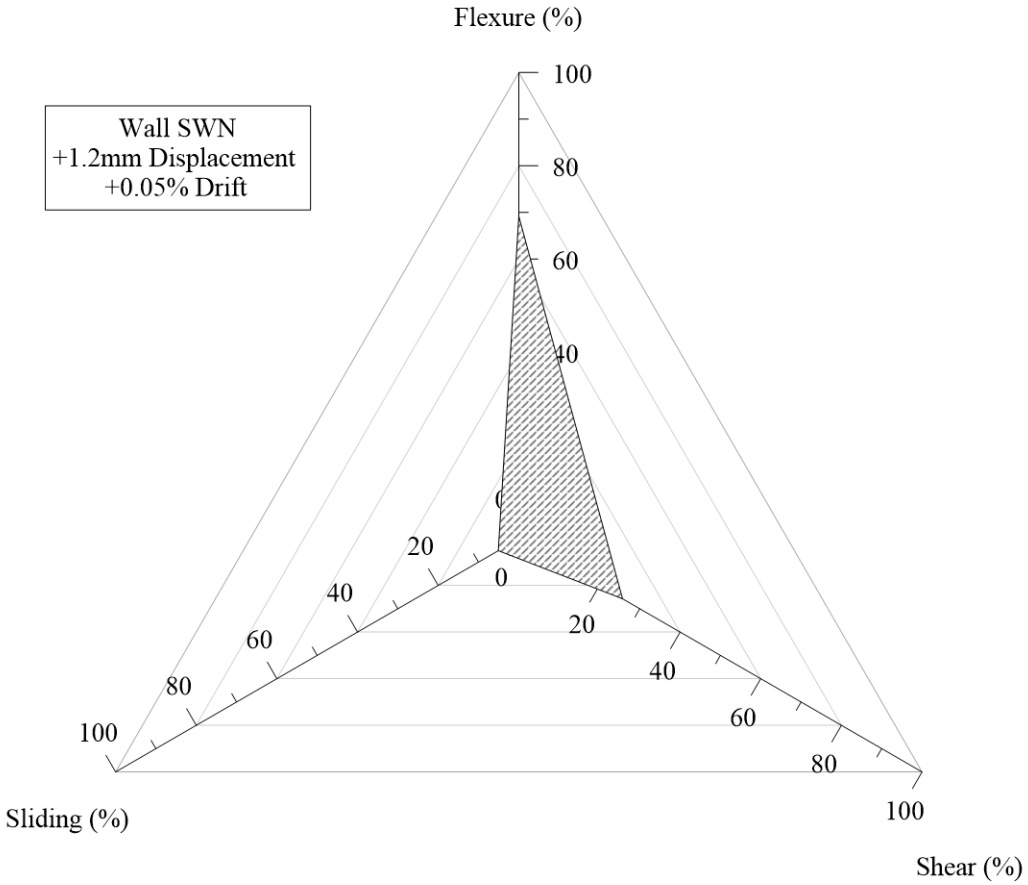

Figure K.23. Distribution of flexure, shear, and sliding of wall SWN at positive 1.2mm displacement.

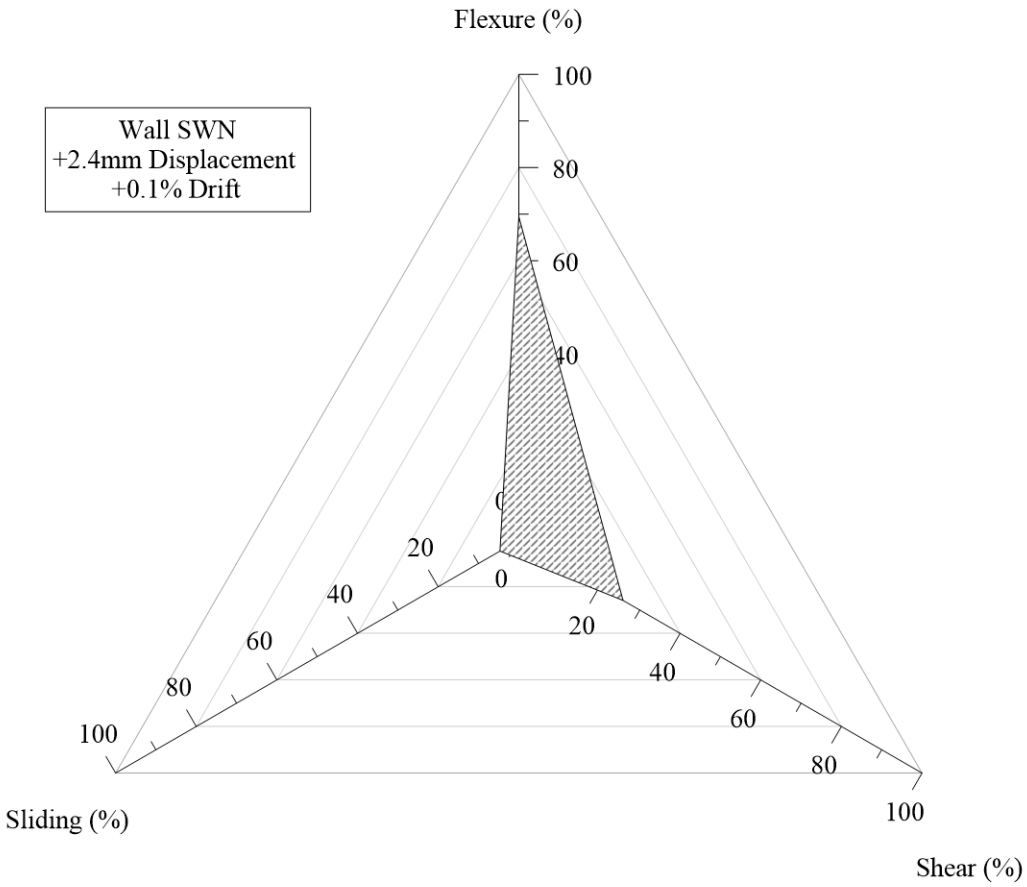

Figure K.24. Distribution of flexure, shear, and sliding of wall SWN at positive 2.4mm displacement.

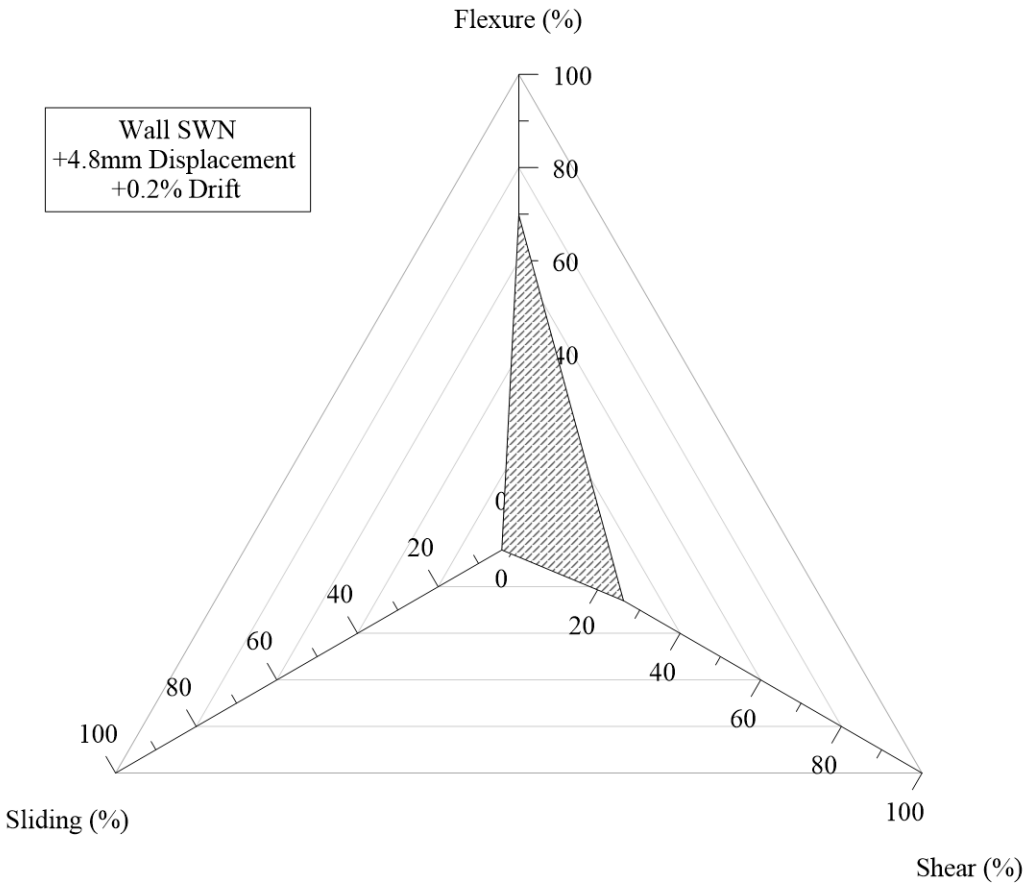

Figure K.25. Distribution of flexure, shear, and sliding of wall SWN at positive 4.8mm displacement.

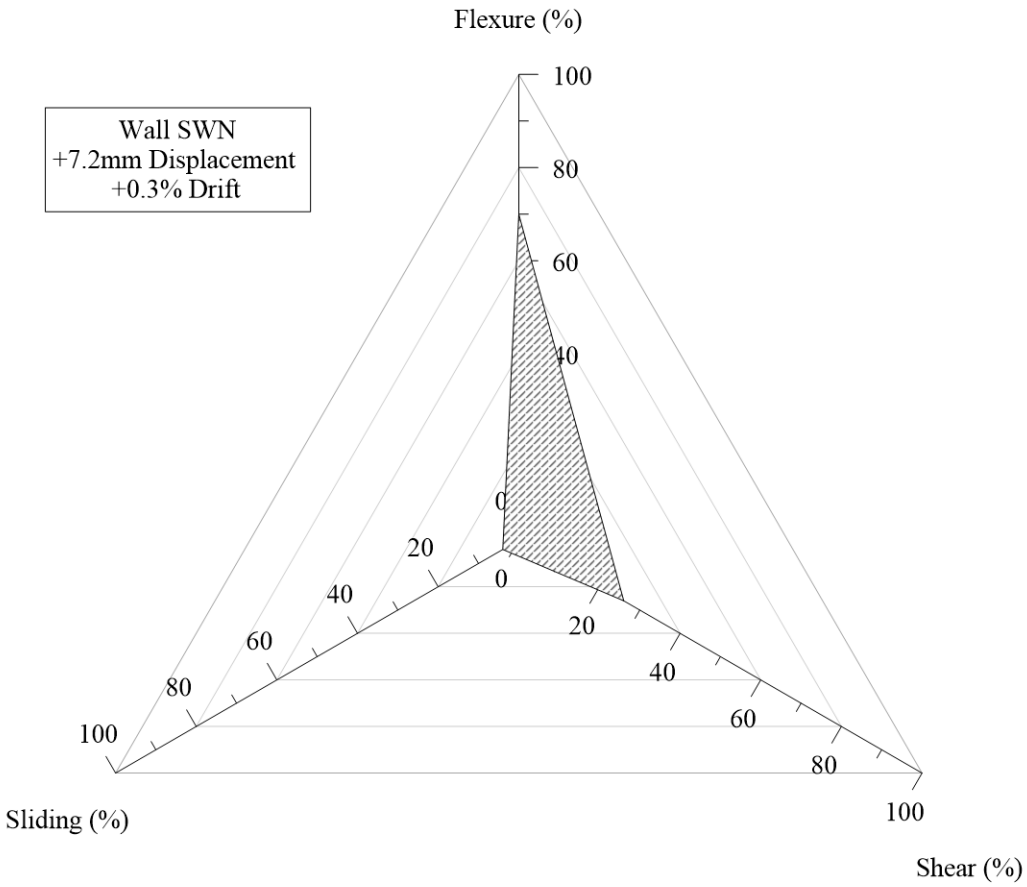

Figure K.26. Distribution of flexure, shear, and sliding of wall SWN at positive 7.2mm displacement.

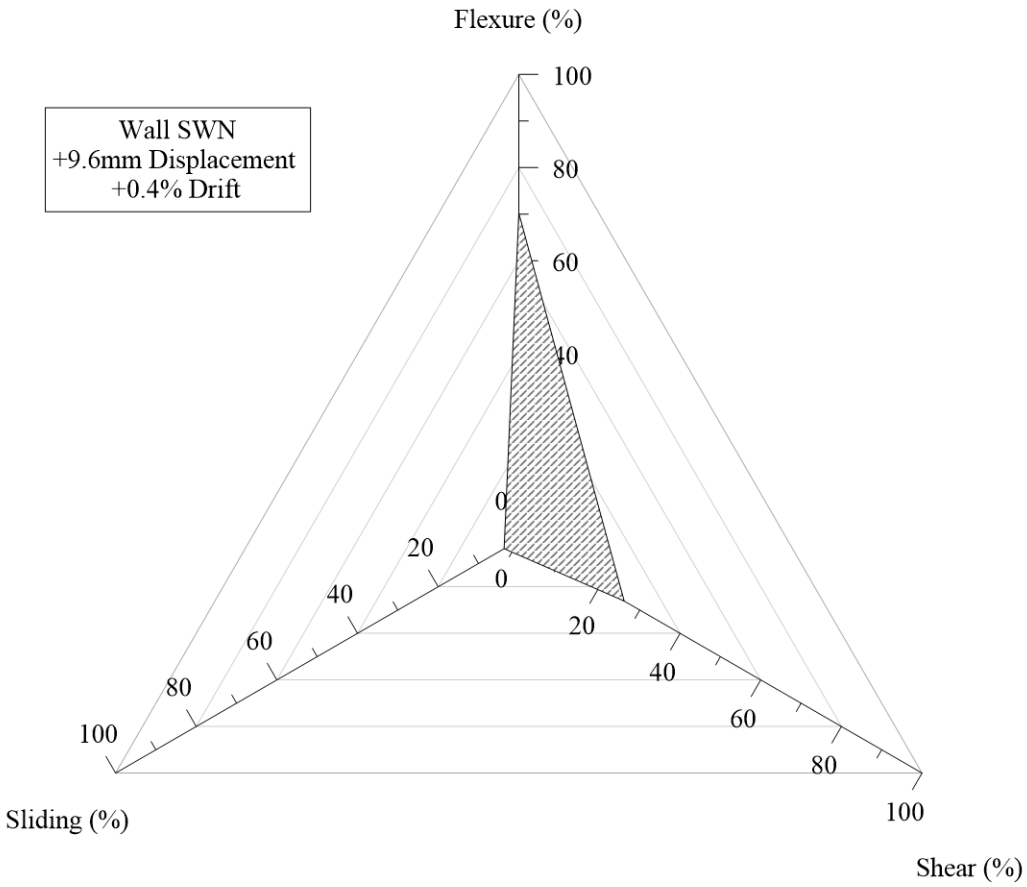

Figure K.27. Distribution of flexure, shear, and sliding of wall SWN at positive 9.6mm displacement.

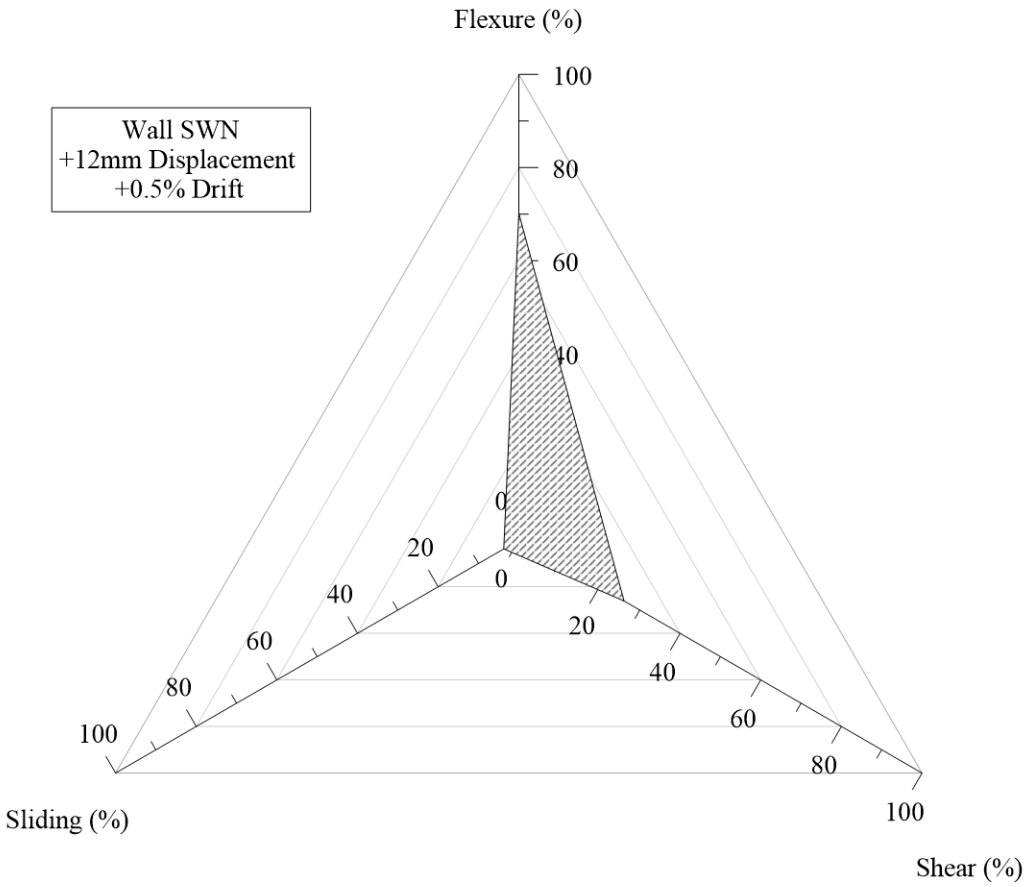

Figure K.28. Distribution of flexure, shear, and sliding of wall SWN at positive 12mm displacement.

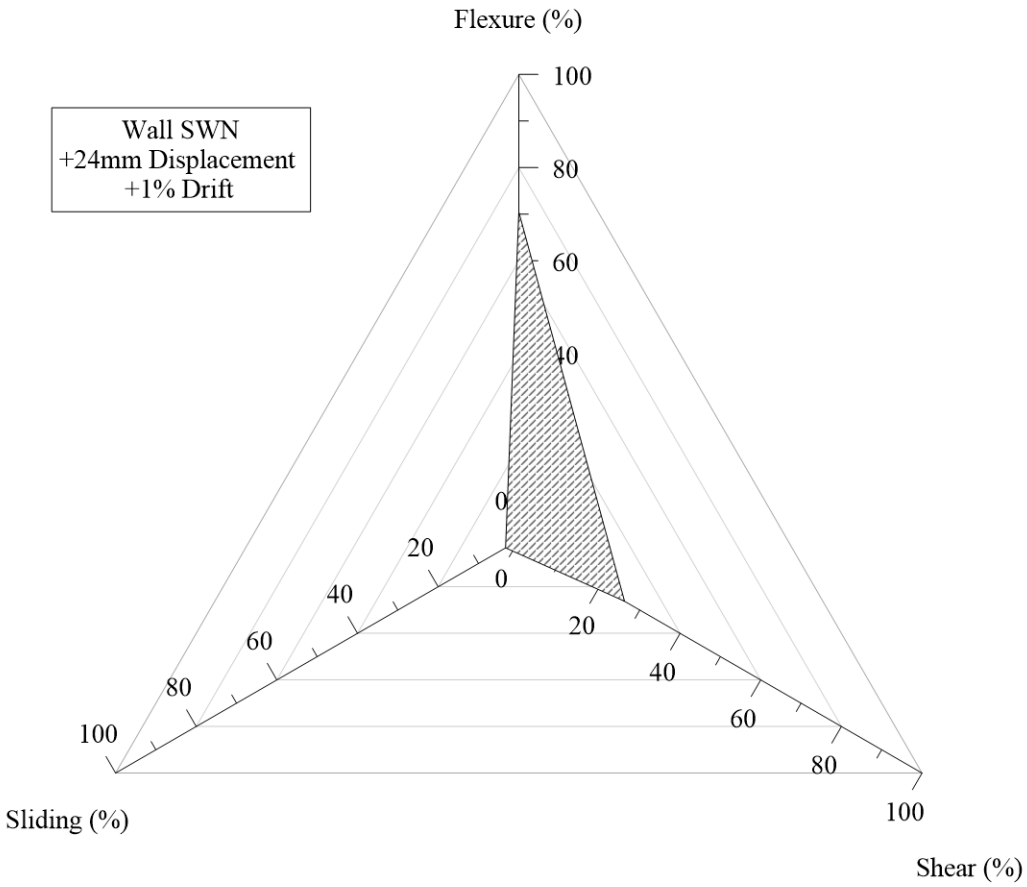

Figure K.29. Distribution of flexure, shear, and sliding of wall SWN at positive 24mm displacement.

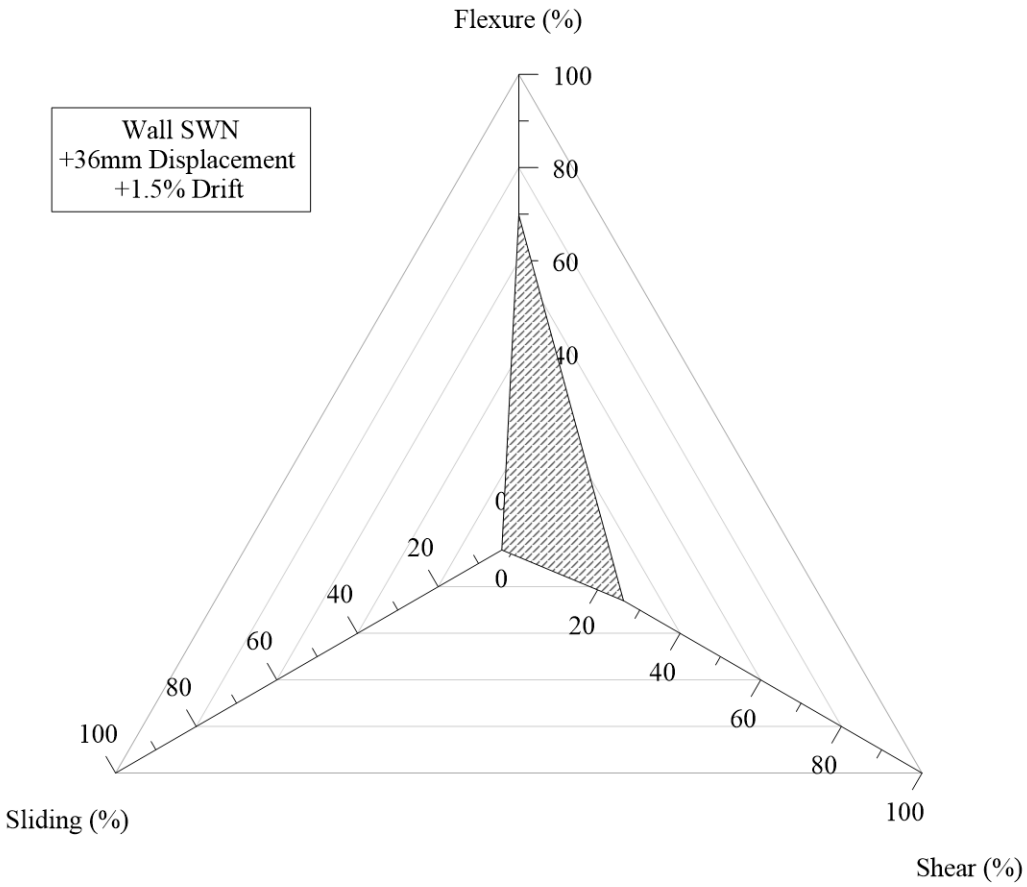

Figure K.30. Distribution of flexure, shear, and sliding of wall SWN at positive 36mm displacement.

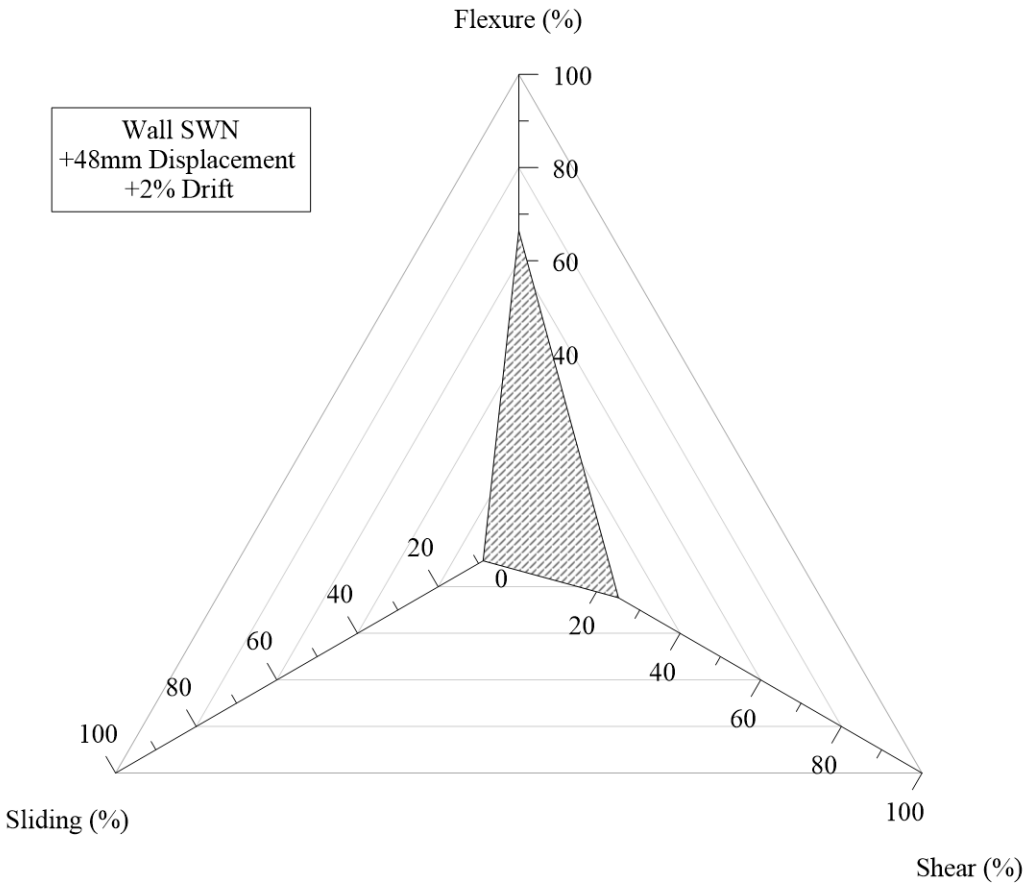

Figure K.31. Distribution of flexure, shear, and sliding of wall SWN at positive 48mm displacement.

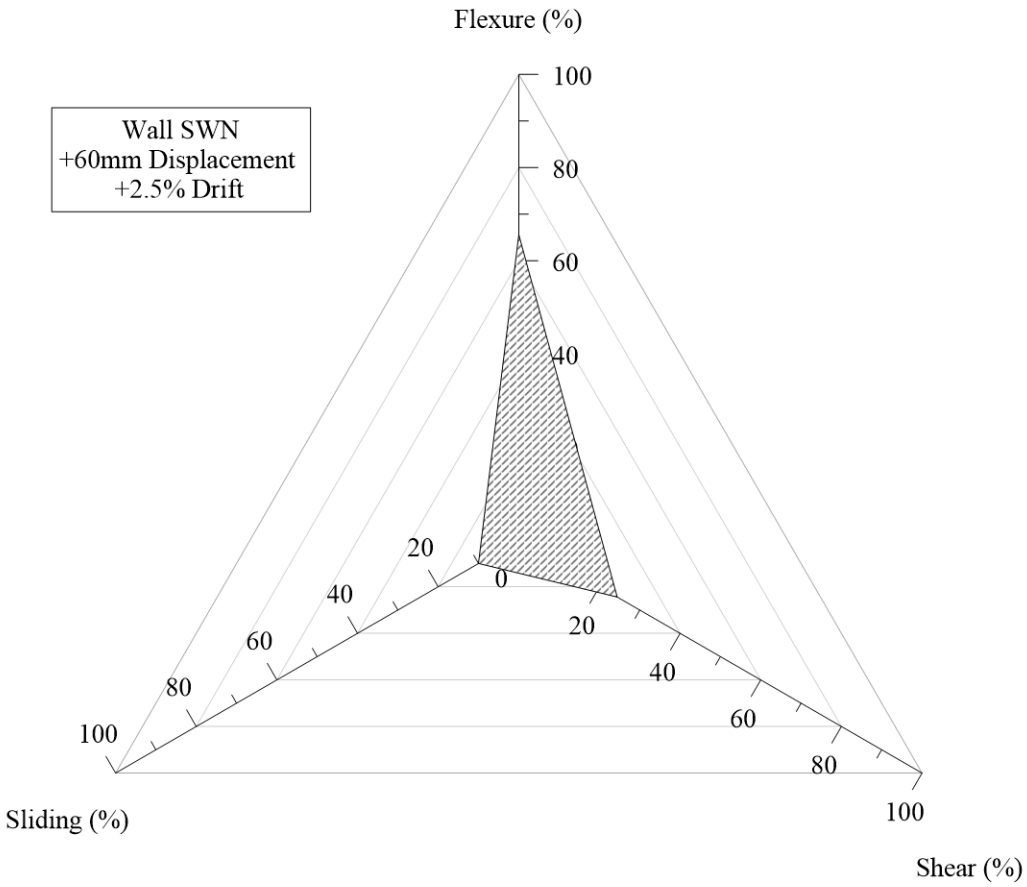

Figure K.32. Distribution of flexure, shear, and sliding of wall SWN at positive 60mm displacement.

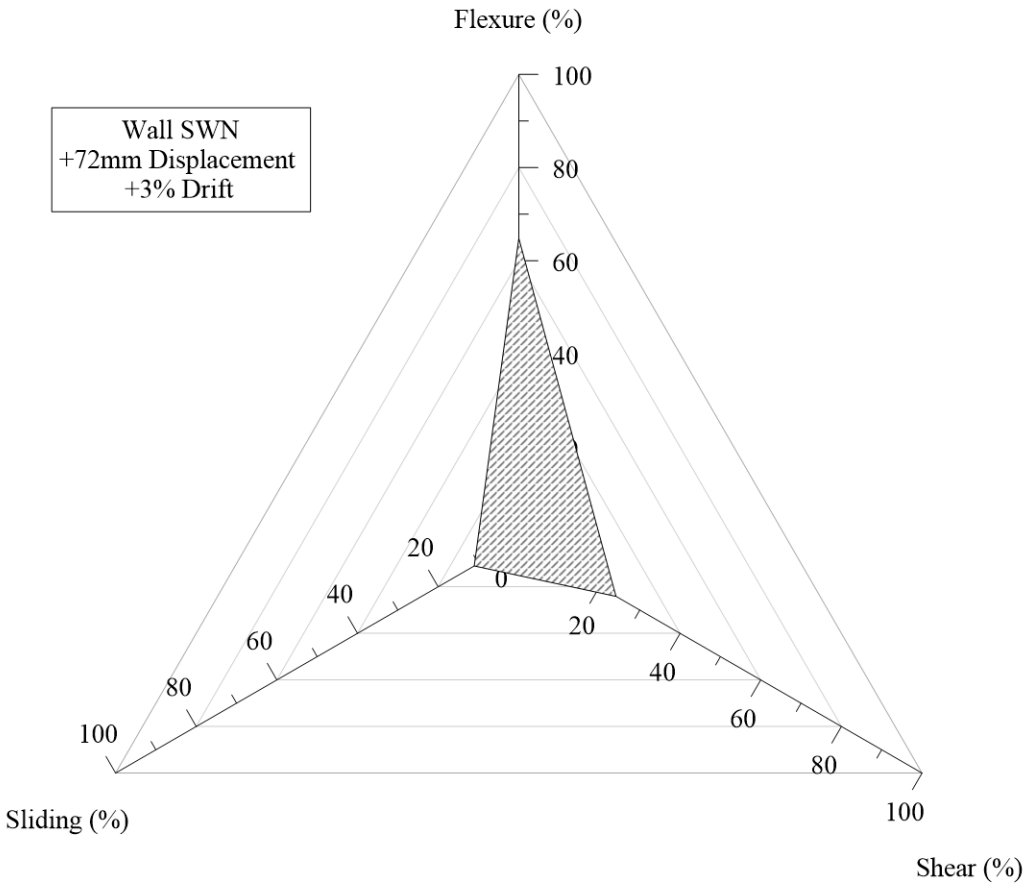

Figure K.33. Distribution of flexure, shear, and sliding of wall SWN at positive 72mm displacement.

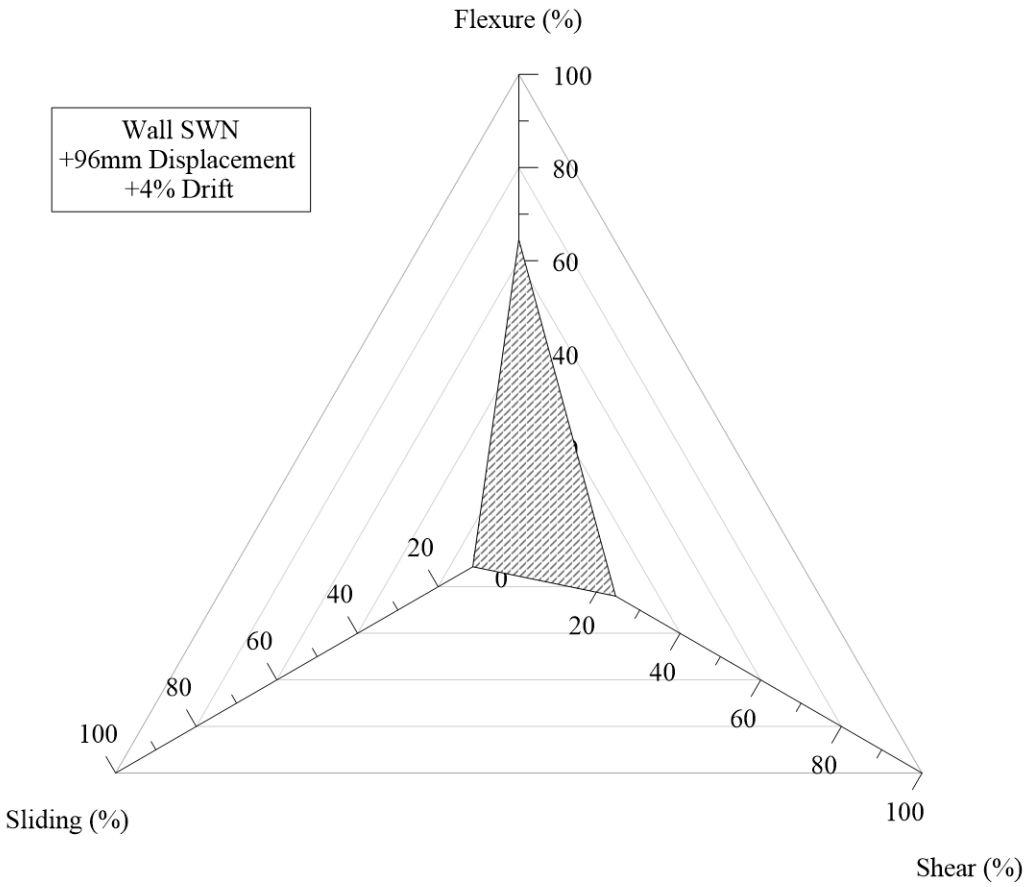

Figure K.34. Distribution of flexure, shear, and sliding of wall SWN at positive 96mm displacement.

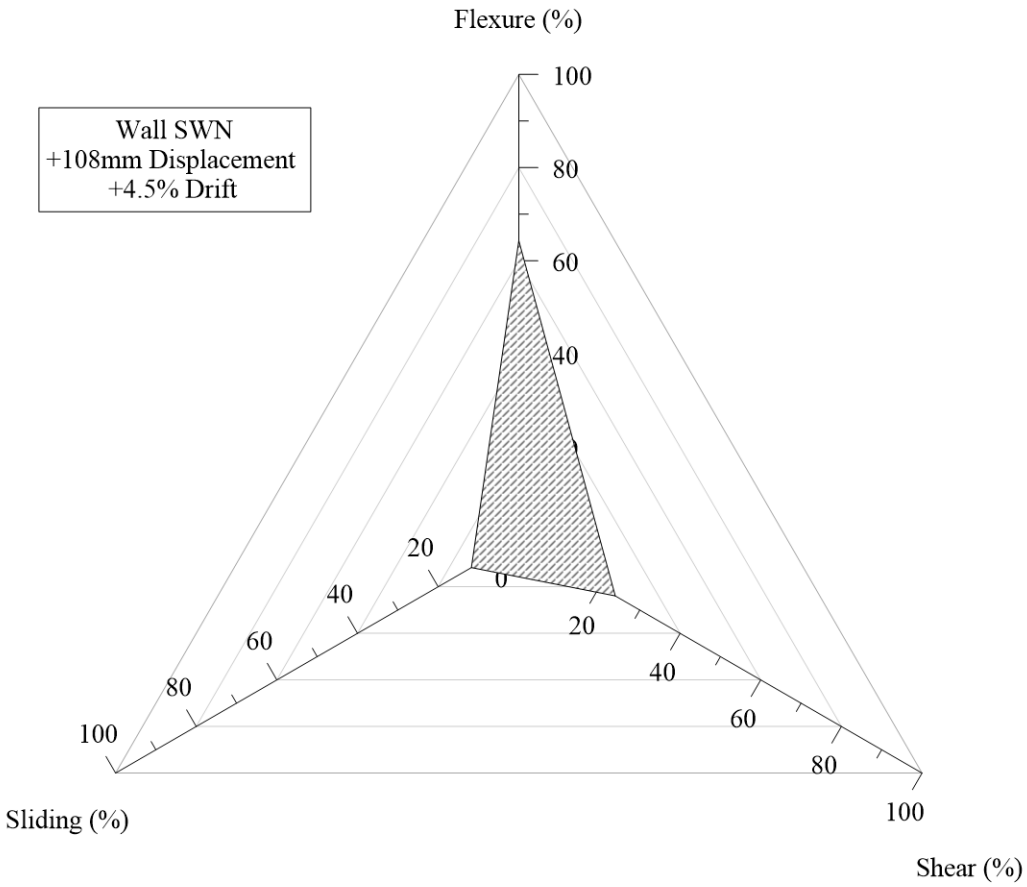

Figure K.35. Distribution of flexure, shear, and sliding of wall SWN at positive 108mm displacement.

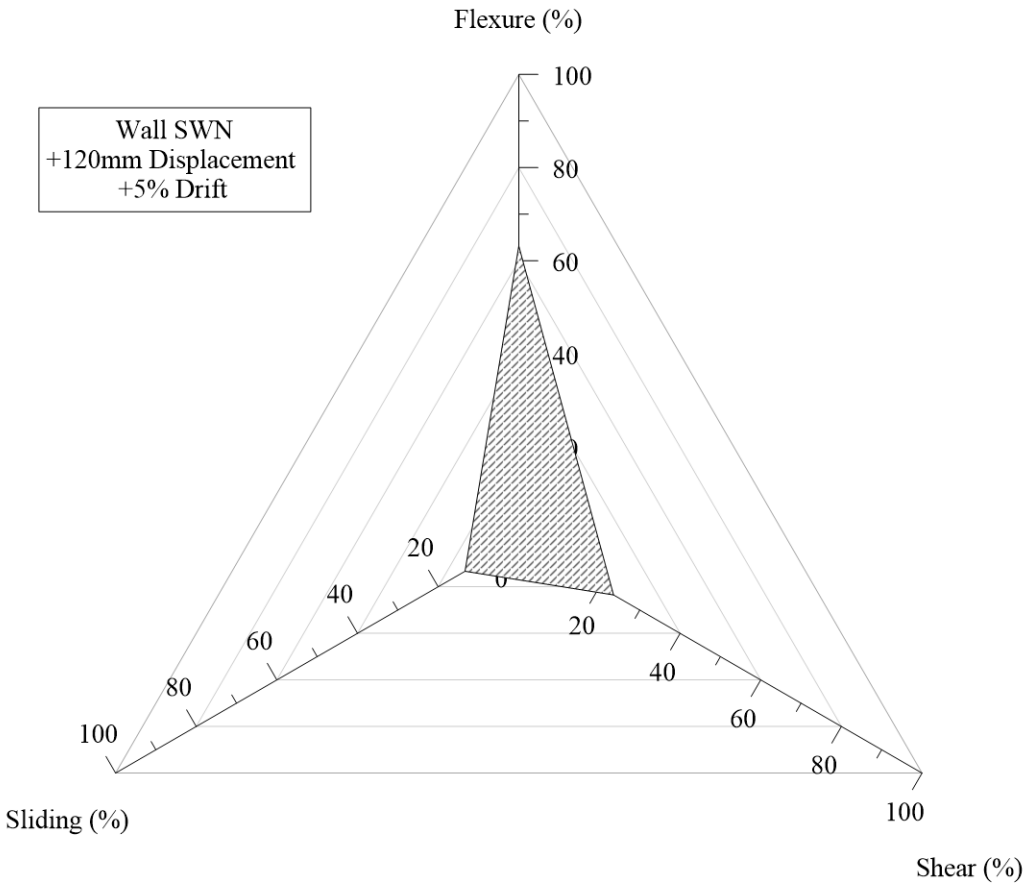

Figure K.36. Distribution of flexure, shear, and sliding of wall SWN at positive 120mm displacement.

Wall SWN Distributions – Negative Loading

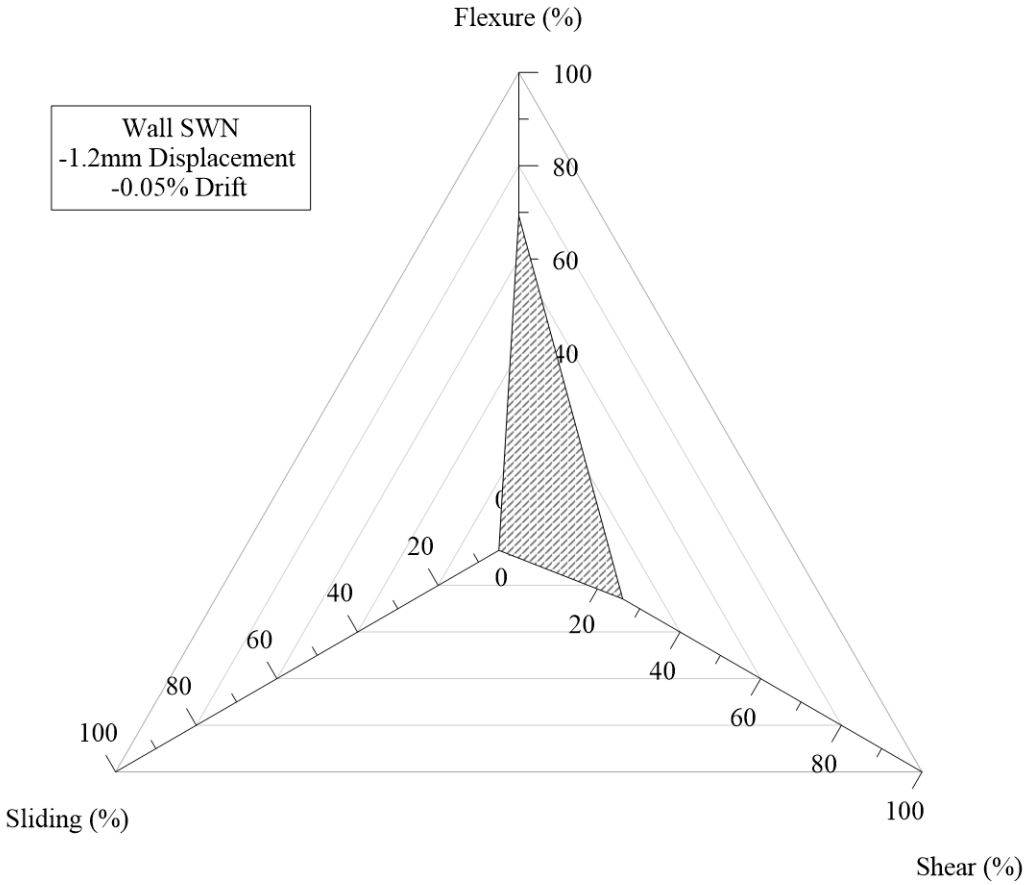

Figure K.37. Distribution of flexure, shear, and sliding of wall SWN at negative 1.2mm displacement.

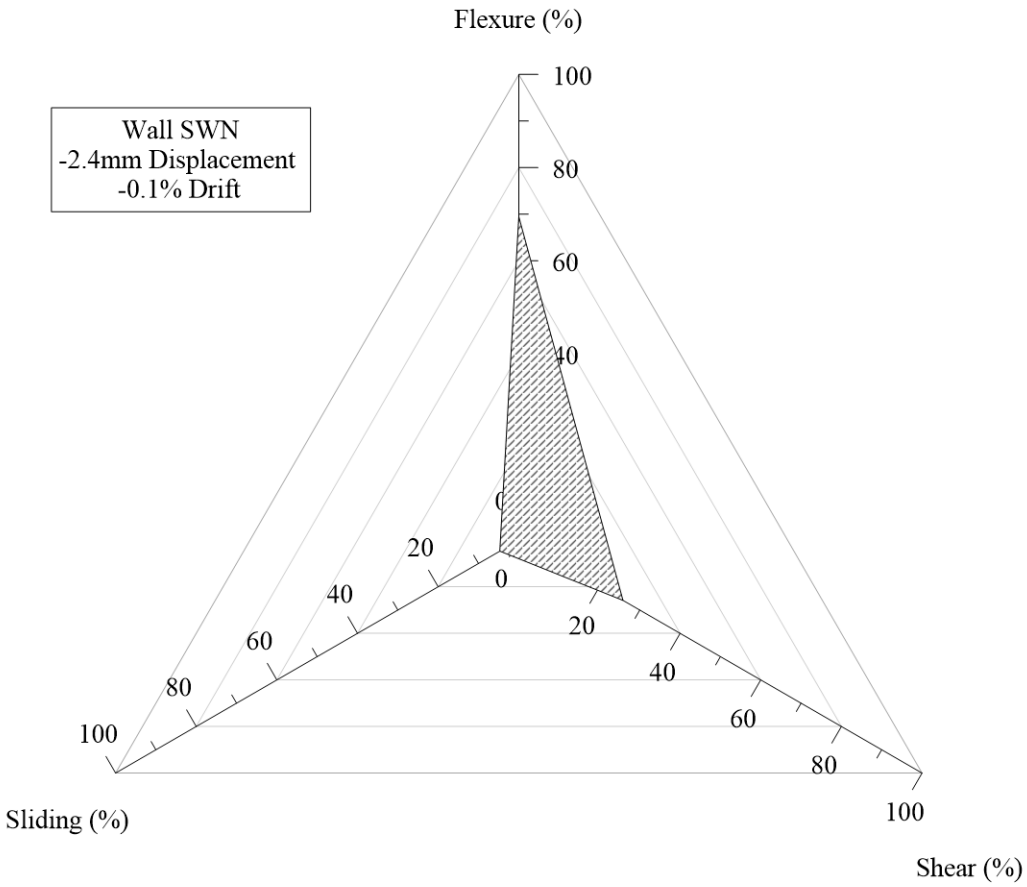

Figure K.38. Distribution of flexure, shear, and sliding of wall SWN at negative 2.4mm displacement.

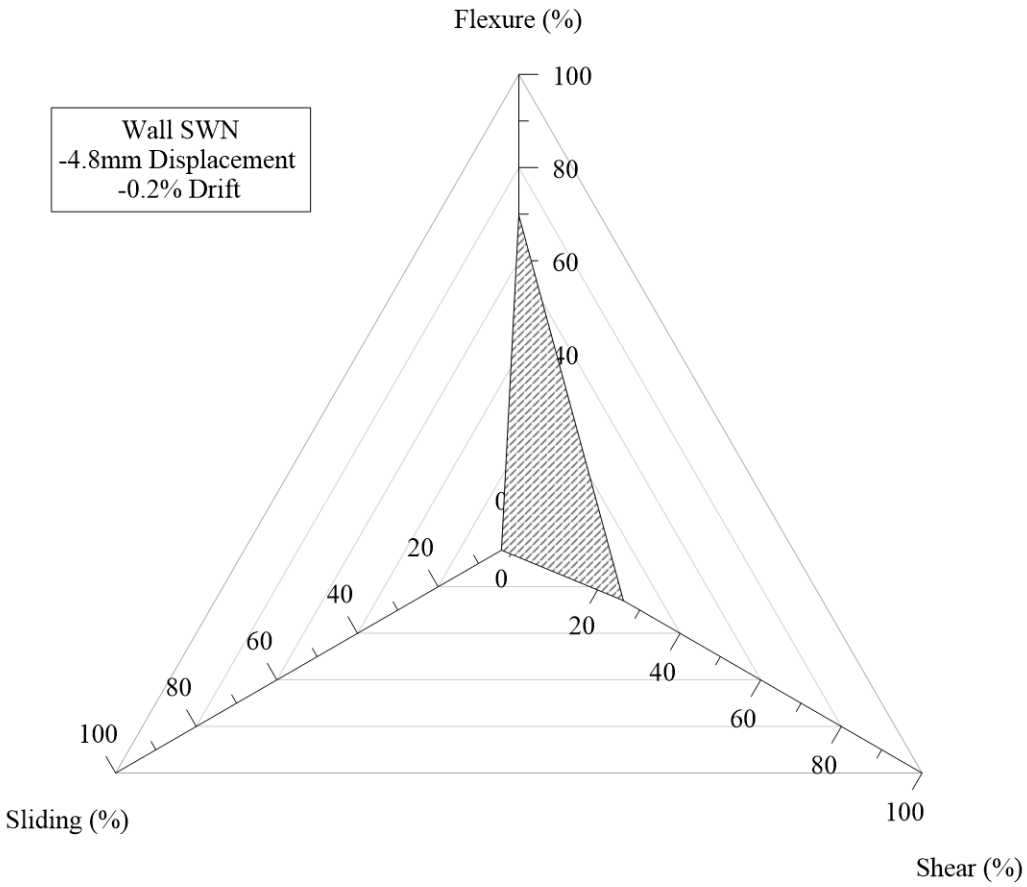

Figure K.39. Distribution of flexure, shear, and sliding of wall SWN at negative 4.8mm displacement.

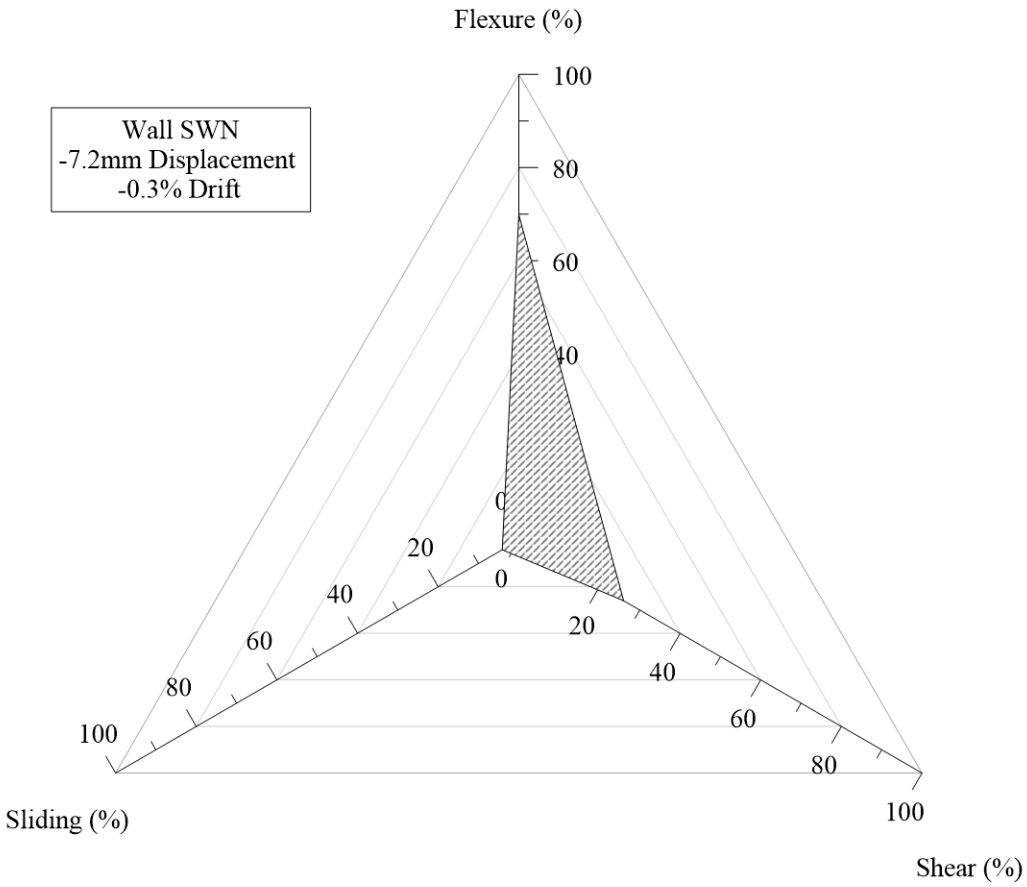

Figure K.40. Distribution of flexure, shear, and sliding of wall SWN at negative 7.2mm displacement.

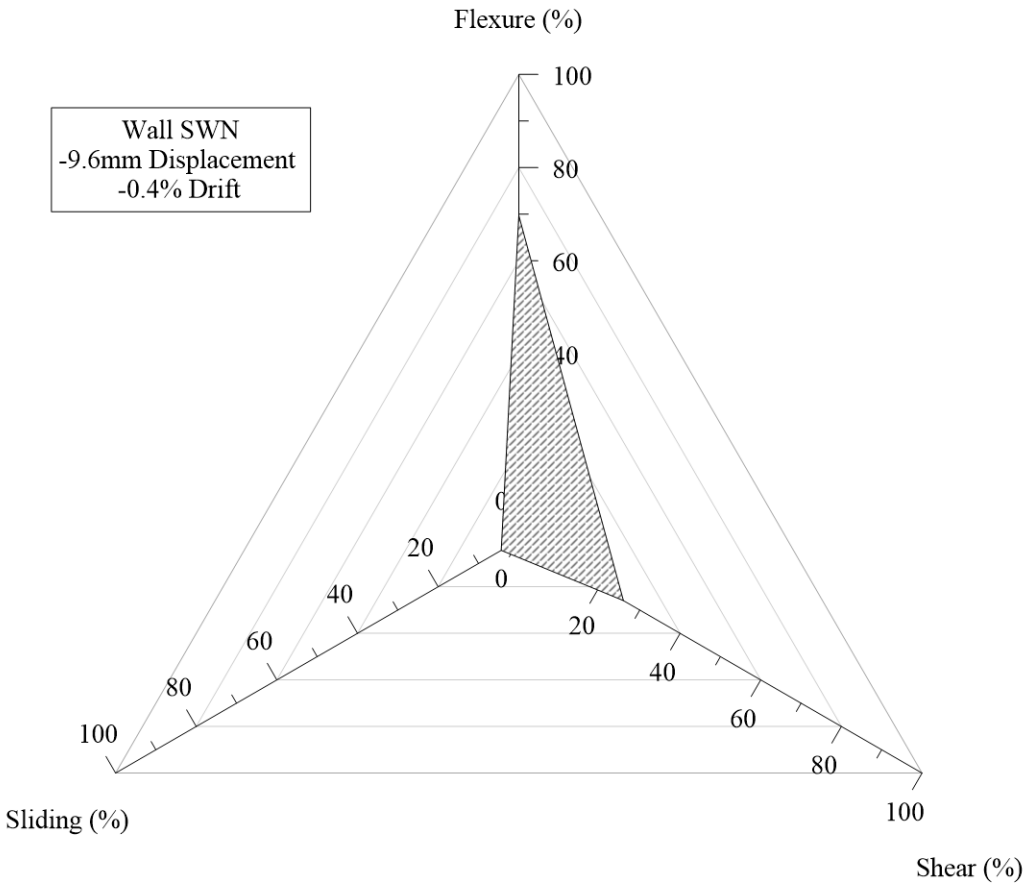

Figure K.41. Distribution of flexure, shear, and sliding of wall SWN at negative 9.6mm displacement.

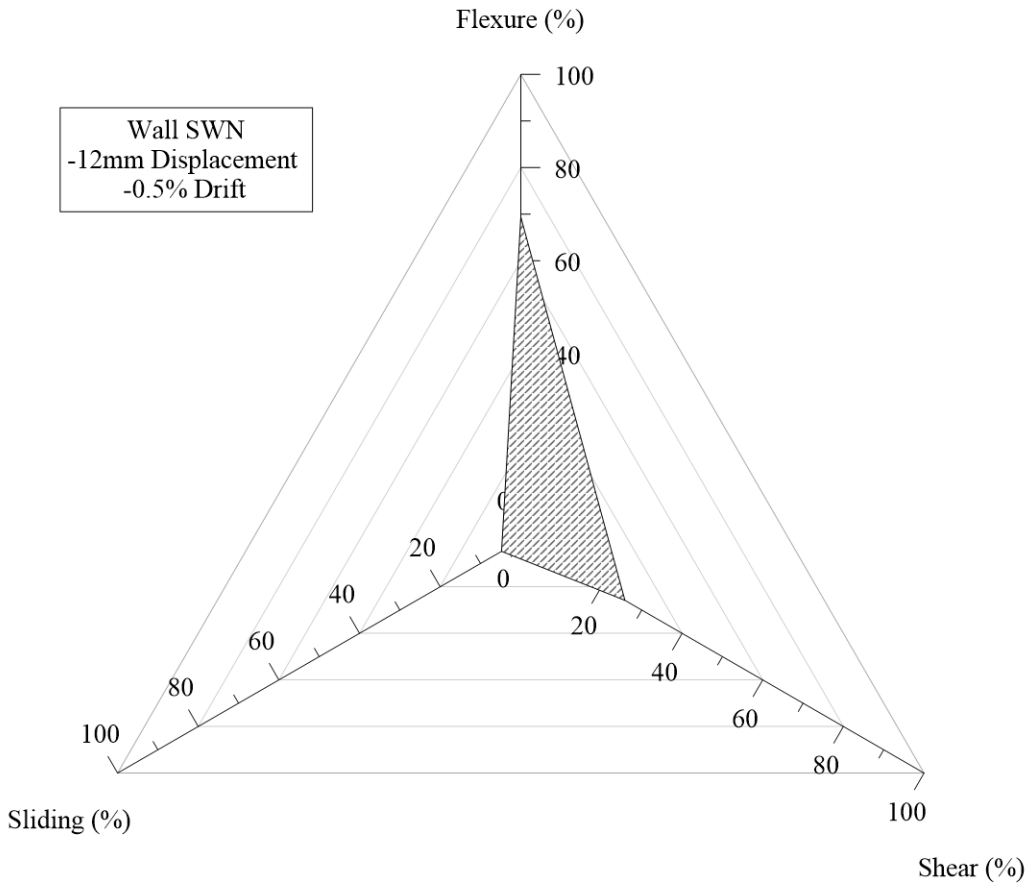

Figure K.42. Distribution of flexure, shear, and sliding of wall SWN at negative 12mm displacement.

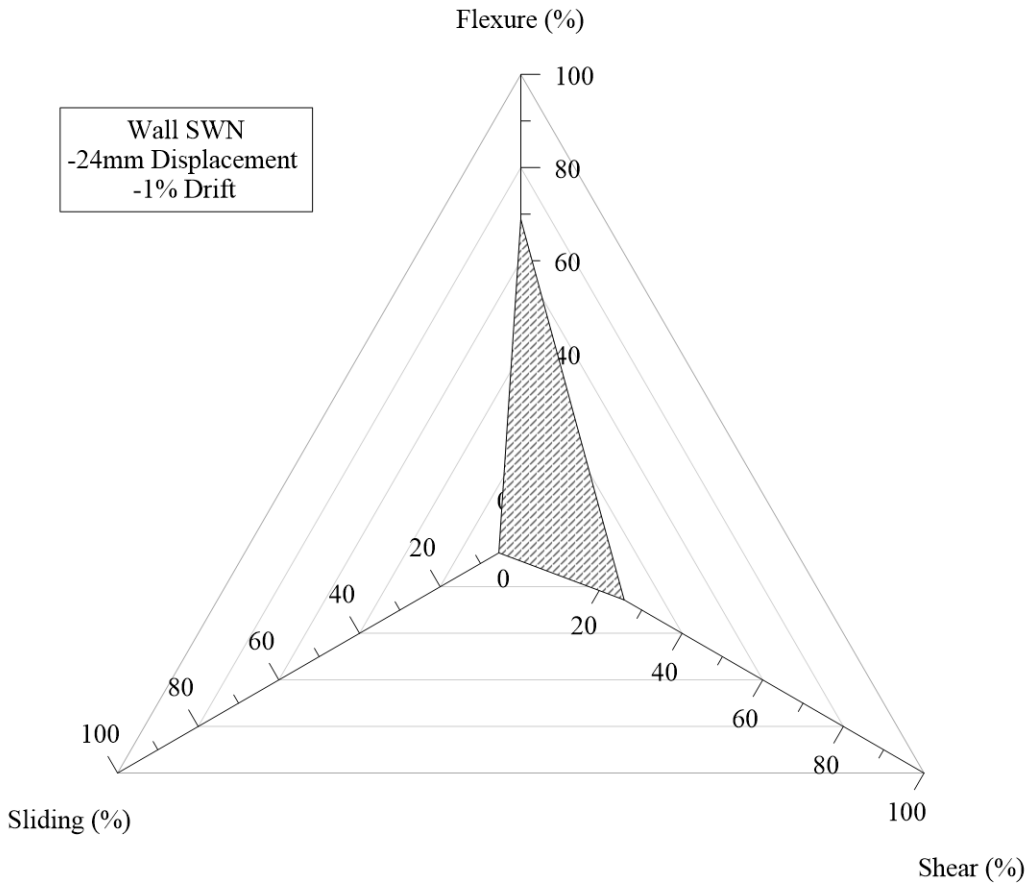

Figure K.43. Distribution of flexure, shear, and sliding of wall SWN at negative 24mm displacement.

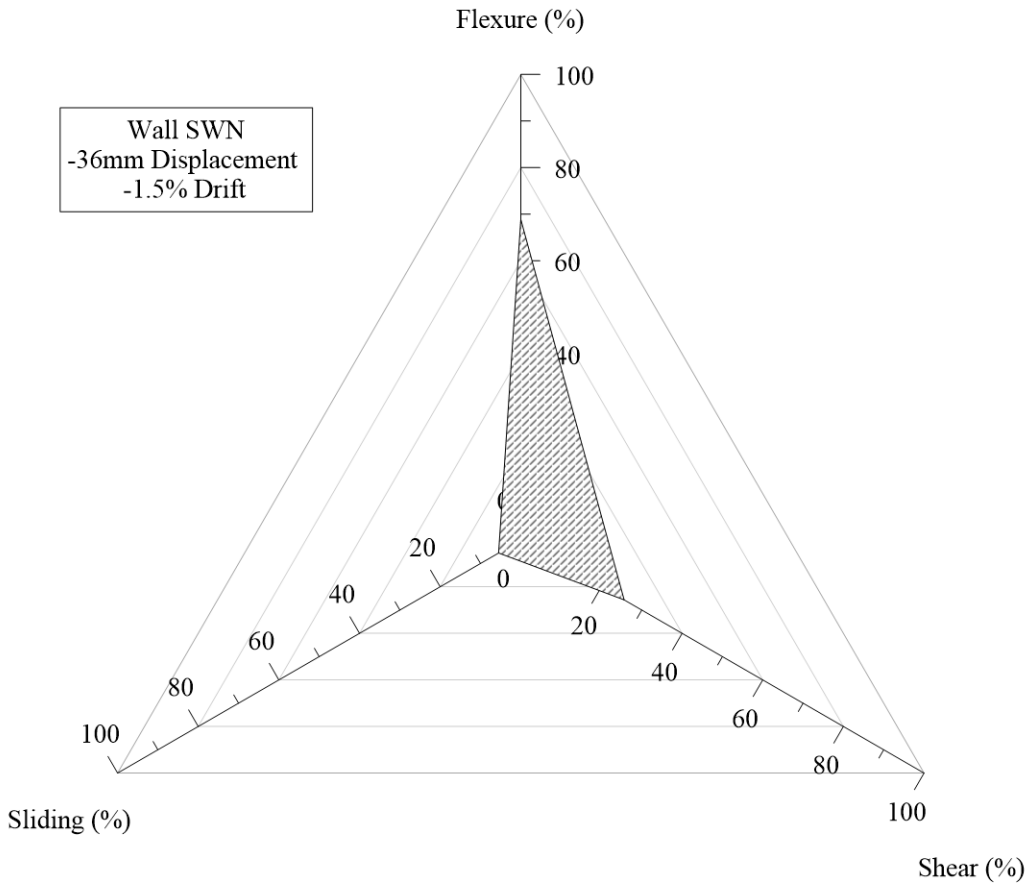

Figure K.44. Distribution of flexure, shear, and sliding of wall SWN at negative 36mm displacement.

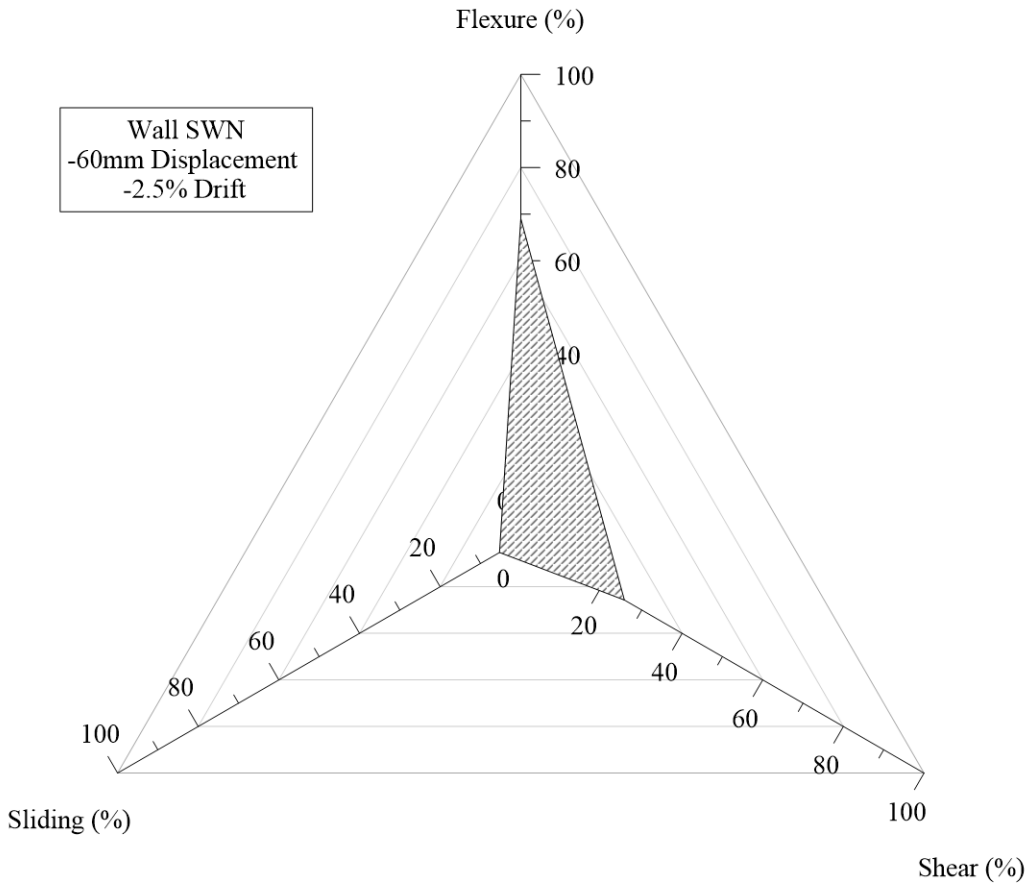

Figure K.45. Distribution of flexure, shear, and sliding of wall SWN at negative 60mm displacement.

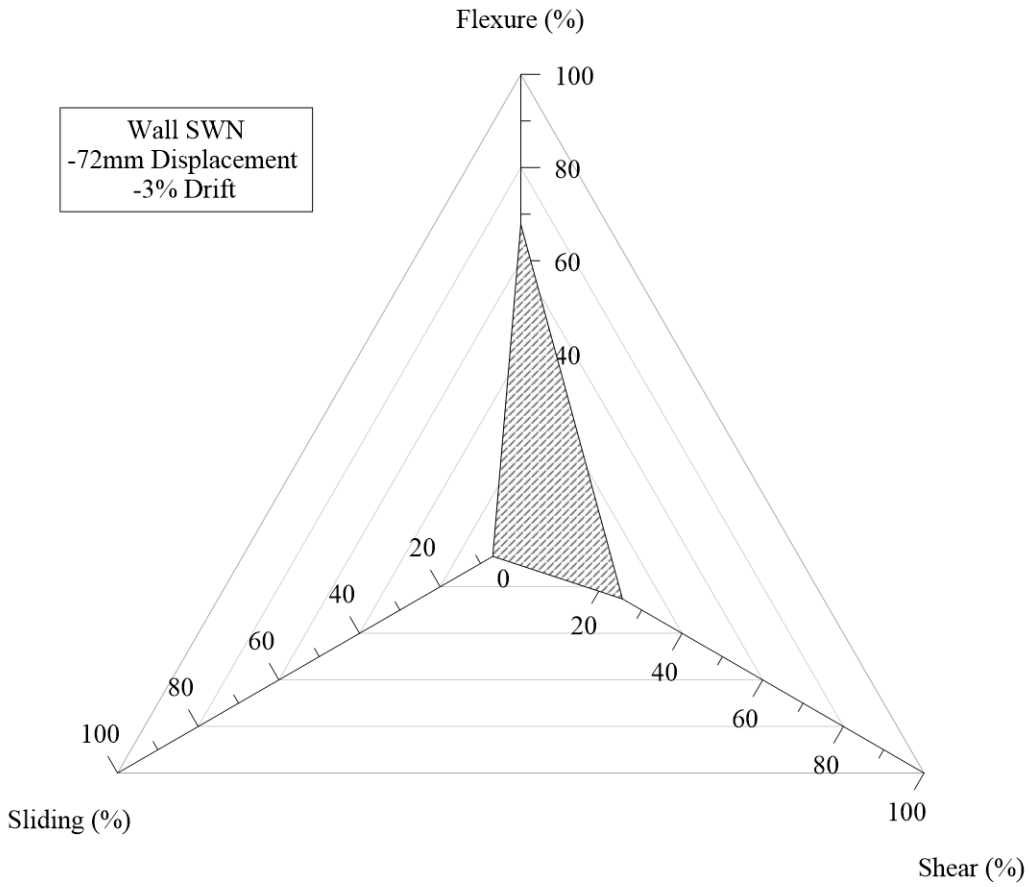

Figure K.46. Distribution of flexure, shear, and sliding of wall SWN at negative 72mm displacement.

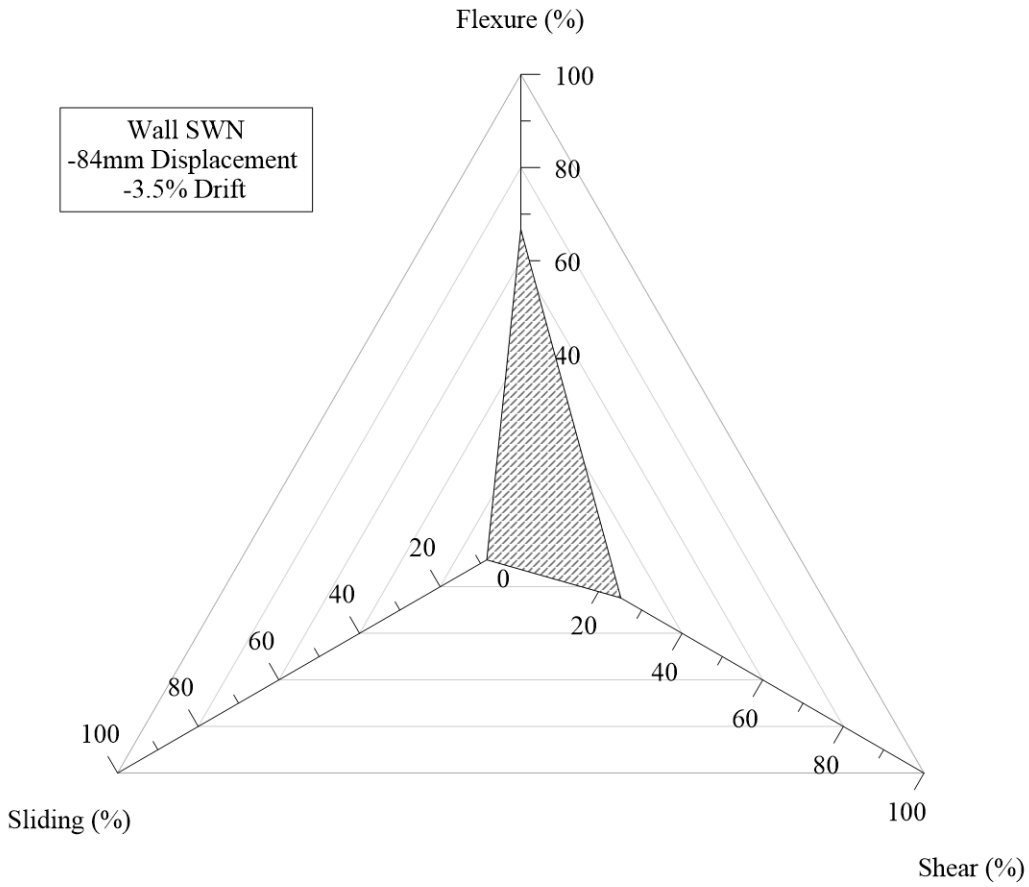

Figure K.47. Distribution of flexure, shear, and sliding of wall SWN at negative 84mm displacement.

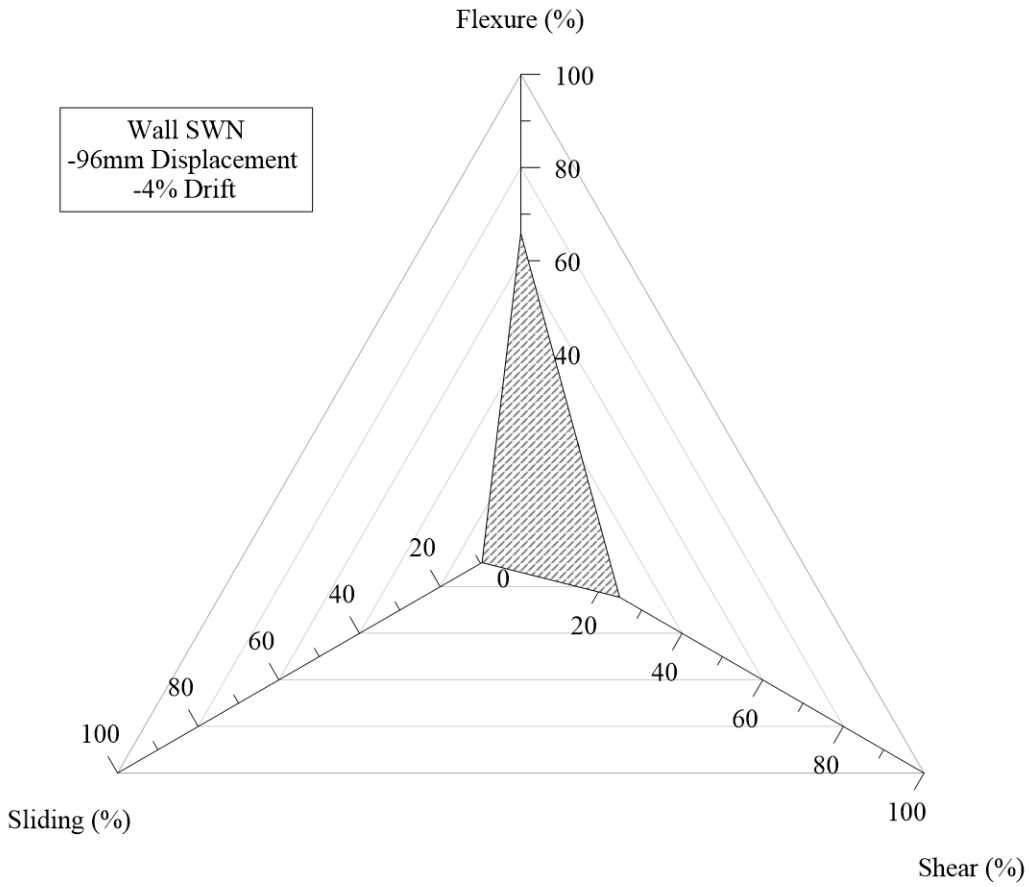

Figure K.48. Distribution of flexure, shear, and sliding of wall SWN at negative 96mm displacement.

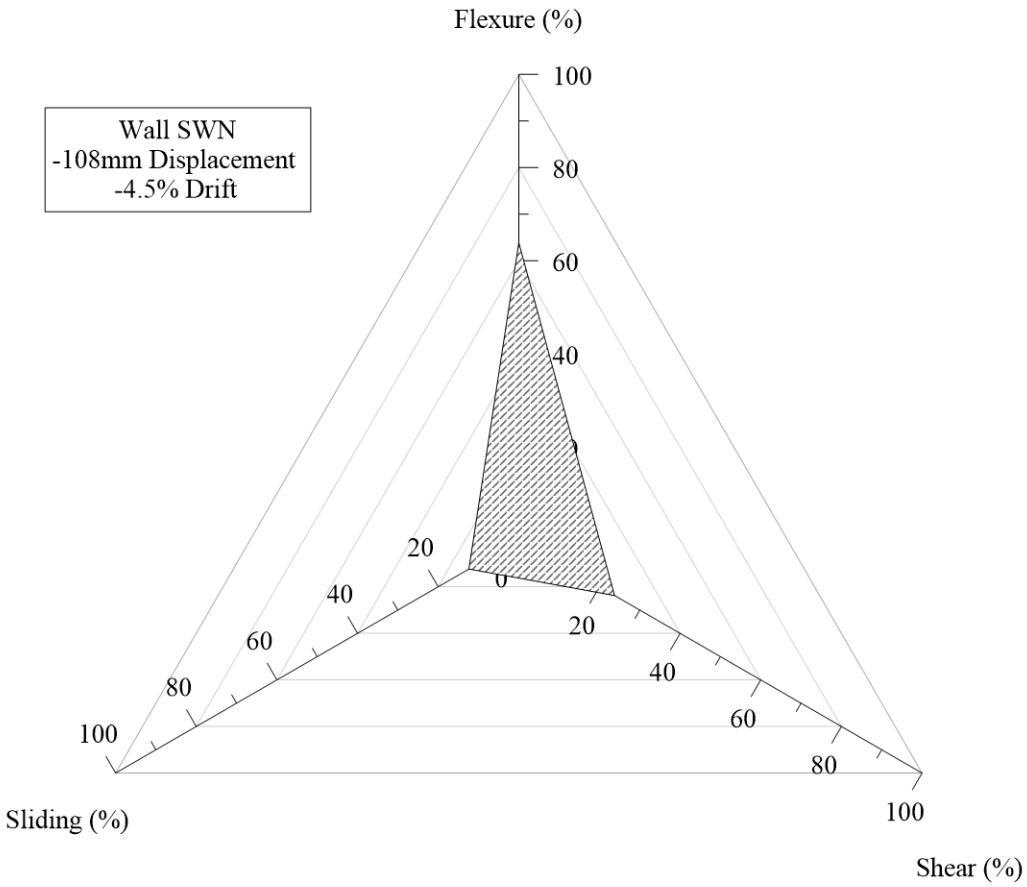

Figure K.49. Distribution of flexure, shear, and sliding of wall SWN at negative 108mm displacement.

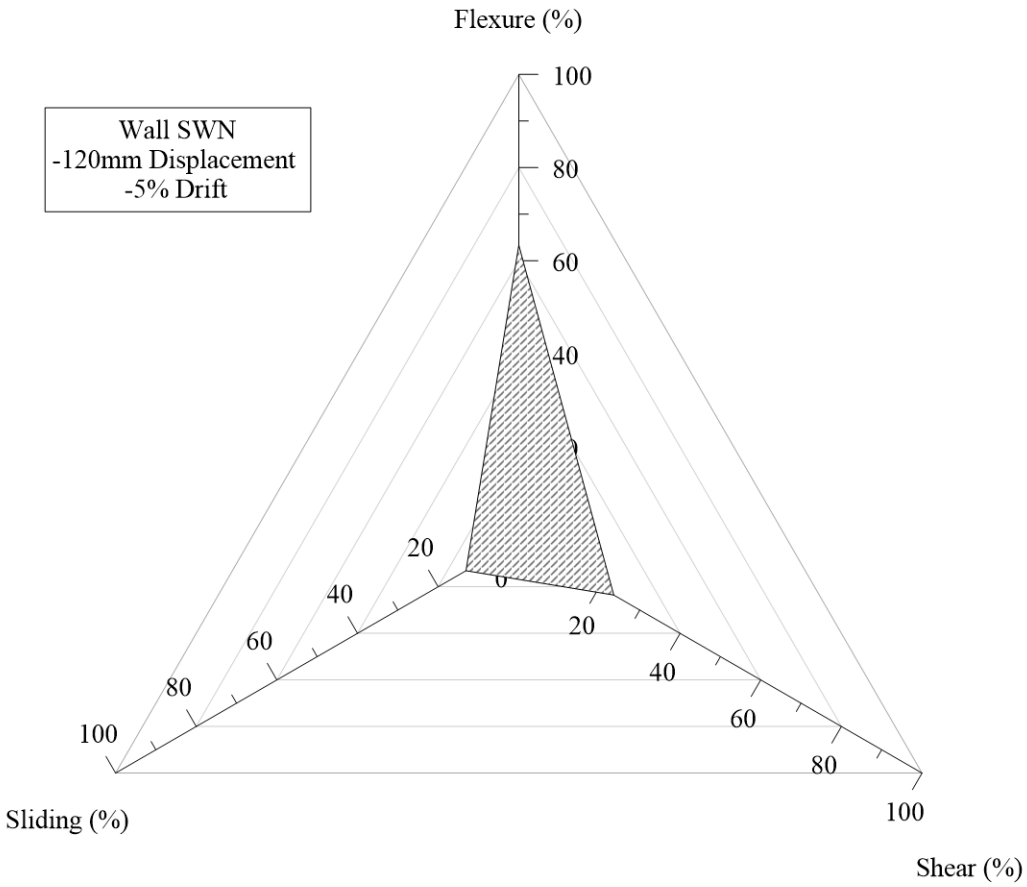

Figure K.50. Distribution of flexure, shear, and sliding of wall SWN at negative 120mm displacement.